1. Report No.	2. Government Accession No.	3. Recipient's Catalog No.
FHWA/TX-06/0-4184-1		

4. Title and Subtitle	5. Report Date
CHARACTERIZING THE EFFECTS OF ROUTINE OVERWEIGHT TRUCK TRAFFIC ON SH4/48	January 2006 Resubmitted: April 2006
	6. Performing Organization Code

7. Author(s)	8. Performing Organization Report No.
Emmanuel G. Fernando, Sonia Ramos, Jeongho Oh, John Ragsdale, Zhaoxia Xie, Robert Atkins and Henry Taylor	Report 0-4184-1

9. Performing Organization Name and Address	10. Work Unit No. (TRAIS)
Texas Transportation Institute The Texas A&M University System College Station, Texas 77843-3135	11. Contract or Grant No. Project 0-4184

12. Sponsoring Agency Name and Address	13. Type of Report and Period Covered
Texas Department of Transportation Research and Technology Implementation Office P. O. Box 5080 Austin, Texas 78763-5080	Technical Report: September 2000 – August 2003
	14. Sponsoring Agency Code

15. Supplementary Notes

Project performed in cooperation with the Texas Department of Transportation and the Federal Highway Administration.

Project Title: Characterize the Effects of Permitted Overweight Loads on SH4/48 at the Port of Brownsville

URL: http://tti.tamu.edu/documents/0-4184-1.pdf

16. Abstract

The 75th and 76th Texas Legislatures passed bills allowing trucks with gross vehicle weights (GVWs) of up to 125,000 lb to routinely use a route in south Texas along the Mexican border. This route proceeds from the border checkpoint at the terminus of US77 to the Port of Brownsville via US77, SH4, and SH48. The portion of the route along US77 is on a new concrete pavement and includes an elevated structure over half of its length. Most of the permitted truck route runs along SH4 and SH48 in Brownsville. Concerned about the effects of routine overweight truck traffic on its roadways, the Texas Department of Transportation sponsored a research project with the Texas Transportation Institute to characterize the effects of routine overweight truck traffic along SH4/48 and develop pavement design guidelines for roadways subjected to routine overweight trucks. This report documents research efforts and findings to characterize the effects of routine overweight truck loads on SH4/48 in Brownsville. The project offered the first opportunity to study the effects of routine overweight truck traffic on pavement performance. The characterization of these effects showed that accelerated pavement deterioration is expected due to the higher rate of accumulation of 18-kip equivalent single axle loads (ESALs), and the fact that routine overweight truck use was not considered in the original pavement design for SH4/48. The higher loading rate is a consequence of the additional overweight trucks that the route now serves, and the higher allowable axle loads on these trucks that produce more pavement damage per application relative to legal or non-permitted trucks. While the findings summarized herein were probably expected based on engineering principles and experience, this project provided evidences based on test data, which point to the conclusion that accelerated pavement deterioration is likely as a consequence of routine overweight truck use on SH4/48.

17. Key Words	18. Distribution Statement
Overweight Loads, Overweight Permits, Nondestructive Testing, Pavement Evaluation, Modulus Backcalculation, Dynamic Analysis, Dynamic Modulus Testing, Pavement Response Models, Pavement Damage Assessment, Fiber-Optic Sensors, Weigh-in-Motion Measurements	No restrictions. This document is available to the public through NTIS: National Technical Information Service Springfield, VA 22161 http://www.ntis.gov

19. Security Classif.(of this report)	20. Security Classif.(of this page)	21. No. of Pages	22. Price
Unclassified	Unclassified	386	

CHARACTERIZING THE EFFECTS OF ROUTINE OVERWEIGHT TRUCK TRAFFIC ON SH4/48

by

Emmanuel G. Fernando
Research Engineer
Texas Transportation Institute

Sonia Ramos
Former Graduate Research Assistant
Texas Transportation Institute

Jeongho Oh
Associate Transportation Researcher
Texas Transportation Institute

John Ragsdale
Research Associate
Texas Transportation Institute

Zhaoxia Xie
Former Graduate Research Assistant, Department of Electrical and Computer Engineering
Texas A&M University

Robert Atkins
Technical Laboratory Coordinator, Department of Electrical and Computer Engineering
Texas A&M University

Henry Taylor
Professor, Department of Electrical and Computer Engineering
Texas A&M University

Report 0-4184-1
Project 0-4184
Project Title: Characterize the Effects of Permitted Overweight Loads on SH4/48 at the Port of Brownsville

Performed in cooperation with the
Texas Department of Transportation
and the
Federal Highway Administration

January 2006
Resubmittted: April 2006

TEXAS TRANSPORTATION INSTITUTE
The Texas A&M University System
College Station, Texas 77843-3135

DISCLAIMER

The contents of this report reflect the views of the authors, who are responsible for the facts and the accuracy of the data presented. The contents do not necessarily reflect the official views or policies of the Texas Department of Transportation (TxDOT) or the Federal Highway Administration. This report does not constitute a standard, specification, or regulation, nor is it intended for construction, bidding, or permit purposes. The United States Government and the State of Texas do not endorse products or manufacturers. Trade or manufacturers' names appear herein solely because they are considered essential to the object of this report. The engineer in charge of the project was Dr. Emmanuel G. Fernando, P.E. # 69614.

ACKNOWLEDGMENTS

The work reported herein was conducted as part of a research project sponsored by the Texas Department of Transportation and the Federal Highway Administration. The authors gratefully acknowledge the steadfast support and guidance of the project director, Mr. Joe Leidy, of the Materials and Pavements Section of TxDOT. Mr. Leidy ran TxDOT's ground penetrating radar equipment on SH4/48 as part of efforts to characterize the pavement sections along the route. In addition, the contributions of the following individuals are noted and sincerely appreciated:

1. Mr. Luis Carlos Peralez of the Pharr District provided invaluable assistance to the data collection activities conducted along SH4/48. Mr. Peralez provided staff and equipment for collection of falling weight deflectometer, multi-depth deflectometer, and profile data at different times during the project; pavement instrumentation at the weigh-in-motion site along SH48; and collection of material samples for laboratory testing.
2. The pavement management staff of the Pharr District, in particular, Mr. Rene Castro, collected FWD data, profile data, and asphalt concrete cores along SH4/48.
3. Mr. Niño Gutierrez and Ms. Jo Saban of the Brownsville Navigation District provided researchers access to the port for monitoring permitted trucks and static axle weight data on these trucks.
4. Mr. Richard Peters, Mr. Jeff Reding, and Ms. Carolyn Markert provided weigh-in-motion data that were used to characterize the existing truck traffic along SH4/48.
5. Dr. Robert Lytton provided expert advice in the analyses of the data presented in this report. The guidance he gave was invaluable to the comprehensive characterization of the effects of routine overweight truck traffic on SH4/48.
6. Mr. Lee Gustavus and Mr. Gerry Harrison provided technical expertise on pavement instrumentation, sample preparation, and laboratory and field testing.
7. Mr. Tom Freeman collected visual survey data on the FWD stations established along SH4/48 that researchers monitored during this study.
8. Dr. Wenting Liu wrote the data acquisition program for MDD testing and assisted in the field data collection activities.

TABLE OF CONTENTS

CHAPTER Page

APPENDIX Page

LIST OF FIGURES

Figure Page

Figure Page

Figure Page

Figure Page

Figure Page

Figure Page

Figure Page

Figure Page

Figure Page

Figure Page

Figure Page

Figure Page

Figure Page

Figure Page

Figure Page

Figure Page

Figure Page

Figure Page

Figure Page

Figure Page

LIST OF TABLES

Table Page

Table Page

CHAPTER I. INTRODUCTION

Many highway facilities experience deterioration due to high traffic volumes and a service life that has been extended beyond facility design life. As aging road network conditions deteriorate, there is a need to increase investments and rehabilitation treatments in order to restore and maintain road conditions at acceptable levels. The 75th and 76th Texas Legislatures passed bills allowing trucks of gross vehicle weights (GVW) up to 125,000 lb to routinely use a route in south Texas, along the Mexican border. The Texas Department of Transportation (TxDOT) is concerned about the impact of overweight truck traffic on its highways. There is a need to establish the potential impact of overweight truck traffic on Texas roads and evaluate structural requirements for pavements that carry axle loads above legal limits on a routine basis.

In this project researchers investigated the effects of overweight truck traffic on a permitted truck route in the city of Brownsville. This route proceeds from the border checkpoint at the terminus of US77 to the Port of Brownsville via US77, SH4 and SH48. The portion of the route along US77 is on a new concrete pavement and includes an elevated structure over half of its length. Most of the permitted truck route runs along SH4 and SH48. This research focused on studying the behaviour of the asphalt pavement supporting routine overweight truck traffic on SH4/48. According to the Brownsville Navigation District, 95 percent of the truck traffic originates from the Port of Brownsville where the route starts at the FM511 bridge, and runs along SH48 until its intersection with Boca Chica Blvd. From there, truckers proceed along SH4 up to the US77 intersection, where they turn left to go to Mexico. Figure 1.1 gives an overview of the permitted truck route.

The payloads carried by permitted trucks are mostly coiled metal sheets, oil, and powder mineral (fluorite), which are transported from the Port of Brownsville to Mexico and vice versa. Figure 1.2 illustrates the types of payloads transported along the permitted truck route. The route was established in response to the need expressed by truckers to haul cargo at their trucks' operating capacities to improve operational efficiency. This need meant hauling in excess of legal load limits, thus requiring permits to be issued. Table 1.1 presents the weight limits used along the route.

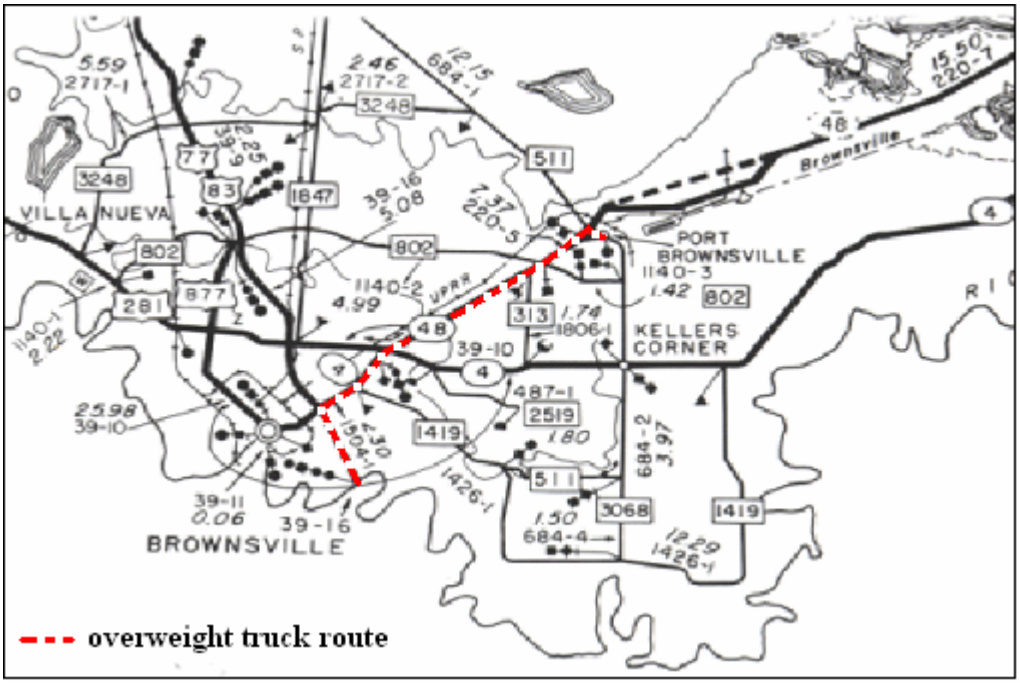

Figure 1.1. Overweight Truck Route along SH4/48.

Figure 1.2. Types of Loads Carried by Permitted Trucks.

Table 1.1. Weight Limits Used for Permitting Trucks along SH4/48.

Weight Criterion	Weight Limit (kips)
Single axle	25
Tandem axle	46
Tridem axle	60
4-axle group	70
5-axle group	81.4
Gross vehicle weight	125

The permit fee is US $30 each way. From the time TxDOT first issued the permits in March 1998 to the end of 2002, about US $4.5 million were collected from permit sales, based on figures provided by the Brownsville Navigation District. The navigation district retains 15 percent of the funds to cover administrative costs, and the remainder goes to the TxDOT Pharr District to pay for route maintenance. On average, about 2700 permitted overweight trucks use the route per month. Considering that the route was not designed to sustain routine overweight truck traffic, the potential for accelerated pavement deterioration exists. Since it is likely that TxDOT will receive requests for similar permitted routes in the future, it becomes prudent to study the effects of routine overweight loads on SH4/48 and to develop guidelines for evaluating and/or designing routine overweight truck routes.

OBJECTIVES

The primary objectives of this research are to:

- characterize the effects of routine overweight truck loads on the performance of SH4/48, and
- evaluate pavement design requirements for dedicated overweight truck routes.

These objectives were accomplished by carrying out nondestructive pavement testing, pavement instrumentation, laboratory materials testing, evaluation of material properties from field and laboratory test data, and modeling of pavement response and performance. Researchers developed a methodology for evaluating the suitability of using an existing route

for routine overweight truck use. This methodology includes procedures to estimate overlay thickness requirements for upgrading a route to accommodate routine overweight truck traffic. A documentation of the methodology developed from this project is presented in two companion reports by Fernando and Oh (2004) and by Fernando and Liu (2004). The present report documents research efforts and findings to characterize the effects of routine overweight truck loads on SH4/48 in Brownsville. This project offered the first opportunity to study the effects of routine overweight truck traffic on pavement performance. In the researchers' opinion, the data collected will be useful in establishing and developing ways to achieve the best accommodation of increased truck use on Texas highways.

PROBLEM STATEMENT

The nature of this complex problem can be stated as follows:

- The initial design for this route was based on conventional truck traffic conforming to legal load limits. Routine use of SH4/48 by overweight trucks began in March 1998.
- Routine overweight truck traffic increased in severity due to the increased flow of trade from the Port of Brownsville to Mexico. The deterioration on the route is mainly along the southbound lanes, K6 and K7.
- The impact of overweight truck traffic is a concern because the service life of highways under these conditions is unknown.

SCOPE OF RESEARCH REPORT

The research conducted in this TxDOT project is documented in nine chapters. Chapter I is the introductory chapter that gives the impetus for this study. Chapter II describes the concepts involved in the nondestructive test methods used to evaluate the effects of routine overweight truck traffic on SH4/48. Chapter III details the field data and laboratory testing methodology. It also describes how the SH4/48 route was segmented into different sections on the K6 and K7 lanes for the purpose of field data collection. The chapter also identifies the locations (FWD stations) where cores were taken for laboratory testing. These FWD stations are referred to as "core stations" in this report. Chapter IV summarizes the results of the analyses of the field data collected during the project. The field data taken with the falling weight deflectometer (FWD) and ground penetrating radar (GPR) are analyzed in

this chapter in order to predict pavement layer thickness profiles and static layer moduli values. Chapter V reports on the analysis of FWD data to characterize the dynamic modulus and the creep compliance properties of the asphalt concrete layer using dynamic analysis. The dynamic moduli backcalculated by system identification are compared to the backcalculated moduli from the static analysis. The dynamic analysis of full-time FWD data was conducted using the Dynamic Backcalculation by System Identification (DBSID) program developed in a research project with the Florida Department of Transportation (Fernando and Liu, 2002). Static backcalculations were performed using MODULUS.

Chapter VI presents the results from laboratory tests conducted on field cores taken from SH4/48. Researchers conducted frequency sweep tests at different temperatures to characterize the time- and temperature-dependency of the asphalt concrete modulus. The dynamic moduli of cores from laboratory tests are also compared to the backcalculated asphalt concrete moduli based on FWD peak deflections.

Chapter VII presents the temperature corrections of backcalculated moduli beginning with the pavement temperature predictions. Researchers examined the corrected moduli as well as the modulus-temperature relationships determined from the test data as part of assessing pavement damage along the route. For this analysis, FWD stations on the K6 and K7 lanes were grouped, taking into consideration the modulus values and the stations' proximity to each other. The temperature corrections of backcalculated moduli were done using the Chen, TxDOT, and Witczak-Fonseca equations that are implemented in TxDOT's Modulus Temperature Correction Program (Fernando, Liu and Ryu, 2001).

Chapter VIII provides an evaluation of damage potential due to overweight truck loading through comparisons of measured multi-depth deflectometer (MDD) displacements under overweight and legal truck loads. In addition, pavement condition data collected along the K6 and K7 lanes of SH4/48 provided evidence of pavement damage from truck traffic using the route. Chapter VIII also presents an evaluation conducted by researchers that showed a strong association between the backcalculated moduli on the K6 and K7 lanes and the cumulative 18-kip equivalent single axle loads each lane has sustained.

Finally, Chapter IX summarizes the findings from this project and provides recommendations for future studies. The appendices present results from analyses of test data and document the instrumentation work done at the WIM site along SH48, the evaluation of

alternative models for predicting pavement response, and the experiments conducted to investigate the use of fiber-optic sensors for weigh-in-motion measurement.

CHAPTER II. FIELD TESTING PROCEDURES AND PAVEMENT ANALYSIS TOOLS

This chapter presents field test methods and analysis procedures used to characterize the effects of permitted overweight loads on SH4/48. For this purpose, researchers conducted tests with TxDOT's ground penetrating radar and falling weight deflectometer to characterize layer thickness and moduli variations along the permitted route. The analyses of data from these measurements were accomplished using COLORMAP, static and dynamic backcalculation procedures, and the Modulus Temperature Correction Program (MTCP). In addition, researchers instrumented two locations along the route with multi-depth deflectometers to estimate damage potential due to overweight truck traffic through comparisons of measured pavement deflections under permitted and non-permitted trucks.

GPR APPLICATIONS

Applying GPR techniques for nondestructive testing on highways and bridge decks has become more common in recent years. Recent applications have demonstrated GPR to be an accurate and practical tool for nondestructive evaluation and inspection of highway structures. Different types of radar may be used for different applications on highway pavements. Depending on the way they operate, radar falls into two categories: air-coupled and ground-coupled.

Air-coupled GPR (Figure 2.1) operates with the antenna mounted at a specific height perpendicular to the pavement surface. This type of GPR is ideal for highway speed data collection since there is no contact between the pavement surface and the antenna (Nguyen, Lau and Scullion, 1995). Ground-coupled GPR operates with its planar antennas in close contact with the pavement. This contact allows a better horizontal resolution in the direction of the survey motion. This antenna is particularly suited to investigating defects in concrete pavements and bridge decks. The drawback is its data acquisition speed, which is limited to less than 6 mph.

Air-coupled radar systems work at the central frequency of approximately 1 GHz, while most ground-coupled radar systems work at lower frequencies, typically from 20 to 500 MHz (Scullion et al., 1997). Figure 2.2 illustrates two ground-coupled radar antennas used in this project. The smaller unit on top of the tray at the back of the cart is a 1.5 GHz antenna,

Figure 2.1. GPR Van with Air-Coupled, Front-Mounted Antenna.

Figure 2.2. GPR Van with Ground-Coupled Antennas.

while the other unit shown on the cart is a 200 MHz ground-coupled system. The lower the frequency is, the greater is its penetration depth. However, lower-frequency antennas offer less in near-surface resolution. For instance, under similar soil conditions, 100 MHz antennas may provide subsurface information to depths of 50 ft. However, these antennas will not be able to identify the presence of thin surface layers. On the other hand, a high frequency ground-coupled system may only penetrate to a depth of 3 ft, but it can identify thin layers close to the surface. The Texas Transportation Institute's air-coupled GPR unit operates at highway speeds (60 mph) and transmits and receives 50 pulses per second. It can effectively penetrate to a depth of 2 ft.

For the practical implementation of a GPR system, automated signal processing is needed so that the mass of waveforms collected in a GPR survey can be transformed into information meaningful to highway engineers. In the past, TTI researchers used a signal processing system named DACQ to analyze GPR data (Scullion, Lau and Chen, 1994). Its main feature is an automated peak tracking system, in which the user identifies significant peaks within the GPR trace. The software then automatically traces those peaks throughout the entire file. For each peak, the amplitudes and arrival times of reflections were determined from the GPR data and used to compute the layer dielectrics and thicknesses. Other advanced features of DACQ are a correction procedure for antenna bounce and several signal clean-up routines, which are applied prior to processing. However, there were several drawbacks with DACQ such as slow data processing if long lengths of highway were to be processed. Additionally, it was difficult to identify section breaks and the peak tracking system was difficult to use on several projects with badly distressed pavements.

Because of these limitations, a new processing package was subsequently developed to match TxDOT's needs more closely. These needs are the capability of rapidly evaluating long sections of highway, defining section changes, estimating layer thickness, and locating subsurface problem areas. COLORMAP is the software package that succeeded DACQ (Scullion, Chen and Lau, 1995). It was developed to provide a simple program that non-GPR experts can easily understand and use to interpret GPR data for pavement evaluation. In order to evaluate massive amounts of data in a timely fashion, COLORMAP employs several innovative data processing techniques. It relies on a color graphics display of GPR data to

identify breaks and surface problems, and the manual tracking of layer interfaces in the layer computation routine.

FALLING WEIGHT DEFLECTOMETER

A nondestructive test is one from which the necessary information can be obtained to define physical properties of a sample without destroying it. In pavement evaluation, this involves a large mechanical device to duplicate vehicle loads without breaking up the pavement. By measuring the pavement response induced by loads, the structural integrity or stress-strain properties of the pavement structure can be determined (Magnuson, 1993).

The FWD (Figure 2.3) is an impulse device used in the nondestructive testing of pavements because it reasonably simulates the shape and temporal nature of a moving wheel loading (Magnuson, 1993). In addition, during FWD tests, the pavement's stress and strain conditions are similar to the conditions under a heavy vehicle load (Lytton et al., 1990). The major advantages of FWD testing are that:

- The impulse dropweight force on the pavement simulates traffic loads at highway speed.
- It is nondestructive.
- Pavement layer materials remain undisturbed.
- Asphalt concrete (AC) creep compliance data can be computed from FWD full-time history data and dynamic analysis. Pavement cracking and rutting can then be predicted from the creep compliance properties.

FWD is used in pavement evaluations to estimate layer moduli for predicting remaining life. Most backcalculation procedures currently implemented predict the layer moduli from the peak load and the peak deflections measured by geophones. In this analysis, it is assumed that the FWD load is applied statically to the pavement, which is represented as an elastic layered system with linear or nonlinear (stress-dependent) material properties. These properties are backcalculated by minimizing the sum of the absolute or the square of the errors between the predicted and the measured peak deflections at the geophone locations.

Figure 2.3. Falling Weight Deflectometer.

The FWD works by applying an impulse load to the pavement, which generates body waves and surface waves (Lytton, 1989). These waves travel at finite velocities and are recorded at different times by the geophones. The time lag of the response of the geophones is determined by transforming the load and the deflection histories from the time domain to the frequency domain by using the fast Fourier transform (FFT) method. Then, the FFT of the deflection history is divided by the FFT of the load history in order to obtain the pavement system transfer function. The magnitude of the deflection per unit force and the phase angle are then determined, frequency by frequency.

The layered elastic backcalculation program MODULUS (Michalak and Scullion, 1995) was used to analyze the FWD deflection data. Specifically, researchers used MODULUS to backcalculate layer moduli at different locations along the permitted overweight truck route from the FWD data.

DYNAMIC ANALYSIS OF FWD DATA FOR PAVEMENT EVALUATION

Lytton (1989) explained that there is more information in the FWD data than load and displacement amplitudes and showed how other properties may be backcalculated using the load and displacement histories from the FWD. These properties include the creep compliance coefficients that may be determined from the analysis of the FWD load and deflection time histories. These coefficients govern the time-dependency of the AC mix according to the following power law model:

$$D(t) = D_o + D_1 t^m \qquad (2.1)$$

where,

$D(t)$ = creep compliance at loading time t, and

D_o, D_1 and m = coefficients of the power law model given by Eq. (2.1).

The slope m of the log creep compliance vs. log time curve is directly related to the material damping as characterized by the phase angle.

There are several computer programs used to analyze the full-time history data. These programs predict the transfer function or the FWD displacement history for each sensor. Among them are PUNCH (Kausel and Peek, 1982), UTFWIBM (Roesset, 1987), SCALPOT (Magnuson and Lytton, 1997) and FWD-DYN (Foinquinos, Roesset and Stokoe, 1989). The first three methods predict the tranfer function and the fourth, FWD-DYN, predicts the displacement history for a given sensor and pavement.

The FWD-DYN predicts the displacement history for each sensor, given the material properties and thickness of each pavement layer. In this program, the FWD load is first decomposed into its frequency components using FFT. Then, the transfer function, which defines the response of the pavement system to a steady-state unit load, is evaluated. Finally, the transfer function is multiplied by the FFT of the load to determine the Fourier transform of the displacement time history. FWD-DYN performs an inverse FFT on this Fourier transform to determine the time history of the displacement for each FWD sensor. It is significant to point out that the procedure assumes a linear system in view of the use of superposition to predict pavement response to the impulse load (Fernando and Liu, 2002).

The computer program DBSID determines the material properties using FWD full-time load and displacement histories. DBSID was the result of adding a system identification

routine to the FWD-DYN program. This work was conducted by Fernando and Liu (2002) as part of a research project sponsored by the Florida Department of Transportation. In the program, the pavement structure is limited to three layers of pavement, with the first layer (AC) characterized as a viscoelastic material following the power law creep compliance relationship of Eq. (2.1). The other two unbound layers are modeled as damped elastic solids characterized by Young's modulus and the damping coefficient. To backcalculate the creep compliance parameters of Eq. (2.1), the program uses the following relationships between the complex compliance and complex modulus (Lytton, 1989):

$$D'(\omega) = D_0 + \frac{\Gamma(1+m)}{\omega^m}\cos\left(\frac{\pi m}{2}\right) \quad (2.2)$$

$$D''(\omega) = \frac{\Gamma(1+m)}{\omega^m}\sin\left(\frac{\pi m}{2}\right) \quad (2.3)$$

$$E'(\omega) = \frac{D'(\omega)}{D'(\omega)^2 + D''(\omega)^2} \quad (2.4)$$

$$E''(\omega) = \frac{D''(\omega)}{D'(\omega)^2 + D''(\omega)^2} \quad (2.5)$$

$$\zeta(\omega) = \frac{E''(\omega)}{2E'(\omega)} \quad (2.6)$$

where,

$D'(\omega)$ = real part of the complex compliance,
$D''(\omega)$ = imaginary part of the complex compliance,
$E'(\omega)$ = real part of the complex modulus,
$E''(\omega)$ = imaginary part of the complex modulus,
$\zeta(\omega)$ = damping ratio,
$\Gamma(1+m)$ = gamma function with parameter $(1+m)$, and
ω = loading frequency, radians/sec.

TEMPERATURE CORRECTION OF BACKCALCULATED AC MODULUS

The use of surface deflection measurements to evaluate pavements has steadily increased in the majority of highway agencies since the American Association of State Highway Officials (AASHO) road test was conducted. Deflection testing is used to evaluate a variety of pavement characteristics, including axle or vehicle load capacity, structural life and uniformity. Deflection results are dependent upon seasonal variations that are affected by the underlying aggregate base course and subgrade. It is more significant in asphalt pavements, which are dependent on the temperature of the asphalt (Lukanen, Stubstad and Briggs, 1998). In fact, those factors that influence deflections are loading, environment and pavement conditions. The environmental conditions related to seasonal variations are the temperature and moisture distributions within and around the pavement structures. The importance of these major factors is that they change the strength of the pavement materials and their resistance to traffic-induced stresses.

For pavement applications, the asphalt concrete moduli backcalculated from FWD data must be corrected to reference or standard conditions of temperature and loading frequency. Before the temperature correction may be made, it is first necessary to determine the pavement temperature one is correcting from. This temperature is referred to herein as the base temperature, and it corresponds to the pavement temperature when the FWD data were collected. For this purpose, pavement temperatures may be measured directly with a temperature probe, or predicted from measured air and surface temperatures. In this regard, Lukanen, Stubstad and Briggs (1998) developed a set of equations for predicting pavement temperatures. These equations, referred to in the literature as BELLS2 and BELLS3, were developed using pavement temperature data from 41 Seasonal Monitoring Program (SMP) sites in North America.

BELLS2 is the equation used for the FWD testing protocol employed in the Long-Term Pavement Performance (LTPP) program, while BELLS3 is used for routine testing. The latter was developed to account for the effects of shading on the infrared temperatures measured at the SMP sites. Both equations require use of the infrared (IR) surface temperature at the time of the FWD measurements and the average of the previous day's minimum and maximum air temperatures in the area of the project surveyed. The BELLS2 and BELLS3 equations have the following form and are different only in the coefficients β_i:

$$T_d = \beta_o + \beta_1 IR + [\log_{10}(d) - 1.25][\beta_2 IR + \beta_3 T_{(1\text{-day})} + \beta_4 \sin(hr_{18} - 15.5)]$$
$$+ \beta_3 IR \sin(hr_{18} - 13.5) \quad (2.7)$$

where,

T_d = pavement temperature at depth, d (mm), within the asphalt layer in °C,

IR = surface temperature measured with the infrared temperature gauge, °C,

$T_{(1\text{-day})}$ = the average of the previous day's high and low air temperatures in °C,

hr_{18} = time of day in the 24-hour system, but calculated using an 18-hour asphalt temperature rise and fall time according to Stubstad et al. (1998), and

β_i = coefficients of Eq. (2.7), which are given in Table 2.1 for both the BELLS2 and BELLS3 equations.

In TxDOT Project 0-1863, TTI researchers developed an alternative equation, named the Texas-LTPP equation, which is considered more applicable for use in Texas. This equation is given by (Fernando, Liu and Ryu, 2001):

$$T_d = \beta_o + \beta_1 (IR+2)^{1.5} + \log_{10}(d) \times \{\beta_2 (IR+2)^{1.5} + \beta_3 \sin^2(hr_{18} - 15.5) + \beta_4 \sin^2(hr_{18} - 13.5) +$$
$$\beta_5 [T_{(1\text{-day})} + 6]^{1.5}\} + \beta_6 \sin^2(hr_{18} - 15.5) \sin^2(hr_{18} - 13.5) \quad (2.8)$$

The coefficients, β_i, of Eq. (2.8) were determined using multiple linear regression with measured IR and pavement temperature data from the asphalt concrete SMP sites in Texas, New Mexico, and Oklahoma, and from asphalt sections located at the Texas A&M Riverside Campus. Table 2.2 presents the coefficients of the Texas-LTPP equation. The interested reader is referred to the report by Fernando, Liu and Ryu (2001) for additional details on the development of this equation. Comparing the predictions of the BELLS2, calibrated BELLS2, and the Texas-LTPP equations, these researchers found that the most accurate predictions for Texas conditions are obtained using the Texas-LTPP equation.

Project 0-1863 led to the development of TxDOT's Modulus Temperature Correction Program, which may be used to correct asphalt concrete moduli backcalculated from FWD data to reference or standard conditions of temperature and loading frequency (Fernando and Liu, 2001). MTCP provides users with the option of using BELLS2, BELLS3, or the Texas-

Table 2.1. Coefficients of the BELLS2 and BELLS3 Equations.

Coefficient	BELLS2	BELLS3
β_0	+2.780	+0.950
β_1	+0.912	+0.892
β_2	–0.428	–0.448
β_3	+0.553	+0.621
β_4	+2.630	+1.830
β_5	+0.027	+0.042

Table 2.2. Coefficients of the Alternative Model for Predicting Pavement Temperature.

Coefficient	Estimate	*t*-statistic for testing the null hypothesis that $\beta_i = 0$	*p* value
β_0	6.460	21.10	0.0000
β_1	0.199	60.79	0.0000
β_2	–0.083	-43.08	0.0000
β_3	–0.692	-3.46	0.0000
β_4	1.875	7.50	0.0000
β_5	0.059	50.11	0.0000
β_6	–6.784	-11.50	0.0000

LTPP equation for predicting pavement temperature. The program uses the output from MODULUS as an input to the modulus temperature correction. More details on using the program are provided by Fernando and Liu (2001).

MULTI-DEPTH DEFLECTOMETER

Multi-depth deflectometers are used to measure "in-situ" elastic deflections and/or permanent deformations in the various pavement layers of a test section. Figure 2.4 shows a trenched pavement section where an MDD has been installed. The basis of the patented MDD system is a series of linear variable differential transducer (LVDT) modules that are mounted on a rod in a 1.54-inch diameter hole within a test section (from http://www.dynatest.com/hardware/CSIR/mdd.htm). The modules are anchored to the soil by way of small steel balls that are pressed along the circumference of the hole at the depth of the module. The reference rod is anchored into the subgrade at approximately 10 ft below the

Figure 2.4. Picture of Trenched Pavement Showing MDD Installed within Test Section.

pavement surface. The top of the hole is sealed with a cap that contains the connector to the data acquisition system. The reference rod is connected to the anchor rod using a snap head connector so that the MDD modules can be removed for re-use. Generally, the MDD modules are placed at each layer interface.

During testing, the deflections at each module under a moving wheel load are recorded over time. By taking deformation readings as the pavement recovers after loading, the permanent deformation due to the test load may be estimated. This information may be used

to develop transfer functions relating load repetition to plastic strain in road building materials. Pavement engineers can also use the deflection data to determine the effective elastic moduli for each pavement layer.

The MDD may be used to verify layer moduli backcalculated from FWD deflections. To verify the results from FWD backcalculations, the pavement engineer can compare calculated deflections at the locations of the MDD modules against the measured displacements at those depths. In addition, the MDD can provide estimates of layer strain by dividing the difference of measured displacements by the gap length between modules. This permits one to predict service life based on subgrade limiting strain criteria.

CHAPTER III. FIELD DATA COLLECTION

The field data collection on SH4/48 involved the following tasks:

- an initial site investigation,
- instrumentation and monitoring of field sections, and
- material sampling.

This chapter documents the tasks carried out to collect data for characterizing the effects of overweight truck traffic on SH4/48 in Brownsville.

INITIAL SITE INVESTIGATION

The main objective of the initial site investigation was to collect information that may be used to establish test segments for pavement instrumentation and field monitoring. For this purpose, the following tasks were conducted:

- ground penetrating radar measurements along SH4/48;
- identification of homogeneous segments from GPR surveys according to the predicted layer thickness profiles;
- selection of FWD stations on each homogeneous segment;
- prediction of layer thicknesses of the asphalt and flexible base materials; and
- core sampling to verify GPR predictions, assist in data interpretation, and provide cores for laboratory testing.

Two GPR surveys were conducted to estimate the pavement layer thickness profiles along SH4/48. The first survey, conducted in September 2000, was done using TxDOT's air-coupled GPR system. The project director operated the equipment for these tests. From the data collected, researchers predicted the surface layer thickness variations along SH4/48. However, information on the layering beneath the surface material was difficult to get, as the reflections coming after the surface layer were either not visible or very faint. Consequently, researchers conducted another survey in February 2001, using ground-coupled radar antennas manufactured by Geophysical Survey Systems Incorporated (GSSI). This second survey was conducted along the outside and inside southbound lanes of SH4/48 corresponding, respectively, to the K6 and K7 lanes of the permitted overweight truck route. Since most of the permitted trucks (about 95 percent) travel from the Port of Brownsville to Mexico, the decision was made to monitor these lanes during the project.

Two ground-coupled radar antennas were used. One was a GSSI 200 MHz unit that was primarily used to check the depth of the water table along the route. The other was a 1.5 GHz antenna that researchers used to collect data on the near-surface pavement layers. These antennas are shown in Figure 2.2 of the previous chapter. Data from the 1.5 GHz antenna, along with coring information taken at various locations, were used to establish the base layer thickness profiles along the K6 and K7 lanes. It was not possible to see the ground water table from the GPR data collected with the 200 MHz antenna. Researchers note that Pharr District personnel drilled a hole on the shoulder near the location of a weigh-in-motion (WIM) site along SH48. No water table was encountered to a depth of 13 ft from the pavement surface at this location.

ESTABLISHING FWD MONITORING STATIONS AND PAVEMENT INSTRUMENTATION

Based on the GPR measurements, researchers established FWD stations along the K6 and K7 lanes of the permitted truck route. The portion of the route monitored in this study begins at the FM511 and SH48 intersection and ends approximately 0.14 mile south of Cleveland Street along SH4. The K6 lane was segmented into 16 homogeneous sections (A to P), while the K7 lane was divided into 6 homogeneous sections (A to F). Tables 3.1 and 3.2 summarize the locations of the different sections established, respectively, on the K6 and K7 lanes. In these tables, the locations of the section endpoints are referred to the south end of the bridge over FM511. In addition, Appendix A presents figures of the data from the air-coupled GPR antenna. These COLORMAP figures show that the sections reflect the observed variations in the radar reflections from the layer interfaces.

Once the homogeneous sections in each lane were defined, researchers established the locations of the FWD stations in each section. Altogether, there were 56 FWD stations established on the K6 lane, and 50 stations on the K7 lane. Tables 3.3 and 3.4 show the locations of the FWD stations on which data were collected at different times during the project. In this regard, personnel from the Pharr District provided FWD, profile, and rut bar data for evaluating and monitoring pavement performance along the K6 and K7 lanes.

Table 3.1. Locations of the K6 Lane Sections.*

Section	From		To	
	(miles)	(feet)	(miles)	(feet)
K6-A	0	1254	0	1610
K6-B	0	1610	0	1809
K6-C	0	1809	0	1954
K6-D	0	1954	1	1484
K6-E	1	1484	1	2874
K6-F	1	2874	2	1894
K6-G	2	1894	2	2639
K6-H	2	2639	3	3269
K6-I	3	3269	3	3544
K6-J	3	3544	3	3879
K6-K	3	4794	4	49
K6-L	4	49	4	3269
K6-M	4	3269	4	3514
K6-N	4	3514	4	3914
K6-O	4	3914	5	1189
K6-P	5	1189	5	1404

* Referred from south end of bridge over FM511

Table 3.2. Locations of the K7 Lane Sections.*

Section	From		To	
	(miles)	(feet)	(miles)	(feet)
K7-A	0	505	3	3159
K7-B	3	4064	3	4504
K7-C	3	4504	3	5174
K7-D	3	5174	4	399
K7-E	4	399	4	3199
K7-F	4	3199	5	669

* Referred from south end of bridge over FM511

Table 3.3. Locations of FWD Stations on K6 Lane.

Section	FWD Station	Distance of Station from FM511 Bridge (miles)
K6-A	6-1	0.267
K6-B	6-2	0.314
K6-D	6-3	0.379
K6-D	6-4	0.466
K6-D	6-5	0.560
K6-D	6-6	0.655
K6-D	6-7	0.750
K6-D	6-8	0.845
K6-D	6-9	1.009
K6-D	6-10	1.091
K6-D	6-11	1.166
K6-D	6-12	1.261
K6-E	6-13	1.356
K6-E	6-14	1.451
K6-F	6-15	1.545
K6-F	6-16	1.668
K6-F	6-17	1.739
K6-F	6-18	1.829
K6-F	6-19	1.924
K6-F	6-20	2.019
K6-F	6-21	2.113
K6-F	6-22	2.208
K6-F	6-23	2.303
K6-G	6-24	2.398
K6-G	6-25	2.435
K6-G	6-26	2.492
K6-H	6-27	2.530
K6-H	6-28	2.606
K6-H	6-29	2.701
K6-H	6-30	2.805
K6-H	6-31	2.890
K6-H	6-32	2.985
K6-H	6-33	3.079
K6-H	6-34	3.193
K6-H	6-35	3.288
K6-H	6-36	3.382
K6-H	6-37	3.477
K6-H	6-38	3.572
K6-I	6-39	3.657

Table 3.3. Locations of FWD Stations on K6 Lane (cont.).

Section	FWD Station	Distance of Station from FM511 Bridge (miles)
K6-J	6-40	3.685
K6-K	6-41	3.951
K6-K	6-42	3.988
K6-L	6-43	4.083
K6-L	6-44	4.178
K6-L	6-45	4.273
K6-L	6-46	4.339
K6-L	6-47	4.416
K6-L	6-48	4.547
K6-L	6-49	4.613
K6-M	6-50	4.642
K6-O	6-51	4.796
K6-O	6-52	4.838
K6-O	6-53	4.932
K6-O	6-54	5.033
K6-O	6-55	5.163
K6-P	6-56	5.238

Table 3.4. Locations of FWD Stations on K7 Lane.

Section	FWD Station	Distance of Station from FM511 Bridge (miles)
K7-A	7-1	0.288
K7-A	7-2	0.382
K7-A	7-3	0.430
K7-A	7-4	0.523
K7-A	7-5	0.618
K7-A	7-6	0.713
K7-A	7-7	0.808
K7-A	7-8	0.902
K7-A	7-9	0.997
K7-A	7-10	1.092
K7-A	7-11	1.177
K7-A	7-12	1.272
K7-A	7-13	1.366
K7-A	7-14	1.461
K7-A	7-15	1.613
K7-A	7-16	1.707
K7-A	7-17	1.802
K7-A	7-18	1.897
K7-A	7-19	1.991
K7-A	7-20	2.086
K7-A	7-21	2.181
K7-A	7-22	2.389
K7-A	7-23	2.470
K7-A	7-24	2.559
K7-A	7-25	2.654
K7-A	7-26	2.749
K7-A	7-27	2.844
K7-A	7-28	2.938
K7-A	7-29	3.033
K7-A	7-30	3.128
K7-A	7-31	3.222
K7-A	7-32	3.317
K7-A	7-33	3.412
K7-A	7-34	3.506
K7-A	7-35	3.601
K7-A	7-36	3.686
K7-B	7-37	3.961
K7-C	7-38	4.088
K7-D	7-39	4.160
K7-E	7-40	4.255

Table 3.4. Locations of FWD Stations on K7 Lane (cont.).

Section	FWD Station	Distance of Station from FM511 Bridge (miles)
K7-E	7-41	4.349
K7-E	7-42	4.444
K7-E	7-43	4.539
K7-E	7-44	4.595
K7-E	7-45	4.650
K7-E	7-46	4.747
K7-F	7-47	4.842
K7-F	7-48	4.927
K7-F	7-49	5.022
K7-F	7-50	5.145

From examination of the GPR data illustrated in Appendix A, the authors note the significant variability in arrival times of the layer interface reflections for several of the sections established, e.g., K6-G, K6-I, K6-K, K6-L, K7-C and K7-E. Researchers used the observed variability in the GPR data as a factor in establishing the locations of FWD test stations within the sections given in Tables 3.1 and 3.2. Specifically, for each section, a candidate list of FWD stations was established that reflects the observed variability in the GPR data. Once candidate stations were identified, researchers went over each location along the route and selected FWD monitoring stations considering other factors such as proximity to street intersections and driveways, culvert locations and observed surface distress (i.e., cracking and rutting). In general, FWD stations were established away from these areas. Through this process, researchers selected the stations identified in Tables 3.3 and 3.4.

In addition to collecting FWD and pavement condition data, researchers also installed two multi-depth deflectometers at the WIM site along SH48. As described previously, an MDD consists of an array of linear variable differential transducers positioned at different depths within the pavement for measuring displacements under moving loads. For this study, MDDs were installed on the inside wheelpath of the K6 lane, and on the outside wheelpath of the K7 lane at the vicinity of the WIM site. Researchers installed pavement instrumentation at this site for the following reasons:

- Traffic flow at the WIM site is continuous (no stop-and-go movements).
- There is a fenced utility area adjacent to the site, which served as an ideal location for the weather station researchers installed to collect environmental data (air and pavement temperatures, precipitation and moisture content variations).
- Previous drilling showed no water table to a depth of 13 ft from the pavement surface, eliminating the need to retrofit the MDD had a shallow water table been present.

Appendix B describes the pavement instrumentation work conducted by researchers at the WIM site.

MATERIAL SAMPLING

For GPR data interpretation and verification, a total of 20 cores were initially taken from SH4/48: 10 samples in each of the K6 and K7 lanes. Tables 3.5 and 3.6 show the locations where cores were taken. At these locations, the coring crew also measured the base thickness and obtained Shelby tube samples of the subgrade. The measured base thicknesses at the coring locations are also given in Tables 3.5 and 3.6.

During coring, a number of the 6-inch diameter cores broke. These broken cores occurred in the downtown area along SH4 where difficulty was encountered in getting intact cores. Disintegration of the asphalt material during coring suggested possible stripping within the mix. In order to get additional cores for laboratory testing, Pharr District personnel took several more cores from the K6 lane along SH4, specifically at the vicinity of stations K6-48, K6-50, K6-51 and K6-53. This time, smaller diameter cores (3.6 inch) were taken to minimize the possibility of breaking the material. Table 3.7 shows the thicknesses of the additional cores.

In addition, a set of five cores were taken at the WIM site along SH48. These are identified as C2 to C6 in Table 3.7. C2 and C3 were taken from the wheelpaths of the K6 lane, while C4 and C5 were taken from the K7 lane. C6 was taken from the center, left-turn lane along SH48, which receives very little traffic.

Table 3.5. Thickness Measurements from Initial Coring Done on K6 Lane.

Number	Core ID	Core Diameter (in)	Thickness (in)	
			AC	Flexible Base
1	K6-1	5.7	8.0	12
2	K6-4	5.6	7.2	11
3	K6-11	5.6	8.0	12
4	K6-23	5.6	7.6	13
5	K6-29	5.7	8.5	12
6	K6-35	5.7	7.8	12
7	K6-42	5.6	6.3	13
8	K6-45	5.6	8.5	8
9	K6-50	5.6	10.4	6
10	K6-53	5.7	7.5	13

Table 3.6. Thickness Measurements from Initial Coring Done on K7 Lane.

Number	Core ID	Diameter (in)	Thickness (in)	
			AC	Flexible Base
1	K7-3	5.6	9.0	12
2	K7-9	5.6	9.0	12
3	K7-11	5.7	9.5	12
4	K7-12	5.6	8.5	11
5	K7-15	5.6	9.0	11
6	K7-20	5.7	8.3	13
7	K7-31	5.7	8.0	11
8	K7-37	5.7	9.5	10
9	K7-46	5.7	10.8	8
10	K7-40	5.7	7.3	10

Table 3.7. Thickness Measurements on Additional AC Cores from K6 Lane.

Number	Core ID	Core Measurements (in)	
		Diameter	Thickness
1	K6-48-16	3.6	8.2
2	K6-48-12	3.6	6.4
3	K6-50-16	3.6	5.0
4	K6-50-12	3.6	6.2
5	K6-51	3.6	5.3
6	K6-53-10	3.6	5.5
7	C2	4.0	6.5
8	C3	4.0	8.0
9	C4	4.0	8.0
10	C5	4.0	8.1
11	C6	4.0	7.4

CHAPTER IV. PREDICTION OF LAYER THICKNESS AND MODULUS BACKCALCULATION

EVALUATION OF LAYER THICKNESS PROFILES

As mentioned in Chapter III, TTI researchers conducted a GPR survey on the permitted truck route using two ground-coupled antennas having central frequencies of 200 MHz and 1.5 GHz. This survey was conducted on the K6 and K7 lanes of SH4/48, beginning just past the junction of FM511 and SH48 and ending just before the intersection of SH4 and US77. The GPR survey covered the 106 FWD stations established along the route.

Data processing, positioning and interpretation of the ground-coupled measurements were done by Roadscanners Oy of Finland, which analyzed the data using its Road Doctor™ software. The processing methods used included static background removal, signal amplification and horizontal and vertical filtering. Roadscanners Oy reported the thicknesses of the AC and flexible base (FB) layers after verifing its predictions with the layer thicknesses determined from coring. Because the FWD stations are located at approximately 500 ft spacing and Roadscanners Oy made the analysis of layer thickness every foot, the average layer thickness was calculated for each 100 ft. Tables 4.1 and 4.2 show the predicted thickness at each FWD station as reported by Roadscanners Oy, and the average thickness and standard deviation calculated over an interval of ±50 ft about each station.

Researchers plotted the thicknesses of the AC and flexible base layers for both lanes. Figures 4.1 to 4.2 show the results obtained for the K6 lane, while Figures 4.3 to 4.4 show the results for the K7 lane. These charts show the following:

- the point-by-point predictions of layer thickness;
- results from segmentations of the K6 and K7 lanes based on the predicted layer thickness, as delineated by the average thickness over each segment;
- the measured asphalt and flexible base layer thicknesses at the coring locations; and
- the predicted layer thicknesses at the different FWD stations.

From Figures 4.1 and 4.3, it is observed that the K6 lane shows slightly more variations in the predicted AC thickness than the K7 lane. In addition all four figures show that, toward the end of the route (within the downtown area of Brownsville), the AC thickness increases and the flexible base thickness decreases on both lanes.

Table 4.1. Predicted Layer Thicknesses on the K6 Lane.

FWD Station	Layer Thickness* (inches)		Mean Thickness** (inches)		Standard Deviation** (inches)	
	AC	FB	AC	FB	AC	FB
6-1	8.74	11.34	8.61	11.44	0.53	0.32
6-2	8.74	10.79	8.61	11.44	0.53	0.32
6-3	9.57	12.17	8.61	11.44	0.53	0.32
6-4	6.73	11.85	7.22	11.51	0.46	0.32
6-5	8.74	11.85	8.03	11.44	0.59	0.32
6-6	8.35	11.38	8.03	11.44	0.59	0.32
6-7	7.52	11.14	8.03	11.44	0.59	0.32
6-8	8.66	11.85	8.03	11.44	0.59	0.32
6-9	6.93	11.73	7.46	11.48	0.43	0.32
6-10	7.52	11.14	7.46	11.48	0.43	0.32
6-11	8.15	11.46	7.46	11.48	0.43	0.32
6-12	8.98	11.18	8.17	11.54	0.56	0.67
6-13	8.98	11.73	8.17	11.54	0.56	0.67
6-14	7.95	11.34	8.17	11.54	0.56	0.67
6-15	7.76	11.30	8.17	11.54	0.56	0.67
6-16	8.66	11.57	8.17	11.54	0.56	0.67
6-17	8.98	11.46	8.17	11.54	0.56	0.67
6-18	7.76	11.46	8.17	11.54	0.56	0.67
6-19	8.03	11.26	8.17	11.54	0.56	0.67
6-20	8.15	11.50	8.17	11.54	0.56	0.67
6-21	8.15	11.42	8.17	11.54	0.56	0.67
6-22	8.15	12.13	8.17	11.54	0.56	0.67
6-23	7.52	12.83	8.17	11.54	0.56	0.67
6-24	9.17	11.54	8.17	11.54	0.56	0.67
6-25	8.98	11.18	8.17	11.54	0.56	0.67
6-26	8.98	11.30	8.17	11.54	0.56	0.67
6-27	8.15	11.77	8.17	11.54	0.56	0.67
6-28	7.95	11.54	8.17	11.54	0.56	0.67
6-29	7.76	12.24	8.17	11.54	0.56	0.67
6-30	6.54	11.97	7.28	11.68	0.66	0.67
6-31	7.13	11.57	7.28	11.68	0.66	0.67
6-32	8.98	11.02	7.28	11.68	0.66	0.67
6-33	6.81	12.17	7.28	11.68	0.66	0.67
6-34	6.61	12.17	7.28	11.68	0.66	0.67
6-35	7.76	11.81	7.28	11.68	0.66	0.67
6-36	7.76	11.54	7.28	11.68	0.66	0.67
6-37	8.15	12.13	8.18	11.55	0.61	0.67
6-38	6.73	11.77	7.02	11.82	0.23	0.67
6-39	8.98	11.65	8.08	11.55	0.53	0.67
6-40	8.35	10.94	8.08	11.55	0.53	0.67
6-41	6.81	13.35	6.99	11.85	0.46	0.67

Table 4.1. Predicted Layer Thicknesses on the K6 Lane (cont.).

FWD Station	Layer Thickness* (inches)		Mean Thickness** (inches)		Standard Deviation** (inches)	
	AC	FB	AC	FB	AC	FB
6-42	7.32	12.48	6.99	11.85	0.46	0.67
6-43	6.54	11.65	5.94	12.27	0.78	0.67
6-44	8.98	11.65	8.31	12.03	0.88	0.67
6-45	7.32	11.02	6.71	11.38	0.44	0.67
6-46	6.10	11.81	6.71	11.38	0.44	0.67
6-47	6.54	11.18	6.71	11.38	0.44	0.67
6-48	9.25	9.09	9.58	8.63	0.64	0.67
6-49	11.02	6.89	9.58	8.63	0.64	0.76
6-50	9.61	8.03	9.58	8.63	0.64	0.76
6-51	6.54	11.65	6.97	10.71	0.58	0.81
6-52	7.76	10.08	6.97	10.71	0.58	0.81
6-53	7.52	13.11	7.75	12.12	0.52	0.80
6-54	9.25	8.50	9.01	9.06	0.65	0.48
6-55	9.17	8.46	9.01	9.06	0.65	0.48
6-56	8.15	9.37	9.01	9.06	0.65	0.48

*At FWD station

**Computed ±50 ft about each FWD station

Table 4.2. Predicted Layer Thicknesses on the K7 Lane.

FWD Station	Layer Thickness* (inches)		Mean Thickness** (inches)		Standard Deviation** (inches)	
	AC	FB	AC	FB	AC	FB
7-1	8.35	11.81	8.07	11.67	0.64	0.42
7-2	9.37	12.01	8.07	11.67	0.64	0.42
7-3	8.46	12.83	8.07	11.67	0.64	0.42
7-4	8.98	12.01	8.07	11.67	0.64	0.42
7-5	7.32	11.81	8.07	11.67	0.64	0.42
7-6	8.27	12.32	8.07	11.67	0.64	0.42
7-7	7.52	11.42	8.07	11.67	0.64	0.42
7-8	8.35	11.73	8.07	11.67	0.64	0.42
7-9	8.98	11.30	8.07	11.67	0.64	0.42
7-10	7.01	11.54	8.07	11.67	0.64	0.42
7-11	9.37	12.13	8.07	11.67	0.64	0.42
7-12	8.35	11.10	8.07	11.67	0.64	0.42
7-13	7.52	11.93	8.07	11.67	0.64	0.42
7-14	8.35	11.77	8.07	11.67	0.64	0.42
7-15	9.17	11.42	8.07	11.67	0.64	0.42
7-16	8.54	11.22	8.07	11.67	0.64	0.42
7-17	7.83	11.61	8.07	11.67	0.64	0.42
7-18	6.93	11.81	8.07	11.67	0.64	0.42
7-19	8.86	11.61	8.07	11.67	0.64	0.42
7-20	7.17	12.76	8.07	11.67	0.64	0.42
7-21	8.19	11.42	8.07	11.67	0.64	0.42
7-22	7.52	12.09	8.07	11.67	0.64	0.42
7-23	7.52	11.93	8.07	11.67	0.64	0.42
7-24	8.74	11.18	8.07	11.67	0.64	0.42
7-25	7.52	11.50	8.07	11.67	0.64	0.42
7-26	8.54	11.65	8.07	11.67	0.64	0.42
7-27	8.66	11.85	8.07	11.67	0.64	0.42
7-28	8.46	11.89	8.07	11.67	0.64	0.42
7-29	8.66	12.72	8.07	11.67	0.64	0.42
7-30	8.50	11.26	8.07	11.67	0.64	0.42
7-31	7.17	12.17	8.07	11.67	0.64	0.42
7-32	8.82	12.13	8.07	11.67	0.64	0.42
7-33	7.83	12.20	8.07	11.67	0.64	0.42
7-34	8.46	11.89	8.07	11.67	0.64	0.42
7-35	8.31	11.89	8.07	11.67	0.64	0.42
7-36	8.27	11.50	8.07	11.67	0.64	0.42
7-37	8.98	10.94	9.31	11.67	0.38	0.42
7-38	7.32	10.24	7.58	11.67	0.42	0.42
7-39	9.49	8.23	9.65	8.98	0.36	0.52
7-40	9.69	8.98	9.65	8.98	0.36	0.52

Table 4.2. Predicted Layer Thicknesses on the K7 Lane (cont.).

FWD Station	Layer Thickness* (inches)		Mean Thickness** (inches)		Standard Deviation** (inches)	
	AC	FB	AC	FB	AC	FB
7-41	9.84	8.74	9.65	8.98	0.36	0.52
7-42	10.28	8.46	9.65	8.98	0.36	0.52
7-43	9.57	8.74	9.65	8.98	0.36	0.52
7-44	9.53	8.46	9.65	8.98	0.36	0.52
7-45	9.49	8.23	9.65	8.98	0.36	0.52
7-46	7.64	9.06	8.32	8.98	0.52	0.52
7-47	8.74	9.09	8.32	8.98	0.52	0.52
7-48	9.49	8.50	8.32	8.98	0.52	0.52
7-49	7.95	12.24	7.68	11.67	0.36	0.30
7-50	7.83	11.50	7.68	11.67	0.36	0.30

*At FWD station

**Computed ±50 ft about each FWD station

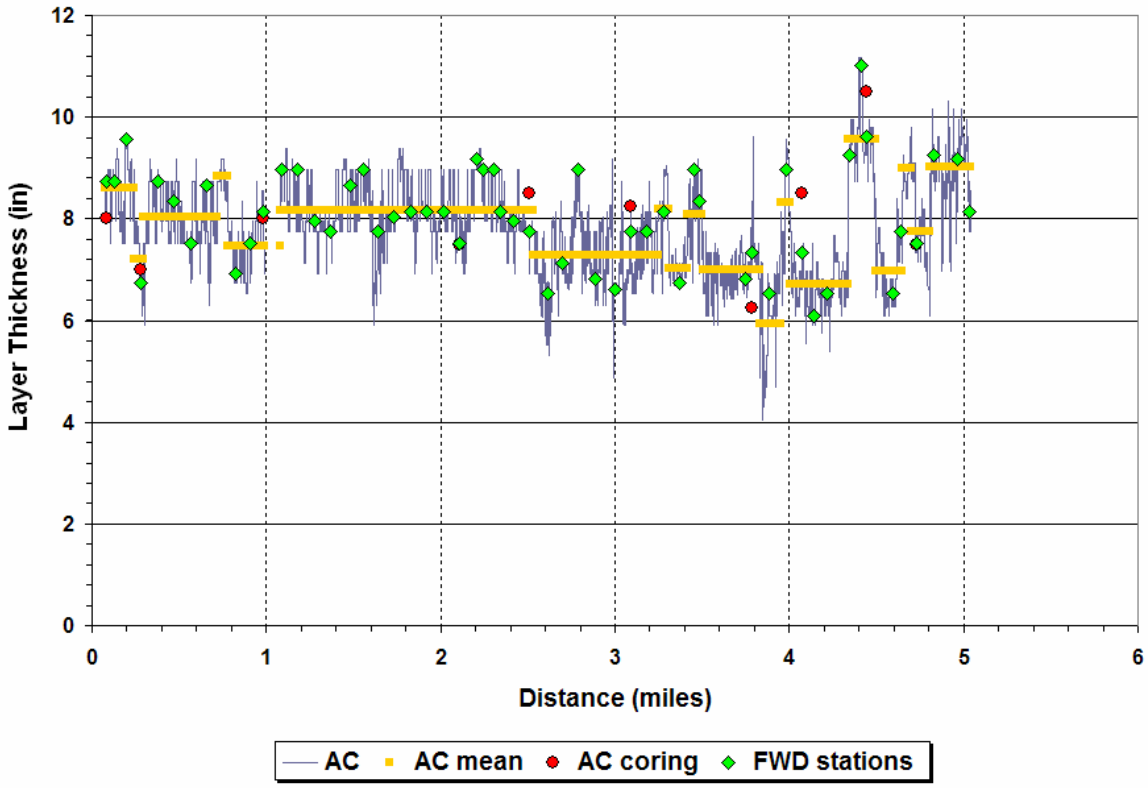

Figure 4.1. AC Thicknesses from GPR Data and Coring on K6 Lane.

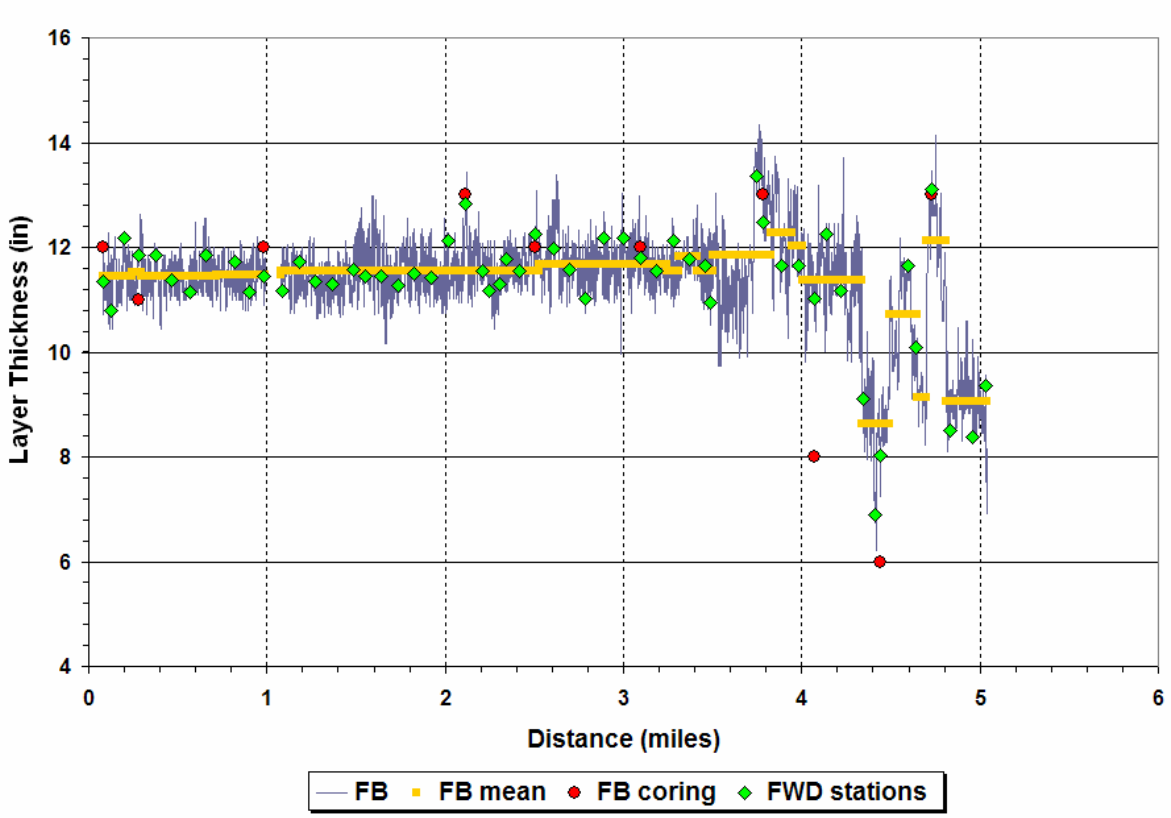

Figure 4.2. Flexible Base Thicknesses from GPR Data and Coring on K6 Lane.

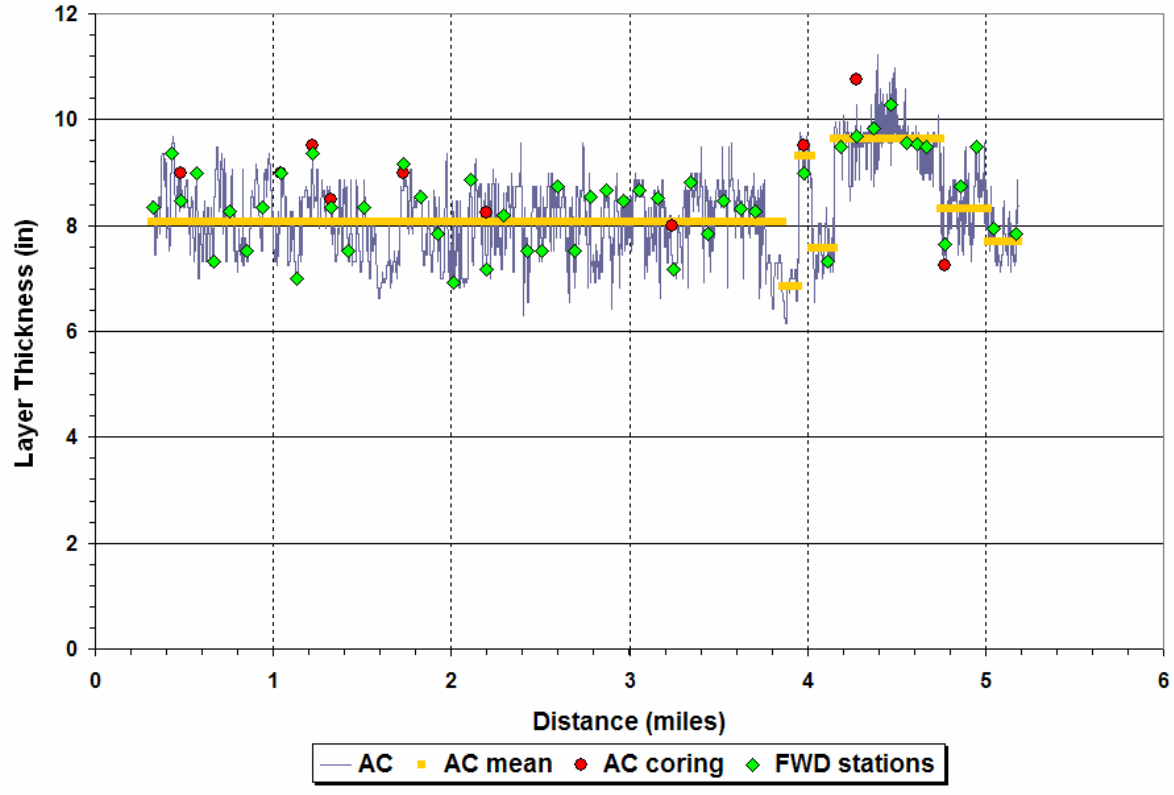

Figure 4.3. AC Thicknesses from GPR Data and Coring on K7 Lane.

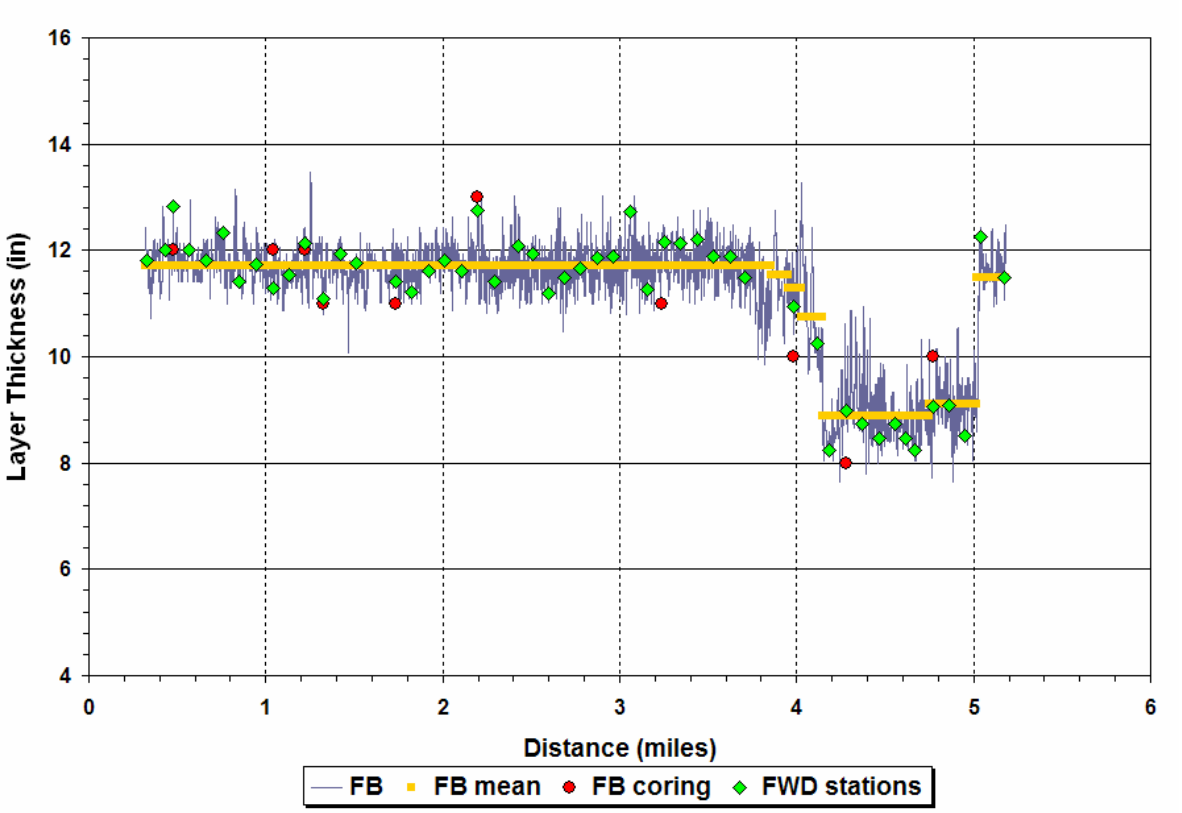

Figure 4.4. Flexible Base Thicknesses from GPR Data and Coring on K7 Lane.

STATIC BACKCALCULATION OF PAVEMENT LAYER MODULI

Pharr District personnel collected FWD data at the monitoring stations on several occasions during the project. Using the MODULUS program, researchers backcalculated the modulus values from the FWD peak deflections. Due to the thickness variations observed in the GPR data, backcalculations were done by station using the predicted layer thicknesses given in Tables 4.1 and 4.2.

Initially, researchers assumed a three-layer pavement system consisting of asphalt, flexible base and subgrade materials for the MODULUS backcalculations. In this three-layer system, the salvaged base and the lime-treated subbase underlying the flexible base were combined with the native soil found along the route to form the "subgrade" layer assumed in the backcalculations. Unfortunately, this three-layer representation of the pavement structure did not produce satisfactory agreement between measured and predicted FWD peak deflections, particularly on stations located within the downtown area where average absolute errors greater than 10 percent were obtained. Thus, researchers evaluated other ways of representing the pavement layering in the MODULUS backcalculations. Two other cases

based on a four-layer pavement system (AC + flexible base + subbase + subgrade) were considered. In one case, the salvaged base was combined with the flexible base to form the "base" layer overlying the lime-treated subbase. In the second case, researchers combined the salvaged base with the lime-treated subbase to form the "subbase" layer used in the MODULUS backcalculations. However, the results obtained were still not satisfactory. Thus, researchers went back to using a three-layer system with the difference being that, the salvaged base and lime-treated subbase were combined with the flexible base to form the "base" layer used in the MODULUS backcalculations. This layer is referred to as the composite flexible base (CFB) in this report.

The three-layer system consisting of the AC, CFB and native subgrade layers produced much better agreement between the measured and predicted peak displacements as reflected in the lower average absolute errors obtained from the MODULUS backcalculations. These error statistics are given in Tables 4.3 and 4.4, where the errors are generally observed to be within 5 percent, over the range of FWD data collected at the different stations and at different times during the project. The backcalculated modulus values are given in Appendix C of this report.

Table 4.3. Percent Absolute Errors/Sensor from Backcalculations on K6 Lane Data.

FWD Station	2001*				2002*			2003*
	Feb	May	July	Aug	Mar	July	Dec	Sept
6-1	5	5	4	6	5	5	4	5
6-2	3	3	2	2	2	3	1	2
6-3	3	4	2	3	3	3	4	2
6-4	1	2	4	1	2	3	2	5
6-5	4	3	3	3	2	2	3	3
6-6	2	2	5	4	2	4	2	4
6-7	4	2	5	4	1	2	4	1
6-8	1	4	2	3		2	2	2
6-9	2	2	4	2				
6-10	1	2	2	1	3	2	2	
6-11	2	1	3	1	2	1	2	
6-12	1	2	2	2	1	3	4	
6-13	3	3	5	4	4	2	5	
6-14	3	1	3	2	3	2	4	
6-15	2	2	3	4	1	3	1	
6-16	2	2	4	4	5	4	2	
6-17	5	2	2	4	2	5	2	
6-18	5	5	3	4	3	5	4	
6-19	2	1	5	5	3	3	4	
6-20	4	2	5	3	4	3	2	
6-21	3	4	5	2	3	3	3	
6-22	3	2	3	2	6	4	1	
6-23	3	4	6	5	5	5	4	
6-24	1	4	5	5	5	5	2	
6-25	3	4	4	5	5	5	4	
6-26	5	2	5	6	1	4	2	
6-27	2	4	2	4	2	4	5	
6-28	3	5	5	5	2	4	5	
6-29	1	3	5	3	3	4	3	
6-30	5	5	5	3	2	5	3	
6-31	1	4	3	4	3	3	5	
6-32	2	2	4	5	5	4	5	
6-33	1	5	4	6	4		5	
6-34	2	2	3	1	3	3	2	
6-35	1	5	5	5	5	5	4	
6-36	4	3	4	1	2	3	4	
6-37	0	4	2	5	5	5	5	
6-38	1	3	4	6	2	5	5	
6-39	1	6	5	5	5	5	4	
6-40	4	5	5	5	5	6	5	
6-41	4	3	5	5	2	5	5	

Table 4.3. Percent Absolute Errors/Sensor from Backcalculations on K6 Lane Data (cont.).

FWD Station	2001*				2002*			2003*
	Feb	May	July	Aug	Mar	July	Dec	Sept
6-42	9	7	12	12	5	2	2	
6-43	7	9	10	19	9	8	6	
6-44	2	2	2	2	1	2	4	
6-45	1	3	3	4	3	3	2	
6-46	5	5	3	4	4	5	4	
6-47	3	3	3	4	3	5	2	
6-48	1	3	3	3	2	2	2	
6-49	4	4	4	5	2	5	2	
6-50	4	3	4	3	3	5	3	
6-51	3	3	3	4	3	5	3	
6-52	4	5	4	4	4	5	3	
6-53	1	2	1	3	1	2	5	
6-54	4	6	7	7	7	7	3	
6-55	1	3	4	5	3	4	4	
6-56	2	4	5	6	3	3	4	

*Shaded cells denote no data available due to construction or maintenance work

Table 4.4. Percent Absolute Errors/Sensor from Backcalculations on K7 Lane Data.

FWD Station	2001*			2002*				2003*	
	Feb	May	Aug	Mar	July	Oct	Dec	Apr	Sept
7-1	1	2	4	1	2	2	1		3
7-2	1	2	5	2	1	2	1	2	2
7-3	1	1	2	2	1	1	1	4	1
7-4	1	1	1	1	1	1	5	1	3
7-5	3	2	3	3	3	2	2	3	4
7-6	2	1		2	2	2	3	3	2
7-7	1	1	1	1	1	4	2	1	1
7-8	1	2	2						
7-9	1	2	3						
7-10	1	1	5	2	3	1	4	2	3
7-11	2	2	4	2	2		5	2	1
7-12	2	5	1	2	4	3	2	1	2
7-13	1	3	1	2	2	1	2	1	2
7-14	2	1	2	2	2	1	1	5	2
7-15	4	5	4	4	5	5	3	1	3
7-16	1	4	1	3	4	3	3	4	2
7-17	1	3	1	1	2	3	2	1	1
7-18	2	2	3	1	4	4	3	1	2
7-19	2	5	4	4	3	4	1	4	2
7-20	1	*	3	1	1	1	2	2	2
7-21	1	5	0	5	1	1	5	4	1
7-22	0	1	1	1	1		4	1	2
7-23	1	1	2	2	2	2	3	3	2
7-24	4	1	1	3	1	2	3	1	1
7-25	2	1	2	3	2	3	4	2	2
7-26	1	2	2	0	2	5	2	1	1
7-27	1	2	2	1	4	3	1	1	2
7-28	4	1	2	1	1	2	2	2	3
7-29	3	3	4	2		3	3	3	3
7-30	4	5	4	4	5	2	2	4	5
7-31	4	3	3	3	4	3	4	3	3
7-32	4	2	4	3	2	2	4	2	4
7-33	1	3	4	2	2	1	3	3	3
7-34	1	2	3	2	1	1	1	1	4
7-35	1	2	3	4	1	2	2	4	3
7-36	1	5	4	5	1	2	1	6	4
7-37	4	5	2	5	5	4	4	4	4
7-38	8	10	6	8	9	11	7	13	17
7-39	1	3	1	3	2	4	4	2	2
7-40	1	2	3	0	2	4	2	1	3
7-41	2	1	3	2	2	2	3	1	1

Table 4.4. Percent Absolute Errors/Sensor from Backcalculations on K7 Lane Data (cont.).

FWD Station	2001*			2002*				2003*	
	Feb	May	Aug	Mar	July	Oct	Dec	Apr	Sept
7-42	4	2	4	1	2	5	5	3	5
7-43	2	2	2	3	3	4	1		1
7-44	1	5	2	1	5	5	1	2	3
7-45	4	3	3	5	3	4	4	3	4
7-46	2	4	4	4	4	4	4	4	4
7-47	2	3	2	5	3	5	3	2	3
7-48	2	1	3	3	4	4	2	1	2
7-49	2	2	2	3	2	3	1	2	1
7-50	3	2	4	3	2	2	4	9	1

*Shaded cells denote no data available due to construction or maintenance work

CHAPTER V. DYNAMIC ANALYSIS OF FWD DATA

The dynamic analysis of FWD data was accomplished using the DBSID computer program (Fernando and Liu, 2002). DBSID uses the FWD full-time histories of load and displacement for the backcalculation of pavement material properties. The program models the pavement as a layered system consisting of three materials overlying bedrock. In the analysis, researchers characterized the first layer as a viscoelastic material. The second and third layers were characterized as damped elastic. The backcalculated material properties were evaluated by examining the agreement between the measured and predicted displacement histories from DBSID. In this evaluation, researchers viewed plots of the measured and predicted displacement histories and determined the root mean square errors (RMSEs) associated with the predictions to assess the reasonableness of the results.

Because of the large volume of data to process, dynamic analyses were limited to FWD data taken at stations where researchers took cores. The results from dynamic analyses were later compared with those from static backcalculations to assess the reasonableness of the DBSID predictions. This comparison is presented in this chapter. Altogether, dynamic analyses were conducted on FWD data from stations K6-1, K6-4, K6-11, K6-23, K6-29, K6-35, K6-48, K7-3, K7-9, K7-11, K7-15, K7-20, K7-31, K7-37 and K7-40.

Appendix D presents plots of the measured and predicted displacement histories on stations analyzed. For each station, results from analyses of FWD data taken at different times are presented, beginning with stations on the K6 lane, then by stations on the K7 lane. These plots generally show that the predicted displacements fit the measured values quite adequately. However, there are stations where the results are mixed, i.e., the displacement histories compare quite well for some of the FWD data files but not for all times FWD full-time history data were collected, e.g., stations K6-1, K6-4, K6-35 and K6-48. On one station, K7-3, the match between predicted and measured displacement histories was generally poor.

Tables 5.1 and 5.2 present the creep compliance parameters and layer moduli backcalculated based on dynamic analysis. Researchers used the same pavement layering from the static backcalculations in this analysis. The creep compliance parameters in Tables 5.1 and 5.2 correspond to the parameters of the storage and loss compliances given in

Table 5.1. Backcalculated Material Properties from Dynamic Analysis of FWD Data on K6 Core Stations.

Station	Month	D_0	D_1	m	Dynamic Modulus (ksi)			RMSE μm
					HMAC	CFB*	Subgrade	
K6-1	May 01	3.30E-05	5.6E-02	0.344	100	10	9	22
	July 01	1.70E-05	3.4E-02	0.417	234	13	11	13
	Aug 01	1.90E-06	6.2E-02	0.354	95	8	8	28
	Mar 02	1.00E-03	4.5E-02	0.474	193	8	9	31
K6-4	May 01	1.00E-05	1.5E-02	0.430	543	13	13	9
	July 01	1.70E-05	1.5E-02	0.435	570	11	10	11
	Mar 02	1.30E-05	1.5E-02	0.415	516	13	12	10
	July 02	1.30E-05	2.7E-02	0.497	417	16	10	14
K6-11	Feb 01	3.30E-06	2.8E-03	0.322	1793	127	14	1
	May 01	7.30E-06	1.7E-02	0.476	592	119	12	2
	July 01	1.40E-05	5.0E-02	0.539	275	133	12	4
	Aug 01	1.90E-05	9.9E-02	0.577	166	119	11	3
	Mar 02	8.30E-06	1.2E-02	0.443	747	111	13	3
	July 02	1.00E-05	3.0E-02	0.498	387	147	13	2
K6-23	Feb 01	5.00E-06	1.37E-02	0.384	490	80	11	2
	May 01	1.67E-05	6.66E-02	0.500	173	46	11	8
	July 01	1.58E-05	5.35E-02	0.398	134	79	10	5
	Aug 01	3.33E-05	1.77E-01	0.485	61	73	11	5
	Mar 02	1.04E-05	1.93E-02	0.413	398	73	10	3
	July 02	1.48E-05	4.59E-02	0.427	179	96	11	5
K6-29	Feb 01	3.50E-06	3.54E-03	0.308	1318	64	14	2
	May 01	1.04E-05	1.33E-02	0.390	517	49	13	4
	July 01	2.78E-07	1.38E-02	0.399	523	82	12	3
	Aug 01	2.27E-05	8.24E-02	0.572	195	48	12	6
	Mar 02	8.77E-06	8.60E-03	0.374	740	76	12	3
	July 02	1.25E-05	1.41E-02	0.441	620	84	12	3
K6-35	Feb 01	4.55E-06	4.55E-03	0.294	958	16	16	11
	July 01	3.13E-05	1.02E-01	0.580	163	14	14	15
K6-48	Feb 01	1.95E-05	3.21E-02	0.416	243	11	12	5
	July 01	5.51E-05	1.99E-01	0.549	72	10	10	12
	Aug 01	8.74E-05	2.40E-01	0.483	44	11	9	14
	Mar 02	3.54E-05	8.67E-02	0.486	125	11	11	8
	July 02	3.98E-05	1.14E-01	0.514	108	10	11	9

* Composite flexible base

Table 5.2. Backcalculated Material Properties from Dynamic Analysis of FWD Data on K7 Core Stations.

Station	Month	D_0	D_1	m	Dynamic Modulus (ksi)			RMSE μm
					HMAC	CFB*	Subgrade	
K7-9	Feb 01	4.08E-06	1.77E-03	0.207	1611	8	16	3
	May 01	5.45E-06	1.89E-03	0.207	1502	7	16	7
	Aug 01	7.70E-06	2.81E-03	0.235	1156	10	16	7
K7-11	May 01	7.00E-06	1.37E-02	0.387	497	70	16	4
	Aug 01	8.30E-06	1.20E-02	0.337	446	69	15	4
	Mar 02	5.00E-06	2.01E-03	0.202	1376	53	15	2
	July 02	1.40E-05	3.27E-02	0.444	271	69	13	3
	Apr 03	5.80E-06	5.95E-03	0.315	810	66	16	3
K7-15	May 01	7.14E-06	1.88E-02	0.356	313	57	17	5
	Aug 01	7.14E-06	9.73E-03	0.289	437	59	16	4
	Mar 02	3.33E-06	4.30E-03	0.229	741	64	17	4
	July 02	1.19E-05	3.13E-02	0.430	266	41	17	6
	Oct 02	9.09E-06	2.96E-02	0.553	498	33	13	11
	Apr 03	4.89E-06	2.74E-03	0.214	1076	42	13	2
K7-20	Feb 01	3.70E-06	2.98E-03	0.221	1026	68	12	2
	Aug 01	8.33E-06	6.48E-03	0.332	803	72	10	3
	Mar 02	3.65E-06	3.85E-03	0.298	1156	74	11	3
	July 02	1.11E-05	1.75E-02	0.424	463	74	11	3
	Oct 02	1.22E-05	3.22E-02	0.488	339	78	10	3
	Apr 03	4.07E-06	3.07E-03	0.241	1095	59	12	3
K7-31	May 01	7.10E-06	5.80E-03	0.415	1329	86	12	3
	Aug 01	1.30E-05	2.40E-02	0.671	1025	122	2	15
	July 02	1.10E-05	1.20E-02	0.501	958	84	10	3
	Oct 02	1.00E-05	3.80E-02	0.528	345	113	11	6
	Apr 03	6.10E-06	2.70E-03	0.341	2005	99	13	3
K7-37	Feb 01	2.60E-06	8.70E-03	0.356	677	63	16	2
	May 01	1.90E-07	3.30E-02	0.456	287	49	15	4
	Aug 01	1.30E-05	4.40E-02	0.467	228	59	16	3
	Mar 02	4.60E-06	1.20E-02	0.356	493	55	16	3
	July 02	1.80E-05	5.00E-02	0.447	180	40	14	9
	Oct 02	2.00E-05	5.90E-02	0.562	259	27	14	12
	Apr 03	7.10E-06	2.70E-02	0.496	417	52	17	6
K7-40	Feb 01	6.40E-06	8.20E-03	0.347	686	18	12	3
	May 01	1.30E-05	2.80E-02	0.452	332	18	11	4
	Aug 01	1.80E-05	2.90E-02	0.461	331	21	11	4
	Mar 02	8.10E-06	9.30E-03	0.343	591	19	11	3
	July 02	2.30E-05	7.30E-02	0.519	172	14	10	9
	Oct 02	1.70E-05	6.40E-02	0.586	267	14	10	11
	Apr 03	1.00E-05	1.60E-02	0.401	446	17	11	3

* Composite flexible base

Eqs. (2.2) and (2.3), respectively. The dynamic moduli in these tables correspond to the frequency f_T of the FWD test, which may be estimated from the equation (Lytton et al., 1990):

$$f_T = \frac{1}{2t} \tag{5.1}$$

where t is the duration of the FWD impulse load in seconds. For a typical load duration of 30 msecs, a test frequency of 16.7 Hz (104.9 rad/sec) is determined from Eq. (5.1). Researchers used this test frequency in Eqs. (2.2) to (2.5) to determine the real and imaginary components of the asphalt concrete complex modulus, given the creep compliance parameters D_0, D_1 and m in Tables 5.1 and 5.2. Knowing these components, researchers determined the absolute value of the complex modulus $|E(\omega)|$ from the equation:

$$|E(\omega)| = \sqrt{E'(\omega)^2 + E''(\omega)^2} \tag{5.2}$$

where $E'(\omega)$ and $E''(\omega)$ are the real and imaginary components, respectively, of the asphalt concrete complex modulus at the frequency ω. Tables 5.1 and 5.2 show the results from these calculations under the column, AC dynamic modulus.

Figures 5.1 and 5.2 compare the AC moduli from dynamic analysis with the corresponding moduli from static analysis for the K6 and K7 core stations, respectively. The data exhibit a significant linear relationship between the logarithms of the backcalculated AC moduli. Consequently, researchers fitted the following simple linear equation to the data:

$$log_{10}(E_{dynamic}) = \beta_0 + \beta_1 log_{10}(E_{static}) \tag{5.3}$$

where,

$E_{dynamic}$ = AC modulus from dynamic analysis, ksi;

E_{static} = AC modulus from static analysis, ksi; and

β_0, β_1 = model coefficients determined by regression analysis.

The results showed that β_0 was not statistically significant. Consequently, researchers fitted Eq. (5.3) to the data but with β_0 set to zero and obtained the following relationships:

K6: $$log_{10}(E_{dynamic}) = 0.981\ log_{10}(E_{static}) \tag{5.4}$$

K7: $$log_{10}(E_{dynamic}) = 0.984\ log_{10}(E_{static}) \tag{5.5}$$

The standard errors of the estimate of the above equations are 0.151 and 0.212 for K6 and K7, respectively. Note that the β_1 coefficients are close to unity, reflecting the good correspondence between the logarithms of the AC moduli from dynamic and static analyses. It is also of interest to note that the coefficients are almost the same between K6 and K7.

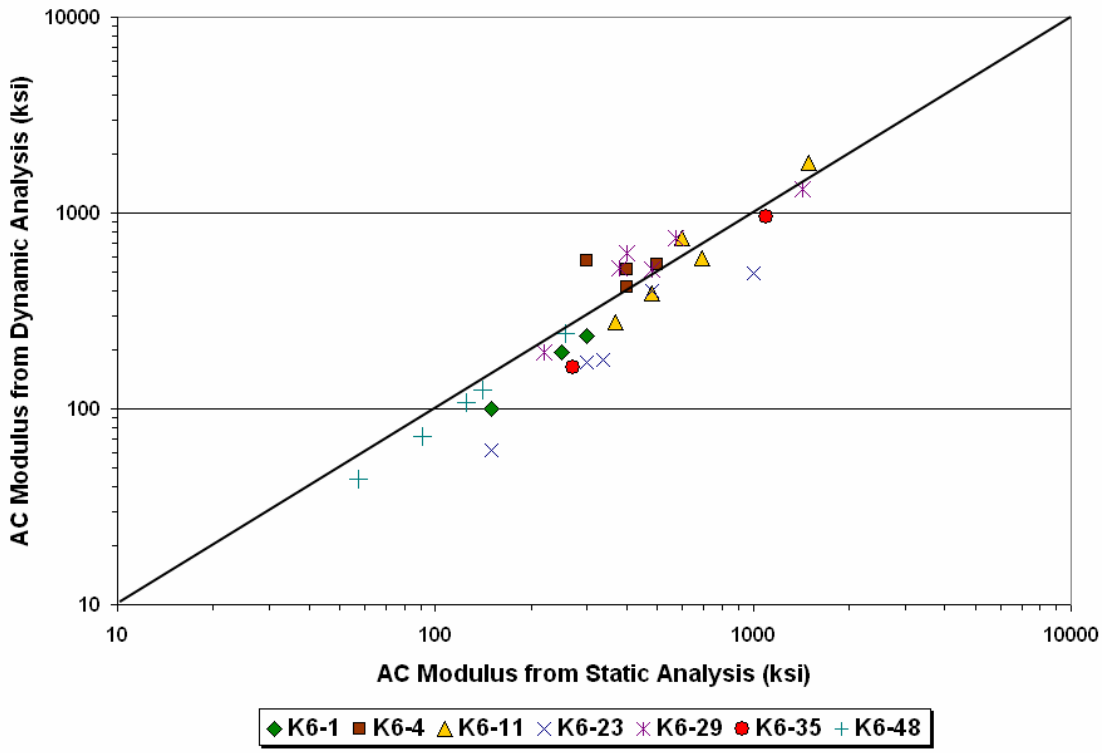

Figure 5.1. Comparison of AC Moduli from Dynamic and Static Analyses (K6 Stations).

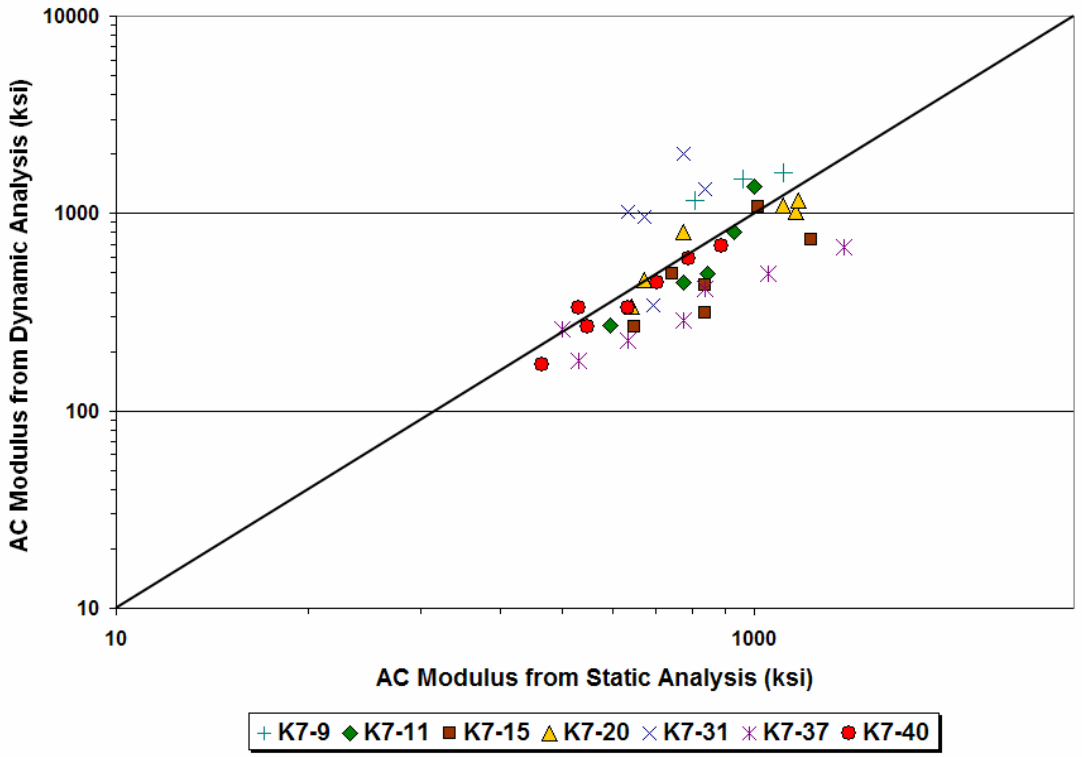

Figure 5.2. Comparison of AC Moduli from Dynamic and Static Analyses (K7 Stations).

CHAPTER VI. LABORATORY TESTING

The main purpose of laboratory testing is to get helpful information about changes in the AC layer as it is affected by routine overweight truck traffic. Because asphalt concrete mixtures undergo time-dependent changes, it is significant to consider this factor in material characterizations. According to the recent Guide for Mechanistic-Empirical Design of New and Rehabilitated Pavement Structures (Applied Research Associates, 2004), long-term, time-dependent property changes in the AC mix come about because of chemical and physical hardening of the asphalt binder due to short- or long-term aging, curing caused by evaporation of moisture inside asphalt emulsion systems, or pozzolanic reactions of cementitious materials. In addition, the design guide indicates that materials subjected to load-related fatigue distress may undergo severe degradation of properties with time and load repetitions. Microcracks may develop, leading to a reduced modulus. The possible reduction in the AC modulus would in turn lead to an increase in predicted pavement strains, and a higher possibility of permanent deformation.

DYNAMIC MODULUS |*E**| OF ASPHALT CONCRETE MIXTURES

Procedures for characterizing the dynamic modulus of AC mixtures are provided in the draft test method developed during the National Cooperative Highway Research Program (NCHRP) 1-37A project (2002) and in the Standard Test Method for Dynamic Modulus of Asphalt Mixtures developed by the American Society for Testing and Materials (ASTM, 1997). The NCHRP test procedure is referred to as the DM1 Draft Standard Test Method for the Dynamic Modulus of Asphalt Concrete Mixtures, while the ASTM test method is designated as ASTM D3497-79. Both methods cover procedures for preparing and testing asphalt concrete specimens to determine the dynamic modulus and phase angle over a range of temperatures and loading frequencies. In these tests, the AC specimen is subjected to a sinusoidal (haversine) axial compressive stress at a given temperature and loading frequency. The applied stress, measured recoverable axial strain and the time lag between the stress and strain pulses are used to calculate the dynamic modulus and phase angle for a given test temperature and loading frequency.

It is noted that DM1 was the draft test procedure for dynamic modulus testing in the new pavement design method being developed (at the time of this project) for the American

Association of State Highway and Transportation Officials (AASHTO). Thus, researchers decided to use DM1 for dynamic modulus testing of cores in the study reported herein. The two methods produce results that vary with the frequencies and temperatures used. ASTM D3497-79 prescribes tests at temperatures of 41, 77 and 104 °F and at frequencies of 1, 4 and 16 Hz for each temperature. On the other hand, DM1 prescribes tests at temperatures of 14, 39, 68, 100 and 130 °F, at frequencies of 25, 10, 5, 1, 0.5 and 0.1 Hz. In this study, test temperatures were established based on field observations of pavement temperatures from FWD tests conducted along SH4/48.

Table 6.1 shows the range in pavement temperatures measured at 1-inch depth at different times on FWD stations established along SH4/48. Also shown are the averages of the measured pavement temperatures at 1-inch depth. Using the Texas-LTPP equation in the Modulus Temperature Correction Program (Fernando, Liu and Ryu, 2001), researchers also predicted the pavement temperatures at mid-depth. The range in the predicted temperatures as well as the averages are given in Table 6.1. Based on these data, researchers decided to conduct tests at 70, 85, 100, 110 and 130 °F.

Table 6.2 identifies the cores tested, shows their dimensions and gives the gauge length (GL) over which deformations were measured during the tests. Most of the cores are 4 inches in diameter, with a few that are slightly smaller than this size. It is noted that DM1 specifies cores with nominal diameters of 4 inches for dynamic modulus testing. The 3.6-inch diameter cores were taken along SH4 in the downtown area of Brownsville. Within this area, Pharr District personnel found it hard to get intact cores as the cores broke easily during coring. Thus, they used a slightly smaller bit.

As is observed in many existing pavements, the cores taken along SH4/48 were not homogeneous, typically consisting of three to four asphalt lifts. Thus, material properties determined from laboratory tests reflect this non-homogeneity and may be considered as composite material properties characteristic of the core tested. This statement also applies for asphalt concrete properties backcalculated from FWD data taken along the route. Note that researchers modeled the entire AC layer in the static and dynamic analyses of FWD data due to the difficulty in reliably backcalculating properties of thin asphalt lifts.

Table 6.1. Minimum, Maximum and Mean Pavement Temperatures along Route.

Lane	FWD Test Date	Measured Temperature at 1-inch Depth (°F)			Predicted Temperature at Mid-Depth (°F)		
		Minimum	Maximum	Mean	Minimum	Maximum	Mean
K6	Feb. 2001	76	91	85	79	88	83
	May 2001	103	124	115	97	108	103
	July 2001	112	127	119	109	116	112
	Aug. 2001	135	145	135	116	126	121
	Mar. 2002	108	119	113	99	105	102
K7	Feb. 2001	78	92	85	89	94	91
	May 2001	115	128	122	99	108	103
	Aug. 2001	*	*	*	107	111	108
	Mar. 2002	89	104	96	94	112	103

*No data

Table 6.2. Core Dimensions and Gauge Lengths for Strain Measurements.

Core ID	Core Dimensions (in)		Gauge Length (in)
	Diameter	Height	
K6-1	4	8	6
K6-4	4	6	5
K6-11	4	8	4
K6-23	4	7	5
K6-29	4	8	5
K6-35	4	8	4
K6-48-16	3.6	8	5
K6-48-12	3.6	6	4
K6-50-16	3.6	5	3
K6-50-12	3.6	6	4
K6-51	3.6	5	3
K6-53-10	3.6	6	4
K7-3	4	8	6
K7-9	4	8	6
K7-11	4	8	6
K7-12	4	8	6
K7-15	4	8	6
K7-20	4	8	6
K7-31	4	8	6
k7-37	4	8	6
K7-40	4	8	6
C2	4	6.5	5
C3	4	7.7	6
C4	4	8.0	6
C5	4	8.1	6
C6	4	7.4	4

To minimize end effects, the position of the linear variable differential transducer clamps were generally set at an offset of 1 inch from the top and bottom ends of the cores. Figure 6.1 illustrates this setup and the resulting gauge length within which deformations were measured during testing. The set of frequencies and load cycles used are as recommended in the selected standard for dynamic modulus testing. Specifically, researchers conducted tests at 25, 10, 5, 1, 0.1 and 0.5 Hz, at load cycles of 200, 200, 100, 20, 15 and 15, respectively. Prior to testing, cores were placed in the environmental chamber to equilibrate them to the required temperature. For this purpose, specimen C2 was fitted with a temperature probe and used as a dummy specimen for monitoring the test temperature inside the environmental chamber.

Researchers processed the laboratory data using a computer program to get complex modulus E^* and complex creep compliance D^* with their corresponding real and imaginary parts. The dynamic modulus $|E^*|$ is the absolute value of the complex modulus, while the phase angle is determined from the time lag between the stress and strain measurements according to the following relation:

$$\phi = (t_i / t_p) \times 360 \qquad (6.1)$$

where,

ϕ = phase angle, degrees;

t_i = time lag, msecs; and

t_p = period of a load cycle, msecs.

Figure 6.2 illustrates how t_i and t_p are determined from the test data. While this figure shows the time lag as the difference between the peak times of the stress and strain pulses, this quantity could also be determined from the times corresponding to the troughs or minimum points of these pulses. Consequently, researchers considered the following cases in characterizing the complex modulus and complex compliance from the frequency sweep tests:

- Case 1: Using regression, a curve is fitted through the data points defining the peak and trough of the stress or strain pulse. The stress and strain amplitudes are then determined from the fitted curves. For calculation of the phase angle, the time lag is determined as the difference in times corresponding to the troughs or minimum points of the stress and strain pulses based on the fitted curves.

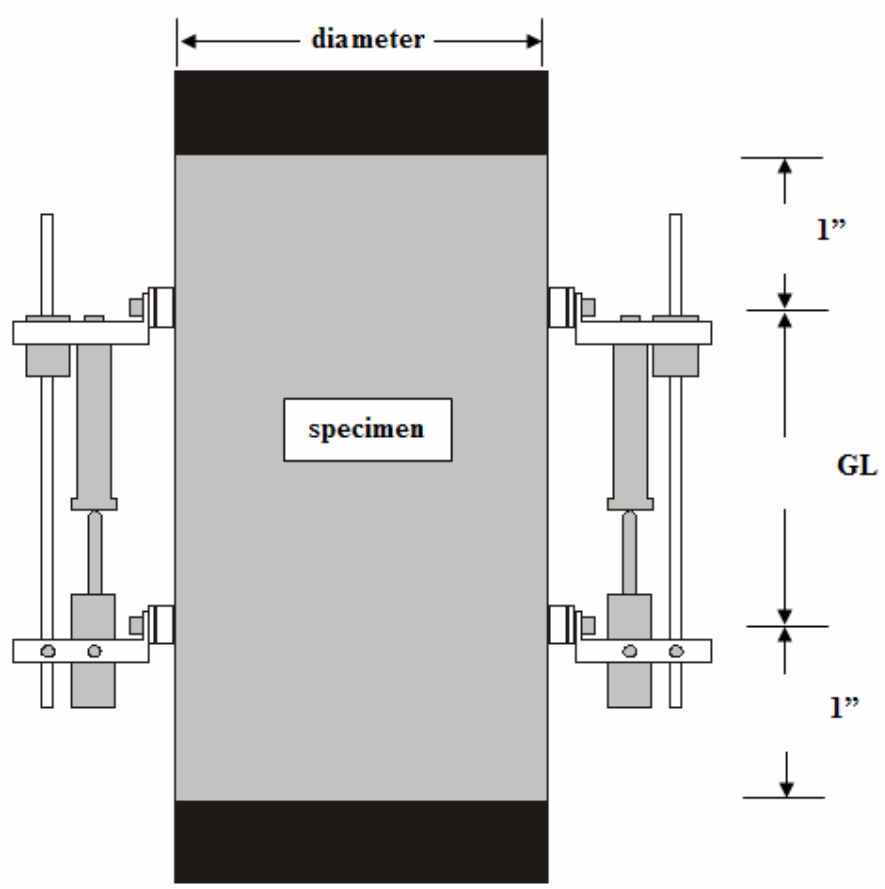

Figure 6.1. Placement of the LVDTs for Testing AC Cores.

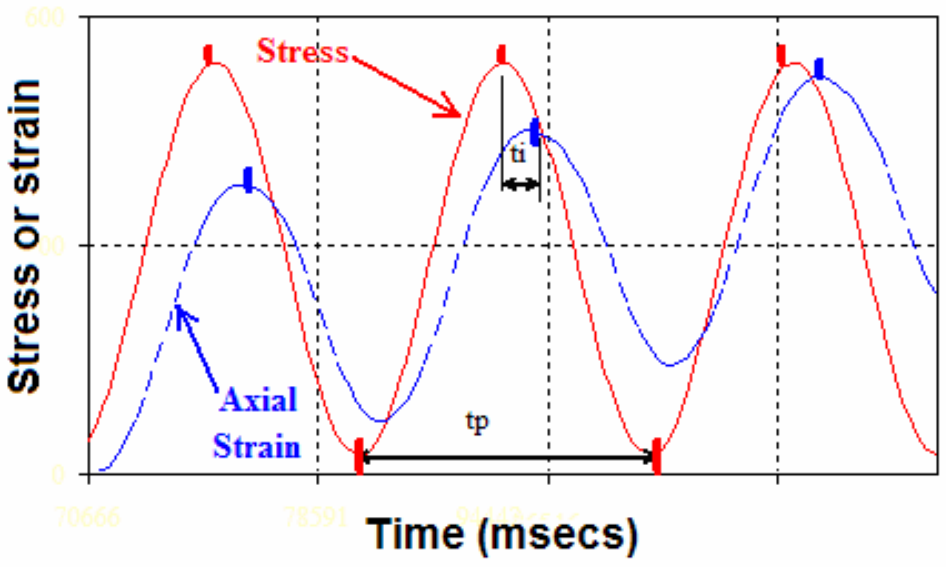

Figure 6.2. Illustration of Stress/Strain Data from Frequency Sweep Tests.

- Case 2: The stress and strain amplitudes are determined from the raw data, without fitting a curve through the points that define the peaks of the stress and strain pulses. However, the time lag is determined from curves fitted through points that define the troughs of these pulses, just like in Case 1.
- Case 3: The stress and strain amplitudes are determined just like in Case 1 (using fitted curves). However, the time lag for calculating the phase angle is determined from curves fitted through points that define the peaks of the stress and strain pulses.
- Case 4: The stress and strain amplitudes are determined just like in Case 2 (from raw data), while the time lag is calculated just like in Case 3 (using curves fitted through points that define the peaks).

Since each core was instrumented with two LVDTs, researchers ran the above cases using the average of the LVDT measurements, as well as the deformation data from each LVDT. Thus, there were 12 possible ways of processing the frequency sweep data to characterize the complex modulus and complex compliance of each core. To select from these results, researchers examined the trends of the dynamic moduli determined at the different test temperatures and frequencies. Assuming that asphalt concrete is a simple thermorheological material, the dynamic modulus should decrease with temperature and increase with frequency. Figures 6.3 to 6.17 present the best results from the laboratory tests conducted.

CREEP COMPLIANCE PARAMETERS

Due to the fact that the creep compliance D is a complex number defined as the inverse of the complex modulus E^* for a linear viscoelastic material, it is possible to backcalculate the parameters of the creep compliance as defined in Eqs. (2.1), (2.2) and (2.3). From the test data, the real and imaginary components of the complex compliance can be determined using the following relations:

$$D'(\omega) = |D^*(\omega)| \cos \phi \quad (6.2)$$

$$D''(\omega) = |D^*(\omega)| \sin \phi \quad (6.3)$$

where,

$|D^*(\omega)|$ = inverse of the absolute value of the complex modulus for a given frequency ω,

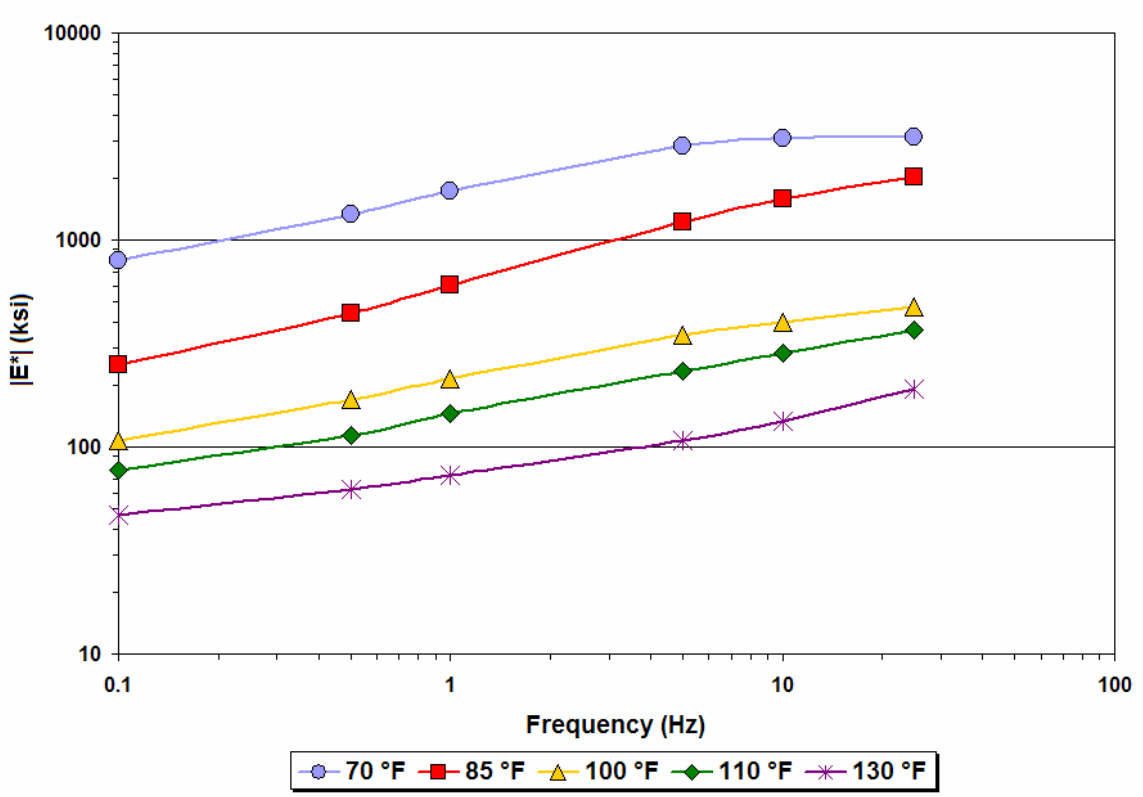

Figure 6.3. Variation of |*E| with Frequency and Temperature for K6-1 Core.**

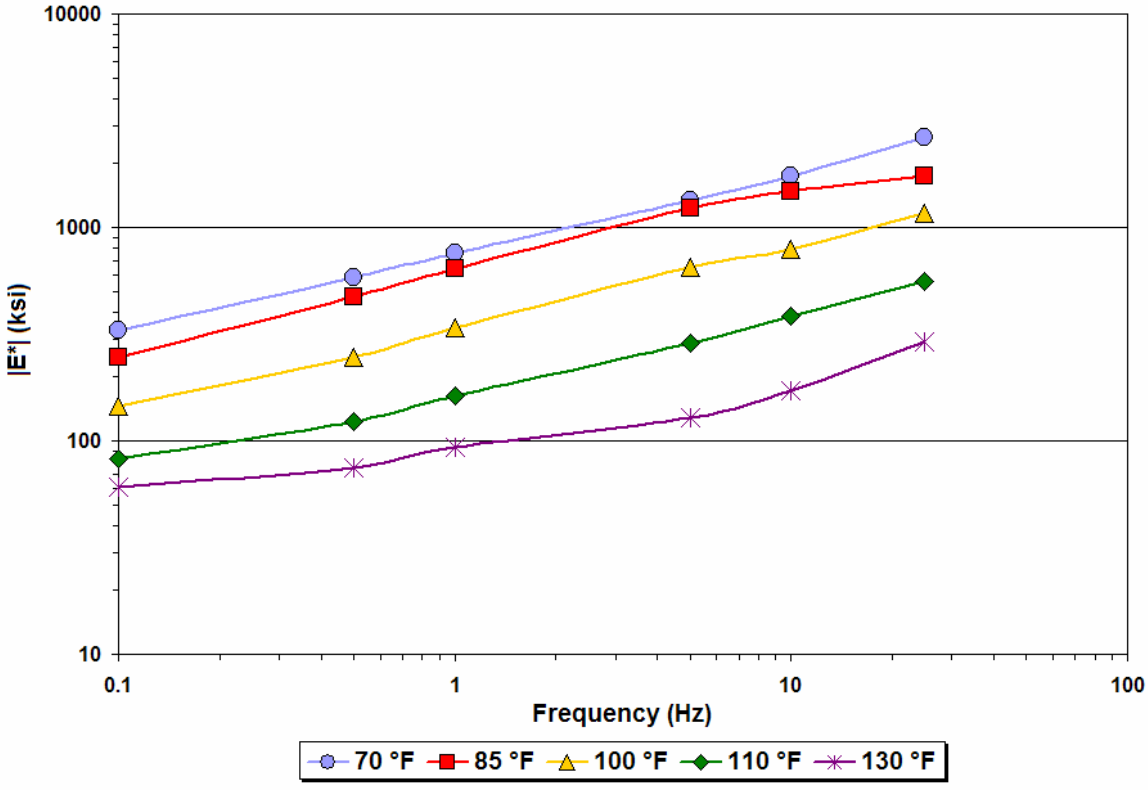

Figure 6.4. Variation of |*E| with Frequency and Temperature for K6-4 Core.**

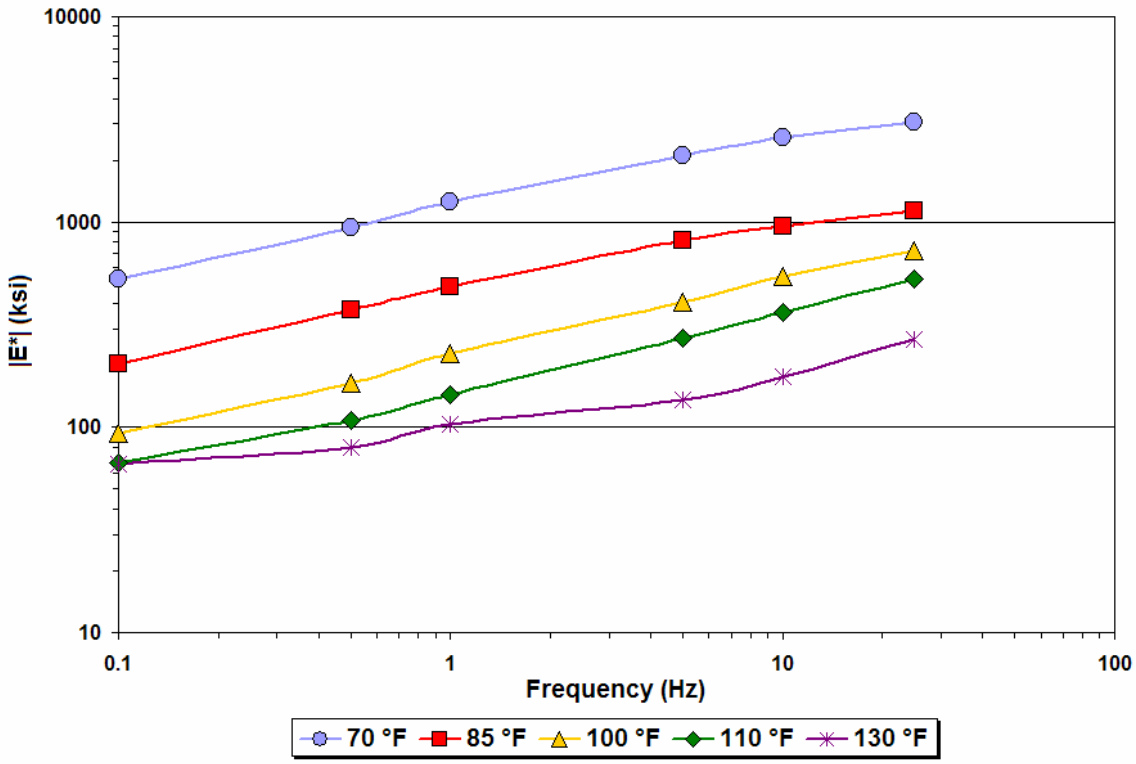

Figure 6.5. Variation of |*E| with Frequency and Temperature for K6-11 Core.**

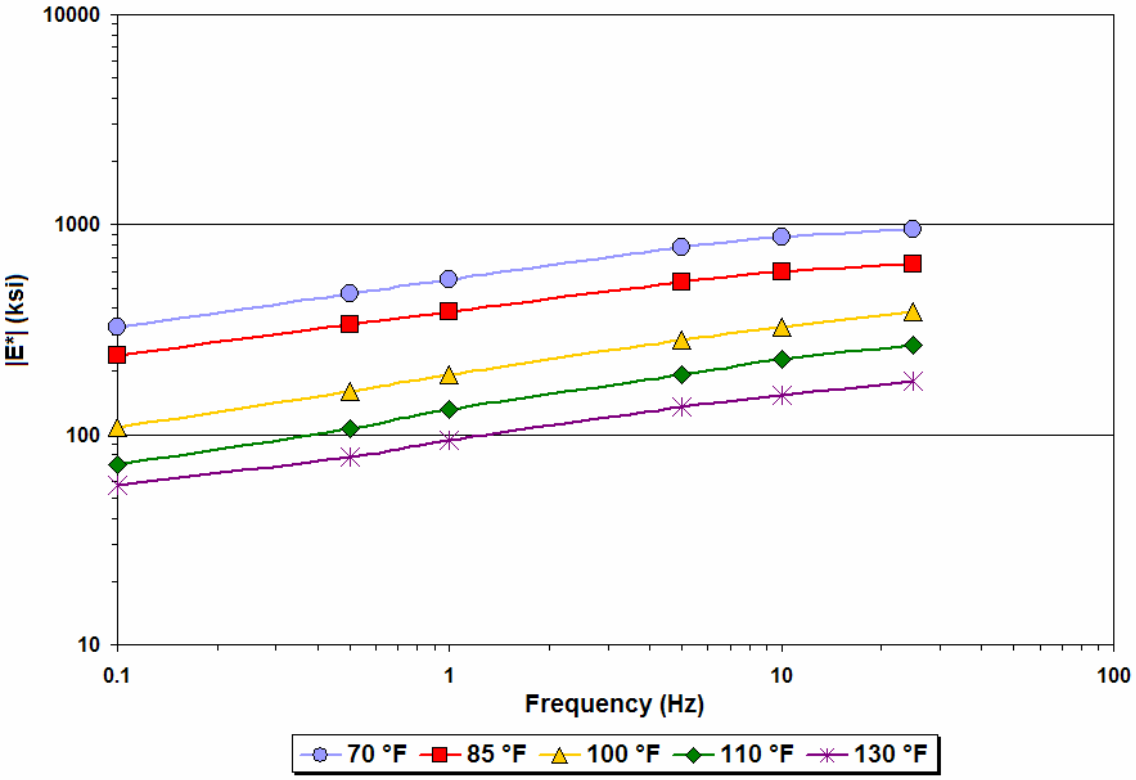

Figure 6.6. Variation of |*E| with Frequency and Temperature for K6-23 Core.**

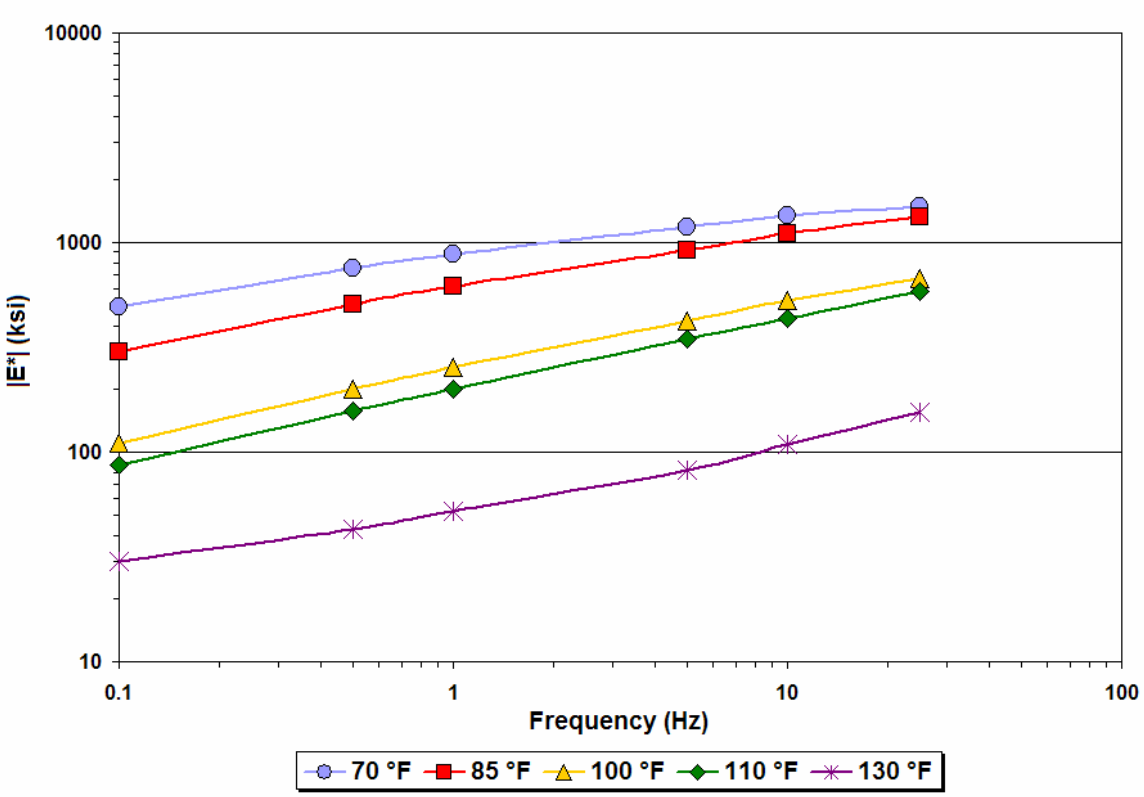

Figure 6.7. Variation of |*E| with Frequency and Temperature for K6-29 Core.**

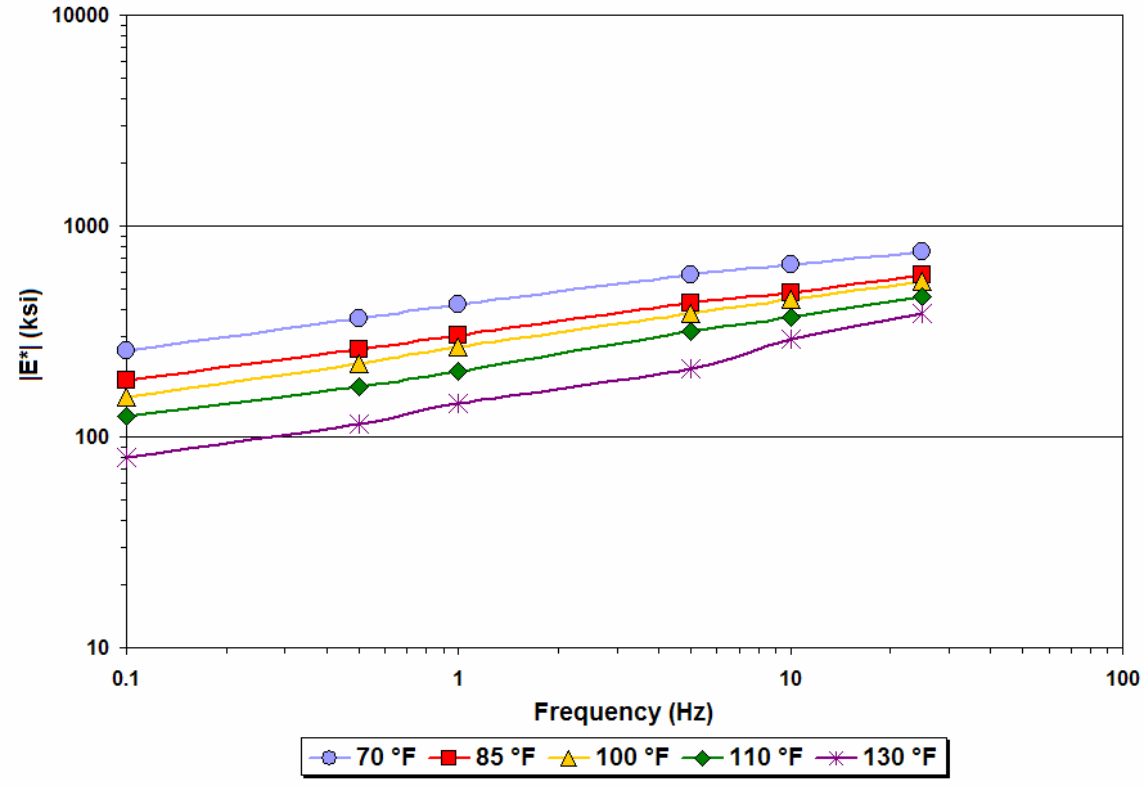

Figure 6.8. Variation of |*E| with Frequency and Temperature for K6-48 Core.**

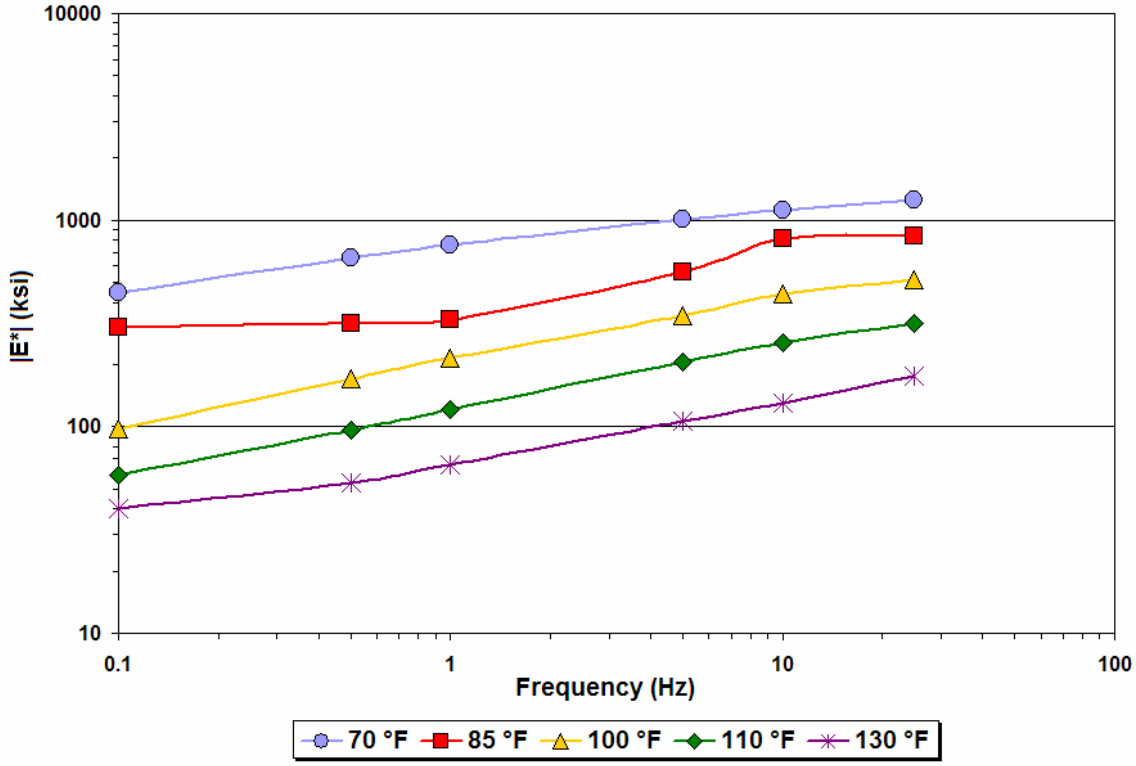

Figure 6.9. Variation of |*E| with Frequency and Temperature for K7-3 Core.**

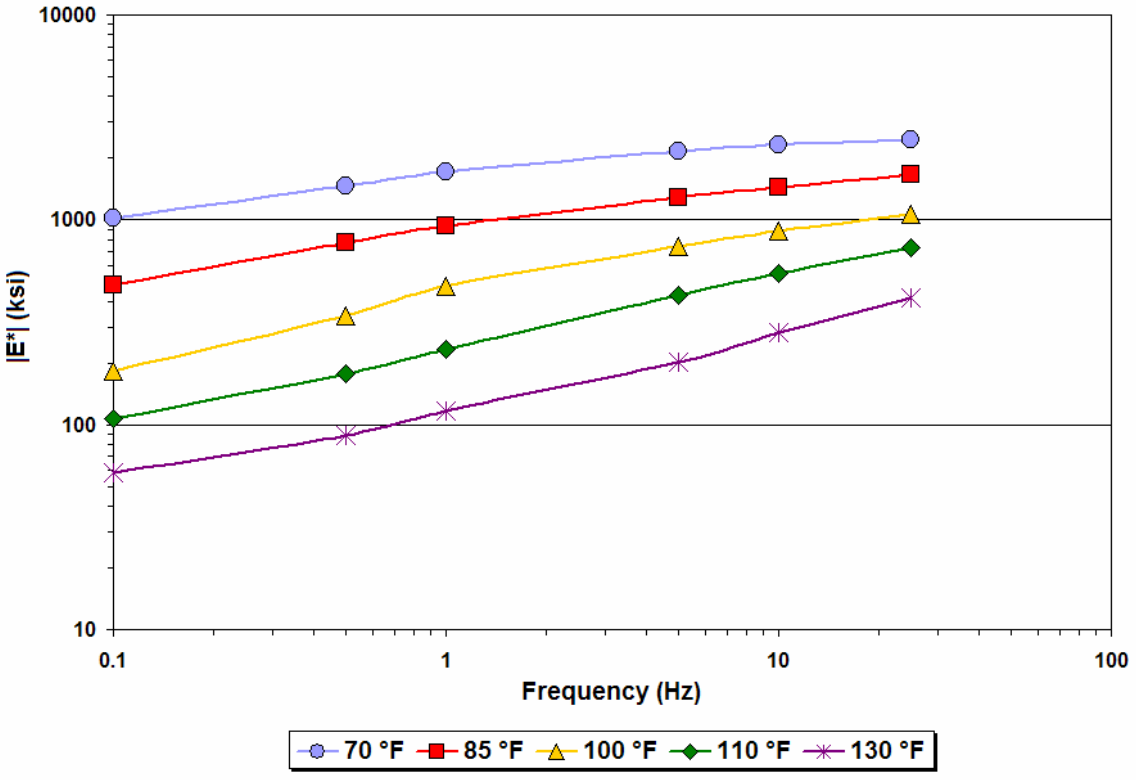

Figure 6.10. Variation of |*E| with Frequency and Temperature for K7-9 Core.**

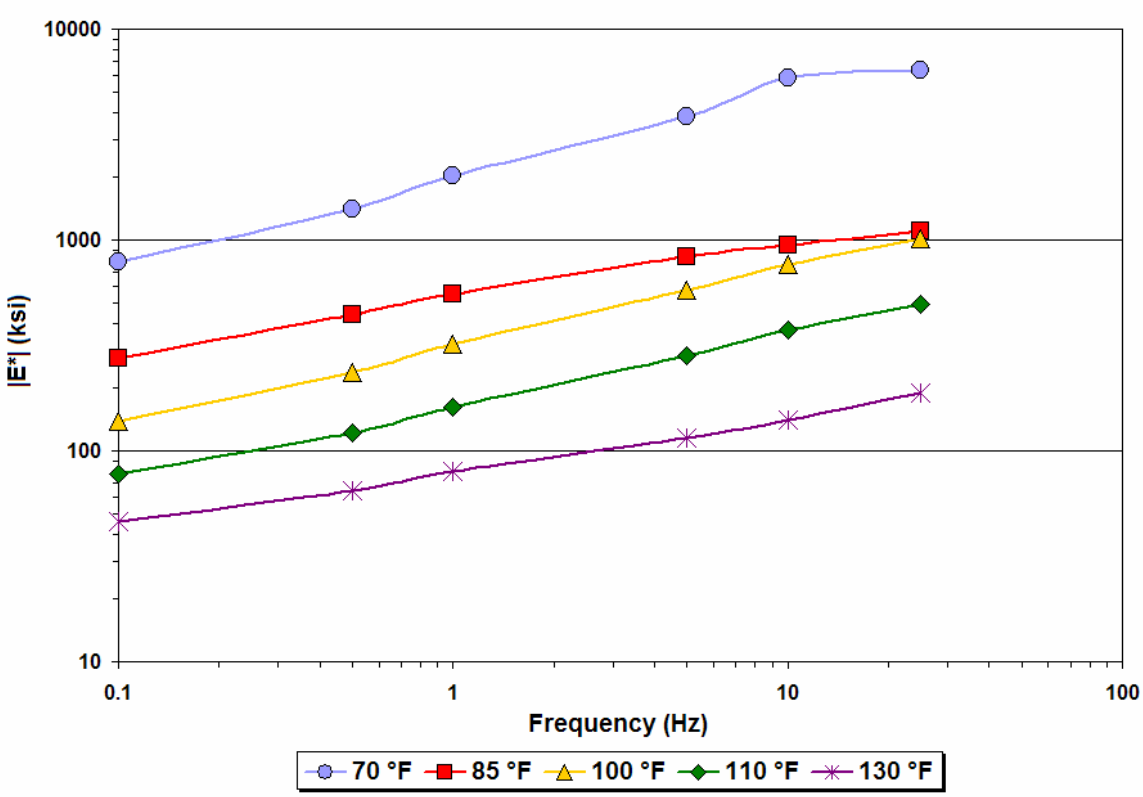

Figure 6.11. Variation of |*E|* with Frequency and Temperature for K7-11 Core.**

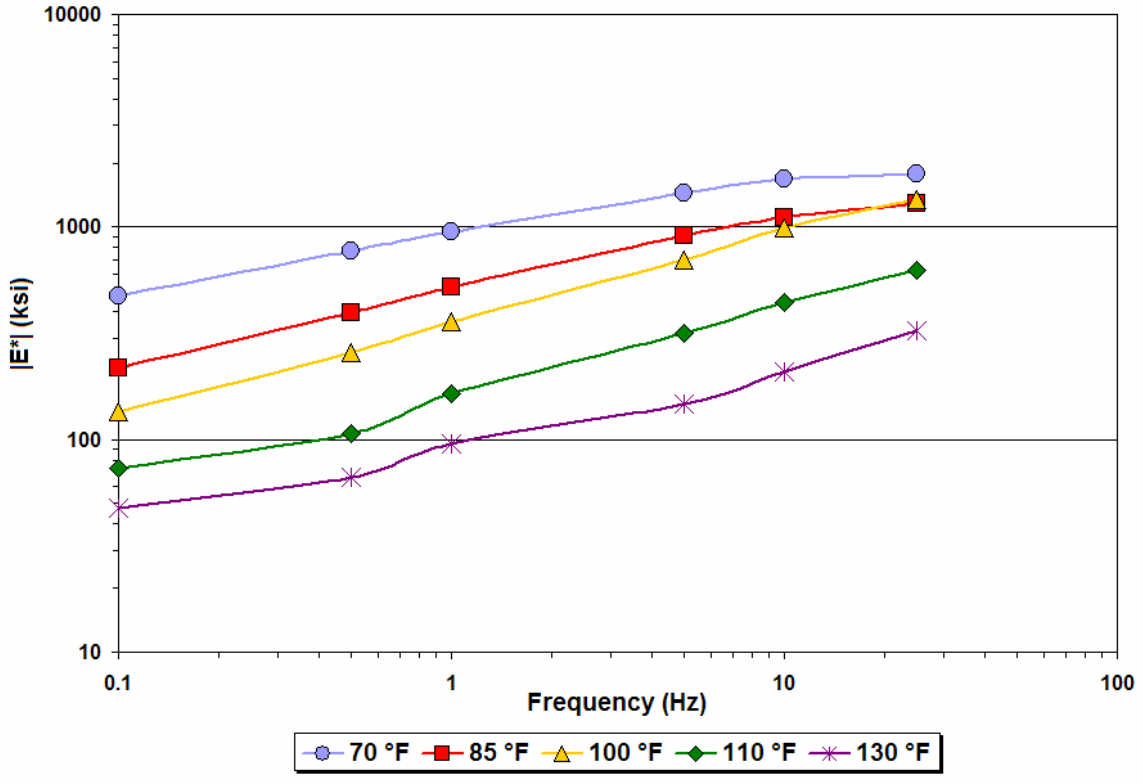

Figure 6.12. Variation of |*E|* with Frequency and Temperature for K7-15 Core.**

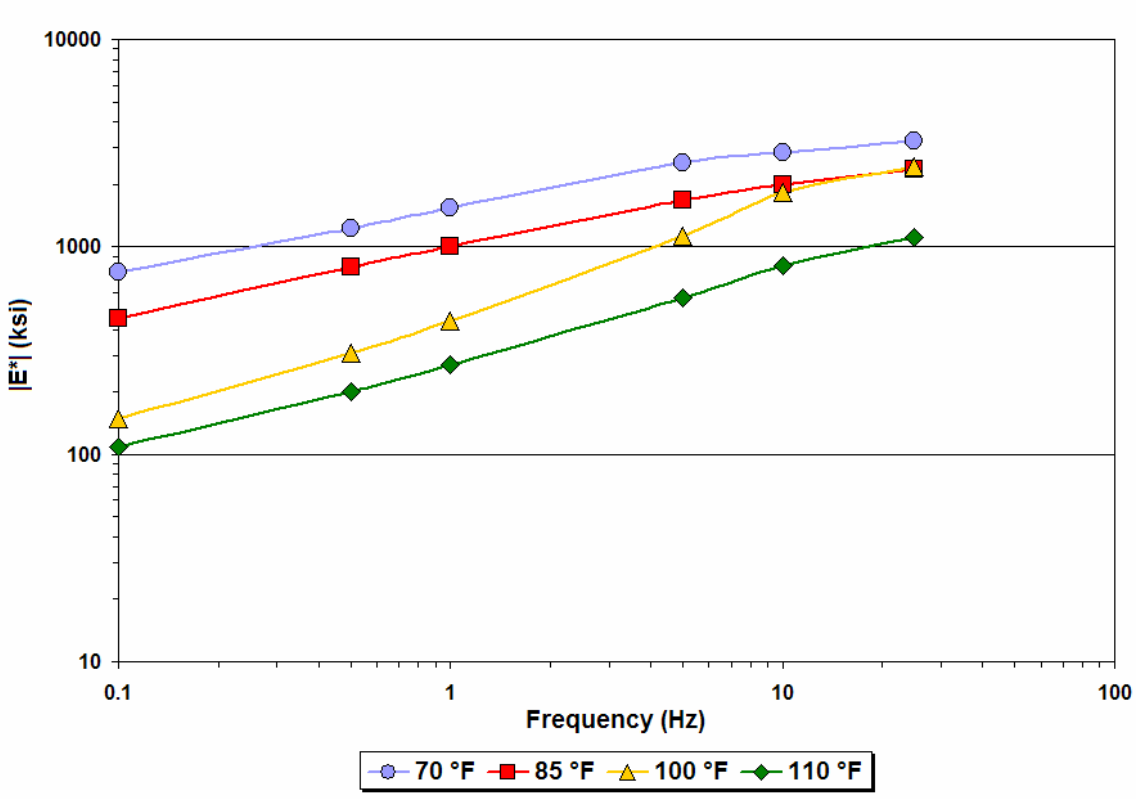

Figure 6.13. Variation of |*E| with Frequency and Temperature for K7-20 Core.**

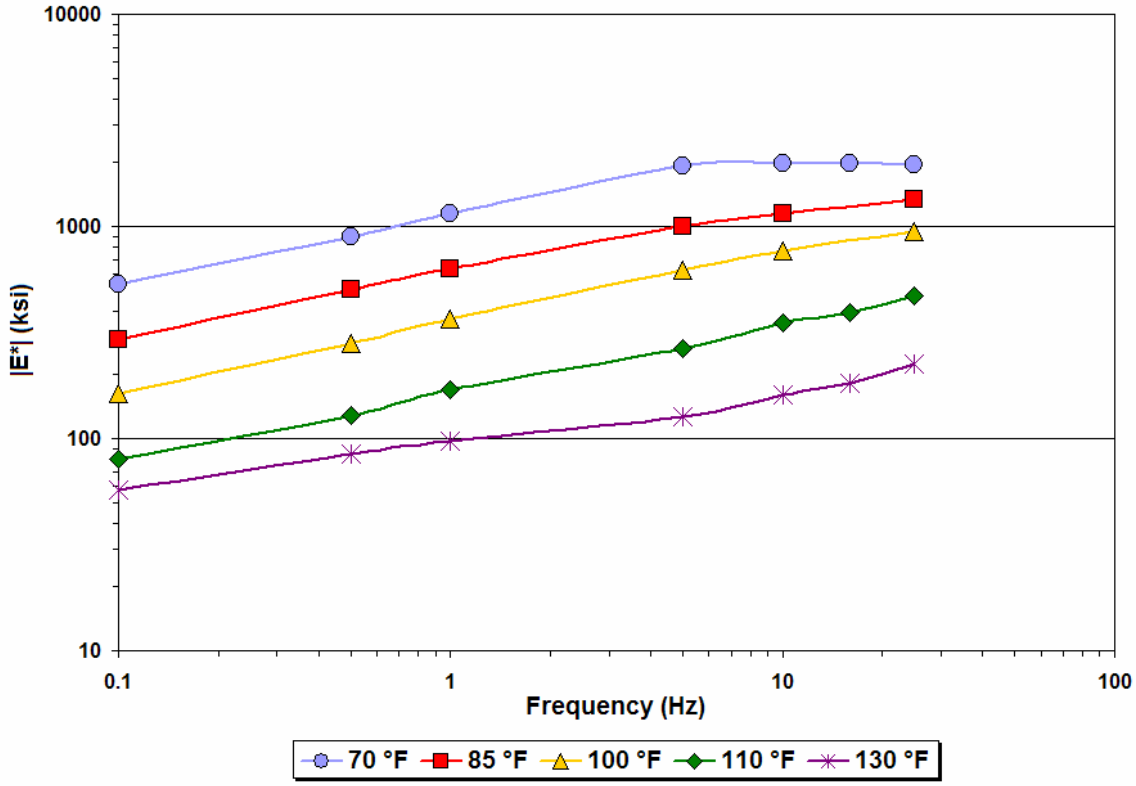

Figure 6.14. Variation of |*E| with Frequency and Temperature for K7-31 Core.**

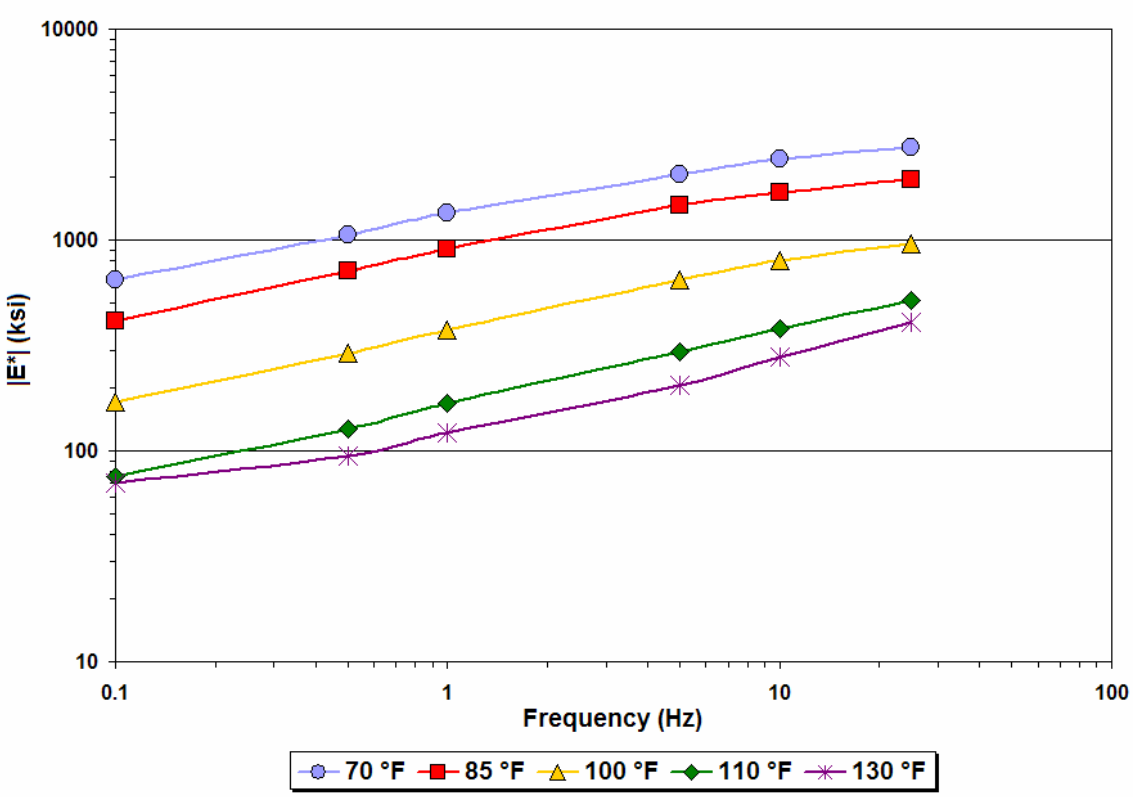

Figure 6.15. Variation of |*E| with Frequency and Temperature for K7-37 Core.**

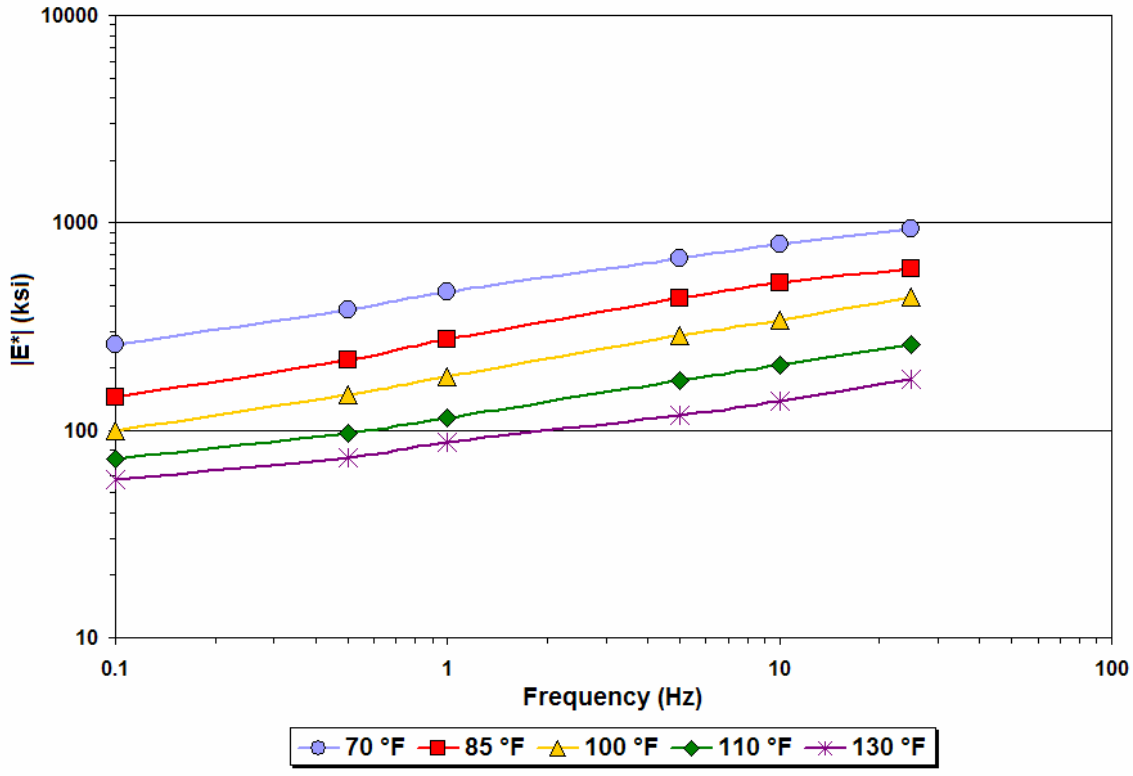

Figure 6.16. Variation of |*E| with Frequency and Temperature for K7-40 Core.**

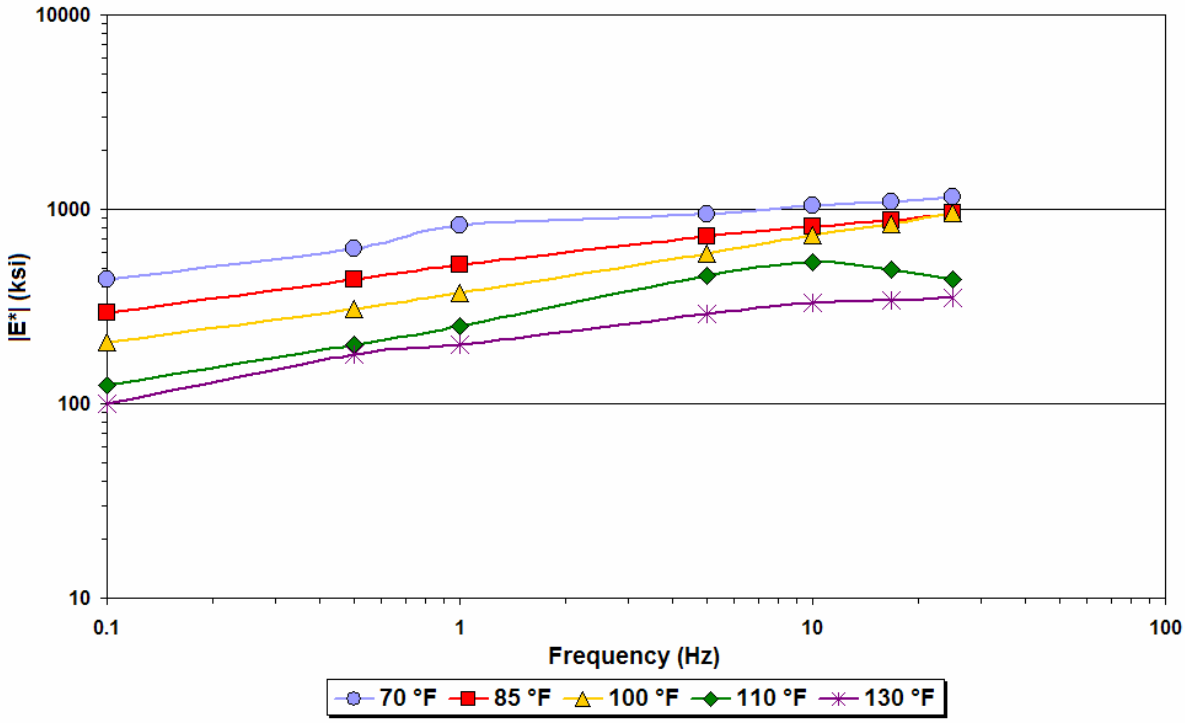

Figure 6.17. Variation of |*E| with Frequency and Temperature for C6 Core.**

$D'(\omega)$ = real part of the complex compliance at the same frequency ω,

$D''(\omega)$ = imaginary part of the complex compliance, and

ϕ = phase angle.

Researchers used the pattern search algorithm (Letto, 1968) with the values of $D'(\omega)$ and $D''(\omega)$ determined from the test data to backcalculate the parameters D_0, D_1 and m of Eqs. (2.2) and (2.3).

Tables 6.3 and 6.4 give the backcalculated creep compliance parameters for the K6 and K7 cores, respectively. Also shown in the tables are the sums of squared errors (SSEs) associated with fitting Eqs. (2.2) and (2.3) to the real and imaginary components of the complex compliance determined from the test data. Charts comparing the predicted and measured components are given in Appendix E.

The m values are expected to increase with test temperature. If the m values given in Tables 6.3 and 6.4 are plotted against temperature, a line fitted to the data does show a positive slope. However, it is interesting to observe from these tables that m tends to drop at the highest temperature of 130 °F for many of the cores tested. This observation may reflect the increased stone-on-stone contact at this test temperature due to binder softening.

Table 6.3. Backcalculated Creep Compliance Parameters for K6 Cores.

FWD Station	Temperature (°F)	D_0	D_1	m	SSE
K6-1	70	1.48E-05	1.76E-04	3.89E-01	2.18E-01
	85	2.69E-11	5.40E-04	4.06E-01	1.68E-01
	100	1.77E-04	1.28E-03	4.29E-01	1.59E-01
	110	3.31E-04	1.39E-03	4.28E-01	5.97E-01
	130	8.68E-04	1.76E-03	5.19E-01	1.46E+00
K6-4	70	4.11E-05	3.47E-04	4.64E-01	2.22E-01
	85	4.89E-05	4.91E-04	4.90E-01	1.52E-01
	100	1.12E-04	1.66E-03	5.31E-01	5.61E-01
	110	3.06E-04	1.24E-03	5.62E-01	1.55E+00
	130	1.27E-04	2.72E-03	3.49E-01	7.72E-01
K6-11	70	2.71E-05	1.97E-04	4.50E-01	2.10E-01
	85	1.16E-04	4.81E-04	5.11E-01	4.40E-01
	100	1.76E-04	1.14E-03	5.17E-01	6.20E-01
	110	2.40E-04	1.88E-03	5.41E-01	7.98E-01
	130	2.69E-11	2.66E-03	2.89E-01	5.43E-01
K6-23	70	3.56E-05	4.58E-04	3.24E-01	1.41E-01
	85	9.64E-05	3.51E-04	3.78E-01	4.26E-02
	100	2.76E-04	1.18E-03	4.27E-01	1.58E-01
	110	4.45E-04	1.69E-03	4.31E-01	2.29E-01
	130	8.31E-04	1.65E-03	4.69E-01	1.12E+00
K6-48	70	1.53E-04	4.01E-04	3.59E-01	4.34E-02
	85	2.05E-04	6.28E-04	3.96E-01	2.47E-01
	100	2.04E-04	6.30E-04	3.99E-01	2.29E-01
	115	3.08E-04	8.23E-04	4.41E-01	7.68E-01
	130	2.69E-11	2.13E-03	3.72E-01	8.33E-01

Table 6.4. Backcalculated Creep Compliance Parameters for K7 Cores.

FWD Station	Temperature (°F)	D_0	D_1	m	SSE
K7-11	70	2.69E-11	1.72E-04	4.08E-01	1.74E-01
	85	9.01E-05	4.79E-04	4.81E-01	1.87E-01
	100	8.74E-05	1.00E-03	5.42E-01	5.60E-01
	110	2.97E-04	1.53E-03	5.84E-01	1.10E+00
	130	7.75E-04	2.36E-03	5.18E-01	1.22E+00
K7-15	70	4.31E-05	2.58E-04	3.99E-01	1.55E-01
	85	5.91E-05	5.41E-04	4.41E-01	1.51E-01
	100	6.85E-05	6.51E-04	4.86E-01	7.87E-01
	110	1.47E-04	1.73E-03	4.96E-01	3.90E-01
	130	2.69E-11	3.26E-03	3.60E-01	4.06E-01
K7-20	70	1.57E-05	1.93E-04	3.93E-01	1.85E-01
	85	3.95E-05	3.25E-04	5.28E-01	4.43E-01
	100	3.39E-05	8.89E-04	6.61E-01	5.71E-01
	110	3.92E-05	1.35E-03	5.24E-01	3.32E-01
K7-31	70	1.25E-05	2.53E-04	3.50E-01	2.86E-01
	85	7.86E-05	3.75E-04	4.39E-01	1.52E-01
	100	1.02E-04	8.12E-04	4.93E-01	1.53E-01
	110	3.72E-04	1.17E-03	7.14E-01	2.13E+00
	130	3.71E-04	8.10E-04	9.88E-01	3.64E+00
K7-37	70	5.90E-06	1.15E-04	4.39E-01	2.73E-01
	85	2.60E-05	2.90E-04	4.63E-01	1.26E-01
	100	1.05E-04	9.87E-04	4.79E-01	9.33E-02
	110	1.31E-04	1.09E-03	5.78E-01	1.99E+00
	130	3.25E-04	2.90E-03	4.32E-01	6.60E-01
K7-40	70	1.05E-04	4.48E-04	3.65E-01	9.51E-02
	85	9.53E-05	8.22E-04	3.81E-01	2.08E-01
	100	2.69E-11	1.47E-03	4.02E-01	1.20E+00
	110	6.26E-04	1.15E-03	5.05E-01	1.40E+00
	130	9.70E-04	1.38E-03	5.63E-01	1.85E+00

COMPARISON OF MODULI FROM LABORATORY AND FWD TESTS

It is of interest to compare the AC modulus from tests done on cores in the laboratory with the modulus obtained from static backcalculations of FWD test data. For this comparison, researchers determined the asphalt concrete moduli at a frequency of 16.7 Hz and at the pavement temperatures corresponding to the FWD tests. Figures 6.18 and 6.19 show the laboratory and backcalculated AC moduli for the K6 and K7 core stations, respectively.

It is observed that there is generally good agreement between the laboratory and backcalculated AC moduli, particularly on K7. However, the differences are comparatively larger on the K6 stations, particularly on K6-48, where the backcalculated AC moduli are much lower than the values determined from laboratory testing. This station is located along SH4 in the downtown area of Brownsville, where as noted previously, Pharr District personnel had problems getting intact cores. Figures 6.20 and 6.21 illustrate materials recovered during coring at the vicinity of stations K6-45 and K6-50, respectively. Researchers note that the cores broke at the bottom lift, which appears to be weak as evidenced in the thinning due to loss of material during coring. The presence of this weak lift seems consistent with the lower backcalculated moduli, not only on K6-48 but at the other stations along the K6 lane of SH4 in the downtown area.

On the other hand, Figure 6.22 shows the intact core obtained at the vicinity of station K6-48. The darker lift in this picture (second from the bottom) appears to be of the same mix as the bottom lift shown in Figure 6.20. However, the core held together during coring and appears to be sound. Researchers note that the coring crew attempted to take an additional core about 12 ft from the sidewalk curb at the same vicinity but the core broke. These observations suggest that the FWD and laboratory data might be reflecting differences in the materials tested, possibly due to construction variability. It is also noted that the laboratory data are specific to the K6-48 core. In the opinion of the researchers, the FWD data are probably more indicative of the pavement condition along the K6 lane of SH4 in the downtown area.

Similar to the comparisons made in Chapter V between the dynamic and static AC moduli from FWD tests, the relationship between the laboratory modulus E_{lab} and the corresponding modulus from static backcalculations was evaluated as follows:

$$log_{10}(E_{static}) = \beta_0 + \beta_1 log_{10}(E_{lab}) \quad (6.4)$$

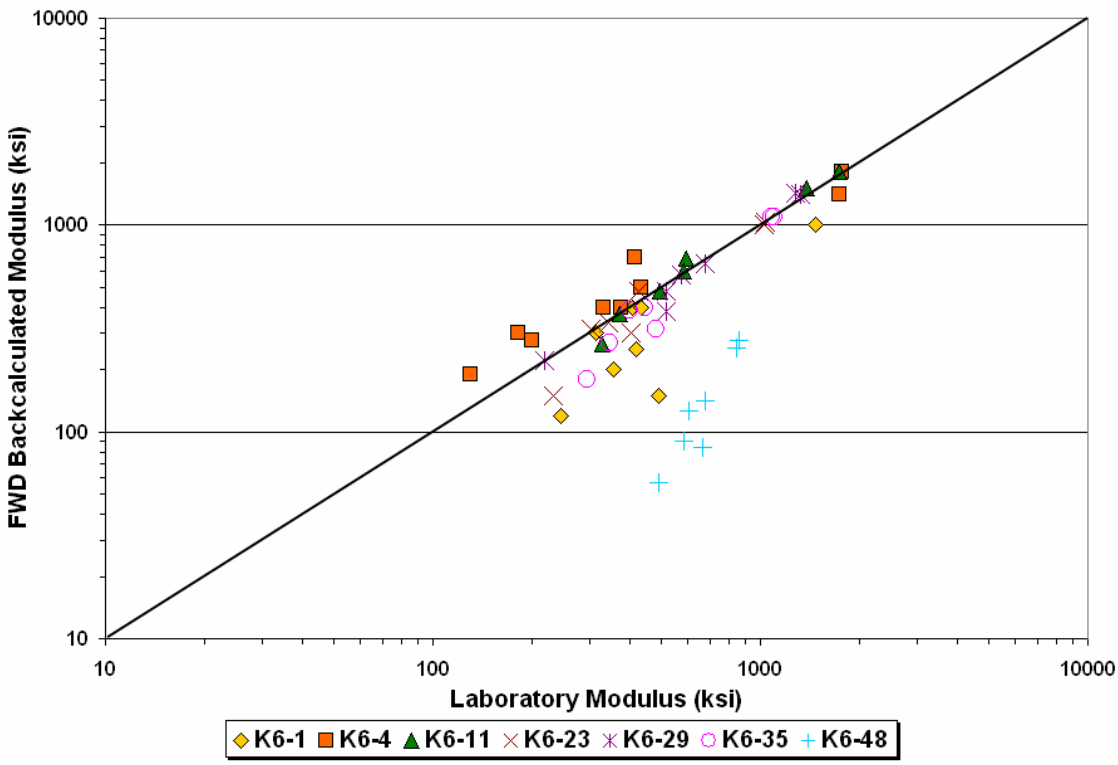

Figure 6.18. Comparison of Backcalculated Modulus from Static Analysis with Laboratory Test Modulus (K6 Stations).

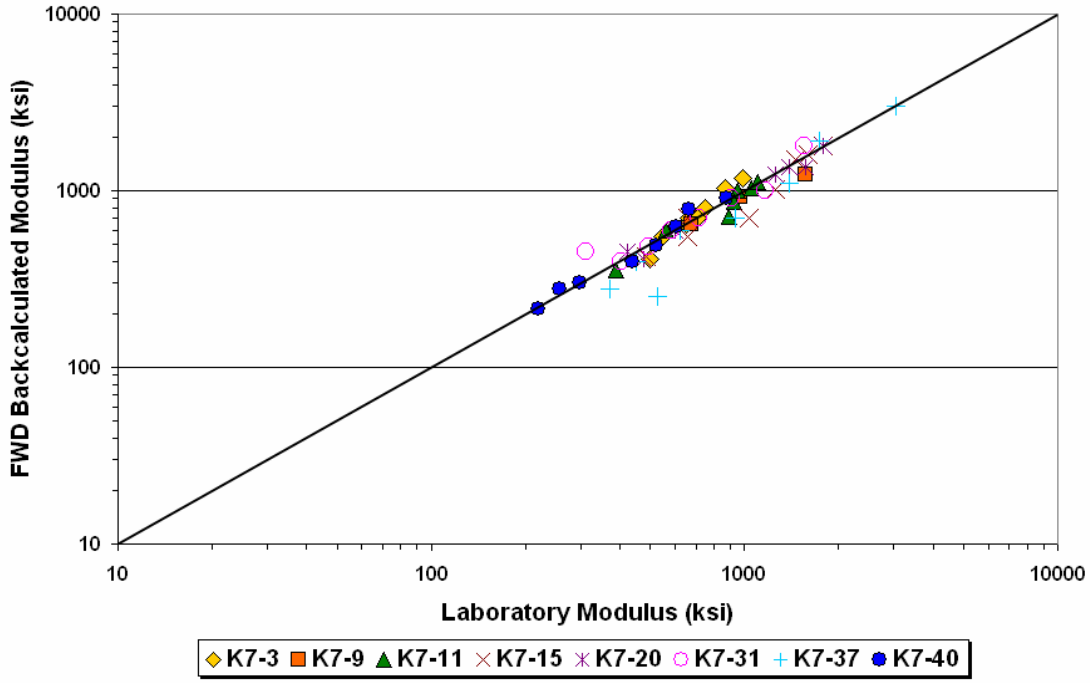

Figure 6.19. Comparison of Backcalculated Modulus from Static Analysis with Laboratory Test Modulus (K7 Stations).

Figure 6.20. Piece of Broken Core Taken from Vicinity of K6-45.

Figure 6.21. Piece of Broken Core Taken from Vicinity of K6-50.

Figure 6.22. Intact Core Taken from Vicinity of K6-48.

In this evaluation, researchers excluded the data from K6-48 since the results appear to reflect differences in the materials tested and are, thus, not comparable.

The results from regression analysis showed β_0 to be not statistically significant. Consequently, researchers fitted Eq. (6.4) to the data but with β_0 set to zero and obtained the following relationships:

K6: $$log_{10}(E_{static}) = 0.987\ log_{10}(E_{lab}) \quad (6.5)$$

K7: $$log_{10}(E_{static}) = 0.993\ log_{10}(E_{lab}) \quad (6.6)$$

The standard errors of the estimate of the above equations are 0.135 and 0.070 for K6 and K7, respectively. Note that the β_1 coefficients are close to unity, reflecting the good correspondence between the logarithms of the AC moduli from laboratory tests and from static backcalculations of FWD deflections.

CHAPTER VII. TEMPERATURE CORRECTION OF BACKCALCULATED ASPHALT CONCRETE MODULUS

PREDICTION OF PAVEMENT TEMPERATURES

Since FWD data were collected at different times along SH4/48, researchers initially examined the temporal variation of the backcalculated AC moduli to look for evidence of pavement damage that can be inferred from the backcalculated values. To examine the temporal variations, it is necessary to correct the backcalculated moduli to a standard or reference temperature. This correction requires the pavement temperatures corresponding to the FWD measurements. To predict pavement temperatures, researchers used the Texas-LTPP equation developed in TxDOT Project 0-1863 by Fernando, Liu and Ryu (2001). This equation is a modification of the BELLS2 and BELLS3 equations developed by Lukanen et al. (1998) in a research project sponsored by the Federal Highway Administration. In that project, researchers used pavement temperature data collected on 41 seasonal monitoring program (SMP) sites in North America to develop BELLS2 and BELLS3. In Project 0-1863, TTI researchers evaluated these equations and came up with a modified form of an equation for predicting pavement temperature that was specifically calibrated to temperature data from SMP sites in Texas, New Mexico and Oklahoma. This work resulted in the Texas-LTPP equation that is given by:

$$\begin{aligned} T_d = {} & 6.460 + 0.199\,(IR+2)^{1.5} + \log_{10}(d) \times \{ -0.083\,(IR+2)^{1.5} - 0.692 \sin^2(hr_{18} - 15.5) \\ & + 1.875 \sin^2(hr_{18} - 13.5) + 0.059\,(T_{1\text{-day}} + 6)^{1.5} \} \\ & - 6.784 \sin^2(hr_{18} - 15.5) \sin^2(hr_{18} - 13.5) \end{aligned} \quad (7.1)$$

where,

T_d = pavement temperature at depth, d, within the asphalt layer, °C;

IR = surface temperature measured with an infrared temperature gauge, °C;

d = depth at which temperature is to be predicted, mm;

$T_{1\text{-day}}$ = the average of the previous day's high and low air temperatures, °C; and

hr_{18} = time of day in the 24-hour system but calculated using an 18-hour asphalt temperature rise and fall time as explained by Stubstad et al. (1998).

Researchers used Eq. (7.1) to predict the pavement temperature at mid-depth on each FWD station, using the infrared surface temperatures taken with a calibrated gauge at the time

of the survey. The Texas Office of the State Climatologist at Texas A&M University provided the previous day's high and low air temperatures for the Brownsville area corresponding to the different times FWD surveys were conducted. Tables 7.1 and 7.2 summarize the predicted pavement temperatures at the FWD stations established on the K6 and K7 lanes, respectively.

VARIATION OF BACKCALCULATED AC MODULI WITH TEMPERATURE

Figures 7.1 to 7.15 show the variation of the backcalculated AC moduli with the predicted pavement temperatures. Due to the large number of stations analyzed (106 stations), results are only exhibited for stations where researchers took cores. These stations were selected to show comparisons between the backcalculated AC moduli and corresponding values determined from dynamic modulus testing in the laboratory. Note that the pavement temperatures corresponding to the FWD tests are not necessarily the same as the temperatures used for the dynamic modulus tests described in Chapter VI. Thus, the laboratory values plotted in Figures 7.1 to 7.15 were determined by interpolation from the moduli obtained at the temperatures selected for dynamic modulus testing. From these figures, it is observed that the agreement between the field and laboratory test results is generally good. There are a couple of stations, 6-1 and 6-48, where significant discrepancies are observed between the field and laboratory moduli but overall, the agreement for the other stations is quite acceptable, in the opinion of the authors.

Note that station 6-48 is located in the downtown area along SH4 where difficulty was encountered in getting intact cores. As noted in Chapter III, the asphalt mix in this area tended to disintegrate during coring. The low backcalculated moduli shown in Figure 7.7 appear more in line with this observation than the corresponding values from dynamic modulus testing of the core taken from the vicinity of this station. In general, Pharr District personnel had to core more than once around the vicinity of each FWD station located in the downtown area before they could obtain an intact core. The test results shown in Figure 7.7 may be indicative of differences between the asphalt material at the FWD station and at the location where the intact core was taken.

Table 7.1. Predicted Pavement Temperatures (°F) on the K6 Lane.

FWD station	2001				2002*			2003*	
	Feb	May	July	Aug	Mar	July	Dec	Apr	Sep
6-1	88	99	110	119	101	102	80	100	107
6-2	79	97	110	118	101	103	80	99	106
6-3	78	98	109	117	101	103	81	100	104
6-4	80	101	113	123	101	105	79	102	110
6-5	79	99	110	118	101	103	80	100	105
6-6	79	99	110	118	101	104	80	100	106
6-7	80	100	112	119	101	105	79	101	108
6-8	80	99	110	117		104	80	100	105
6-9	82	102	112	122					
6-10	81	101	112	120	101	106	79		
6-11	82	101	114	118	101	106	79		
6-12	82	101	114	118	101	106	79		
6-13	82	101	114	118	101	106	79		
6-14	80	102	114	120	101	107	80		
6-15	80	102	114	120	101	107	80		
6-16	80	101	113	119	101	106	80		
6-17	80	101	113	119	101	106	80		
6-18	80	103	115	121	101	109	80		
6-19	80	103	114	120	102	108	80		
6-20	82	102	114	120	101	108	81		
6-21	82	102	112	119	101	108	80		
6-22	82	102	112	119	101	108	80		
6-23	82	103	113	122	101	108	80		
6-24	81	101	111	118	101	106	81		
6-25	81	101	111	118	100	106	80		
6-26	81	101	111	118	101	106	81		
6-27	82	102	112	120	101	106	80		
6-28	82	102	112	120	101	106	80		
6-29	84	103	113	120	101	106	80		
6-30	84	103	113	120	101	106	80		
6-31	84	104	116	123	103	109	80		
6-32	82	101	112	119	102	107	81		
6-33	85	106	116	126	102		80		
6-34	85	107	117	125	102	112	80		
6-35	84	105	114	122	102	108	81		
6-36	84	104	114	123	102	108	81		
6-37	83	104	114	121	102	108	81		
6-38	86	106	116	125	102	111	80		
6-39	83	103	112	119	102	109	81		
6-40	82	103	113	121	100	107	80		

Table 7.1. Predicted Pavement Temperatures (ºF) on the K6 Lane (cont.).

FWD Station	2001				2002*			2003*	
	Feb	May	July	Aug	Mar	July	Dec	Apr	Sep
6-41	86	106	114	123	101	110	80		
6-42	85	103	113	120	100	109	80		
6-43	86	107	115	125	101	111	80		
6-44	83	103	111	119	101	107	81		
6-45	85	106	113	123	113	112	81		
6-46	87	108	115	125	114	114	80		
6-47	86	108	115	126	102	115	80		
6-48	83	102	111	119	101	109	81		
6-49	81	100	109	116	102	107	82		
6-50	82	103	110	118	102	109	81		
6-51	85	108	115	125	102	115	80		
6-52	84	106	113	122	102	113	81		
6-53	83	102	111	119	101	109	81		
6-54	82	103	111	119	102	110	82		
6-55	82	103	111	120	102	109	82		
6-56	85	105	112	122	118	113	81		

*Shaded cells denote no data available due to construction or maintenance work

Table 7.2. Predicted Pavement Temperatures (°F) on the K7 Lane.

FWD station	2001*			2002*				2003*	
	Feb	May	Aug	Mar	July	Oct	Dec	Apr	Sep
K7-1	83	97	108	91	113	99	77		102
K7-2	82	97	107	91	111	98	78	94	104
K7-3	83	99	108	92	115	99	78	95	104
K7-4	83	98	107	91	112	104	78	95	103
K7-5	84	99	108	92	118	107	78	96	104
K7-6	83	98		91	114	106	78	95	103
K7-7	84	100	108	92	116	107	78	96	105
K7-8	83	99	108						
K7-9	83	99	108						
K7-10	84	101	108	92	116	108	78	96	105
K7-11	83	98	107	91	113		79	95	103
K7-12	84	101	107	92	114		79	96	104
K7-13	89	102	108	92	116	110	78	97	105
K7-14	89	99	108	92	114	107	79	95	104
K7-15	89	99	107	91	112	107	78	95	104
K7-16	89	100	107	91	114	109	78	96	104
K7-17	89	102	108	90	117	110	78	96	105
K7-18	89	101	109	92	117	111	78	96	106
K7-19	89	99	107	92	112	108	79	95	104
K7-20	89		108	92	115	112	78	95	105
K7-21	89	100	108	92	114	108	78	96	105
K7-22	89	101	109	92	113	78	97		105
K7-23	89	101	108	92	113	108	78	97	106
K7-24	89	99	107	92	112	106	78	96	104
K7-25	89	102	109	93	115	108	78	97	106
K7-26	89	101	108	93	113	106	79	97	105
K7-27	89	100	108	93	114	107	79	97	104
K7-28	89	101	108	94	115	108	79	97	105
K7-29	89	100	108	94	108	79	97		104
K7-30	89	101	109	96	116	108	79	98	105
K7-31	89	103	110	98	118	108	79	101	107
K7-32	89	101	109	95	116	108	79	98	106
K7-33	89	103	109	97	116	109	79	100	106
K7-34	91	101	110	94	115	106	79	98	106
K7-35	91	103	108	96	115	109	79	100	106
K7-36	91	102	108	95	116	109	79	99	106
K7-37	91	101	110	94	115	106	79	98	105
K7-38	92	104	110	94	116	107	79	99	108
K7-39	91	101	109	93	114	104	79	97	106
K7-40	91	98	108	93	113	106	79	95	105

Table 7.2. Predicted Pavement Temperatures (°F) on the K7 Lane (cont.).

FWD Station	2001*			2002*				2003*	
	Feb	May	Aug	Mar	July	Oct	Dec	Apr	Sep
K7-41	91	101	108	92	112	105	79	97	105
K7-42	91	102	107	92	111	105	79	97	105
K7-43	91	103	107	93	113	105	79		105
K7-44	91	104	108	94	113	105	79	99	106
K7-45	91	103	108	94	114	107	79	99	101
K7-46	91	108	111	95	118	111	79	102	106
K7-47	92	107	110	94	115	108	79	101	105
K7-48	92	107	110	94	115	108	79	101	104
K7-49	92	108	111	95	118	110	79	101	105
K7-50	93	107	110	95	118	107	78	101	105

*Shaded cells denote no data available due to construction or maintenance work

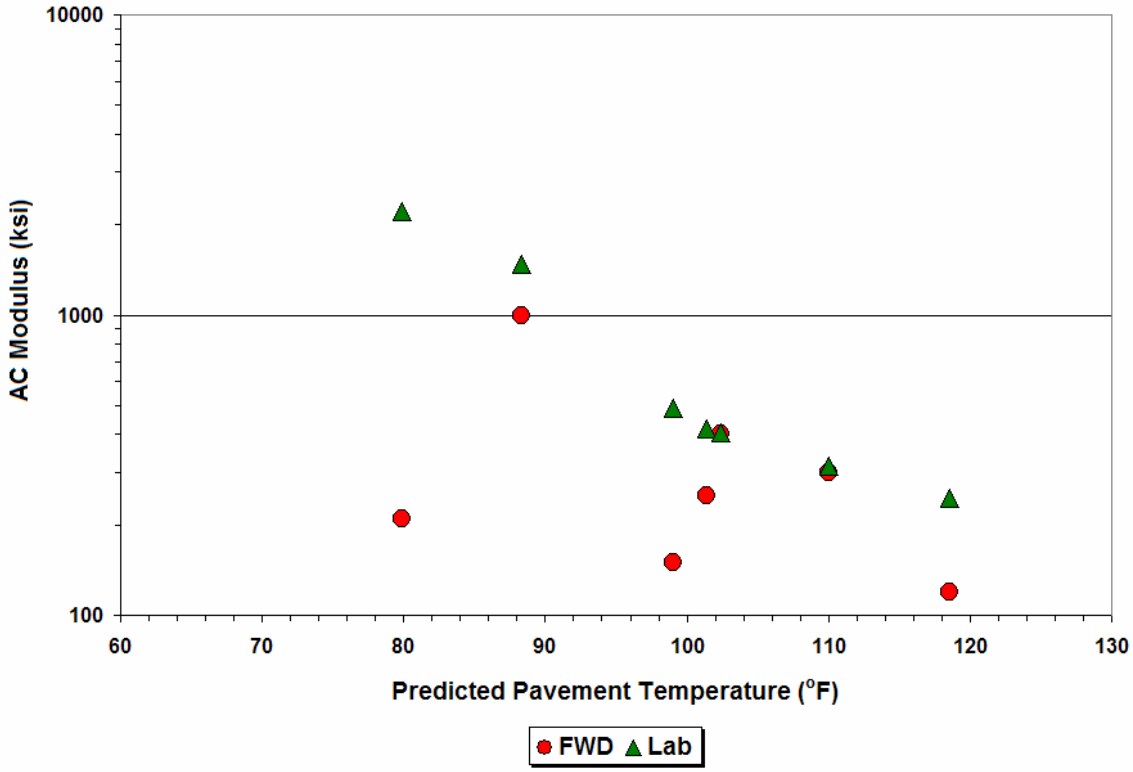

Figure 7.1. Comparison of Backcalculated & Laboratory AC Moduli (Station K6-1).

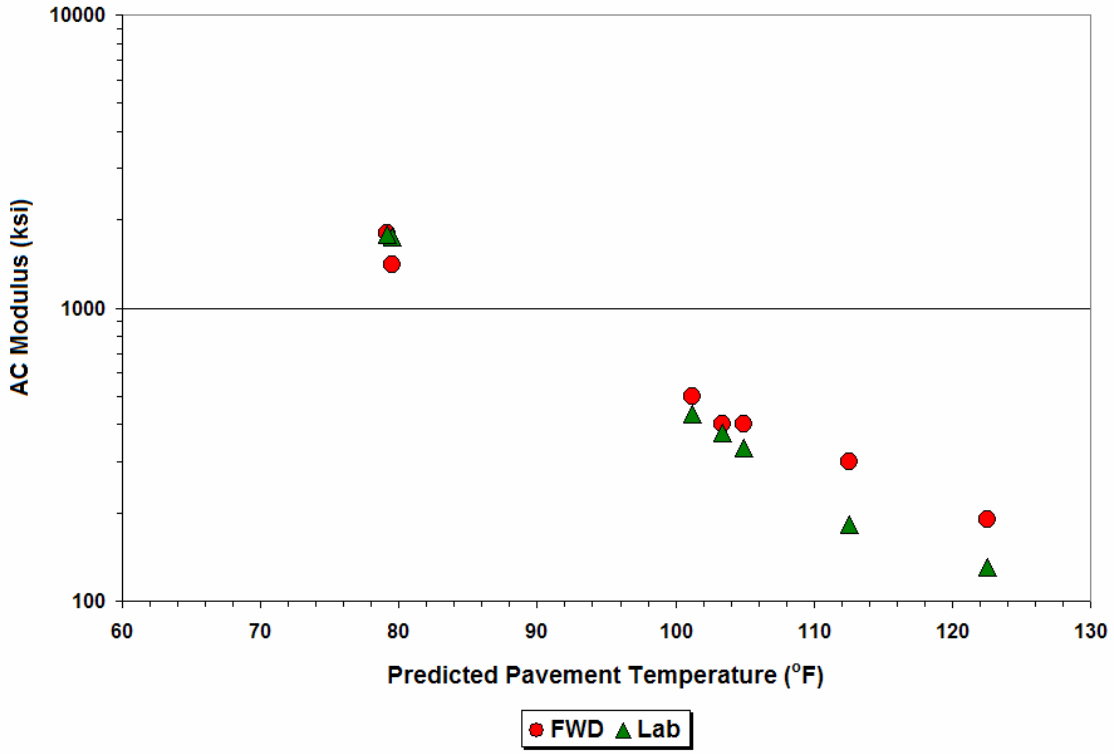

Figure 7.2. Comparison of Backcalculated & Laboratory AC Moduli (Station K6-4).

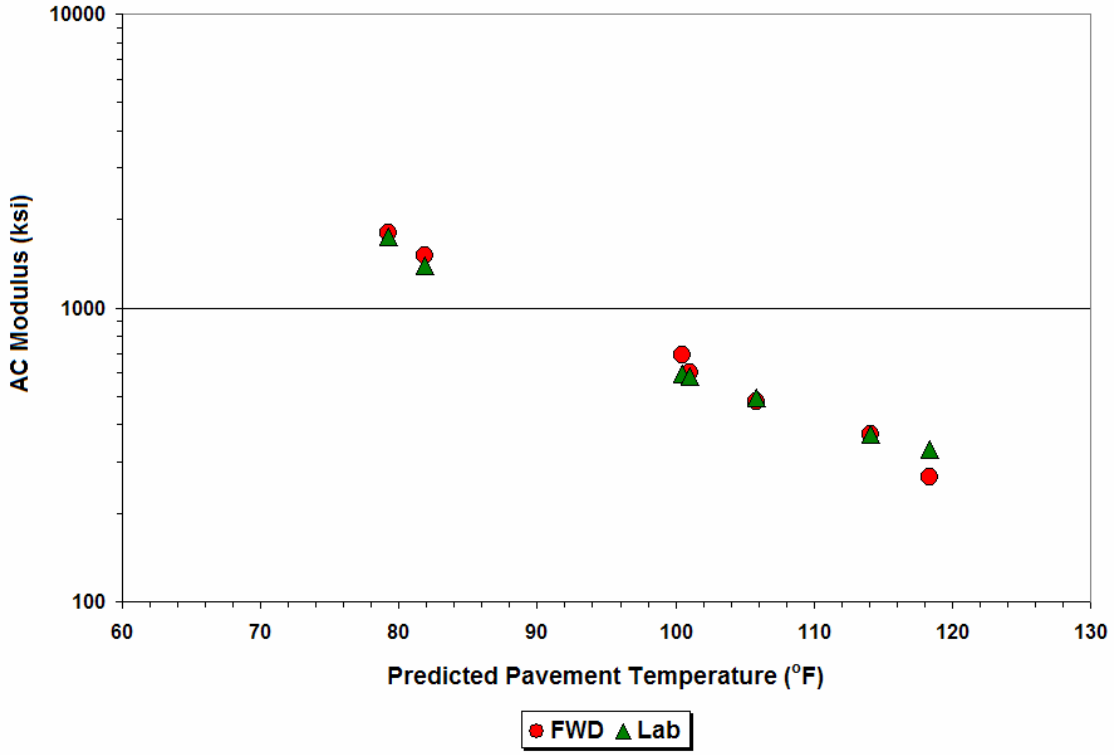

Figure 7.3. Comparison of Backcalculated & Laboratory AC Moduli (Station K6-11).

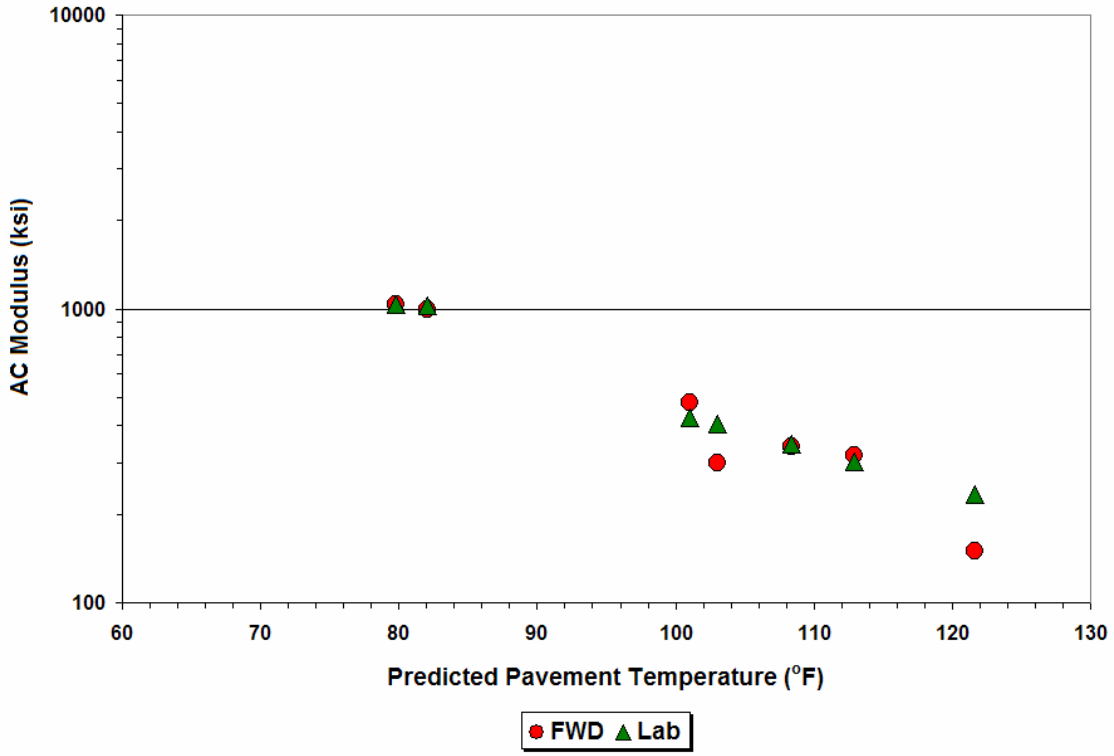

Figure 7.4. Comparison of Backcalculated & Laboratory AC Moduli (Station K6-23).

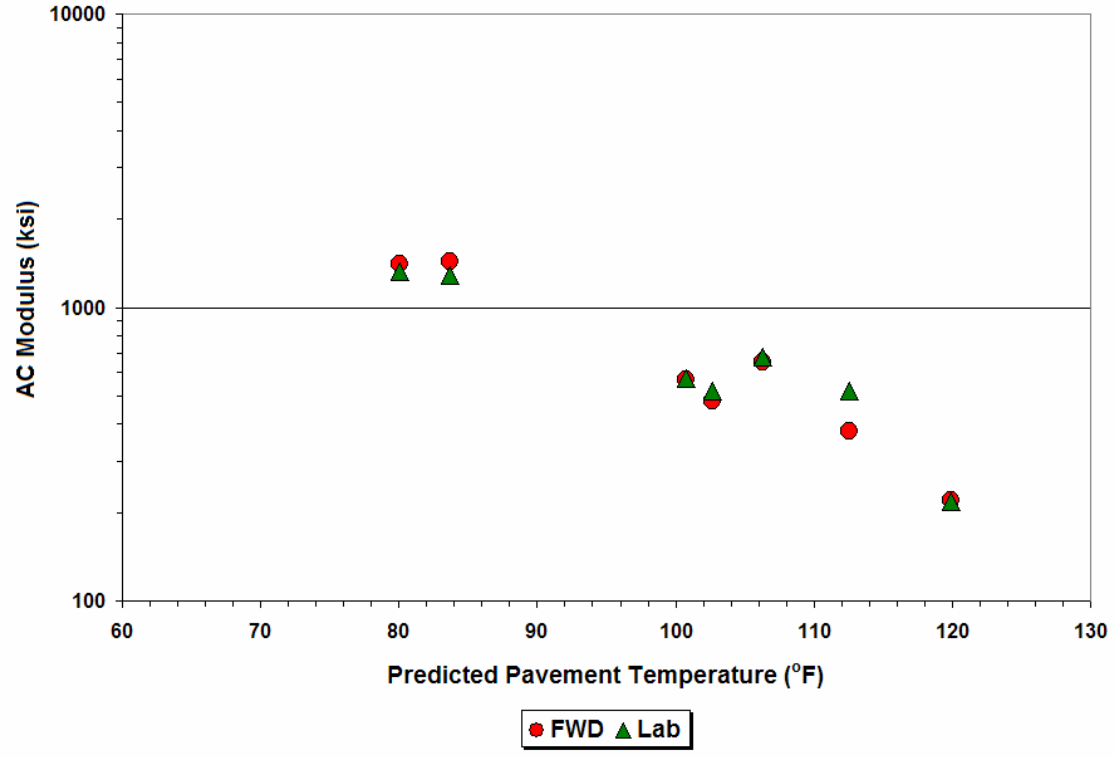

Figure 7.5. Comparison of Backcalculated & Laboratory AC Moduli (Station K6-29).

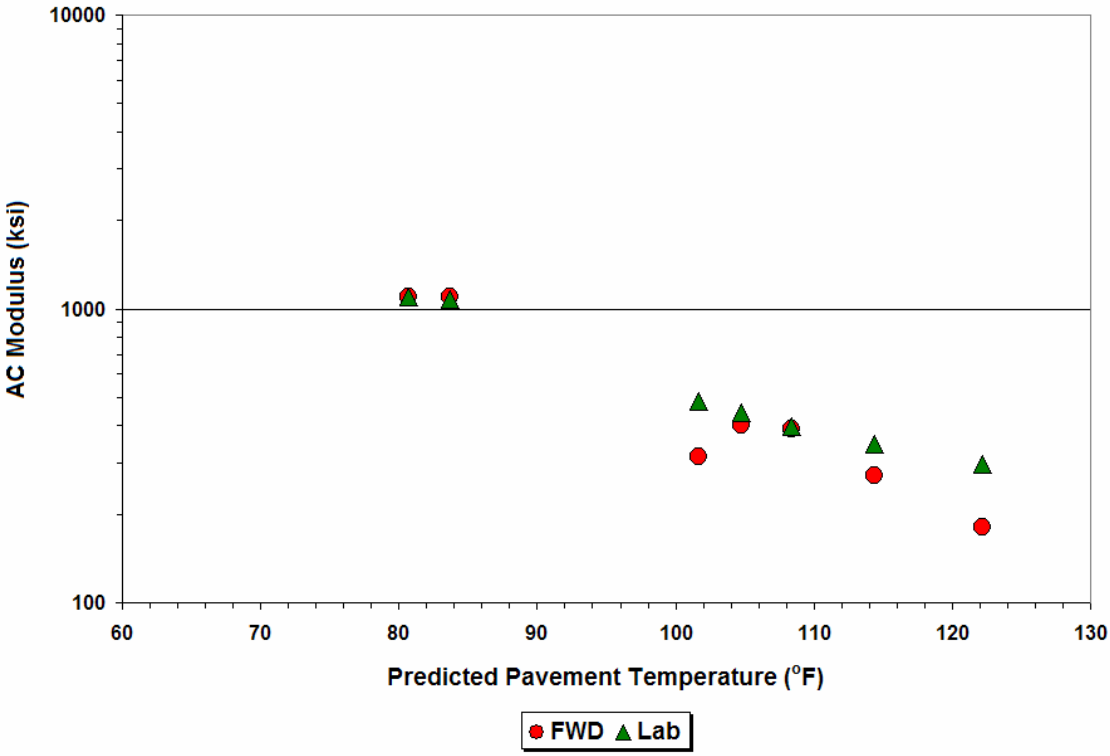

Figure 7.6. Comparison of Backcalculated & Laboratory AC Moduli (Station K6-35).

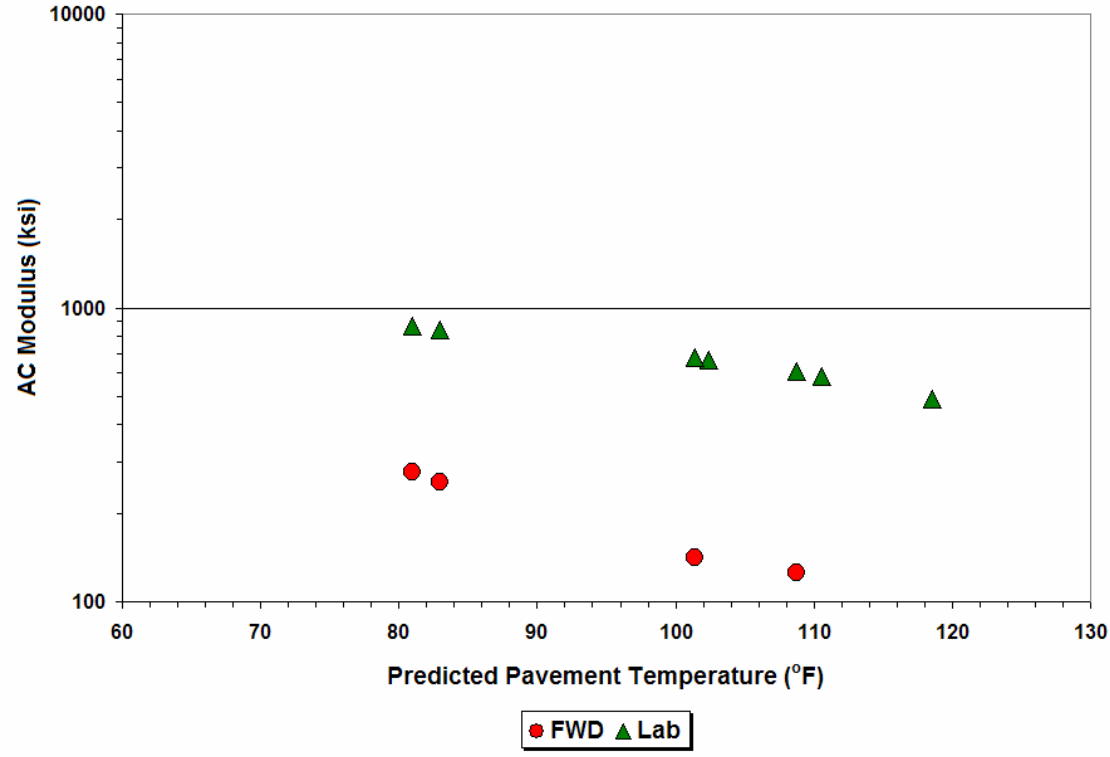

Figure 7.7. Comparison of Backcalculated & Laboratory AC Moduli (Station K6-48).

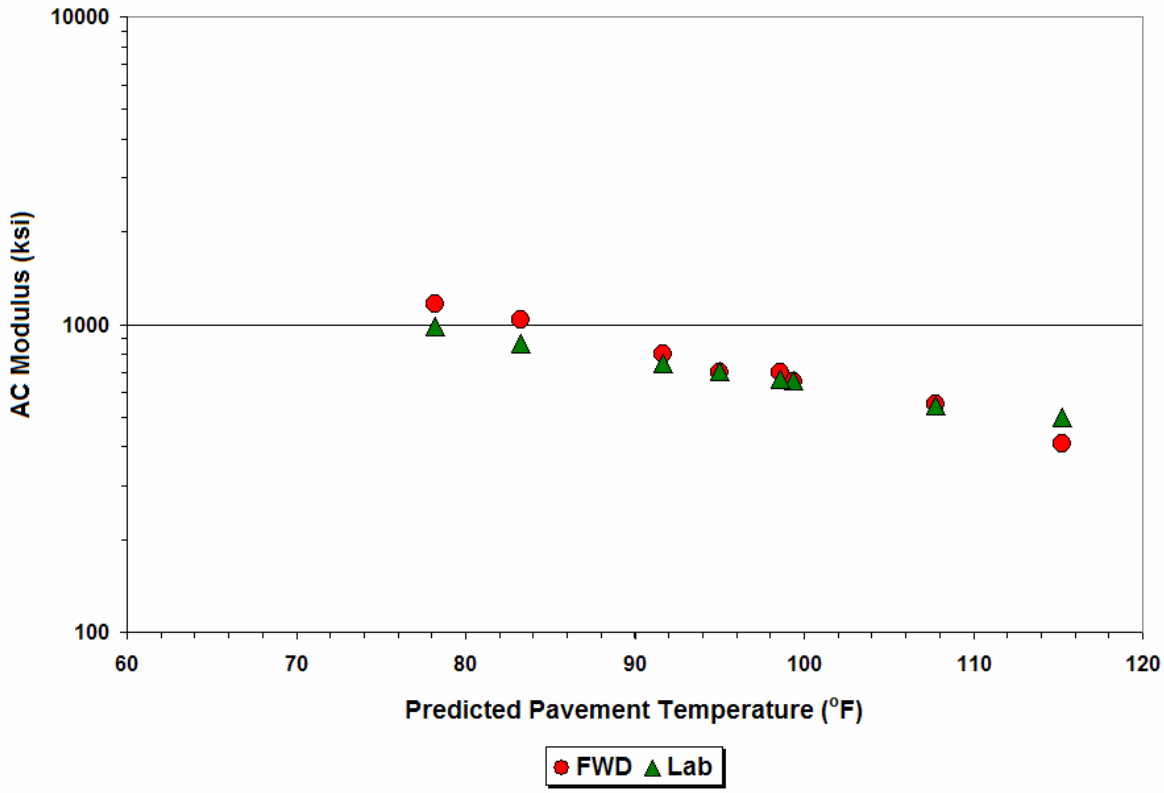

Figure 7.8. Comparison of Backcalculated & Laboratory AC Moduli (Station K7-3).

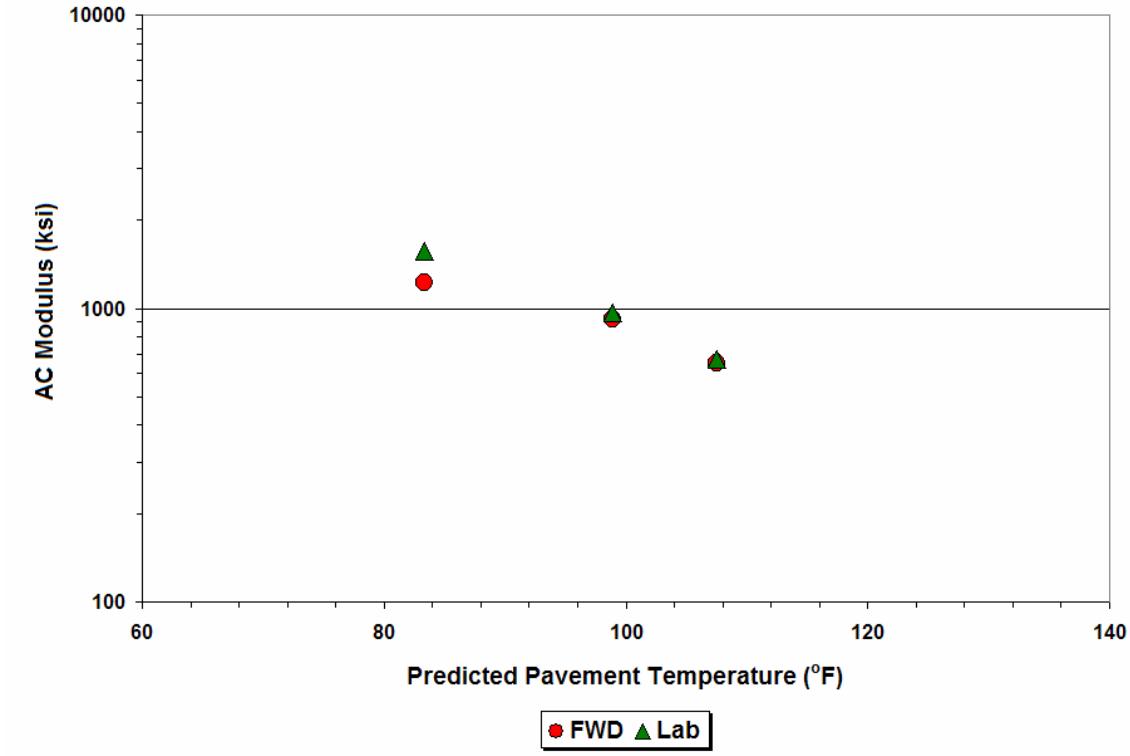

Figure 7.9. Comparison of Backcalculated & Laboratory AC Moduli (Station K7-9).

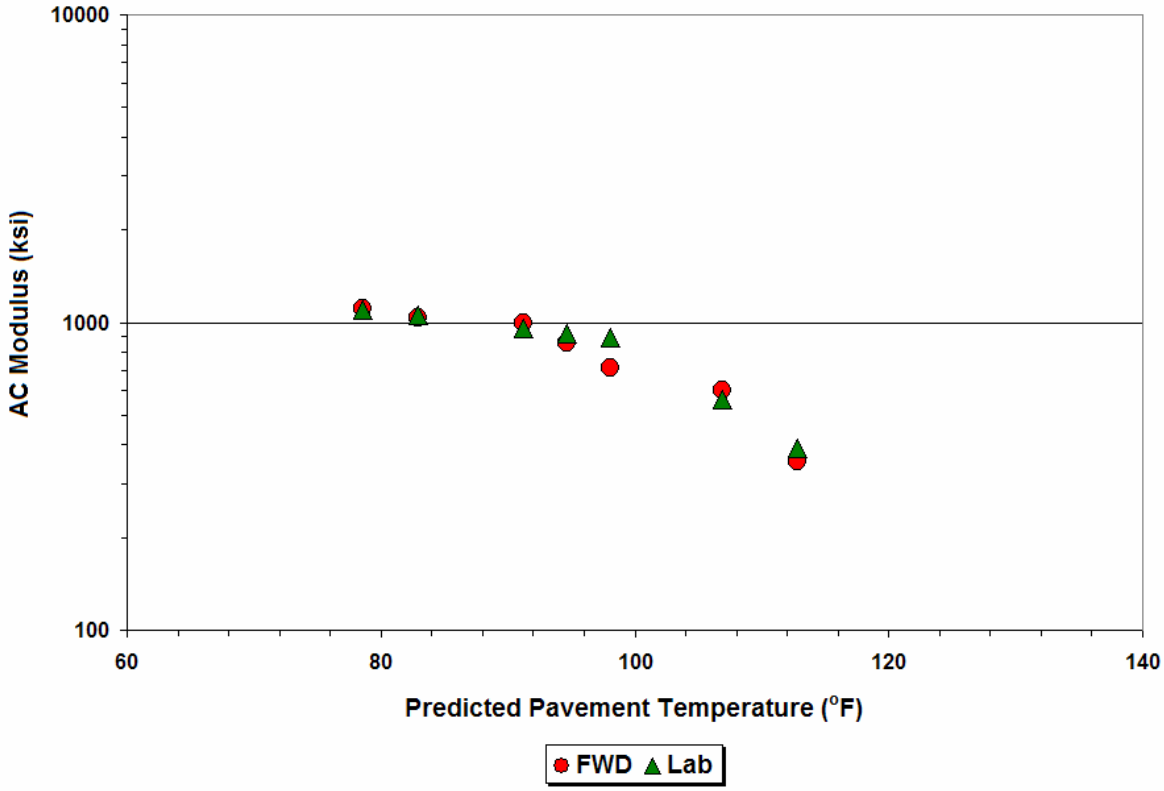

Figure 7.10. Comparison of Backcalculated & Laboratory AC Moduli (Station K7-11).

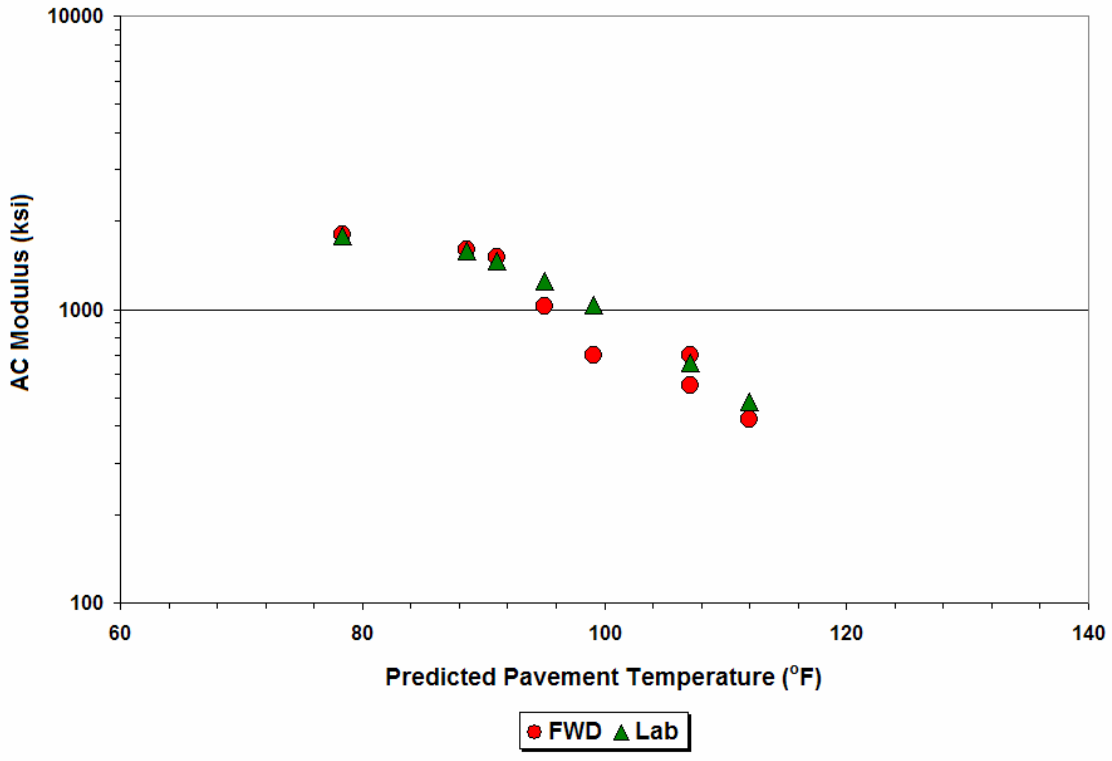

Figure 7.11. Comparison of Backcalculated & Laboratory AC Moduli (Station K7-15).

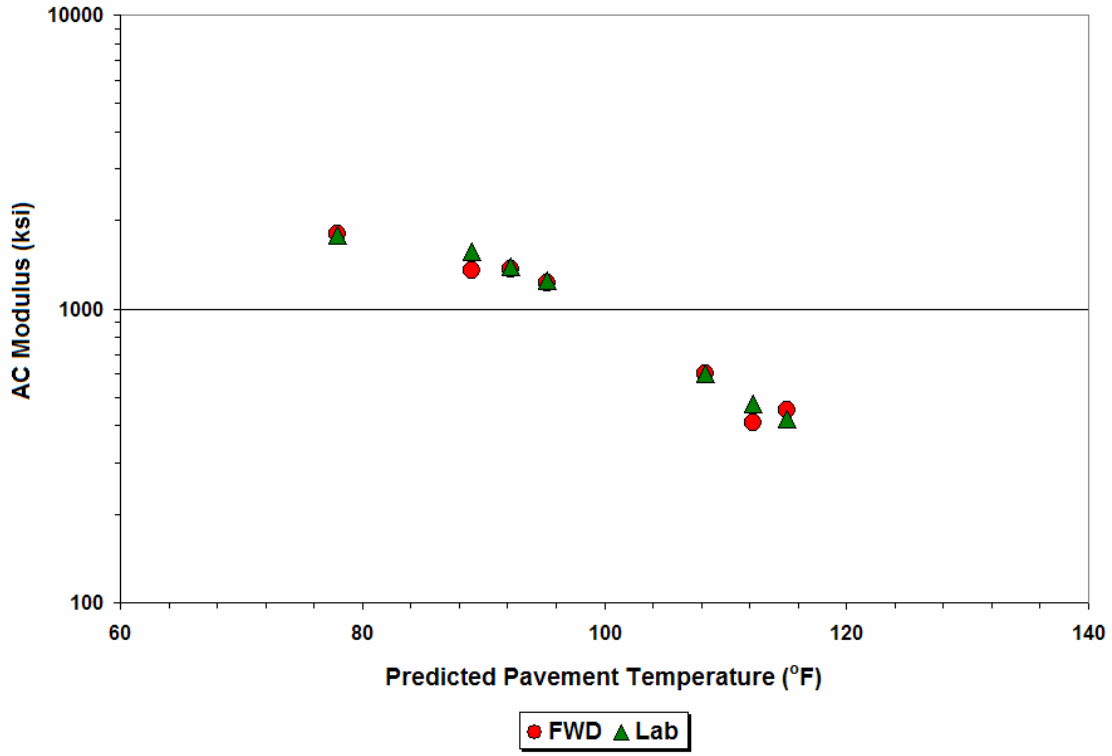

Figure 7.12. Comparison of Backcalculated & Laboratory AC Moduli (Station K7-20).

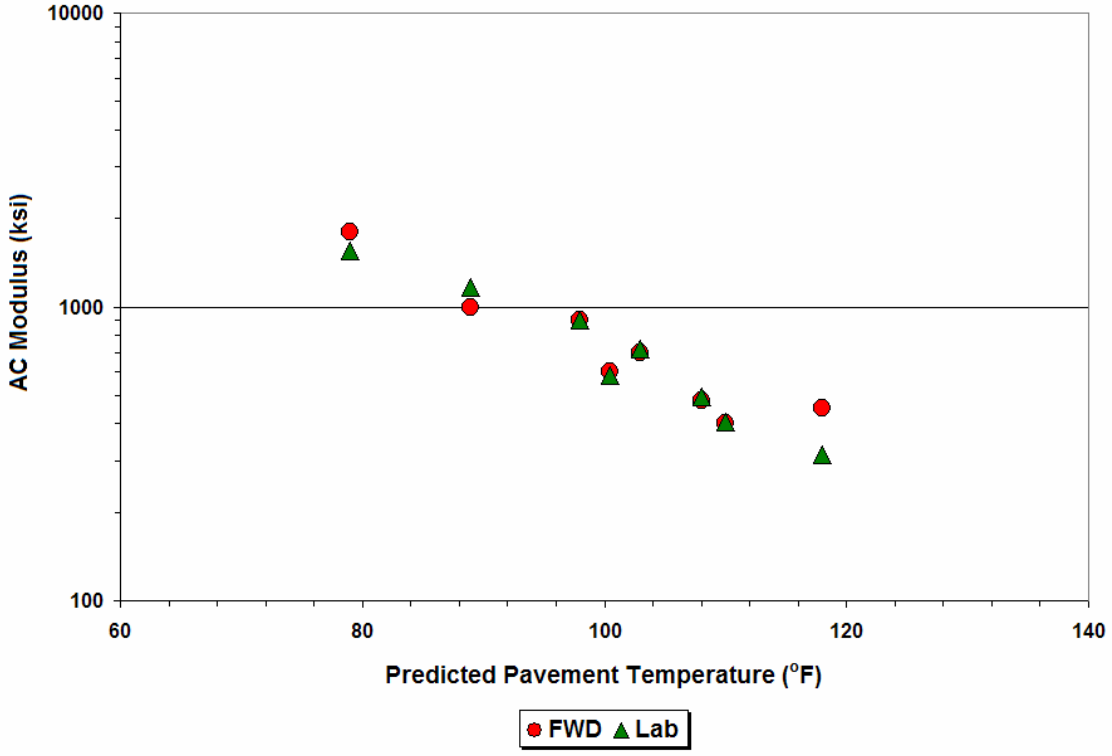

Figure 7.13. Comparison of Backcalculated & Laboratory AC Moduli (Station K7-31).

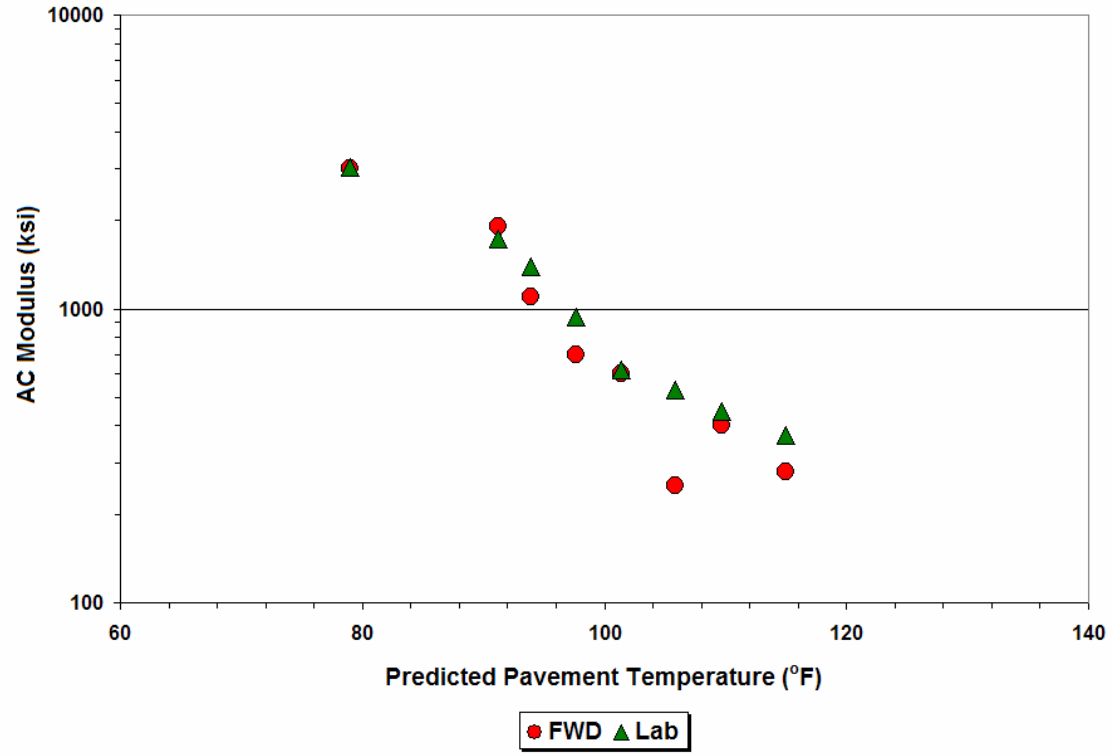

Figure 7.14. Comparison of Backcalculated & Laboratory AC Moduli (Station K7-37).

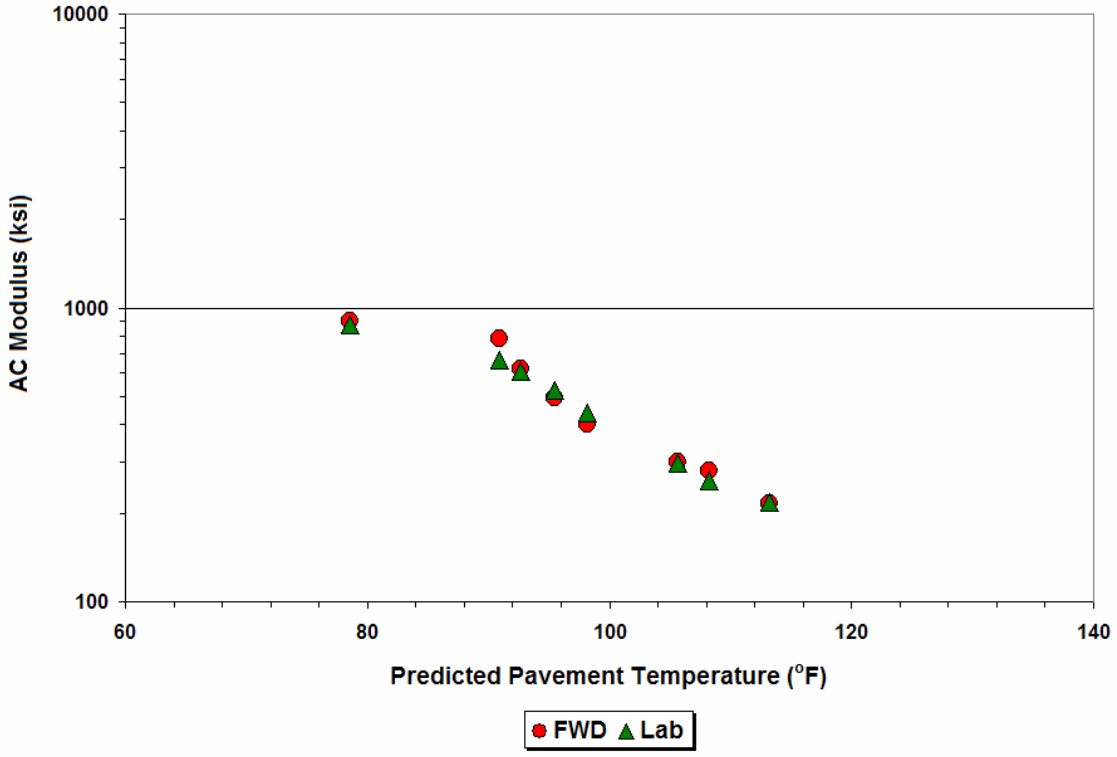

Figure 7.15. Comparison of Backcalculated & Laboratory AC Moduli (Station K7-40).

GROUPING OF FWD STATIONS

To interpret the results from the FWD backcalculations, researchers grouped the FWD stations along the K6 and K7 lanes using the following criteria:

- the physical proximity between FWD stations belonging to a group, and
- similarity in the observed trends between the backcalculated modulus and predicted pavement temperature for FWD stations belonging to the same group.

Application of the above criteria resulted in the formation of the following seven groups on which further evaluations were made:

- Group 1: from FM511 to Coffee Port Road
  - Lane K6: FWD stations 6-1 to 6-15
  - Lane K7: FWD stations 7-1 to 7-15
- Group 2: from Coffee Port to Dunlap Street
  - Lane K6: FWD stations 6-16 to 6-18
  - Lane K7: FWD stations 7-16 to 7-17
- Group 3: from Dunlap to Central Avenue
  - Lane K6: FWD stations 6-19 to 6-23
  - Lane K7: FWD stations 7-18 to 7-21
- Group 4: from Central to Austin Road
  - Lane K6: FWD stations 6-24 to 6-26
  - Lane K7: FWD stations 7-22 to 7-23
- Group 5: from Austin to Fruitdale Road
  - Lane K6: FWD stations 6-27 to 6-36
  - Lane K7: FWD stations 7-24 to 7-33
- Group 6: from Fruitdale to Boca Chica Boulevard
  - Lane K6: FWD stations 6-37 to 6-41
  - Lane K7: FWD stations 7-34 to 7-37
- Group 7: from Boca Chica to Cleveland Street
  - Lane K6: FWD stations 6-42 to 6-56
  - Lane K7: FWD stations 7-38 to 7-50

TEMPERATURE CORRECTION METHODS

Researchers examined the results from the FWD analysis to check for evidence of possible pavement damage that might be discerned from the spatial and temporal variations in the backcalculated asphalt concrete moduli along the route. Since FWD deflections are affected by load and temperature, researchers initially corrected the backcalculated moduli to a common reference temperature to isolate the load effects. For this purpose, temperature corrections were made using the following equations:

- Chen's equation developed from FWD and pavement temperature data collected from TxDOT's Mobile Load Simulator (MLS) investigations (Chen at al., 2000),
- the existing equation used by TxDOT to correct backcalculated AC moduli to a standard temperature of 75 °F, and
- the equation developed by Witczak and Fonseca (1996) that is included as a method for predicting dynamic modulus in the mechanistic-empirical design method developed from NCHRP Project 1-37A.

Researchers then compared the spatial and temporal variations of the corrected AC moduli between the FWD groups to assess the progression of pavement damage along the route. The findings from these comparisons are presented later in this chapter. The equations for temperature correction are presented in the following.

Chen's equation (Chen et al., 2000):

$$E_{T_r} = E_T \times \left(\frac{T}{T_r} \right)^{2.4462} \tag{7.2}$$

where,

E_{T_r} = modulus corrected to a reference temperature of T_r (°F), and

E_T = modulus corresponding to the test temperature T (°F) determined at mid-depth of the asphalt concrete layer.

Existing TxDOT equation based on a standard temperature of 75 °F:

$$E' = \frac{E_T \times T^{2.81}}{185{,}000} \tag{7.3}$$

where,

E' = modulus corrected to a standard temperature of 75 °F, and

E_T = modulus corresponding to the test temperature T (°F).

Witczak–Fonseca equation (1996):

$$\begin{aligned}\log_{10} E = {} & -0.261 + 0.008225\,p_{200} - 0.00000101\left(p_{200}\right)^2 + 0.00196\,p_4 \\ & - 0.03157\,V_a - 0.415\,\frac{V_{beff}}{\left(V_{beff} + V_a\right)} \\ & + \frac{\left[1.87 + 0.002808\,p_4 + 0.0000404\,p_{3/8} - 0.0001786\left(p_{3/8}\right)^2 + 0.0164\,p_{3/4}\right]}{1 + e^{\left(-0.716\,\log_{10} f - 0.7425\,\log_{10}\eta\right)}}\end{aligned} \tag{7.4}$$

where,

E = asphalt mix dynamic modulus, 10^5 psi;

η = bitumen viscosity at a given temperature and degree of aging, 10^6 poises;

f = loading frequency, Hz;

Va = percent of air voids, by volume;

V_{beff} = percent effective binder content, by volume;

$p_{3/4}$ = percent retained on ¾-inch sieve, by total aggregate weight;

$p_{3/8}$ = percent retained on ⅜-inch sieve, by total aggregate weight;

p_4 = percent retained on No. 4 sieve, by total aggregate weight; and

p_{200} = percent passing No. 200 sieve, by total aggregate weight.

Based on Eq. (7.4), Fernando, Liu and Ryu (2001) derived the following relationship for temperature and frequency correction of asphalt concrete modulus:

$$\log_{10} E_R = \log_{10} E_T + \alpha\left[\frac{1}{1 + e^{-\left(B_R + 0.7425\log_{10}\eta_R\right)}} - \frac{1}{1 + e^{-\left(B_T + 0.7425\log_{10}\eta_T\right)}}\right] \tag{7.5}$$

where,

$$\alpha = 1.87 + 0.003\, p_4 + 0.00004\, p_{3/8} - 0.00018\, (p_{3/8})^2 + 0.0164\, p_{3/4} \quad (7.6)$$

$$B_R = 0.716 \log 10\, f_R \quad (7.7)$$

$$B_T = 0.716 \log 10\, f_T \quad (7.8)$$

E_R = AC modulus corrected for the selected reference temperature and loading frequency;

E_T = modulus corresponding to the test temperature T (°F);

η_R = binder viscosity corresponding to the reference temperature, 10^6 poises;

η_T = binder viscosity corresponding to the test temperature, 10^6 poises;

f_R = reference loading frequency, Hz; and

f_T = test frequency, Hz.

Note that Eqs. (7.2), and (7.5) to (7.8) permit the correction to be made for any user-specified reference temperature. In addition, Eqs. (7.5) to (7.8) permit the correction to a reference frequency of loading. Note that Chen's equation does not require AC mixture properties for the correction. This equation was developed for the typical mixtures used in Texas, which were predominantly dense-graded mixes at the time. On the other hand, Eqs. (7.5) to (7.8) require the input of binder and mixture properties, and are applicable for a wider range of asphalt concrete mixes. Note that the binder viscosities corresponding to the test and reference temperatures are used in Eq. (7.5) to adjust the measured or backcalculated modulus to the specified reference temperature. For this purpose, the binder viscosity-temperature relationship is characterized using the following equation from ASTM standard specification D-2493:

$$\log_{10} \log_{10} \eta = A + VTS \log_{10} T_{\circ R} \quad (7.9)$$

where,

η = the binder viscosity, centipoises;

$T_{\circ R}$ = temperature, degrees Rankine; and

A, VTS = model coefficients determined from testing.

In practice, *A* and *VTS* are determined by conducting dynamic shear rheometer (DSR) tests on the binder at a range of temperatures. DSR tests may be conducted at an angular frequency of 10 rad/sec and for a temperature range of 40 to 130 °F. From the binder complex shear modulus G^* and phase angle δ determined at a given temperature, the corresponding binder viscosity is determined from the equation:

$$\eta = \frac{G^*}{10}\left(\frac{1}{\sin\delta}\right)^{4.8628} \qquad (7.10)$$

The binder viscosities determined at the different test temperatures are used in a regression analysis to get the *A* and *VTS* coefficients of Eq. (7.9).

EVALUATION OF MODULUS–TEMPERATURE RELATIONSHIPS

Since FWD data were taken at different times during the project, researchers took the approach of characterizing modulus-temperature relationships using the AC moduli and pavement temperatures determined from the FWD measurements. This same approach was utilized by Fernando, Liu and Ryu (2001) in TxDOT Project 0-1863 to characterize the modulus-temperature relationships of asphalt concrete mixtures found on LTPP test sections. For this task, the authors used the same functional form of the model adopted by Witczak and Fonseca (1996) in developing their dynamic modulus prediction equation (Eq. 7.4). Note that this equation can be expressed in the following form:

$$y = \delta + \frac{\alpha}{1 + e^{(\beta - \gamma x)}} \qquad (7.11)$$

where,

y = $\log_{10} E$;

δ, α = model coefficients that are functions of the volumetric mixture properties;

β = $-0.716 \log_{10} f$;

f = $\frac{1}{2t}$;

t = load duration (secs);

γ = 0.7425; and

x = $\log_{10} \eta$.

The independent variable x in Eq. (7.11) may be expressed as a function of the test temperature using Eq. (7.9). Thus, by nonlinear regression, researchers fitted Eq. (7.11) to the test data from each of the seven FWD groups to get the coefficients A, VTS, δ and α that characterize the temperature dependency of the asphalt mixtures at these locations. In this analysis, a test frequency of 16.7 Hz was used, corresponding to the 30 msec FWD impulse load duration. Tables 7.3 and 7.4 summarize the coefficients determined by researchers, while Tables 7.5 and 7.6 show the analysis of the variance (ANOVA) tables from the regression analyses. The small p values in these tables indicate the strong statistical significance of the relationships determined, as may be observed in Figures 7.16 to 7.29, which compare the predicted backcalculated AC moduli with the values determined from the FWD test data. The fitted curves agree adequately with the trends in the backcalculated moduli, in the researchers' opinion.

It is observed from these figures that the backcalculated AC moduli from the K6 lane are generally lower than the moduli from the corresponding FWD group on the K7 lane. Since K6 and K7 are adjacent lanes, it is not likely that different asphalt concrete mixtures would have been placed on these lanes, particularly for FWD stations that have the same group number. In the authors' opinion, the differences in the backcalculated AC moduli between the K6 and K7 lanes reflect the effect of truck loading. Note that K6 receives most of the truck traffic along SH4/48 and has, thus, carried a greater number of 18-kip equivalent single axle load applications (ESALs) compared to the K7 lane. Relationships between the backcalculated AC moduli and cumulative 18-kip ESALs are evaluated later in this report.

MODULUS–TEMPERATURE CORRECTIONS

It is of interest to examine the temporal variation of the AC moduli backcalculated from the FWD measurements to further establish the effect of truck loading on pavement deterioration. Since FWD data were collected at different times, researchers corrected the backcalculated moduli to a reference temperature of 75 °F to remove the influence of temperature on FWD measurements. In this way, the effect of truck loading can be readily discerned.

Table 7.3. Coefficients of the Modulus-Temperature Relationships for the FWD Groups on the K6 Lane.

Group	Range of FWD Stations	A	VTS	α	δ
1	6-1 to 6-15	10.0	-3.350	3.2	-0.5
2	6-16 to 6-18	9.0	-3.000	3.0	-0.5
3	6-19 to 6-23	9.0	-3.000	3.0	-0.2
4	6-24 to 6-26	9.0	-2.989	2.5	-0.5
5	6-27 to 6-36	10.0	-3.343	2.7	-0.5
6	6-37 to 6-41	12.2	-4.247	6.8	0.1
7	6-42 to 6-56	10.0	-3.380	2.5	-0.5

Table 7.4. Coefficients of the Modulus-Temperature Relationships for the FWD Groups on the K7 Lane.

Group	Range of FWD Stations	A	VTS	α	δ
1	7-1 to 7-15	10.0	-3.329	2.5	-0.5
2	7-16 to 7-17	10.0	-3.338	3.0	-0.5
3	7-18 to 7-21	10.0	-3.329	2.5	-0.5
4	7-22 to 7-23	10.0	-3.323	2.5	-0.5
5	7-24 to 7-33	10.0	-3.331	2.6	-0.5
6	7-34 to 7-37	10.0	-3.353	3.6	-0.5
7	7-38 to 7-50	11.4	-3.846	2.5	-0.4

Table 7.5. ANOVA Results for K6 Lane FWD Groups.

Group	Source	df	Sum of squares	Mean square	F-value	Approx. pr > F (*p*)
1	Regression	3	75.66	25.22	184.66	<.0001
	Residual	114	2.88	0.03		
	Uncorrected total	117	78.54			
	Corrected total	116	12.21			
2	Regression	3	3.48	1.16	15.54	0.0001
	Residual	18	0.58	0.03		
	Uncorrected total	21	4.06			
	Corrected total	20	1.58			
3	Regression	3	23.58	7.86	109.15	<.0001
	Residual	32	0.37	0.01		
	Uncorrected total	35	23.95			
	Corrected total	34	2.90			
4	Regression	3	5.85	1.95	9.69	0.0014
	Residual	18	2.27	0.13		
	Uncorrected total	21	8.13			
	Corrected total	20	4.72			
5	Regression	3	36.27	12.09	828.40	<.0001
	Residual	66	0.96	0.01		
	Uncorrected total	69	37.23			
	Corrected total	68	6.02			
6	Regression	4	11.37	2.84	9.24	0.0002
	Residual	31	1.09	0.04		
	Uncorrected total	35	12.46			
	Corrected total	34	2.06			
7	Regression	3	5.05	1.68	42.43	<.0001
	Residual	102	4.05	0.04		
	Uncorrected total	105	9.10			
	Corrected total	104	8.92			

Table 7.6. ANOVA Results for K7 Lane FWD Groups.

Group	Source	df	Sum of squares	Mean square	F-value	Approx. pr > F (*p*)
1	Regression	2	99.81	49.91	6341.85	<.0001
	Residual	117	0.92	0.01		
	Uncorrected Total	119	100.70			
	Corrected Total	118	4.10			
2	Regression	3	17.60	5.87	86.74	<.0001
	Residual	15	0.09	0.01		
	Uncorrected Total	18	17.69			
	Corrected Total	17	1.18			
3	Regression	4	32.38	8.09	102.09	<.0001
	Residual	31	0.18	0.01		
	Uncorrected Total	35	32.56			
	Corrected Total	34	2.01			
4	Regression	2	17.53	8.77	2043.87	<.0001
	Residual	15	0.06	0.004		
	Uncorrected Total	17	17.60			
	Corrected Total	16	0.70			
5	Regression	4	75.69	18.92	146.05	<.0001
	Residual	85	0.75	0.01		
	Uncorrected Total	89	76.44			
	Corrected Total	88	4.61			
6	Regression	3	27.64	9.21	62.38	<.0001
	Residual	33	0.78	0.02		
	Uncorrected Total	36	28.42			
	Corrected Total	35	3.72			
7	Regression	4	34.99	8.75	60.5	<.0001
	Residual	112	3.47	0.03		
	Uncorrected Total	116	38.46			
	Corrected Total	115	9.10			

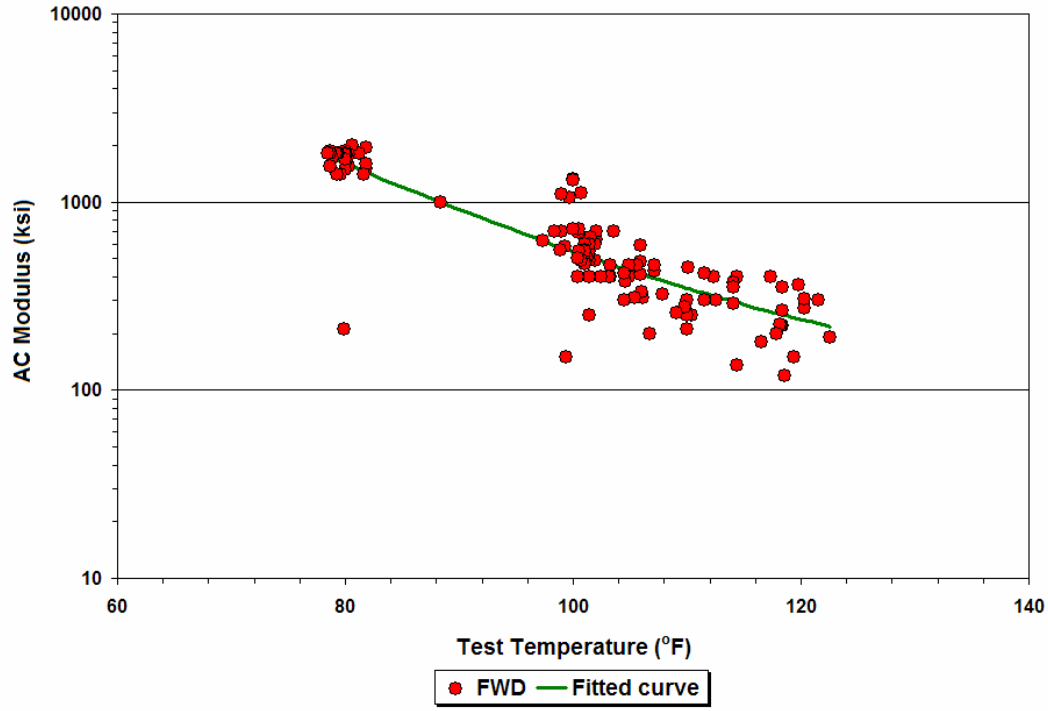

Figure 7.16. Relationship between Backcalculated AC Modulus and Pavement Temperature (Group 1, K6 Lane).

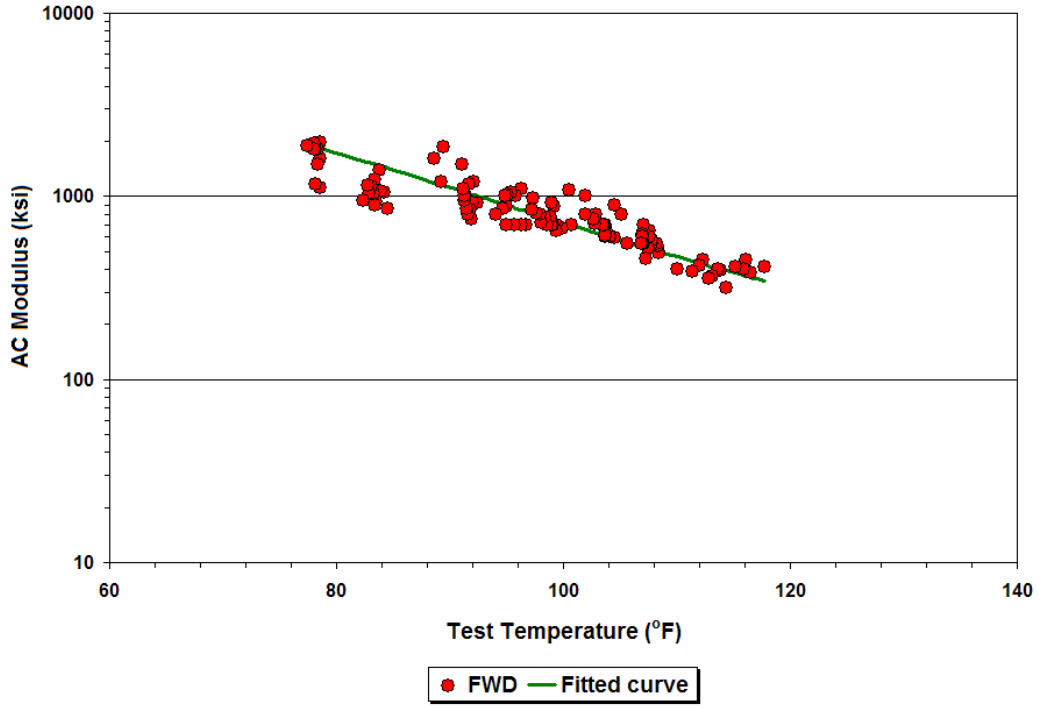

Figure 7.17. Relationship between Backcalculated AC Modulus and Pavement Temperature (Group 1, K7 Lane).

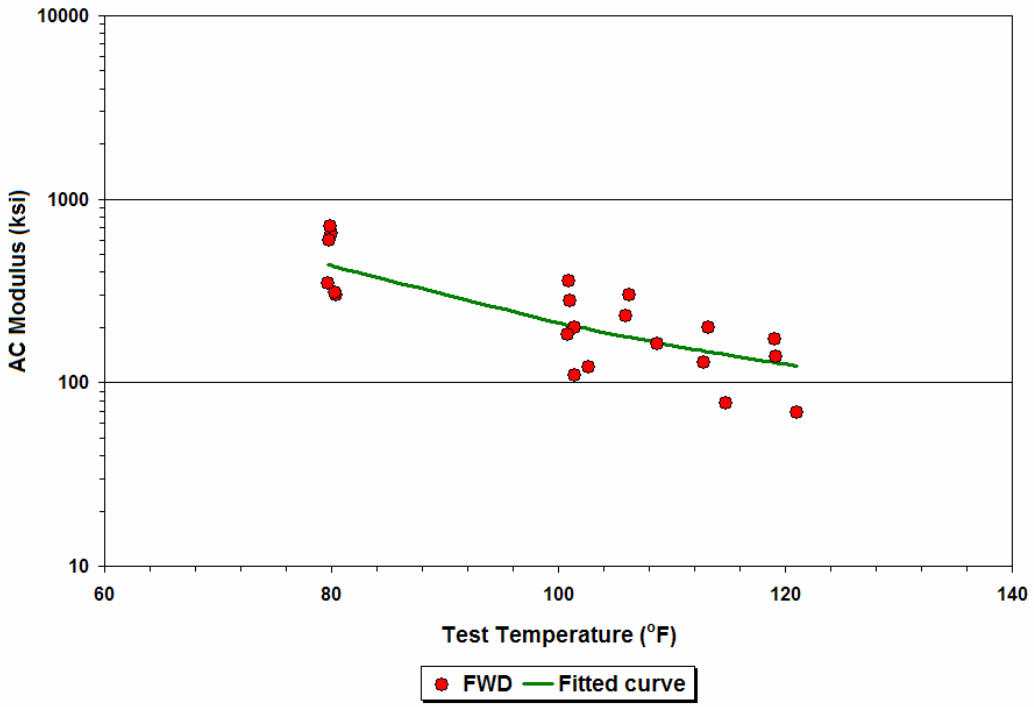

Figure 7.18. Relationship between Backcalculated AC Modulus and Pavement Temperature (Group 2, K6 Lane).

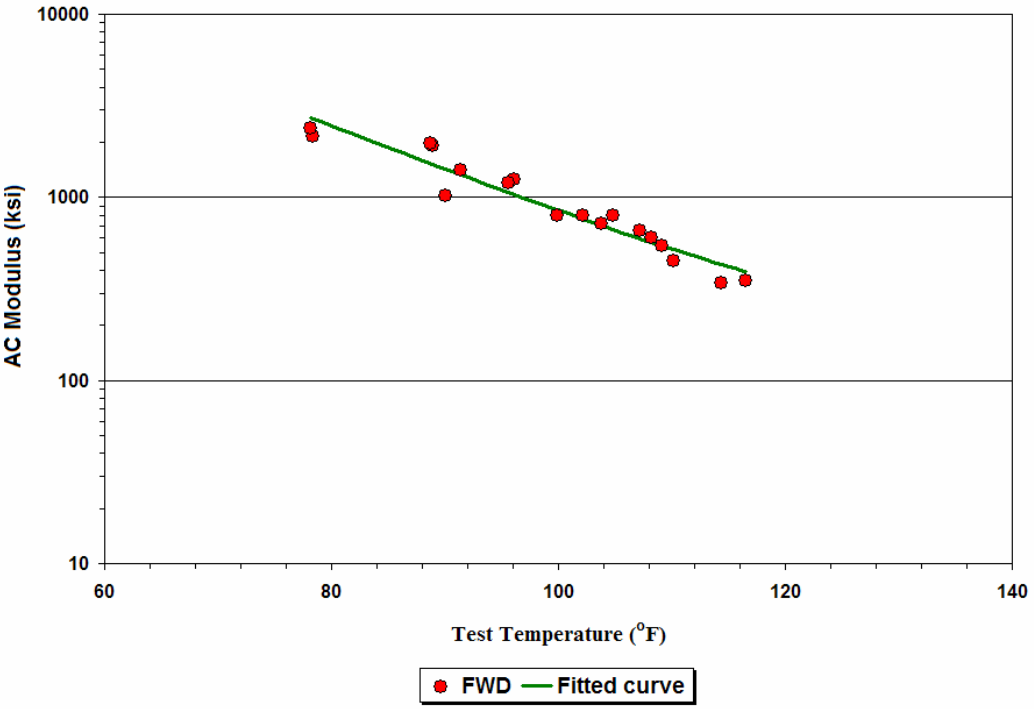

Figure 7.19. Relationship between Backcalculated AC Modulus and Pavement Temperature (Group 2, K7 Lane).

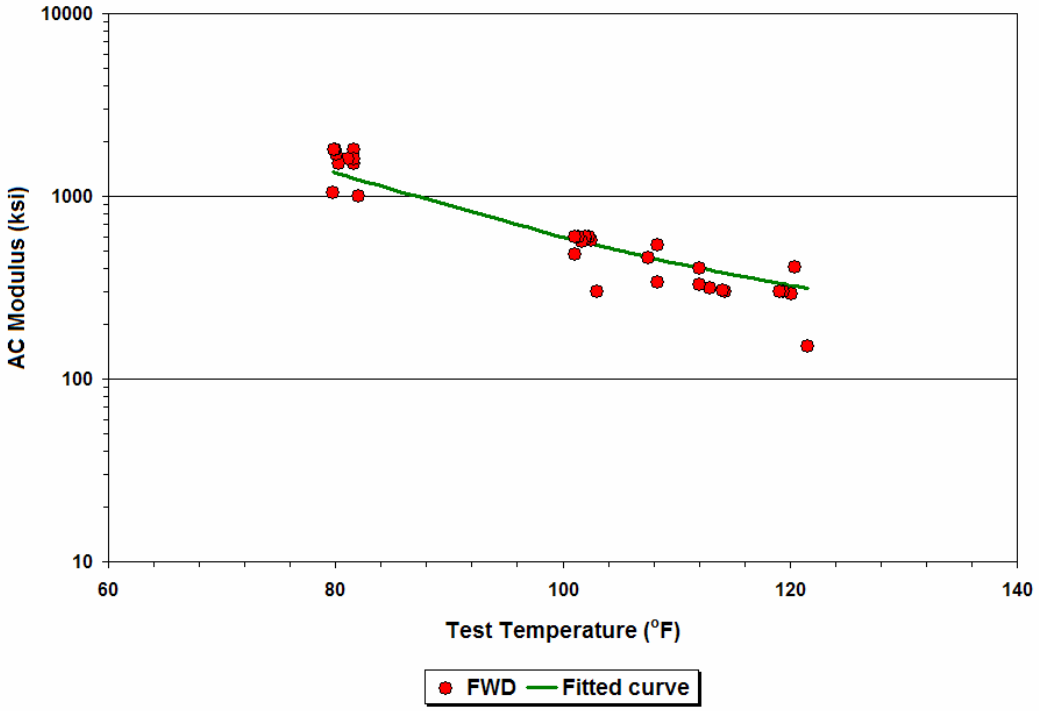

Figure 7.20. Relationship between Backcalculated AC Modulus and Pavement Temperature (Group 3, K6 Lane).

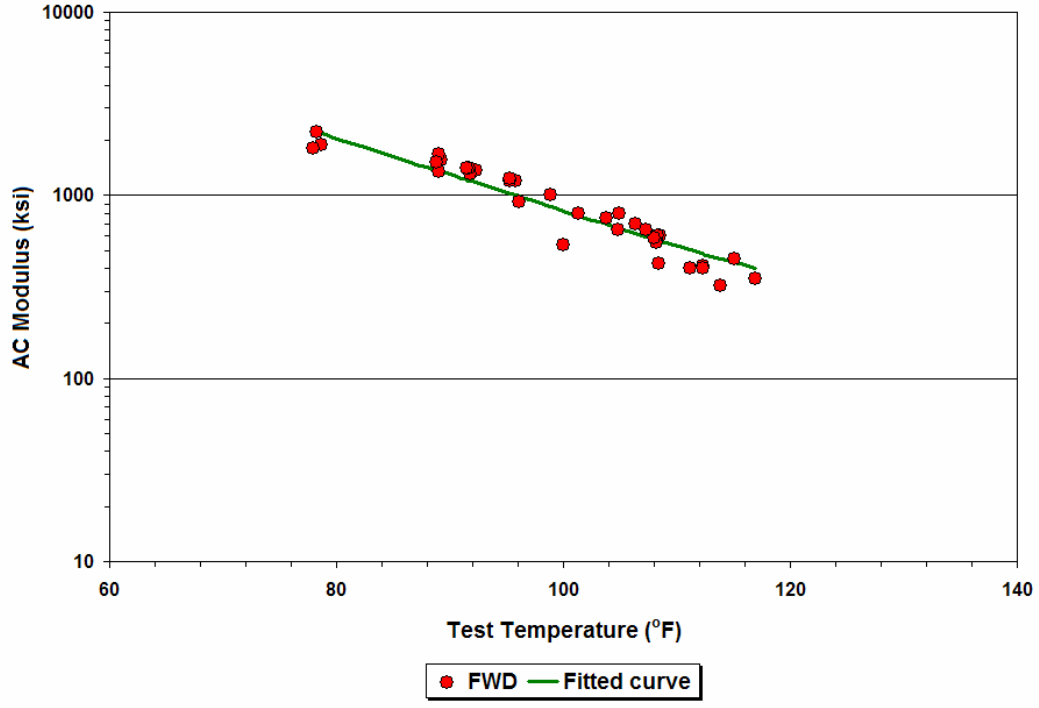

Figure 7.21. Relationship between Backcalculated AC Modulus and Pavement Temperature (Group 3, K7 Lane).

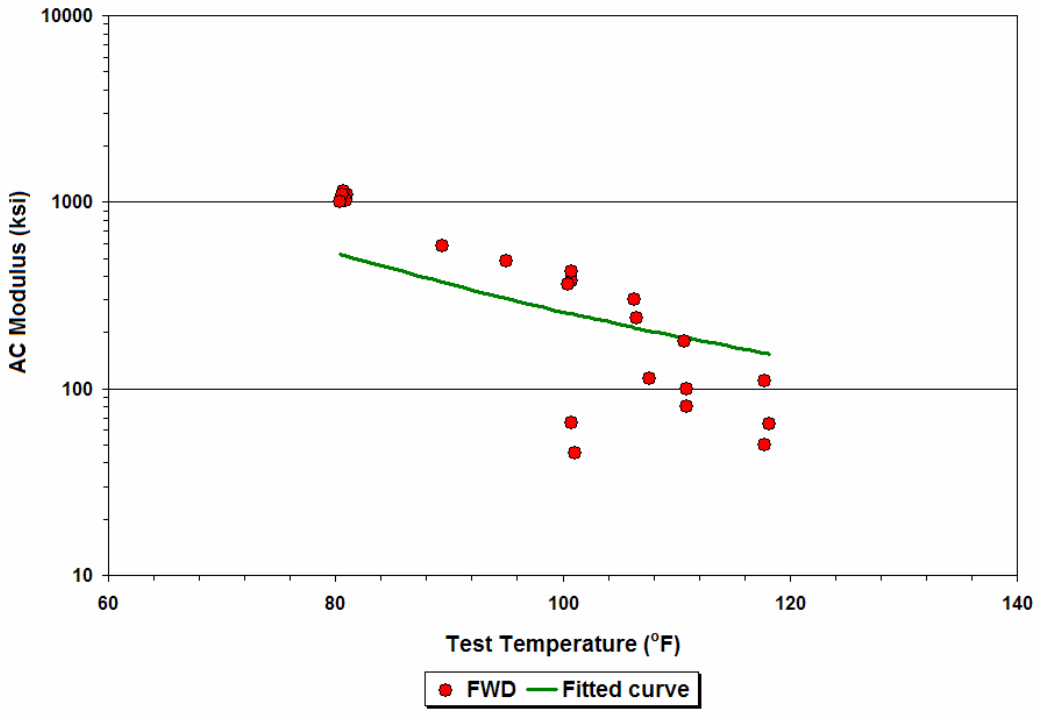

Figure 7.22. Relationship between Backcalculated AC Modulus and Pavement Temperature (Group 4, K6 Lane).

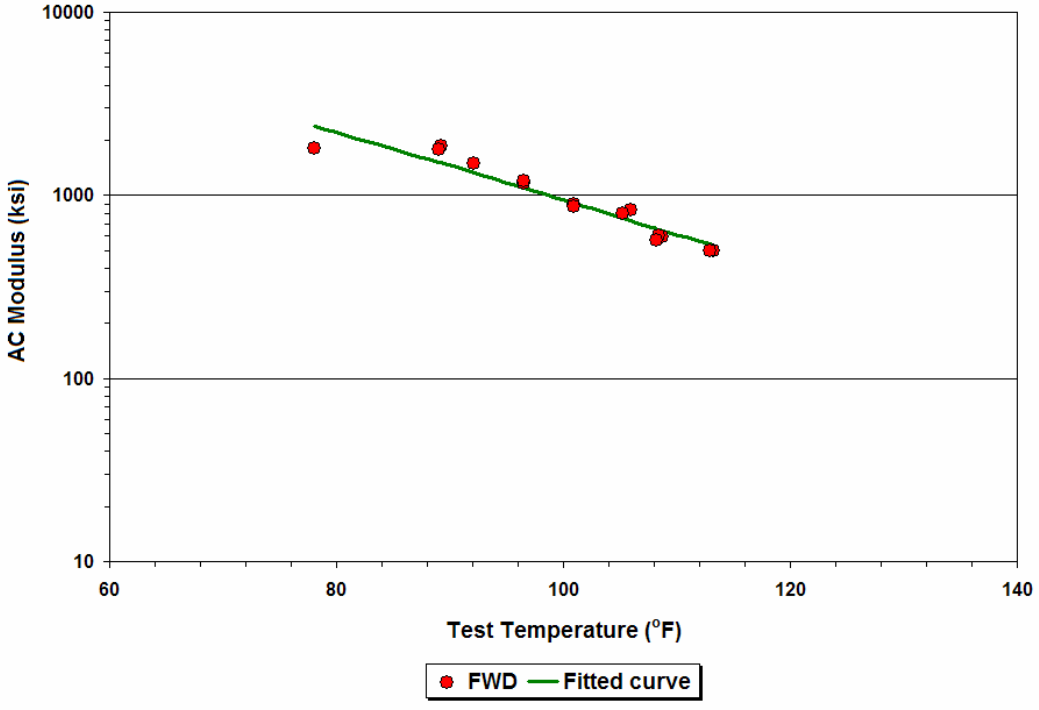

Figure 7.23. Relationship between Backcalculated AC Modulus and Pavement Temperature (Group 4, K7 Lane).

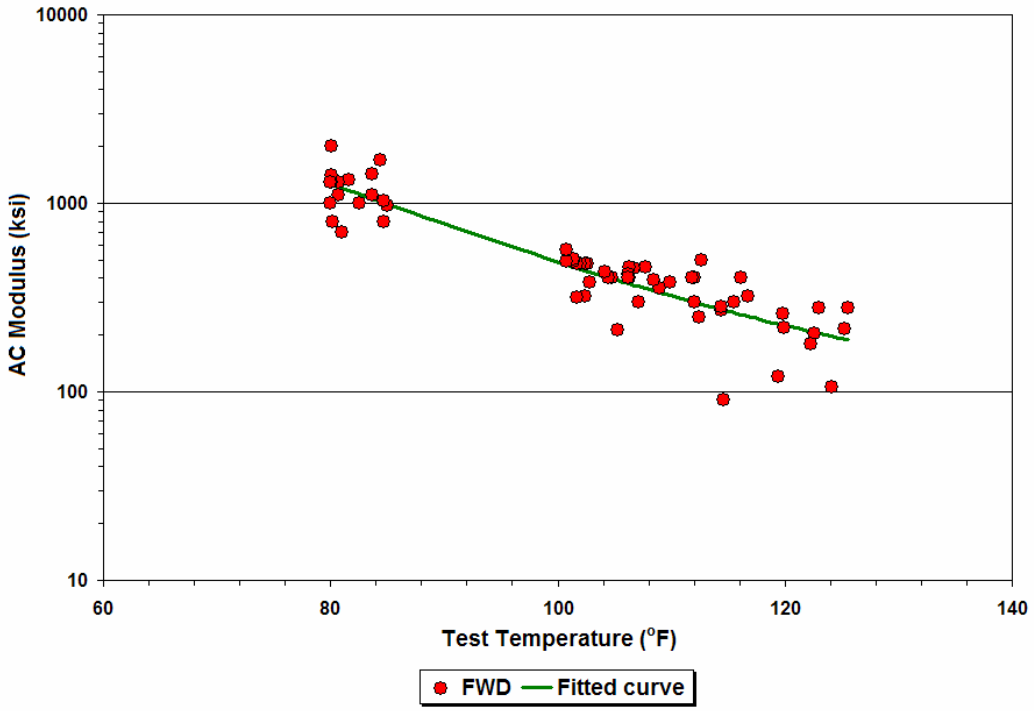

Figure 7.24. Relationship between Backcalculated AC Modulus and Pavement Temperature (Group 5, K6 Lane).

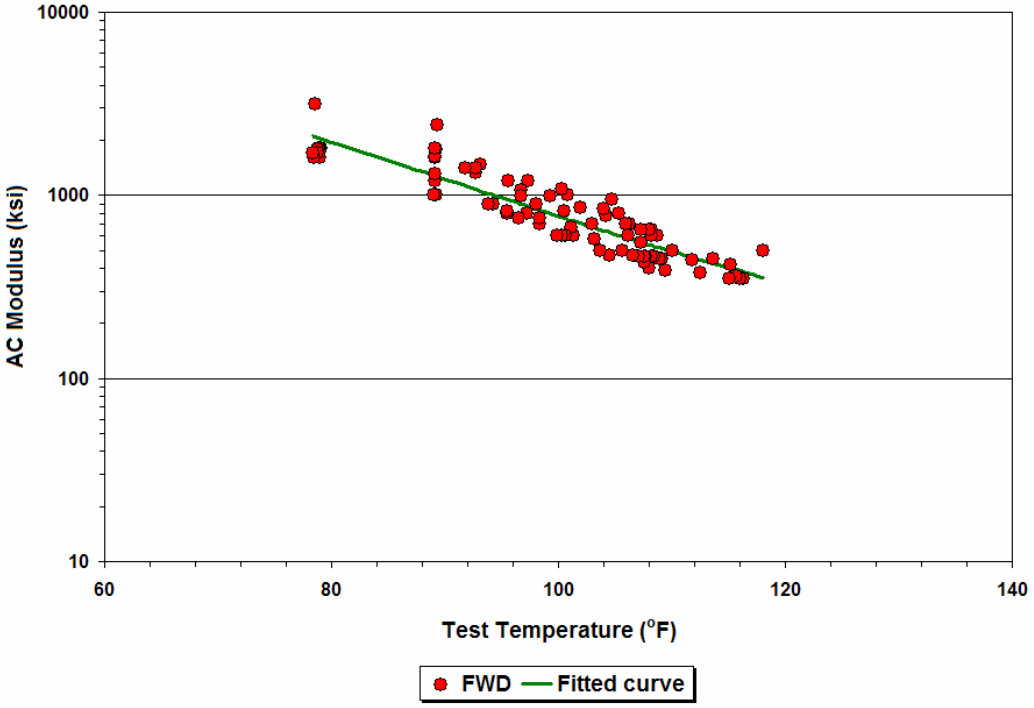

Figure 7.25. Relationship between Backcalculated AC Modulus and Pavement Temperature (Group 5, K7 Lane).

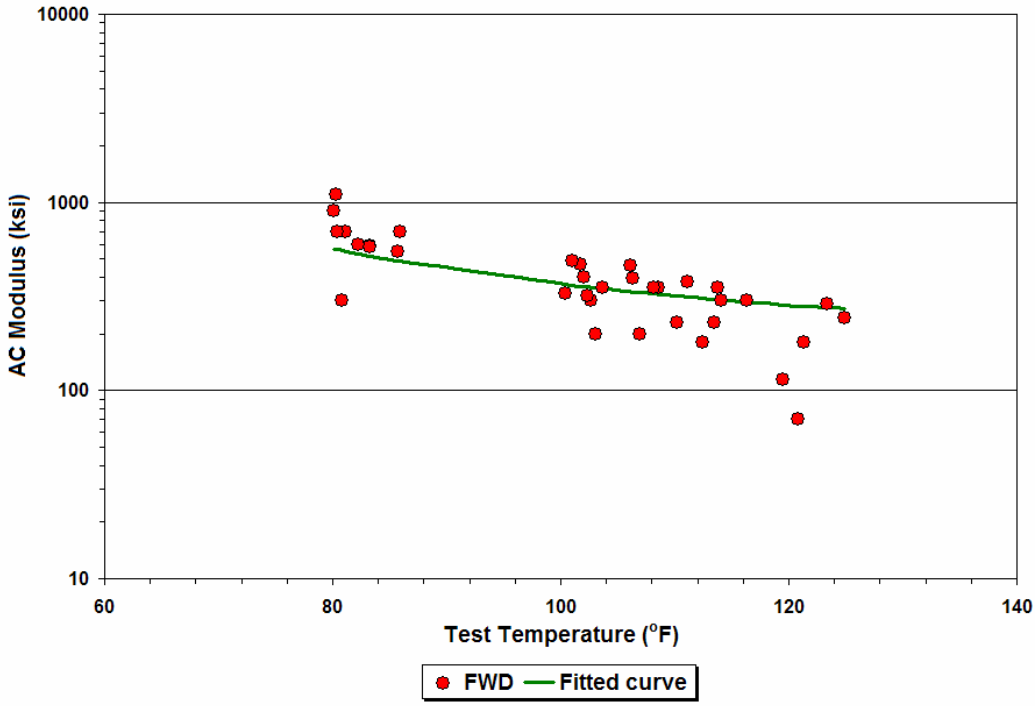

Figure 7.26. Relationship between Backcalculated AC Modulus and Pavement Temperature (Group 6, K6 Lane).

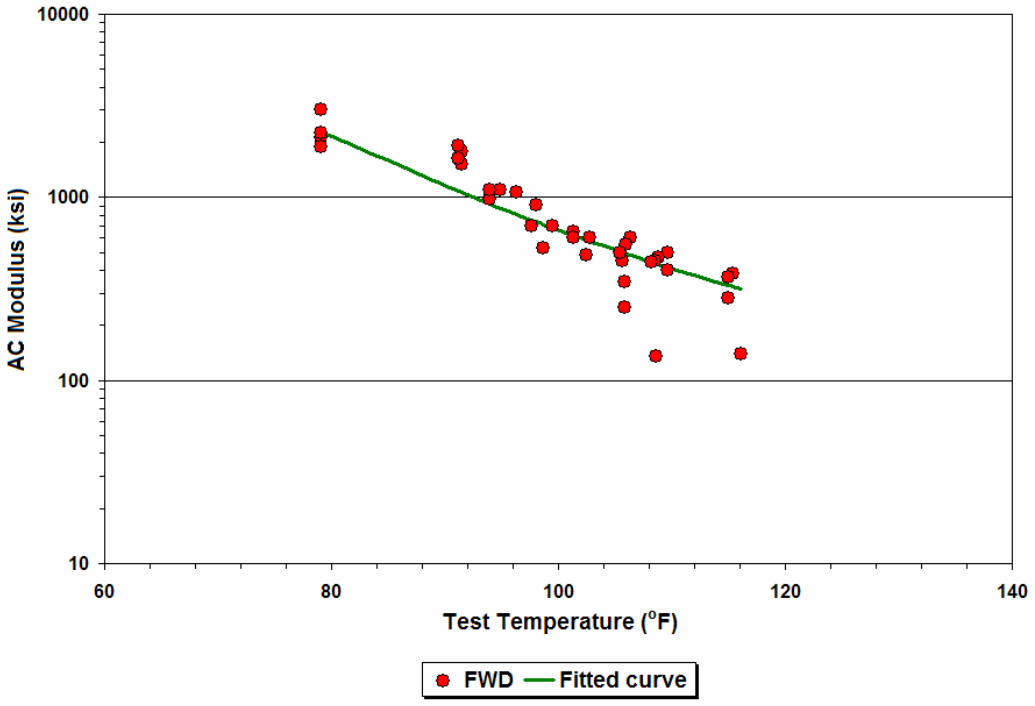

Figure 7.27. Relationship between Backcalculated AC Modulus and Pavement Temperature (Group 6, K7 Lane).

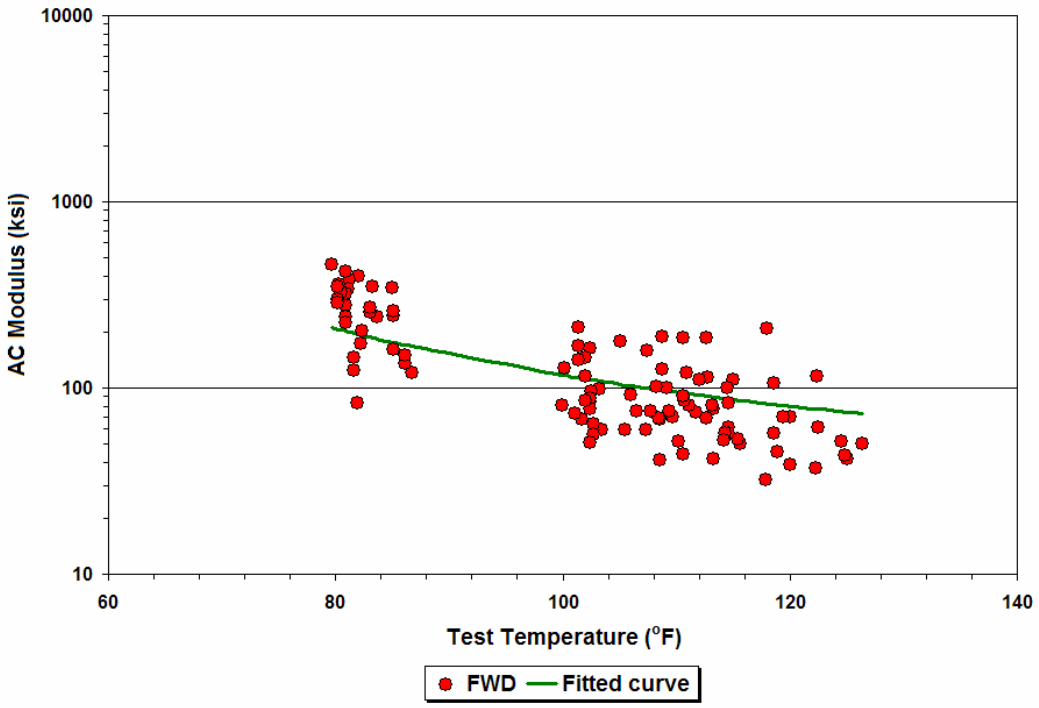

Figure 7.28. Relationship between Backcalculated AC Modulus and Pavement Temperature (Group 7, K6 Lane).

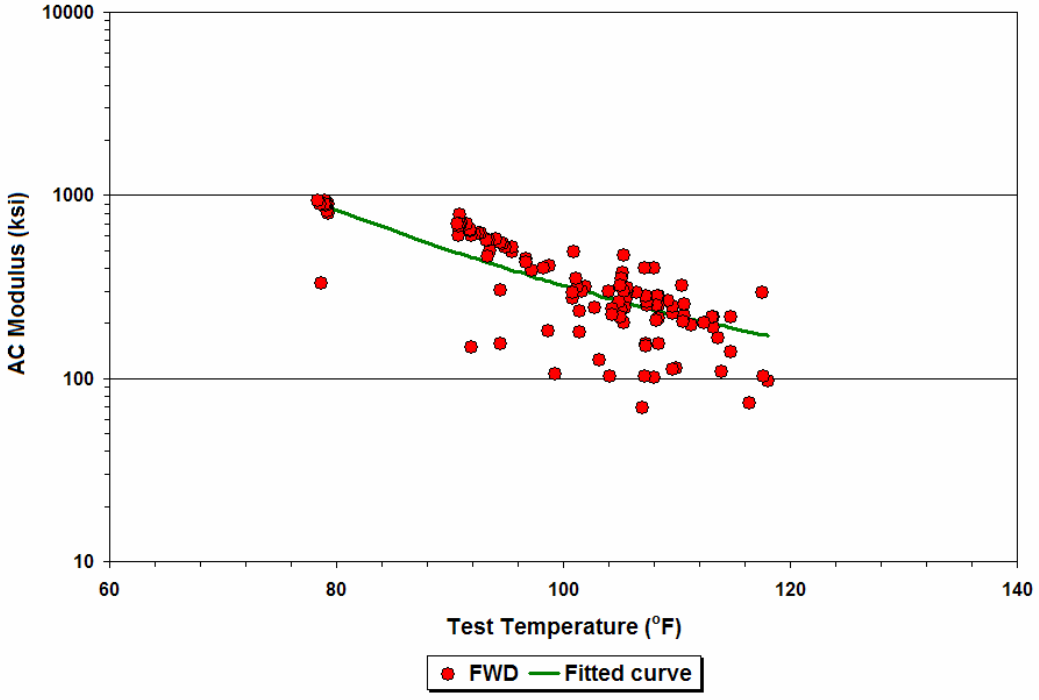

Figure 7.29. Relationship between Backcalculated AC Modulus and Pavement Temperature (Group 7, K7 Lane).

As noted previously, researchers used three methods to perform the temperature correction of backcalculated AC moduli. This section presents the results from application of Eq. (7.5), which is based on the Witczak-Fonseca equation for predicting dynamic modulus of asphalt concrete mixtures. Appendix F shows the results obtained using Eqs. (7.2) and (7.3).

To perform the temperature corrections based on Eq. (7.5), researchers used results from the dynamic modulus tests conducted on core C6. As stated previously, this core was taken from the center lane at the vicinity of the WIM site along SH48. This lane receives very little traffic as it is only used for left-turn movements. Consequently, the properties of this core are not expected to include load-associated effects due to truck traffic. While modulus-temperature relationships were previously evaluated from the backcalculated moduli along SH4/48, the deflection data on which these relationships are based include the effects of both vehicular loading and pavement temperature. Thus, corrections using these relationships will likely mask the effect of traffic loading on asphalt concrete modulus. Consequently, researchers performed the temperature corrections using the modulus-temperature relationship for core C6, as established from laboratory testing. This relationship is shown in Figure 7.30, which shows the dynamic moduli corresponding to the FWD test frequency. Also shown is the fitted curve to the test data determined using Eq. (7.11).

Figures 7.31 to 7.37 compare the average corrected AC moduli for the different FWD groups along the K6 and K7 lanes. In general, the average corrected moduli show a decreasing trend over time, particularly for the FWD groups on the K6 lane. These observations provide additional indications of the effects of truck loading on pavement deterioration along the route.

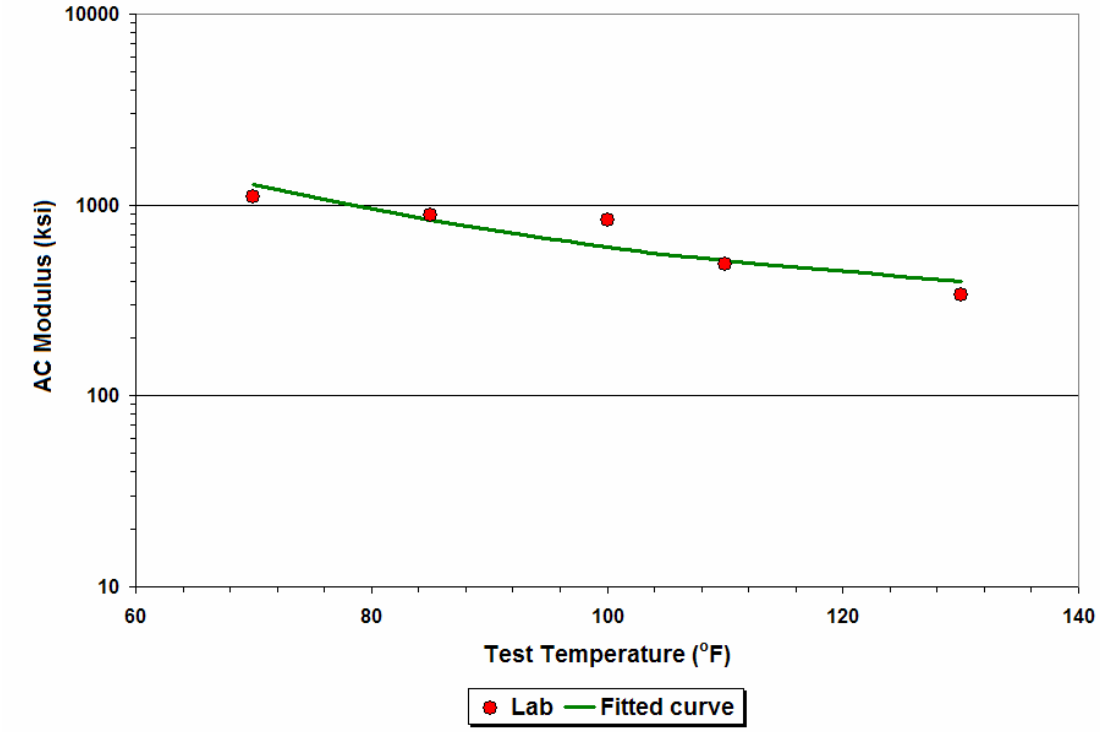

Figure 7.30. Relationship between Dynamic Modulus and Test Temperature (Core C6).

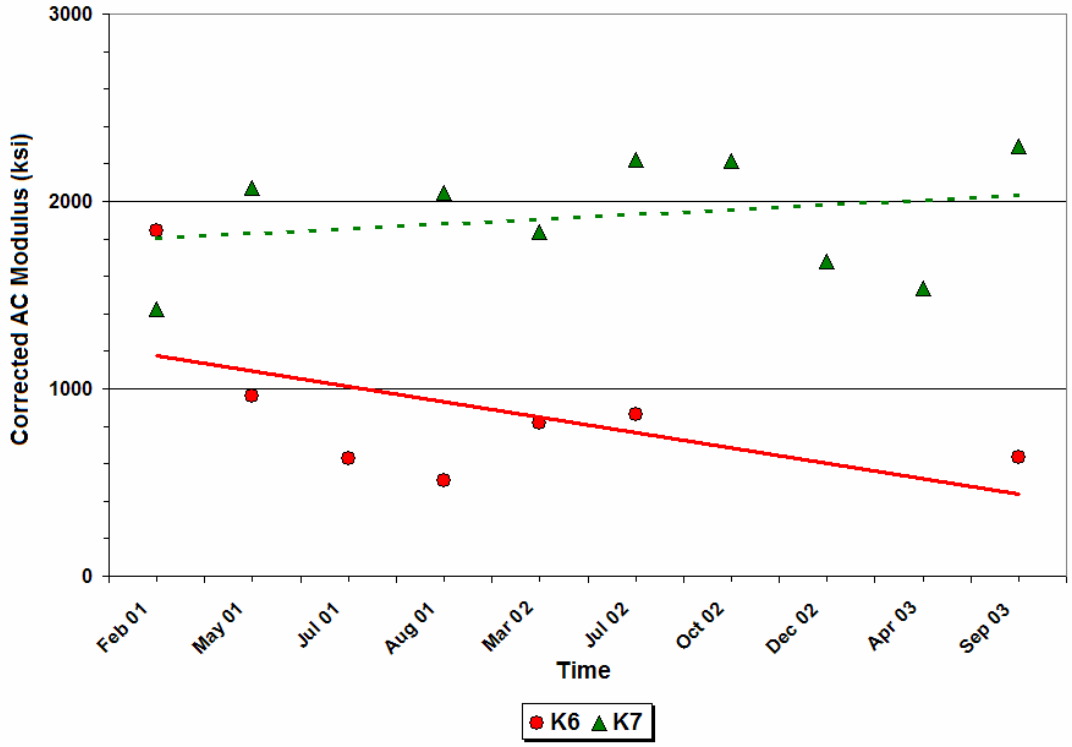

Figure 7.31. Temporal Trends in the Corrected AC Moduli (Group 1).

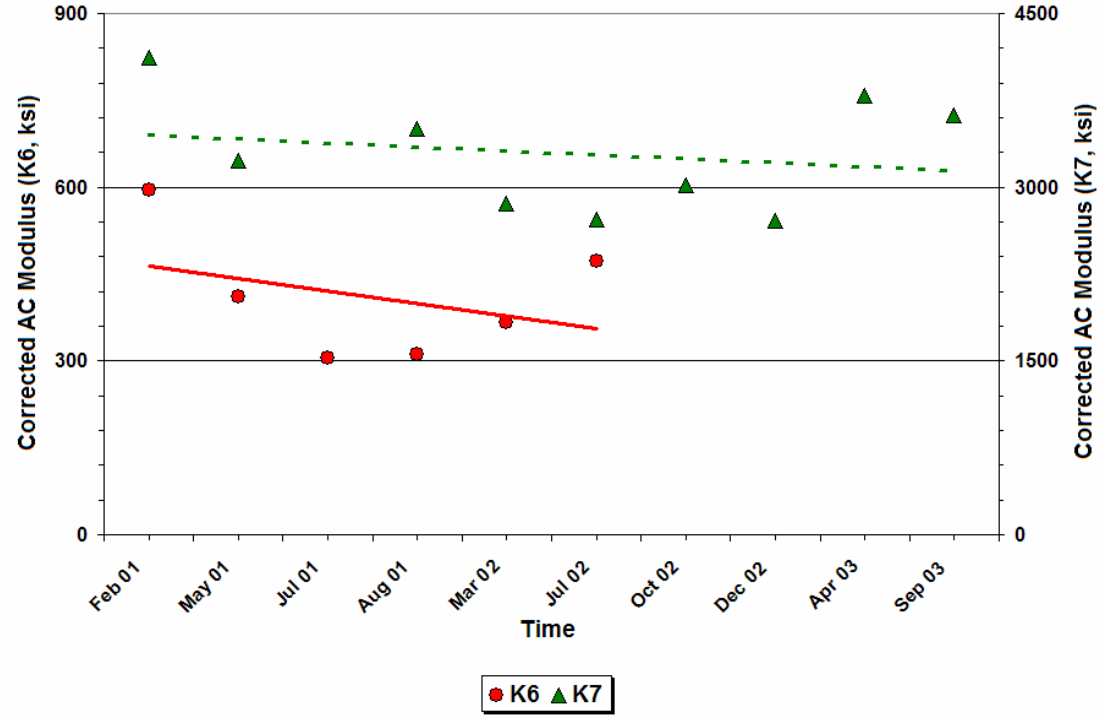

Figure 7.32. Temporal Trends in the Corrected AC Moduli (Group 2).

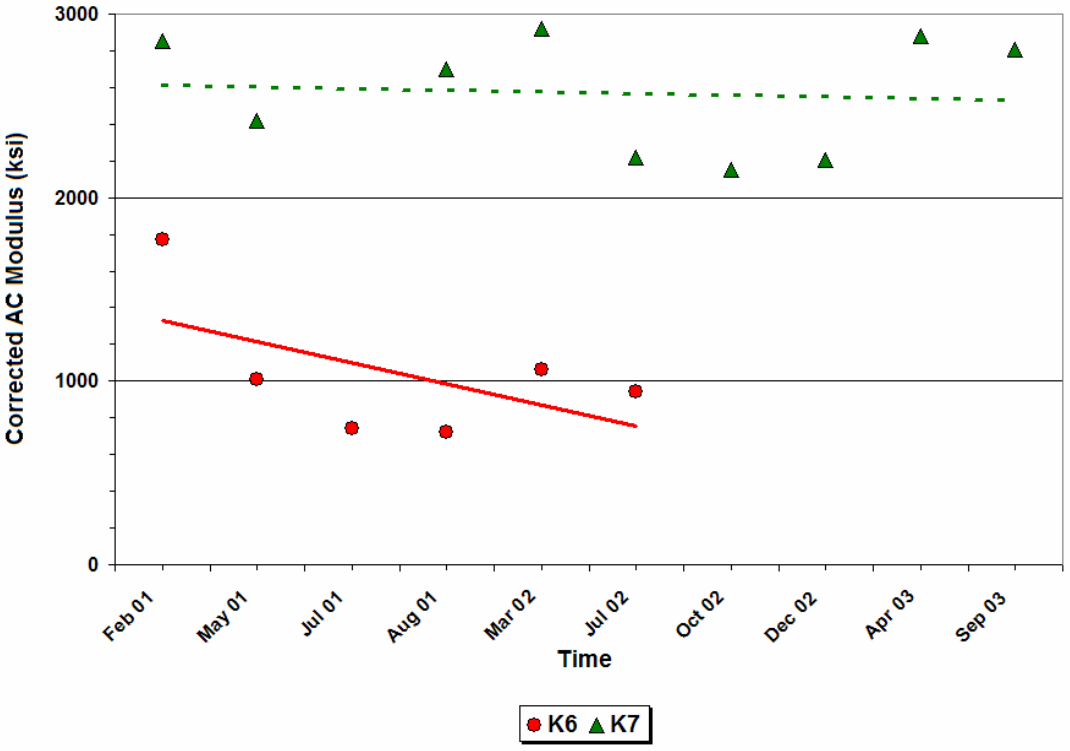

Figure 7.33. Temporal Trends in the Corrected AC Moduli (Group 3).

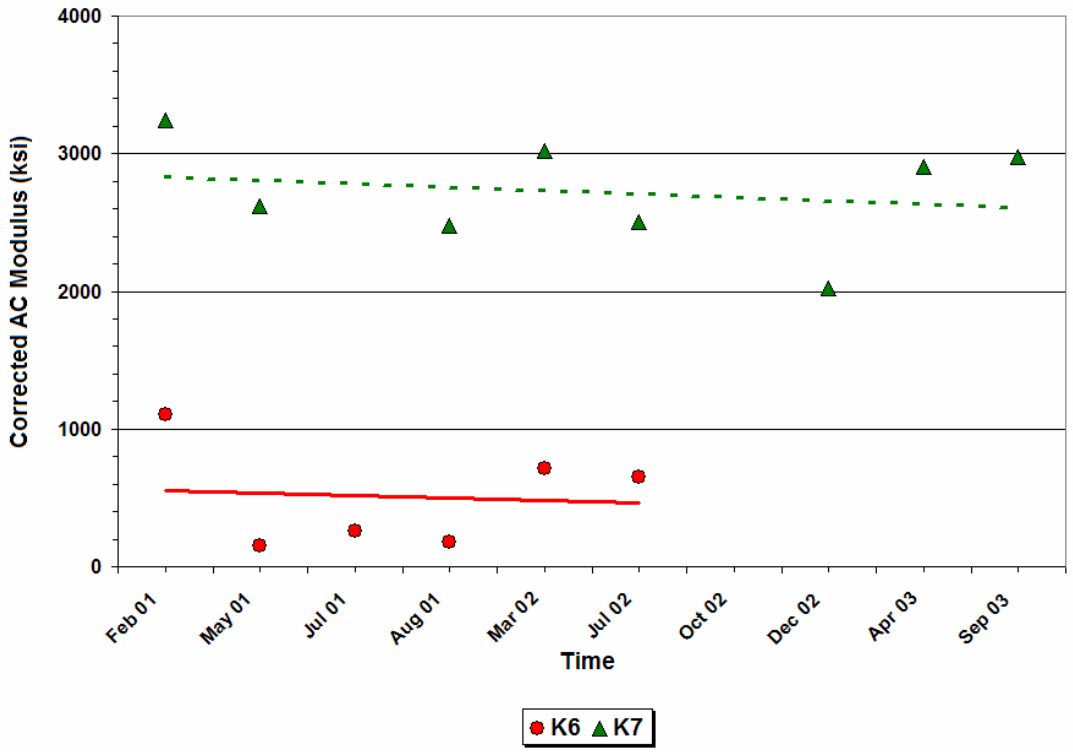

Figure 7.34. Temporal Trends in the Corrected AC Moduli (Group 4).

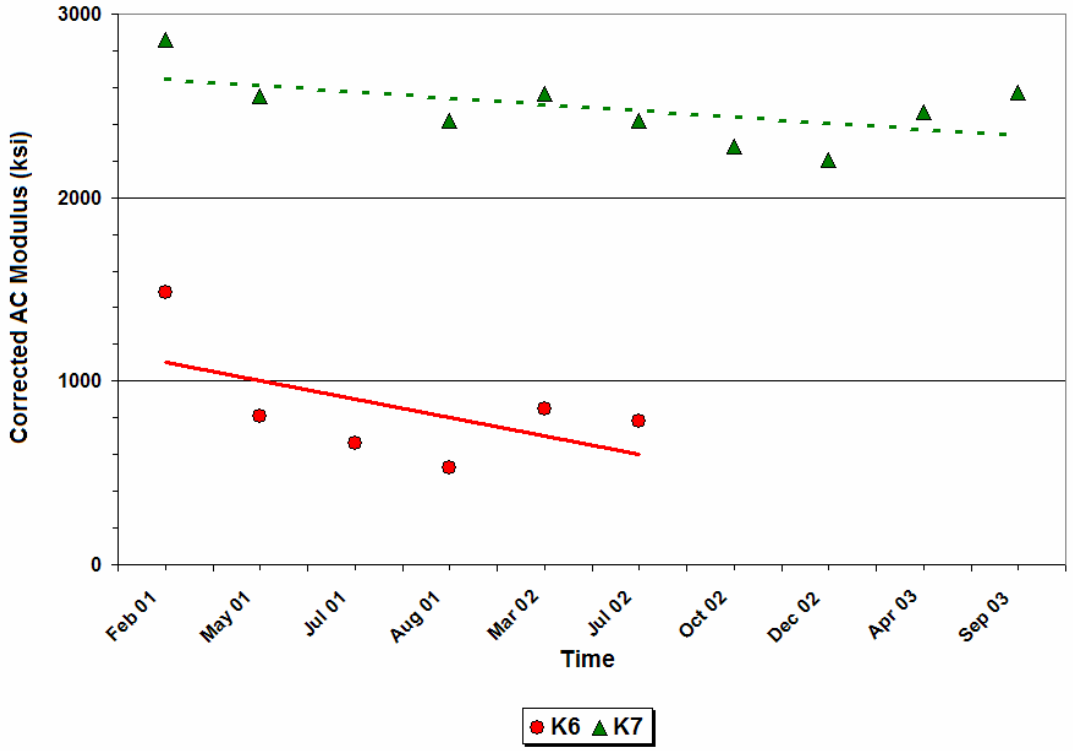

Figure 7.35. Temporal Trends in the Corrected AC Moduli (Group 5).

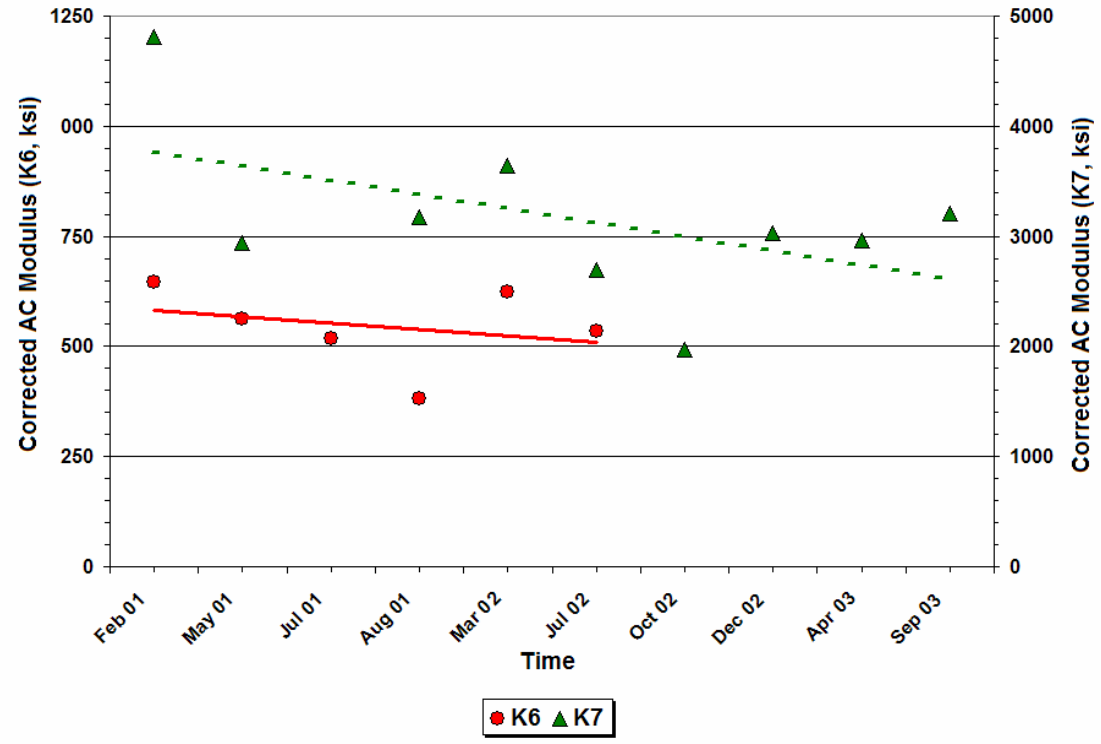

Figure 7.36. Temporal Trends in the Corrected AC Moduli (Group 6).

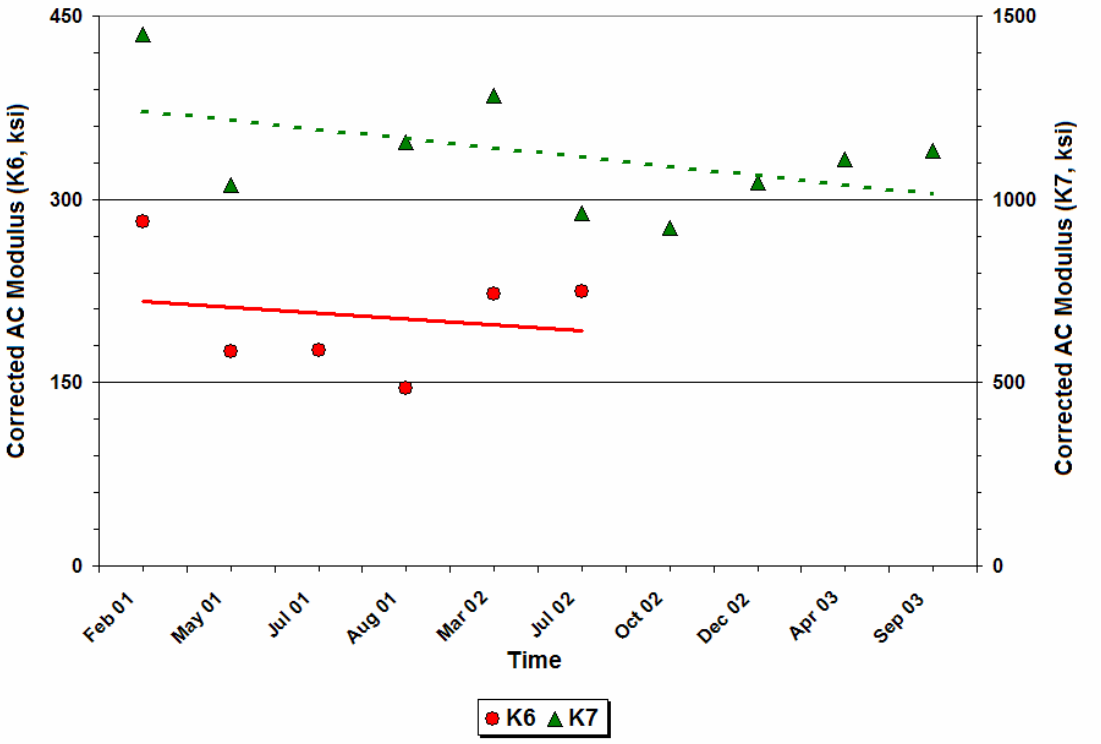

Figure 7.37. Temporal Trends in the Corrected AC Moduli (Group 7).

CHAPTER VIII. EVALUATION OF DAMAGE POTENTIAL

INTRODUCTION

As stated in Chapter I, this project aims to characterize the effects of routine overweight truck loads on the performance of SH4/48 in Brownsville. Toward this objective, researchers installed MDDs at the TxDOT WIM site located along SH48 to assess the potential for accelerated pavement damage due to routine overweight truck use. Note that no dedicated truck lane was established to service overweight truck traffic. Since the travel lanes receive both non-permitted (legal) and overweight truck loads, separating the effects of legal and permitted trucks becomes an issue. To address this problem, researchers used the MDDs to monitor pavement deflections under both legal and permitted trucks, and assessed the potential for pavement damage from overweight trucks on the basis of the measured deflections. For this purpose, tags were placed on the permitted trucks as the vehicles were about to leave the Port of Brownsville. These tags identified each truck with a number that researchers recorded as the truck passed the WIM site, along with the date of test, time of arrival at the site and the test lane (K6 or K7). The tag also referred back to the particular permit issued for the truck. With this information, researchers obtained the specific permits for the different trucks monitored at the WIM site to get the measured axle loads recorded on the permits as each truck is weighed at the port. Researchers later used these axle loads in analyzing the MDD deflections.

In addition to the permitted trucks, researchers monitored deflections under legal trucks that passed the WIM site. These measurements were made when both types of trucks were observed to be approaching the WIM site. In this way, deflection data were obtained under very similar environmental conditions to minimize the effects of differences in the data due to pavement temperature and moisture variations. Researchers assigned a label for each legal truck, and recorded its date, time of arrival at the WIM site and the test lane. This information was later used to estimate the axle loads of the non-permitted trucks from the WIM data supplied by TxDOT.

In addition to evaluating the potential for accelerated pavement damage due to overweight trucks, researchers used the MDD measurements to verify a number of alternative models for predicting pavement response. Appendix G presents this evaluation. The current chapter focuses on the assessment of pavement damage potential.

EVALUATION OF DAMAGE POTENTIAL FROM MDD DEFLECTIONS

To compare predicted damage potential due to permitted and non-permitted trucks, researchers analyzed MDD deflections from corresponding truck pairs, which were monitored at the WIM site at close to the same times. Figures 8.1 and 8.2 illustrate MDD traces measured under legal and overweight trucks, respectively. The peaks in these figures correspond to the different axles that passed the MDD station, beginning with the steering axle, the axles of the drive assembly, and the semi-trailer axles. Four traces are shown in each figure, which show the deflections at different depths corresponding to the locations of the LVDTs. Figure 8.3 provides the pavement cross-sections at the K6 and K7 MDD stations along with the positions of the LVDTs on the MDD assemblies.

The displacements decrease with depth, as observed in Figures 8.1 and 8.2, and show peaks corresponding to the times each axle came closest to the MDD. To determine the positions of the wheel loads that passed the MDD, researchers viewed the video recordings that were made as the different trucks passed through the station. The offset distance from a given tire and the MDD on the test lane was estimated from the position of the tire on grid lines painted on the pavement when the MDDs were installed. In this way, researchers were able to consider the effect of tire offset from the MDD in the analysis of the measured pavement deflections.

Pavement performance is related to the pavement response under load. In current practice, the horizontal tensile strain at the bottom of the asphalt and the vertical compressive strain at the top of the subgrade are typically used to predict service life based on fatigue cracking and rutting, respectively. To assess the potential pavement damage from permitted trucks relative to legal trucks, researchers used the Asphalt Institute equations to predict the life consumed due to the passage of a given truck. The performance equations based on rutting and fatigue cracking are given by (Asphalt Institute, 1982):

$$(N_f)^r = 1.365\times10^{-9}\left(\frac{1}{\varepsilon_z}\right)^{-4.477} \tag{8.1}$$

$$(N_f)^c = 7.9488\times10^{-2}\left(\frac{1}{\varepsilon_{ac}}\right)^{3.29}\left(\frac{1}{E_{ac}}\right)^{0.854} \tag{8.2}$$

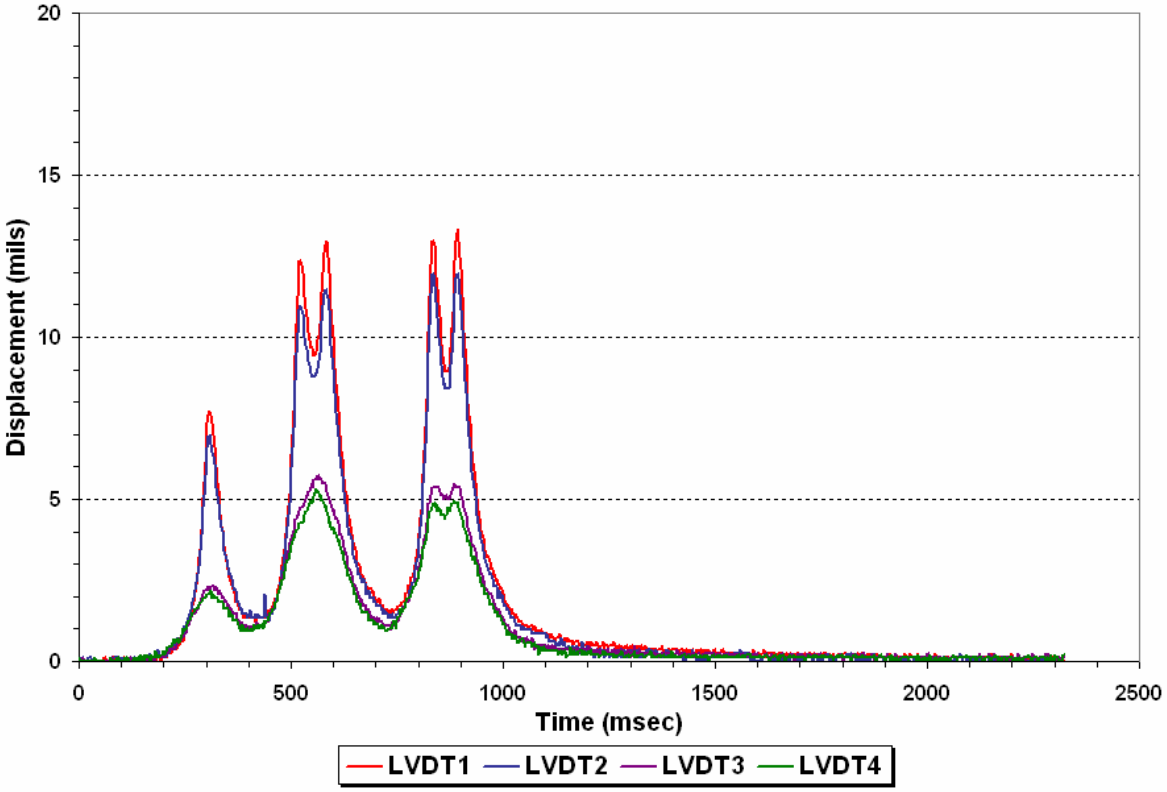

Figure 8.1. Illustration of MDD Response under a Legal Truck.

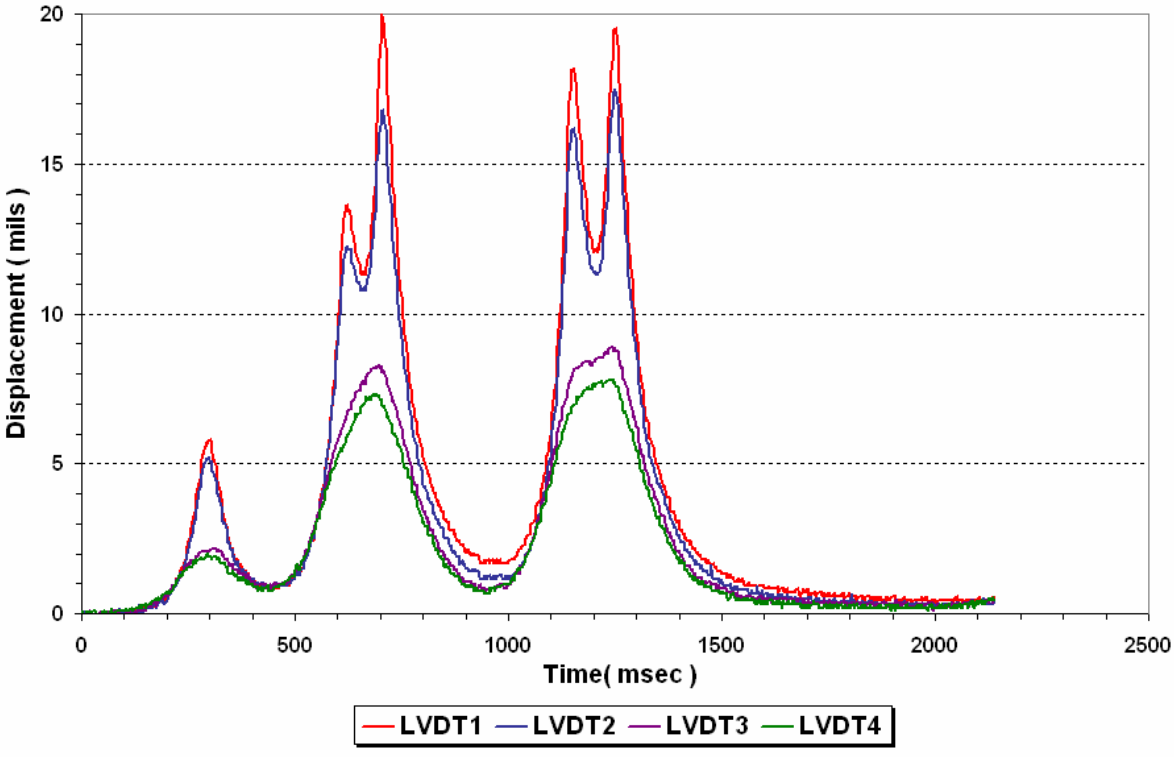

Figure 8.2. Illustration of MDD Response under a Permitted Overweight Truck.

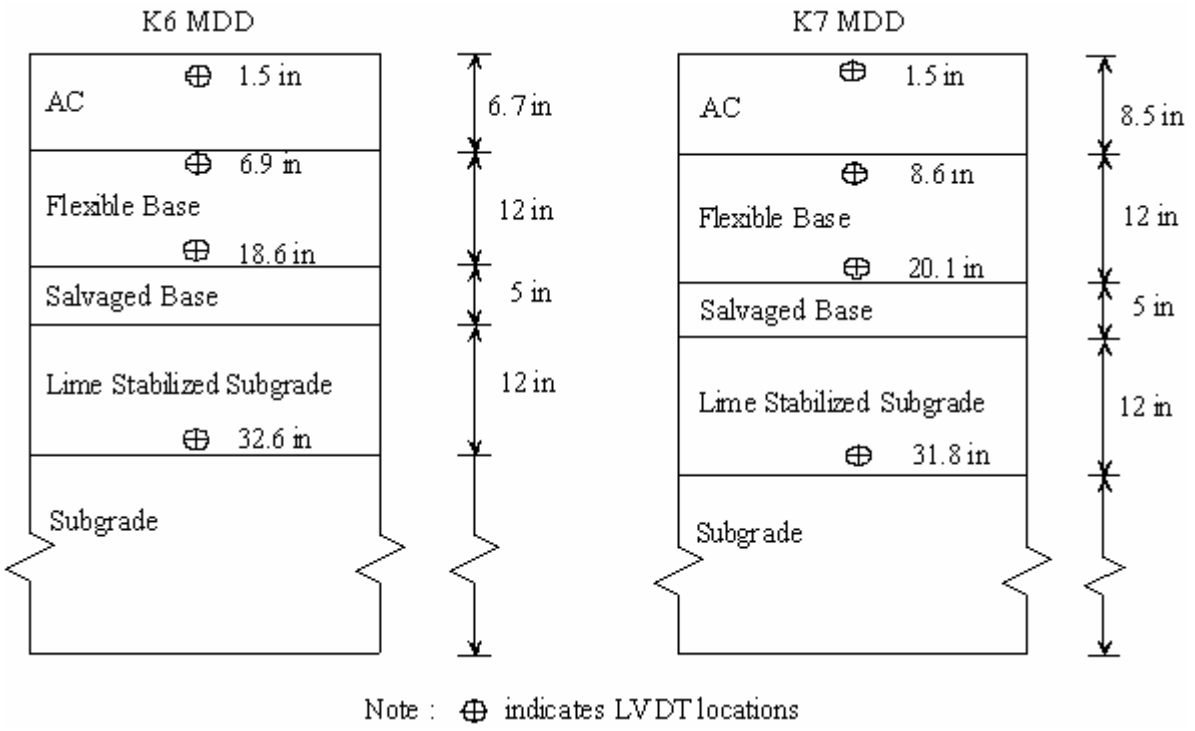

Figure 8.3. Pavement Cross-Sections at MDD Stations and LVDT Positions.

where,

$(N_f)^r$ = allowable number of load repetitions based on rutting,

$(N_f)^c$ = allowable number of load repetitions based on fatigue cracking,

ε_z = predicted vertical compressive strain at the top of the subgrade,

ε_{ac} = predicted horizontal tensile strain at the bottom of the AC layer, and

E_{ac} = asphalt concrete modulus.

To predict the subgrade compressive strain and the AC tensile strain from the measured MDD displacements, researchers established relationships between these performance predictors and the MDD displacements. In the authors' opinion, this approach is rational since the deflections, strains and stresses are related to the material properties of the different pavement layers and the applied loads through the laws of mechanics. Fernando, Luhr and Anderson (1986) used a similar approach in developing a simplified flexible pavement evaluation and overlay design procedure that uses relationships between subgrade compressive strain, AC tensile strain and surface deflections to predict pavement service life.

To establish relationships for predicting subgrade compressive strain and AC tensile strain from MDD displacements, researchers used a finite element program to predict these pavement response parameters for a range of layer moduli, tire loads and offset distances

(from the MDD), which covered the range of these variables as observed from the test data. Appendix G presents the finite element model used in this evaluation. To predict pavement response, researchers characterized the base, subbase and subgrade layers as nonlinear cross-anisotropic materials. This constitutive model was found to provide the best agreement between measured and predicted MDD displacements relative to other constitutive models evaluated by researchers. These other constitutive models are the linear elastic, isotropic; nonlinear elastic, isotropic; and the linear elastic, cross-anisotropic formulations. Appendix G presents the comparative evaluation of these different constitutive models.

Using the data generated from the finite element runs, researchers conducted regression analyses to establish relationships for predicting the strain parameters in Eqs. (8.1) and (8.2). The equations developed are given below, along with the corresponding coefficients of determination (R^2), standard errors of the estimate (SEE) in micro-strains (με) and the number of observations (N) used to determine the relationships:

$$\varepsilon_{sg,K6} = -5.667 + 19.914\,D_4 + 10.681(D_1 - D_4) \quad (8.3)$$

$R^2 = 99.4\%$ N=144 SEE = 6.028 με

$$\varepsilon_{sg,K7} = 12.851\,D_2 + 7.276\left(\frac{D_1 - D_3}{\Delta + 1}\right) \quad (8.4)$$

$R^2 = 98.3\%$ N=144 SEE = 14.411 με

$$\varepsilon_{ac,K6} = 29.4 + 10.036\,D_4 - 0.844\,\Delta^2 + 52.219\,(D_1 - D_2) \quad (8.5)$$

$R^2 = 98.8\%$ N=144 SEE = 7.695 με

$$\varepsilon_{ac,K7} = 8.317 + 6.044\,D_1 - 0.227\,\Delta^2 + 9.348\left(\frac{D_1 - D_3}{\Delta + 1}\right) \quad (8.6)$$

$R^2 = 98.7\%$ N=144 SEE = 4.145 με

where,

$\varepsilon_{sg,K6}$ = vertical compressive strain (με) at the top of the subgrade (K6 MDD),
$\varepsilon_{sg,K7}$ = vertical compressive strain (με) at the top of the subgrade (K7 MDD),
$\varepsilon_{ac,K6}$ = horizontal tensile strain (με) at the bottom of AC layer (K6 MDD),
$\varepsilon_{ac,K7}$ = horizontal tensile strain (με) at the bottom of AC layer (K7 MDD),
D_i = displacement (mils) at i^{th} LVDT of MDD, and
Δ = offset distance (inch) of wheel load from MDD.

Figures 8.4 to 8.7 compare the predicted strains from the above equations with the corresponding theoretical strains from the finite element program. In the authors' opinion, the predictions are generally in good agreement with the theoretical values for the range of layer moduli, wheel loads and offsets covered in the finite element runs. It was found that the MDD displacements are highly correlated with the subgrade compressive and AC tensile strains and that the displacements adequately account for differences in layer moduli and wheel loads, as may be inferred from Eqs. (8.3) to (8.6), which are functions of the MDD displacements and the load offset. Researchers used these equations to predict the subgrade compressive and AC tensile strains from the measured MDD displacements under legal and overweight trucks. Note that these equations are specific to the pavement sections in which the MDDs were installed. Thus, differences in the prediction equations reflect the differences in the K6 and K7 pavement sections at the WIM site.

To compare overweight and legal trucks on the basis of predicted pavement damage potential, researchers estimated the service life consumed from one passage of a given truck using the following equation:

$$\frac{1}{(N_f)_{steering}} + \frac{1}{(N_f)_{drive}} + \frac{1}{(N_f)_{trailer}} = \frac{1}{(N_f)_{truck}} \tag{8.7}$$

where $(N_f)_{steering}$, $(N_f)_{drive}$ and $(N_f)_{trailer}$ are the predicted allowable repetitions corresponding to the steering, drive and trailer axle loads, and $(N_f)_{truck}$ is the computed allowable repetitions of the given truck. The allowable repetitions of the steering, drive and trailer axle loads are determined by first using the measured MDD displacements in Eqs. (8.3) to (8.6) to predict the strains at the MDD station for the given wheel load, and then using the predicted strains in Eqs. (8.1) and (8.2) to predict the number of allowable load repetitions based on rutting and fatigue cracking criteria.

Researchers used MDD data taken under permitted and non-permitted trucks at close to the same time to assess the pavement damage potential of permitted overweight trucks relative to legal or non-permitted trucks. Table 8.1 identifies the truck pairs evaluated by researchers. Truck IDs that begin with a *T* refer to legal or non-permitted trucks while those that are numeric refer to permitted overweight trucks. As used herein, a truck pair refers to a pair of legal and overweight trucks that happened to pass the MDD station within a short time interval of each other. In this way, environmental effects on the measured MDD displacements are minimized if not eliminated, and differences in pavement response

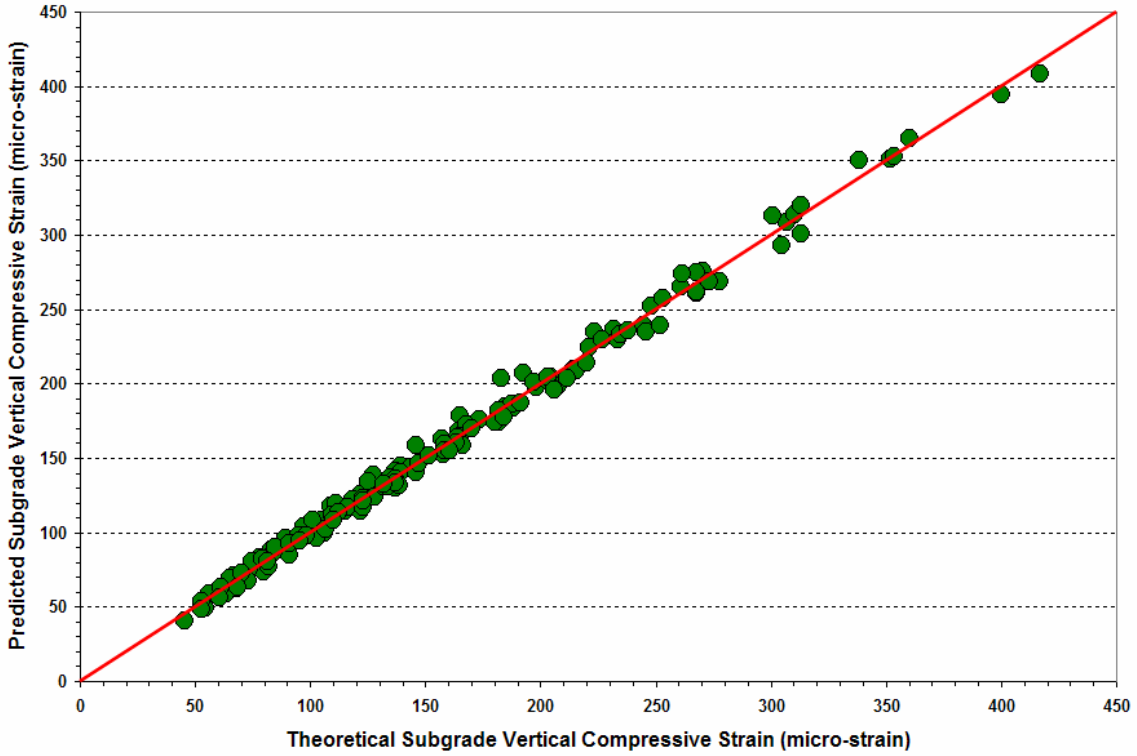

Figure 8.4. Comparison of Predicted versus Theoretical Vertical Compressive Strains at the Top of the Subgrade (K6 MDD).

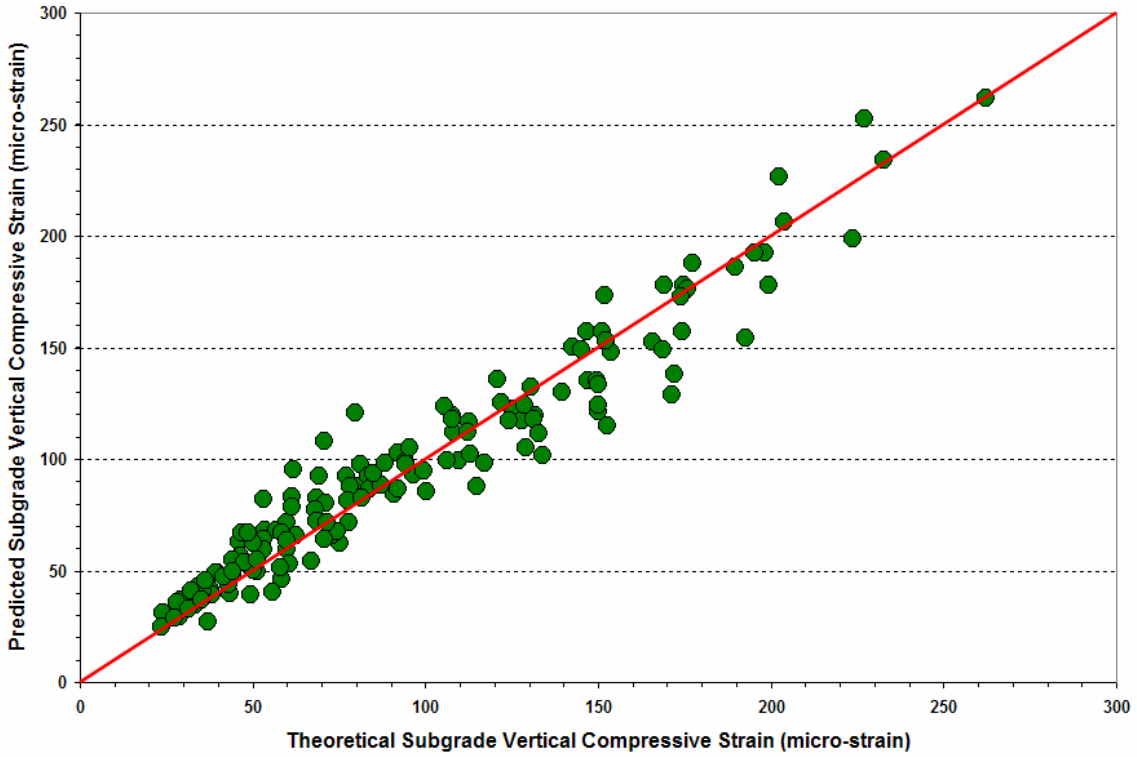

Figure 8.5. Comparison of Predicted versus Theoretical Vertical Compressive Strains at the Top of the Subgrade (K7 MDD).

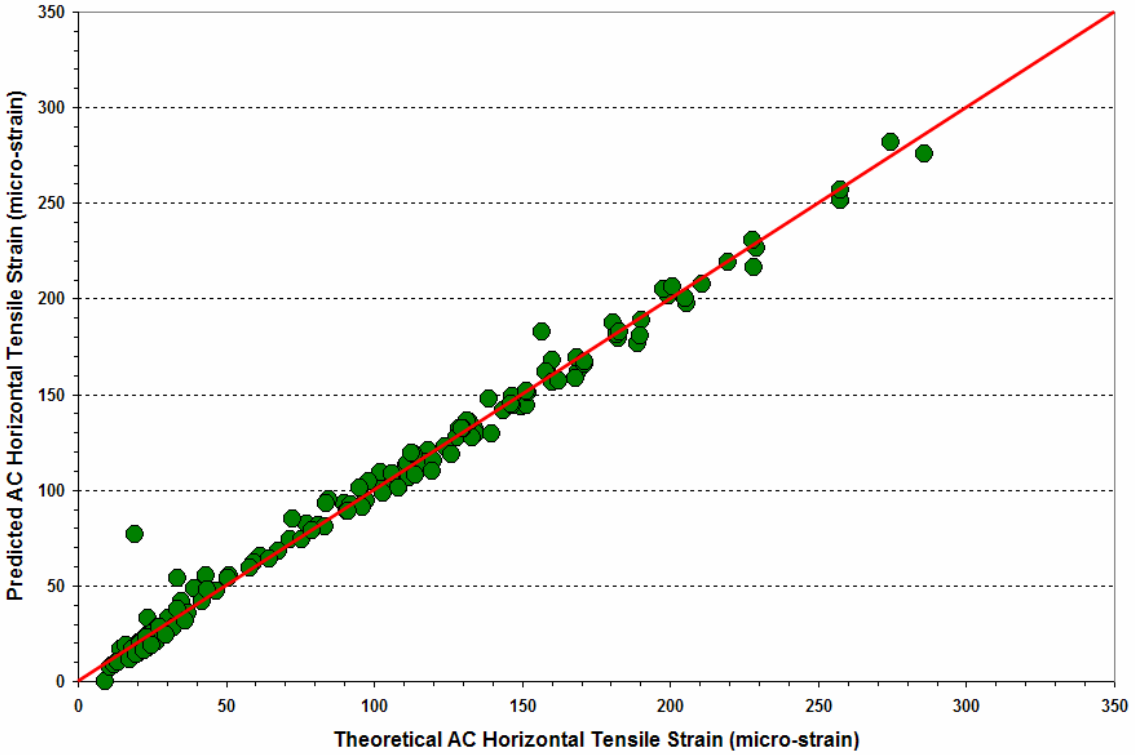

Figure 8.6. Comparison of Predicted versus Theoretical Horizontal Tensile Strains at the Bottom of the AC Layer (K6 MDD).

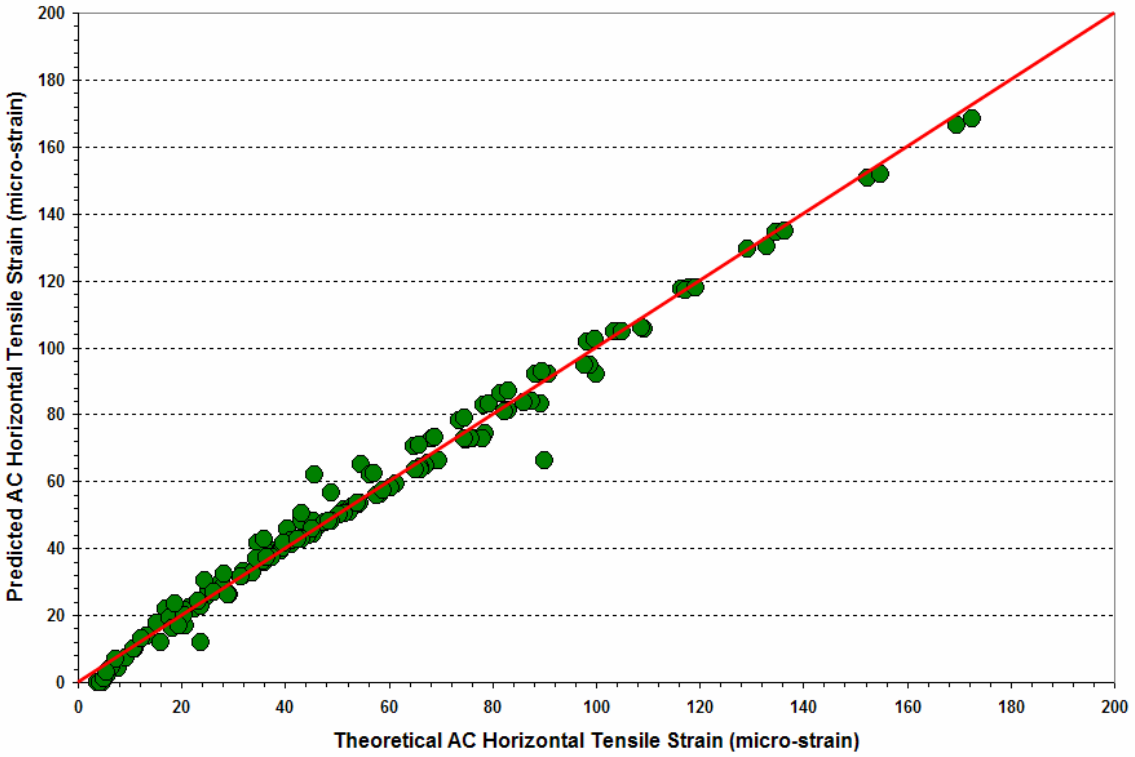

Figure 8.7. Comparison of Predicted versus Theoretical Horizontal Tensile Strains at the Bottom of the AC Layer (K7 MDD).

Table 8.1. Truck Pairs Used in Evaluating Pavement Damage Potential.

MDD Station	Date	Time	Truck ID	Axle Weight (kips)		
				Steering	Drive	Trailer*
K6 MDD	10/02	12:18:43	T26	10.2	38.1	56.0 (3)
	10/02	12:21:47	414	12.1	44.9	55.6 (2)
	10/02	12:46:07	T27	13.9	37.2	58.7 (2)
	10/02	12:49:43	415	12.7	41.2	56.1 (3)
	10/02	16:29:17	T32	15.0	38.0	38.3 (2)
	10/02	16:33:57	441	12.1	44.2	52.0 (3)
	10/02	18:30:55	T35	12.5	31.7	26.9 (3)
	10/02	18:17:12	470	10.0	44.1	39.6 (2)
	10/02	18:32:57	T37	11.6	31.8	20.3 (2)
	10/02	18:33:48	472	12.5	40.0	43.7 (2)
	10/02	18:42:18	T41	10.6	25.0	24.0 (2)
	10/02	18:41:16	474	11.7	41.4	57.5 (3)
	12/02	12:03:25	T14	11.4	33.3	31.4 (2)
	12/02	12:05:35	509	9.5	42.1	43.4 (2)
	12/02	13:05:11	T30	10.6	25.0	24.0 (2)
	12/02	13:07:11	512	9.6	39.1	34.1 (2)
	12/02	14:21:44	T41	10.6	35.0	44.0 (2)
	12/02	14:22:59	520	12.9	45.2	56.4 (3)
K7 MDD	12/02	15:04:52	T2	8.6	37.9	43.7 (2)
	12/02	15:00:25	484	11.3	41.8	55.6 (3)
	12/02	15:14:16	T3	10.7	32.2	38.4 (2)
	12/02	15:09:24	485	10.8	42.4	44.8 (2)
	12/02	15:25:55	T4	9.8	32.4	31.7 (2)
	12/02	15:28:52	486	12.5	41.3	43.7 (2)
	12/02	15:50:23	T5	9.5	32.4	31.7 (2)
	12/02	15:50:13	493	8.7	43.2	42.0 (3)
	12/02	16:09:20	T9	9.8	35.1	39.6 (2)
	12/02	16:03:28	497	9.0	37.7	44.5 (2)

***** The number within parentheses following the axle weight denotes the trailer axle configuration: 2 = tandem axle assembly and 3 = triple axle. The drive axles for trucks listed in the table are all tandems.

between trucks can primarily be attributed to differences in axle loads and offset distances from the MDD station.

Table 8.1 shows the axle weights for the trucks used in the comparisons of predicted pavement damage potential. It is observed that a number of legal trucks (i.e., T2, T3, T9, T26, T27, T32 and T41) had axle weights that exceeded the legal limits based on the data from the piezoelectric WIM sensors installed by TxDOT. From this perspective, researchers are of the opinion that the term non-permitted (in lieu of legal) is a more appropriate descriptor of these trucks. Researchers estimated the service life consumed based on the MDD displacements measured as each truck passed the given MDD station. Table 8.2 shows these estimates determined based on rutting and fatigue cracking criteria. For each truck pair, researchers determined the ratio of the service life consumed from one pass of the permitted truck to the corresponding service life consumed due to passage of the non-permitted truck. It is observed from Table 8.2 that the ratios are all greater than one, indicating greater potential for accelerated pavement deterioration on the route due to permitted overweight truck use. The averages of the service life consumption ratios based on rutting and fatigue cracking criteria are about 5.3 and 4.0, respectively, on the K6 MDD station. The corresponding averages on the K7 MDD station are about 3.4 and 2.4, respectively. Since K6 is the outside travel lane that generally receives truck traffic, researchers attribute the higher service life consumption ratios on K6 to the greater deterioration that has occurred at this station relative to the K7 MDD station. This observation is consistent with the findings presented in Chapter VII where it was shown that the backcalculated AC moduli from FWD measurements are lower on the K6 lane compared to the K7 lane. In the succeeding sections, researchers compare the K6 and K7 lanes on the basis of pavement condition survey data collected during this project.

PAVEMENT CONDITION SURVEY DATA ON K6 AND K7 LANES

In current practice, pavement performance is measured by monitoring the variation of functional and structural indicators over time or with cumulative traffic. The functional performance of a given pavement is typically measured by monitoring its ride quality from periodic measurements of pavement profile. On the other hand, structural performance is typically evaluated from temporal measurements of deformation and cracking that develop while the pavement is in service.

Table 8.2. Comparison of Non-Permitted and Permitted Trucks Based on Pavement Damage Predictions.

MDD Station	Truck ID	Predicted Service Life Consumed per Truck		Predicted Damage Ratio	
		Rutting	Fatigue Cracking	Rutting	Fatigue Cracking
K6 MDD	T26	1.55E-07	3.79E-09	1.30	2.82
	414	2.02E-07	1.07E-08		
	T27	5.94E-08	3.31E-09	1.94	1.96
	415	1.15E-07	6.48E-09		
	T32	9.39E-08	5.66E-09	2.50	2.39
	441	2.35E-07	1.35E-08		
	T35	1.22E-08	4.30E-10	10.05	9.55
	470	1.23E-07	4.10E-09		
	T37	7.02E-08	5.76E-09	2.49	1.22
	472	1.75E-07	7.00E-09		
	T41	2.65E-08	1.71E-09	8.80	8.66
	474	2.33E-07	1.48E-08		
	T14	1.36E-08	1.63E-10	7.90	5.10
	509	1.07E-07	8.32E-10		
	T30	1.06E-08	1.73E-09	11.22	1.55
	512	1.19E-07	2.67E-09		
	T41	4.74E-08	6.06E-10	1.50	3.18
	520	7.10E-08	1.93E-09		
Average Damage Ratio on K6 MDD				5.30	4.05
K7 MDD	T2	1.88E-09	2.19E-10	1.32	1.30
	484	2.48E-09	2.85E-10		
	T3	1.87E-09	2.26E-10	7.51	4.02
	485	1.40E-08	9.08E-10		
	T4	1.47E-10	1.98E-11	5.36	3.08
	486	7.88E-10	6.09E-11		
	T5	1.89E-09	1.16E-10	1.79	2.52
	493	3.38E-09	2.93E-10		
	T9	1.50E-09	2.17E-10	1.02	1.09
	497	1.53E-09	2.36E-10		
Average Damage Ratio on K7 MDD				3.40	2.40

During the course of this project, Pharr District personnel collected pavement smoothness and rut depth data on SH4/48. Researchers used the profile measurements provided by the District to monitor the change in pavement smoothness on the K6 and K7 lanes based on the International Roughness Index (IRI). In addition, researchers monitored the development of rutting from rut bar data collected during profile measurements, and conducted visual surveys at different times to check the progression of cracking along the route. In what follows, the performance data compiled by researchers are presented for the different FWD groups established along the K6 and K7 lanes, as identified in Chapter VII.

Analysis of Rut Bar Data

Rut depths were estimated using elevation data collected with the Pharr District's profiler rut bar. This device is mounted at the front of the inertial profiler van and houses two laser and three acoustic sensors that measure the heights aboveground at five different transverse locations corresponding to the middle of the rut bar, at the two wheel paths and 4 ft from the middle at each end. Height measurements are taken at specific intervals along the test lane (typically at 3.5-ft intervals on this project).

Researchers used the string line method to calculate the rut depth per wheel path from the rut bar data within ±50 ft of each FWD station. The averages of the left and right wheel path rut depths were then determined for each FWD group and plotted in Figures 8.8 to 8.14. Researchers used a power law model to characterize the trends in the data as illustrated in the figures. As shown, more rutting is observed on the K6 lane compared to K7, particularly within groups 1, 6 and 7. There are also indications of an accelerated rate of rut development on the K6 lane as inferred from the trend lines that show an increase in the progression of rutting within each group. Again, this observation is logical considering that K6 receives most of the truck traffic on SH4/48.

Researchers note that after October 2002, the K6 lane was milled beginning past the intersection of SH48 and FM802 to the junction of SH48 and Boca Chica Boulevard. In addition, maintenance seals were placed at various intervals along the K6 lane from Boca Chica to Cleveland Street along SH4. This maintenance work might have been in response to the observed rate of rut development on the K6 lane. Because of the maintenance performed, no data are reported for FWD stations within Groups 2 to 7 on the K6 lane after October 2002.

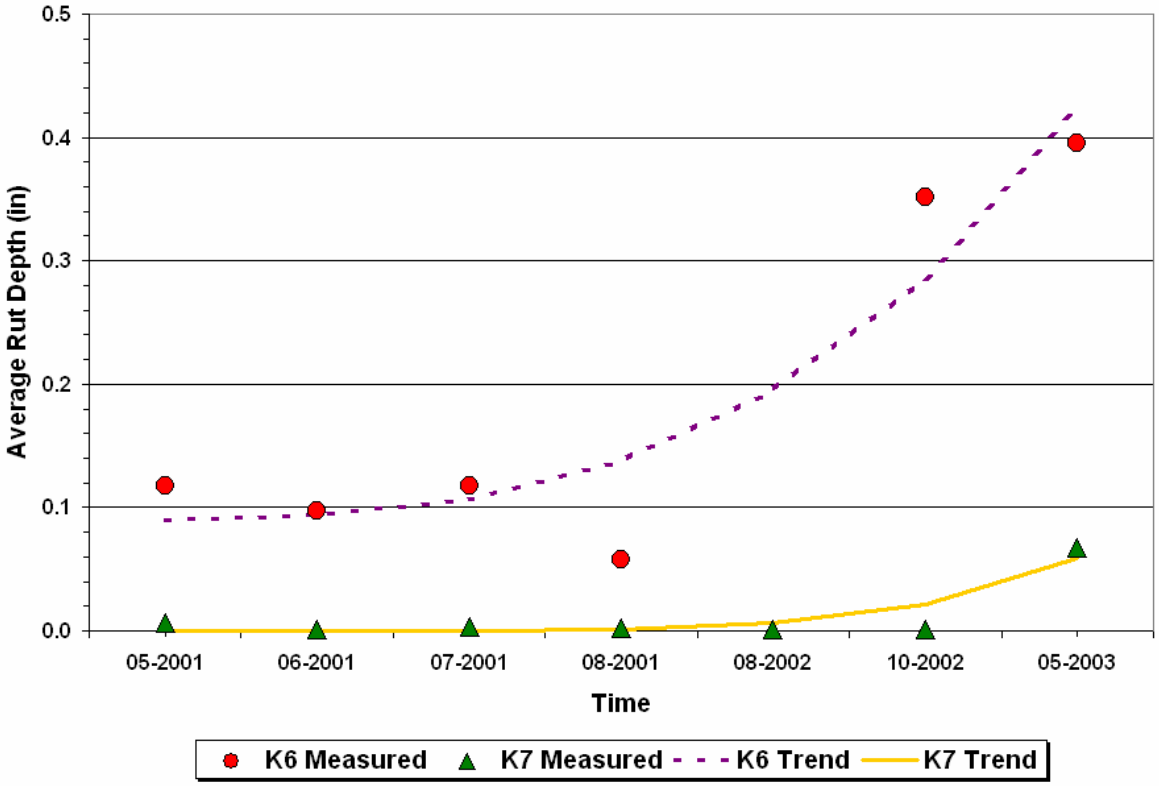

Figure 8.8. Progression of Rutting on Group 1 FWD Stations.

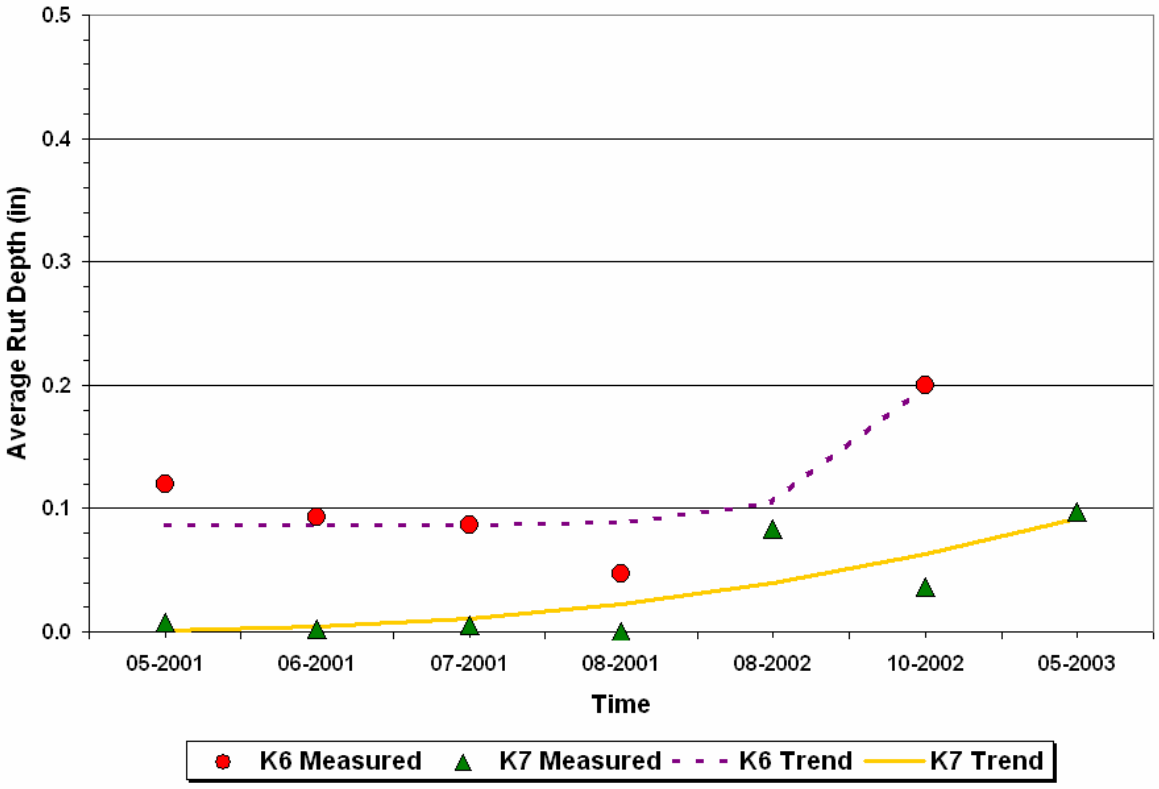

Figure 8.9. Progression of Rutting on Group 2 FWD Stations.

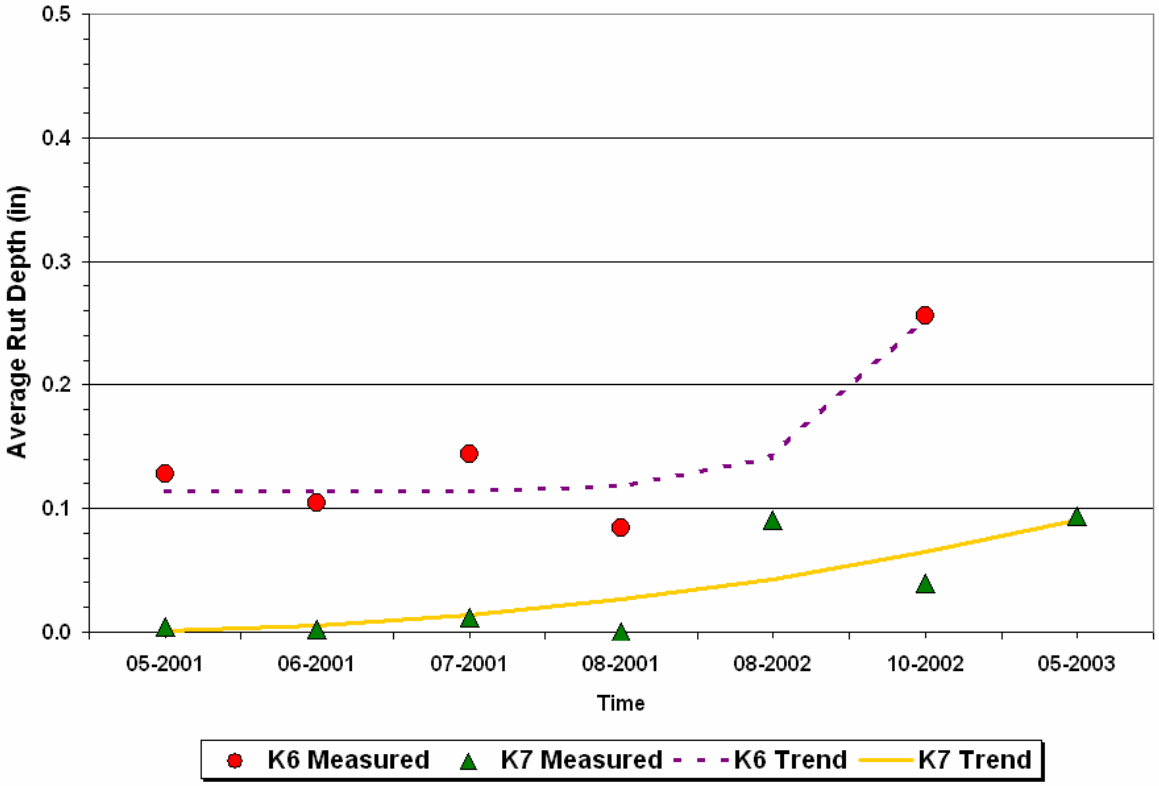

Figure 8.10. Progression of Rutting on Group 3 FWD Stations.

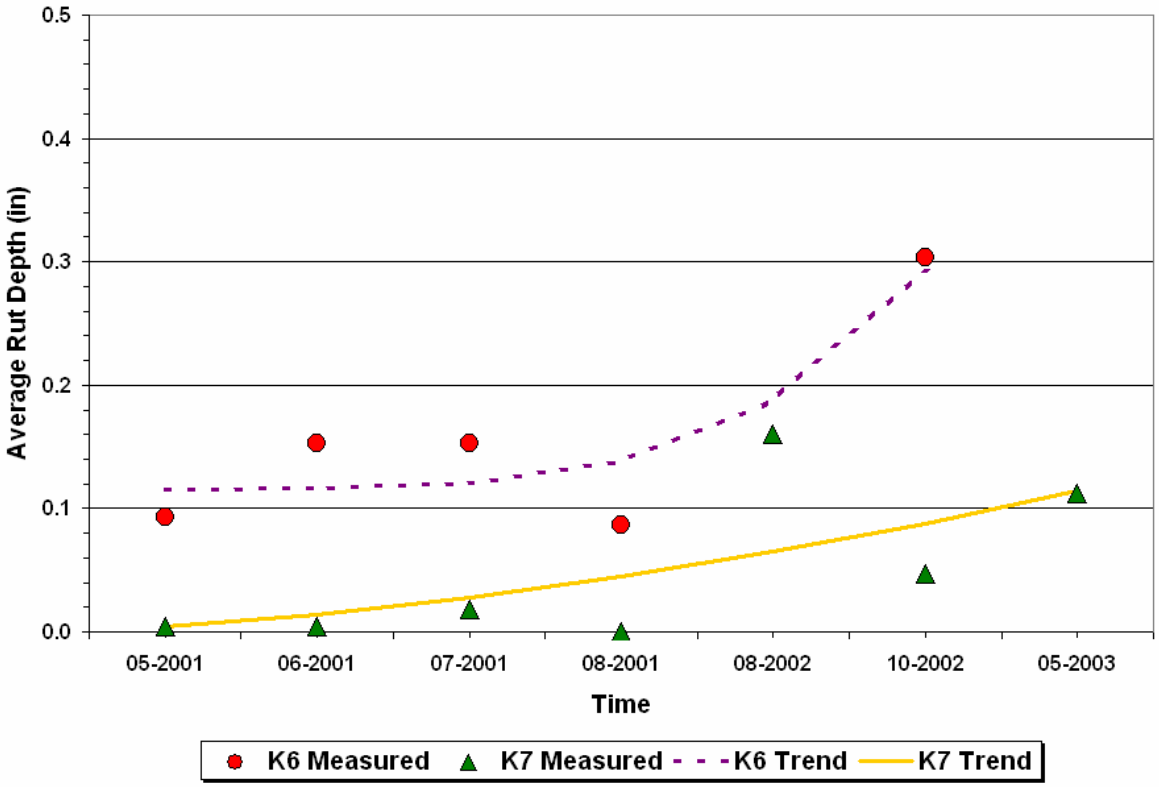

Figure 8.11. Progression of Rutting on Group 4 FWD Stations.

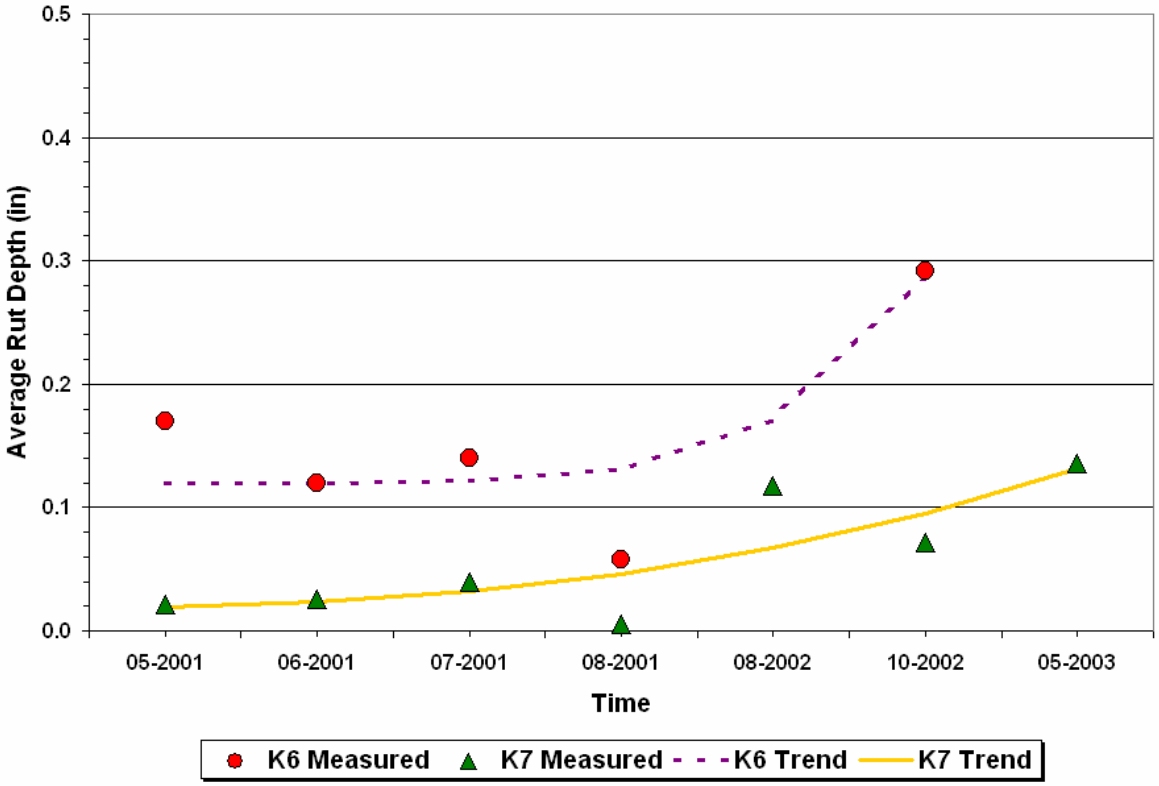

Figure 8.12. Progression of Rutting on Group 5 FWD Stations.

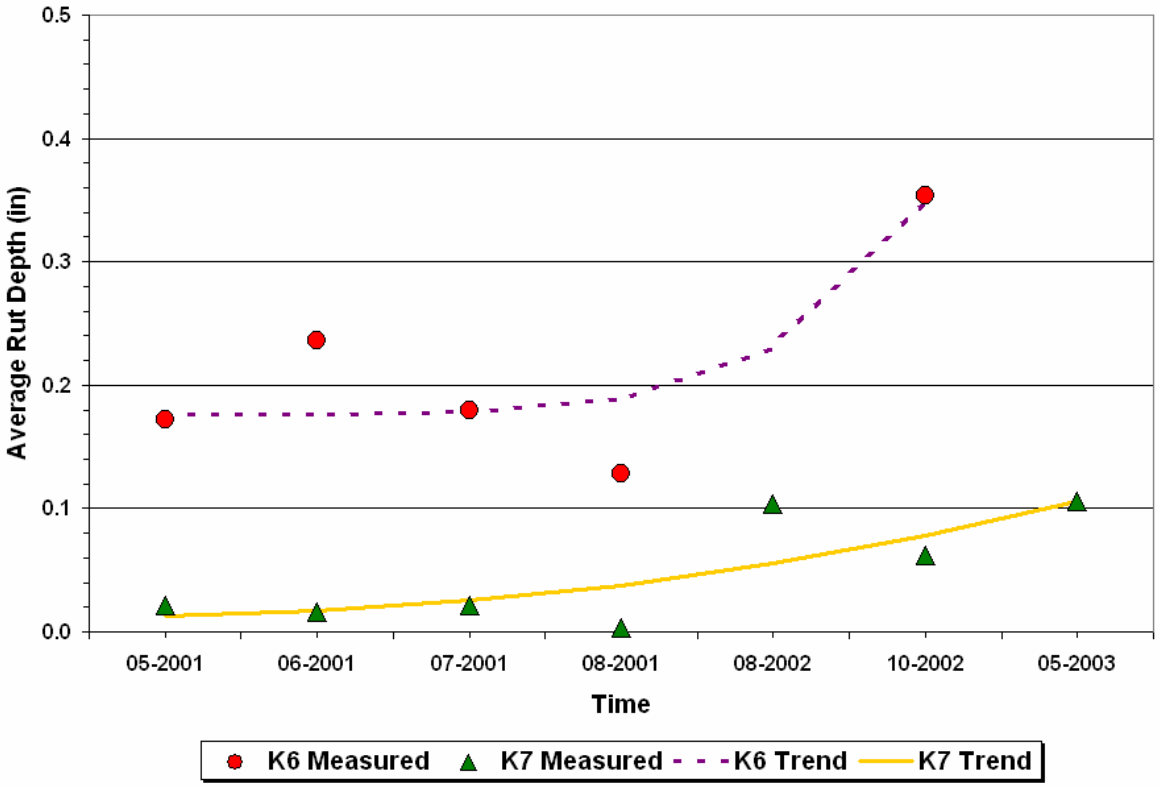

Figure 8.13. Progression of Rutting on Group 6 FWD Stations.

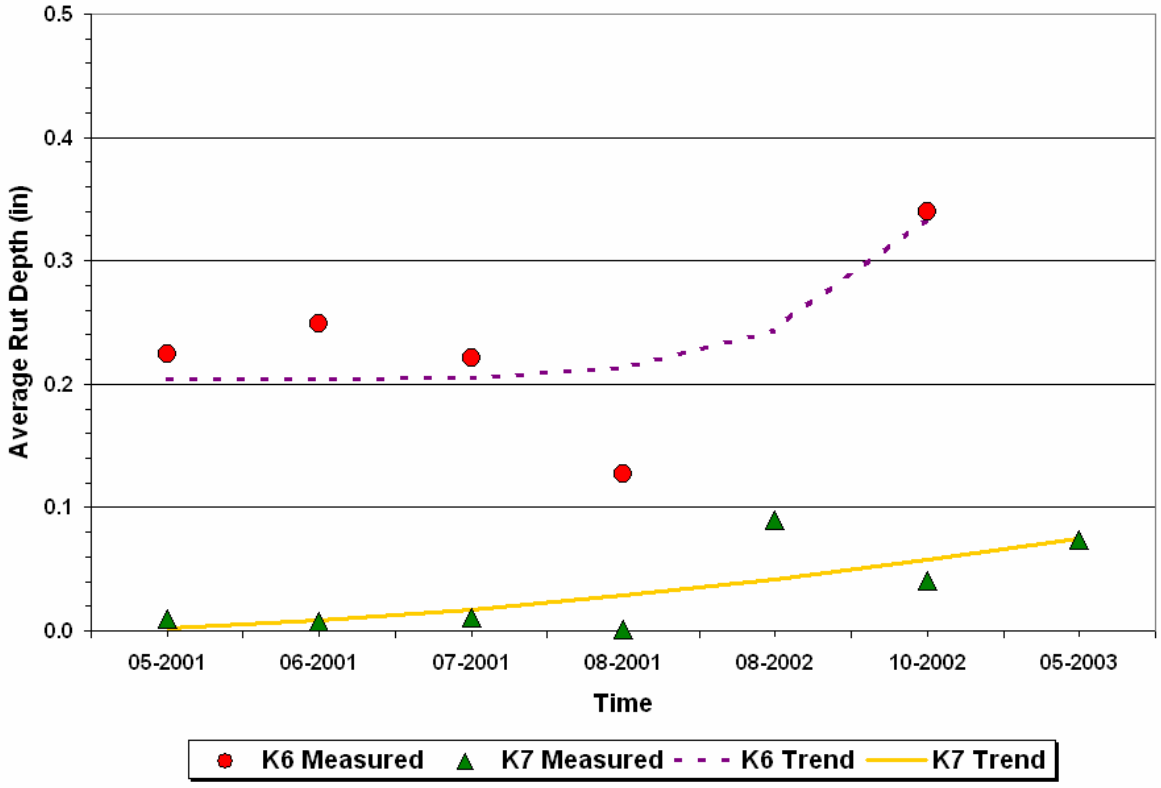

Figure 8.14. Progression of Rutting on Group 7 FWD Stations.

Analysis of Roughness Data

To quantify the surface smoothness along the K6 and K7 lanes, researchers computed the International Roughness Index from the wheel path profiles measured with the District's inertial profiler at different times during the project. Similar to the analysis of rut bar data, wheel path IRIs were determined within a ±50-ft interval of each FWD station using a program by Sayers (1995). The averages of the left and right wheel path IRIs were then determined for each FWD group and plotted in Figures 8.15 to 8.21.

It is observed that the K6 lane is rougher than the K7 lane as evidenced by the higher IRIs computed for K6 where the overall means of the measured IRIs range from 91 to 129 inches/mile. This range in IRIs is characteristic of medium-smooth pavements. On K7, the corresponding range is from 44 to 87 inches/mile, which indicates a smoother lane. In fact, 58 percent of the average IRIs determined from the profiles collected on K7 are less than 60 inches/mile, a threshold used in TxDOT's Item 585 (2004) smoothness specification to identify pavement sections that merit bonuses due to above standard riding quality.

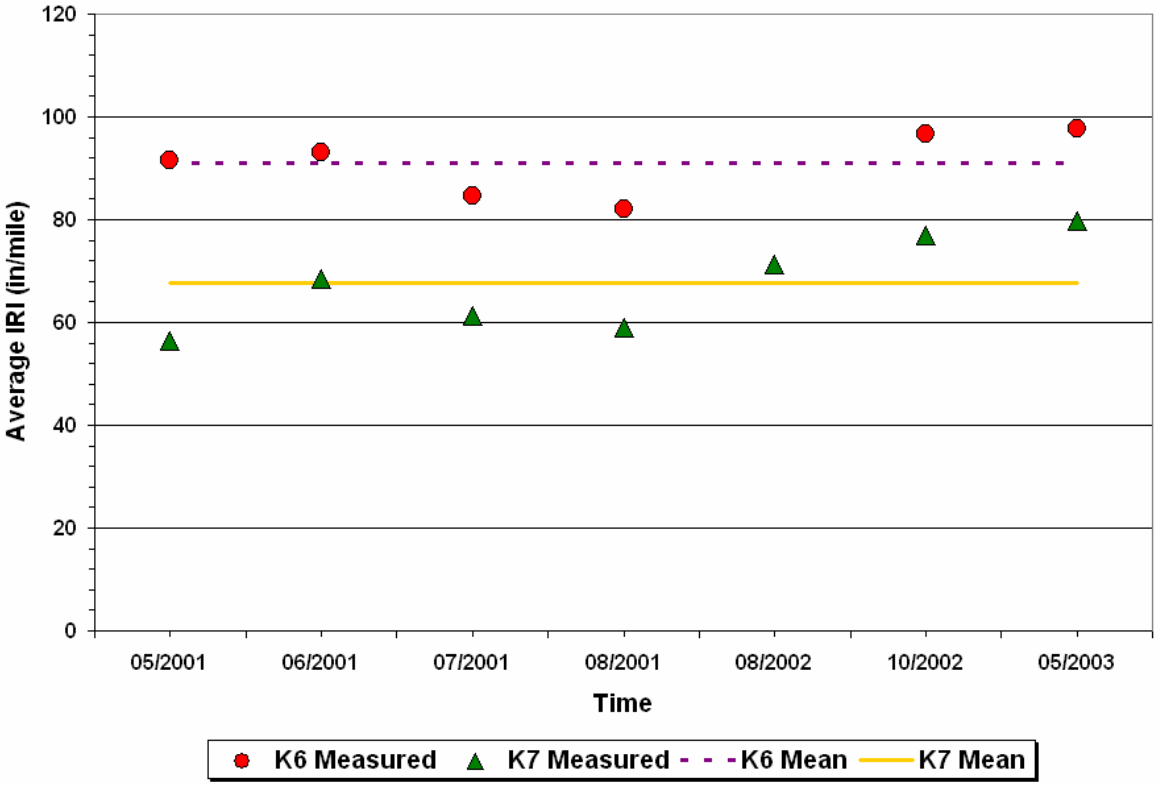

Figure 8.15. Average IRIs of Group 1 FWD Stations.

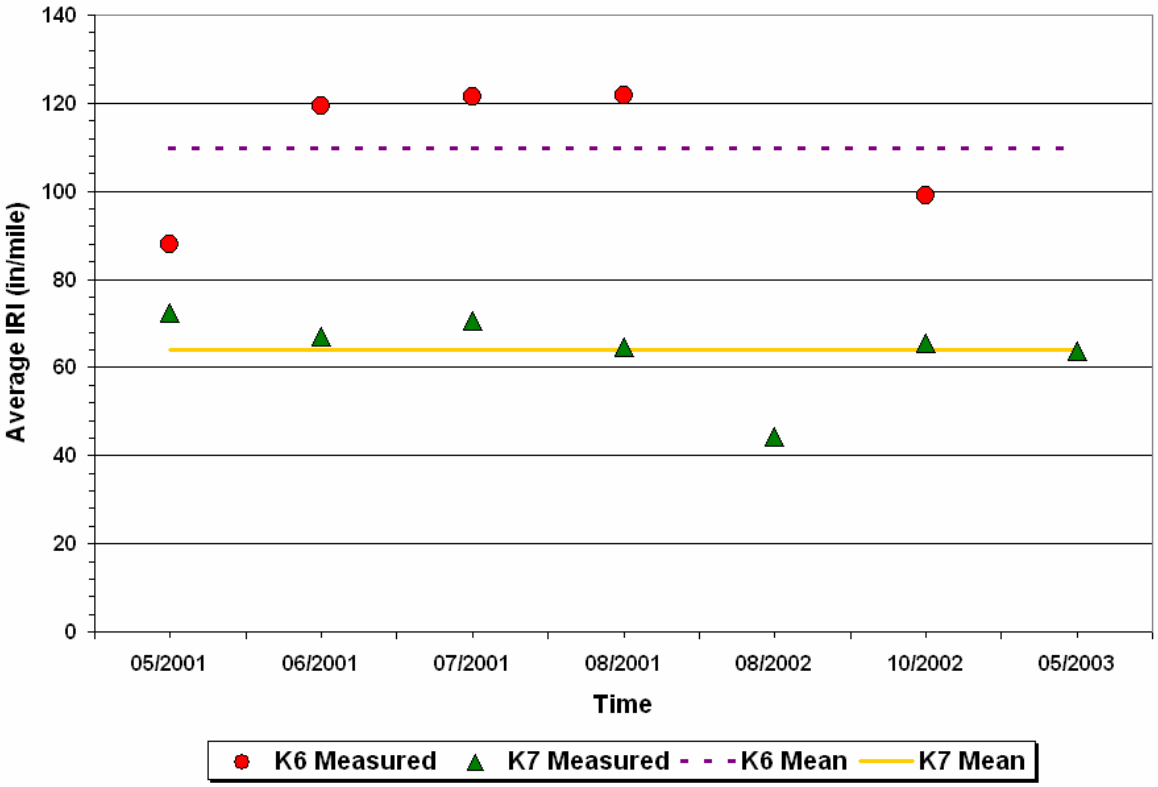

Figure 8.16. Average IRIs of Group 2 FWD Stations.

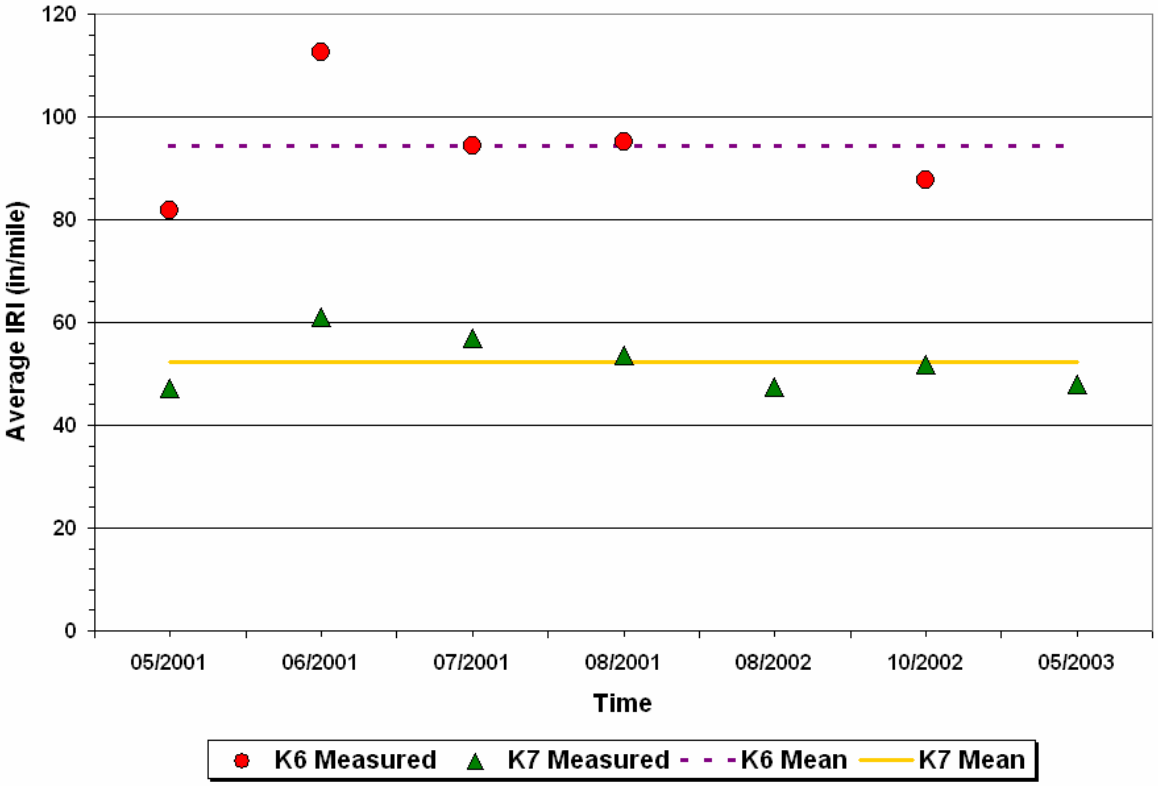

Figure 8.17. Average IRIs of Group 3 FWD Stations.

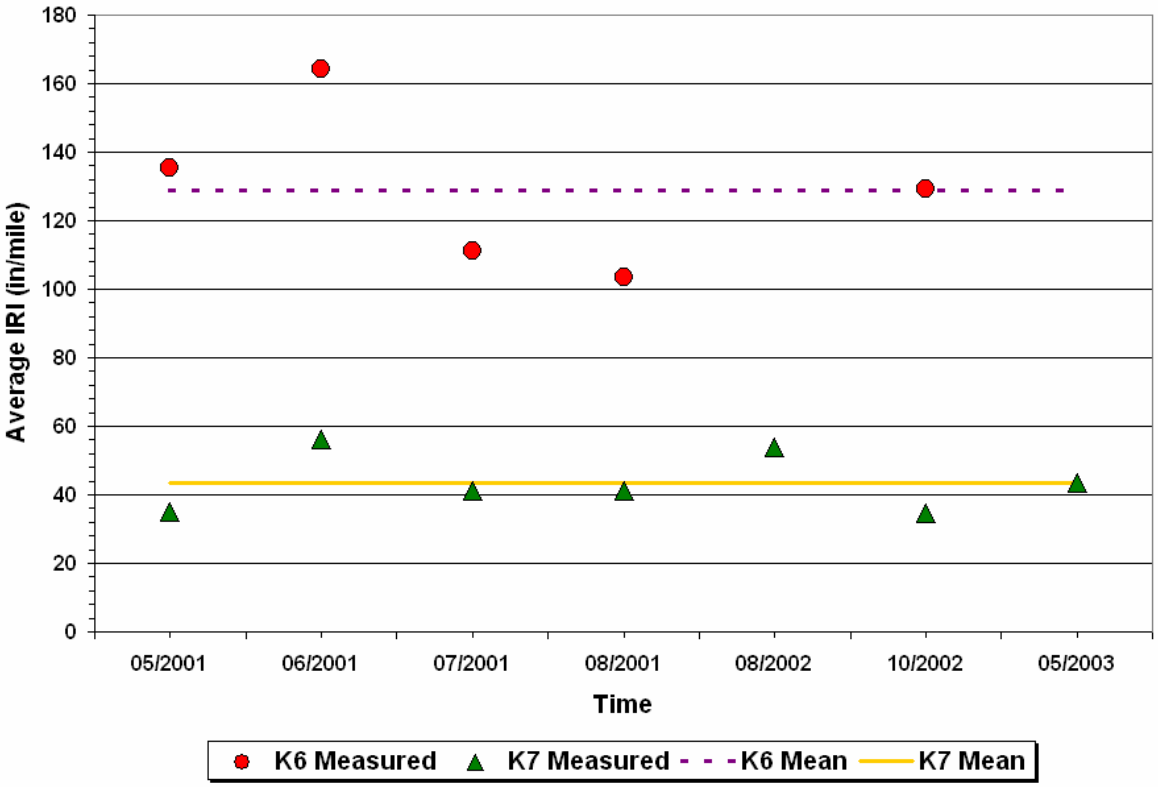

Figure 8.18. Average IRIs of Group 4 FWD Stations.

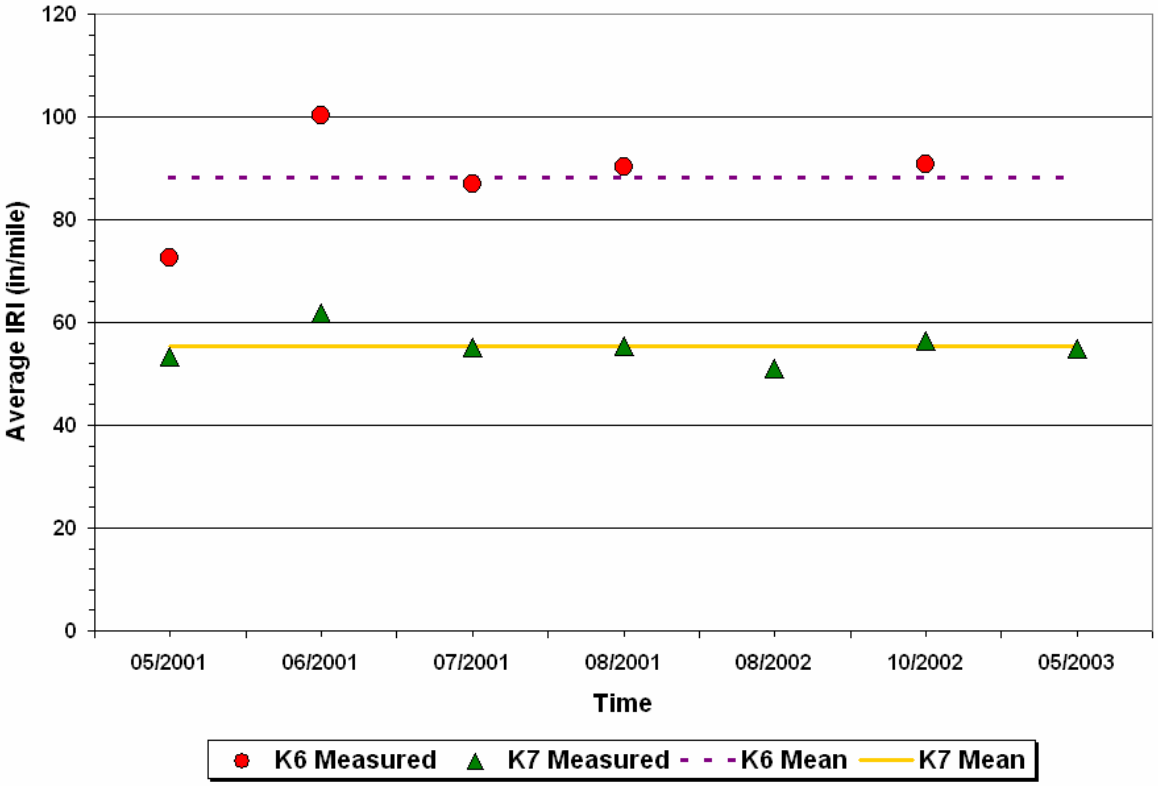

Figure 8.19. Average IRIs of Group 5 FWD Stations.

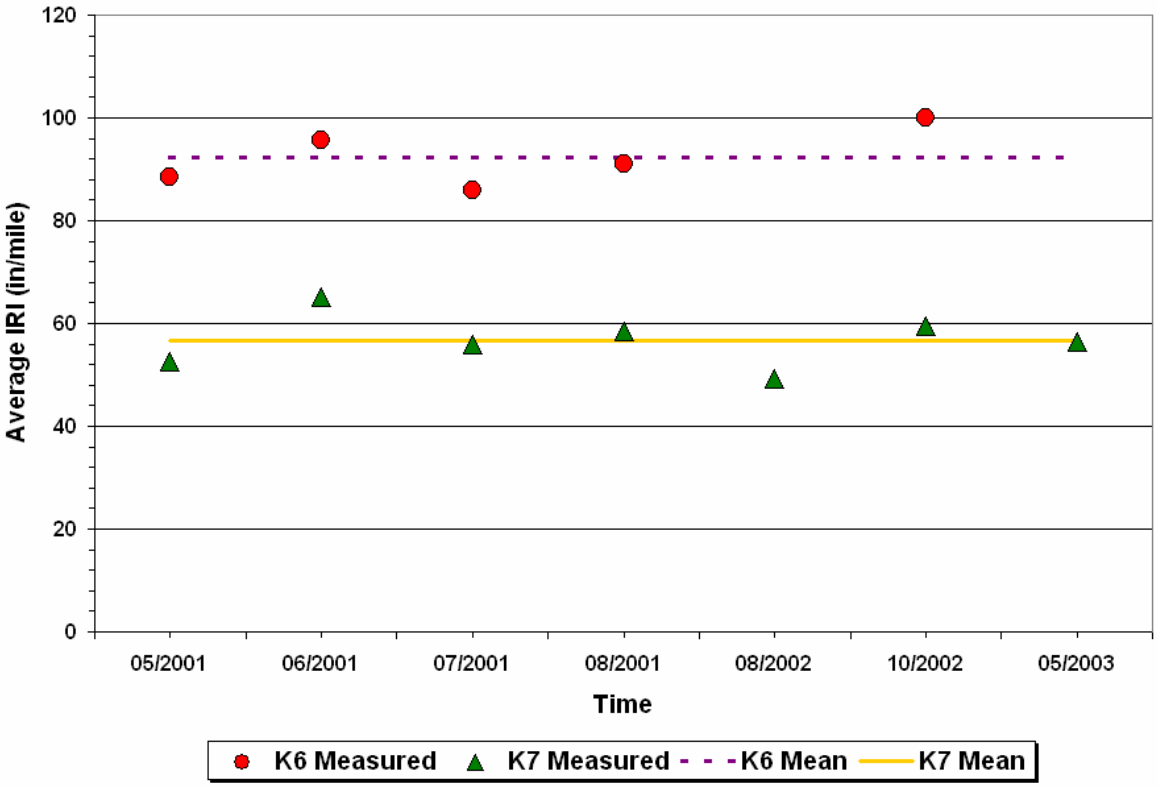

Figure 8.20. Average IRIs of Group 6 FWD Stations.

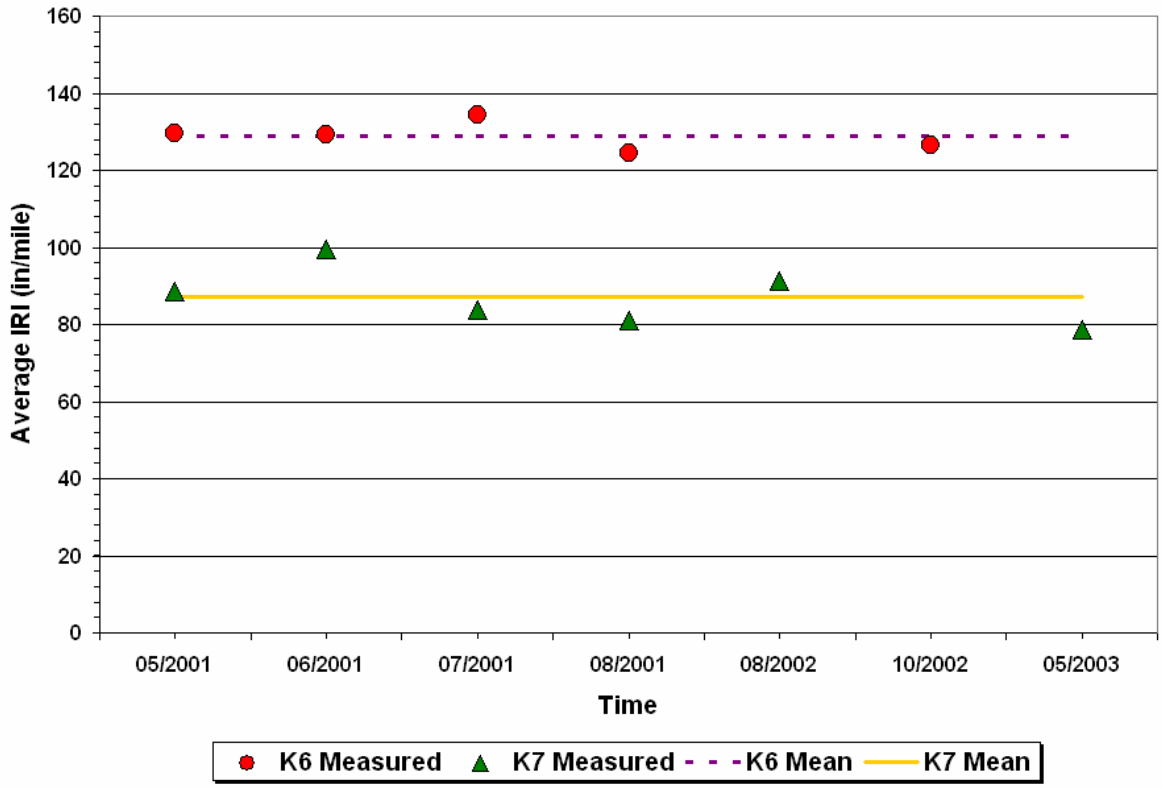

Figure 8.21. Average IRIs of Group 7 FWD Stations.

Analysis of Cracking Data

To monitor the development of cracking, researchers conducted visual surveys within ±50 ft of each FWD station at different times during the project. Within each 100-ft interval, researchers surveyed the pavement surface to check for the occurrence of alligator, longitudinal and transverse cracking. Alligator cracks form a pattern resembling that of an alligator's skin and develop from fatigue of the surface material due to repeated wheel load applications. Current TxDOT practice (2002) quantifies this distress in terms of the percentage of the rated section's total wheel path area covered by alligator cracking.

Longitudinal cracking consists of cracks or breaks that run approximately parallel to the pavement centerline. This distress is quantified in terms of the average linear feet of cracking per 100 ft of pavement surface. On the other hand, transverse cracks travel at right angles to the pavement centerline and are quantified in terms of the average number of cracks per 100 ft of surface.

Charts presenting the crack survey data are provided in Appendix H of this report. Most of the cracks observed on the K6 and K7 lanes were longitudinal cracks. Since differential movement beneath the surface is a primary cause of this crack, its occurrence

might be associated with the development of rutting on the lanes tested. As expected, cracking was more predominant on the K6 lane than on K7.

Appendix H also presents charts of the pavement scores determined from the survey data. These scores range from a low of zero to a perfect score of 100. It is observed from the charts that the FWD groups on the K7 lane generally scored 100, reflecting the minimal distress on this lane.

INVESTIGATION OF PAVEMENT DAMAGE FROM CUMULATIVE TRUCK LOAD APPLICATIONS BASED ON BACKCALCULATED AC MODULUS

Analyses of FWD data presented in Chapter VII revealed lower backcalculated modulus values in the K6 lane compared to the K7 lane. This finding is reflected in the comparisons between the modulus-temperature relationships, determined based on the Witczak-Fonseca (1996) model (Eq. 7.10), and in the comparisons between the temperature-corrected AC moduli from both lanes. Since the K6 lane receives more truck traffic than the adjacent K7 lane, the lower backcalculated AC moduli from K6 indicates (in the authors' opinion) the greater deterioration that has occurred due to this difference. To quantify this difference, researchers characterized the traffic in both lanes based on the cumulative 18-kip equivalent single axle loads. For this task, the Pharr District provided historical data on average daily traffic (ADT) along SH4/48. In addition, TxDOT's Transportation Planning and Programming (TPP) Division provided weigh-in-motion data from the piezoelectric sensors installed along SH48 that covered the period from September 2002 to August 2003. The WIM data permitted researchers to characterize the axle load distributions and, thus, estimate the cumulative 18-kip ESALs for the 2003 fiscal year using load equivalency factors from the design guide published by the American Association of State Highway and Transportation Officials (AASHTO, 1993).

From the historical ADT data, researchers estimated the traffic growth rate based on the trend line fitted to the data. Since SH4/48 was subdivided into seven FWD groups, researchers determined traffic growth rates for the different roadway intervals corresponding to these groups. Figure 8.22 shows the historical trend in the ADTs for the section of the route where the Group 1 FWD stations are found. The points plotted are the ADTs for different years as obtained from the Pharr District data. The trend in the plotted points is given by the fitted line. To determine the growth rate g, researchers used the equation:

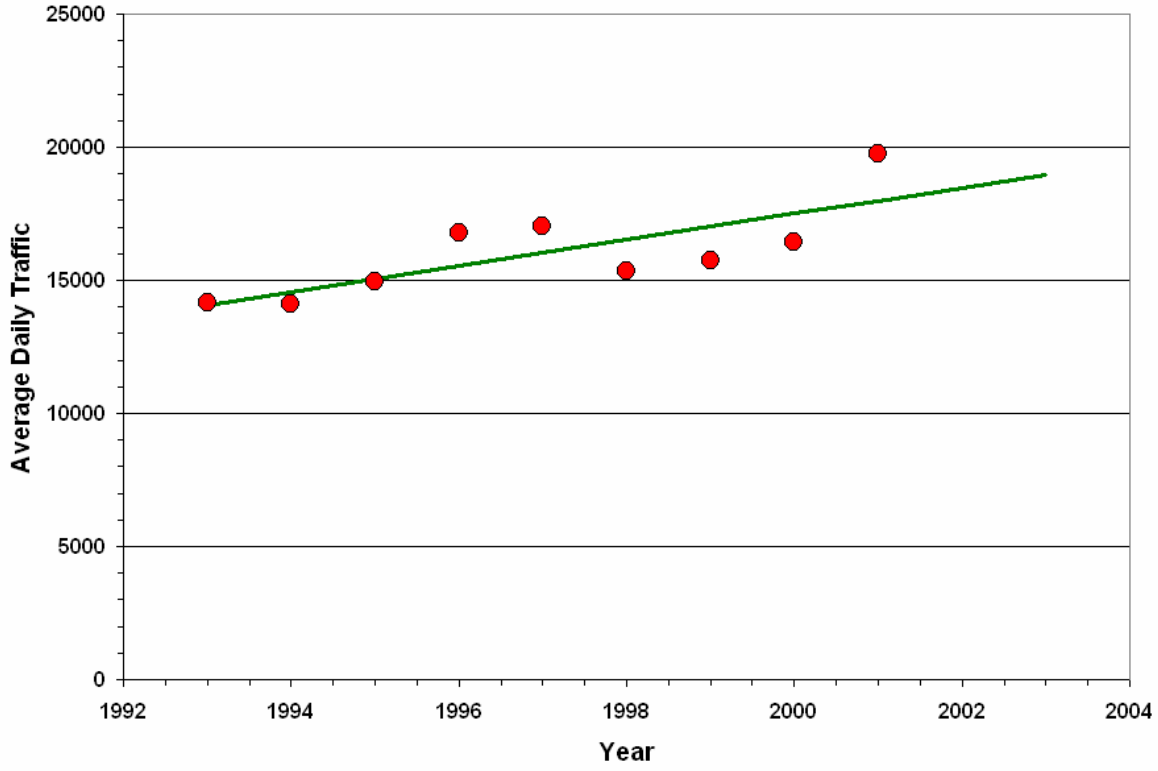

Figure 8.22. Historical Trend of ADTs for Group 1 FWD Stations.

$$g = \left(\frac{ADT_n}{ADT_0}\right)^{\frac{1}{n}} - 1 \qquad (8.8)$$

where,

ADT_0 = average daily traffic at start of the evaluation period,

ADT_n = average daily traffic at end of the evaluation period, and

n = length of the evaluation period in years.

In the analysis, researchers used 1993 as the start of the evaluation period as this was the last reported year of resurfacing along SH4/48. In addition, the length of the evaluation period was taken as 10 years. To estimate the growth rate, researchers determined the beginning and ending ADTs based on the trend line fitted to the data. These values were then used in Eq. (8.8) to calculate the traffic growth rate. Table 8.3 shows the rates determined from these calculations. Researchers used these growth rates, along with the estimated number of 18-kip ESALs for 2003, to backcalculate the number of 18-kip ESALs at the base year of the evaluation period (1993). This value was then used in the following equation to estimate the cumulative 18-kip ESALs for each year of the evaluation period:

Table 8.3. Estimated Growth Rates along Different Sections of SH4/48.

FWD Group	ADT_0 (1993)	ADT_n (2003)	Traffic Growth Rate (percent)	Base Year 18-kip ESALs (1993)*
1	14,079	18,974	3.03	234,762
2, 3, 4, 5	23,511	28,344	1.89	262,437
6	28,022	34,356	2.06	258,055
7	27,148	29,253	0.75	293,618

* Estimates are for the westbound K6 and K7 lanes.

$$ESAL_t = ESAL_0 \times \left[\frac{(1+g)^n - 1}{g} \right] \quad (8.9)$$

where,

$ESAL_t$ = cumulative 18-kip ESALs up to year t, and

$ESAL_0$ = number of 18-kip ESALs in base year (1993).

Table 8.4 gives the estimates of cumulative 18-kip ESALs for the different times FWD data were collected during this project. These estimates are given for different sections of the route corresponding to the FWD groups established by researchers.

To evaluate the effect of truck traffic on backcalculated AC modulus, researchers plotted the temperature-corrected AC modulus (based on 75 °F) versus the cumulative 18-kip ESALs at the different test dates. Figures 8.23 to 8.29 illustrate the relationships determined. In these figures, the averages of the corrected AC moduli are plotted versus the corresponding cumulative 18-kip ESALs for the various test dates. Table 8.5 gives the averages of the temperature-corrected AC moduli.

To quantify the relationship between temperature-corrected AC moduli and cumulative 18-kip ESALs, researchers fitted a sigmoidal curve to the data based on the equation:

$$E'_{ac} = \alpha + \gamma \left(1 - e^{-\left(\frac{\rho}{N}\right)^{\beta}} \right) \quad (8.10)$$

where,

E'_{ac} = backcalculated AC modulus (ksi) corrected to a reference temperature of 75 °F,

N = cumulative 18-kip ESALs, and

$\alpha, \gamma, \rho, \beta$ = model coefficients determined by nonlinear regression.

Table 8.4. Estimates of Cumulative 18-kip ESALs on Different Dates of Testing.

Lane	Date of Test	FWD Group			
		1	2 to 5	6	7
K6	Feb. 2001	1,349,509	1,455,800	1,439,168	1,572,194
	May 2001	1,402,305	1,510,392	1,493,484	1,628,655
	July 2001	1,437,503	1,546,786	1,529,695	1,666,295
	Aug. 2001	1,455,101	1,564,983	1,547,800	1,685,116
	Mar. 2002	1,579,891	1,693,392	1,675,655	1,817,281
	July 2002	1,652,418	1,767,553	1,749,568	1,893,127
	Sept. 2003	1,911,205	2,030,268	2,011,684	2,159,866
K7	Feb. 2001	499,134	538,447	532,295	581,496
	May 2001	518,661	558,638	552,385	602,379
	Aug. 2001	538,188	578,829	572,474	623,262
	Mar. 2002	584,343	626,323	619,763	672,145
	July 2002	611,168	653,753	647,100	700,198
	Oct. 2002	631,287	674,325	667,603	721,237
	Dec. 2002	644,700	688,040	681,272	735,263
	Apr. 2003	672,337	715,987	709,172	763,526
	Sept. 2003	706,884	750,921	744,048	798,854

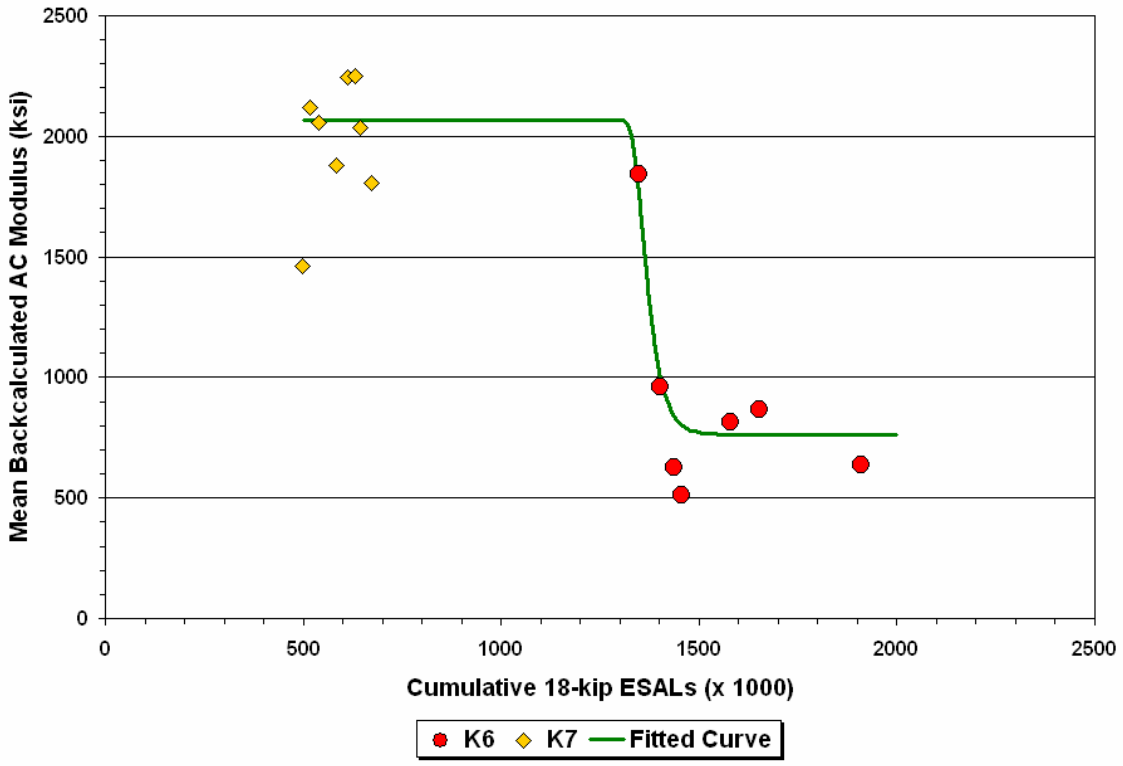

Figure 8.23. Plot of the Average Corrected AC Moduli vs. Cumulative 18-kip ESALs for Group 1 FWD Stations.

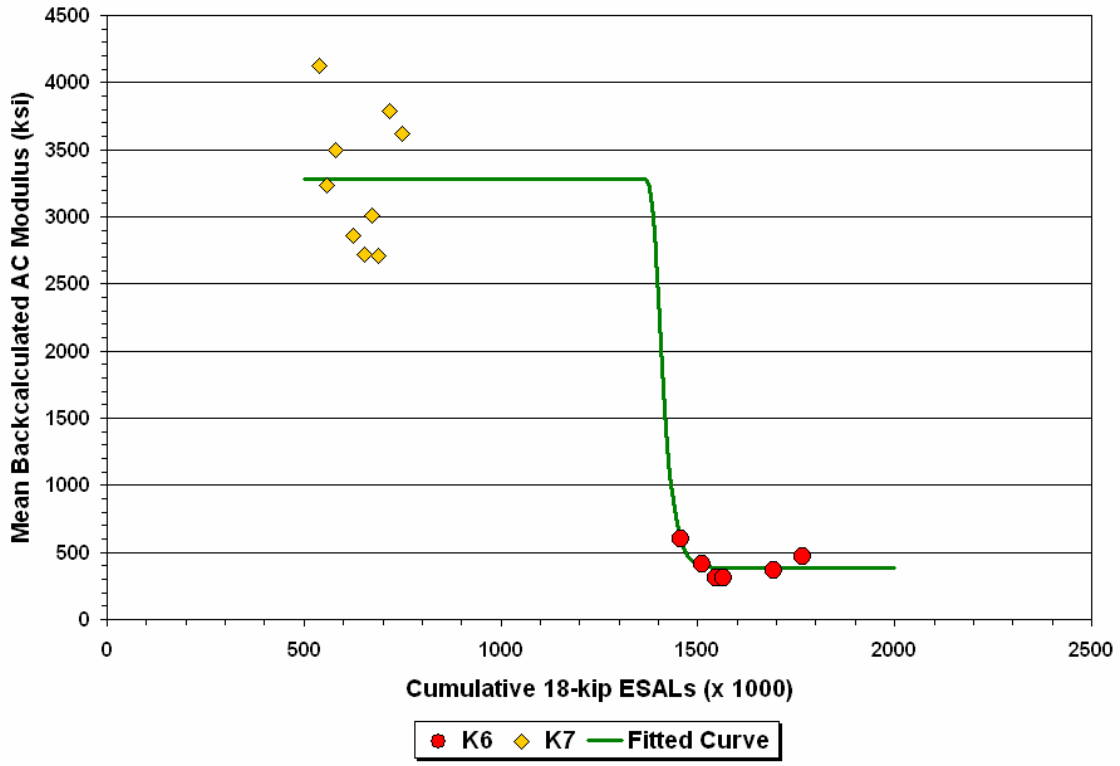

Figure 8.24. Plot of the Average Corrected AC Moduli vs. Cumulative 18-kip ESALs for Group 2 FWD Stations.

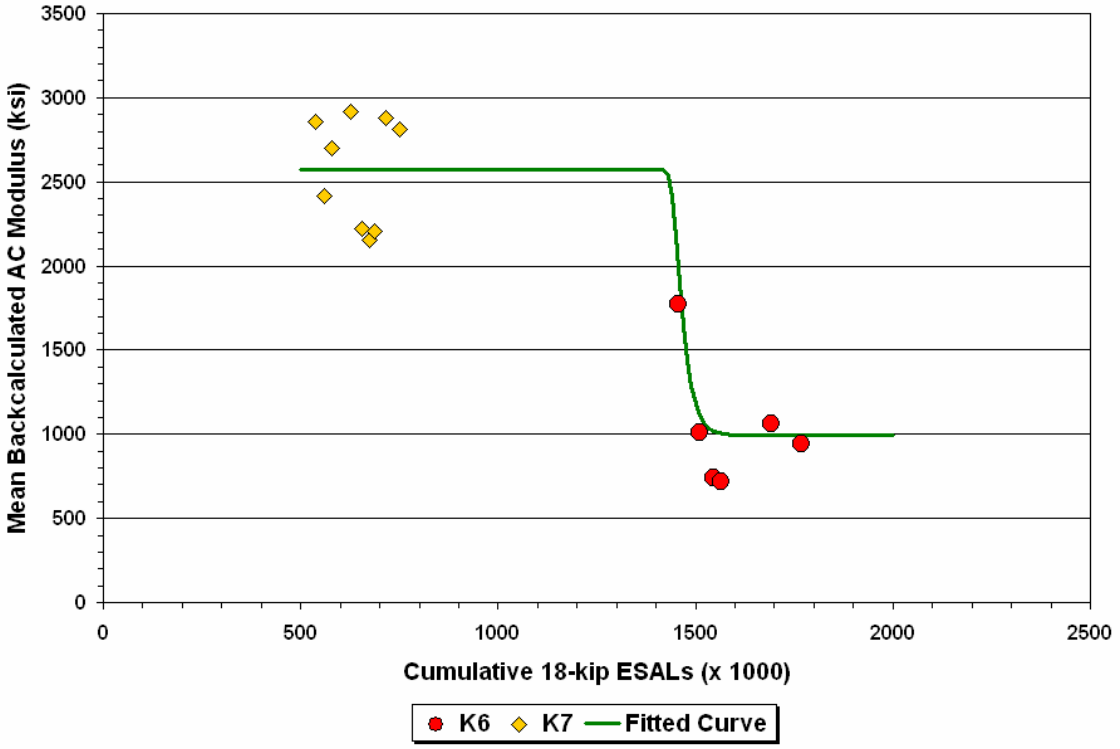

Figure 8.25. Plot of the Average Corrected AC Moduli vs. Cumulative 18-kip ESALs for Group 3 FWD Stations.

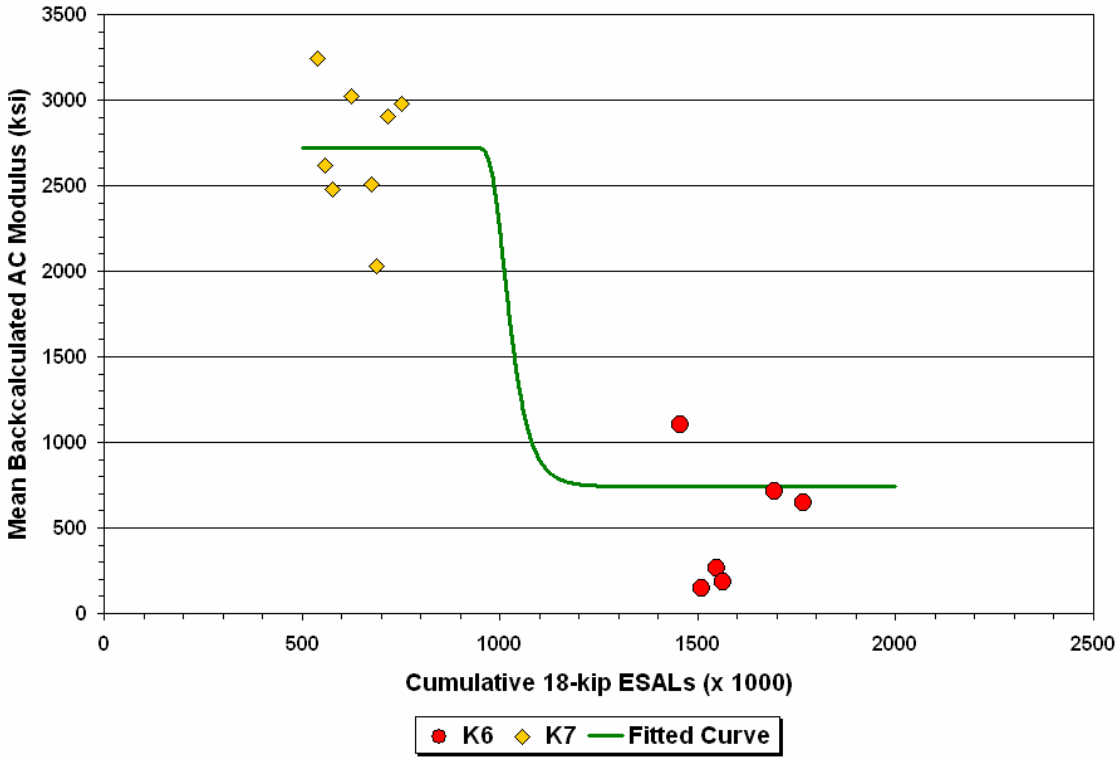

Figure 8.26. Plot of the Average Corrected AC Moduli vs. Cumulative 18-kip ESALs for Group 4 FWD Stations.

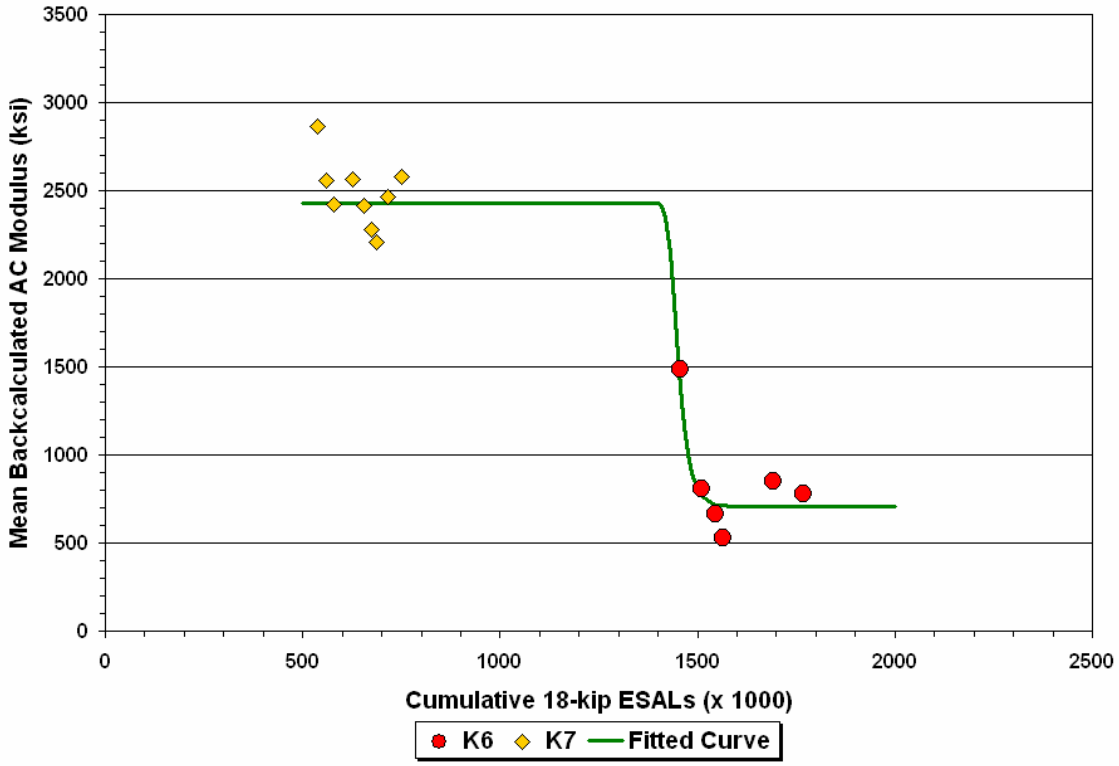

Figure 8.27. Plot of the Average Corrected AC Moduli vs. Cumulative 18-kip ESALs for Group 5 FWD Stations.

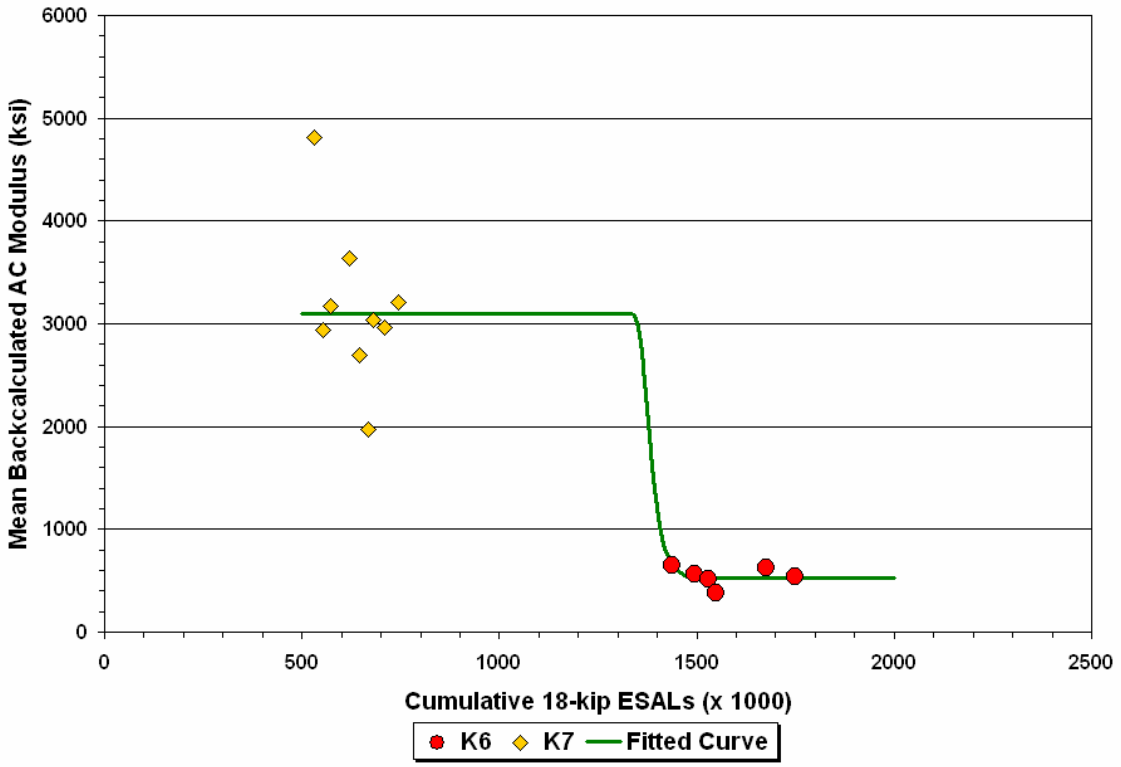

Figure 8.28. Plot of the Average Corrected AC Moduli vs. Cumulative 18-kip ESALs for Group 6 FWD Stations.

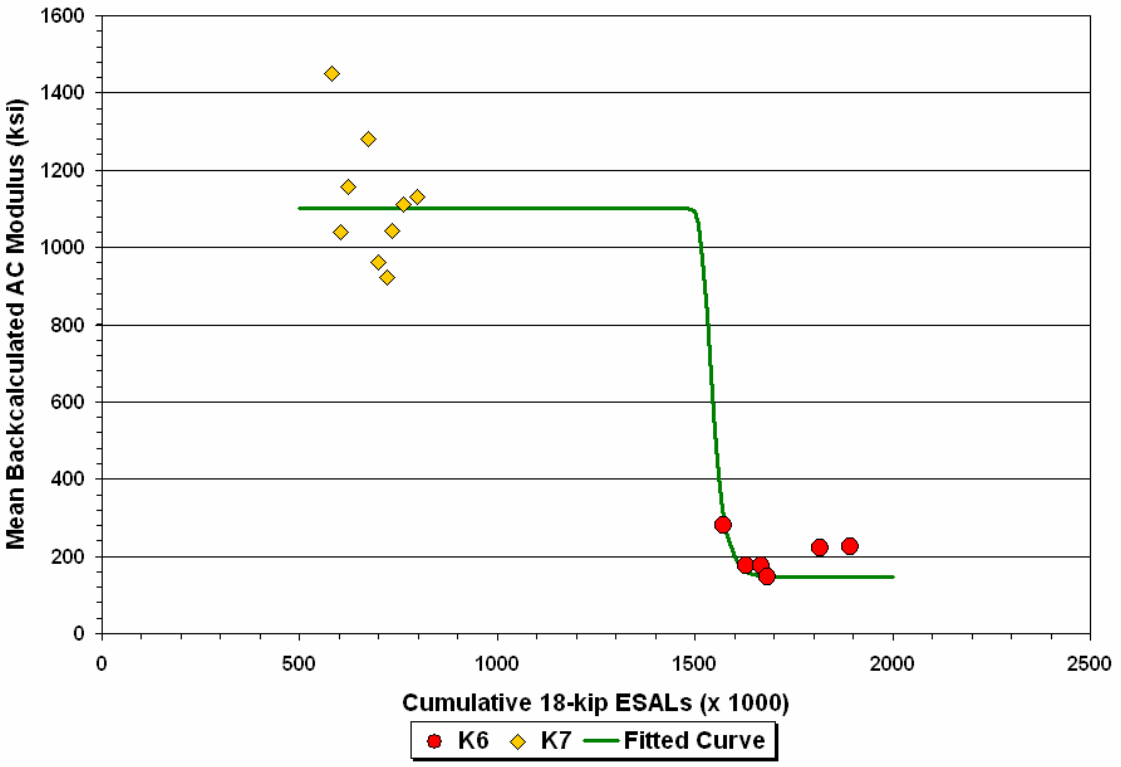

Figure 8.29. Plot of the Average Corrected AC Moduli vs. Cumulative 18-kip ESALs for Group 7 FWD Stations.

Table 8.5. Average Temperature-Corrected AC Moduli on K6 and K7 Lanes.

Lane	Date of Test	Corrected AC Modulus (ksi) by FWD Group*						
		1	2	3	4	5	6	7
K6	Feb. 2001	1841	596	1773	1101	1486	646	281
	May 2001	961	410	1006	147	808	561	175
	July 2001	629	306	744	261	662	519	177
	Aug. 2001	511	312	720	180	528	382	145
	Mar. 2002	817	366	1060	716	851	625	223
	July 2002	865	471	940	650	782	535	225
	Sept. 2003	637						
K7	Feb. 2001	1460	4124	2856	3239	2863	4816	1449
	May 2001	2121	3230	2417	2618	2554	2937	1041
	Aug. 2001	2055	3500	2698	2481	2420	3172	1157
	Mar. 2002	1876	2863	2920	3020	2568	3640	1282
	July 2002	2244	2721	2218	2505	2415	2696	962
	Oct. 2002	2249	3014	2153		2276	1968	922
	Dec. 2002	2035	2711	2203	2026	2206	3033	1044
	Apr. 2003	1805	3790	2882	2903	2466	2958	1110
	Sept. 2003	2750	3616	2809	2978	2575	3211	1132

* Shaded cells show dates where no data are available.

Table 8.6 summarizes the parameters of the sigmoidal curve for each FWD group. In addition, Table 8.7 gives the analysis of variance results. This table shows that the relationships between the corrected AC modulus and the cumulative 18-kip ESALs are statistically significant, as reflected in the low *p* statistics given in the last column. The relationships given in Figures 8.23 to 8.29 clearly demonstrate that the higher cumulative 18-kip ESALs are associated with lower corrected AC moduli on the K6 lane. This finding verifies the damaging effect of truck traffic and implies a greater potential for accelerated pavement deterioration along SH4/48 from the additional overweight truck traffic that uses the route.

Table 8.6. Parameters of the Sigmoidal Relationship between Corrected AC Modulus and Cumulative 18-kip ESALs.

FWD Group	Model Parameter			
	α	γ	ρ	β
1	762	1305	1,358,229	50
2	384	2901	1,403,440	70
3	994	1580	1,456,682	70
4	742	1980	1,011,486	30
5	706	1724	1,442,190	70
6	521	2577	1,374,560	65
7	147	954	1,534,960	70

Table 8.7. Analysis of Variance Results from Sigmoidal Curve Fitting.

FWD Group	Source	df	Sum of Squares	Mean Square	F-value	Approx. Pr > F (*p*-value)
1	Regression	3	45,040,517	15,013,506	166	<0.0001
	Residual	13	1,178,459	90,651		
	Uncorrected Total	16	46,218,976			
	Corrected Total	15	7,605,180			
2	Regression	3	98,195,065	32,731,688	193	<0.0001
	Residual	12	2,037,067	169,756		
	Uncorrected Total	15	100,230,000			
	Corrected Total	14	31,839,626			
3	Regression	3	66,578,186	22,192,729	250	<0.0001
	Residual	12	1,065,291	88,774		
	Uncorrected Total	15	67,643,477			
	Corrected Total	14	10,023,397			
4	Regression	3	60,469,580	20,156,527	106	<0.0001
	Residual	11	2,093,336	190,303		
	Uncorrected Total	14	62,562,915			
	Corrected Total	13	18,543,367			
5	Regression	3	60,133,474	20,044,491	444	<0.0001
	Residual	12	541,666	45,139		
	Uncorrected Total	15	60,675,140			
	Corrected Total	14	10,405,033			
6	Regression	3	91,572,515	30,524,172	77	<0.0001
	Residual	12	4,783,480	398,623		
	Uncorrected Total	15	96,355,995			
	Corrected Total	14	29,367,555			
7	Regression	3	11,568,756	3,856,252	195	<0.0001
	Residual	12	237,711	19,809		
	Uncorrected Total	15	11,806,468			
	Corrected Total	14	3,255,912			

CHAPTER IX. SUMMARY OF FINDINGS AND RECOMMENDATIONS

This research investigated the potential impact of routine overweight truck traffic on segments of SH4/48 in Brownsville. To characterize the effects of permitted truck loads on the performance of the affected route, researchers carried out a work plan that covered:

- nondestructive pavement testing,
- pavement instrumentation,
- laboratory materials testing,
- evaluation of material properties from field and laboratory test data, and
- modeling of pavement response and performance.

Based on the research conducted, the following findings are noted:

- Application of backcalculation procedures often require a trial-and-error process to achieve reasonable results. Such was the researchers' experience in this project where a number of alternative schemes had to be investigated to establish how the pavement structure should be modeled in the static backcalculations. In the end, researchers found that the lowest absolute errors per sensor were obtained when a three-layer system, comprising an AC surface, composite flexible base and native subgrade, was used to model the pavement on the permitted truck route.

- While small errors between predicted and measured surface deflections are good to have, this agreement does not always guarantee realistic results since there may be multiple solutions that yield close agreement between predicted and measured FWD peak deflections. Thus, it is necessary to assess the backcalculated moduli against previous experience from tests done on the same or similar materials. Alternatively, the backcalculated moduli may be compared with other test data to establish whether the values are realistic or not. In this project, researchers verified the static backcalculation results through comparisons with corresponding values from laboratory measurements and from analyses of full-time FWD displacement histories.

- From analyses of test data on cores taken from SH4/48, researchers found a good correlation between the backcalculated AC modulus and the dynamic modulus from laboratory testing, particularly on the K7 lane. Researchers fitted a simple linear

regression equation between the logarithms of the AC moduli from static backcalculations and the corresponding dynamic moduli from laboratory measurements. This analysis showed that the intercept term β_0 is not statistically significant. Thus, researchers conducted a regression through the origin and found the slope β_1 to be 0.987 for the K6 lane and 0.993 for the K7 lane. Note that these slopes are close to unity, reflecting the good correspondence between the logarithms of the laboratory and backcalculated AC moduli and providing verification of the results from static backcalculations of FWD deflections.

- While the correlation between laboratory and backcalculated AC moduli from the tests conducted in this project is generally good, this agreement is not always observed in practice. On the K6 lane for example, there was one station, K6-48, where the backcalculated AC moduli are much lower than the values determined from laboratory tests. Based on a review of the coring operations and the test data, researchers are of the opinion that the discrepancies on station K6-48 reflect differences between the asphalt material at this FWD station and at the location where the intact core was taken. These differences may arise due to construction variability, such as variability in the production of the mix or in laydown and compaction. Note that the laboratory data are specific to the core tested and that District personnel had problems getting intact cores along SH4 in the downtown area of Brownsville. Because of these considerations, the authors are of the opinion that the FWD test results are probably more indicative of the pavement condition along the K6 lane of SH4 in the downtown area.

- Researchers also conducted dynamic analyses of FWD full-time displacement histories and backcalculated, among other properties, the creep compliance parameters of the AC layer tested. The asphalt concrete moduli corresponding to the FWD test frequency of 16.7 Hz were determined based on the backcalculated creep compliance parameters and compared with the corresponding moduli from static backcalculations of FWD peak deflections. This comparison showed good correlation between the AC moduli from dynamic and static analyses. Researchers fitted a simple linear regression equation between the logarithms of the AC moduli from dynamic and static backcalculations. This analysis showed that the intercept term β_0 is not statistically significant. A subsequent regression through the origin showed that the slopes of the

regression equations are almost the same between the K6 and K7 lanes (0.981 and 0.984, respectively). Note that these slopes are close to unity, indicating a good correspondence between the logarithms of the AC moduli from dynamic and static backcalculations. This good correlation between AC moduli backcalculated using two different methods provides further verification of the FWD test results. This finding is encouraging since dynamic analysis provides additional properties that are not determined from static backcalculation based on FWD peak deflections. In particular, the slope *m* of the creep compliance curve has been shown, from theoretical considerations, to be a predictor of material parameters that govern the development of fatigue cracking and permanent deformation in flexible pavements. The authors recommend that TxDOT renew efforts to implement this pavement evaluation tool, which has been developed in research projects conducted for the department in the late 1980s to early 1990s. Initial implementation could target forensic investigations.

- Using FWD data collected at different times during this project, researchers evaluated relationships between backcalculated asphalt concrete modulus and pavement temperature for the different FWD groups established on the K6 and K7 lanes. Researchers fitted the Witczak-Fonseca model (1996) to the backcalculated moduli at different temperatures and found that this model adequately agrees with the observed trends in the backcalculated moduli (see Figures 7.16 to 7.29). The relationships determined based on the model were also found to be statistically significant. This finding agrees with earlier results reported by Fernando, Liu and Ryu (2001) who used the Witczak-Fonseca model to characterize the modulus-temperature relationships of asphalt concrete mixtures found on LTPP test sections.

- The modulus-temperature relationships for FWD groups on the K6 lane yield generally lower HMAC modulus values than those determined for corresponding groups on the K7 lane. For a given pavement temperature, it is observed that the predicted AC modulus on the K6 lane is lower than the corresponding prediction on the K7 lane. Since K6 and K7 are adjacent lanes, it is not likely that different asphalt concrete mixtures would have been placed on these lanes, particularly for FWD stations that have the same group number. In the authors' opinion, the observed differences primarily reflect the effect of truck loading. Note that K6 receives most of the truck traffic along SH4/48. Thus, it has carried a greater number of 18-kip equivalent single

axle load applications. This difference, coupled with the slightly thinner HMAC material on K6, contributed, in the researchers' opinion, to a higher rate of deterioration on K6 that is reflected in the lower backcalculated AC moduli on that lane.

- Researchers further verified the effect of truck loading by comparing the backcalculated AC moduli between lanes after correcting the values to a reference temperature of 75 °F. This comparison also showed that the corrected AC moduli are lower on the K6 lane than on the K7 lane. Moreover, researchers observed that the corrected moduli show a decreasing trend over time, particularly for FWD groups on the K6 lane. These observations provide further verification of the effects of truck loading on pavement deterioration along the route evaluated in this project.
- Another corroboration of the effect of truck loading was made when researchers estimated the cumulative 18-kip ESALs from traffic data provided by TxDOT. This evaluation verified the higher 18-kip ESALs sustained by FWD groups on the K6 lane compared to the corresponding ESALs on the K7 lane. Researchers evaluated the relationships between the corrected AC moduli and cumulative 18-kip ESALs for the different FWD groups along the route. It was found that a sigmoidal model fits the data quite adequately (see Figures 8.23 to 8.29) and that the fitted curves have strong statistical significance. In the opinion of the researchers, the relationships from this analysis clearly demonstrate that the higher cumulative 18-kip ESALs are associated with lower corrected AC moduli on the K6 lane. This finding provides further corroboration of the damaging effect of truck traffic and implies a greater potential for accelerated pavement deterioration along SH4/48 from the additional overweight truck traffic that uses the route.
- Researchers also compared the pavement condition survey data collected along the K6 and K7 lanes during this project. This comparison showed a higher level of observed pavement distress on the K6 lane compared to the K7 lane. The following observations are noted:
  - Based on rut bar data provided by TxDOT, researchers found more rutting on the K6 lane compared to K7, particularly within groups 1, 6 and 7. There are also indications of an accelerated rate of rut development on the K6 lane as inferred

from the trend lines that show an increase in the progression of rutting within each group. Again, this observation is logical considering that K6 receives most of the truck traffic on SH4/48.

- The K6 lane is rougher than the K7 lane as evidenced by the higher IRIs computed for K6 where the overall means of the measured IRIs range from 91 to 129 inches/mile. This range in IRIs is characteristic of medium-smooth pavements. On K7, the corresponding range is from 44 to 87 inches/mile, which indicates a smoother lane. In fact, 58 percent of the average IRIs determined from the profiles collected on K7 are less than 60 inches/mile, a threshold used in TxDOT's Item 585 (2004) smoothness specification to identify pavement sections that merit bonuses due to above standard riding quality.
- The K6 lane also exhibits more cracking than the K7 lane, with the predominant type being longitudinal cracking along the wheel paths. The higher occurrence of cracking on the K6 lane is consistent with the higher cumulative 18-kip ESALs that this lane has received compared to K7.
- The computed pavement scores are lower on the K6 lane than on K7. These scores range from a low of zero to a perfect score of 100. The FWD groups on the K7 lane generally scored 100, reflecting the minimal distress on this lane.

The findings summarized thus far clearly point to a strong direct association between the level of pavement deterioration and the amount of load applications a pavement has sustained. With the adoption of a policy permitting overweight trucks on SH4/48, an accelerated rate of pavement deterioration may be expected, given these findings. This projection is based on the higher rate of 18-kip ESALs that the route now services due to the addition of overweight trucks into the traffic stream. It does not necessarily mean that overweight trucks produce greater damage than legal or non-permitted trucks, although this might be suspected.

Since the travel lanes on SH4/48 service both non-permitted and overweight trucks, separating the effects of legal and permitted trucks becomes an issue. To address this problem, researchers used the MDDs installed at the WIM site along SH48 to monitor pavement deflections under both truck types and compare overweight versus non-permitted trucks on the basis of damage estimates made from the measured MDD deflections. This task required

the evaluation and application of models to predict pavement response and performance. The findings from this task are summarized as follows:

- A nonlinear anisotropic (NA) model gave the closest predictions to measured MDD peak displacements relative to the other models evaluated by researchers, specifically, nonlinear isotropic (NI), linear anisotropic (LA) and linear isotropic (LI) models. The accuracy of the predictions diminished in the order: NA $\rightarrow$ NI $\rightarrow$ LA $\rightarrow$ LI. This order suggests the importance of modeling the stress-dependency of base and subgrade materials to predict pavement response for assessing the potential pavement damage due to routine overweight truck loads. It also suggests the need for considering the anisotropic behavior of pavement materials in predicting pavement response under load. To address this need, the authors are of the opinion that further research is required and recommend additional studies to:
  - review pavement evaluation and design procedures to assess the impact of implementing an NA model and establish a staged plan for revising existing procedures to consider the effects of material anisotropy;
  - characterize anisotropic properties and evaluate the factors that affect these properties;
  - revise methodologies presently used for pavement evaluation and design to model, where appropriate, the anisotropic behavior of pavement materials; and
  - develop a standard test method for characterizing material anisotropy that specifies the test equipment and procedure to be used, and associated data acquisition and reduction programs.

  In view of the additional studies proposed to improve existing practice by developing procedures to consider anisotropic effects in pavement evaluation and design, researchers recommend that a nonlinear isotropic approach be used to develop the initial methodology for evaluating routes proposed for routine overweight truck use.
- To assess the potential pavement damage from permitted trucks relative to legal trucks, researchers used performance equations based on fatigue cracking and rutting criteria. For this evaluation, equations were developed to predict the tensile strain at the bottom of the asphalt and the vertical compressive strain at the top of the subgrade to predict

the life consumed due to the passage of a given truck. From this work, researchers found that the MDD displacements are highly correlated with these performance-related pavement response parameters, and that the displacements adequately account for differences in layer moduli and wheel loads.

- Researchers used MDD data taken under permitted and non-permitted trucks at close to the same time to assess the pavement damage potential of permitted overweight trucks relative to legal or non-permitted trucks. In this way, deflection data were obtained under very similar environmental conditions to minimize the effects of differences in the data due to pavement temperature and moisture variations. For each truck pair, researchers determined the ratio of the service life consumed from one pass of the permitted truck to the corresponding service life consumed due to passage of the non-permitted truck. This analysis showed all ratios to be greater than one, indicating greater potential for accelerated pavement deterioration on the route due to permitted overweight truck use. The averages of the service life consumption ratios based on rutting and fatigue cracking criteria were determined to be about 5.3 and 4.0, respectively, on the K6 MDD station. The corresponding averages on the K7 MDD station are about 3.4 and 2.4, respectively.

In summary, the characterization of the effects of overweight truck traffic on SH4/48 showed that accelerated pavement deterioration can be expected due to the higher rate of accumulation of 18-kip ESALs, and the fact that routine overweight truck use was not considered in the pavement design for this route. The higher loading rate is a consequence of the additional overweight trucks that the route now serves, and the higher allowable axle loads on these trucks that produce more pavement damage per application relative to legal or non-permitted trucks. While the findings summarized herein were probably expected based on engineering principles and experience, this project provided evidences based on test data, which point to the conclusion that accelerated pavement deterioration is likely as a consequence of routine overweight truck use on SH4/48. Before concluding this report, the researchers offer the following additional recommendations for TxDOT's consideration:

- Support should be provided to continue the monitoring and evaluation of the overweight truck route investigated in this study. In view of the maintenance work that has been done on various segments of this route during the course of the project,

researchers propose that the monitoring effort be focused on the segment of SH48 between FM511 and FM802, which received no maintenance treatments during the project. As a minimum, researchers recommend that inertial profile and rut bar data be collected at three-month intervals, and that FWD and visual surveys be conducted at six-month intervals. These measurements will be made on both the K6 and K7 lanes to track the pavement condition over time and provide further verification of the findings from this project.

- Enforcement of permitted axle weights is important to minimize the likelihood of non-permitted but overweight vehicles blending in with the permitted truck traffic. For monitoring purposes, researchers placed tags on permitted trucks to identify these vehicles for MDD measurements. In practice, there are no tags to differentiate between permitted and legal or non-permitted trucks. Thus, the potential exists that some amount of non-permitted but overweight trucks would use the route. As noted in Chapter VIII, researchers have observed non-permitted trucks on SH48 that had axle loads exceeding the legal limits based on the data from the piezoelectric WIM sensors installed by TxDOT. These observations indicate the need for enforcement, which will entail monitoring trucks to check axle loads and identifying between permitted and non-permitted trucks. To this end, the use of visible or electronic tags can help differentiate permitted from non-permitted trucks, without the need to stop vehicles to view the permit papers. For axle load measurements, the existing WIM site along SH48 can be used. However, piezoelectric WIM sensors, while relatively cheap, are not as accurate as the load cells or bending plates used on high-end WIM installations. Thus, research toward developing or identifying alternative methods for weigh-in-motion measurement on routine overweight truck routes would be useful, in the authors' opinion. In connection with this, researchers evaluated the application of fiber-optic sensors in an ancillary task conducted for this project. Appendix I documents this evaluation. While the the sensors exhibited a strong response and consistently reproduced the expected characteristics of truck wheel crossings in the tests conducted, the correlation between peak fiber-optic sensor response and static truck weight data was poor. Thus, further development work is necessary. In this regard, calibration methods to relate the response of multiple sensors to actual truck

weights need to be investigated before fiber-optic sensors can be established as a viable alternative for a practical weigh-in-motion system.

REFERENCES

AASHTO Guide for Design of Pavement Structures. American Association of State Highway and Transportation Officials, Washington, D.C., 1993.

ASTM Designation: D-3497-79, Standard Test Method for Dynamic Modulus of Asphalt Mixtures. American Society for Testing and Materials, Vol. 04.03, 1997, pp. 334-336.

Adu-Osei, A. *Characterization of Unbound Granular Layers in Flexible Pavements*. Ph.D. Dissertation, Department of Civil Engineering, College of Engineering, Texas A&M University, College Station, Tex., 2000.

Applied Research Associates. *Guide for Mechanistic-Empirical Design of New and Rehabilitated Pavement Structures*. Final Report, National Cooperative Highway Research Program, Transportation Research Board, National Research Council, Washington, D.C., 2004.

Asphalt Institute. *Research and Development of the Asphalt Institute's Thickness Design Manual (MS-1) Ninth Edition*. Research Report No. 82-2, Asphalt Institute, Lexington, Ky., 1982.

Chen, D., J. Bilyeu, H. H. Lin and M. Murphy. Temperature Correction on Falling Weight Deflectometer Measurements. Transportation Research Record 1716, Transportation Research Board, Washington, D.C., 2000, pp. 30-39.

CIRCLY 4: User's Manual. MINCAD System Pty. Ltd., Victoria, Australia, 1999.

Fernando, E. G., D. Luhr and D. Anderson. *Development of a Simplified Mechanistic Pavement Evaluation and Overlay Design Procedure for Flexible Pavements*. Transportation Research Record 1095, Transportation Research Board, Washington, D.C., 1986, pp. 37-44.

Fernando, E. G. *PALS 2.0 User's Guide*. Research Report 3923-1, Texas Transportation Institute, Texas A&M University, College Station, Tex., 1997.

Fernando, E. G., W. Liu and D. Ryu. *Development of a Procedure for Temperature Corrections of Backcalculated AC Modulus*. Research Report 1863-1, Texas Transportation Institute, Texas A&M University, College Station, Tex., 2001.

Fernando, E. G. and W. Liu. *User's Guide for the Modulus Temperature Correction Program (MTCP)*. Research Report 1863-2, Texas Transportation Institute, Texas A&M University, College Station, Tex., 2001.

Fernando, E. G. and W. Liu. *Dynamic Analysis of FWD Data for Pavement Evaluation*. Proceedings, 6th International Conference on the Bearing Capacity of Roads and Airfields, Lisbon, Portugal, Vol. 1, 2002, pp. 159-167.

Fernando, E. G. and J. Oh. *Guidelines for Evaluating Routine Overweight Truck Routes*. Product 0-4184-P2, Texas Transportation Institute, Texas A&M University, College Station, Tex., 2004.

Fernando, E. G. and W. Liu. *User's Guide to the Overweight Truck Route Analysis (OTRA) Program*. Product 0-4184-P3, Texas Transportation Institute, Texas A&M University, College Station, Tex., 2004.

Foinquinos, R., J. Roesset and K. Stokoe. *FWD-DYN: A Computer Program for Forward Analysis and Inversion of Falling Weight Deflection Data*. Research Report 1970-1F, Center for Transportation Research, The University of Texas, Austin, Tex., 1989.

Gazetas, A. M. *Stresses and Displacements in Cross-Anisotropic Soils*. Journal of Geotechnical Engineering, American Society of Civil Engineers, Vol. 108, No. GT4, 1982, pp. 532-553.

Jooste, F. J. and E. G. Fernando. *Modeling of Pavement Response under Superheavy Loads*. Transportation Research Record 1448, Transportation Research Board, Washington, D.C., 1994, pp. 69-74.

Jooste, F. J. and E. G. Fernando. *Development of a Procedure for the Structural Evaluation of Superheavy Load Routes*. Research Report 1335-3F, Texas Transportation Institute, Texas A&M University, College Station, Tex., 1995.

Kausel, E. and R. Peek. *Dynamic Loads in the Interior of a Layered Stratum: An Explicit Solution*. Bulletin of the Seismological Society of America, 72(5), 1982, pp. 1459-1481.

Leknitskii, S. G. *Theory of Elasticity of an Anisotropic Elastic Body*. Holden-Day Inc. San Francisco, Calif., 1963.

Letto, A. R. *A Computer Program for Function Optimization Using Pattern Search and Gradient Summation Techniques*. M.E. Thesis, Department of Industrial Engineering, College of Engineering, Texas A&M University, College Station, Tex., 1968.

Lukanen, E., N. Stubstad and R. Briggs. *Temperature Predictions and Adjustment Factors for Asphalt Pavements*. Research Report FHWA-RD-98-085, Federal Highway Administration, McLean, Va., 1998.

Lytton, R. *Backcalculation of Pavement Layer Properties. Nondestructive Testing of Pavements and Backcalculations of Moduli*. ASTM STP 1026, A. J. Bush III and G. Y. Baladi (eds.). American Society for Testing and Materials. Philadelphia, Pa., 1989, pp. 7-38.

Lytton, R., F. Germann, J. Chou and S. Stoffels. *Determining Asphaltic Concrete Pavement Structural Properties by Nondestructive Testing*. National Cooperative Highway Research Program, Report 327, Transportation Research Board, Washington, D.C., 1990.

Magnuson, A. *Calculation of the Pavement Layer Properties Using Dynamic Analysis of Falling Weight Deflectometer Data*. Final Report SHRP-88-ID025, Texas Transportation Institute, Texas A&M University, College Station, Tex., 1993.

Magnuson, A. and R. Lytton. *Development of Dynamic Analysis Techniques for Falling Weight Deflectometer Data*. Research Report 1175-2, Texas Transportation Institute, Texas A&M University, College Station, Tex., 1997.

Michalak, C. and T. Scullion. *MODULUS 5.0: User's Manual*. Research Report 1987-1, Texas Transportation Institute, Texas A&M University, College Station, Tex., 1995.

NCHRP 1-37A Draft Test Method DM-1: Standard Test Method for Dynamic Modulus of Asphalt Concrete Mixtures. Arizona State University, Tempe, Ariz., 2002.

Nguyen, C., C. Lau and T. Scullion. *Design Concepts for a Miniature Pavement GPR Antenna*. Research Report 1341-3F, Texas Transportation Institute, Texas A&M University, College Station, Tex., 1995.

Owen, D. R. J. and E. Hinton. *Finite Elements in Plasticity: Theory and Practice*. Pineridge Press Ltd., Swansea, United Kingdom, 1980.

Porter, D.W. *Technical Basis of Austroads Pavement Design Guide: Part 1 – 1992 Guide Procedures for Design of Flexible Pavements*. Austroads Publication No. AP-T33/04, Austroads Incorporated, Sydney, Australia, 2004.

Roesset, J. *Computer Program UTFWIBM*. Center for Transportation Research, The University of Texas, Austin, Tex., 1987.

Sayers, M. W. *On the Calculation of International Roughness Index from Longitudinal Road Profile*. Transportation Research Record 1501, Transportation Research Board, Washington, D.C., 1995, pp. 1-12.

Scullion, T., C. Lau and Y. Chen. *Implementation of the Texas Ground Penetrating Radar System*. Research Report 1233-1, Texas Transportation Institute, Texas A&M University, College Station, Tex., 1994.

Scullion, T., Y. Chen and C. Lau. *COLORMAP – User's Manual with Case Studies*. Research Report 1341-1, Texas Transportation Institute, Texas A&M University, College Station, Tex., 1995.

Scullion, T., S. Servos, J. Ragsdale and T. Saarenketo. *Applications of Ground-Coupled GPR to Pavement Evaluation*. Research Report 2947-S, Texas Transportation Institute, Texas A&M University, College Station, Tex., 1997.

Stubstad, N., E. Lukanen, C. Ritcher and S. Baltzer. *Calculation of AC Layer Temperatures from FWD Field Data*. Proceedings, 5th International Conference on the Bearing Capacity of Roads and Airfields, Trondheim, Norway, Vol. II, 1998, pp. 919-928.

Texas Department of Transportation. *Pavement Management Information System Rater's Manual*. Texas Department of Transportation, Austin, Tex., 2002.

Texas Department of Transportation. *Standard Specifications for Construction of Roads and Bridges – Item 585: Ride Quality for Pavement Surfaces*. Texas Department of Transportation, Austin, Tex., 2004.

Tutumluer, E. *Prediction Behavior of Flexible Pavements with Granular Bases*. Ph.D. Dissertation, School of Civil and Environmental Engineering, Georgia Institute of Technology, Atlanta, Ga., 1995.

Uzan, J. *Granular Material Characterization*. Transportation Research Record 1022, Transportation Research Board, Washington, D.C., 1985, pp. 52-59.

Uzan, J. *Resilient Characterization of Pavement Materials*. International Journal for Numerical and Analytical Methods in Geomechanics, Vol. 16, 1992, pp. 435-459.

Weave, J. W. and P. R. Johnston. *Finite Elements for Structural Analysis*. Prentice-Hall, Inc., 1984.

Witczak, M. W. and O. A. Fonseca. *Revised Predictive Model for Dynamic (Complex) Modulus of Asphalt Mixtures*. Transportation Research Record 1540, Transportation Research Board, Washington, D.C., 1996, pp. 15-23.

Zienkiewicz, O. C. and R. L. Taylor. *The Finite Element Method: Volume 1, Basic Formulation and Linear Problems*. 4th Edition, McGraw Hill Book Company, United Kingdom, 1989.

APPENDIX A
AIR-COUPLED GPR DATA ON K6 AND K7 LANES

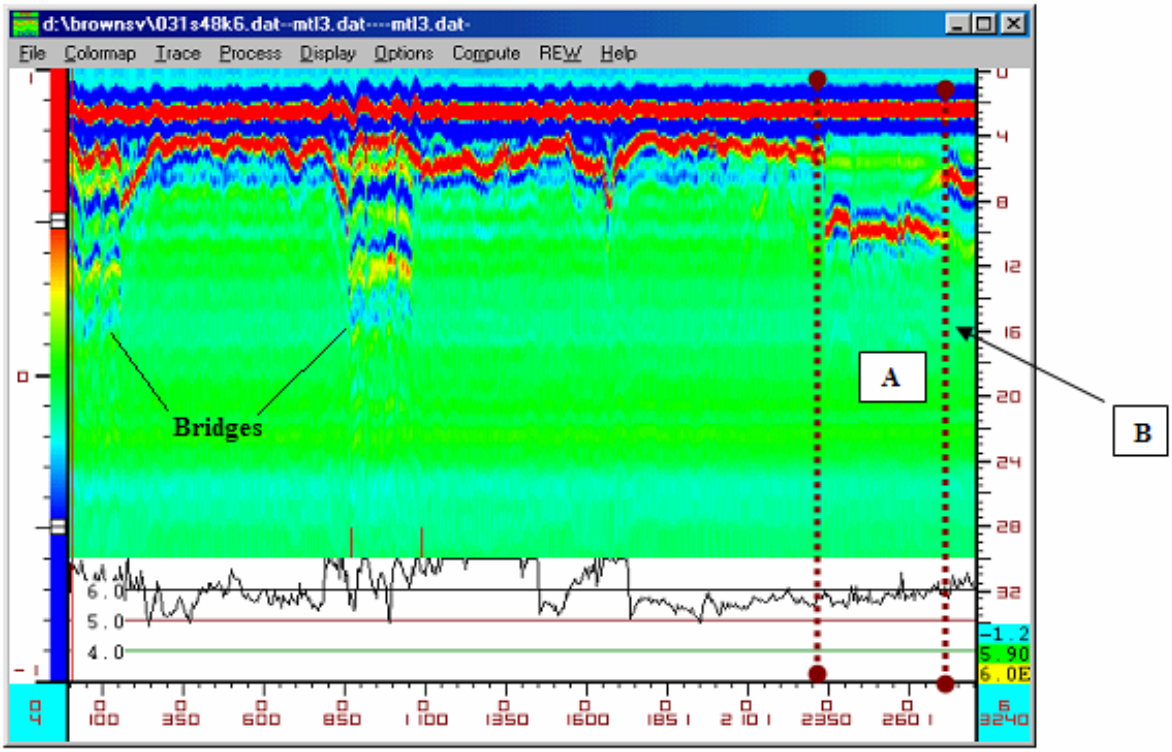

Figure A1. GPR Data on K6-A and K6-B Sections.

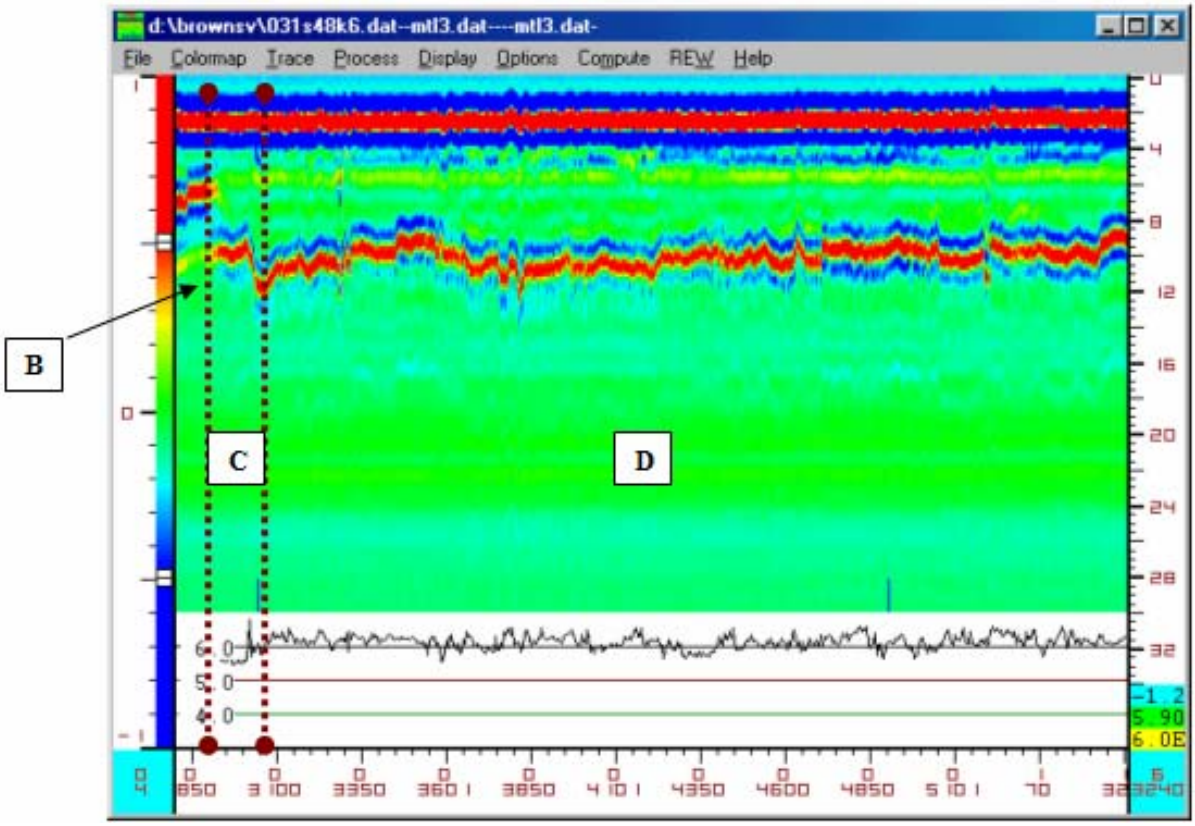

Figure A2. GPR Data on K6-B, K6-C and K6-D Sections.

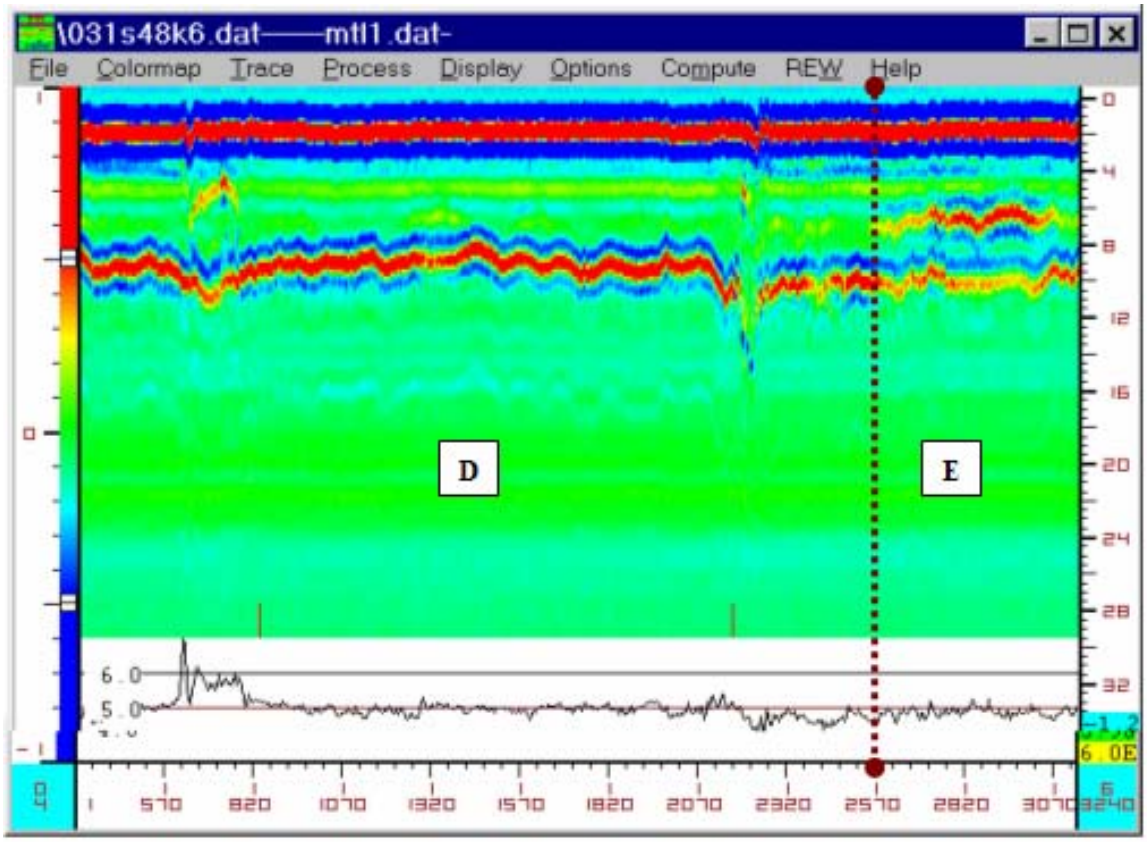

Figure A3. GPR Data on K6-D and K6-E Sections.

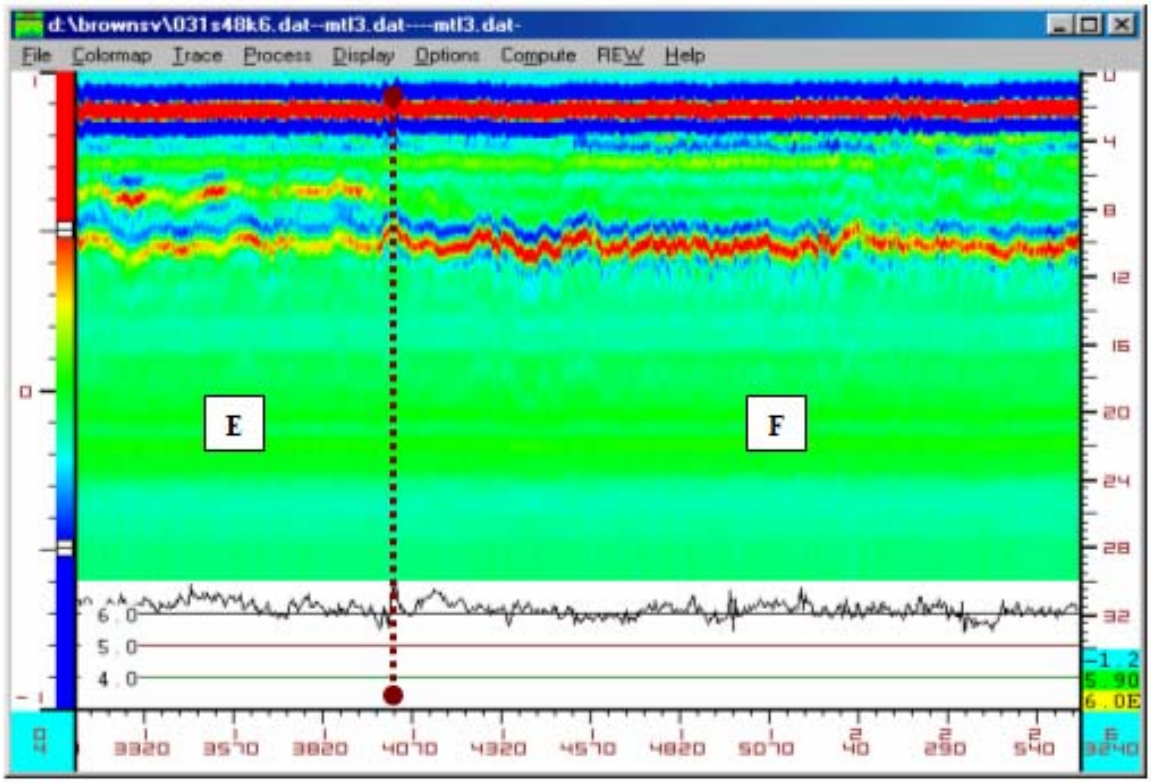

Figure A4. GPR Data on K6-E and K6-F Sections.

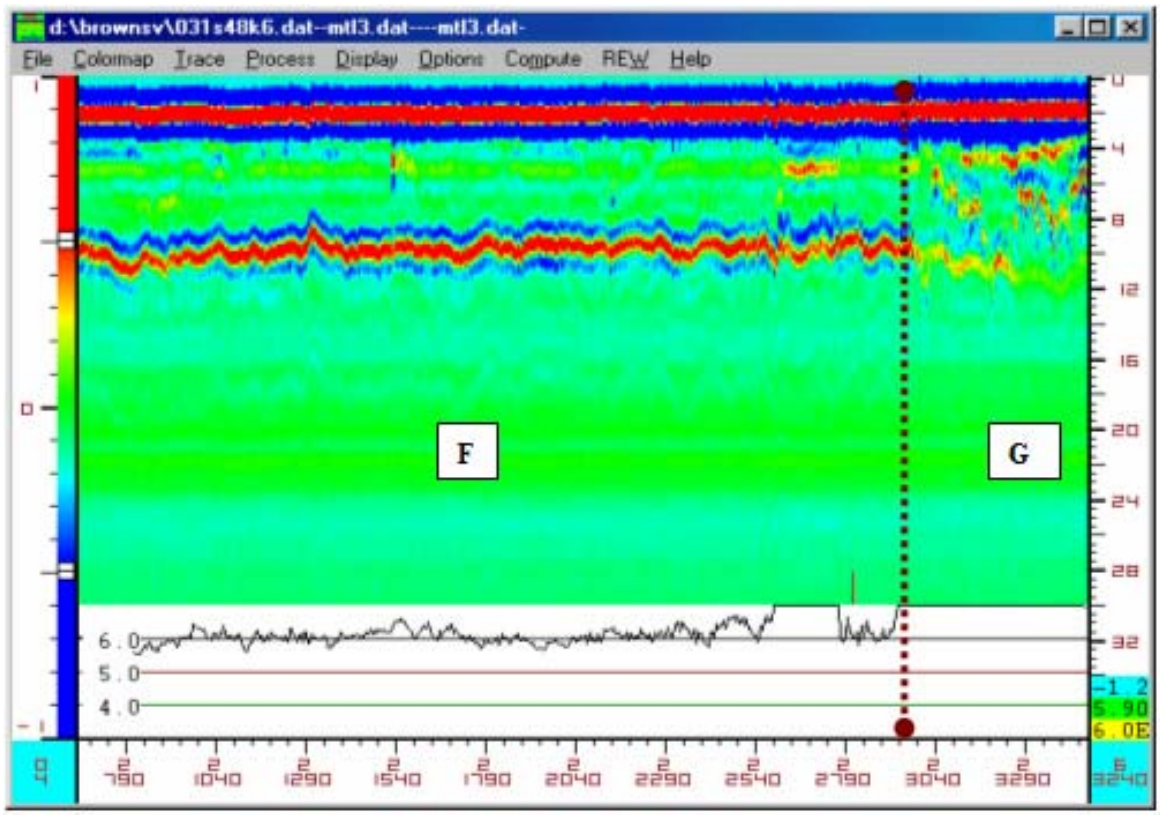

Figure A5. GPR Data on K6-F and K6-G Sections.

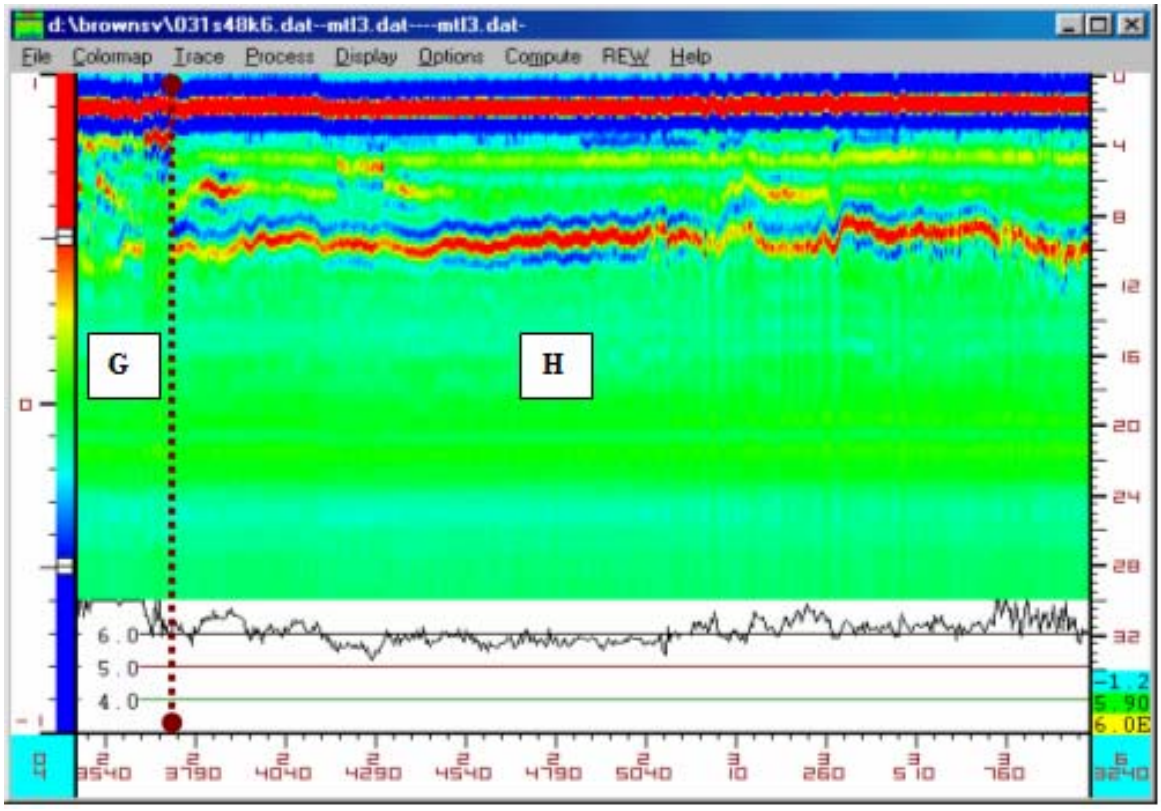

Figure A6. GPR Data on K6-G and K6-H Sections.

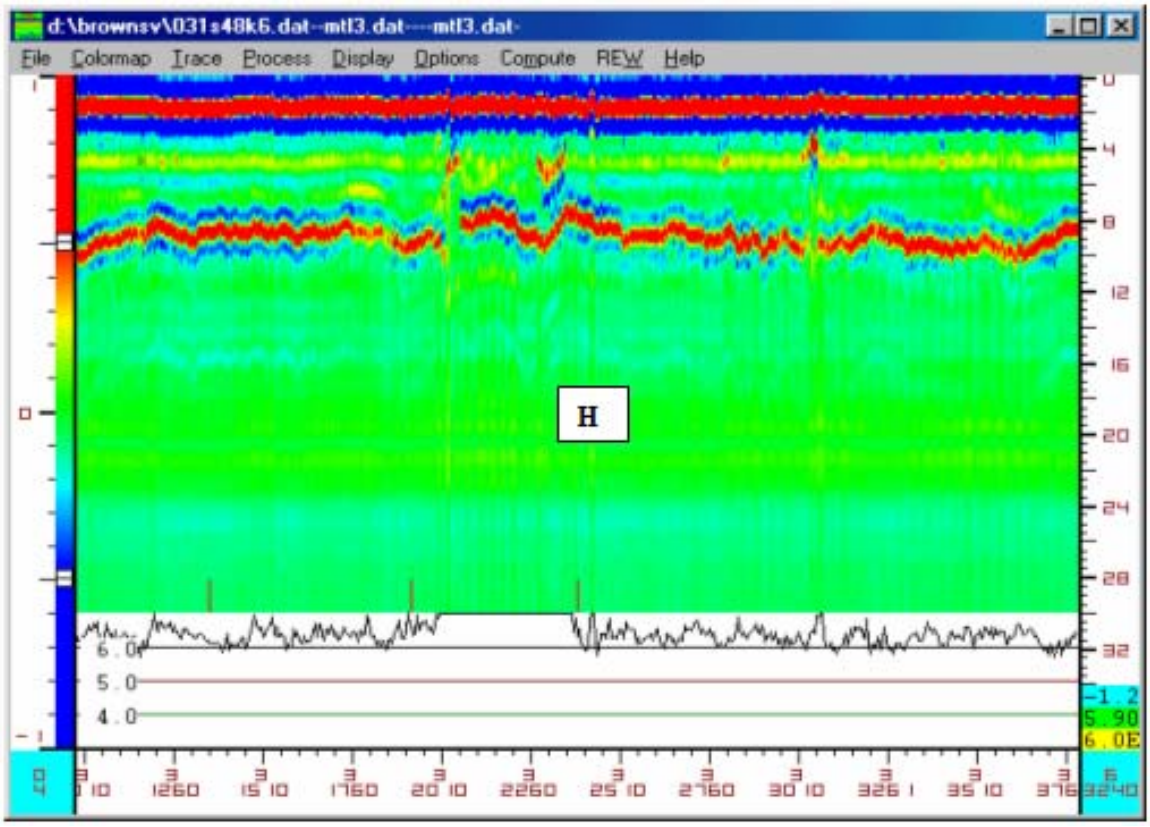

Figure A7. GPR Data on K6-H Section (continued).

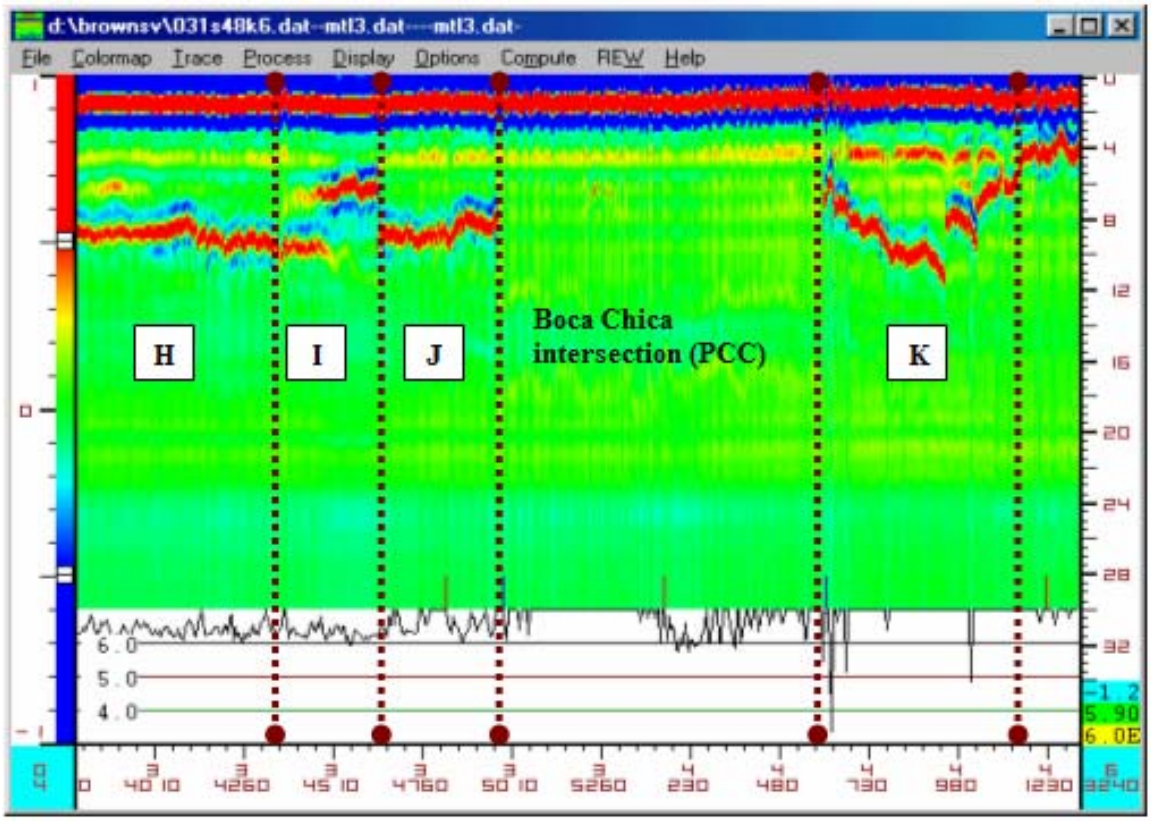

Figure A8. GPR Data on K6-H, K6-I, K6-J and K6-K Sections.

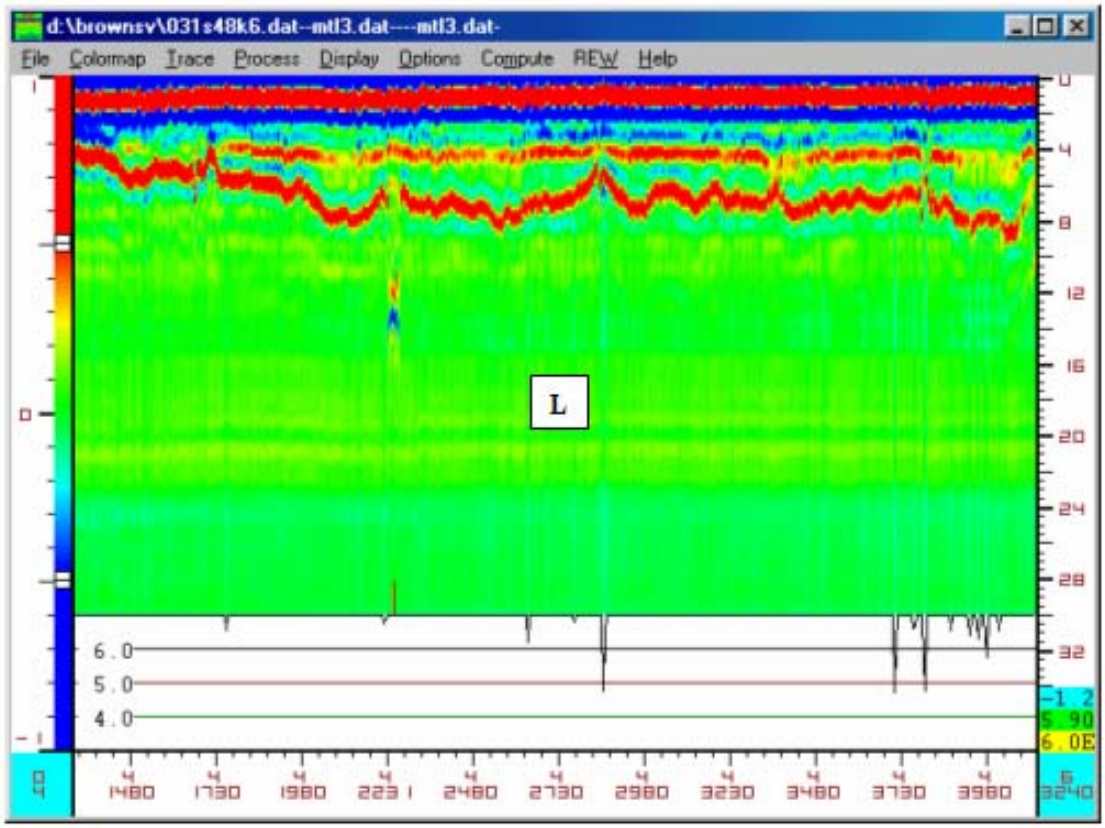

Figure A9. GPR Data on K6-L Section.

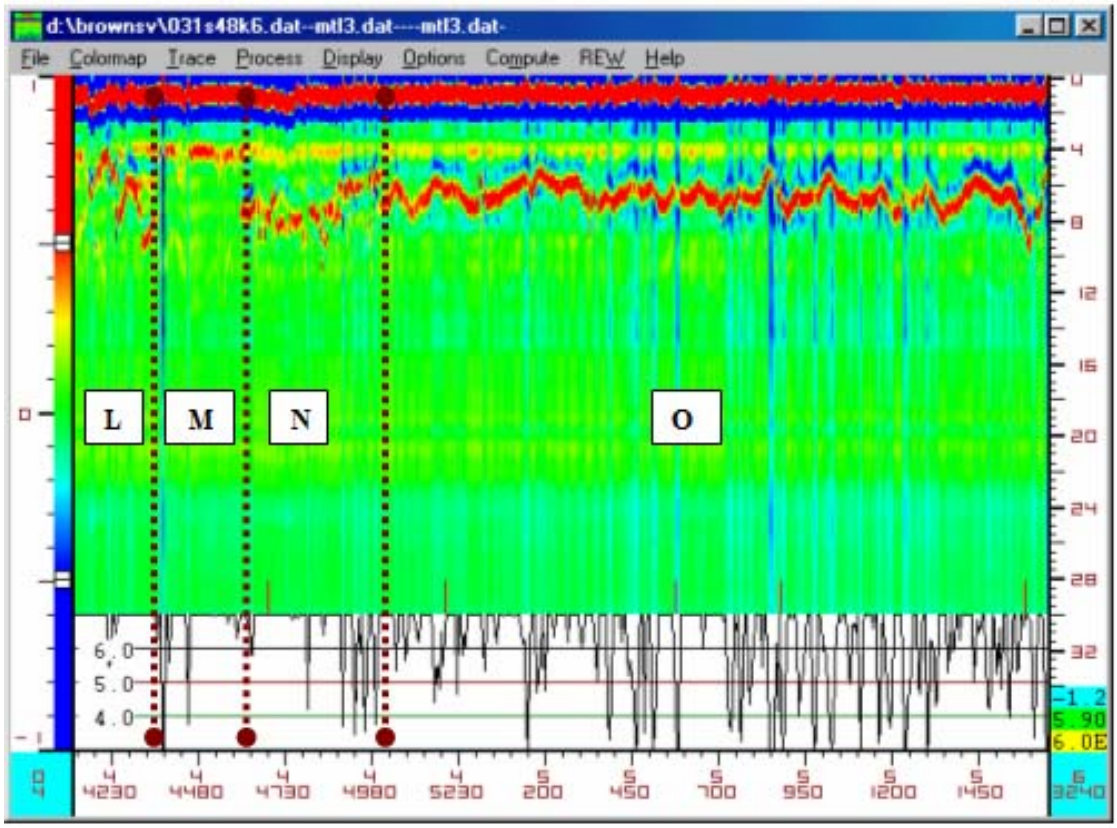

Figure A10. GPR Data on K6-L, K6-M, K6-N and K6-O Sections.

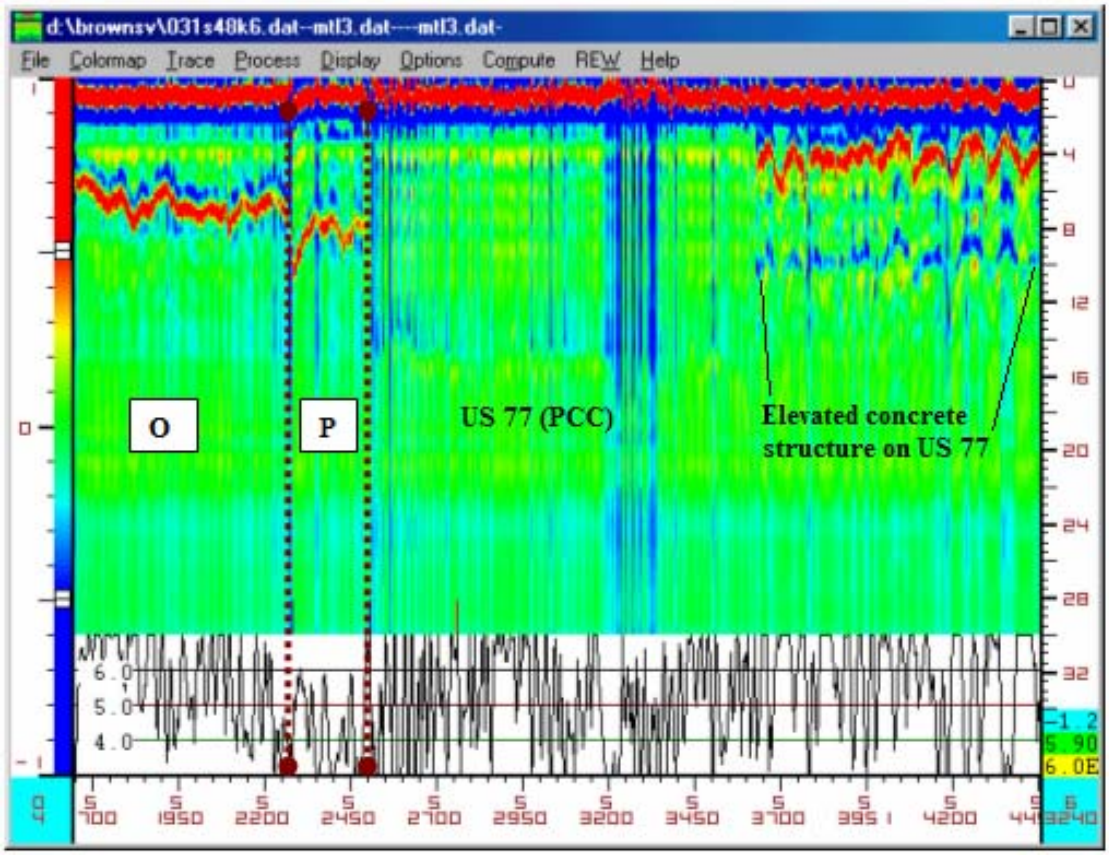

Figure A11. GPR Data on K6-O and K6-P Sections.

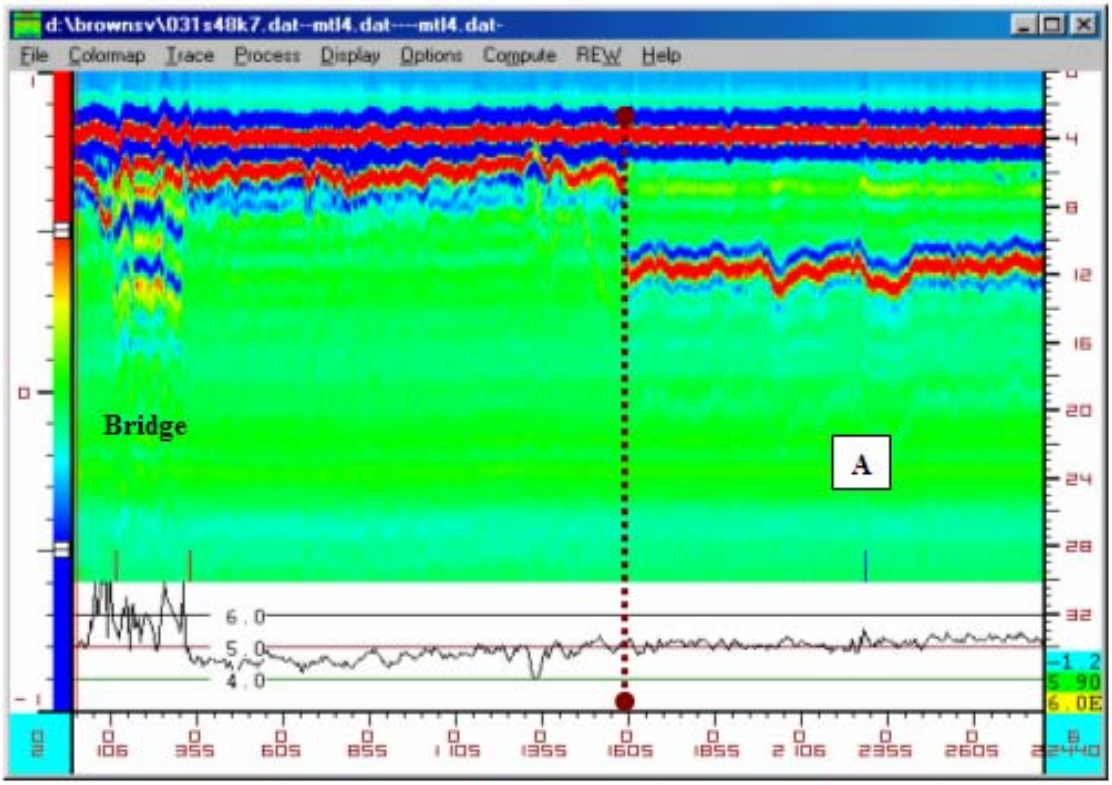

Figure A12. GPR Data on K7-A Section.

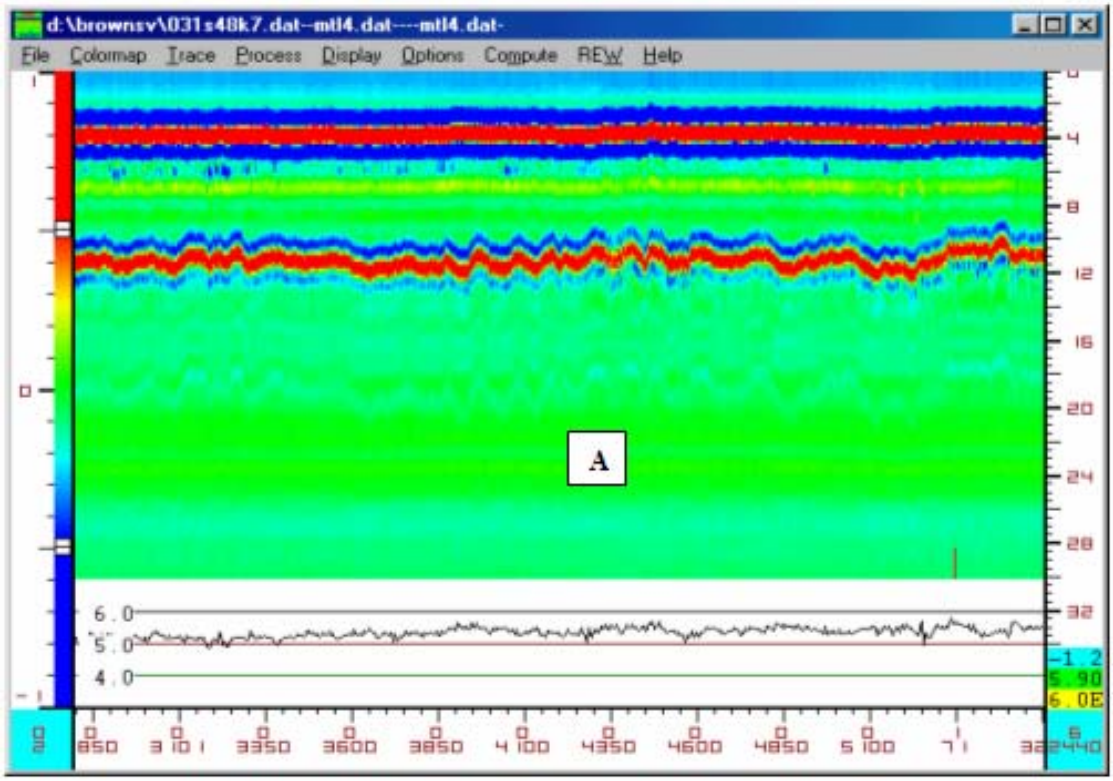

Figure A13. GPR Data on K7-A Section (continued).

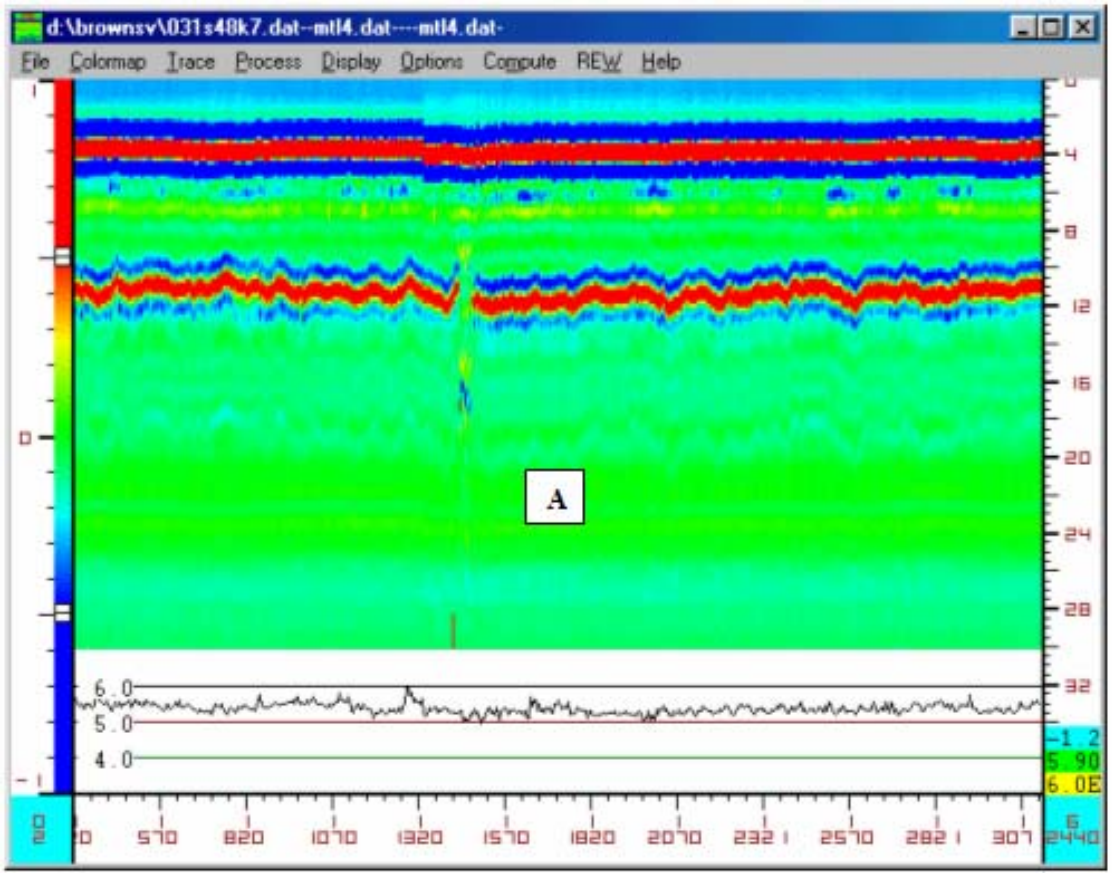

Figure A14. GPR Data on K7-A Section (continued).

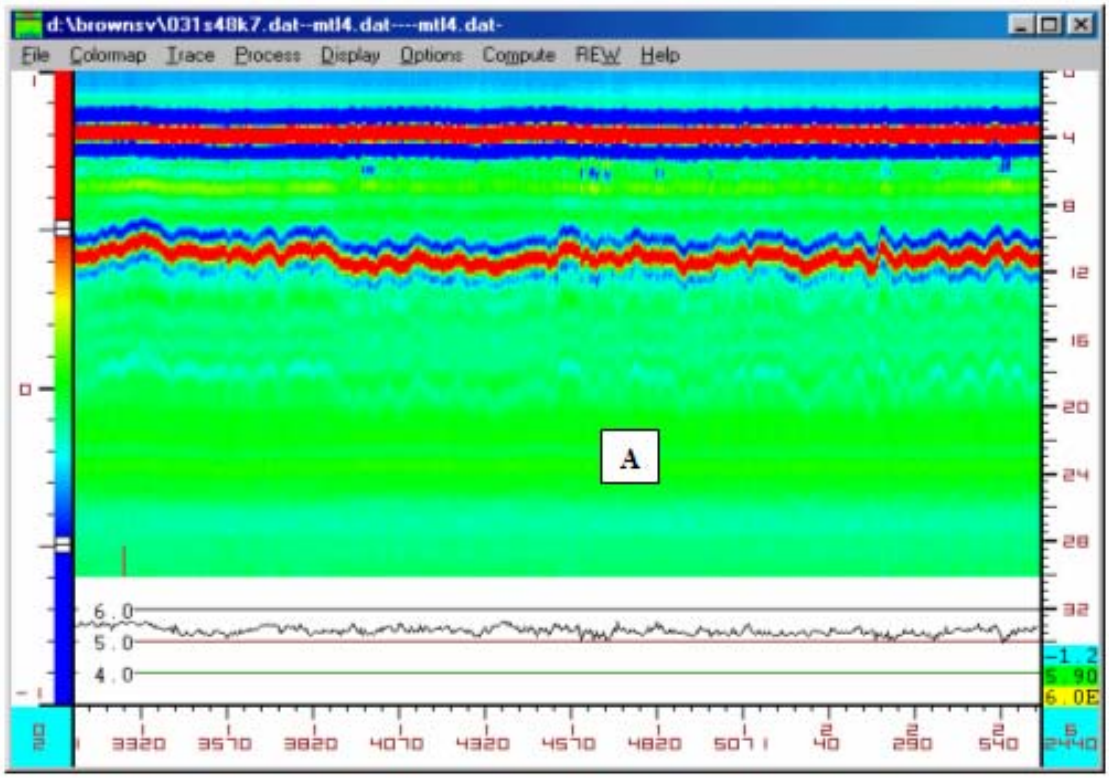

Figure A15. GPR Data on K7-A Section (continued).

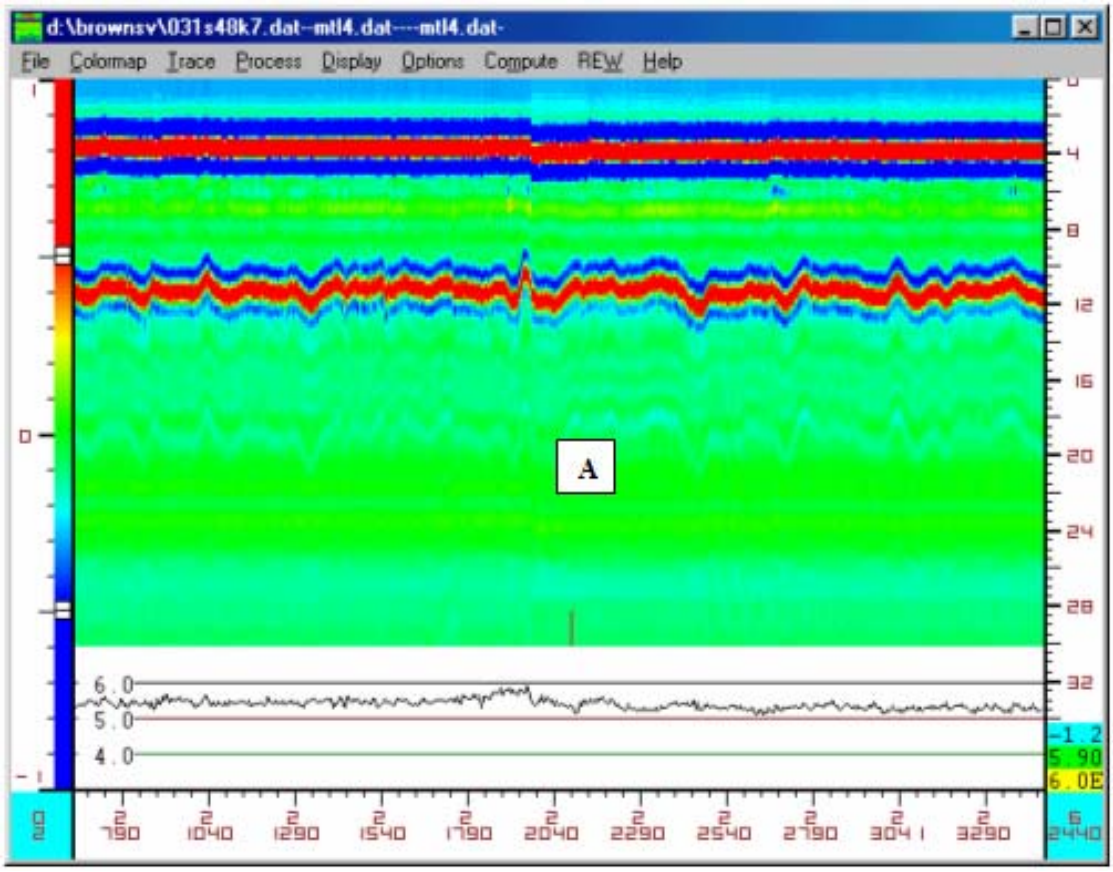

Figure A16. GPR Data on K7-A Section (continued).

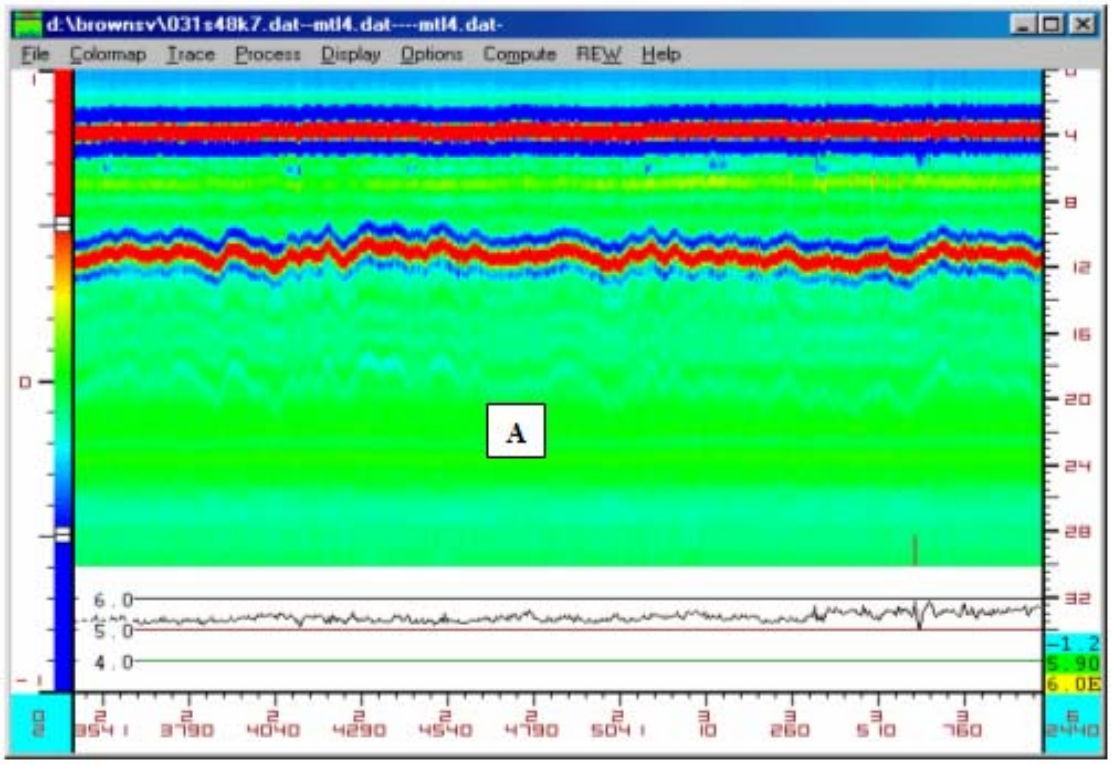

Figure A17. GPR Data on K7-A Section (continued).

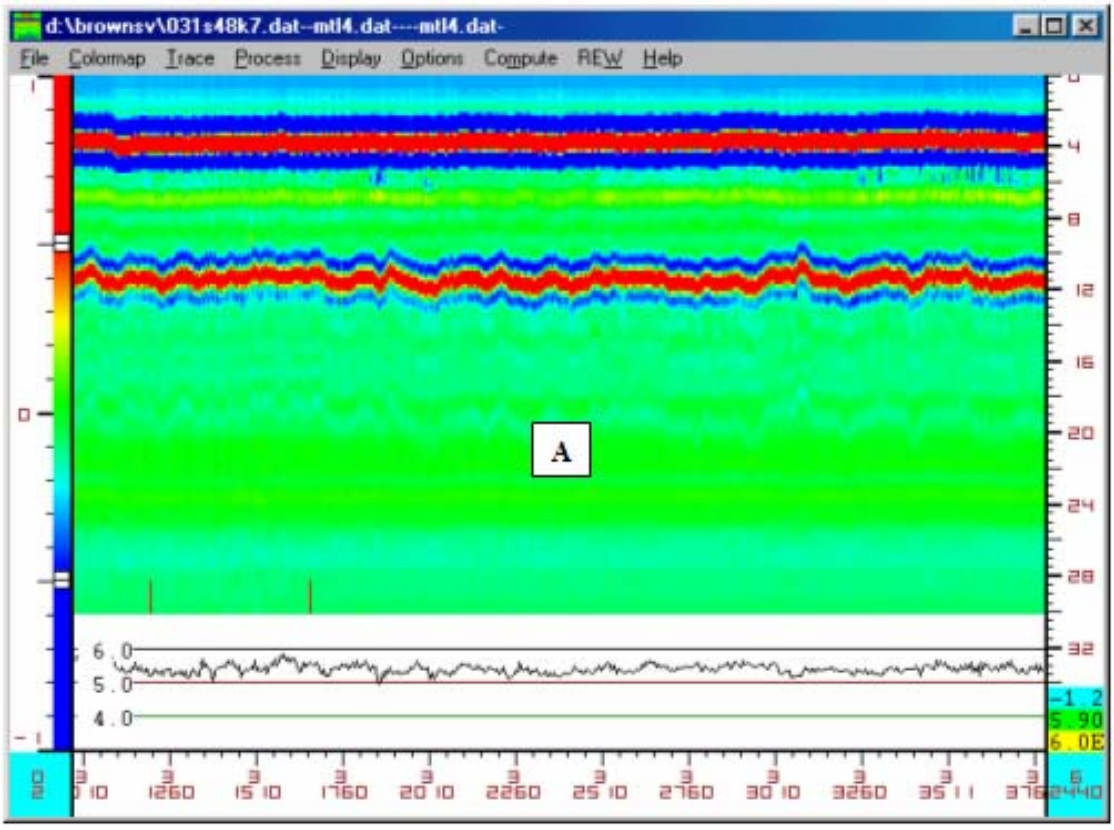

Figure A18. GPR Data on K7-A Section (continued).

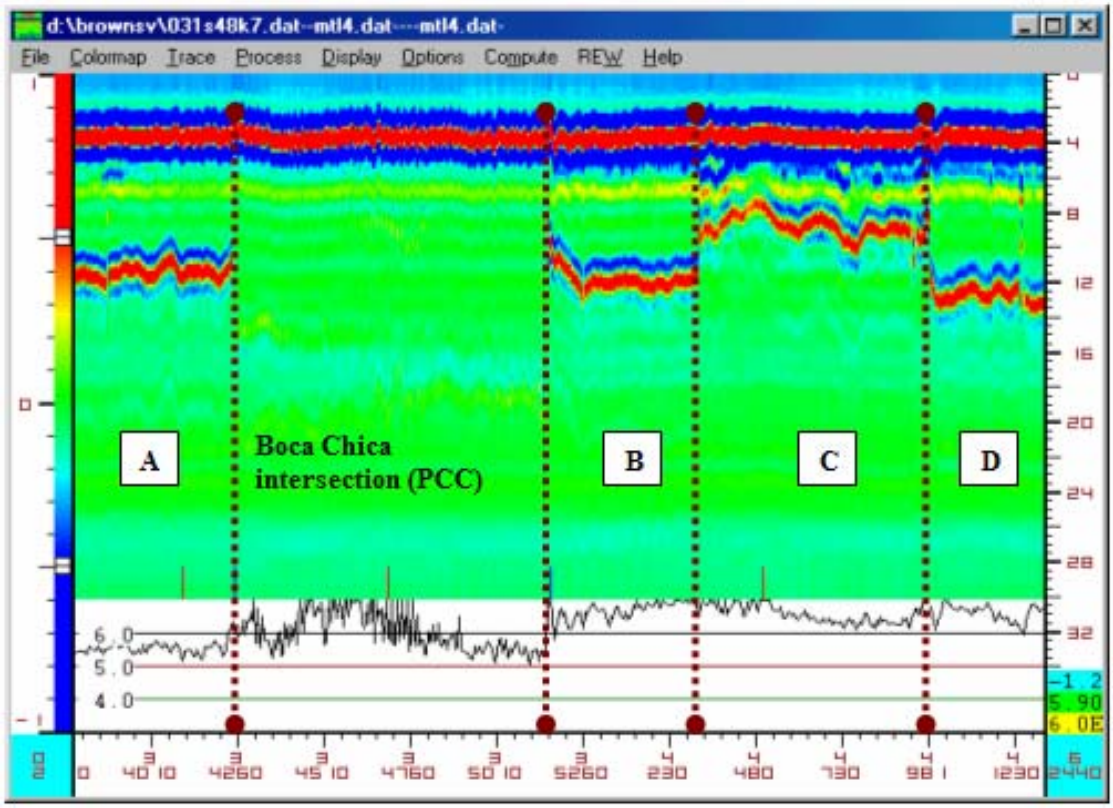

Figure A19. GPR Data on K7-A, K7-B, K7-C and K7-D Sections.

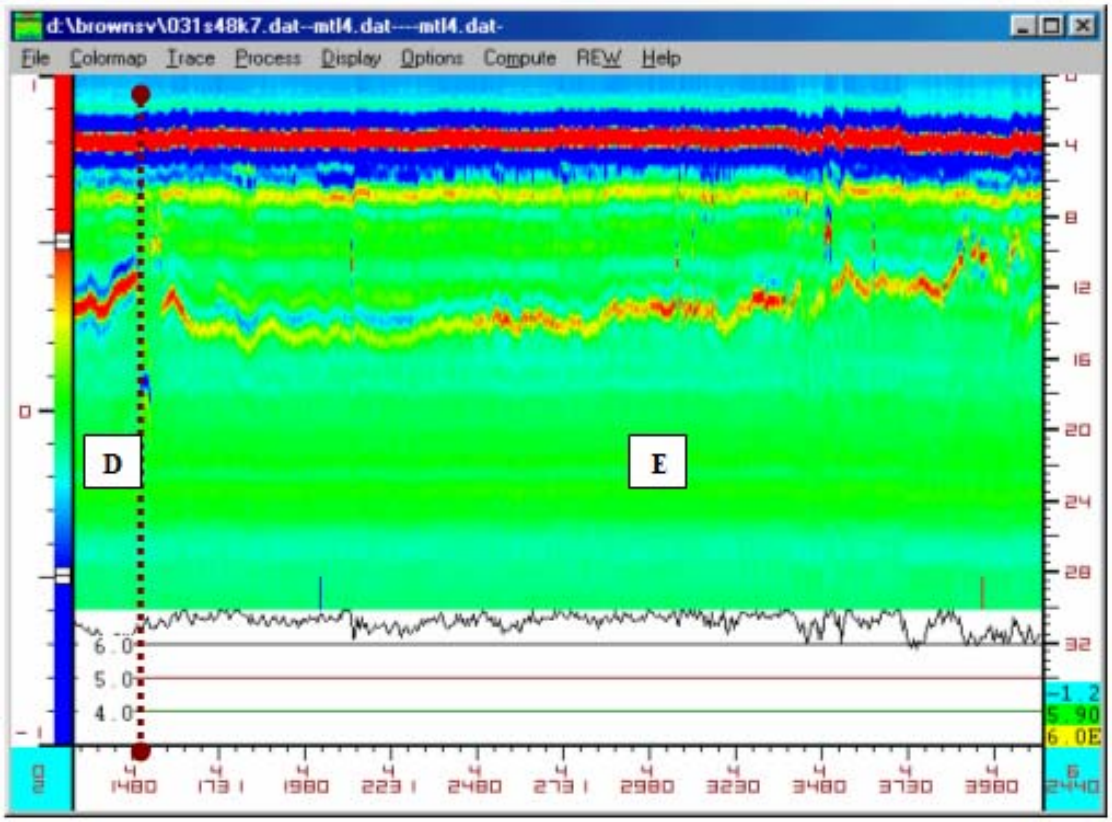

Figure A20. GPR Data on K7-D and K7-E Sections.

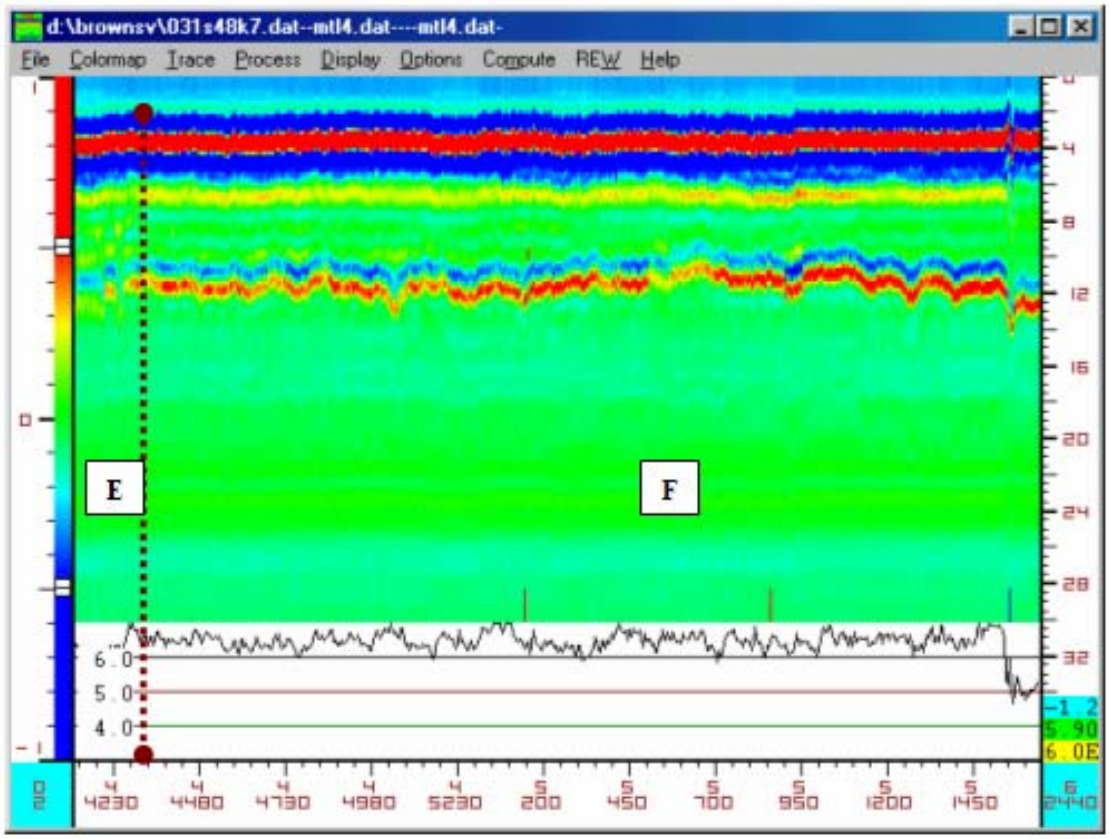

Figure A21. GPR Data on K7-E and K7-F Sections.

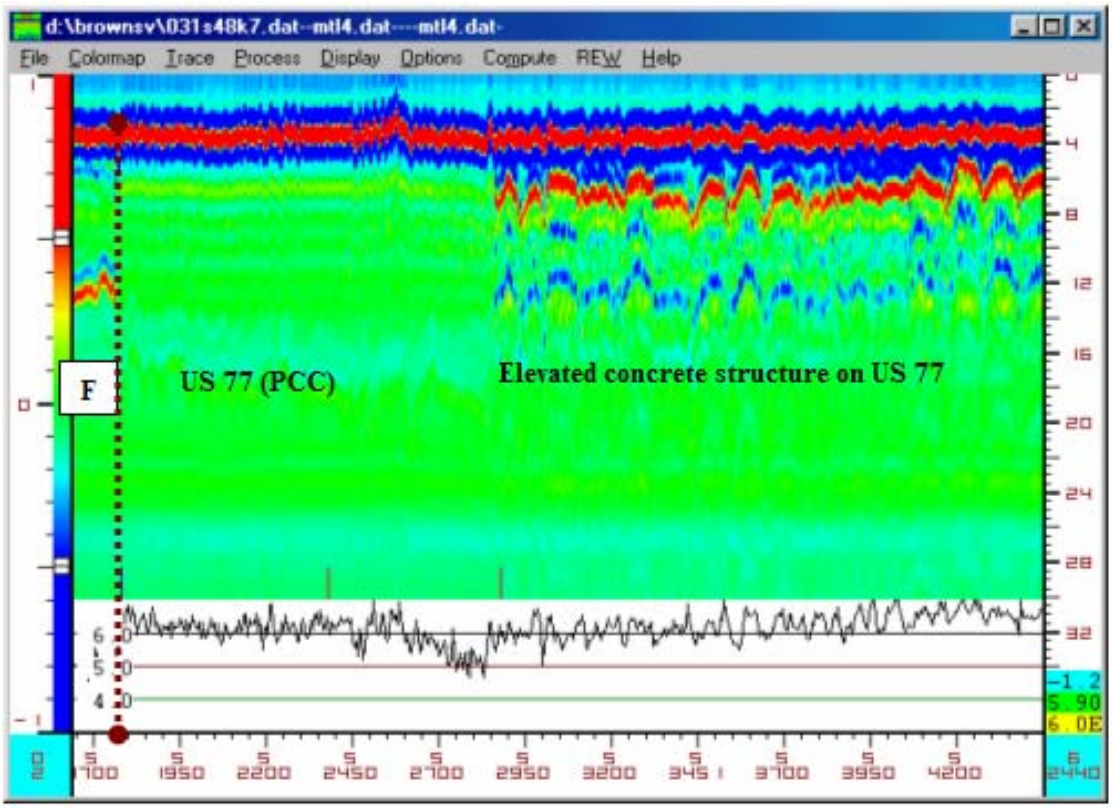

Figure A22. GPR Data on K7-F Section.

APPENDIX B

PAVEMENT INSTRUMENTATION AT WEIGH-IN-MOTION SITE ALONG SH48

This appendix provides a pictorial description of the pavement instrumentation work conducted at an existing weigh-in-motion site located along SH48, approximately 0.5 mile from the bridge over FM511. The WIM site uses piezoelectric sensors and was set up by TxDOT prior to the start of this project. Pavement instrumentation included the installation of MDDs and a weather station for monitoring pavement temperature and moisture variations. The field work conducted is described in the following.

INSTALLATION OF MDDs AND WEATHER STATION

Researchers installed MDDs on both the K6 and K7 lanes at the vicinity of the WIM site. This installation was a laborious task. Researchers initially reviewed data from the GPR, FWD and visual condition surveys and considered the flow of traffic in deciding where to locate the MDDs. Once a location was selected, researchers took appropriate steps to verify the presence of underground utilities around the WIM site in order to avoid damaging these utilities during the instrumentation work. Figure B1 shows the location selected for installing MDDs.

Installing multi-depth deflectometers requires a multitude of custom-made parts and a variety of specialized tools. Drilling of the MDD hole requires experience and careful attention so as not to damage the interface layers where deflections are to be measured. The drill is mounted on a tripod as illustrated in Figure B2. This method enables the technician to drill the MDD hole perpendicular to the pavement surface. The drilling process requires a dedicated crew to properly remove the tailings or dust from the drilling operation. A variety of drill bits and reamers are used depending on the road and subgrade.

While MDD installation was ongoing, a crew from TxDOT began digging a hole along the shoulder (Figure B3) so that thermocouples and time domain reflectometry (TDR) probes could subsequently be installed. The existing asphalt concrete surface was carefully removed to minimize disturbance of the base material. After removing the AC surface, a technician took density measurements on top of the base with a nuclear density gauge as

Figure B1. Location Selected for Installing MDDs.

Figure B2. Drill Mounted on a Tripod to Drill a Hole for the MDD.

Figure B3. Pavement Excavation along the Shoulder at the Vicinity of the WIM Site.

depicted in Figure B4. Once these measurements were taken, the base was carefully removed to get to the next material. Samples of the material from each layer were collected in bags as shown in Figure B5 for laboratory testing at TTI. This process continued until the proper depth of subgrade was reached, i.e., excavation went past the lime-treated subgrade and into the depth of the underlying native soil (Figure B6).

After the excavation was completed, the field crew started installing TDR probes and thermocouples. The placement depths of the sensors were measured along the side of the excavation as illustrated in Figure B7. Researchers also recorded the thickness of each layer. A special alignment jig (Figure B8) was fabricated to ensure proper installation of the TDR probes. This jig was used to drill holes where TDRs were inserted at the desired depths. It helped the technician drill holes of the proper diameter and spacing, and as straight and horizontal as possible.

The main difficulty in installing the TDRs was drilling through aggregates found in the base. In particular, some chipping of the base occurred in a few of the holes. Thus, some of the probes were offset slightly as shown in Figure B9, but the procedure followed permitted researchers to install the probes at or close to the insitu density of the underlying

Figure B4. Density Measurement on Base Material.

Figure B5. Samples of Lime-Treated Subgrade Collected from WIM Site.

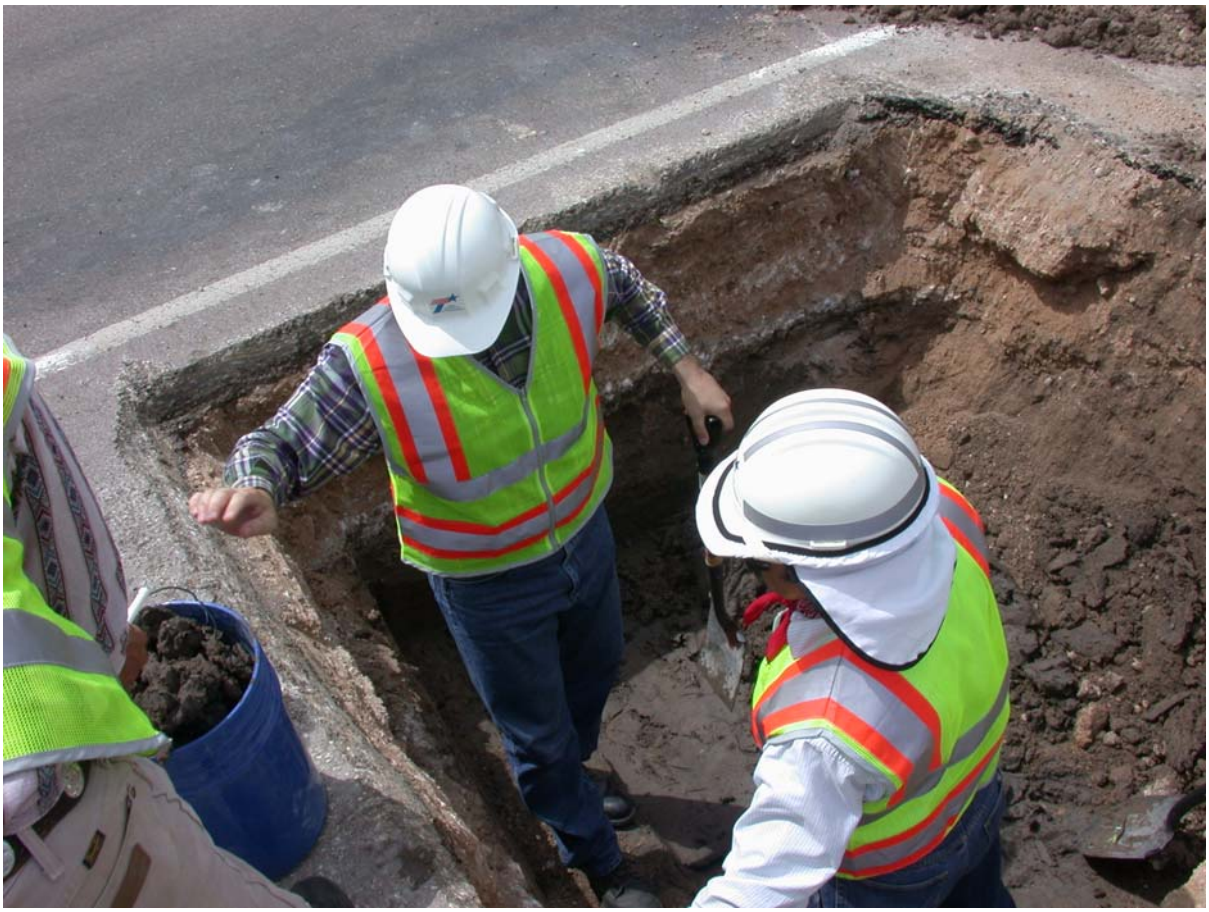

Figure B6. Collecting Samples of the Native Subgrade Material.

Figure B7. Establishing Depths of TDR Probes.

Figure B8. Drilling Holes for Installing TDR Probes.

Figure B9. TDRs Installed at Different Depths.

materials. After installing the TDRs, thermocouples were also placed at the required depths. Then, materials were shoveled back into the excavation in reverse order, carefully compacting at the locations of the sensors to prevent damage. Cables were routed through a conduit leading to a fenced area (Figure B10) operated by the Brownsville Public Utilities Board (PUB) where researchers later placed the weather station that housed the data recording system for the TDRs and thermocouples.

While the moisture sensors were being installed, other members of the field crew worked on finishing the MDD holes, which included placing a rubber liner inside the hole. To assure a good bond between the liner and the hole, technicians used flexible urethane asphalt as a bonding agent. This material is poured into the hole (Figure B11) and fills minute voids between the liner and the hole. The bonding agent is allowed to cure overnight.

Technicians also installed thermocouples near the top, middle and bottom of the AC surface at the vicinity of each MDD. For this purpose, a hole was initially drilled through the surface layer. Thermocouple wires were then attached to the top, middle and bottom of a wooden rod (Figure B12), of length approximately equal to the thickness of the asphalt concrete layer. This rod was then hammered into the hole. Technicians also saw cut cable runs into the pavement to route the MDD and thermocouple wires to an access box placed inside the fenced area shown in Figure B10.

After the bonding agent had set up, the LVDT modules comprising each MDD were installed. At this point, the reference anchor was already in place from the previous day's work, and technicians installed other positive locking devices inside the MDD hole. Each LVDT module was then lowered into the hole (Figure B13) and placed at the desired location. Technicians also took measurements to determine the exact placement depth of each module. After installing the top sensor, the electrical connector was crimped as shown in Figure B14. MDD and thermocouple wires were routed through the cable runs, which were then sealed. Connectors were also placed on the terminating ends of the MDD cables. At this point, the MDDs were ready for initial system tests.

In addition, technicians assembled the weather station and anchored it in place inside the Brownsville PUB fenced area. TDR cables and thermocouple wires were connected to the data recording system (Figure B15) to complete the installation. Figure B16 shows the weather station that researchers set up at the site.

Figure B10. Sensor Cables Routed through a Conduit.

Figure B11. Curing of MDD Bonding Agent.

Figure B12. Wooden Rod Used to Install Thermocouple Wires.

Figure B13. Installation of MDD LVDT Module.

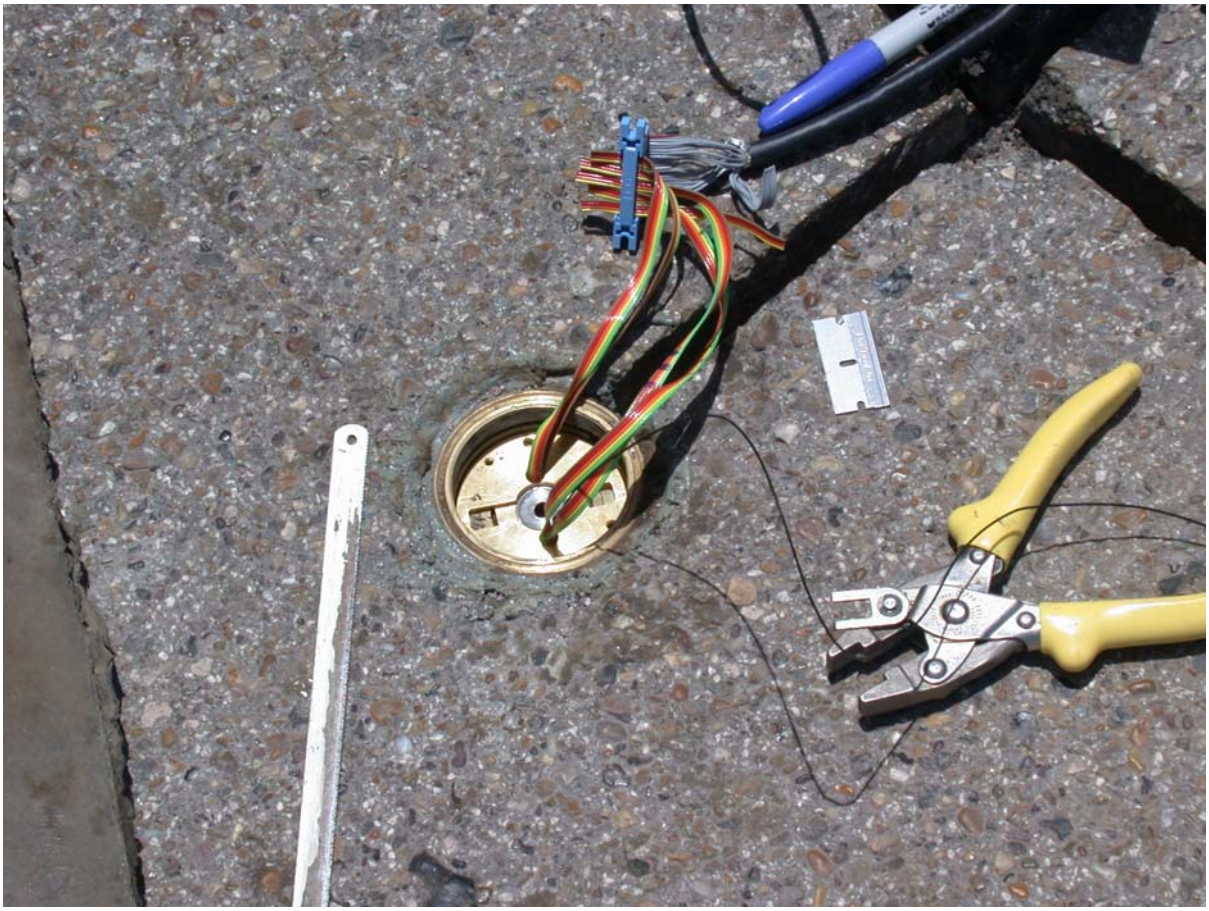

Figure B14. Setup after Installing All MDD Sensors Inside Hole.

Figure B15. Weather Station Controller Box.

Figure B16. Weather Station Installed at WIM Site.

MDD INITIAL SYSTEM CHECK-UP AND DATA COLLECTION

After completing the MDD installation, the field crew verified the operation of the sensors by taking measurements with a falling weight deflectometer (Figure B17) and a calibration truck of known axle weights (Figure B18). Both the FWD and test truck were provided by the Pharr District. For MDD data analysis, it is important to know the position of the load relative to the MDD. Thus, researchers painted a grid on the K6 and K7 lanes so that the wheel load position may be determined during analysis of MDD data from videos taken of trucks passing the WIM site. Figure B19 shows the grid at the MDD locations. The distances between grid lines were also marked on the pavement as shown in the figure.

Researchers verified that all MDD sensors were giving reasonable readings under both the FWD test loads and the calibration truck, and that the signals were stable. The verification done in the field was primarily based on the trends in the deflection readings from the different sensors for the range of test loads used. Later, researchers analyzed the data at TTI and verified that measured deflections were consistent with theoretical predictions. This analysis required backcalculating the stiffness of each layer from the FWD data taken during the tests and reviewing the videos taken of the calibration truck to determine the positions of the wheel load based on the grid for the various runs made.

After verifying the operation of the MDDs, researchers collected deflection data under permitted trucks. This initial data collection served as a dry run or a rehearsal of the procedure established to collect pavement response data under permitted truck traffic. This data collection was done at different times during the project.

Figure B20 shows a permitted truck going over the MDD sensor on the K7 lane. As the truck passes, a technician operates a video camera to record the placement of the tires on the grid. At the same time, a researcher monitors the MDD displacements and records the data into an electronic file for analysis at a later time (Figure B21). To identify each permitted truck, researchers are stationed at the Port of Brownsville where they collect the permit number issued for each truck and affix a tag to the vehicle (Figure B22). The permit number is necessary to retrieve the static axle weights measured on each truck at the port. The tag affixed to the truck has a unique identification number that is radioed back to the researchers stationed at the WIM site. In this way, researchers responsible for collecting MDD data and operating the video camera get advance notice on the trucks that will be passing the WIM site, thus, giving them sufficient time to get ready.

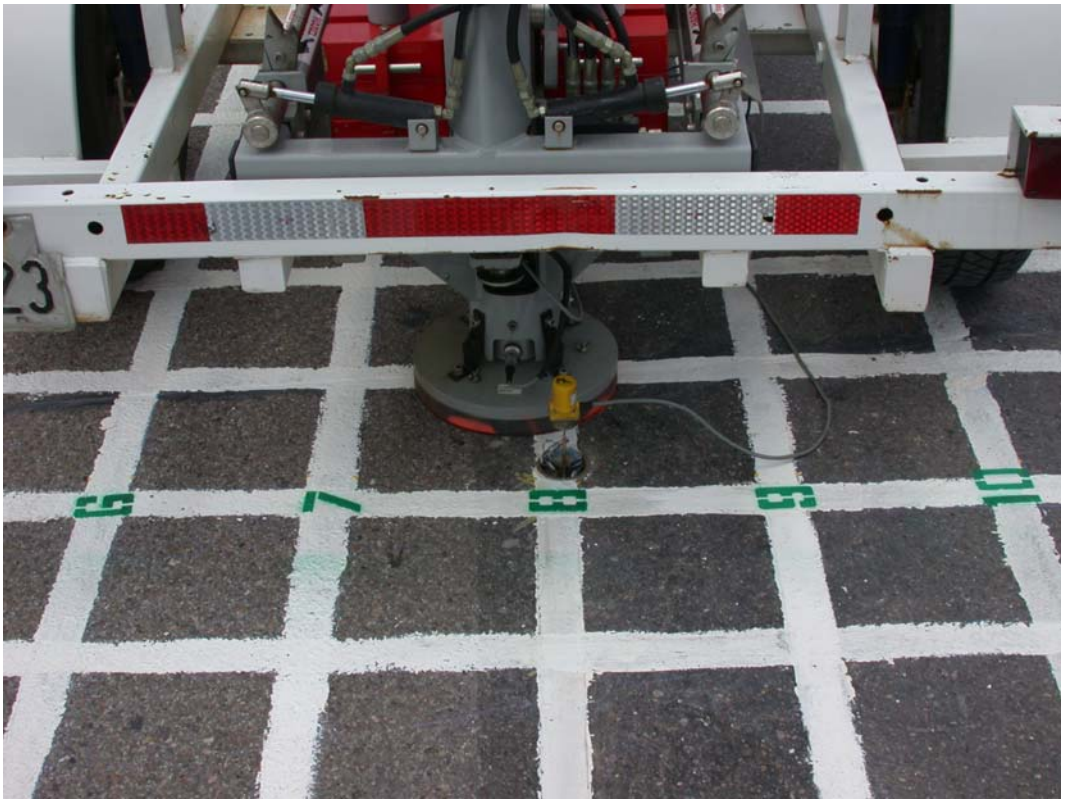

Figure B17. MDD Data Collection under FWD Loading.

Figure B18. MDD Data Collection under Calibration Truck.

Figure B19. Grid Placed on Test Lanes for Determining Tire Placement.

Figure B20. Permitted Truck Going Over MDD on K7 Lane.

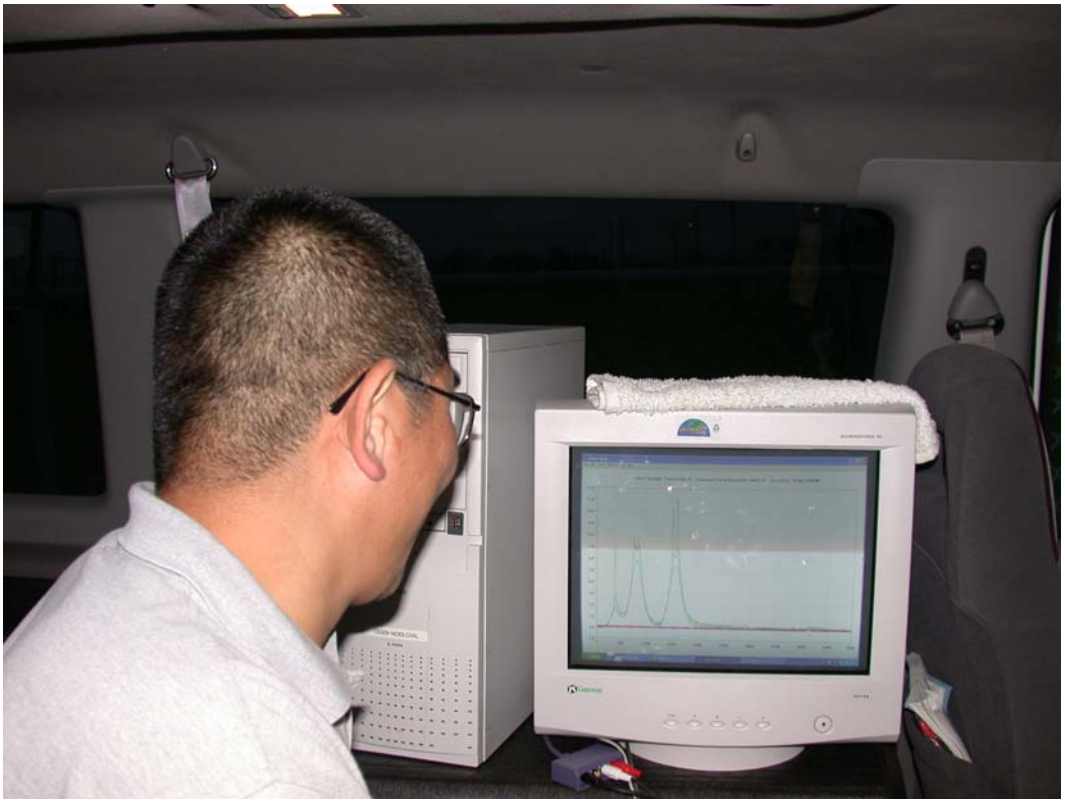

Figure B21. Monitoring and Recording MDD Displacements during Data Collection.

Figure B22. Permitted Truck with Tag Affixed (#118).

APPENDIX C

CHARTS OF BACKCALCULATED LAYER MODULI ON K6 AND K7 FWD STATIONS

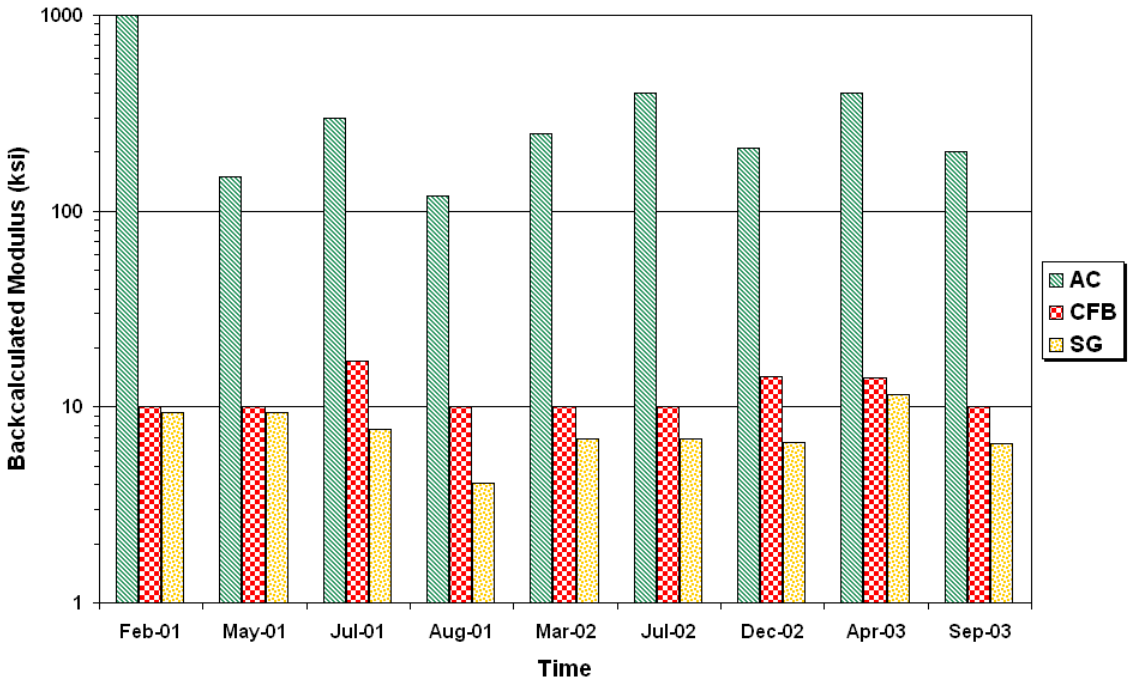

Figure C1. Backcalculated Layer Moduli on FWD Station K6-1.

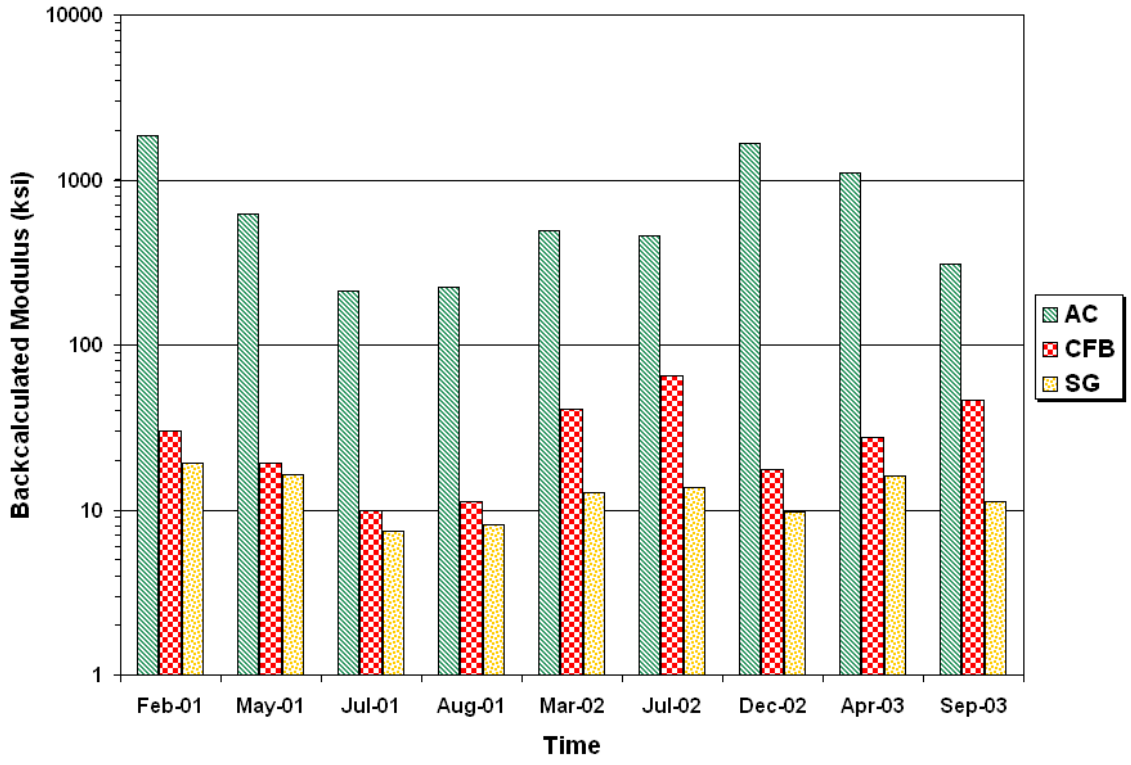

Figure C2. Backcalculated Layer Moduli on FWD Station K6-2.

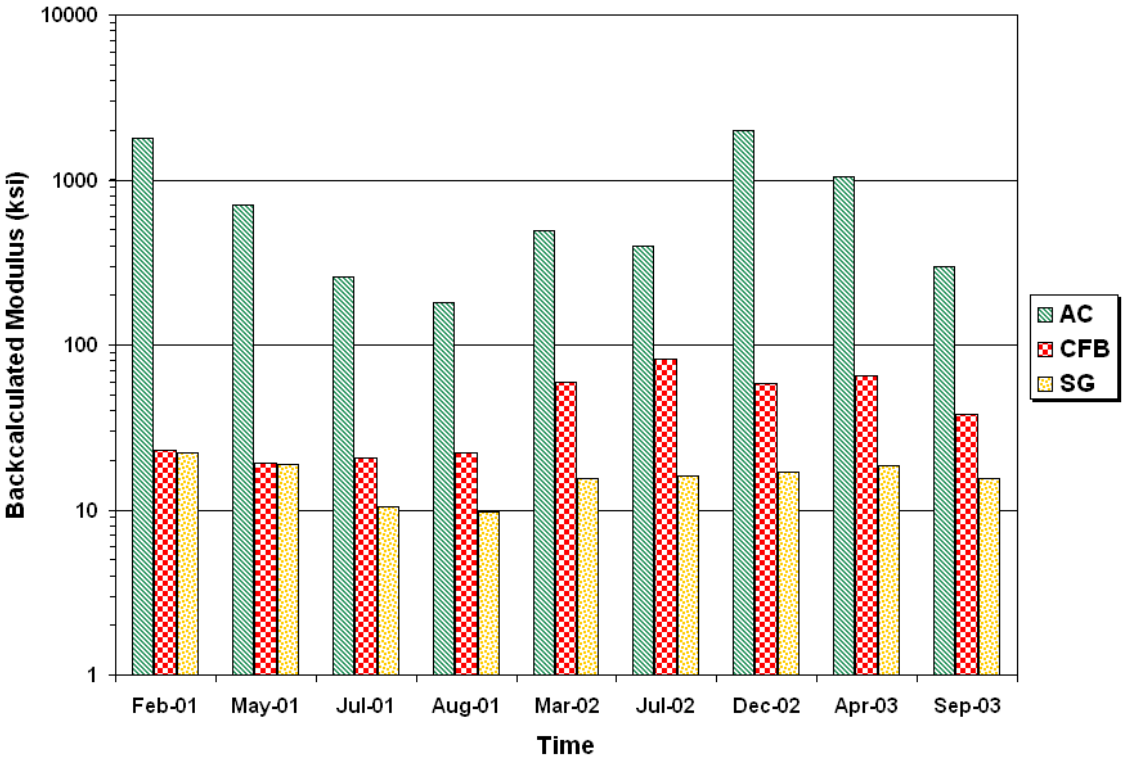

Figure C3. Backcalculated Layer Moduli on FWD Station K6-3.

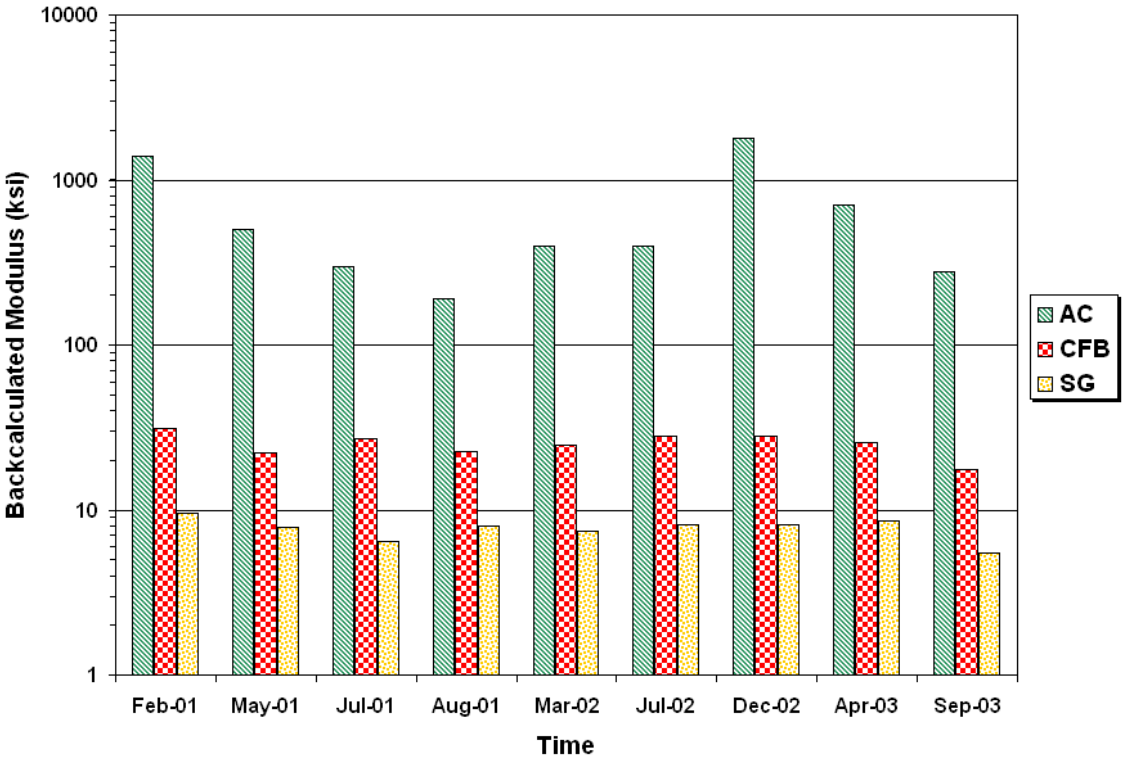

Figure C4. Backcalculated Layer Moduli on FWD Station K6-4.

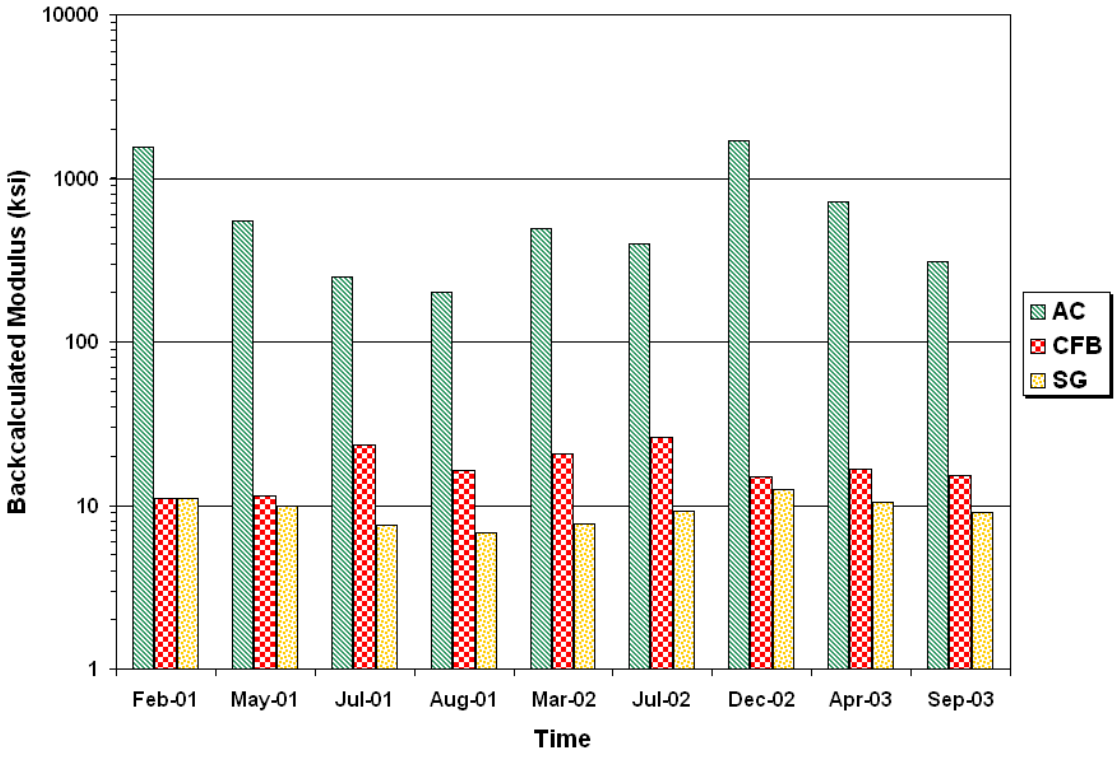

Figure C5. Backcalculated Layer Moduli on FWD Station K6-5.

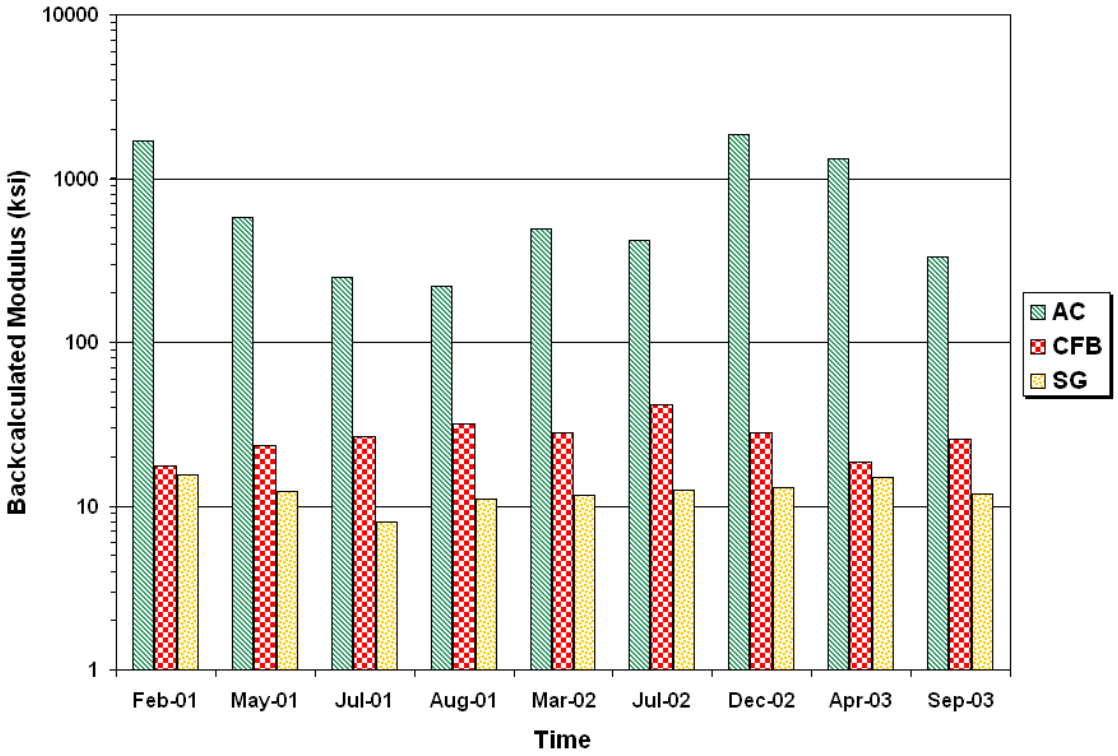

Figure C6. Backcalculated Layer Moduli on FWD Station K6-6.

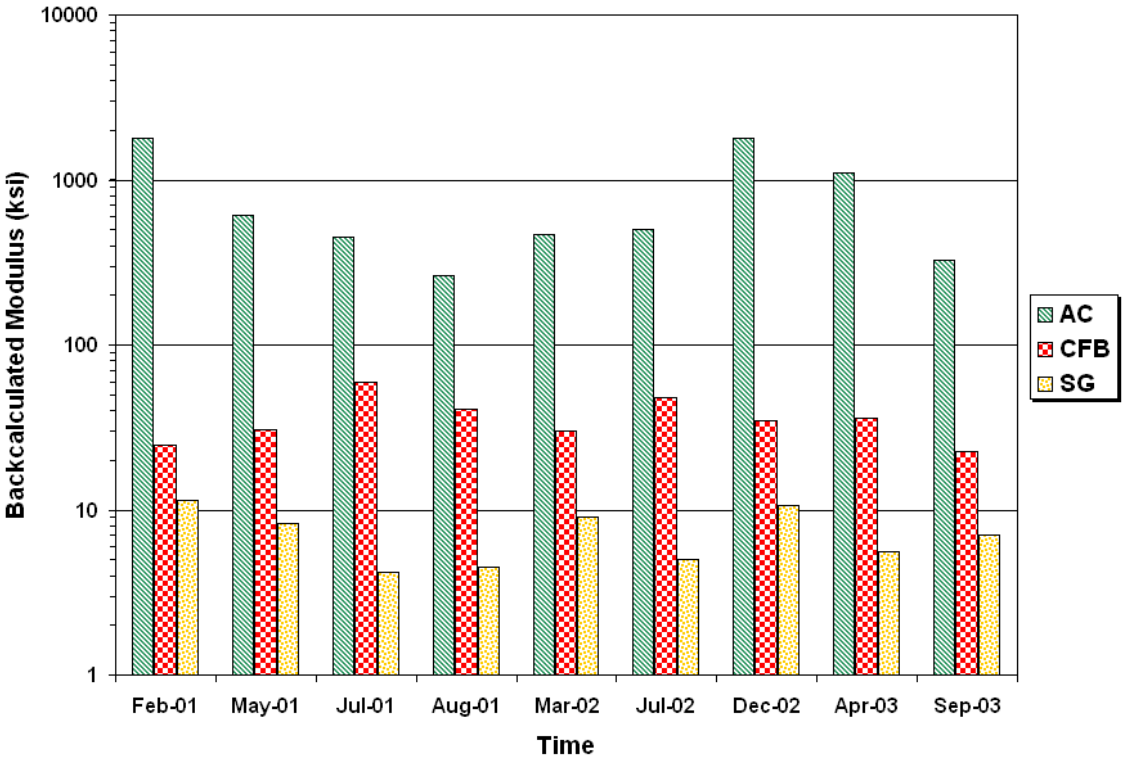

Figure C7. Backcalculated Layer Moduli on FWD Station K6-7.

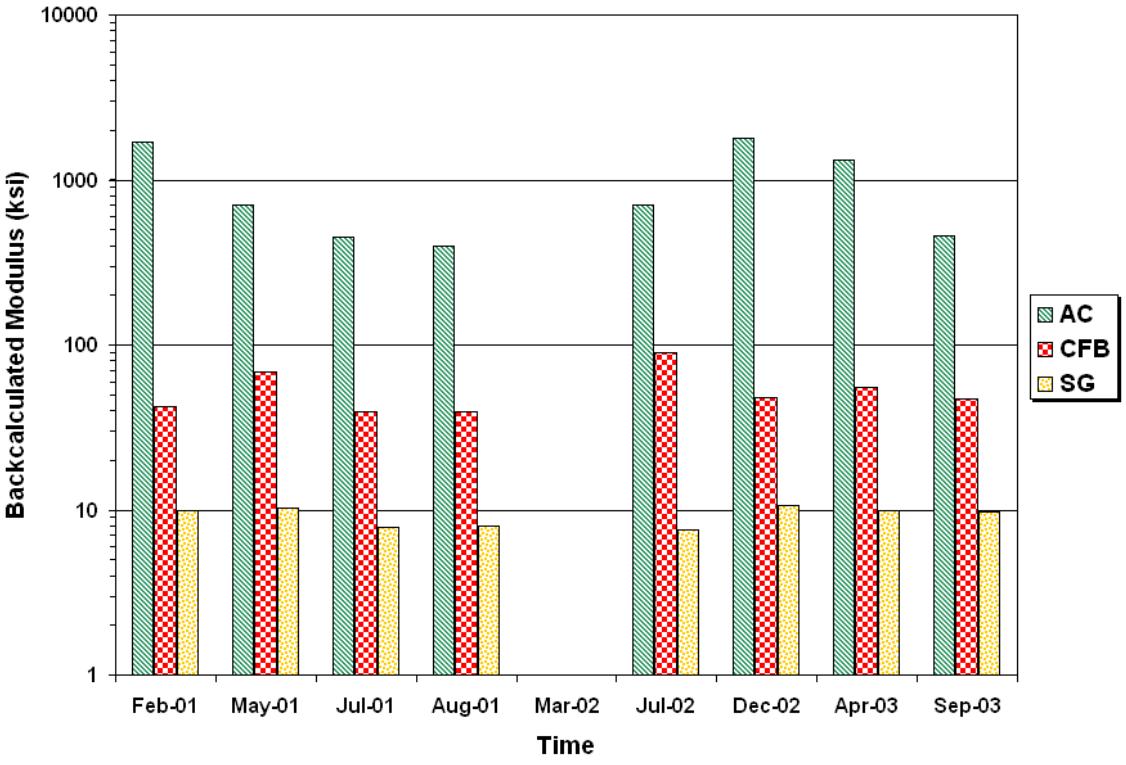

Figure C8. Backcalculated Layer Moduli on FWD Station K6-8.

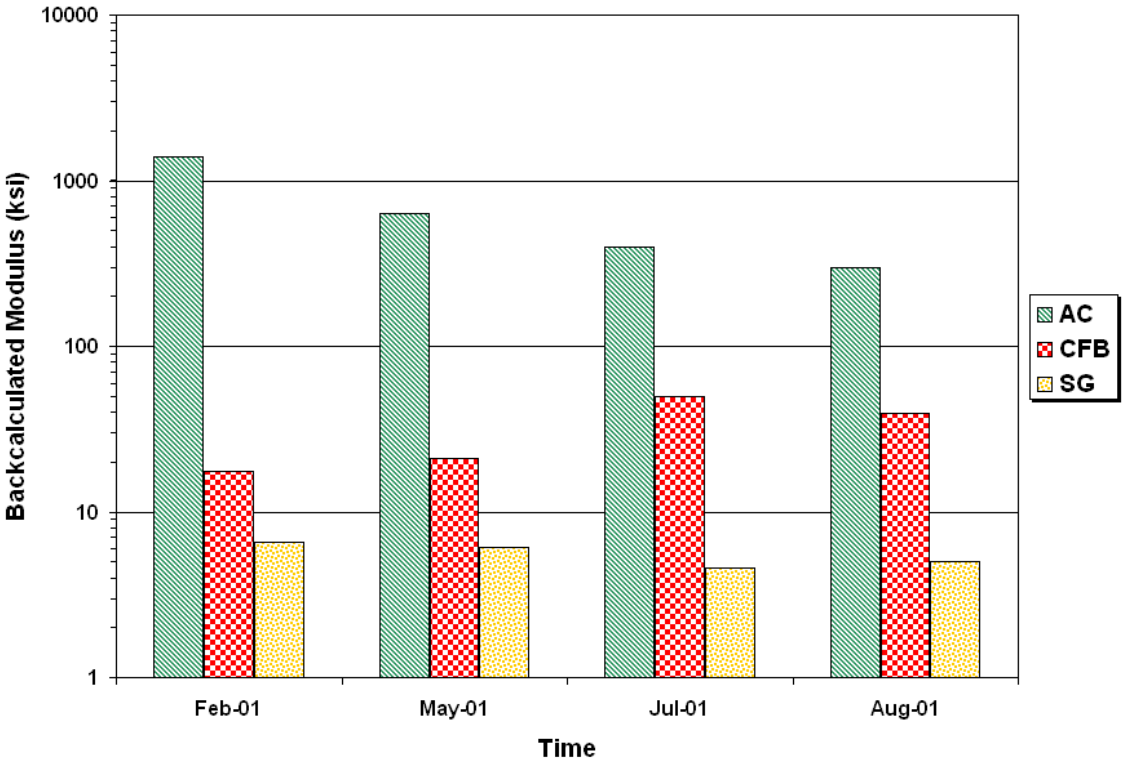

Figure C9. Backcalculated Layer Moduli on FWD Station K6-9.

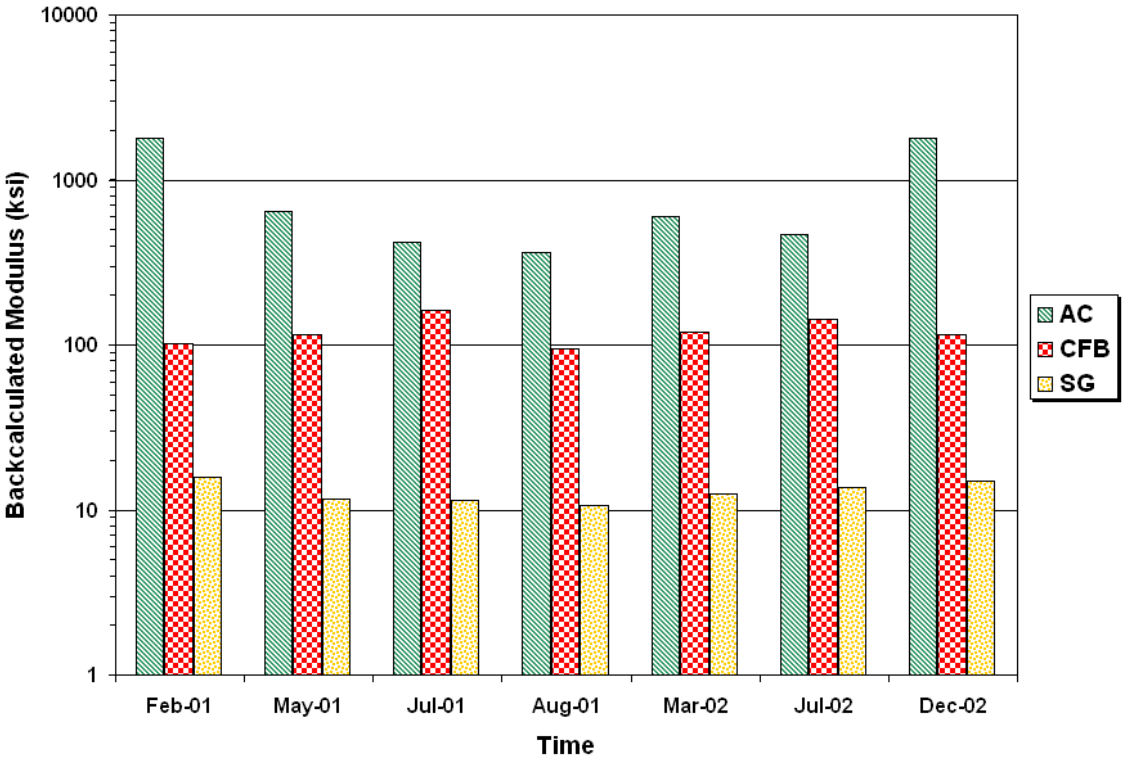

Figure C10. Backcalculated Layer Moduli on FWD Station K6-10.

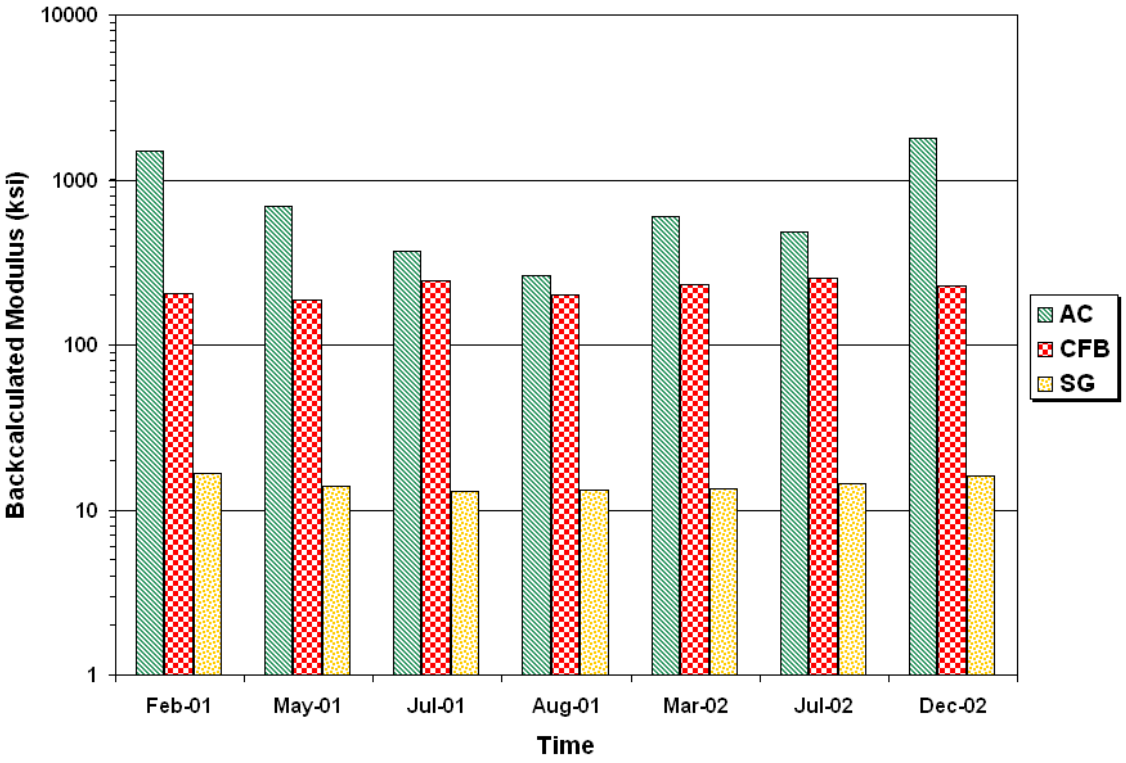

Figure C11. Backcalculated Layer Moduli on FWD Station K6-11.

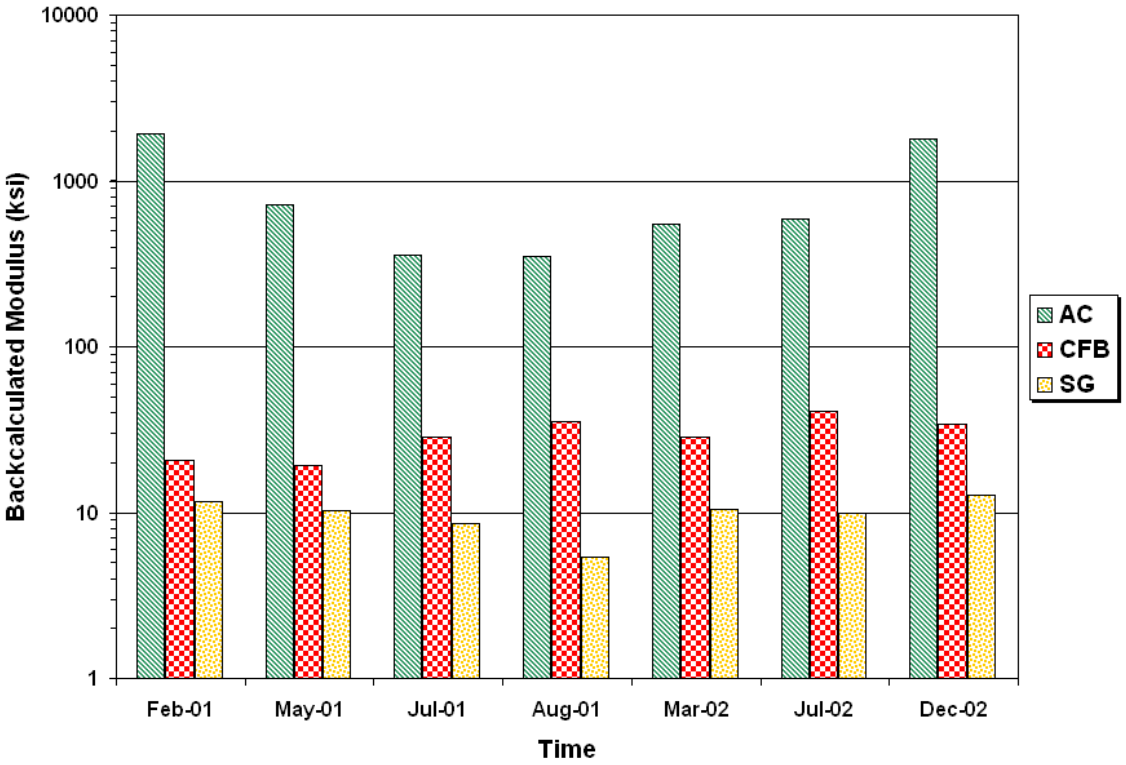

Figure C12. Backcalculated Layer Moduli on FWD Station K6-12.

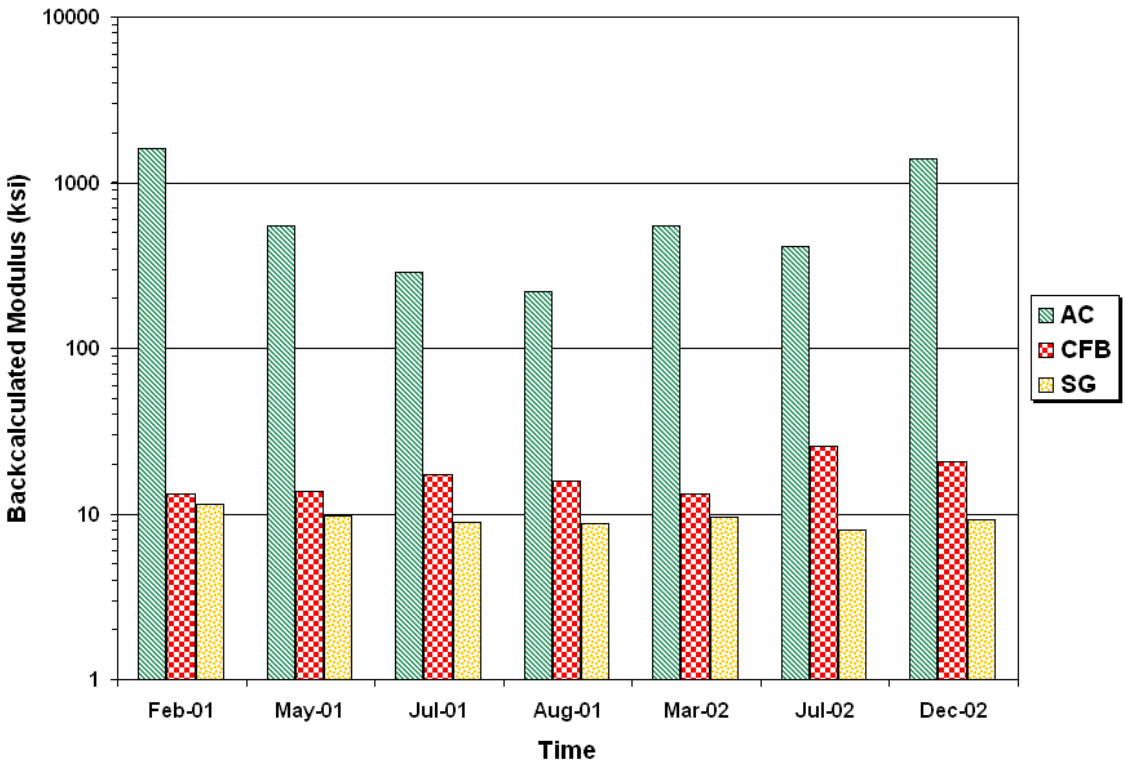

Figure C13. Backcalculated Layer Moduli on FWD Station K6-13.

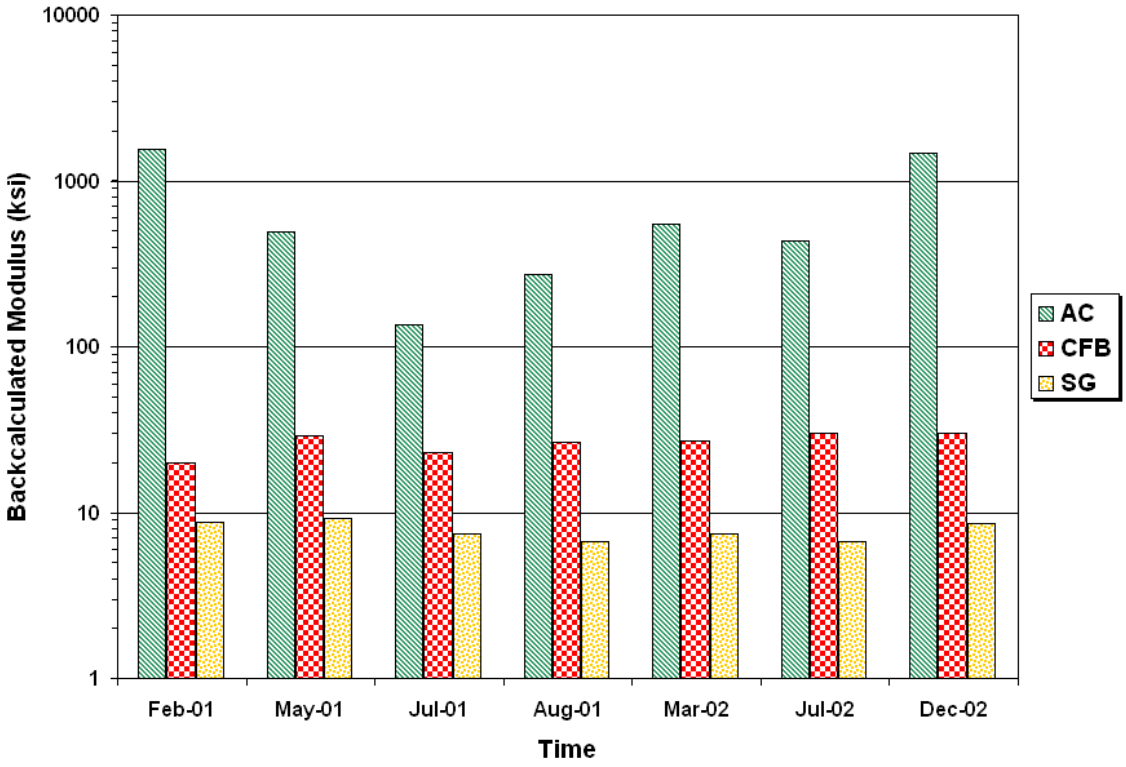

Figure C14. Backcalculated Layer Moduli on FWD Station K6-14.

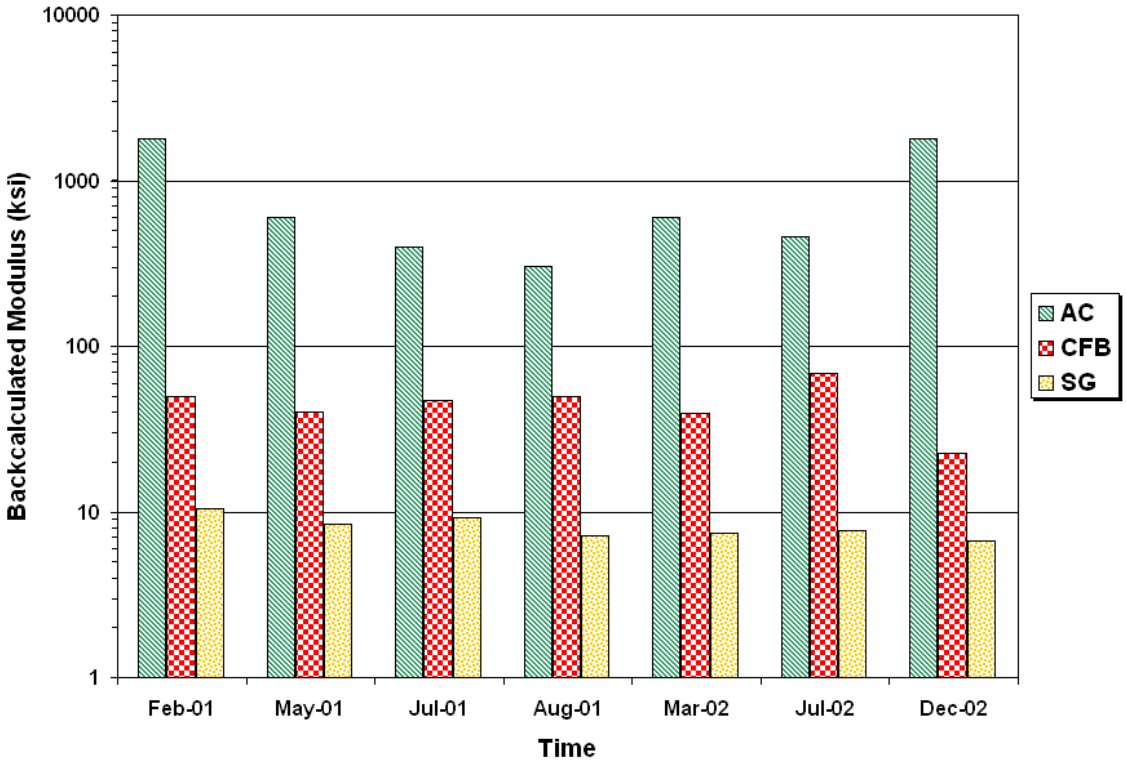

Figure C15. Backcalculated Layer Moduli on FWD Station K6-15.

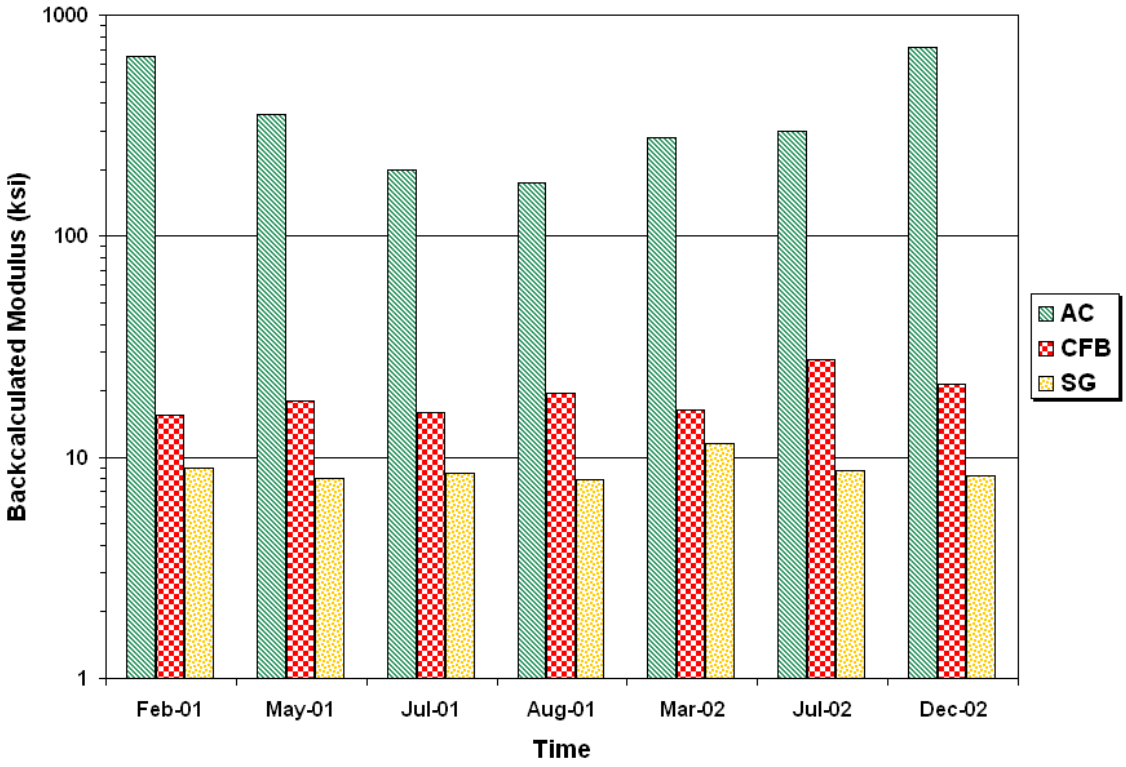

Figure C16. Backcalculated Layer Moduli on FWD Station K6-16.

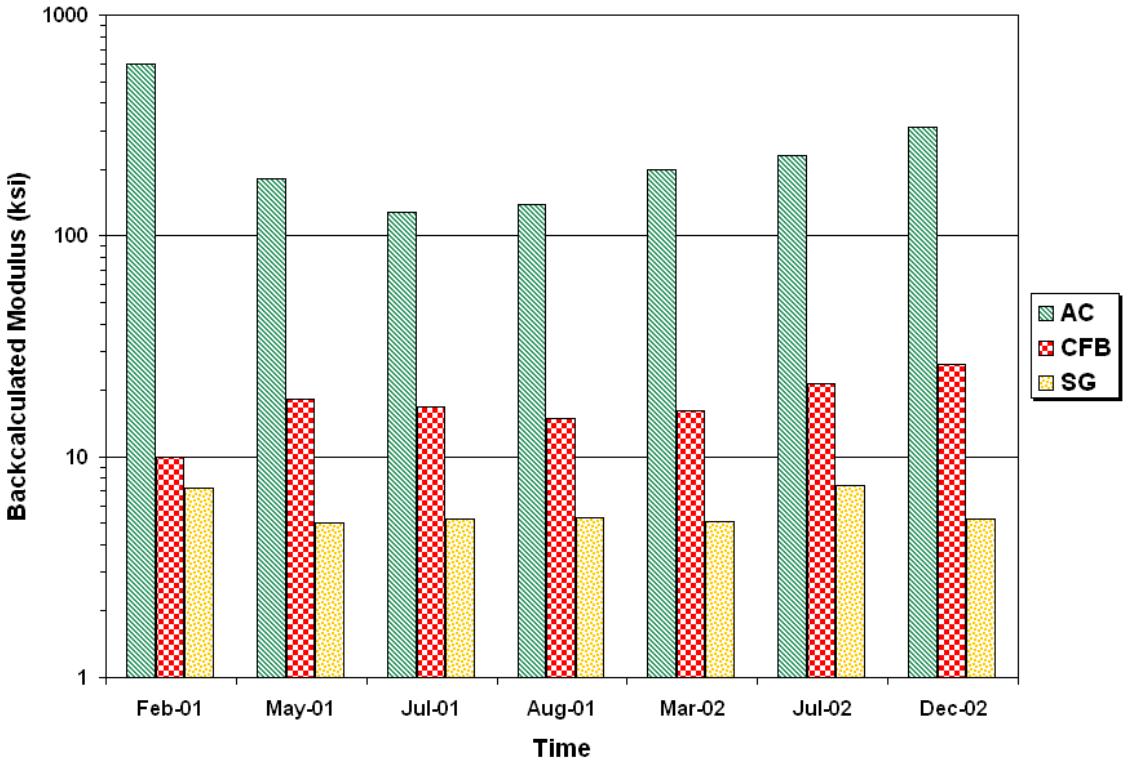

Figure C17. Backcalculated Layer Moduli on FWD Station K6-17.

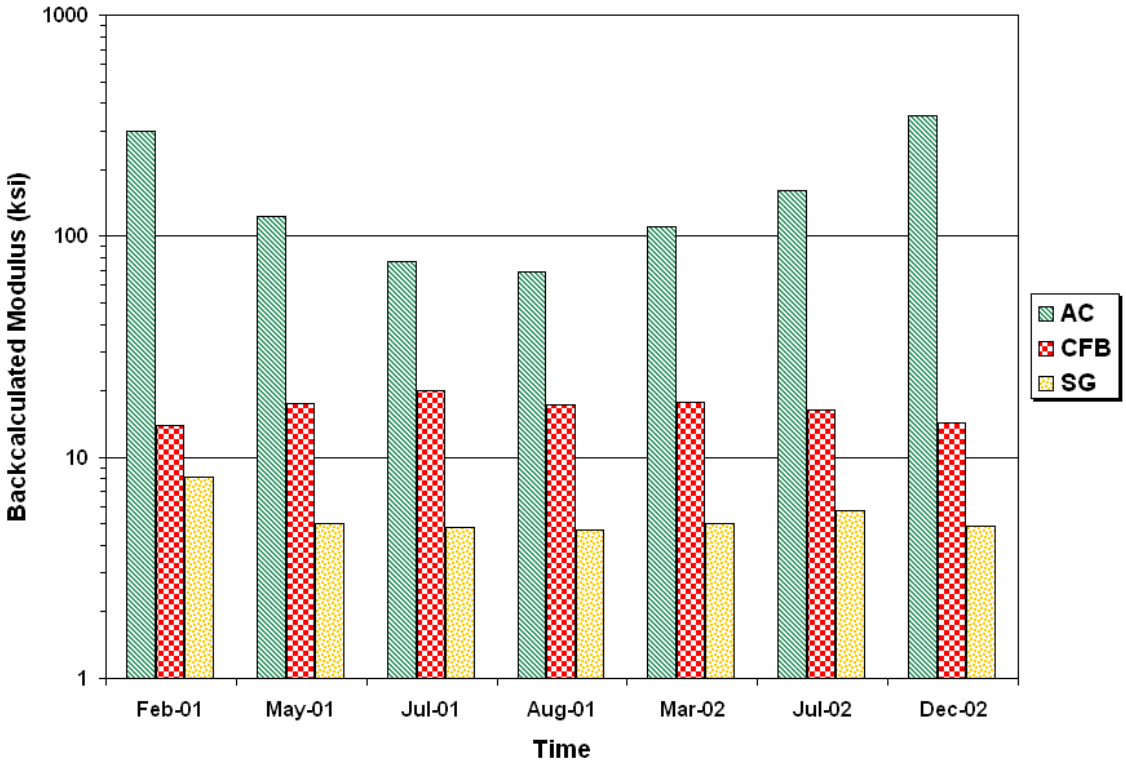

Figure C18. Backcalculated Layer Moduli on FWD Station K6-18.

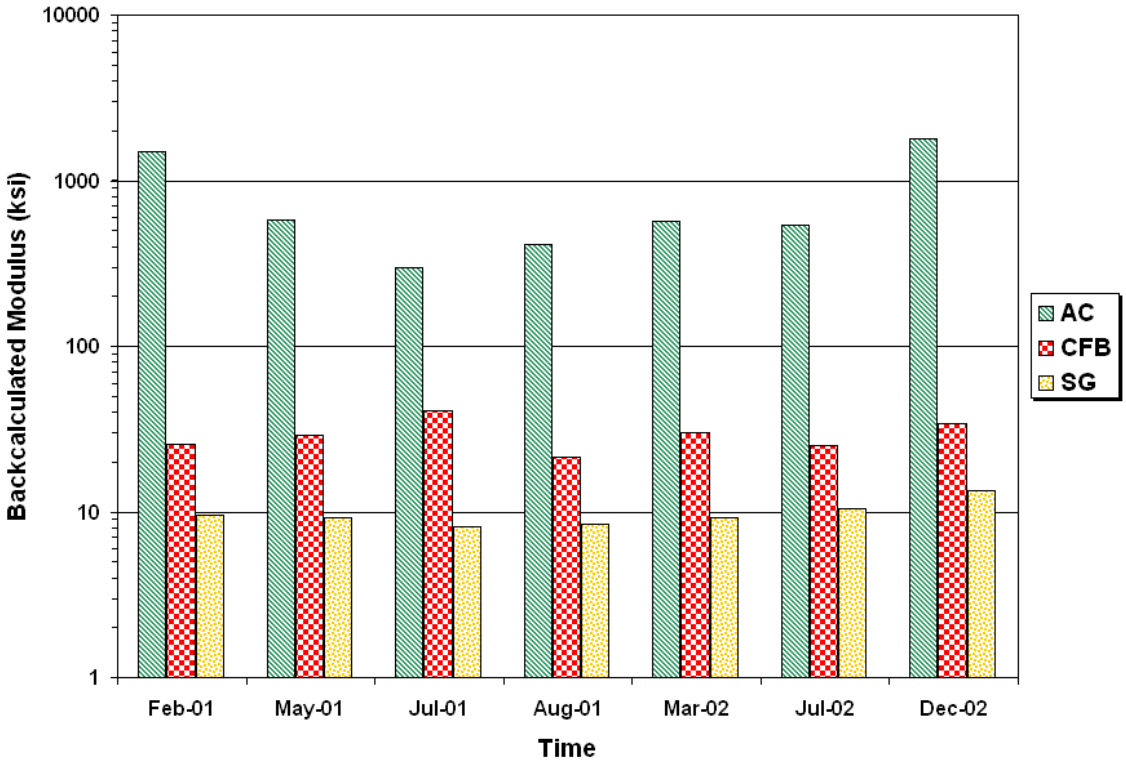

Figure C19. Backcalculated Layer Moduli on FWD Station K6-19.

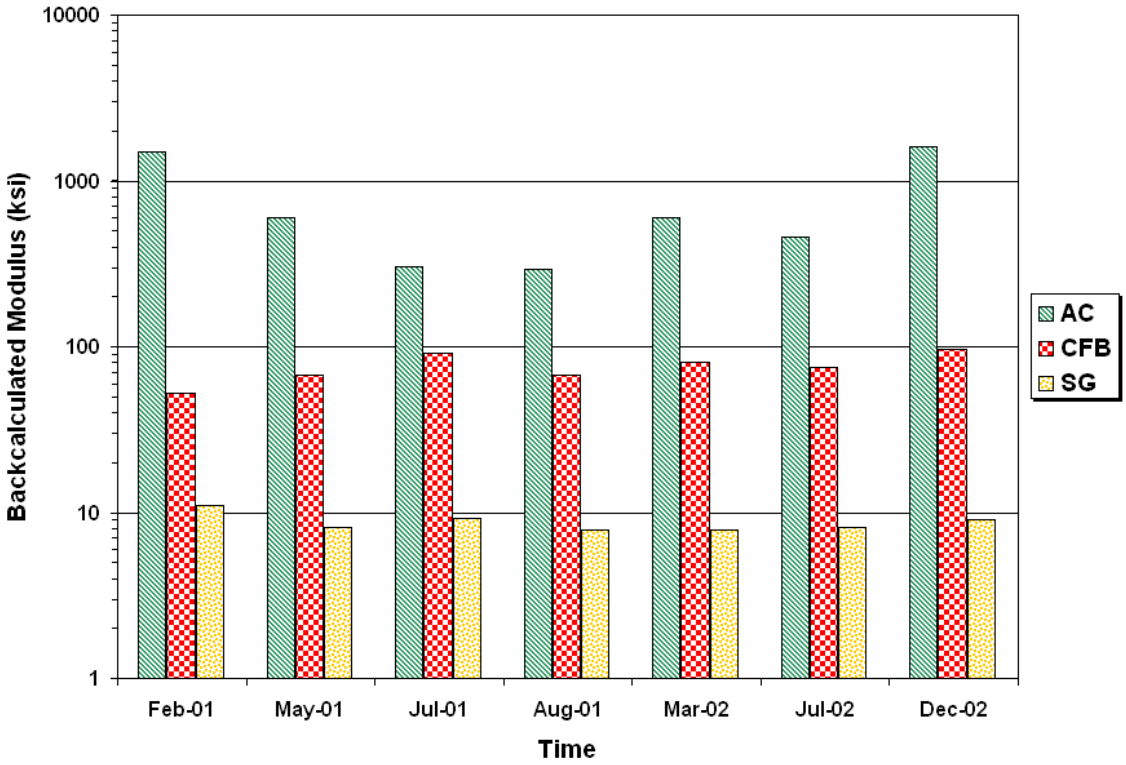

Figure C20. Backcalculated Layer Moduli on FWD Station K6-20.

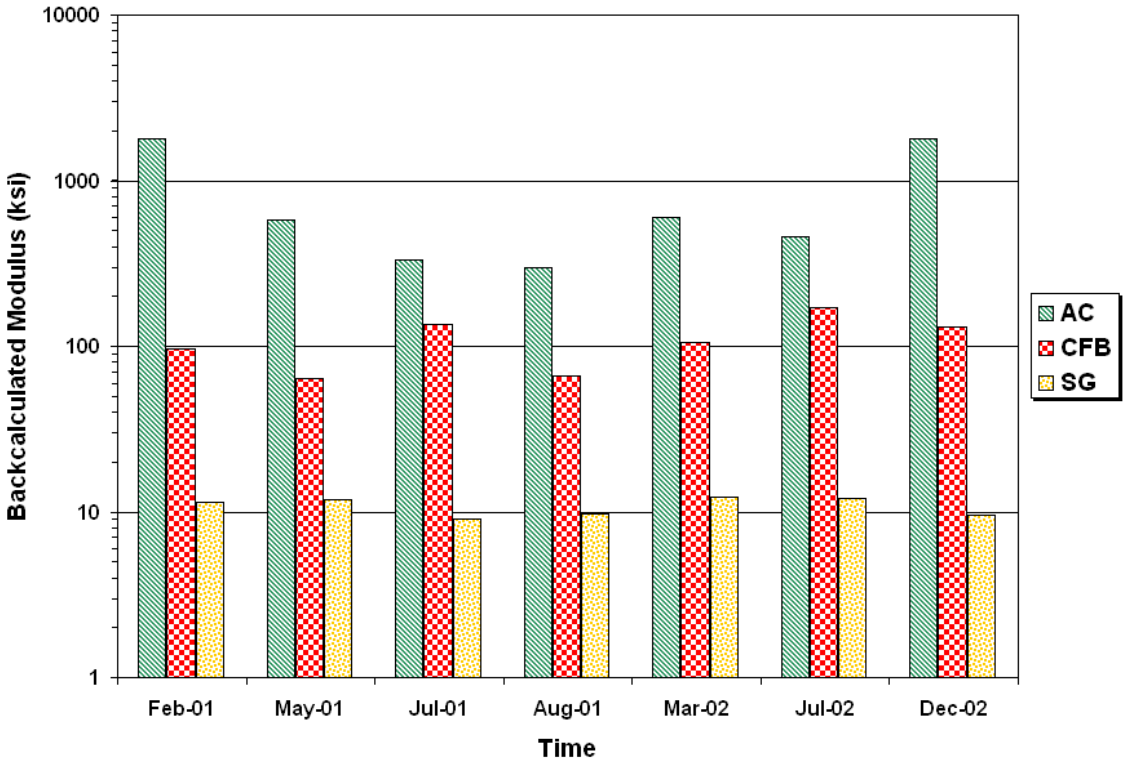

Figure C21. Backcalculated Layer Moduli on FWD Station K6-21.

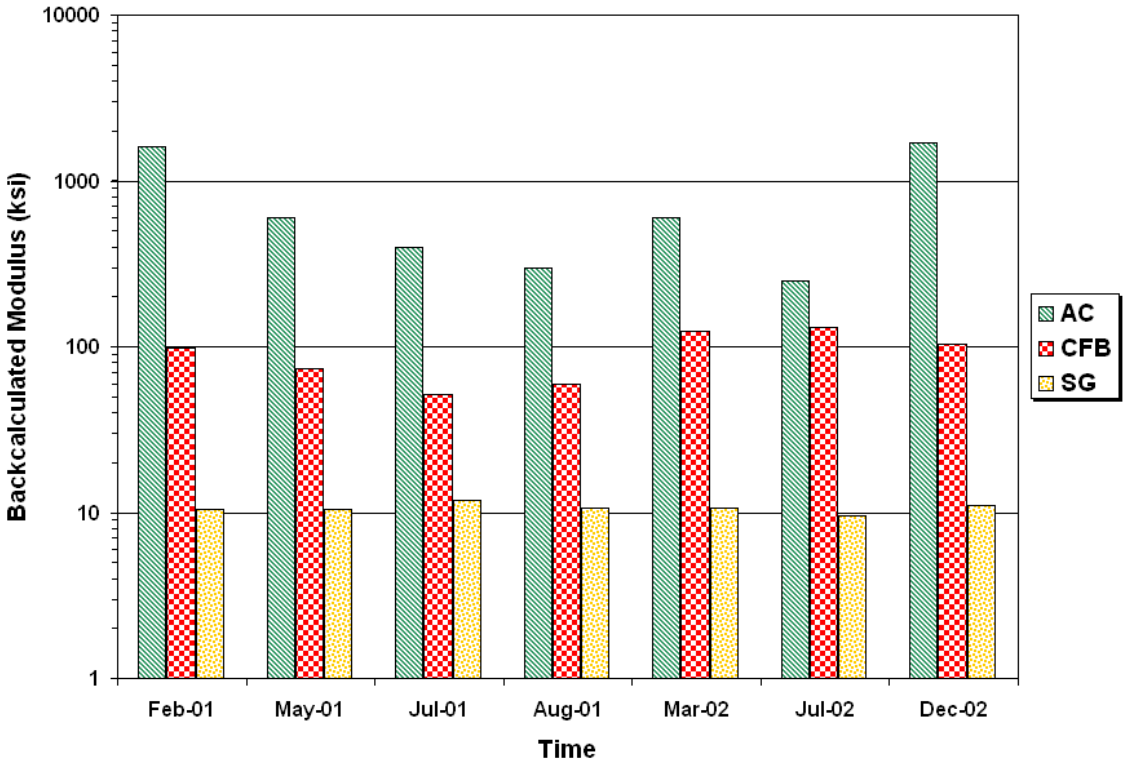

Figure C22. Backcalculated Layer Moduli on FWD Station K6-22.

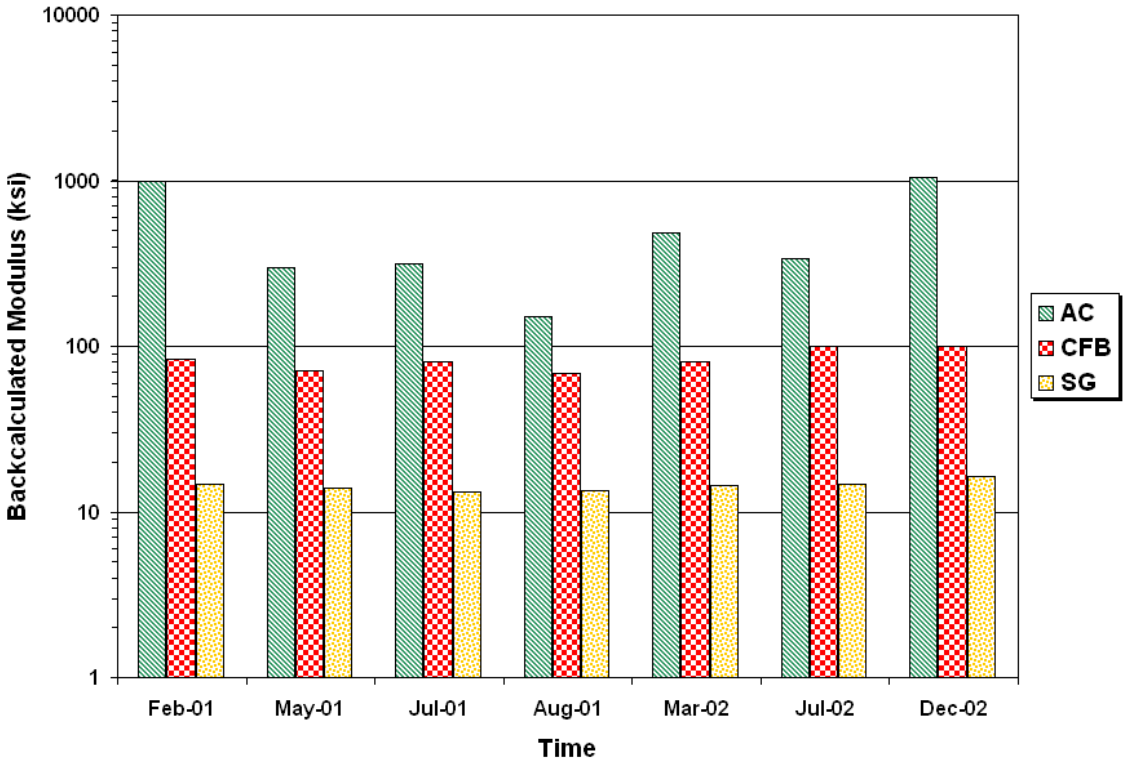

Figure C23. Backcalculated Layer Moduli on FWD Station K6-23.

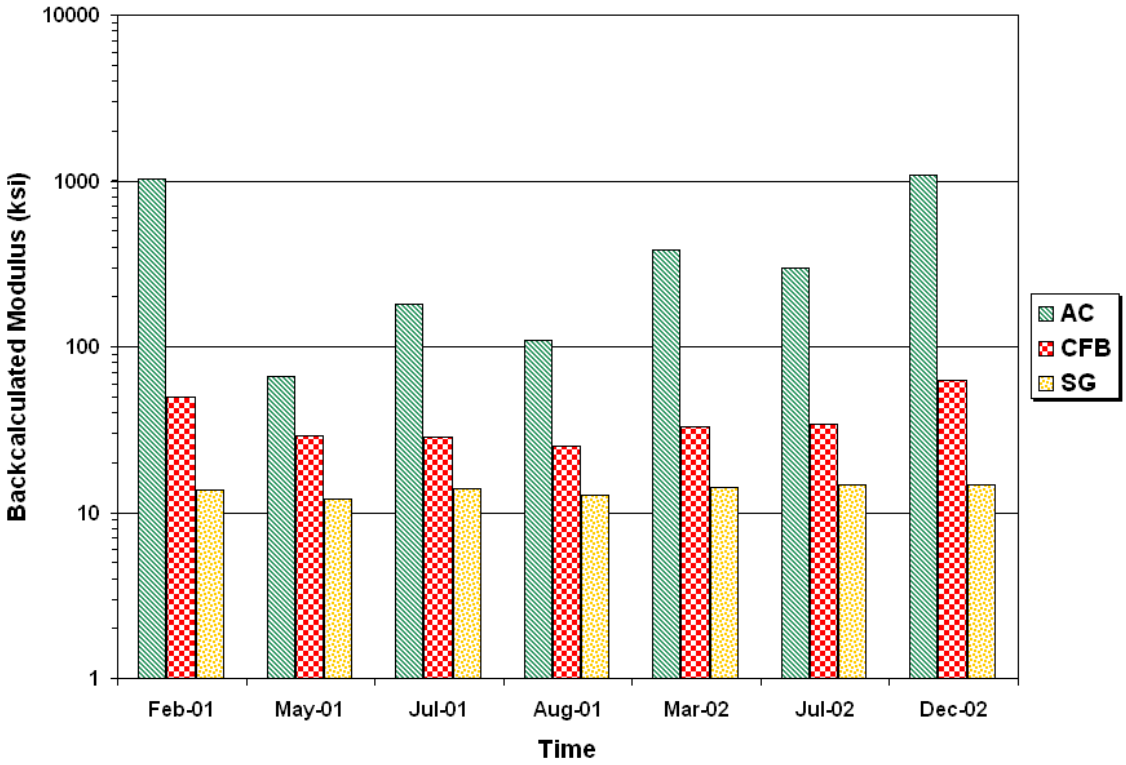

Figure C24. Backcalculated Layer Moduli on FWD Station K6-24.

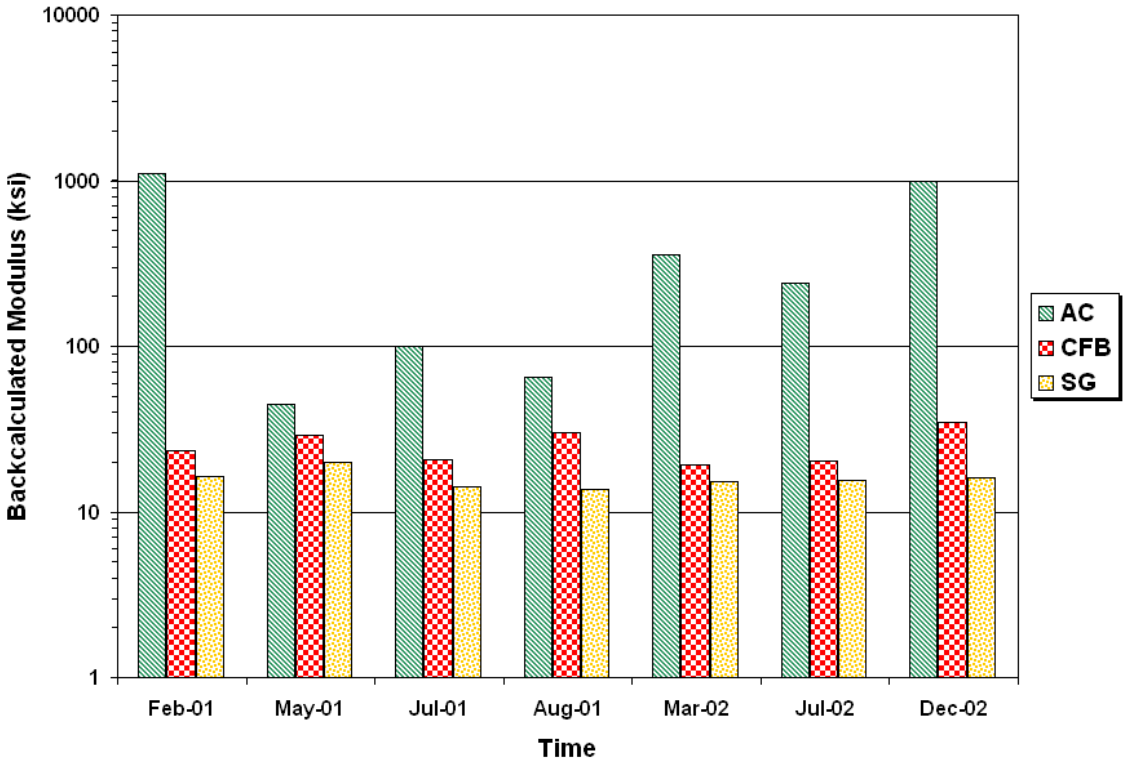

Figure C25. Backcalculated Layer Moduli on FWD Station K6-25.

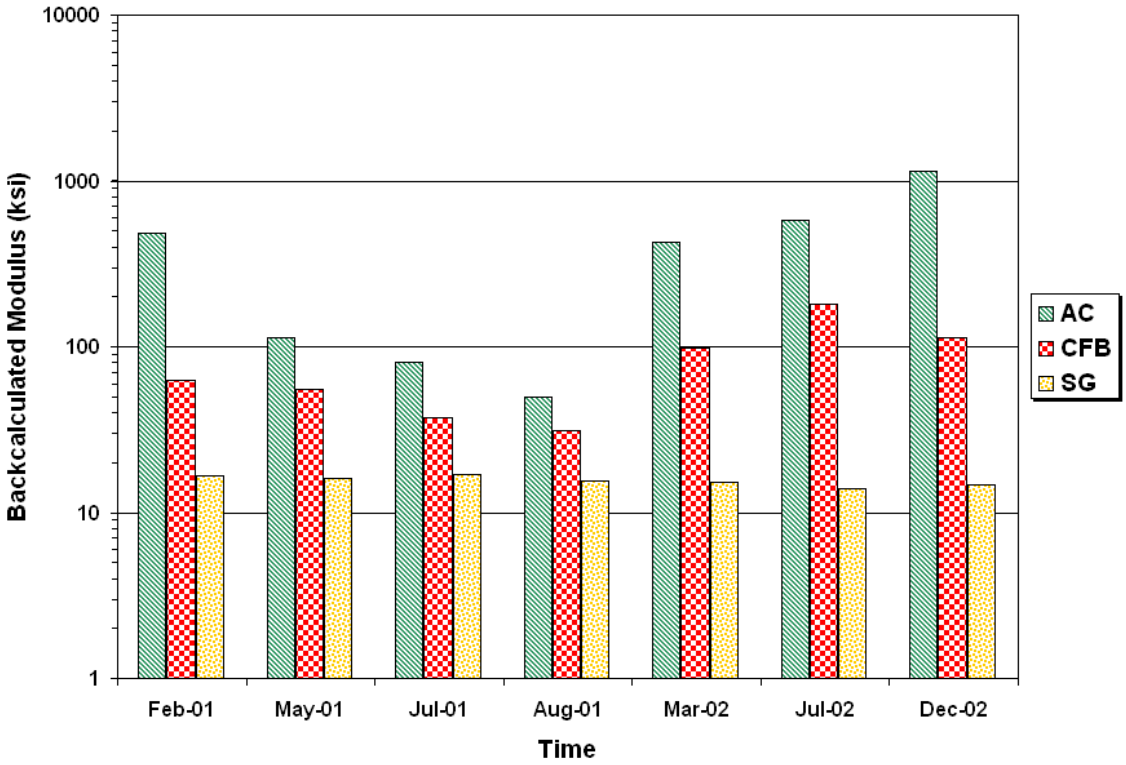

Figure C26. Backcalculated Layer Moduli on FWD Station K6-26.

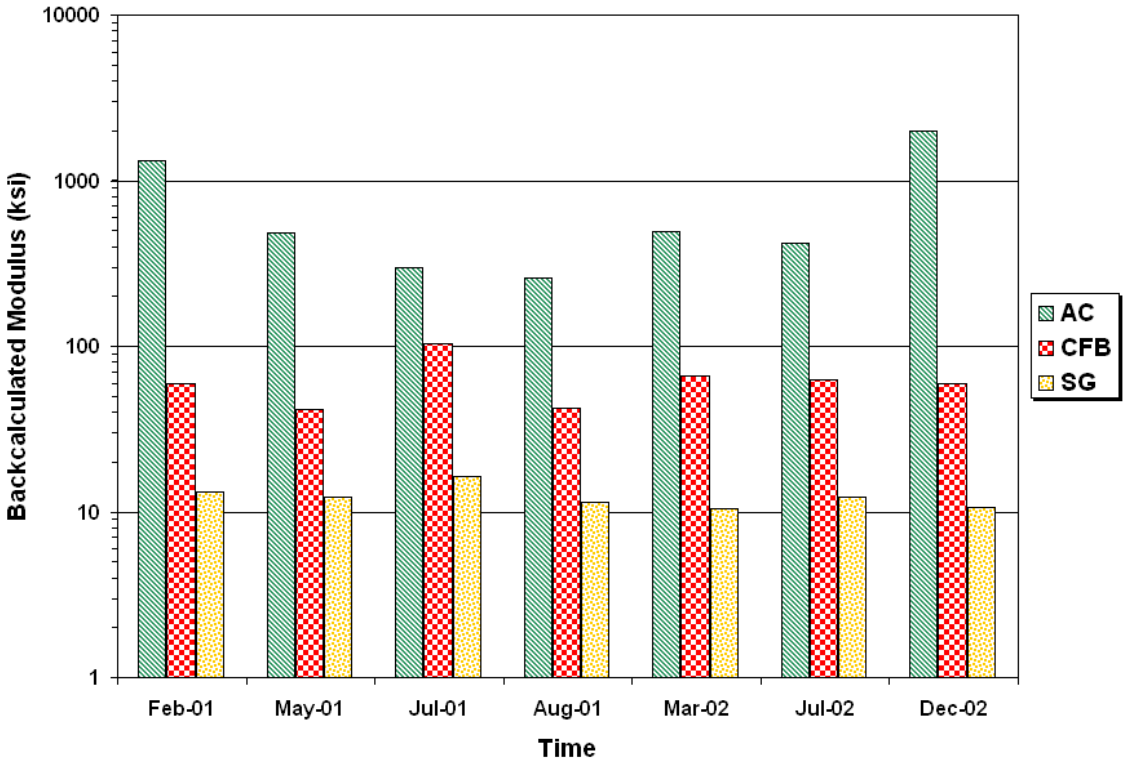

Figure C27. Backcalculated Layer Moduli on FWD Station K6-27.

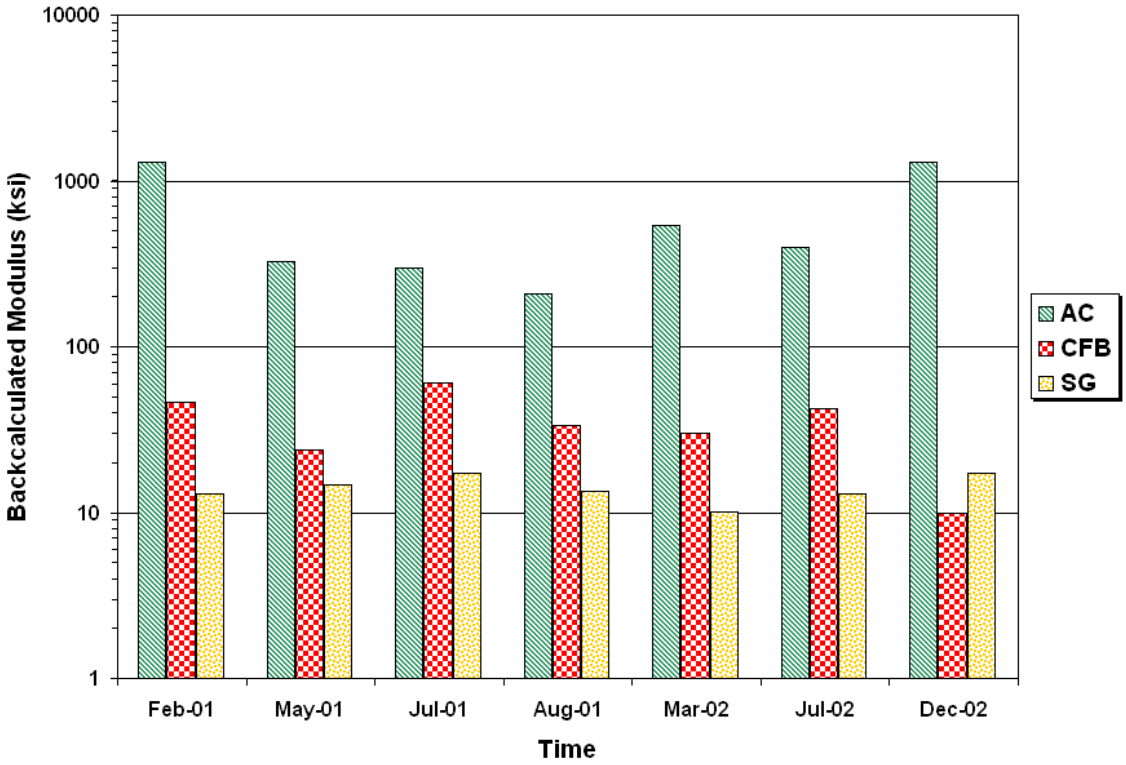

Figure C28. Backcalculated Layer Moduli on FWD Station K6-28.

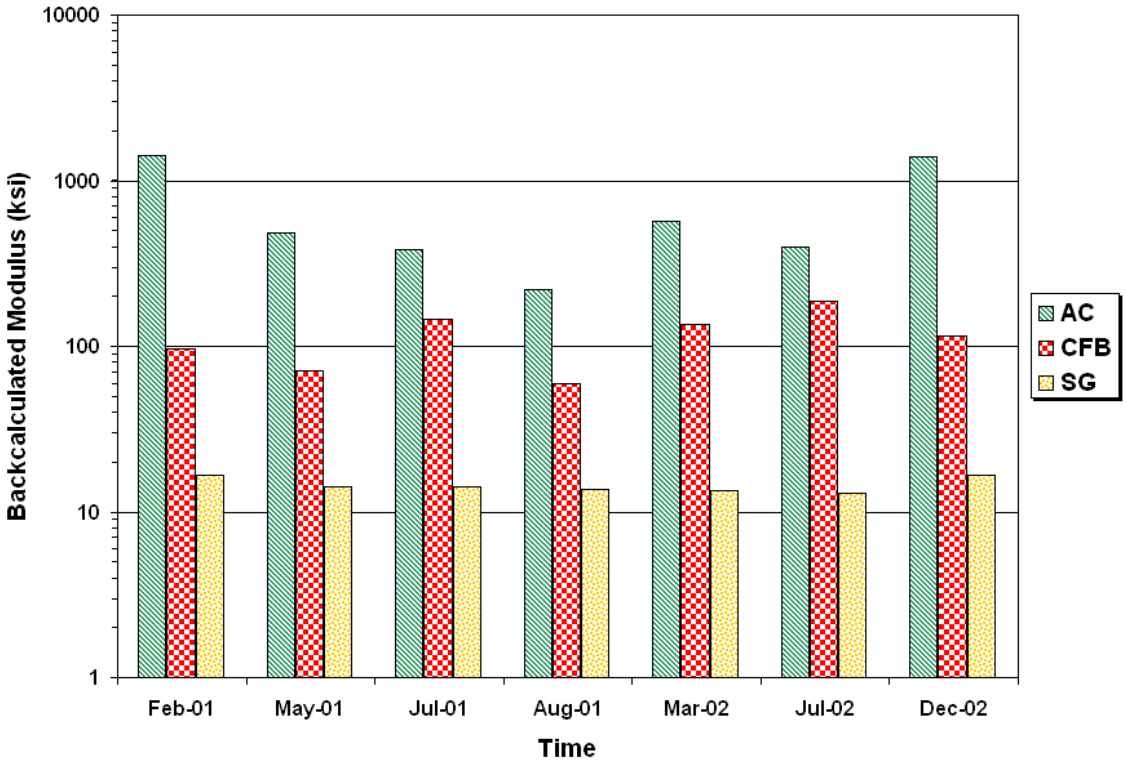

Figure C29. Backcalculated Layer Moduli on FWD Station K6-29.

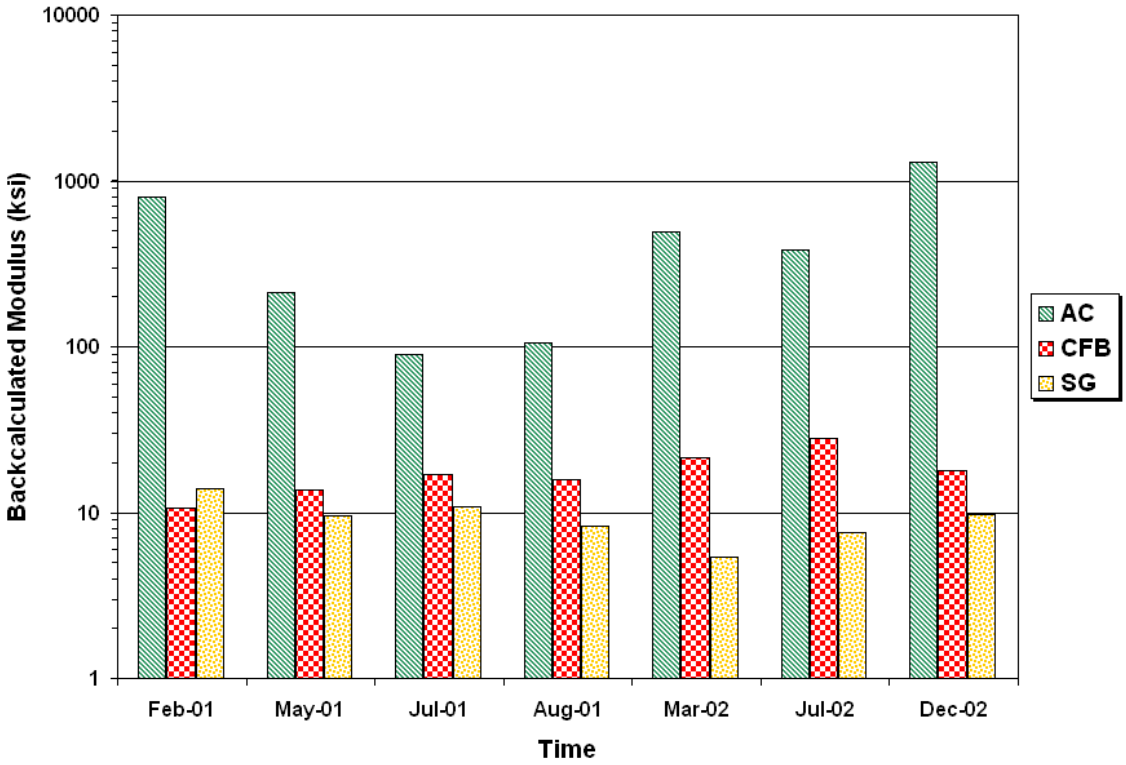

Figure C30. Backcalculated Layer Moduli on FWD Station K6-30.

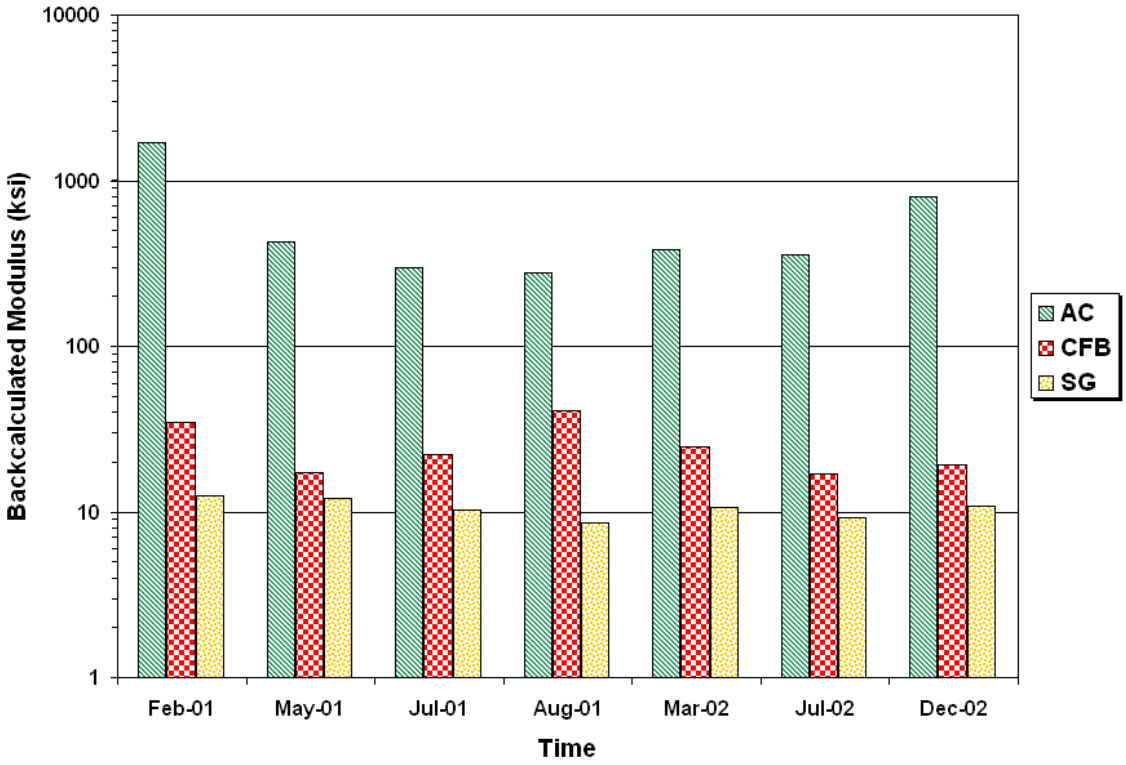

Figure C31. Backcalculated Layer Moduli on FWD Station K6-31.

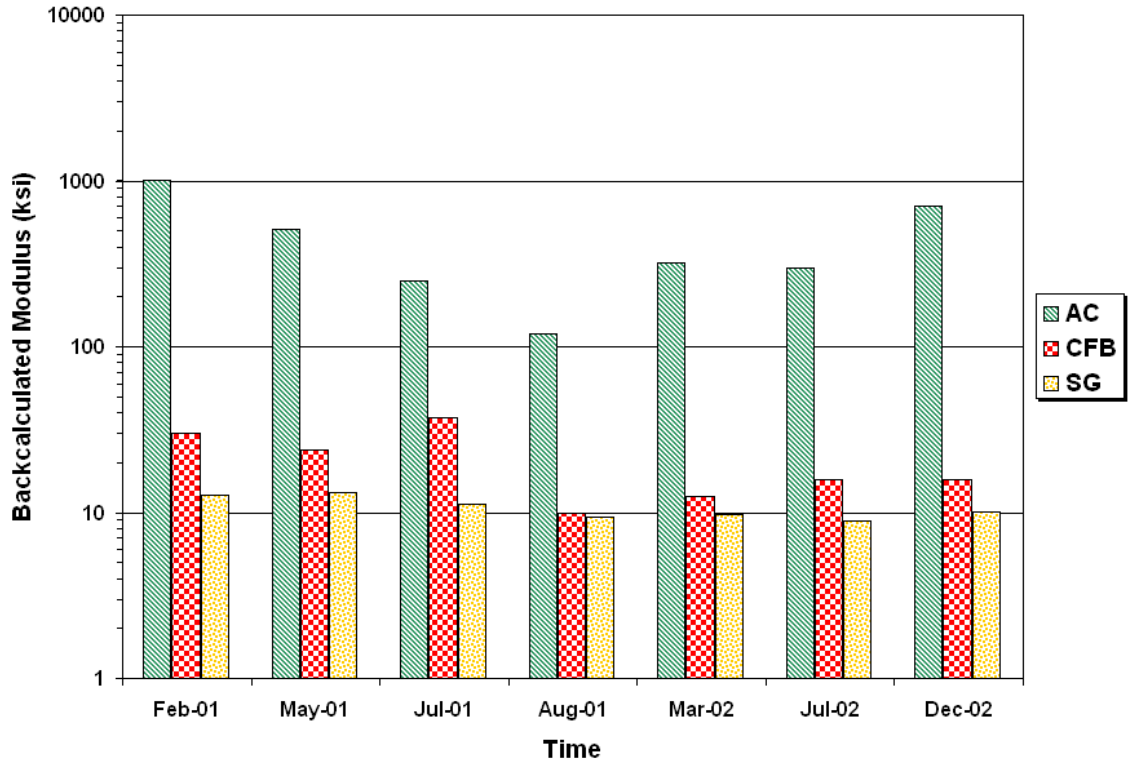

Figure C32. Backcalculated Layer Moduli on FWD Station K6-32.

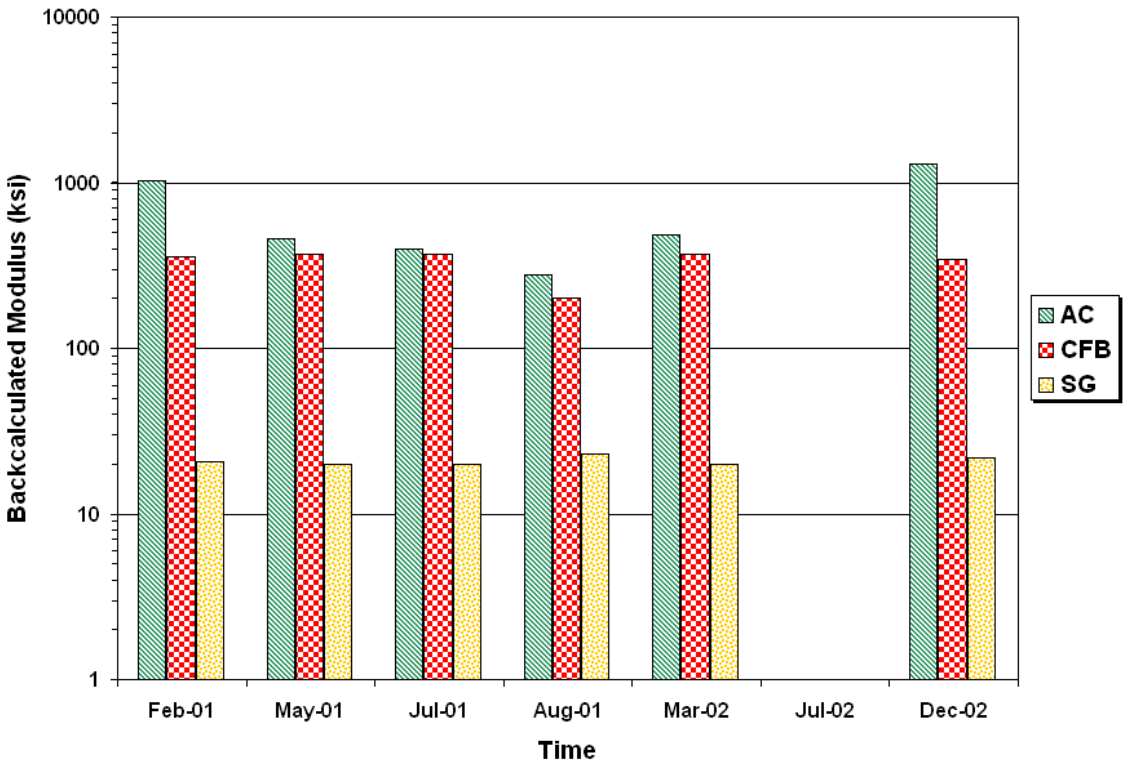

Figure C33. Backcalculated Layer Moduli on FWD Station K6-33.

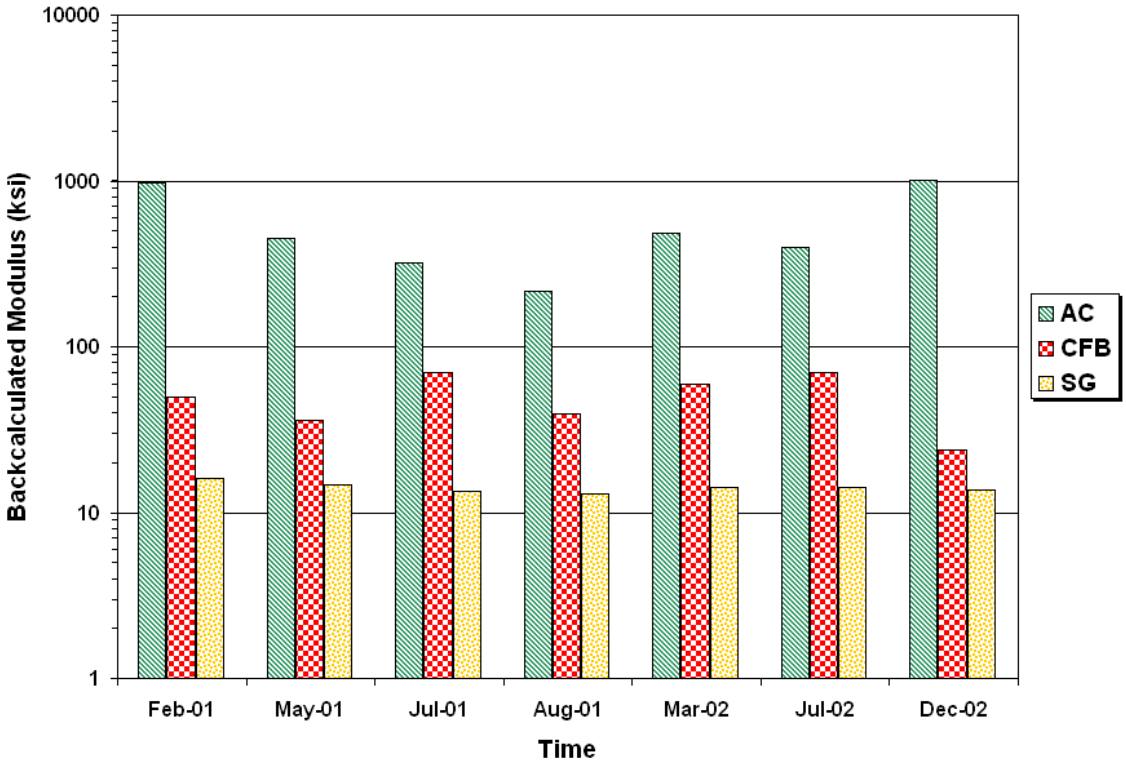

Figure C34. Backcalculated Layer Moduli on FWD Station K6-34.

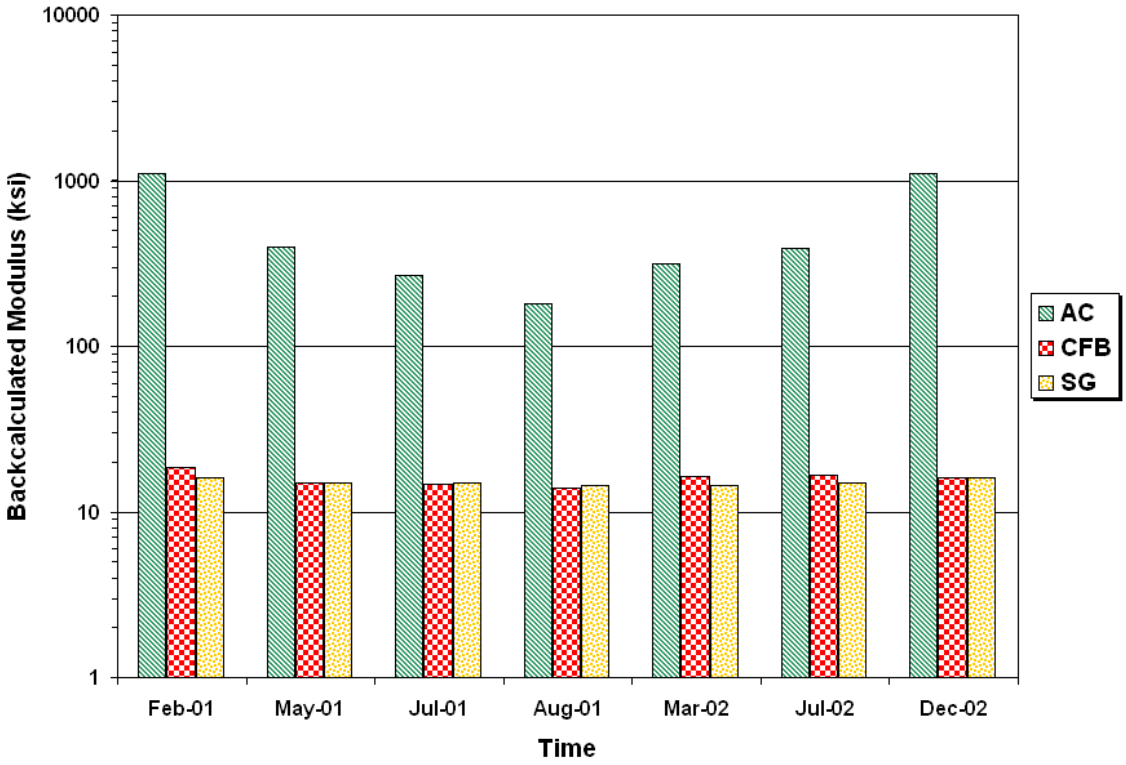

Figure C35. Backcalculated Layer Moduli on FWD Station K6-35.

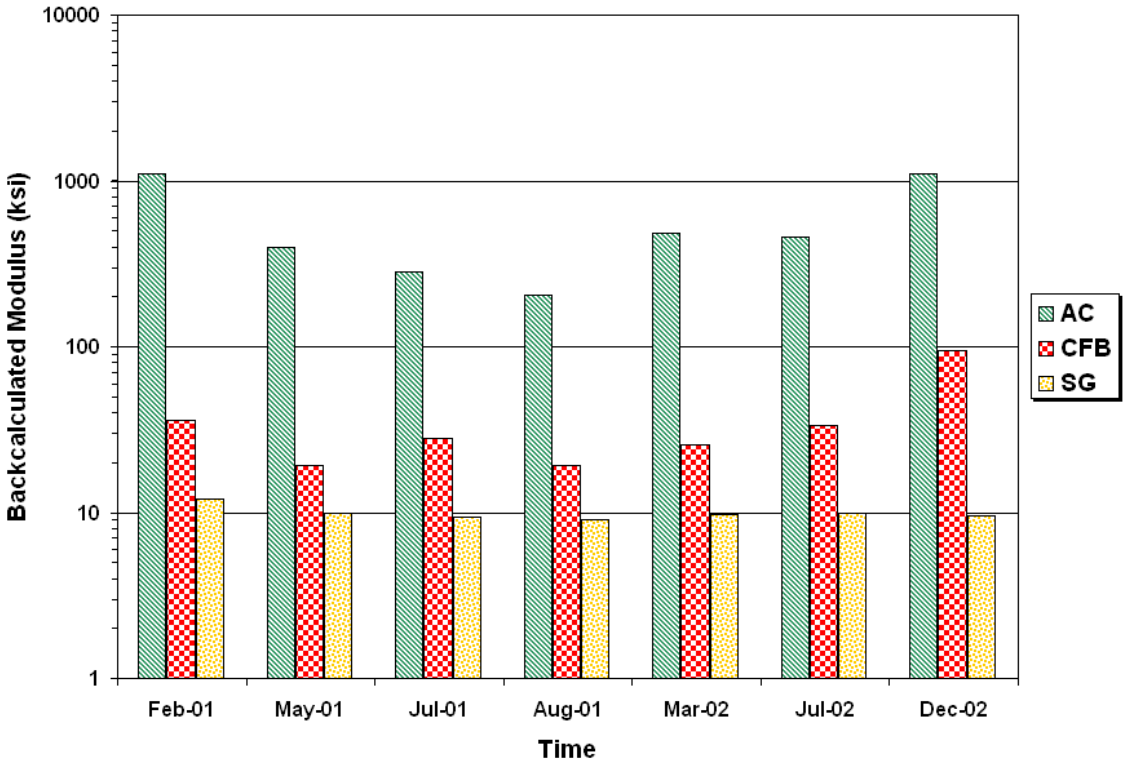

Figure C36. Backcalculated Layer Moduli on FWD Station K6-36.

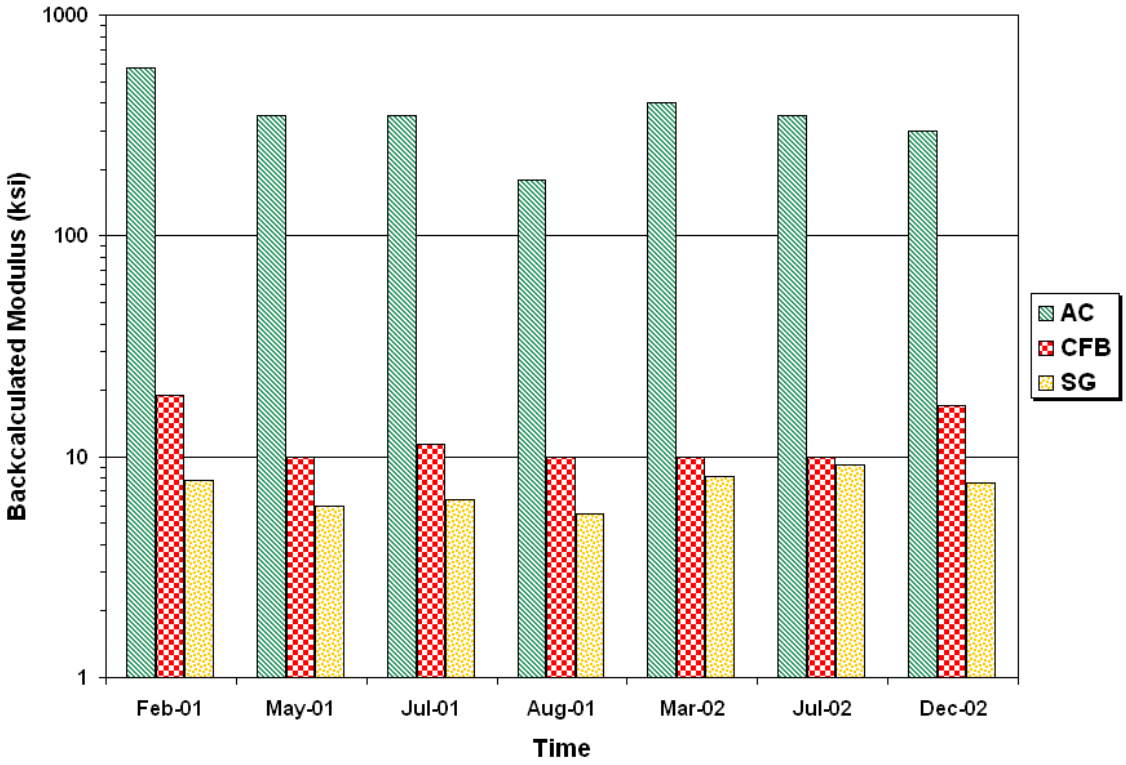

Figure C37. Backcalculated Layer Moduli on FWD Station K6-37.

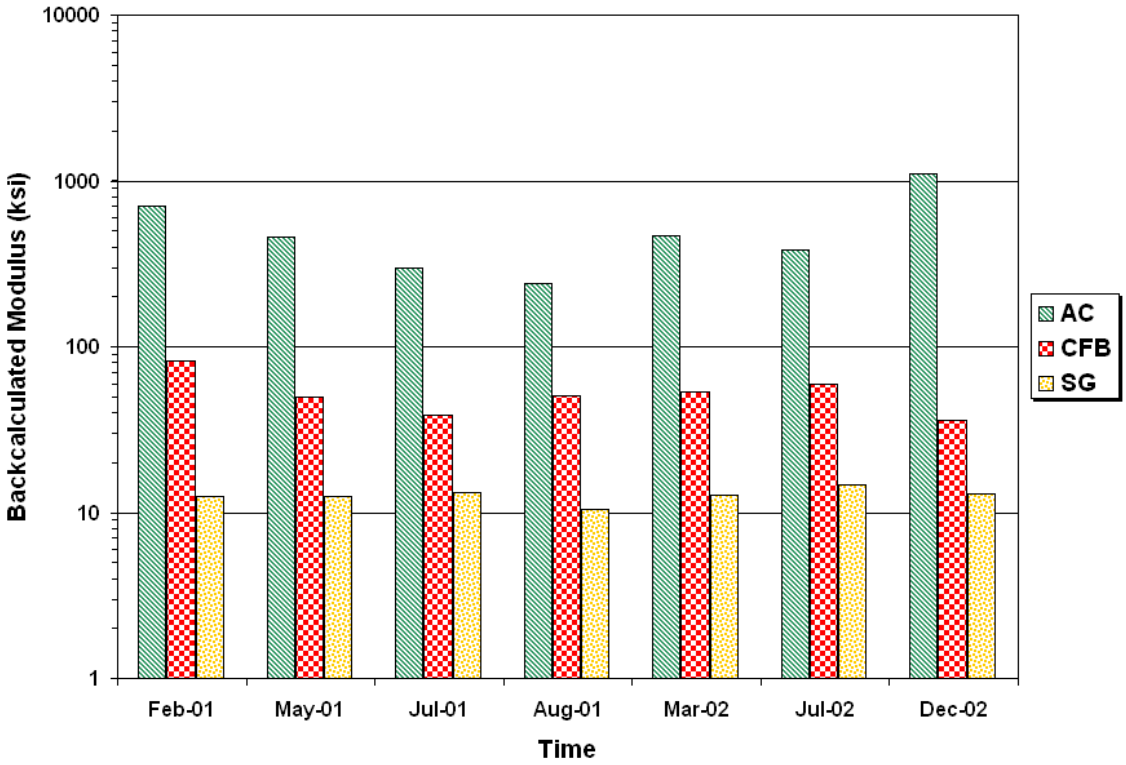

Figure C38. Backcalculated Layer Moduli on FWD Station K6-38.

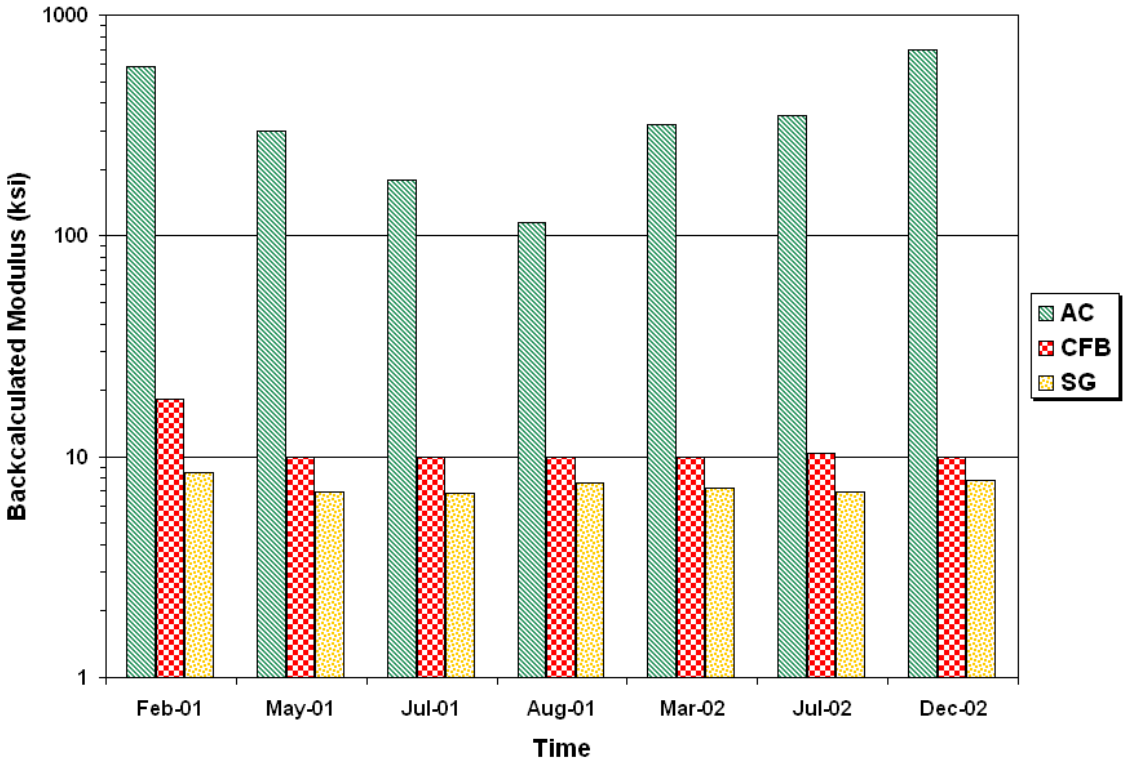

Figure C39. Backcalculated Layer Moduli on FWD Station K6-39.

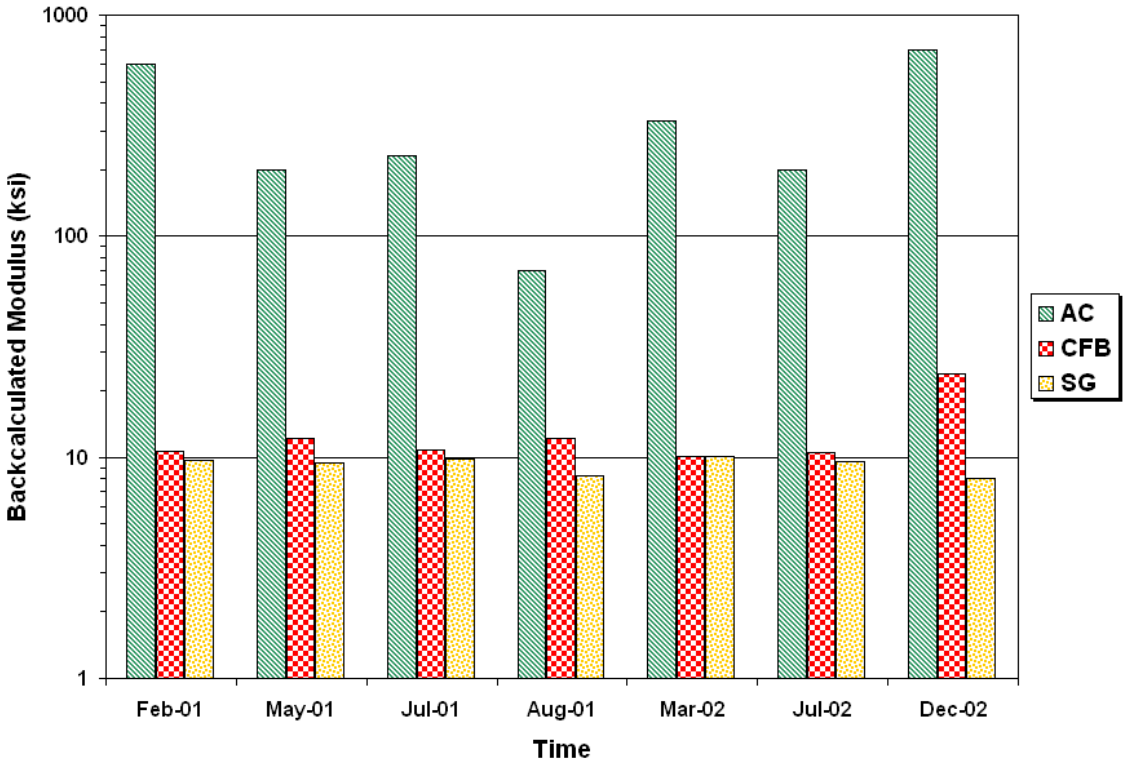

Figure C40. Backcalculated Layer Moduli on FWD Station K6-40.

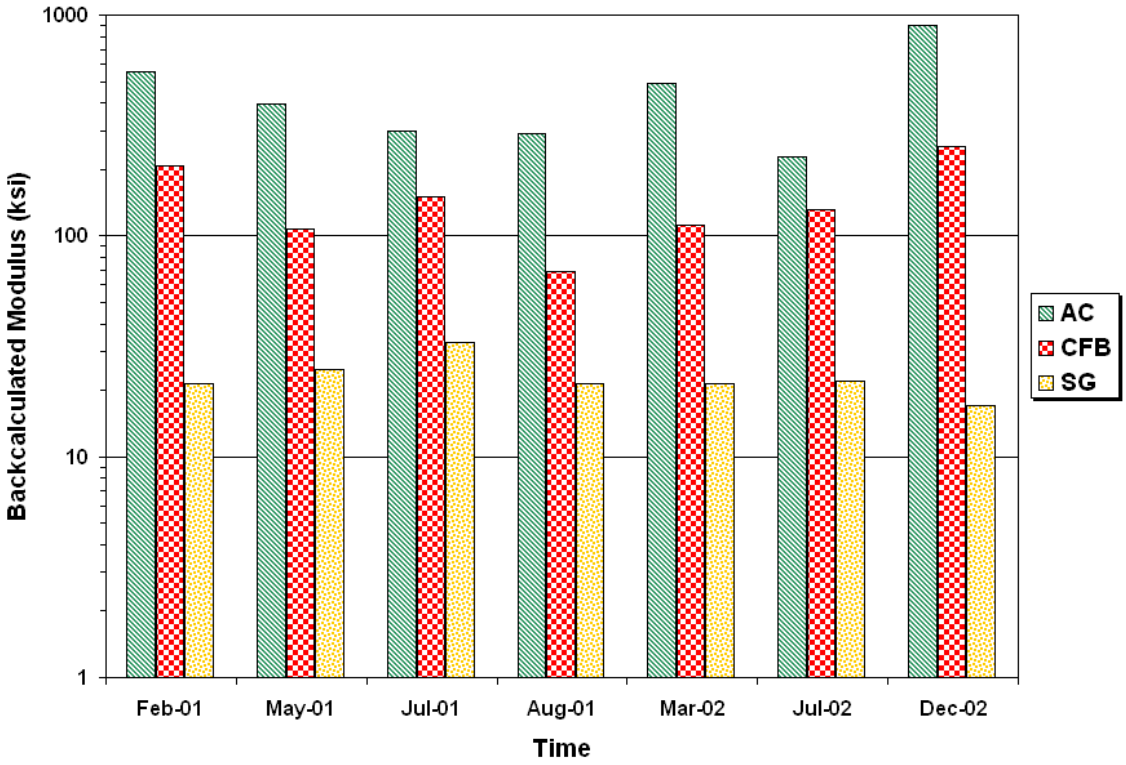

Figure C41. Backcalculated Layer Moduli on FWD Station K6-41.

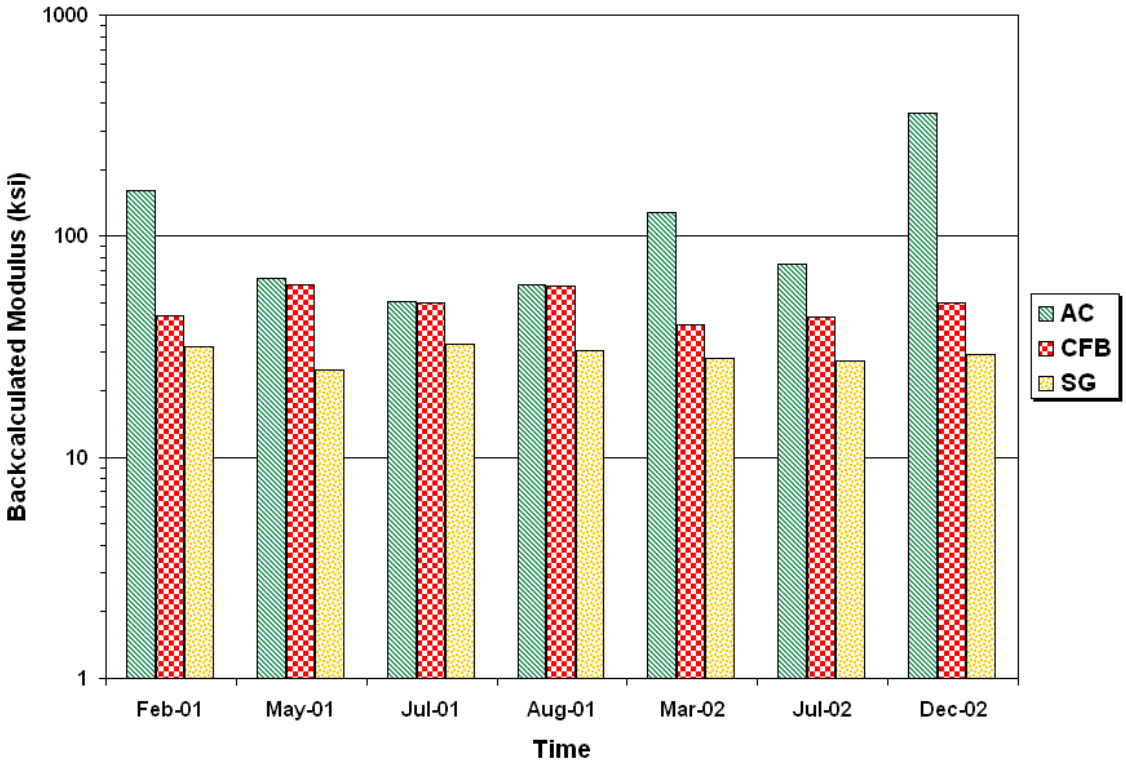

Figure C42. Backcalculated Layer Moduli on FWD Station K6-42.

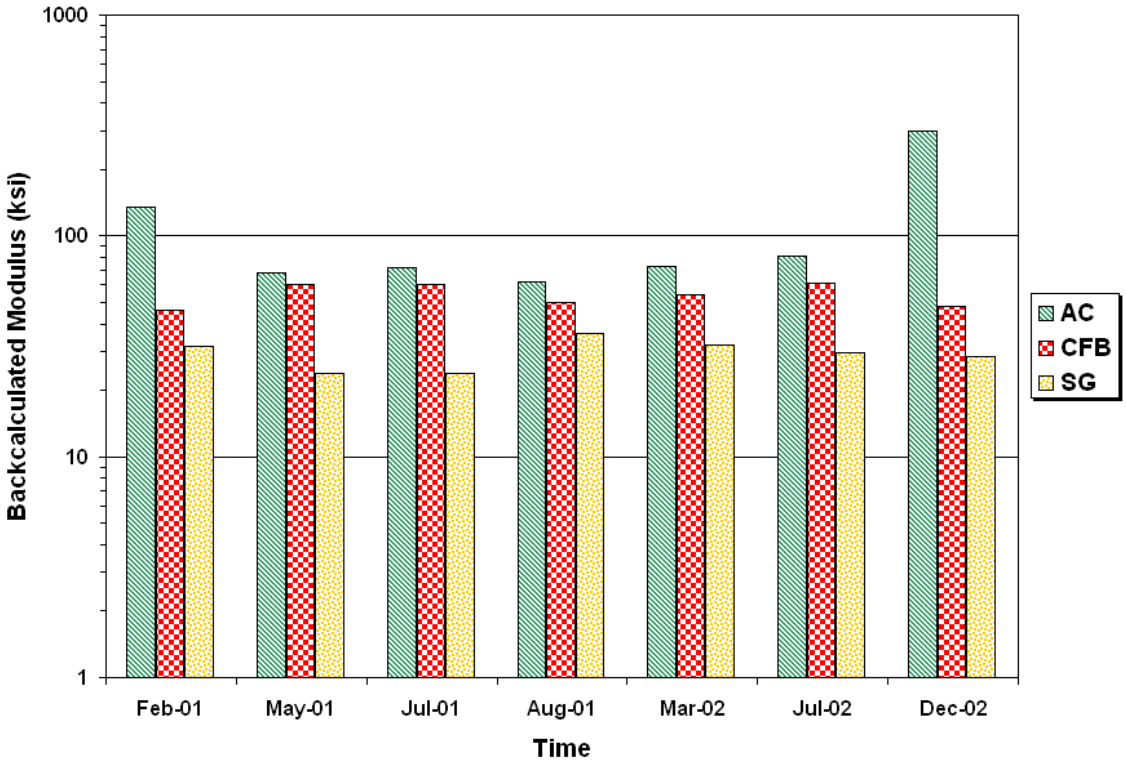

Figure C43. Backcalculated Layer Moduli on FWD Station K6-43.

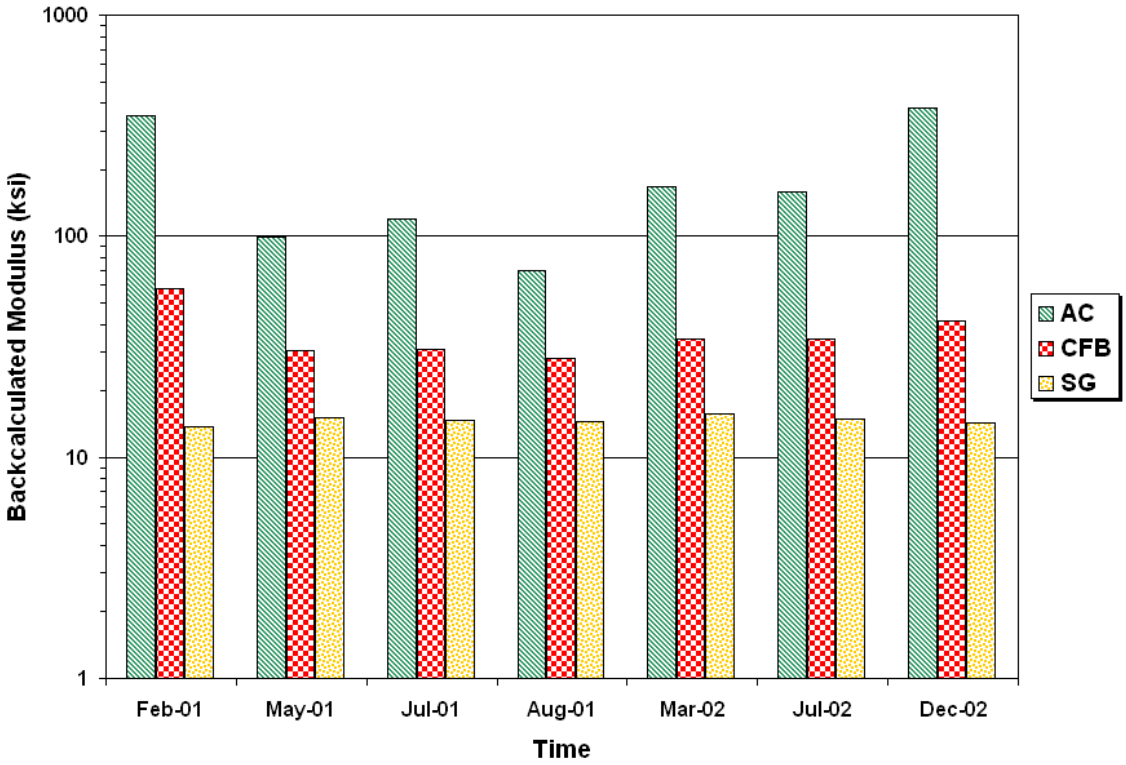

Figure C44. Backcalculated Layer Moduli on FWD Station K6-44.

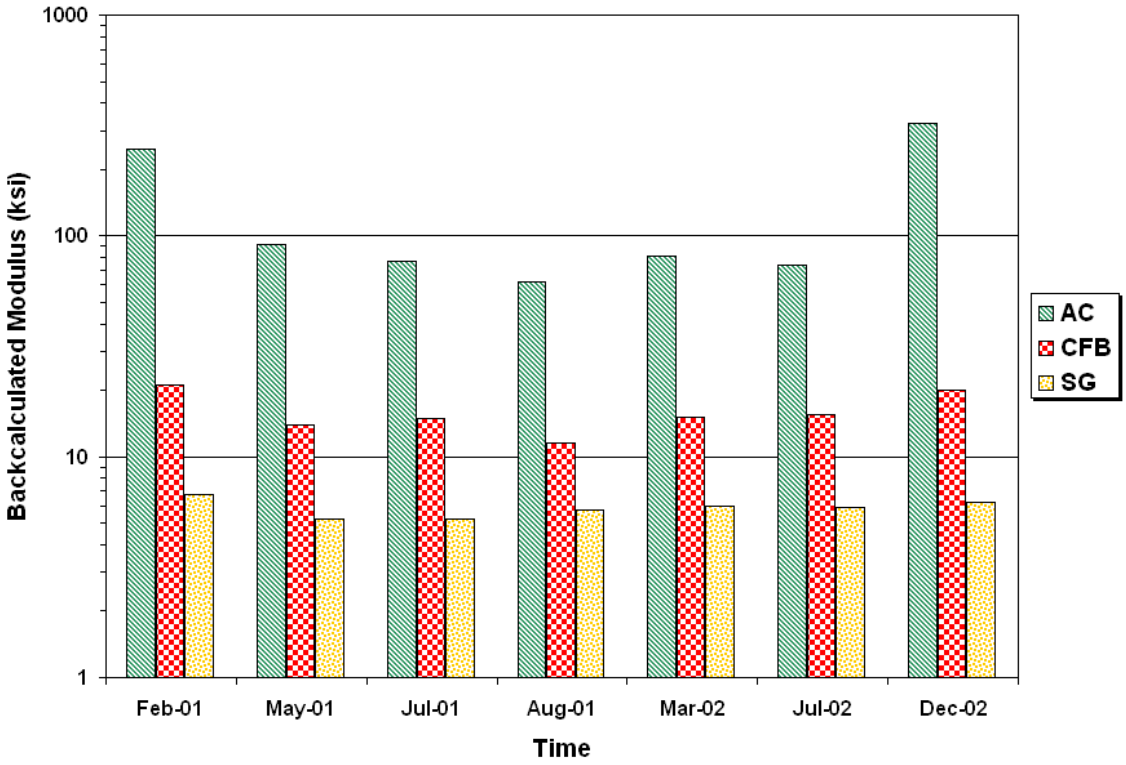

Figure C45. Backcalculated Layer Moduli on FWD Station K6-45.

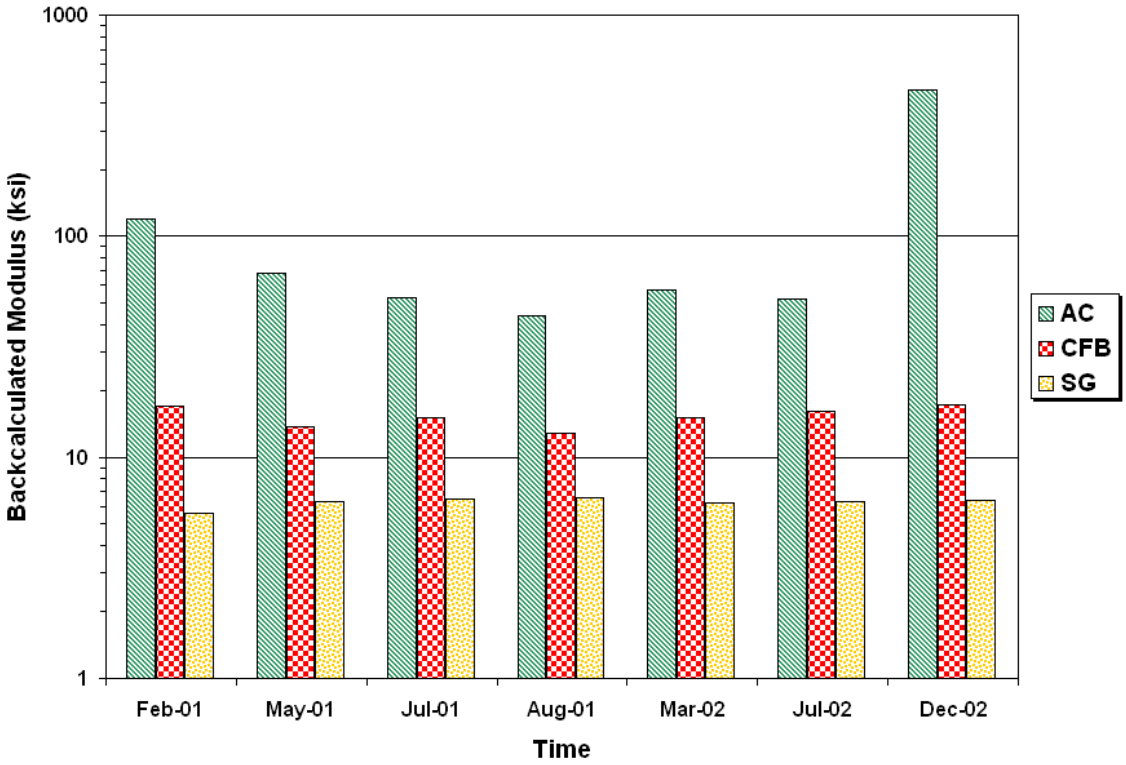

Figure C46. Backcalculated Layer Moduli on FWD Station K6-46.

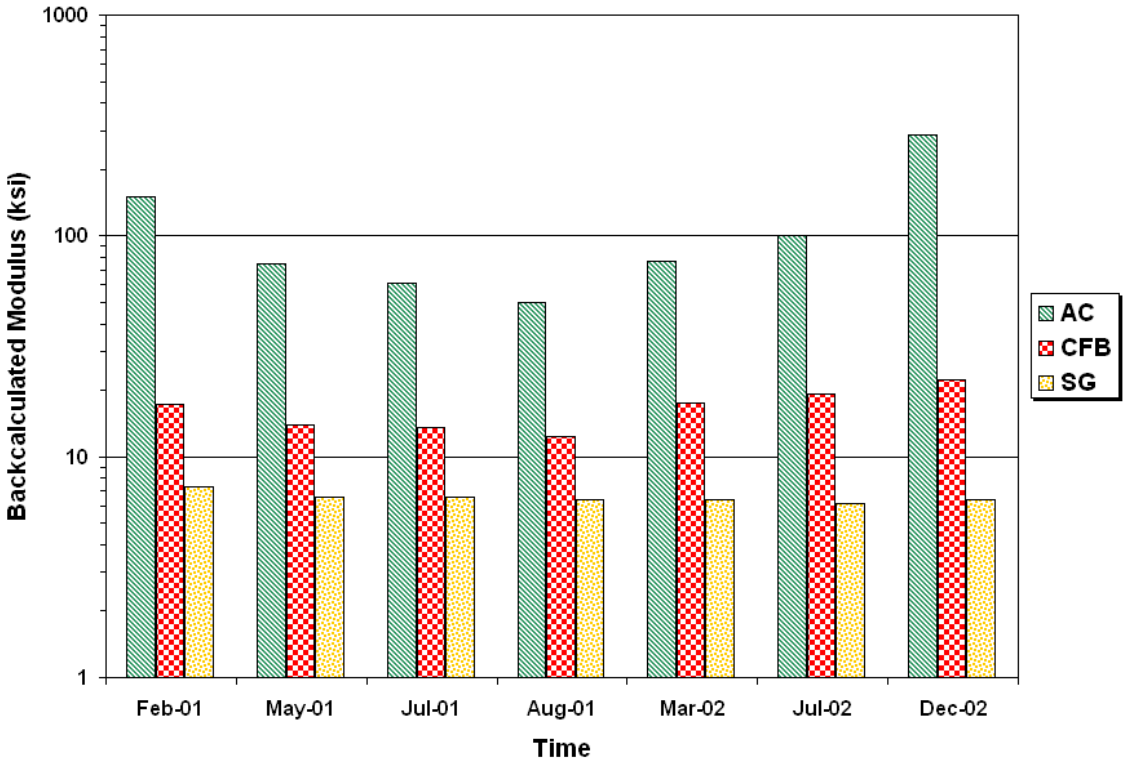

Figure C47. Backcalculated Layer Moduli on FWD Station K6-47.

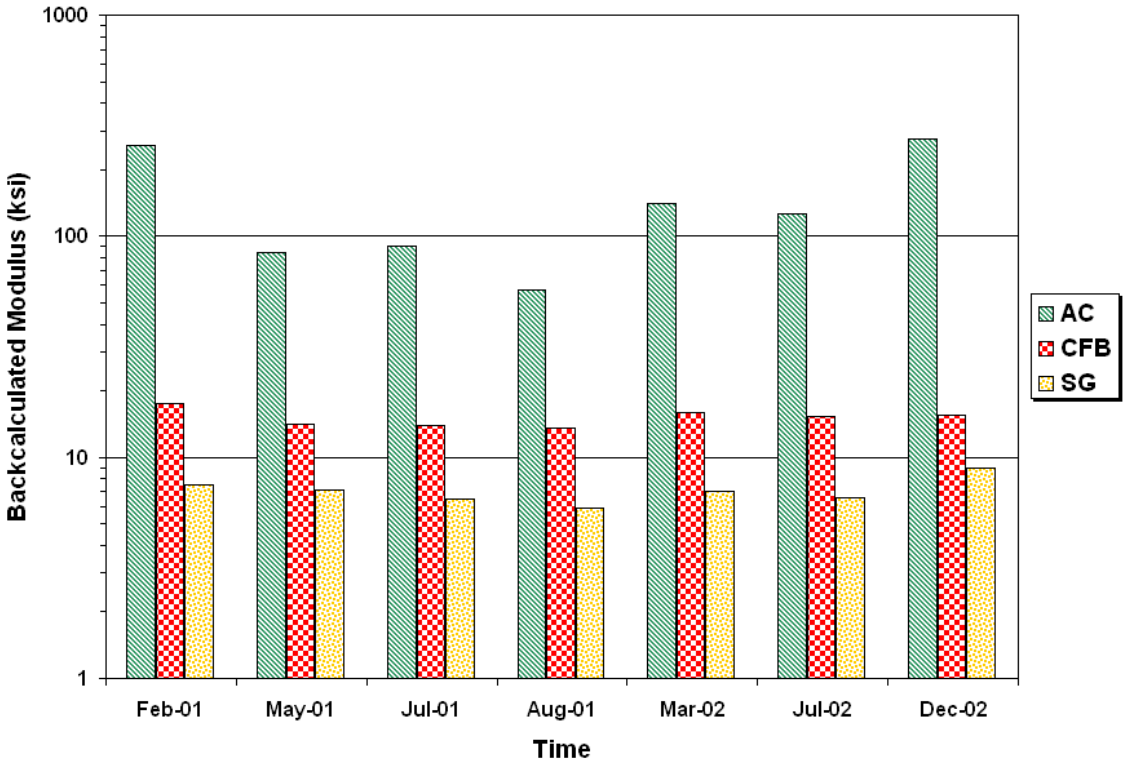

Figure C48. Backcalculated Layer Moduli on FWD Station K6-48.

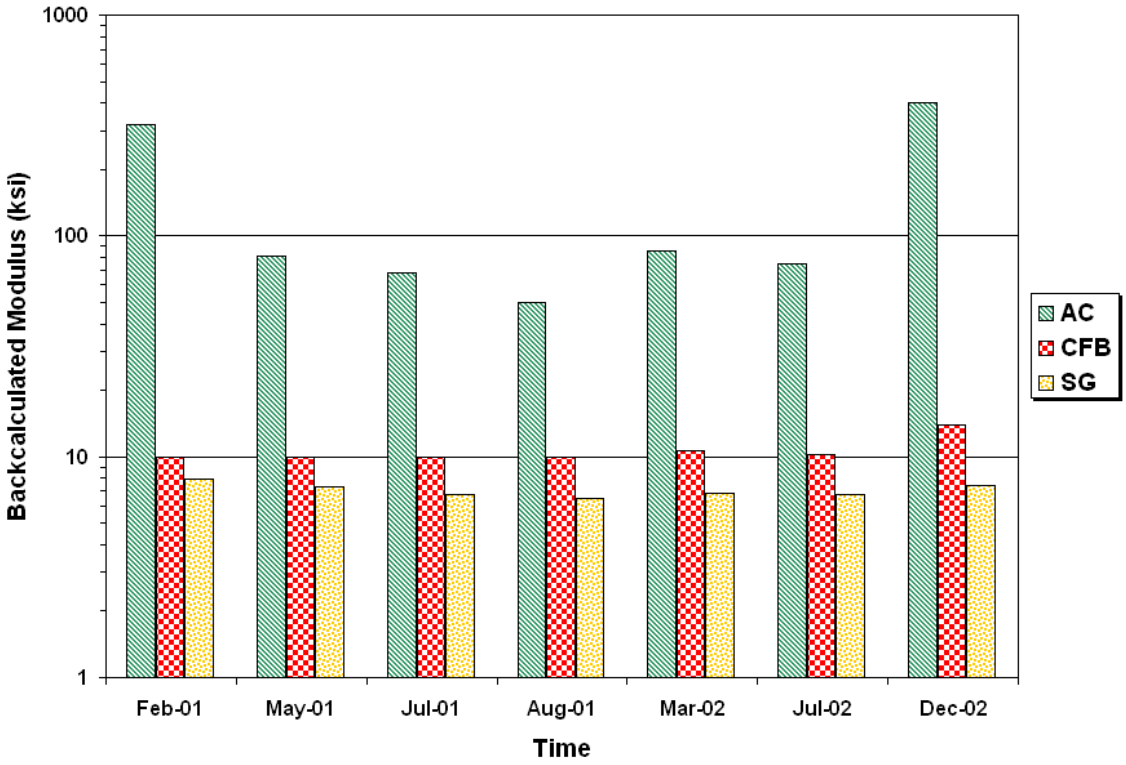

Figure C49. Backcalculated Layer Moduli on FWD Station K6-49.

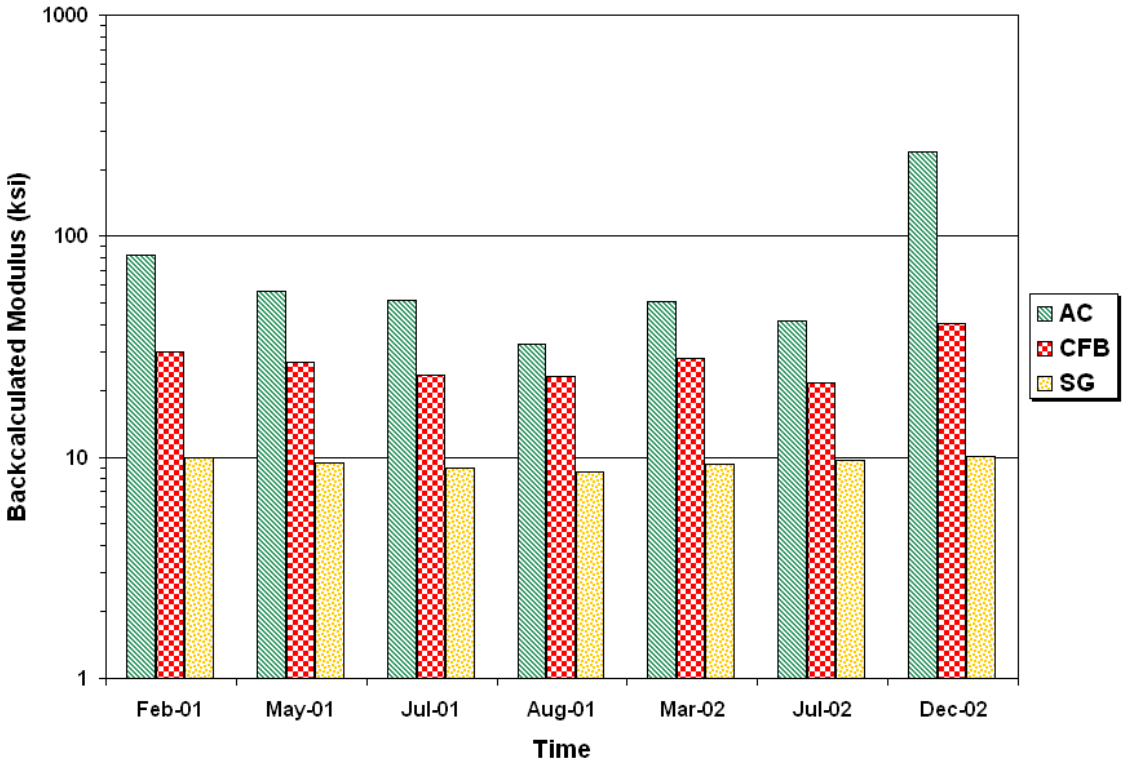

Figure C50. Backcalculated Layer Moduli on FWD Station K6-50.

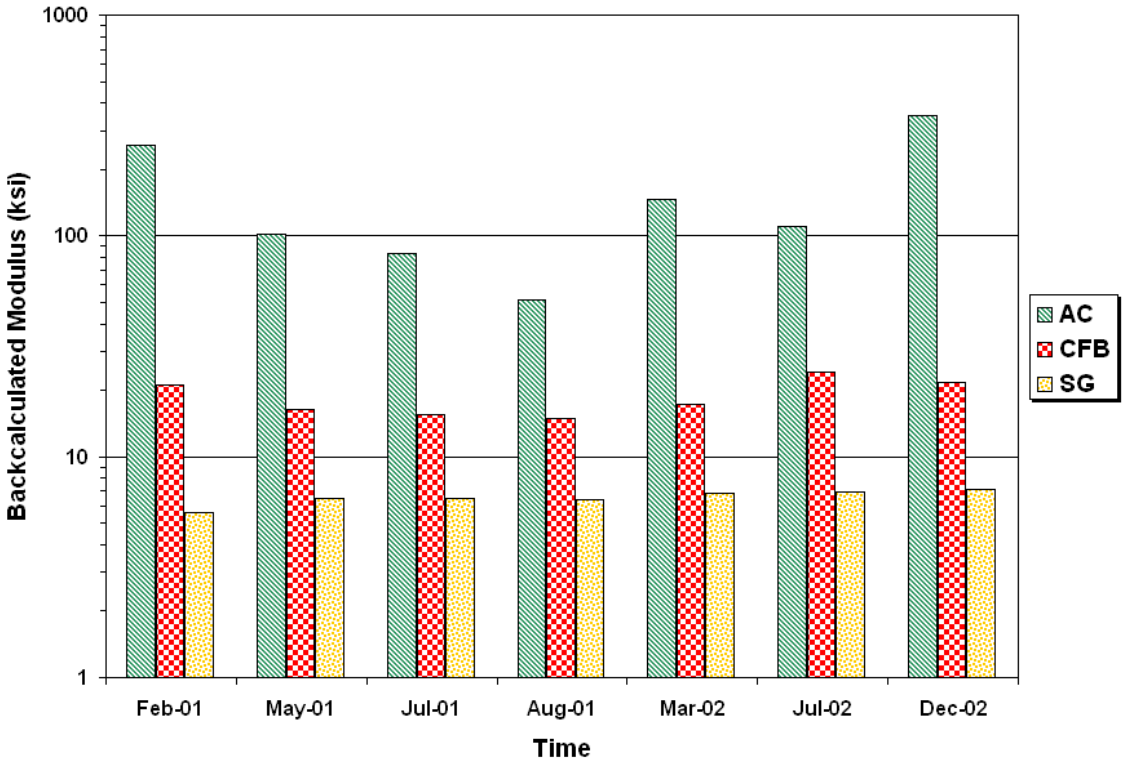

Figure C51. Backcalculated Layer Moduli on FWD Station K6-51.

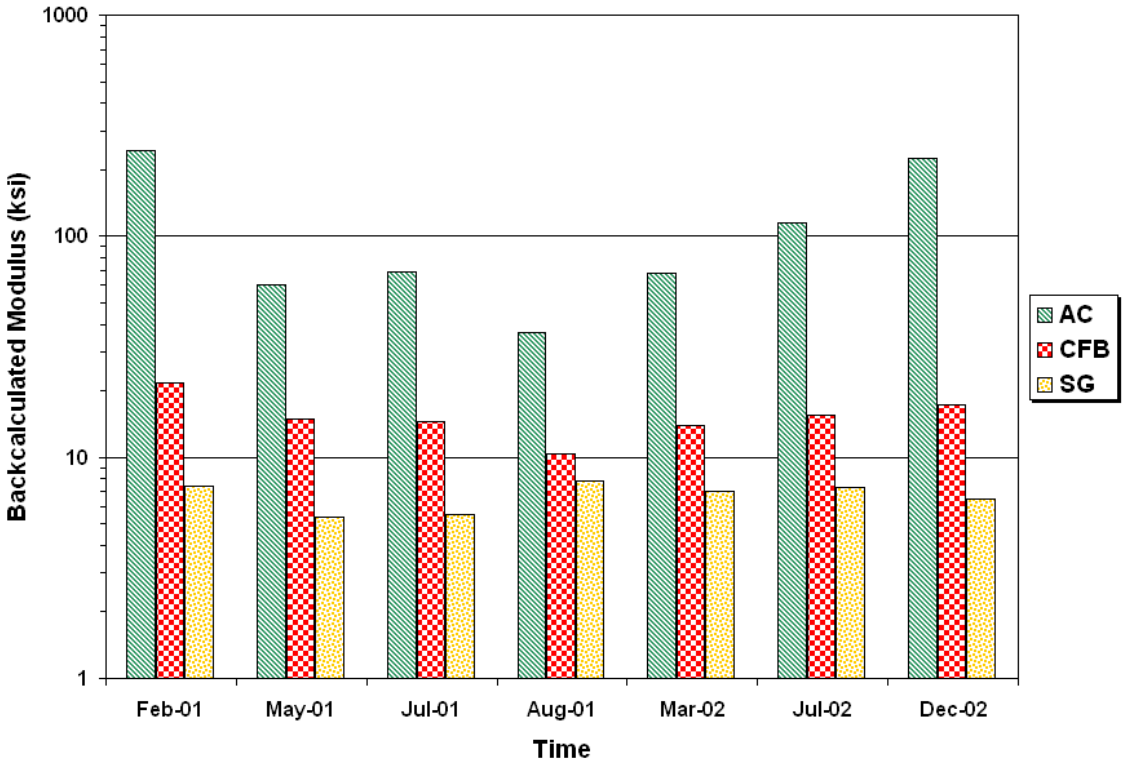

Figure C52. Backcalculated Layer Moduli on FWD Station K6-52.

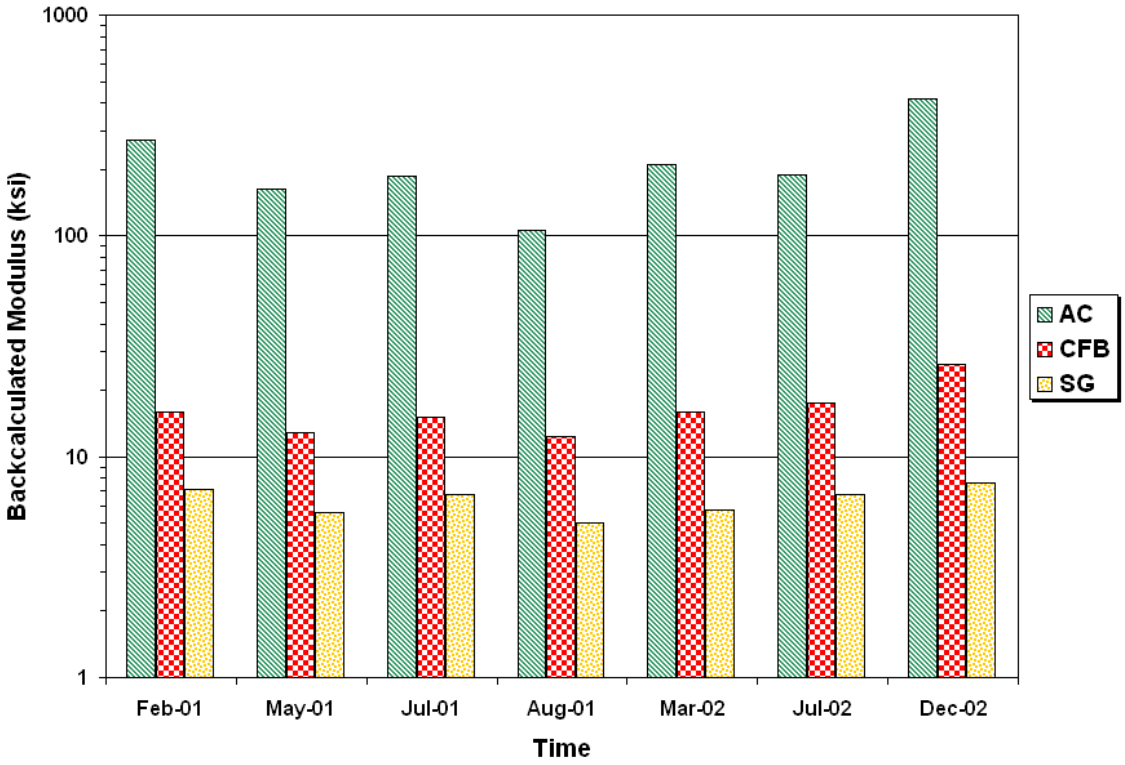

Figure C53. Backcalculated Layer Moduli on FWD Station K6-53.

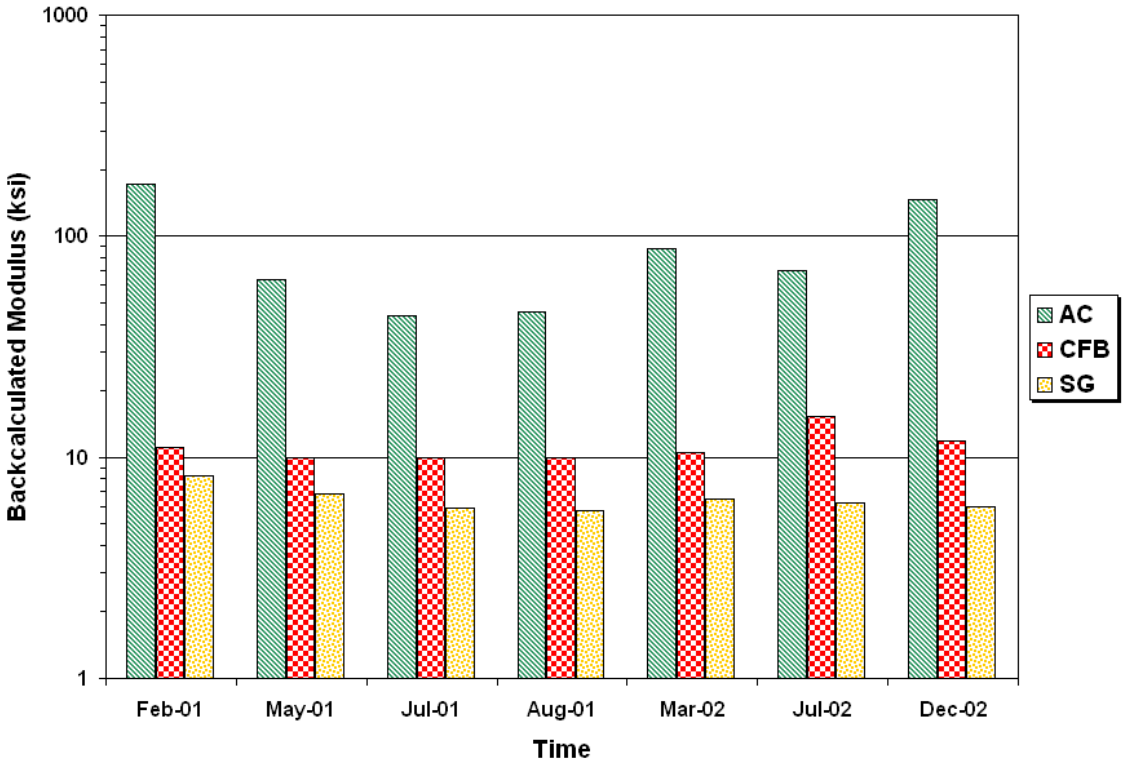

Figure C54. Backcalculated Layer Moduli on FWD Station K6-54.

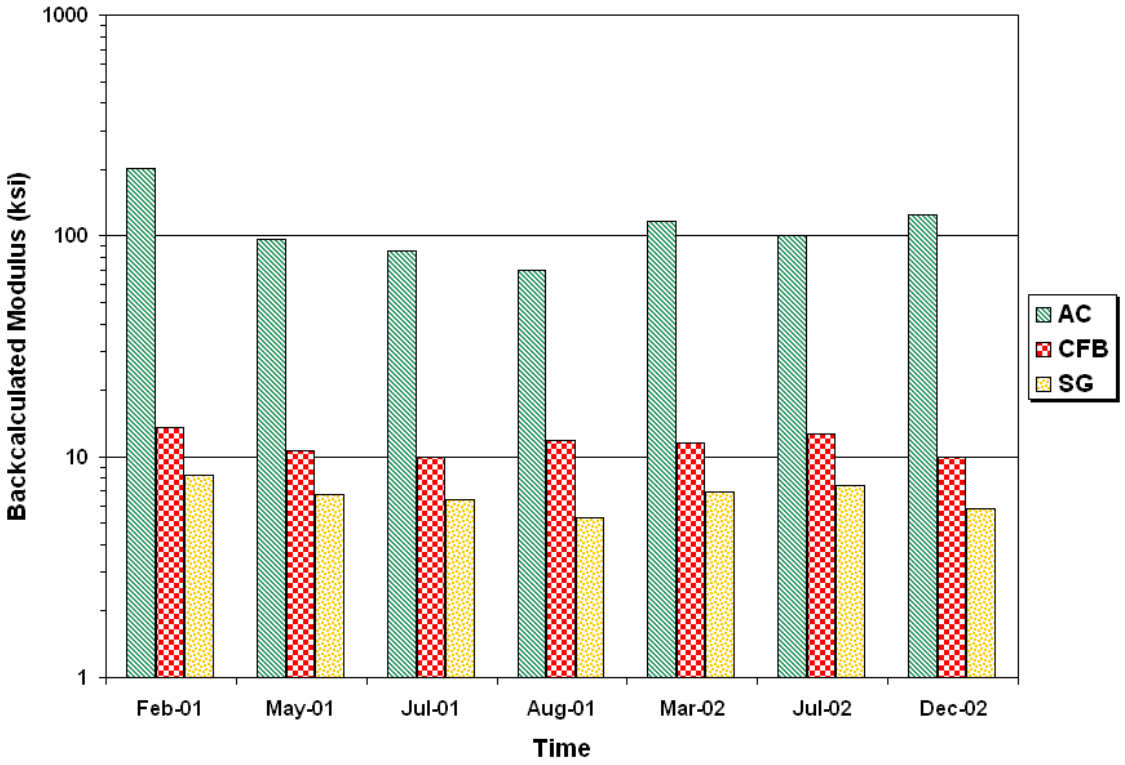

Figure C55. Backcalculated Layer Moduli on FWD Station K6-55.

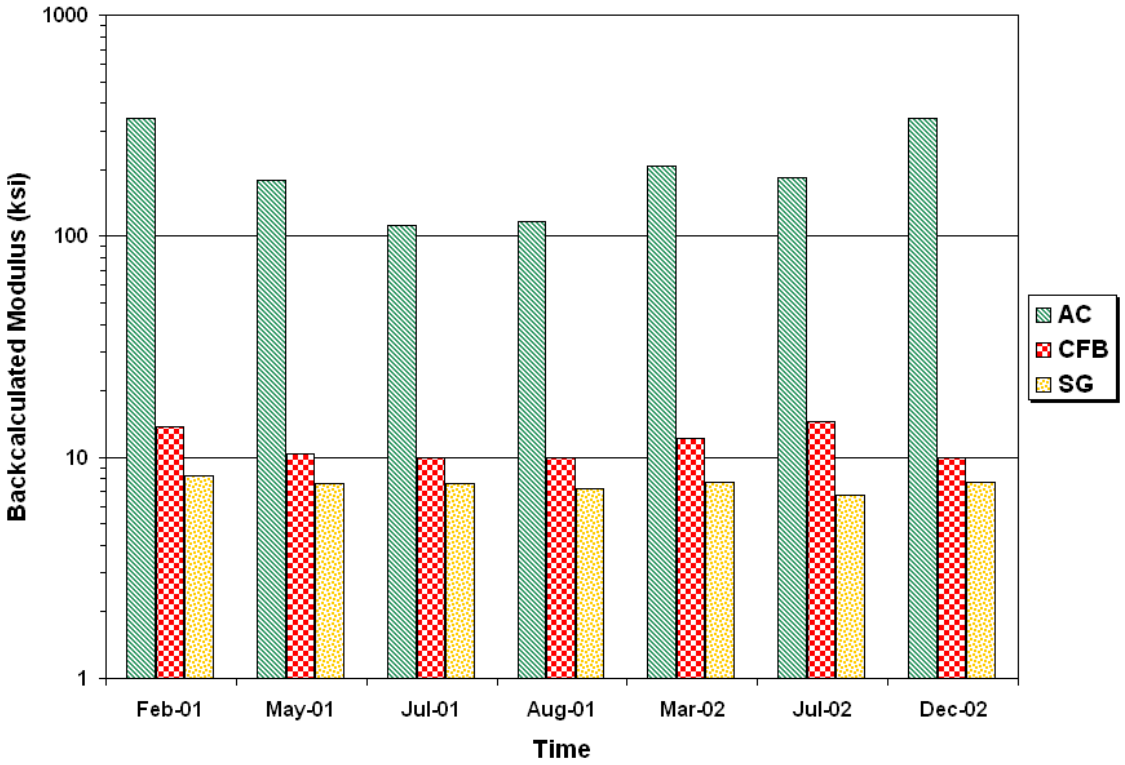

Figure C56. Backcalculated Layer Moduli on FWD Station K6-56.

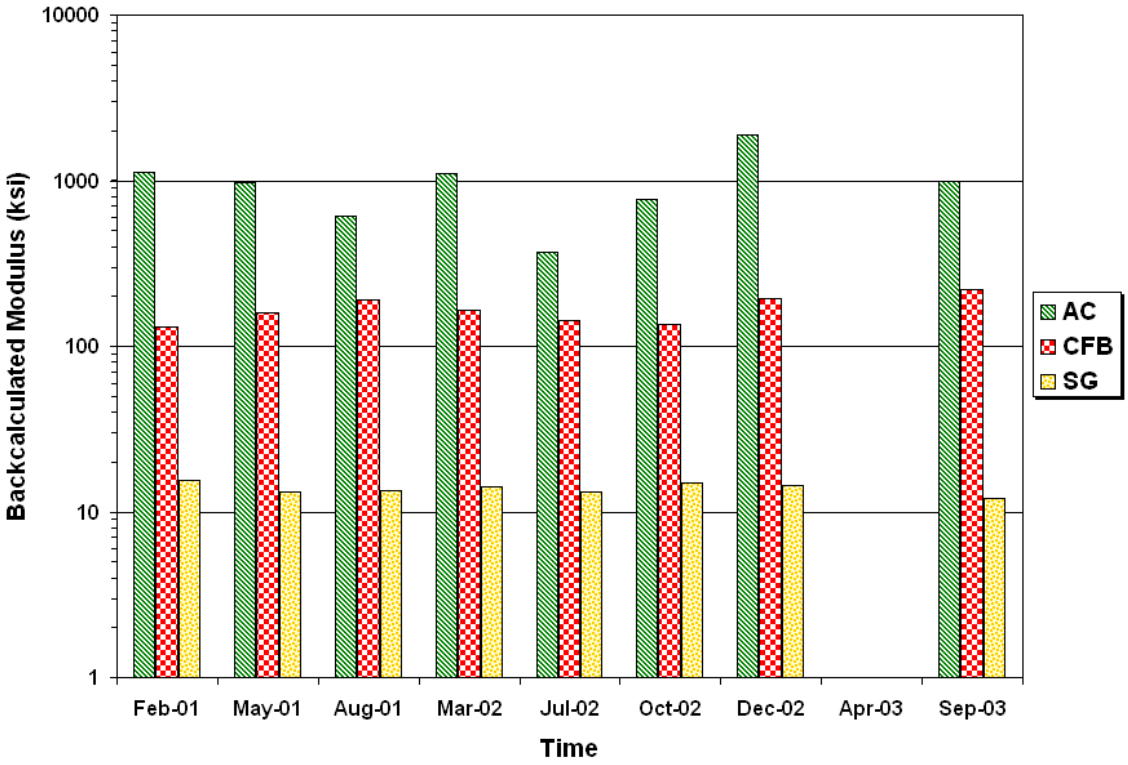

Figure C57. Backcalculated Layer Moduli on FWD Station K7-1.

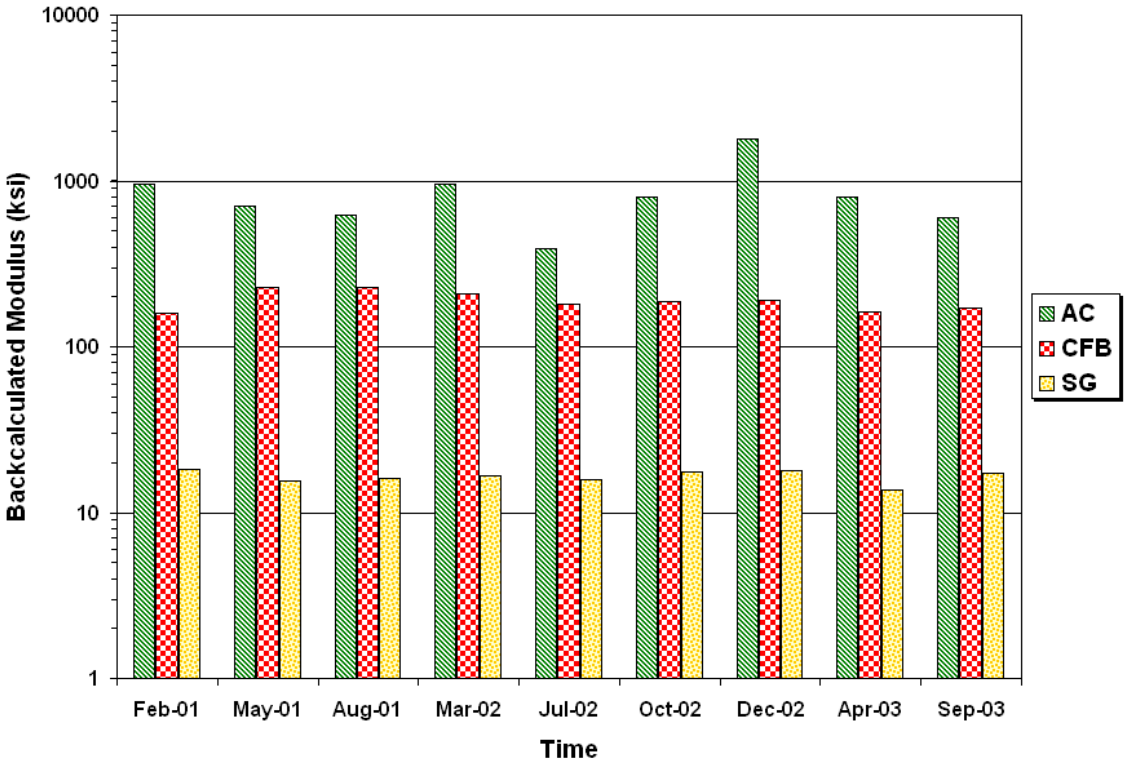

Figure C58. Backcalculated Layer Moduli on FWD Station K7-2.

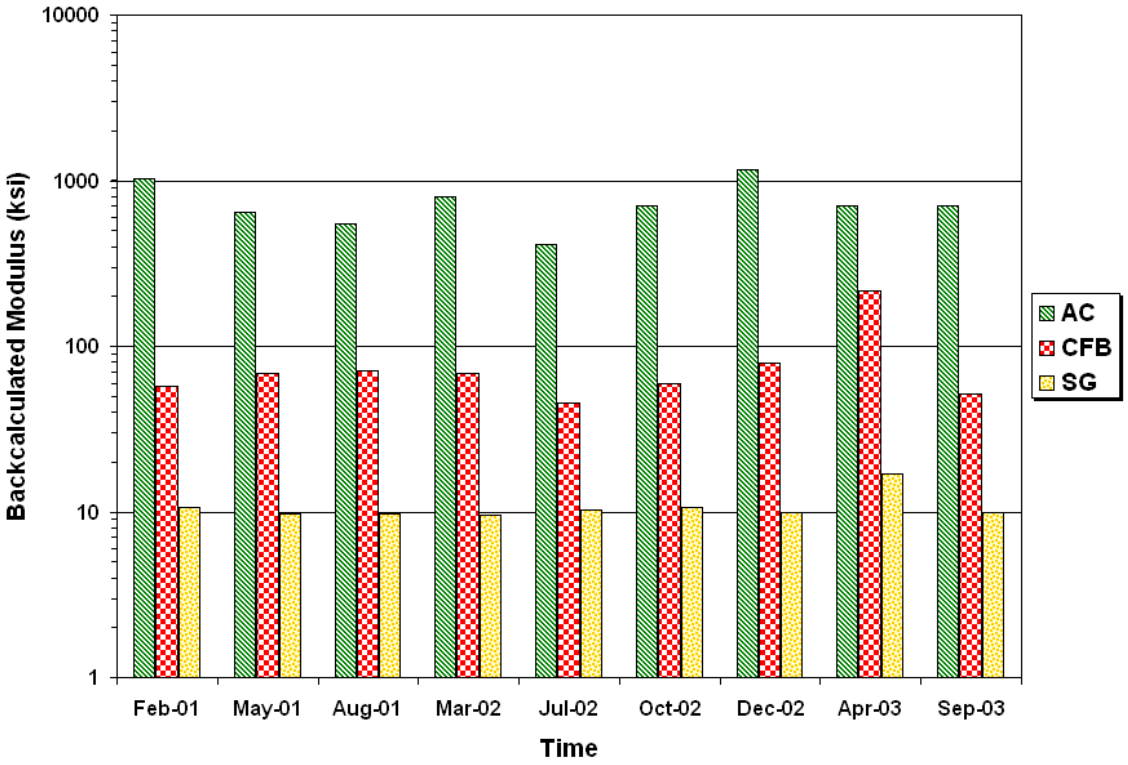

Figure C59. Backcalculated Layer Moduli on FWD Station K7-3.

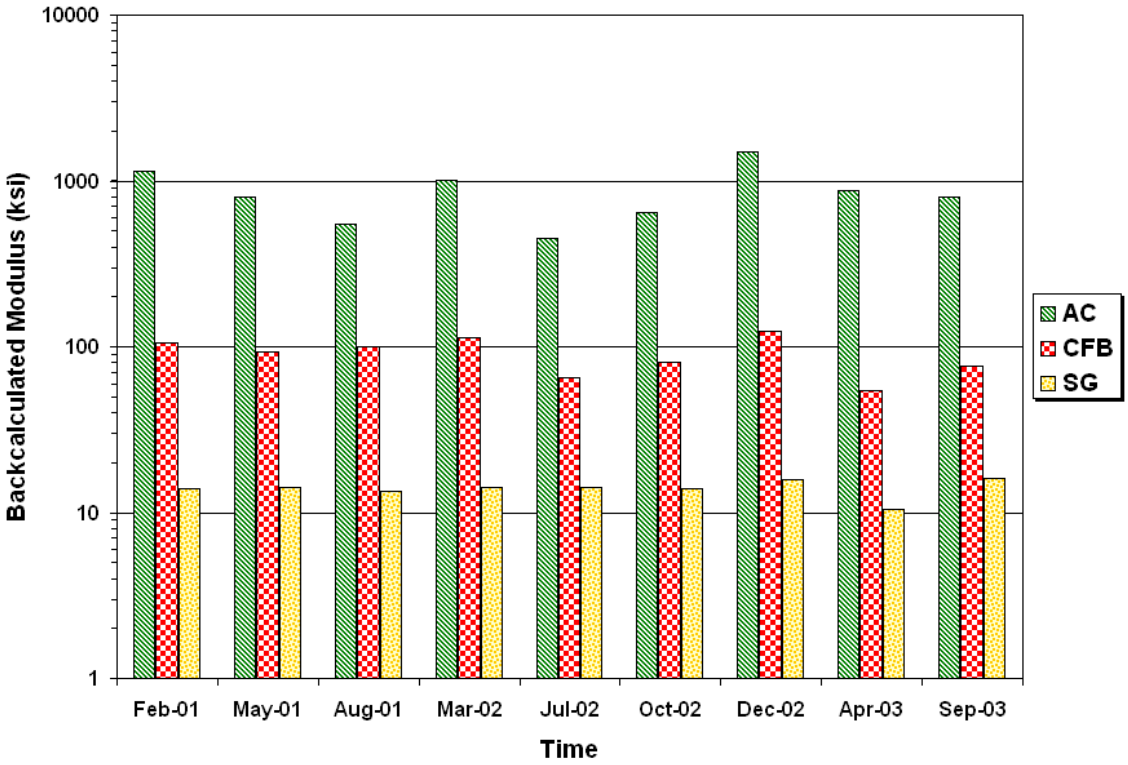

Figure C60. Backcalculated Layer Moduli on FWD Station K7-4.

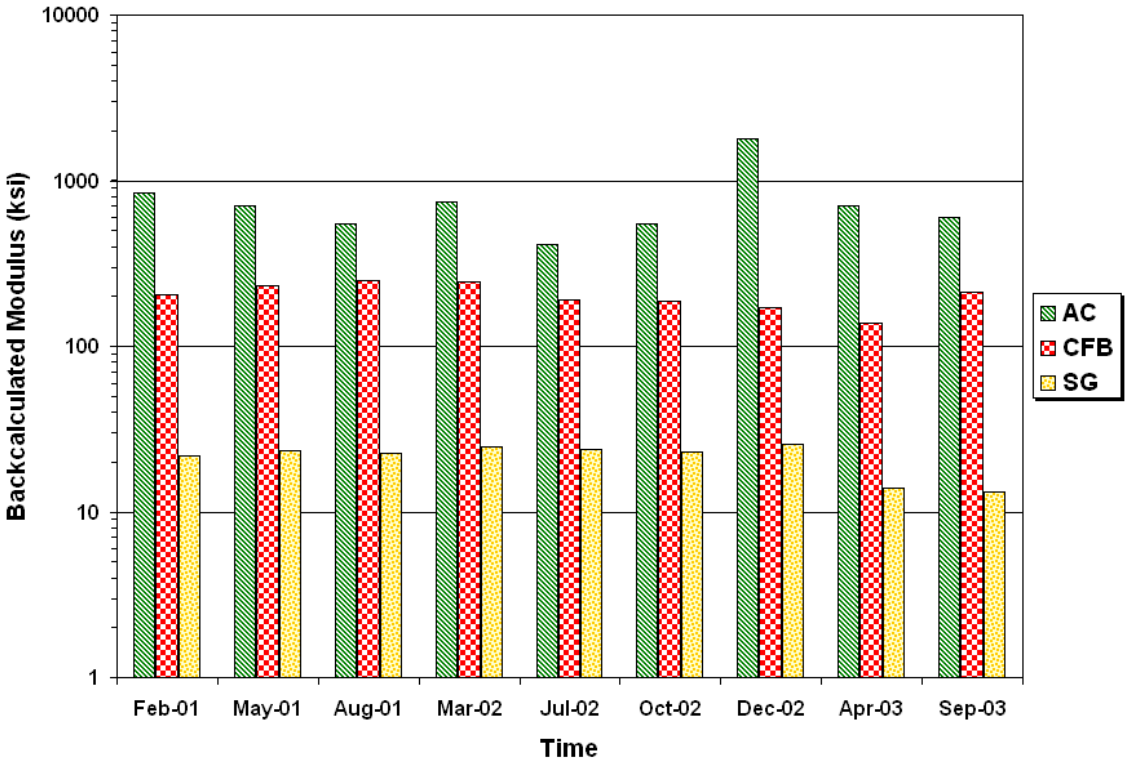

Figure C61. Backcalculated Layer Moduli on FWD Station K7-5.

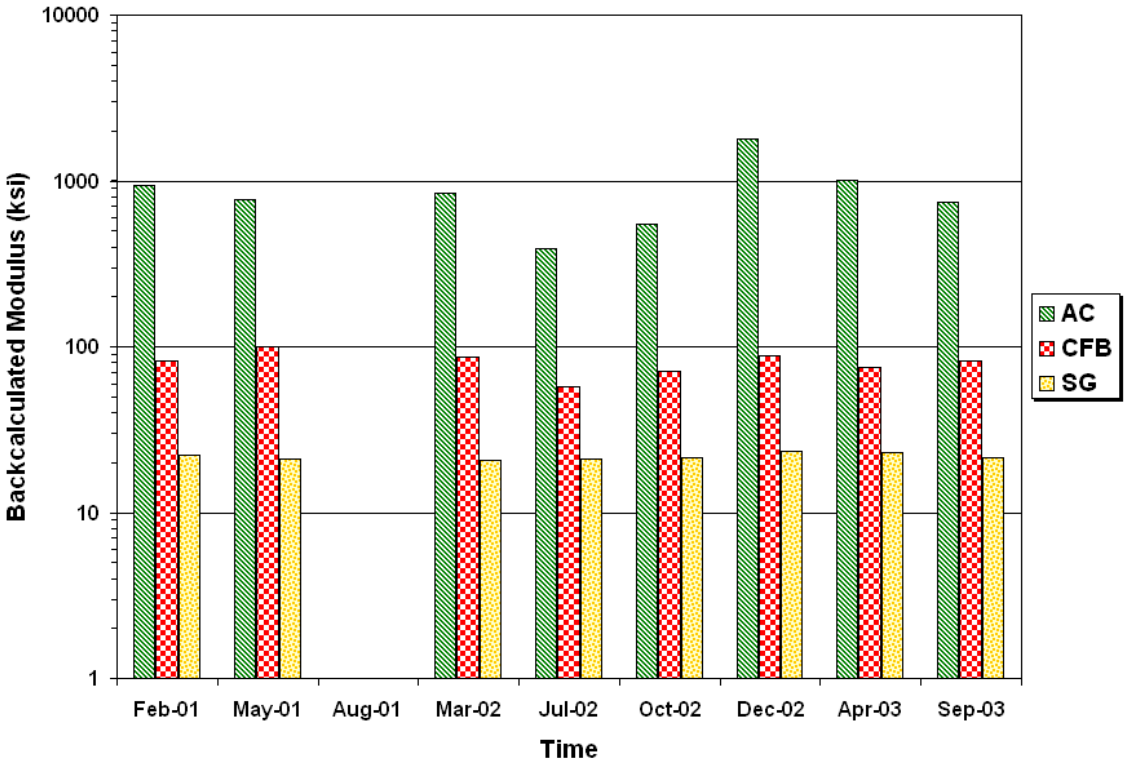

Figure C62. Backcalculated Layer Moduli on FWD Station K7-6.

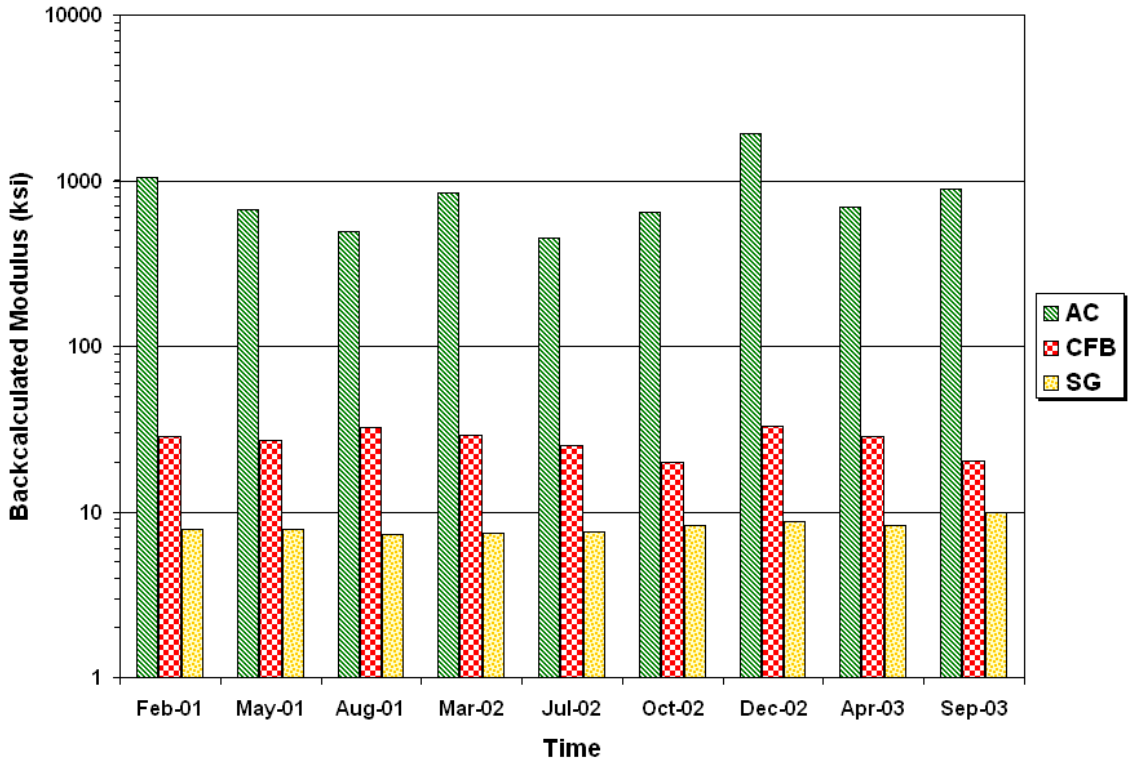

Figure C63. Backcalculated Layer Moduli on FWD Station K7-7.

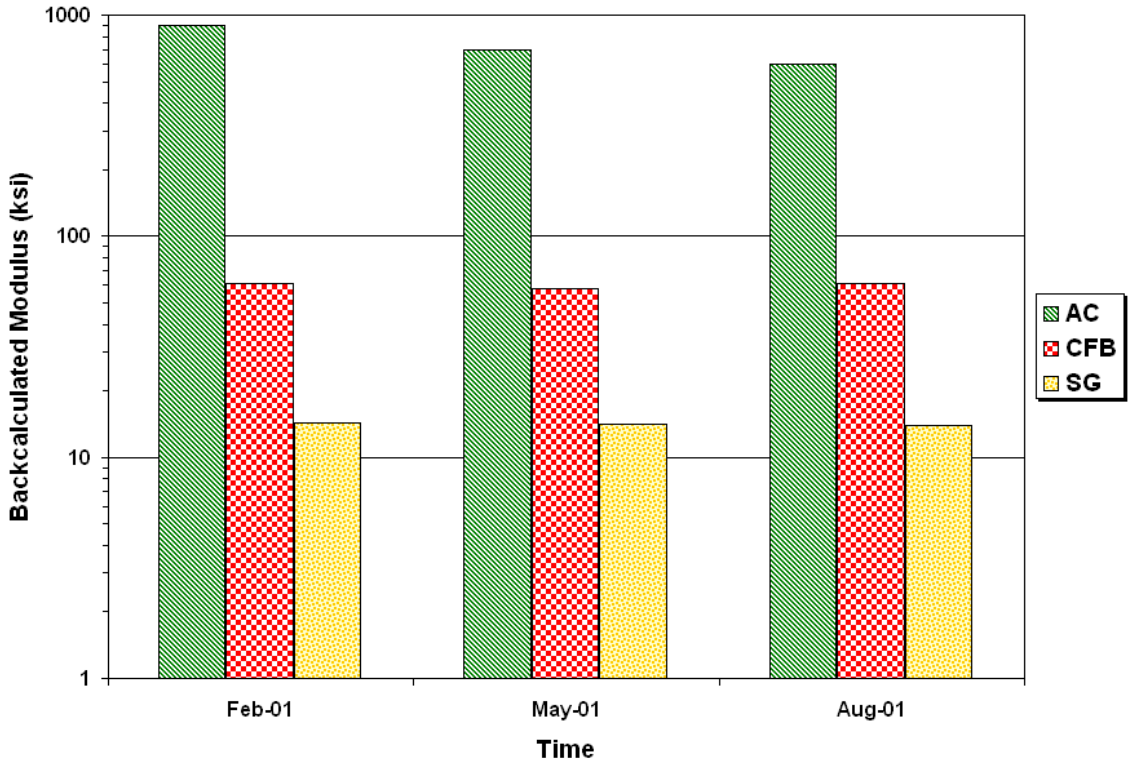

Figure C64. Backcalculated Layer Moduli on FWD Station K7-8.

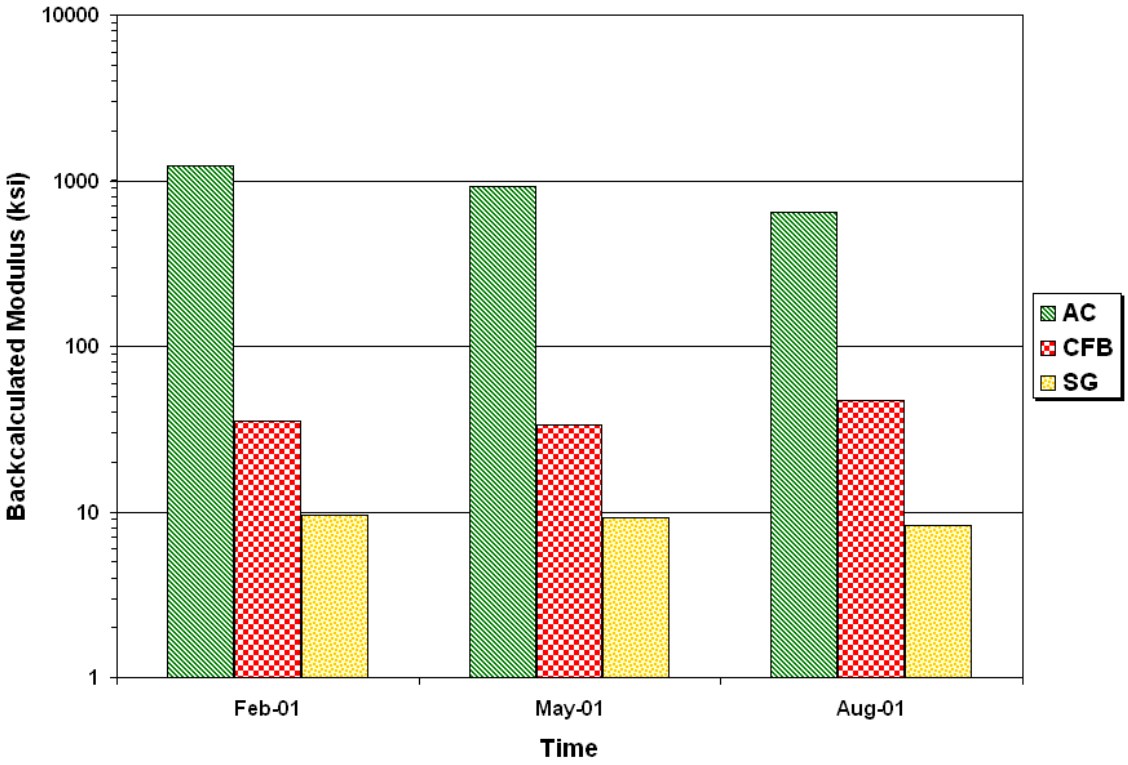

Figure C65. Backcalculated Layer Moduli on FWD Station K7-9.

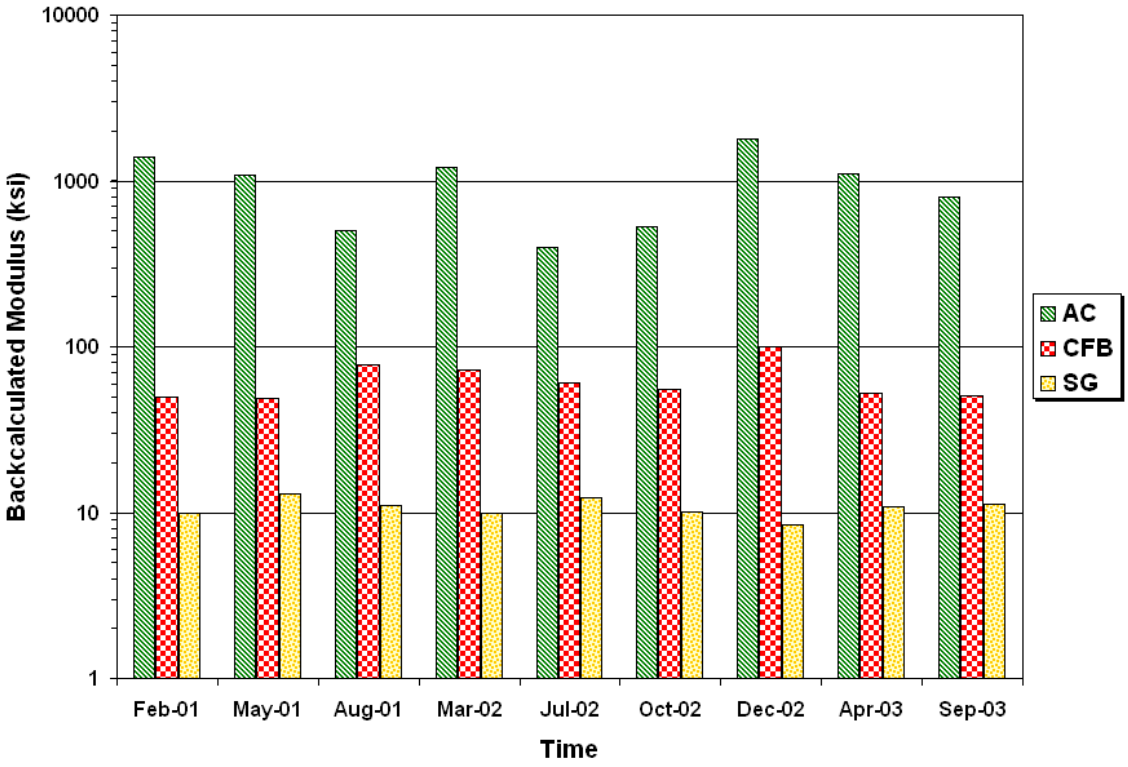

Figure C66. Backcalculated Layer Moduli on FWD Station K7-10.

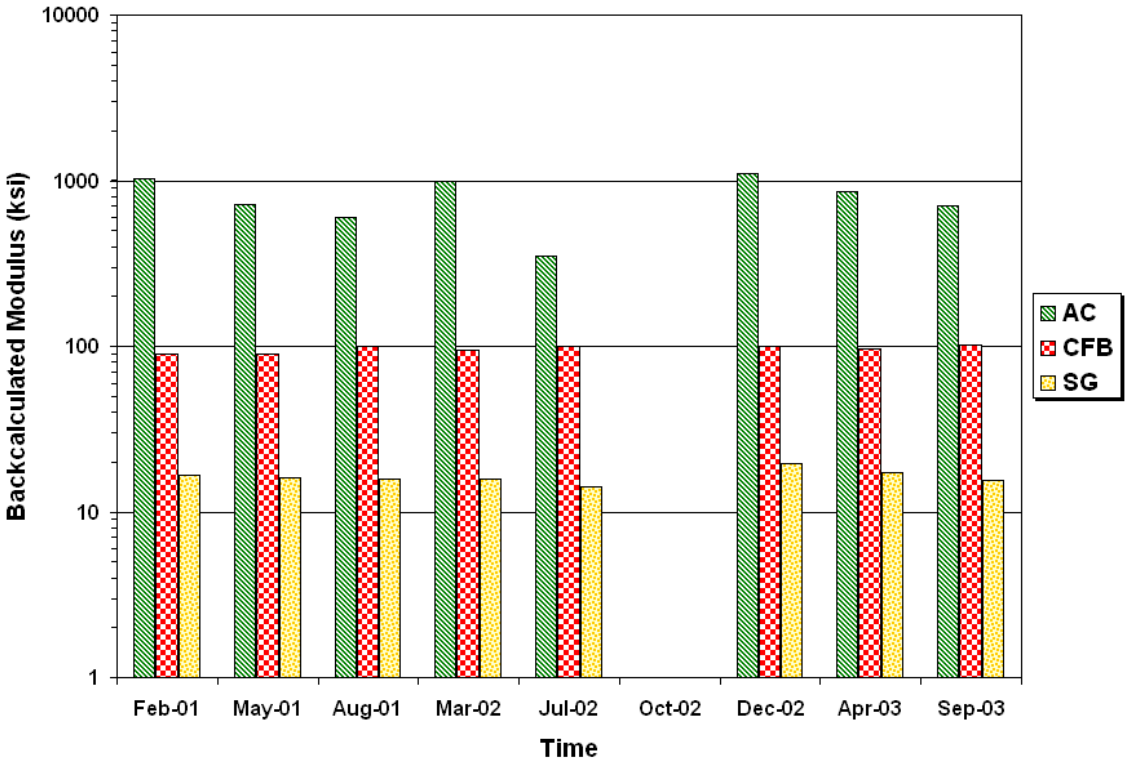

Figure C67. Backcalculated Layer Moduli on FWD Station K7-11.

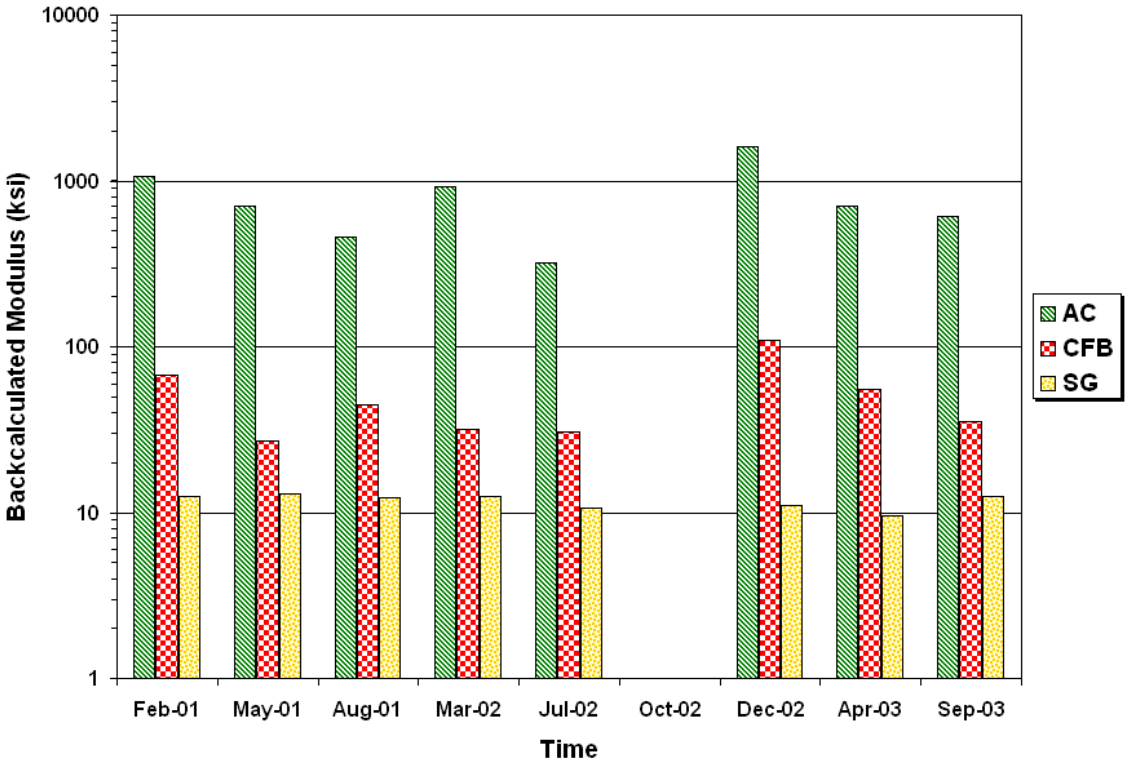

Figure C68. Backcalculated Layer Moduli on FWD Station K7-12.

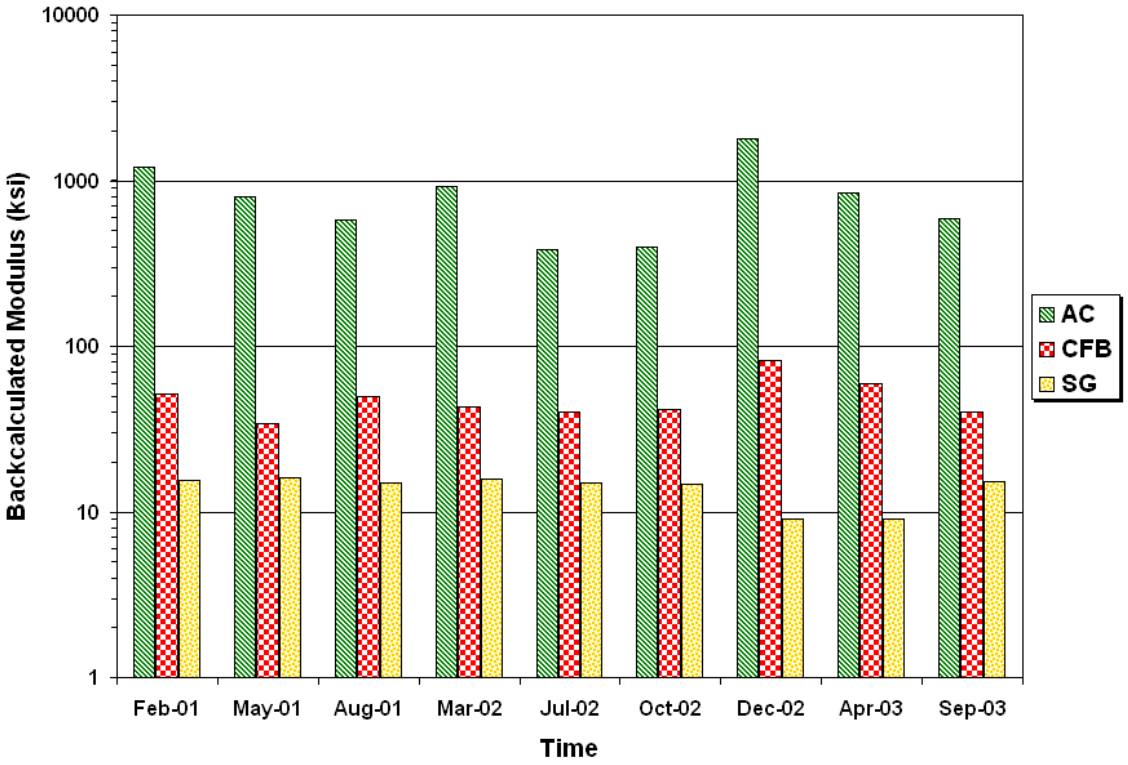

Figure C69. Backcalculated Layer Moduli on FWD Station K7-13.

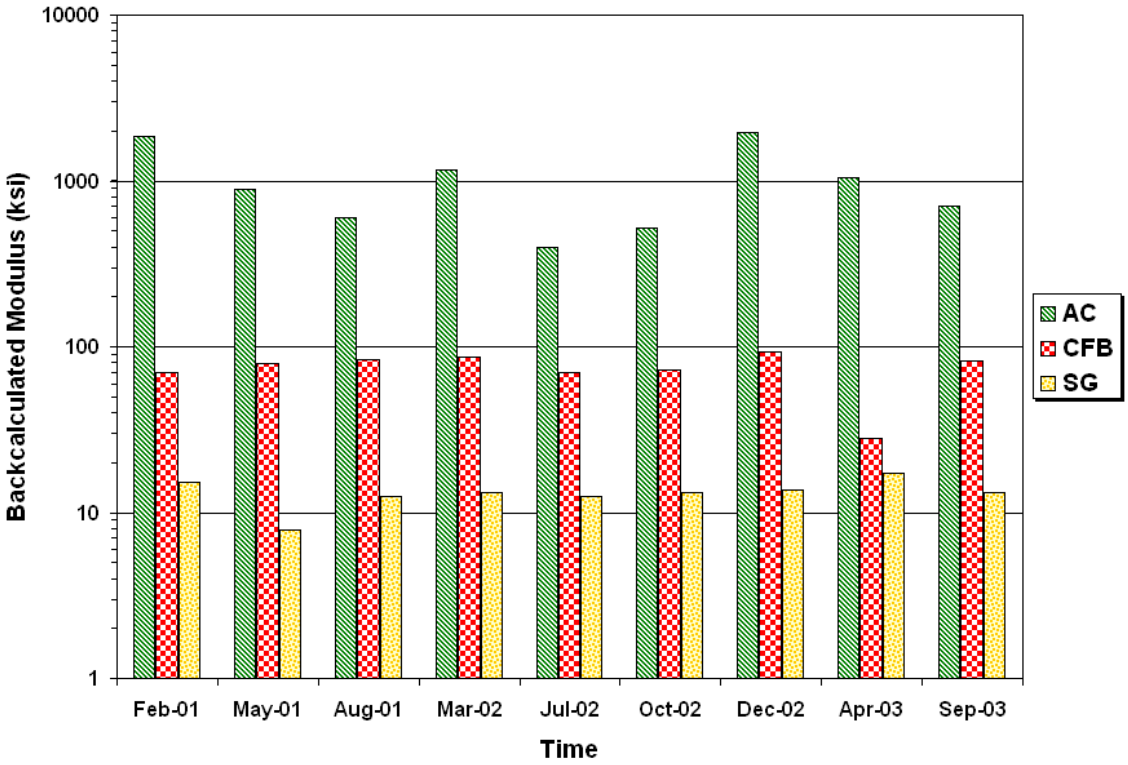

Figure C70. Backcalculated Layer Moduli on FWD Station K7-14.

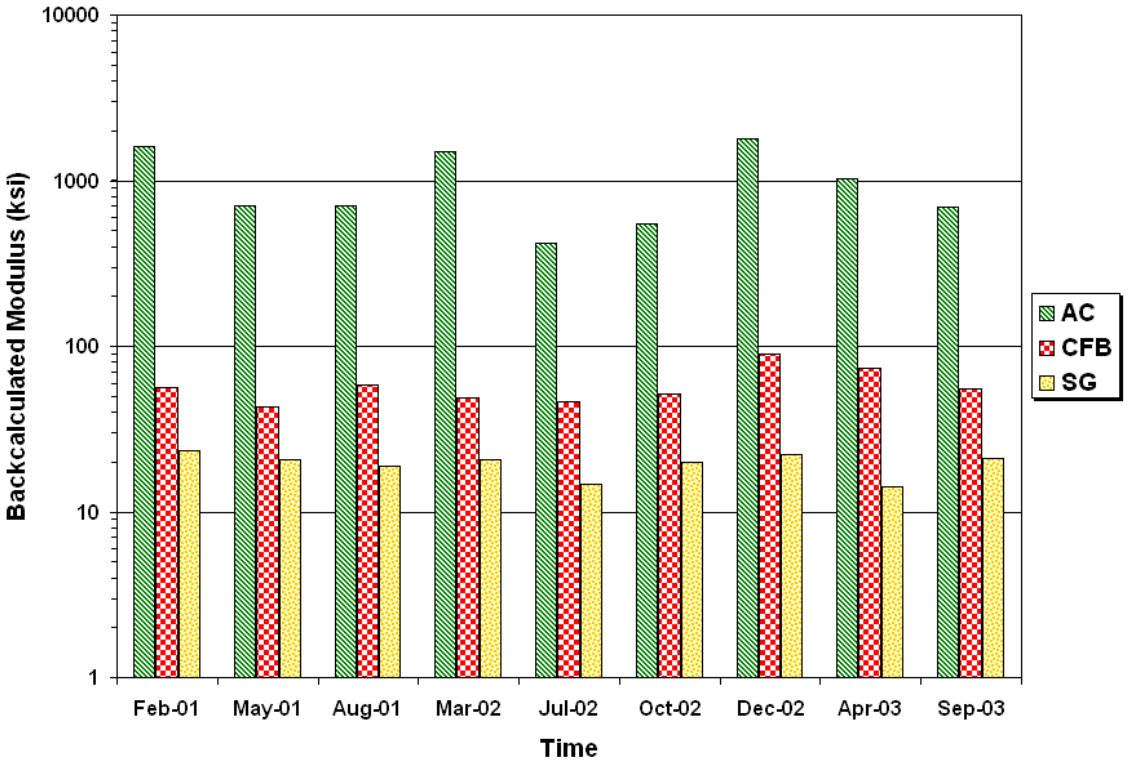

Figure C71. Backcalculated Layer Moduli on FWD Station K7-15.

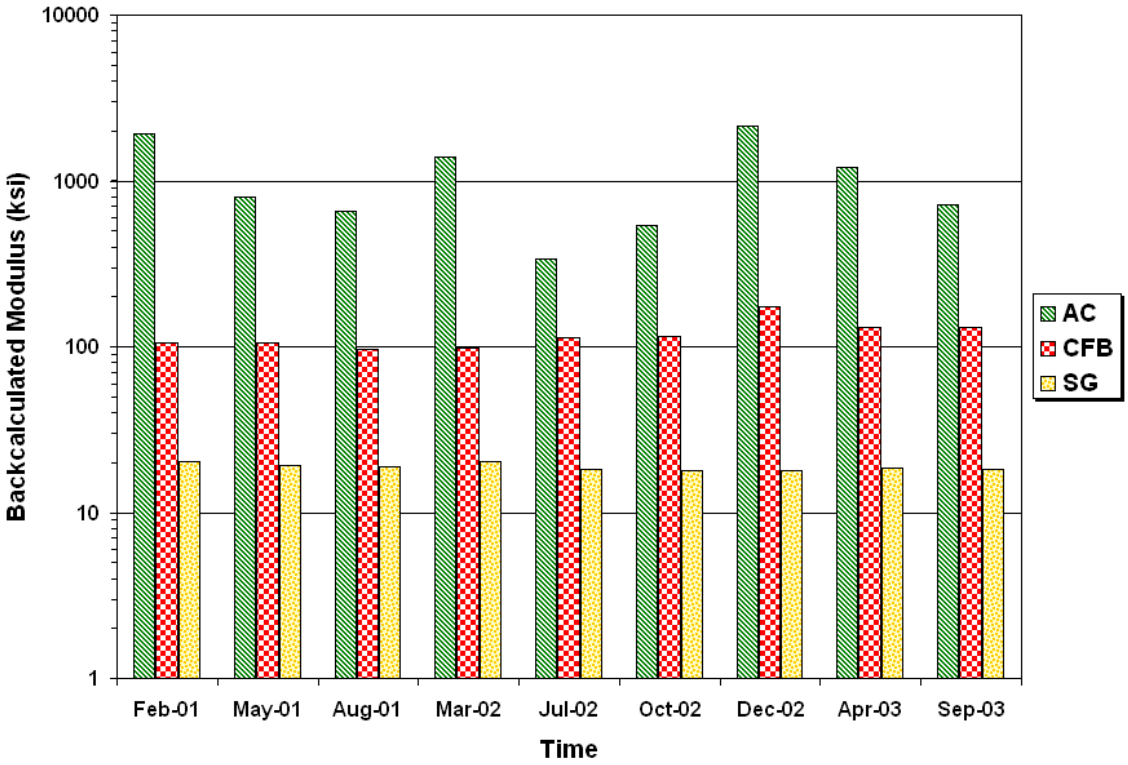

Figure C72. Backcalculated Layer Moduli on FWD Station K7-16.

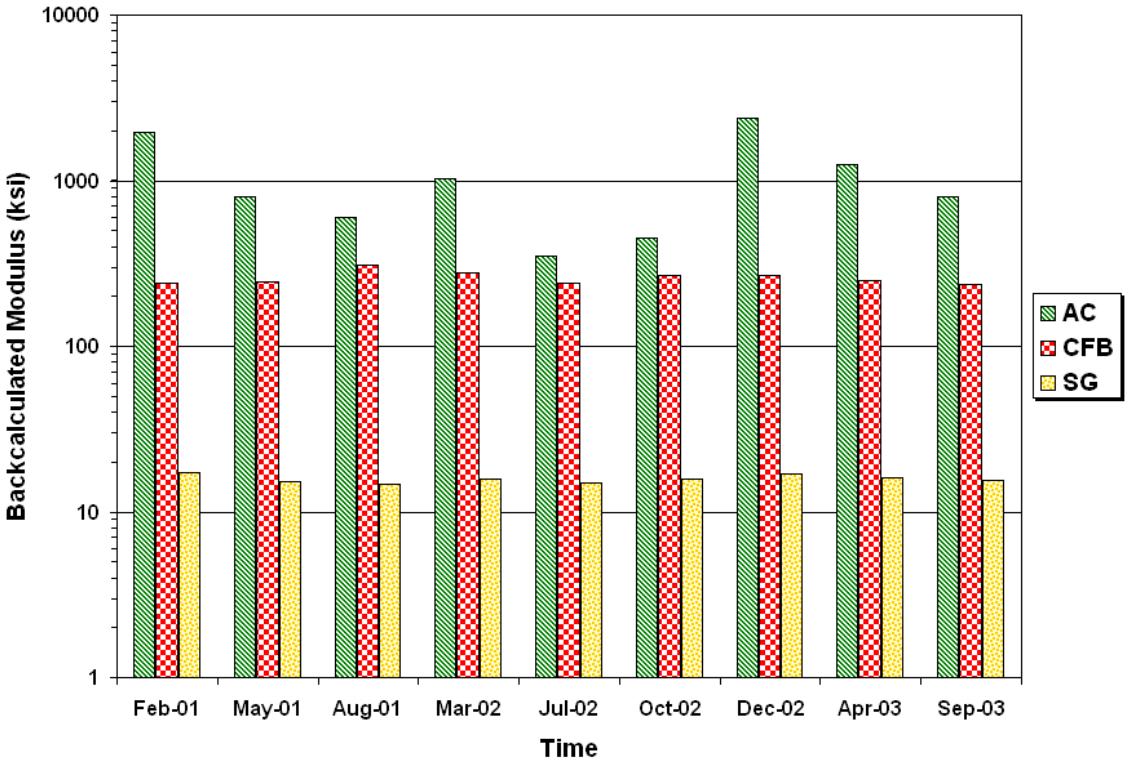

Figure C73. Backcalculated Layer Moduli on FWD Station K7-17.

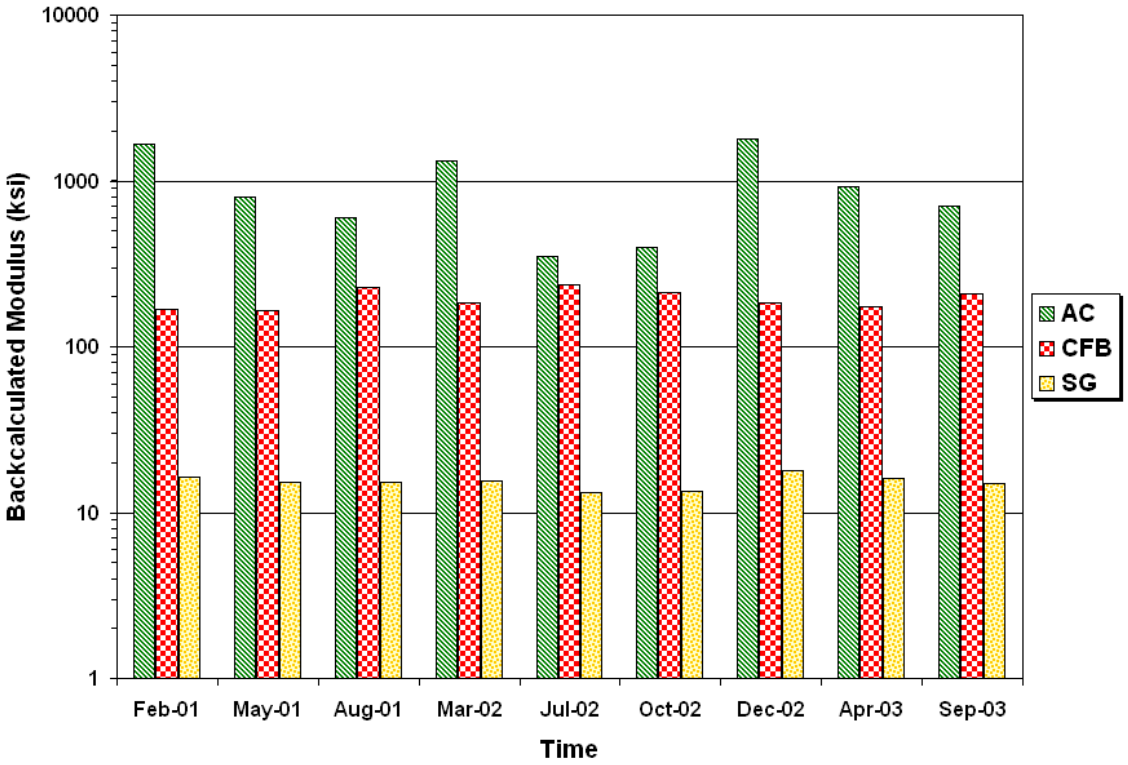

Figure C74. Backcalculated Layer Moduli on FWD Station K7-18.

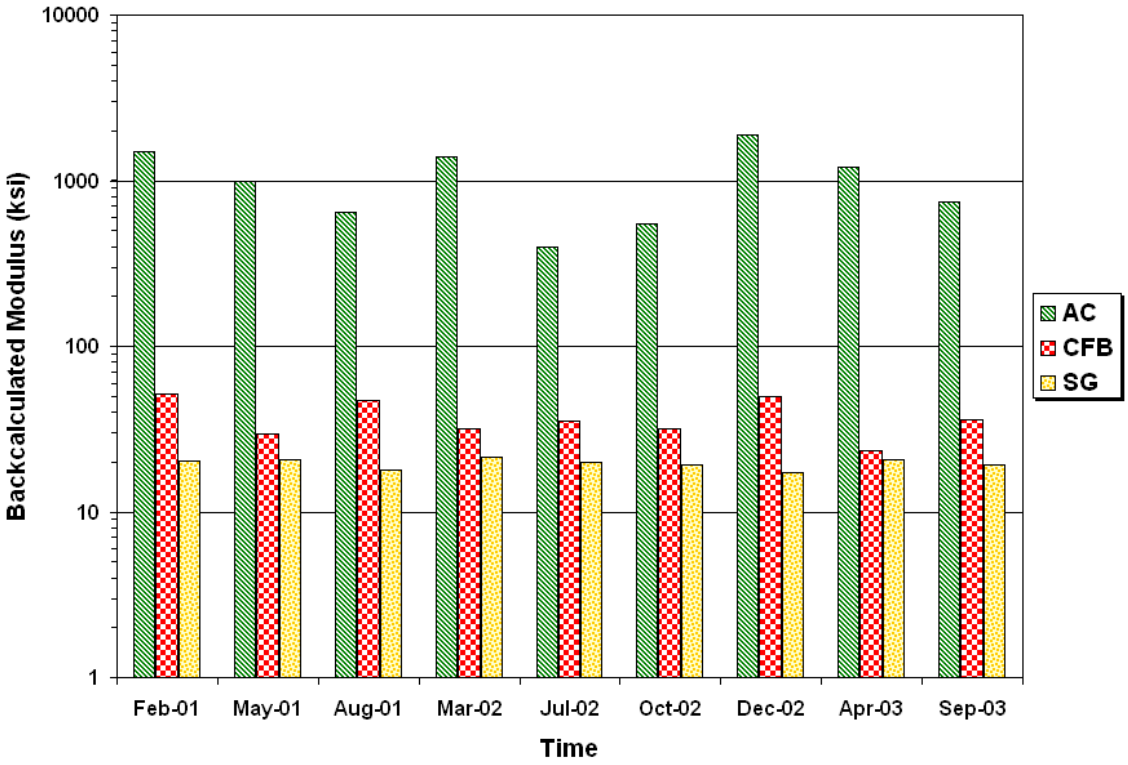

Figure C75. Backcalculated Layer Moduli on FWD Station K7-19.

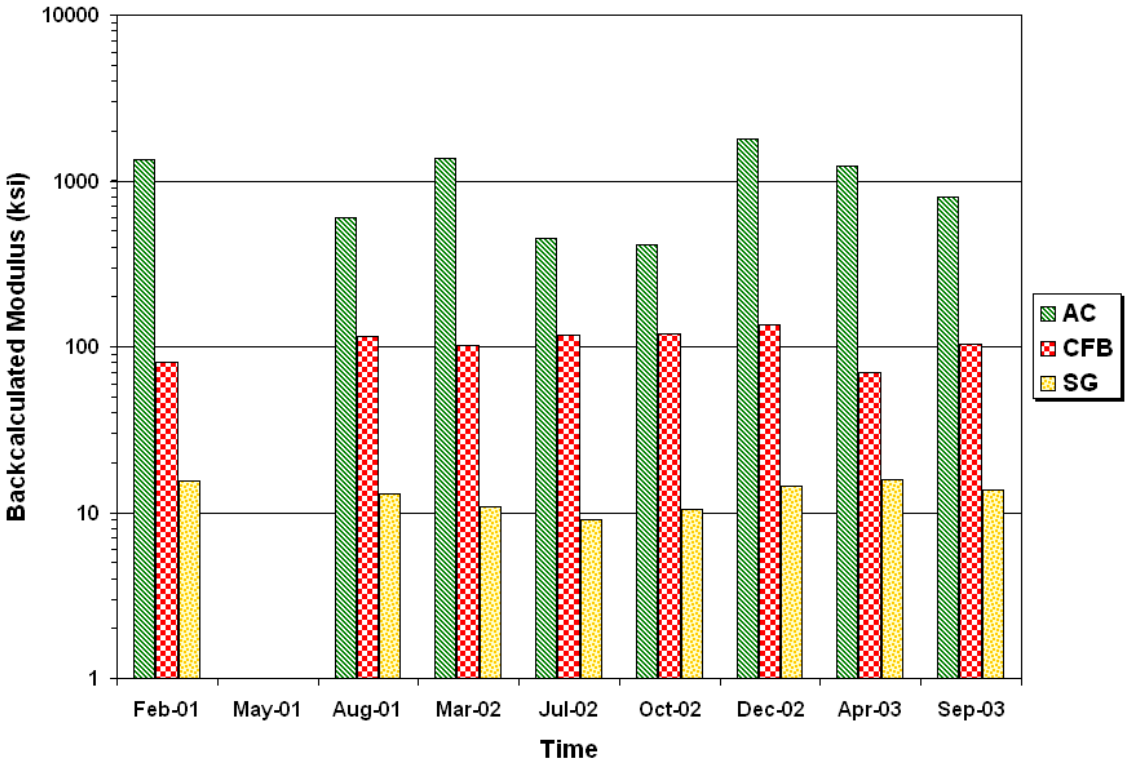

Figure C76. Backcalculated Layer Moduli on FWD Station K7-20.

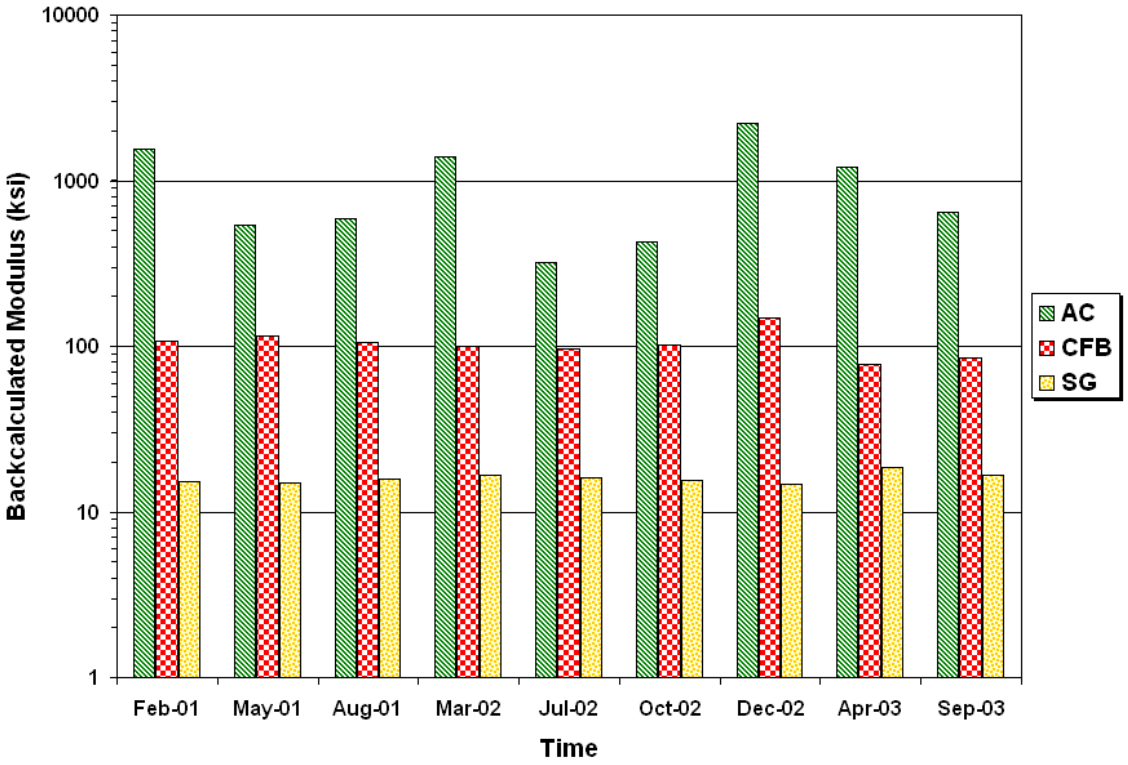

Figure C77. Backcalculated Layer Moduli on FWD Station K7-21.

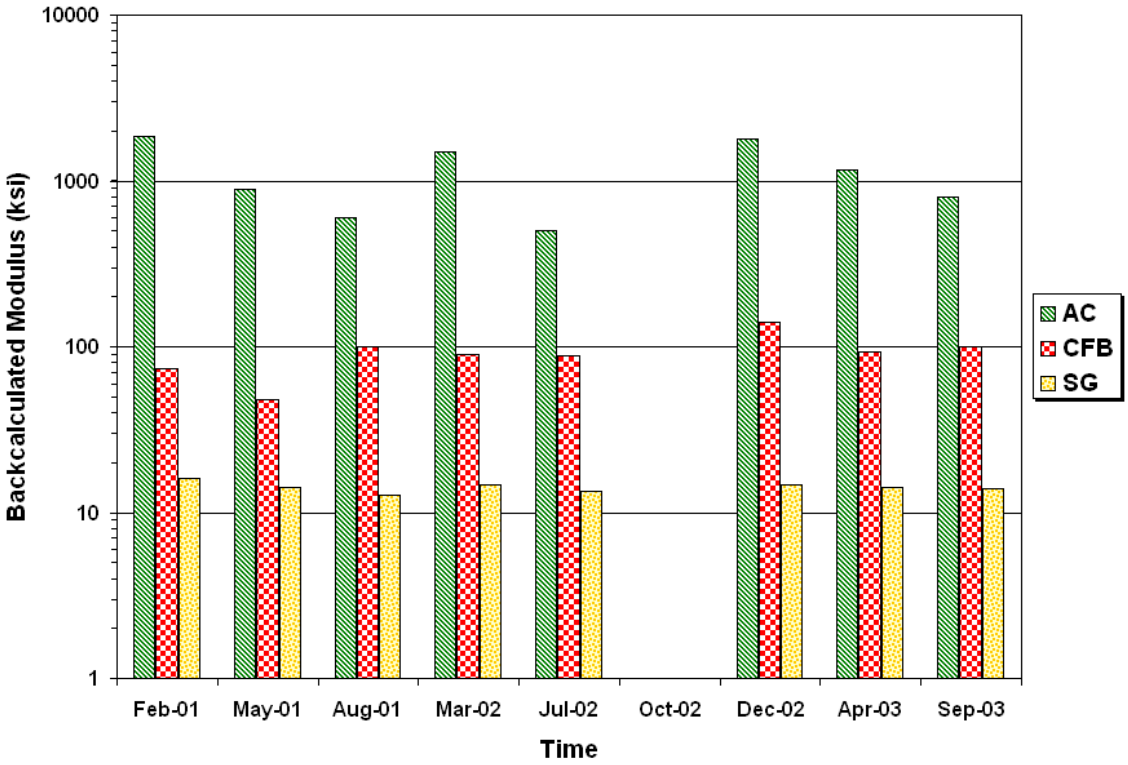

Figure C78. Backcalculated Layer Moduli on FWD Station K7-22.

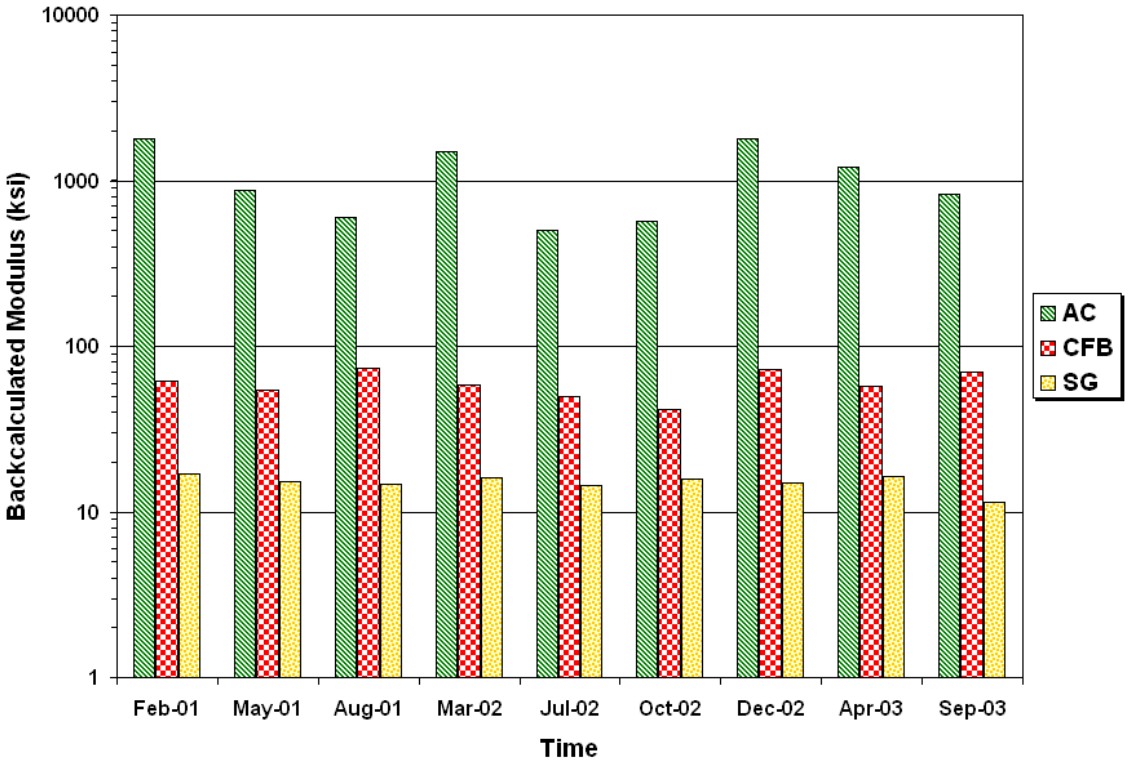

Figure C79. Backcalculated Layer Moduli on FWD Station K7-23.

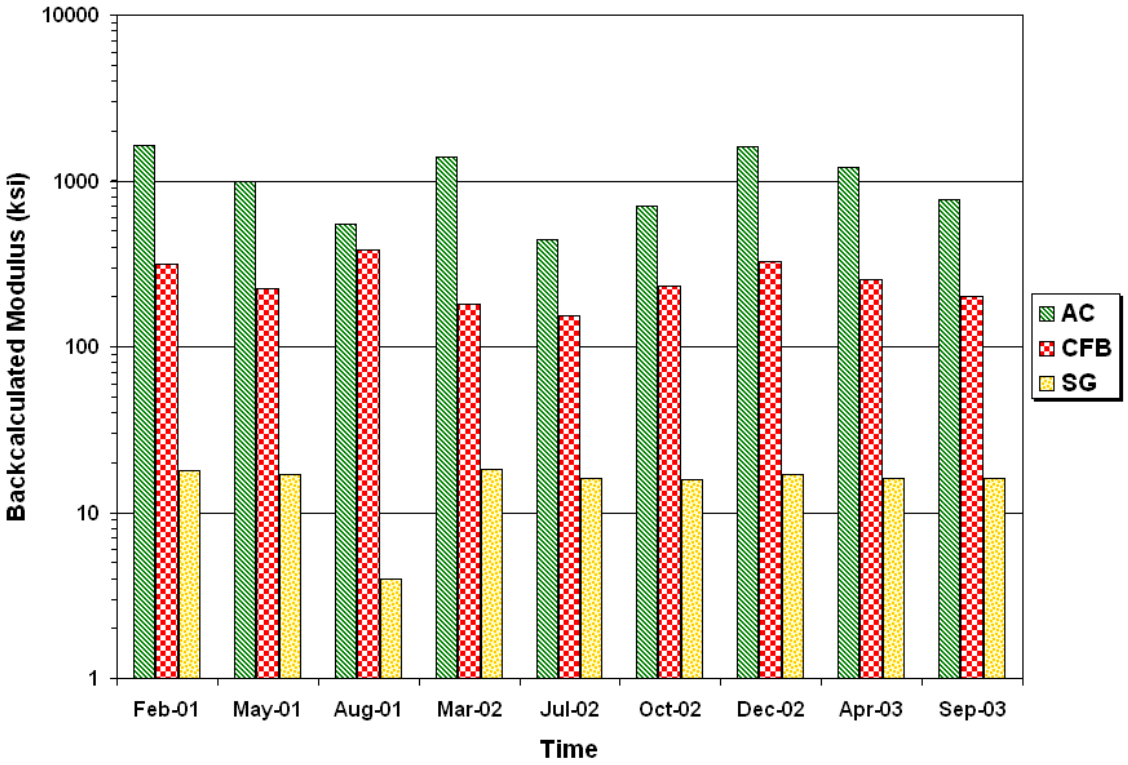

Figure C80. Backcalculated Layer Moduli on FWD Station K7-24.

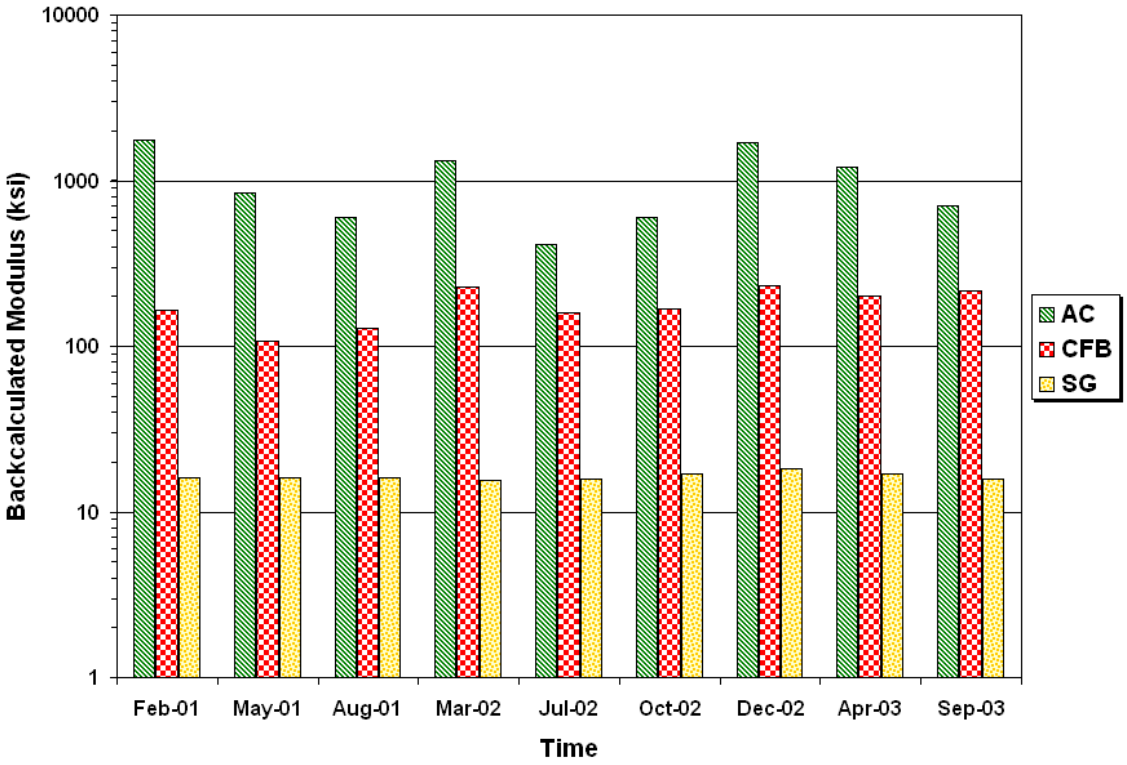

Figure C81. Backcalculated Layer Moduli on FWD Station K7-25.

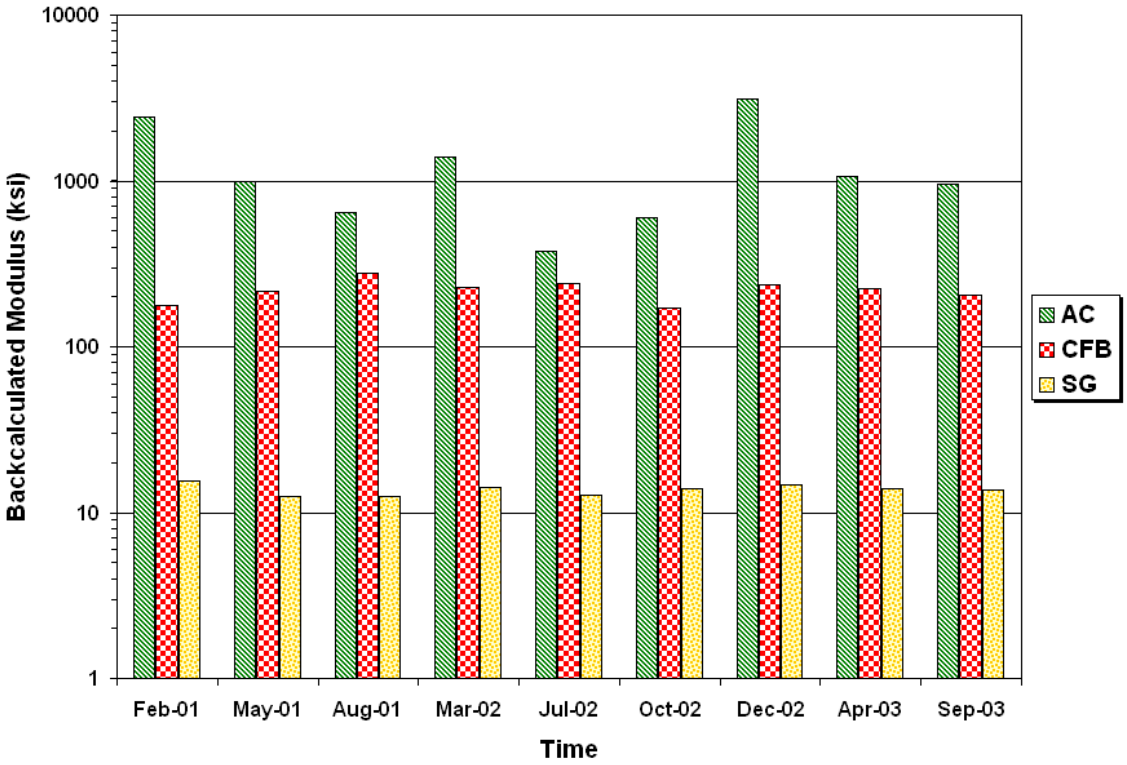

Figure C82. Backcalculated Layer Moduli on FWD Station K7-26.

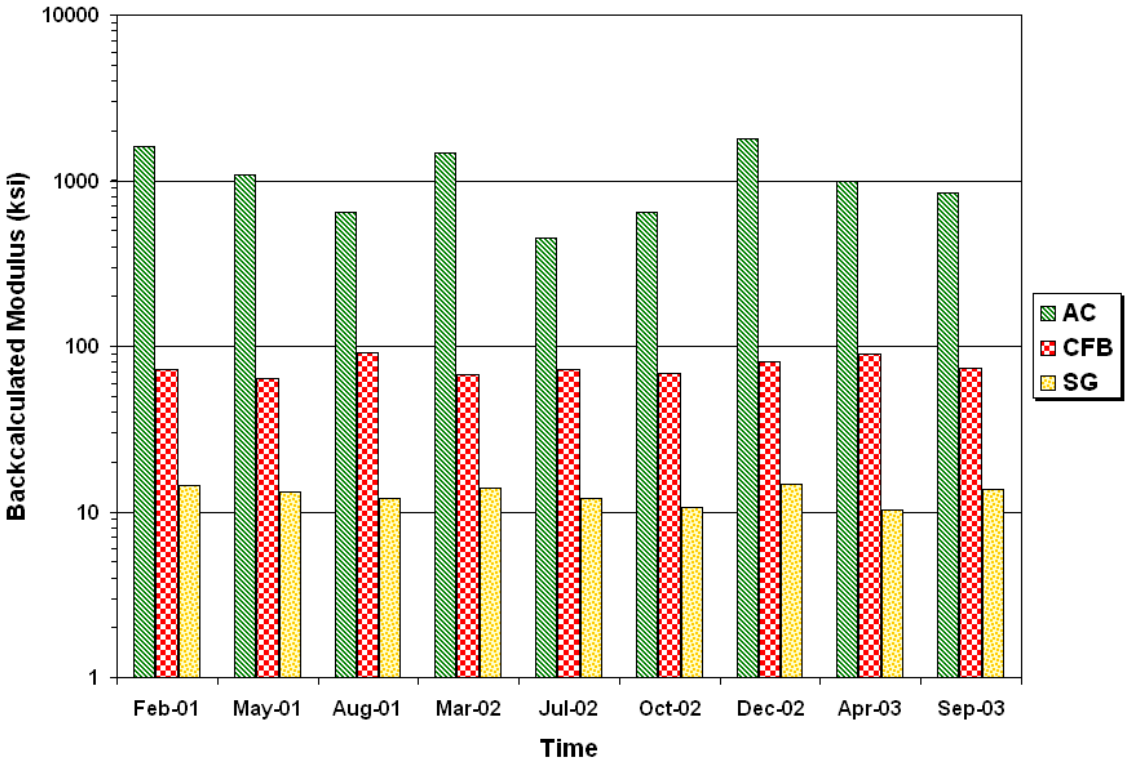

Figure C83. Backcalculated Layer Moduli on FWD Station K7-27.

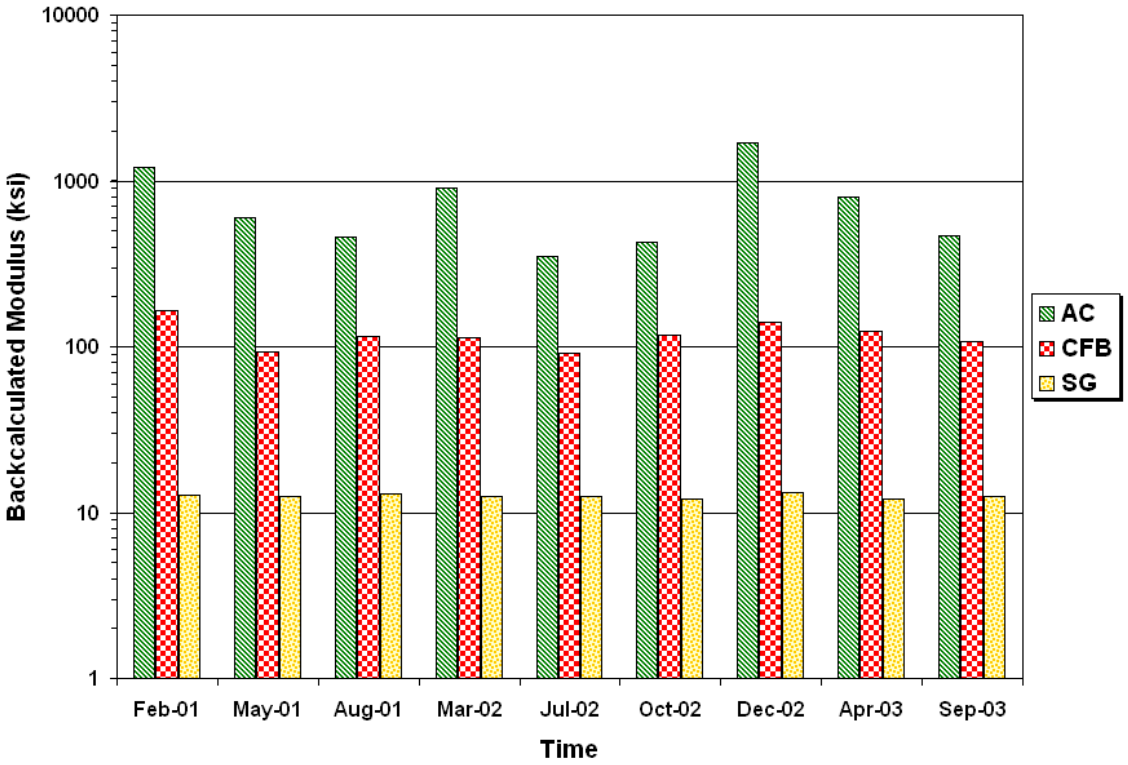

Figure C84. Backcalculated Layer Moduli on FWD Station K7-28.

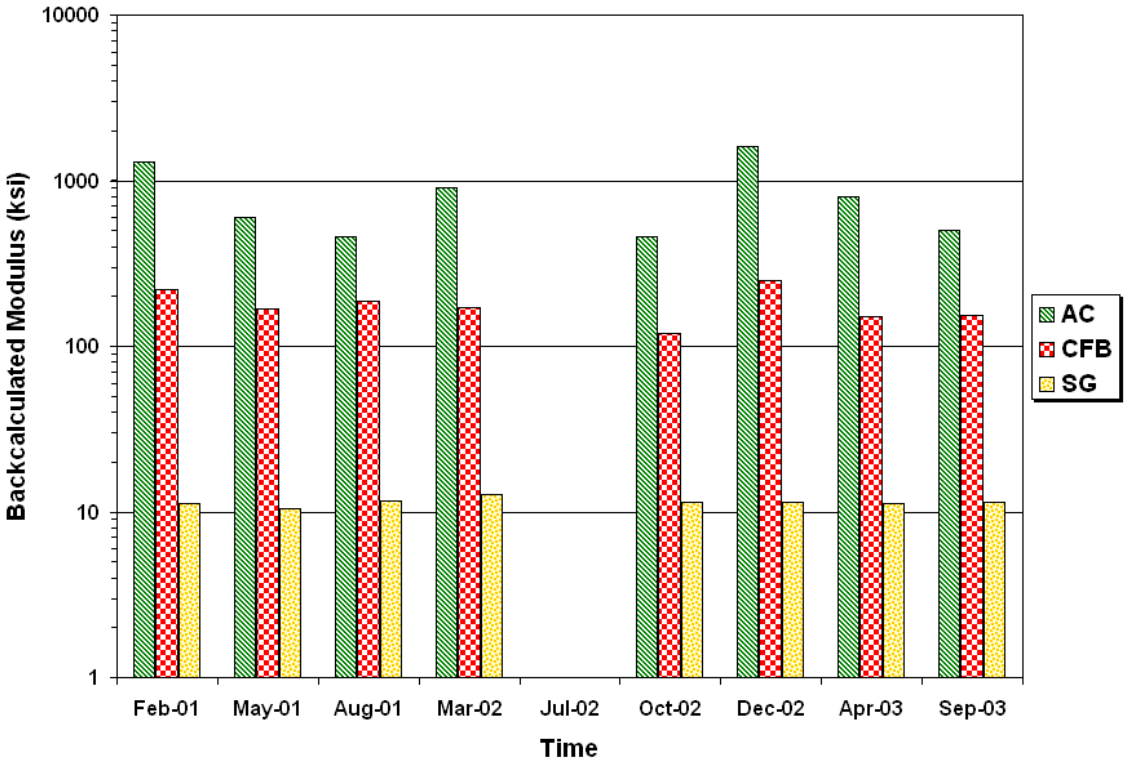

Figure C85. Backcalculated Layer Moduli on FWD Station K7-29.

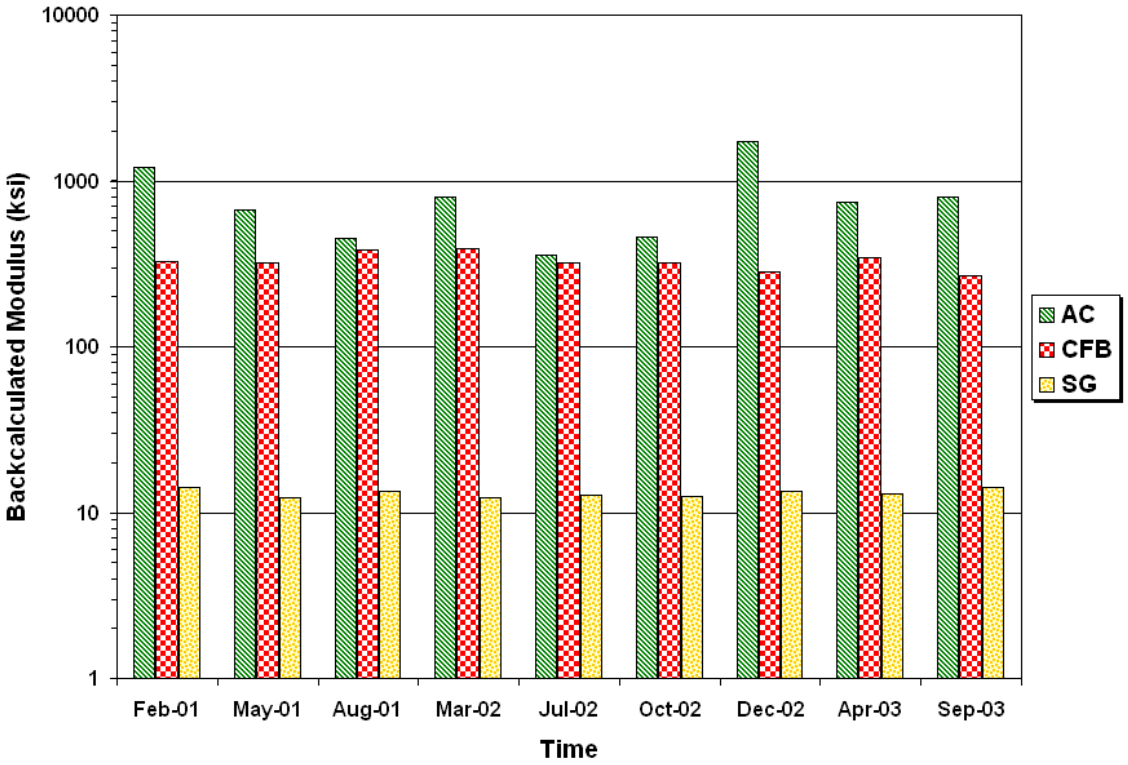

Figure C86. Backcalculated Layer Moduli on FWD Station K7-30.

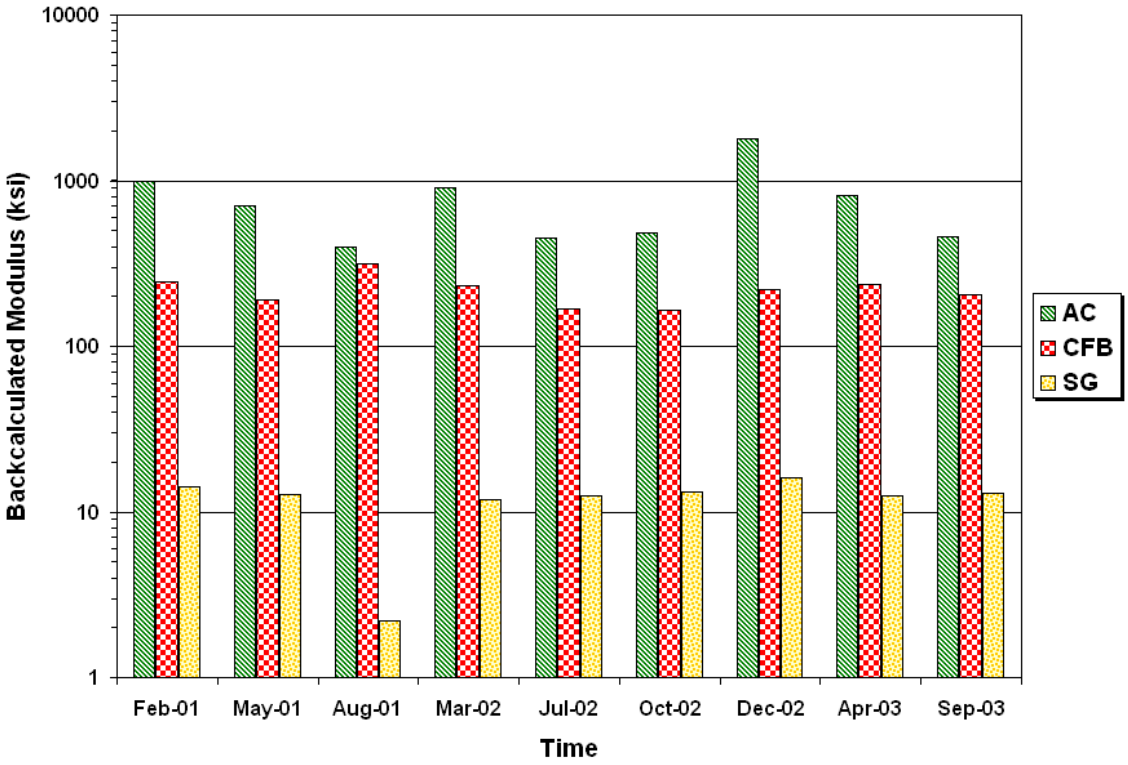

Figure C87. Backcalculated Layer Moduli on FWD Station K7-31.

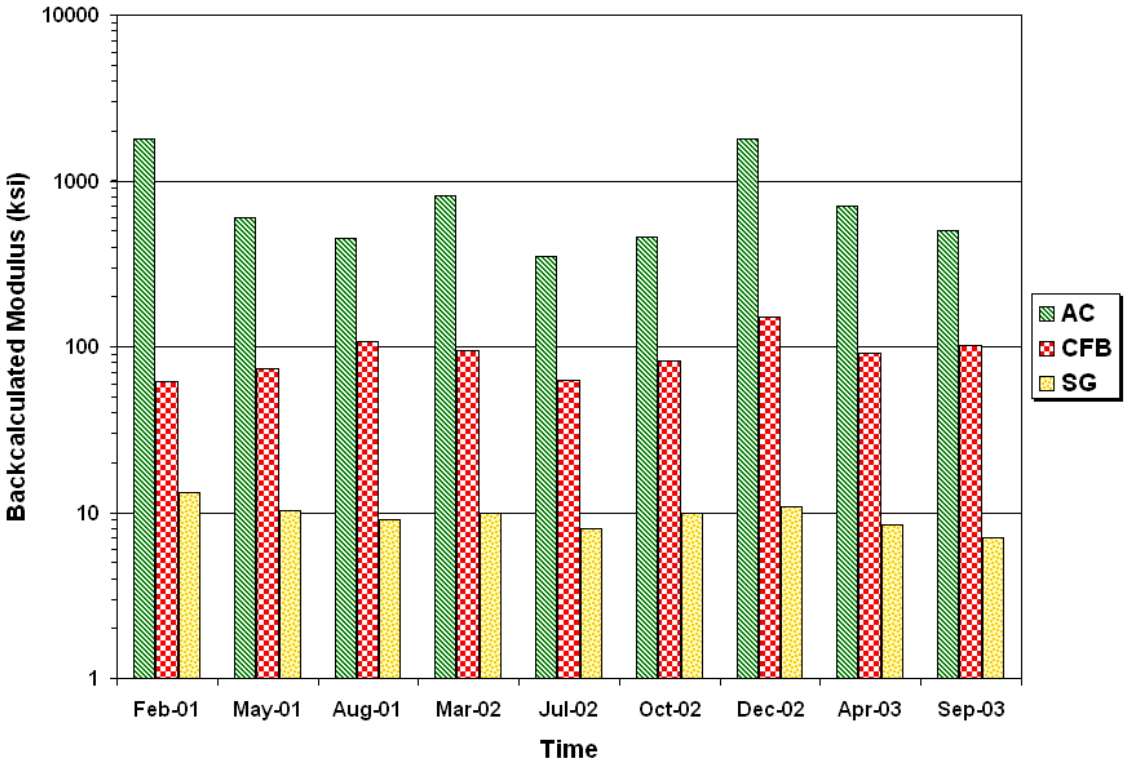

Figure C88. Backcalculated Layer Moduli on FWD Station K7-32.

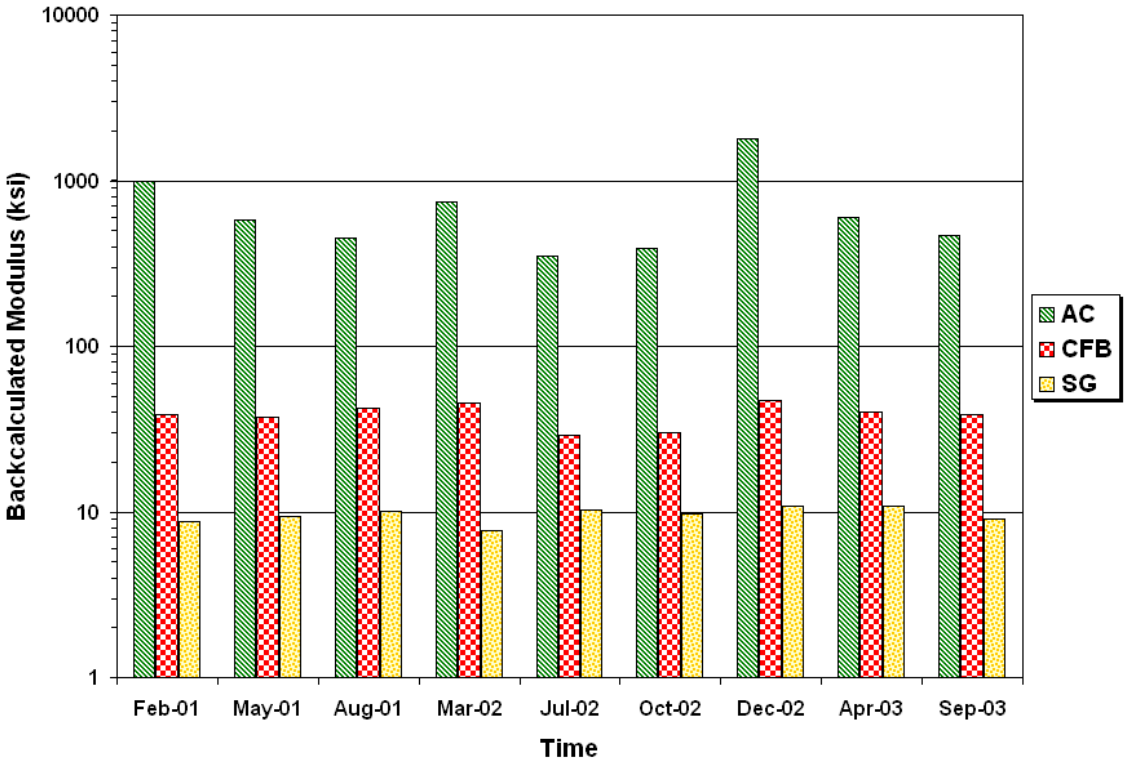

Figure C89. Backcalculated Layer Moduli on FWD Station K7-33.

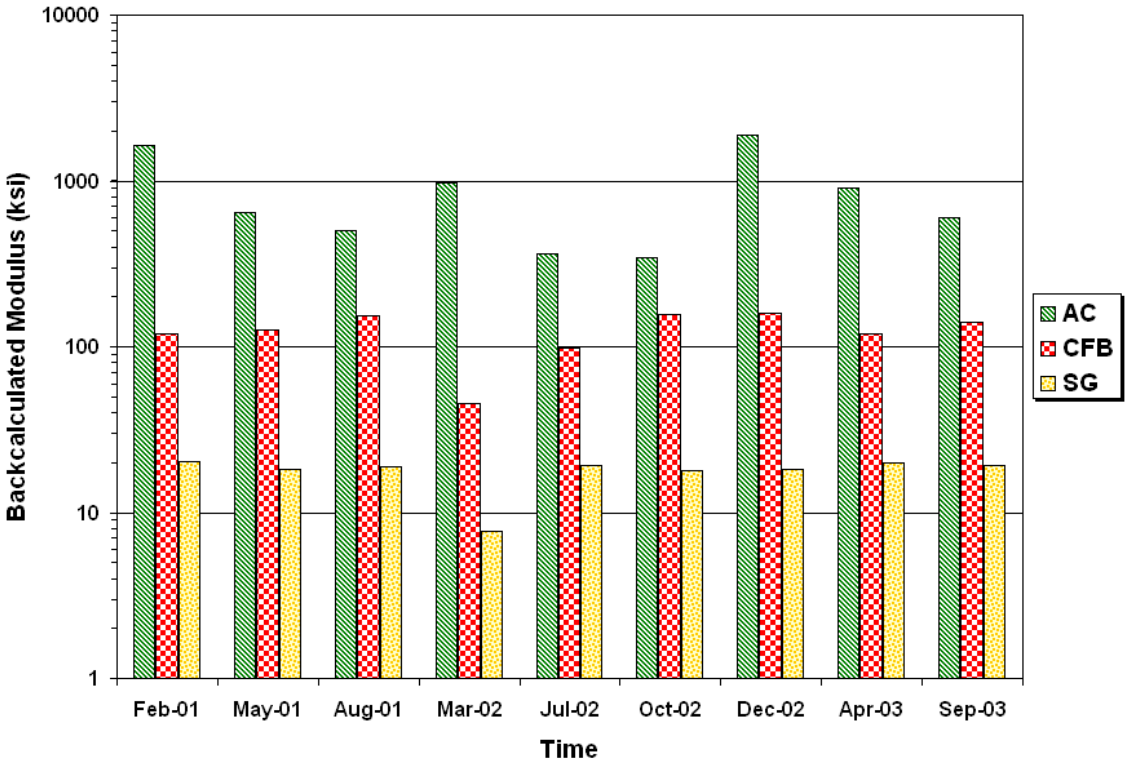

Figure C90. Backcalculated Layer Moduli on FWD Station K7-34.

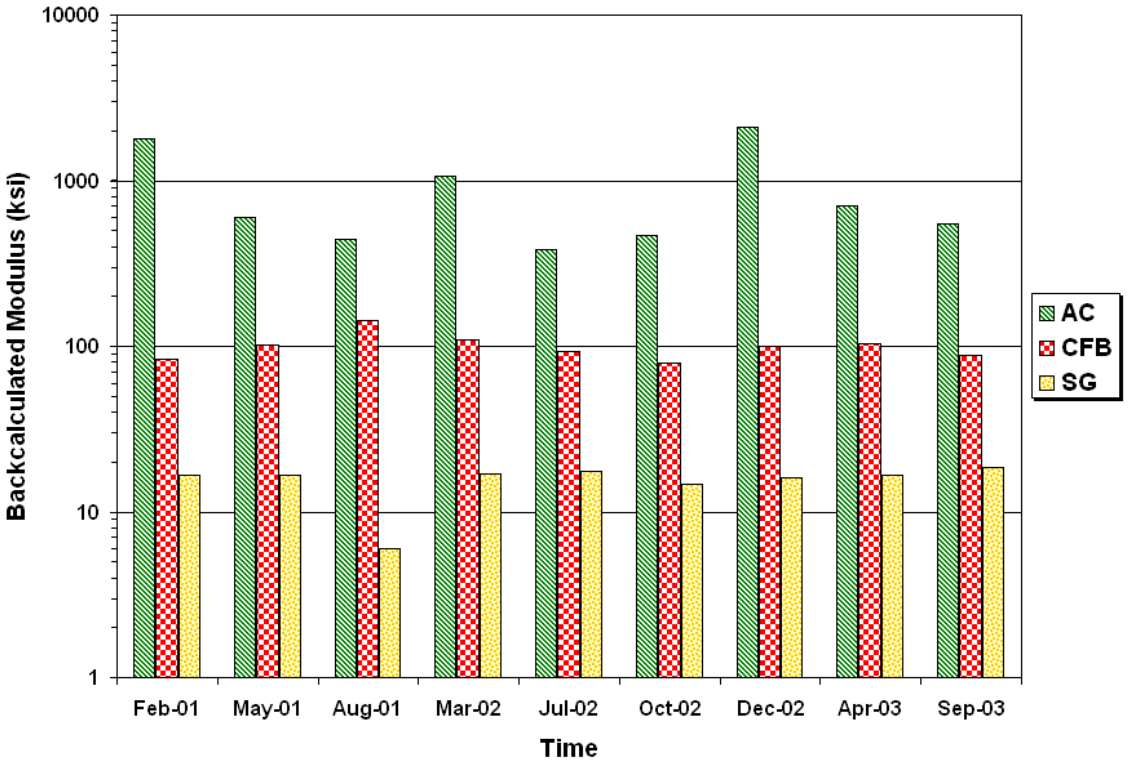

Figure C91. Backcalculated Layer Moduli on FWD Station K7-35.

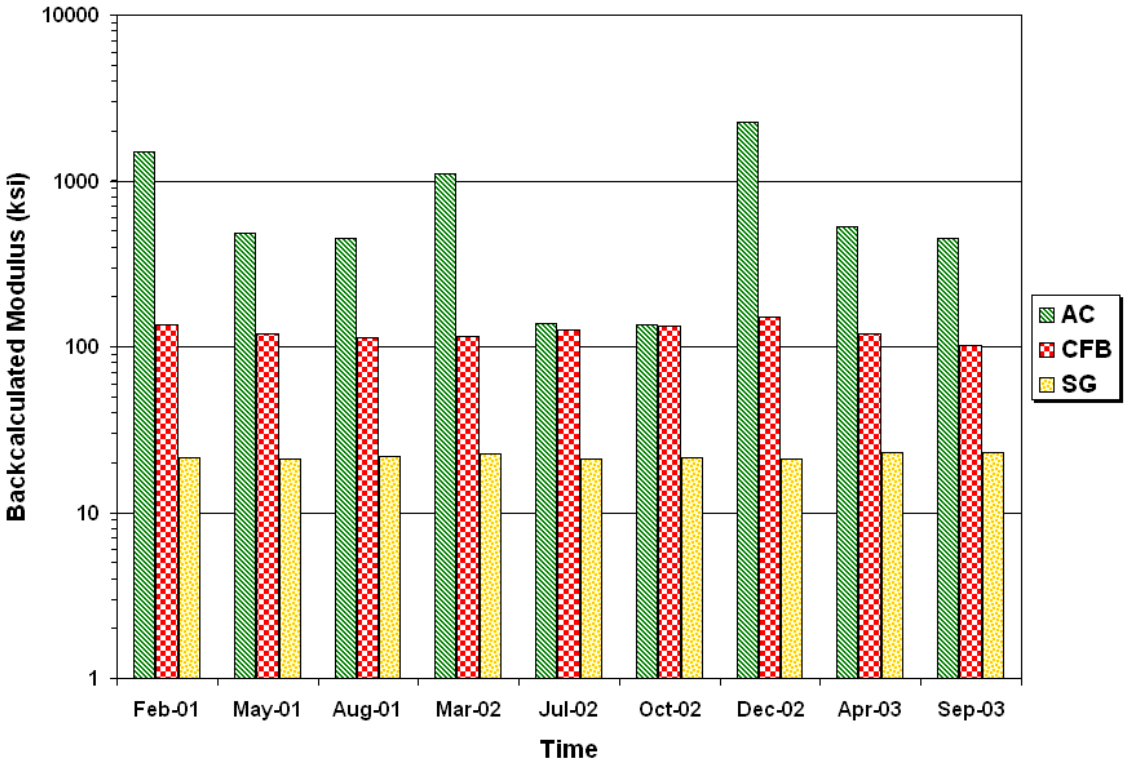

Figure C92. Backcalculated Layer Moduli on FWD Station K7-36.

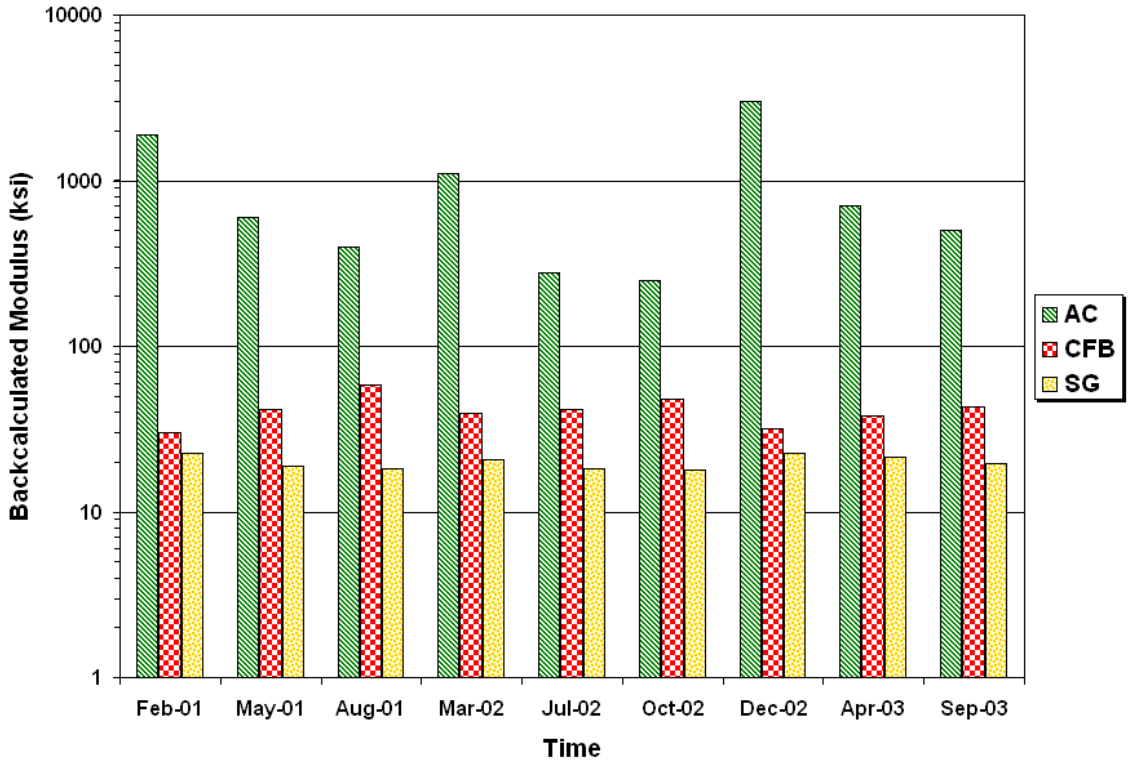

Figure C93. Backcalculated Layer Moduli on FWD Station K7-37.

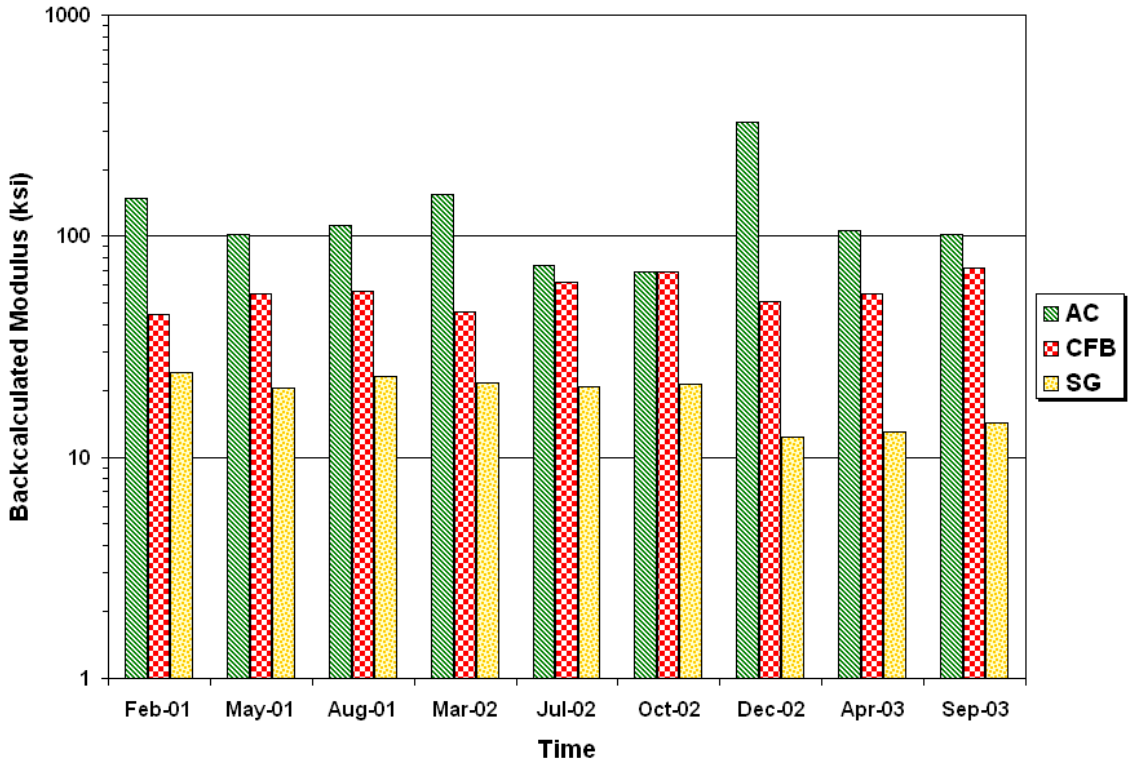

Figure C94. Backcalculated Layer Moduli on FWD Station K7-38.

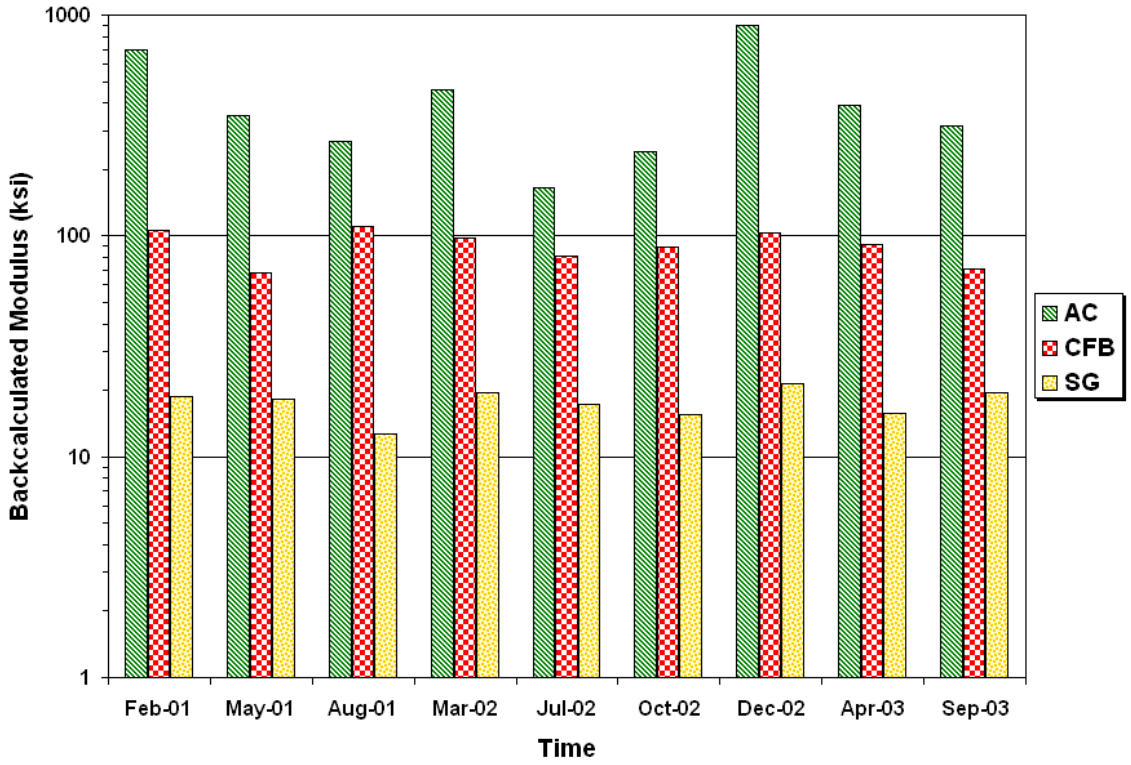

Figure C95. Backcalculated Layer Moduli on FWD Station K7-39.

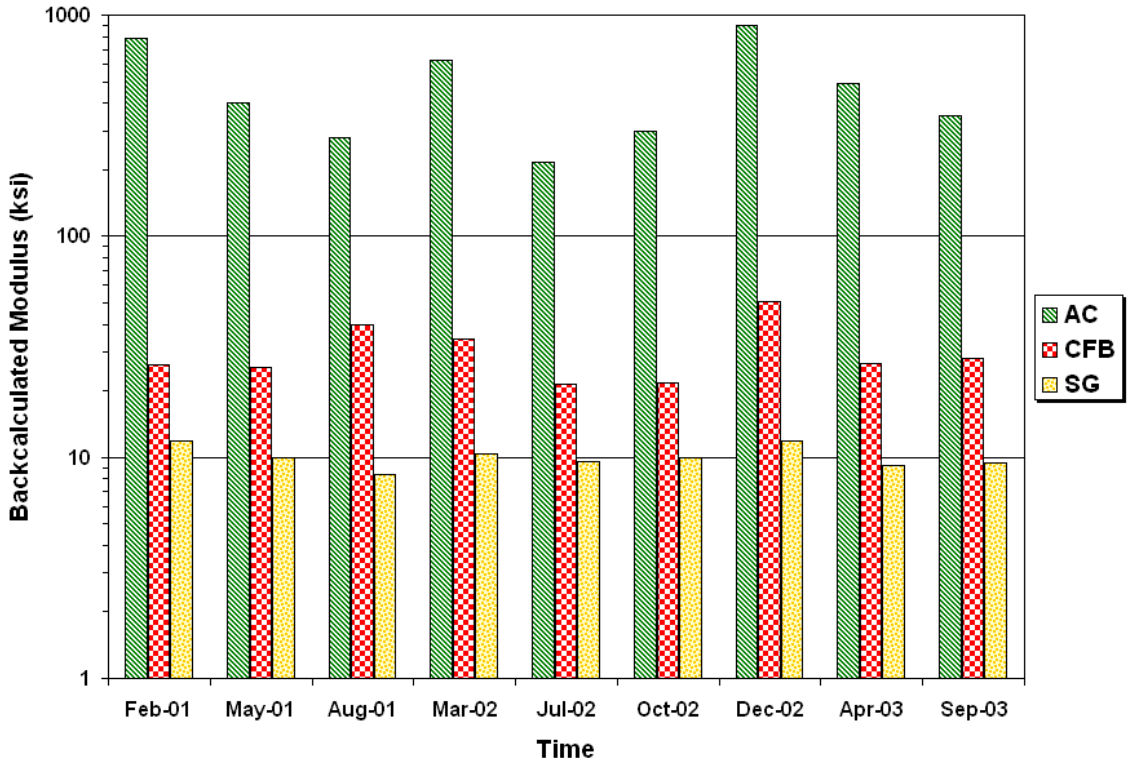

Figure C96. Backcalculated Layer Moduli on FWD Station K7-40.

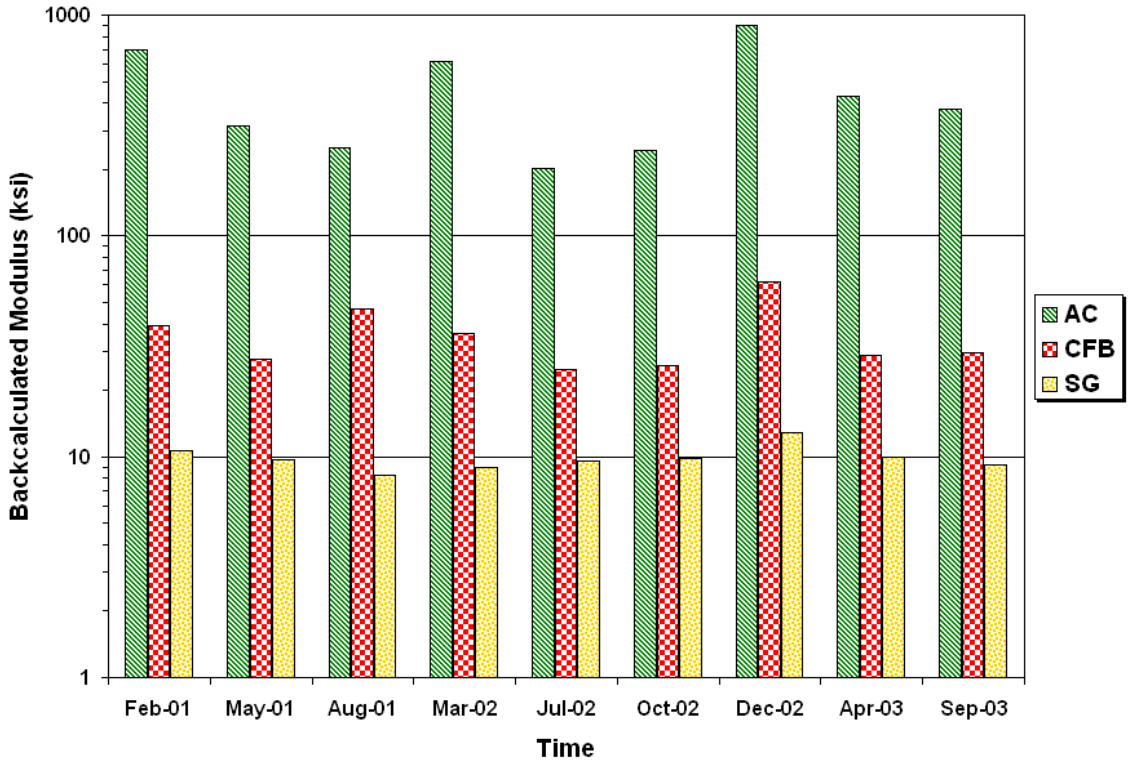

Figure C97. Backcalculated Layer Moduli on FWD Station K7-41.

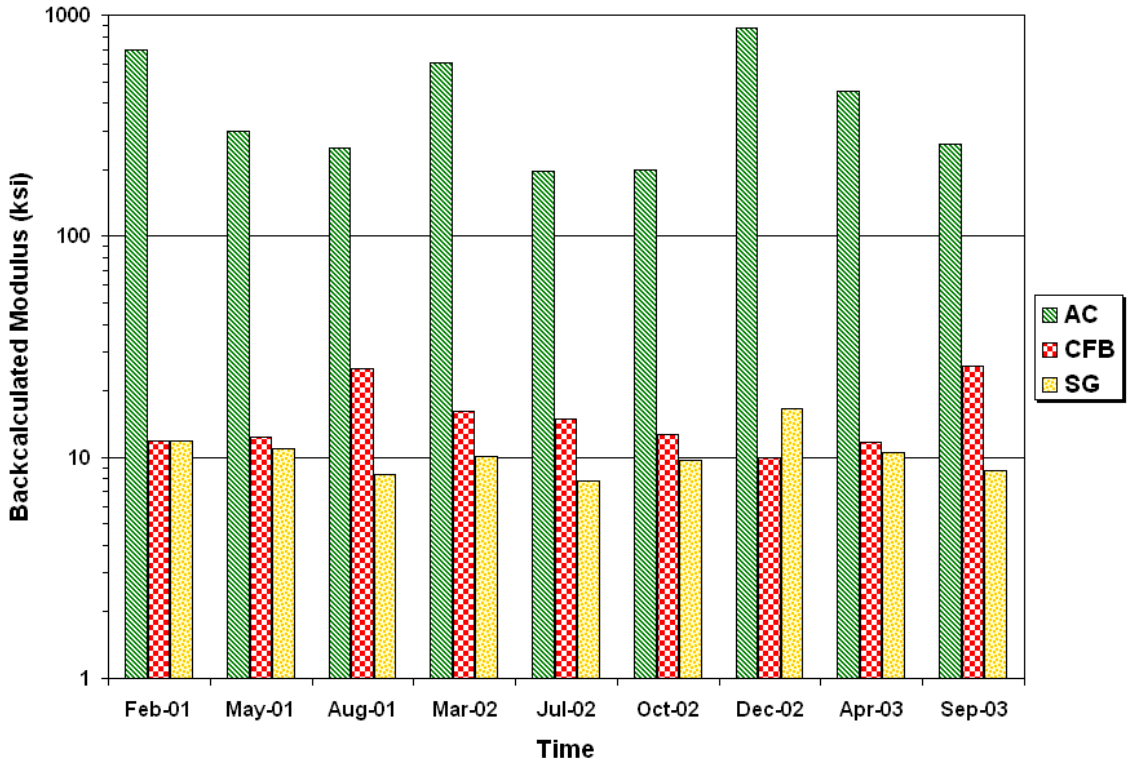

Figure C98. Backcalculated Layer Moduli on FWD Station K7-42.

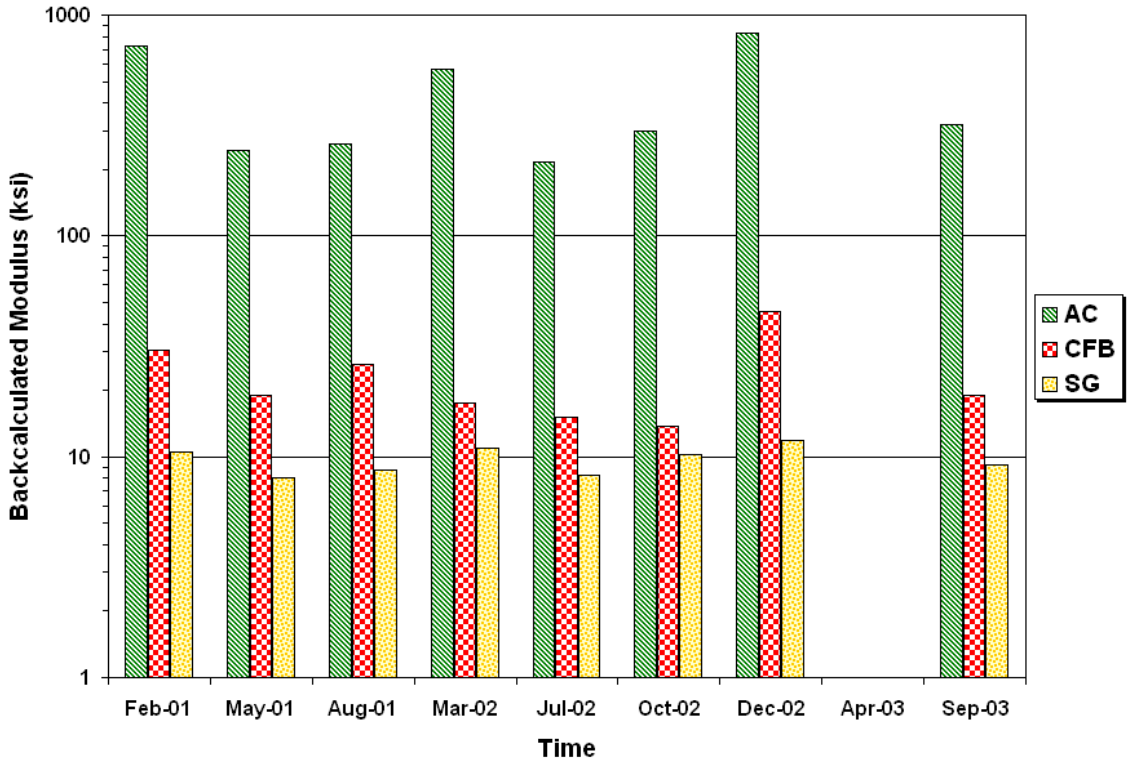

Figure C99. Backcalculated Layer Moduli on FWD Station K7-43.

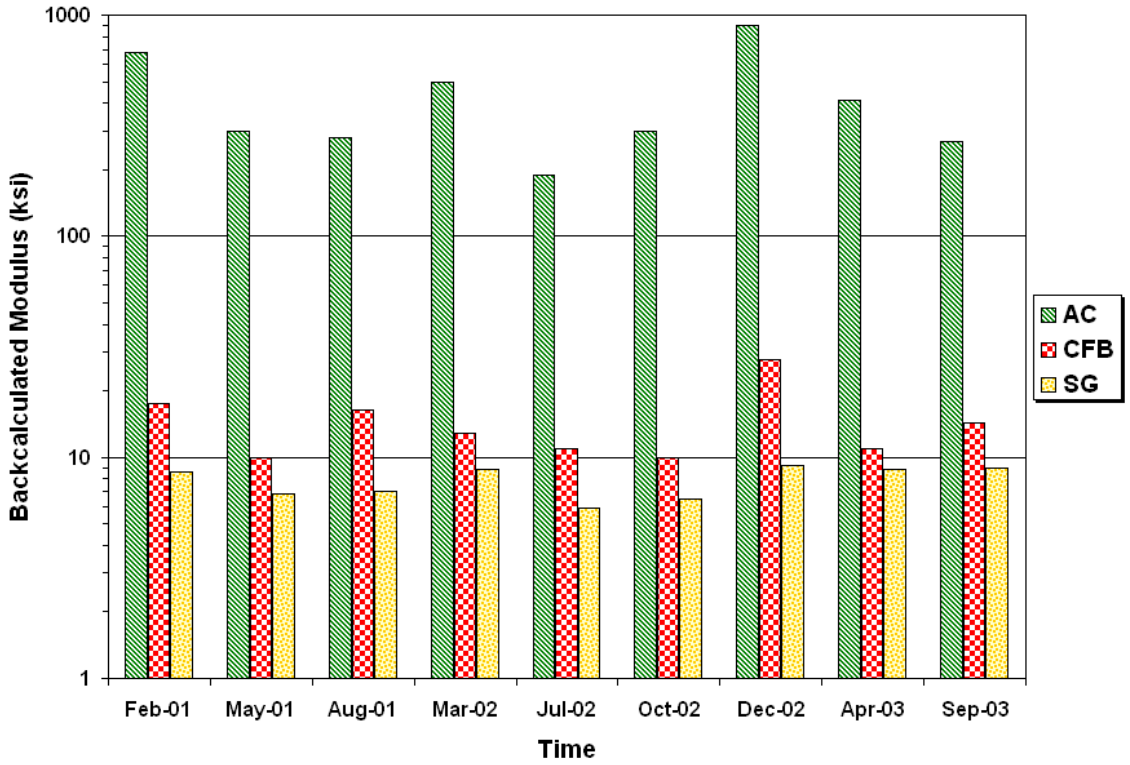

Figure C100. Backcalculated Layer Moduli on FWD Station K7-44.

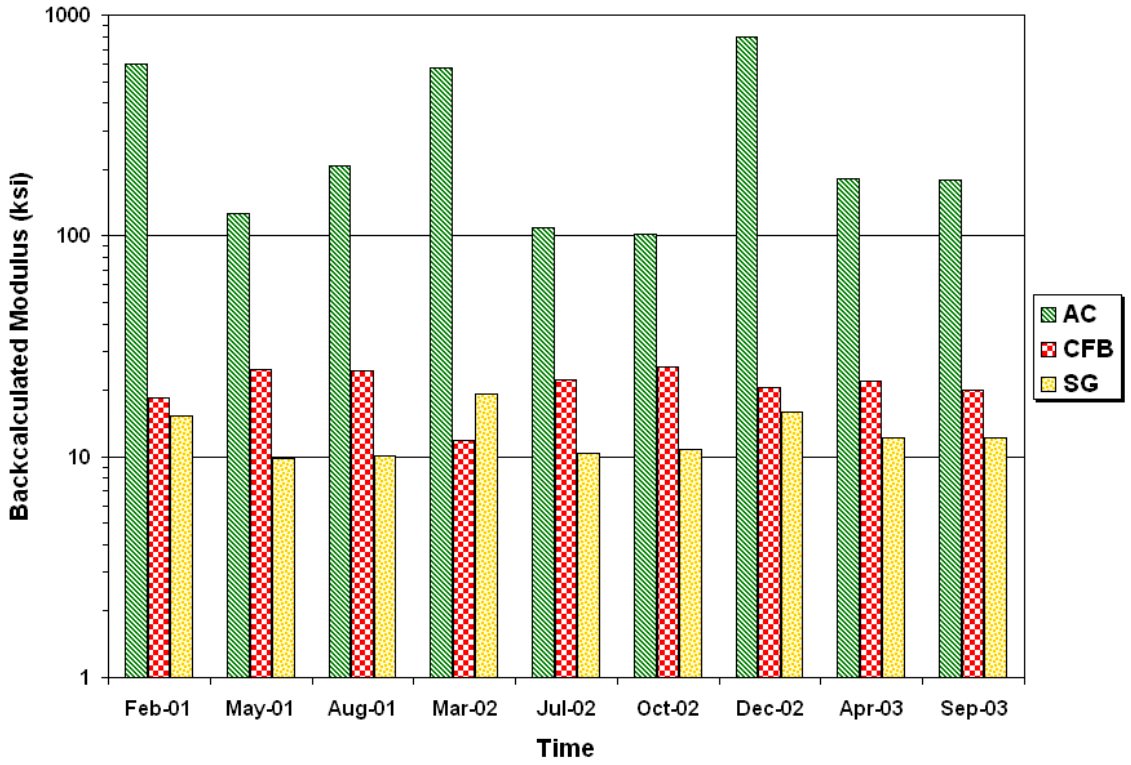

Figure C101. Backcalculated Layer Moduli on FWD Station K7-45.

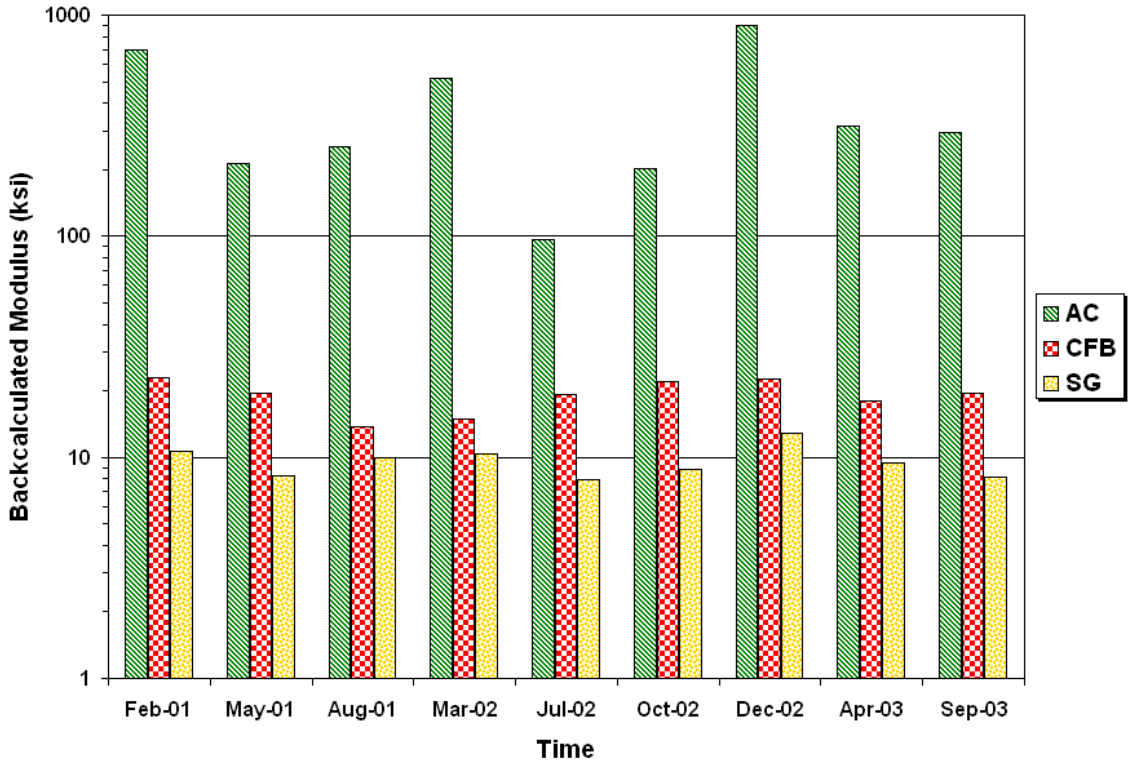

Figure C102. Backcalculated Layer Moduli on FWD Station K7-46.

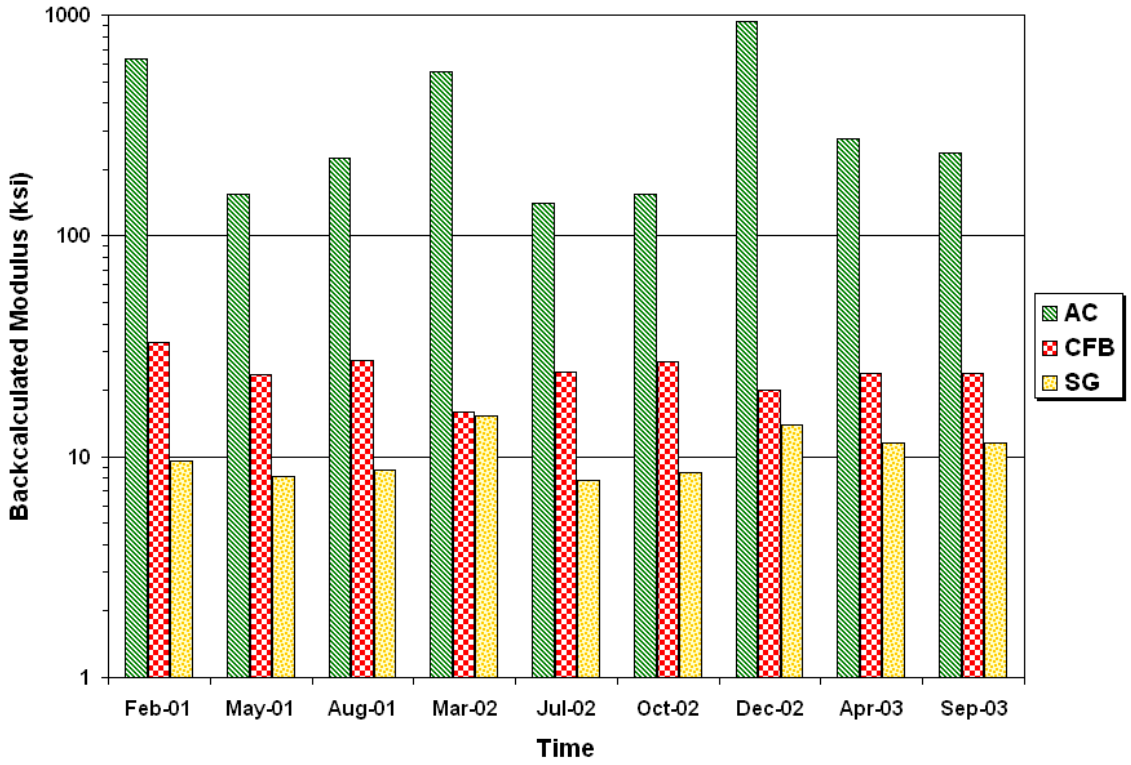

Figure C103. Backcalculated Layer Moduli on FWD Station K7-47.

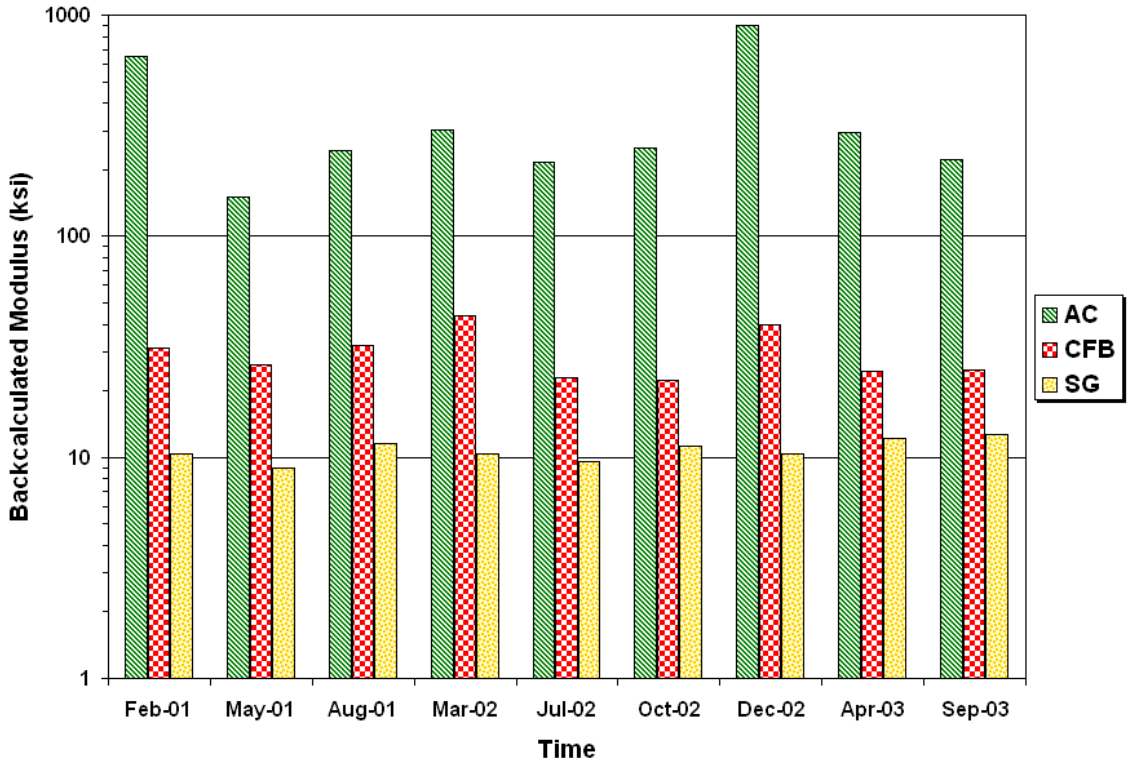

Figure C104. Backcalculated Layer Moduli on FWD Station K7-48.

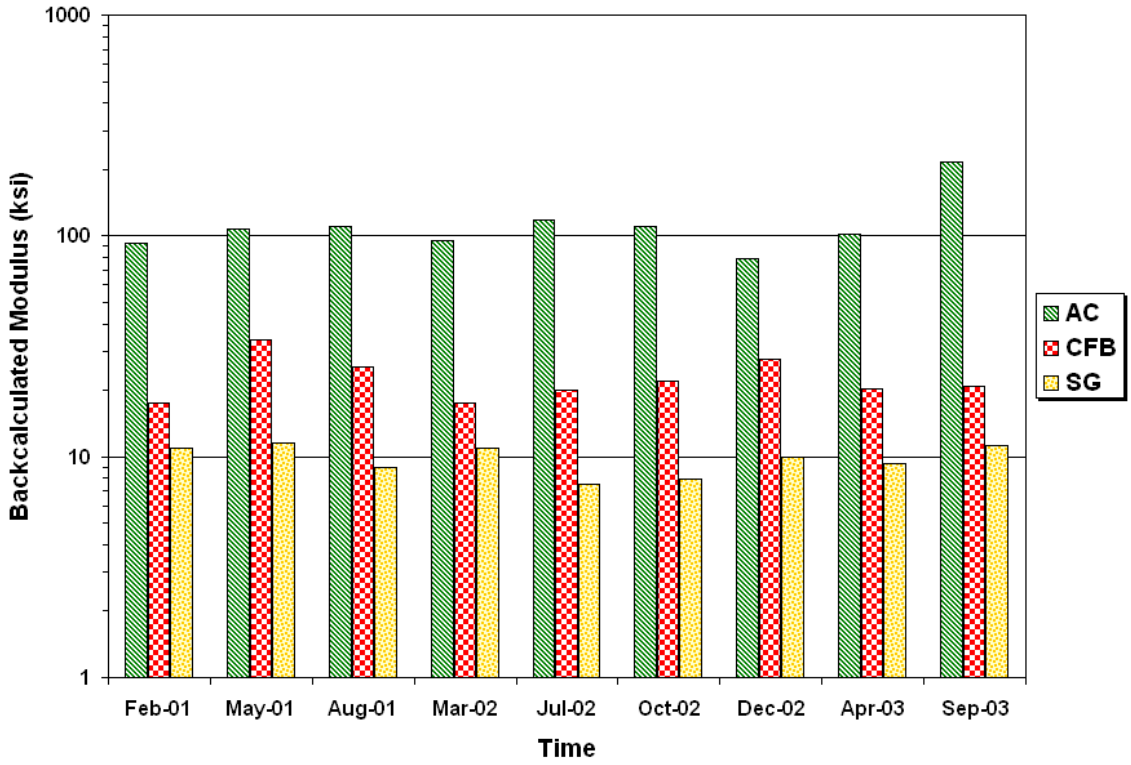

Figure C105. Backcalculated Layer Moduli on FWD Station K7-49.

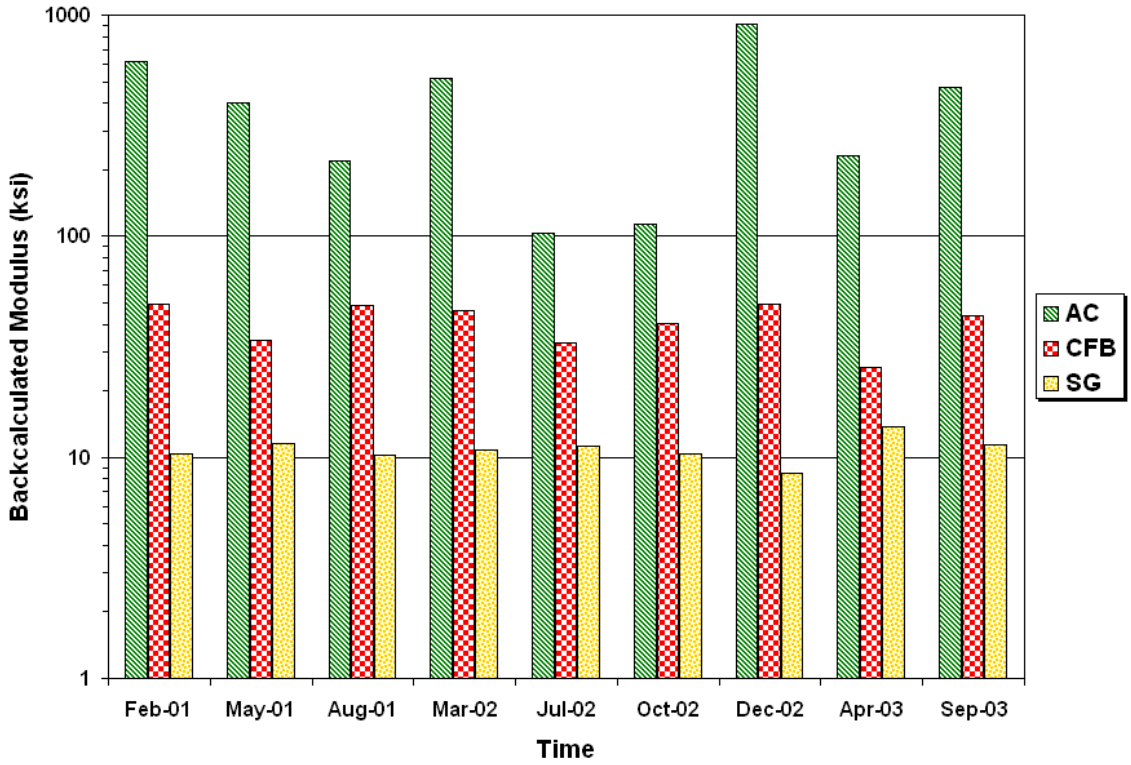

Figure C106. Backcalculated Layer Moduli on FWD Station K7-50.

APPENDIX D
PLOTS OF MEASURED AND PREDICTED FWD DISPLACEMENT HISTORIES

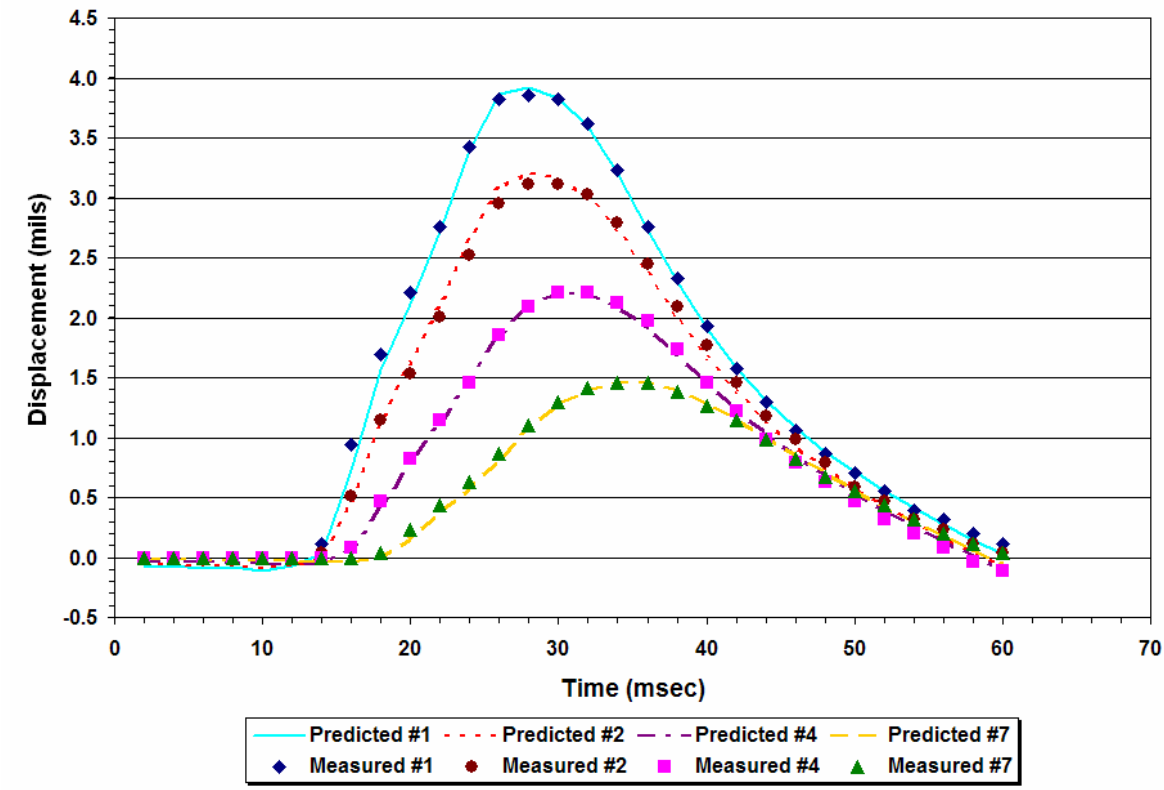

Figure D1. Comparison of Measured and Predicted FWD Displacement Histories on K6-11 (Data Collected in Feb 01).

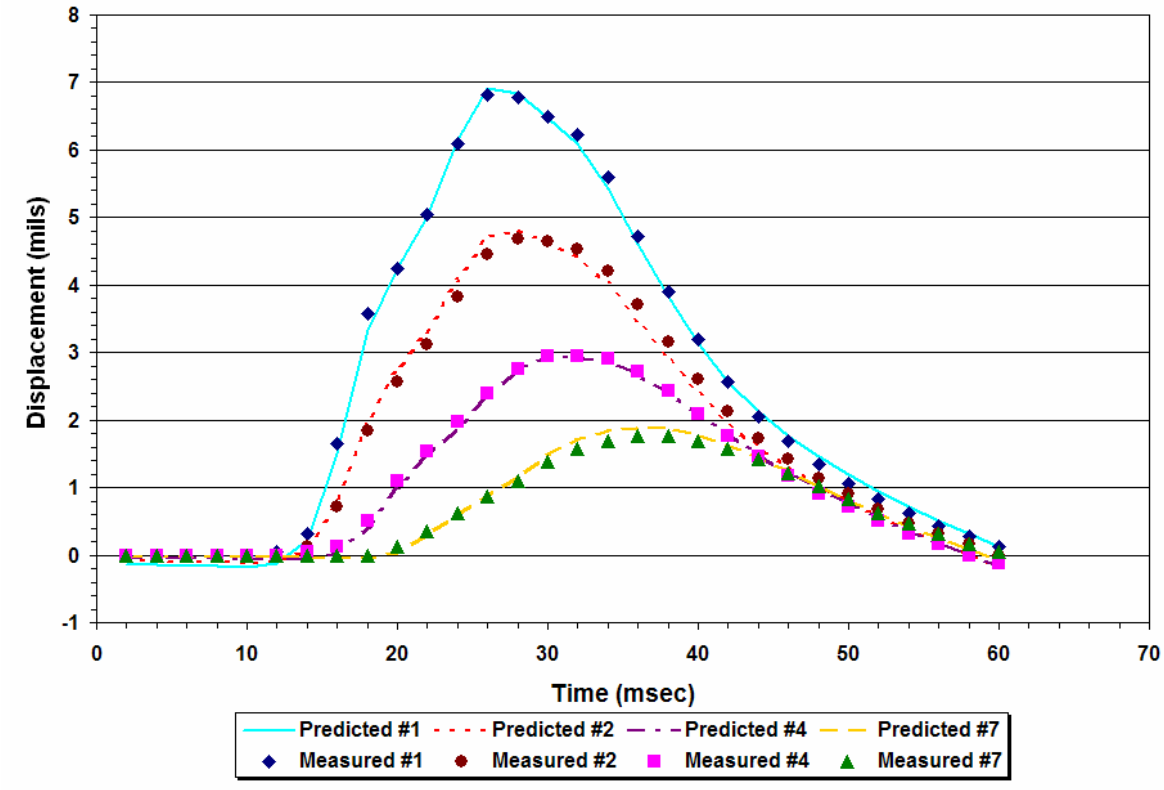

Figure D2. Comparison of Measured and Predicted FWD Displacement Histories on K6-23 (Data Collected in Feb 01).

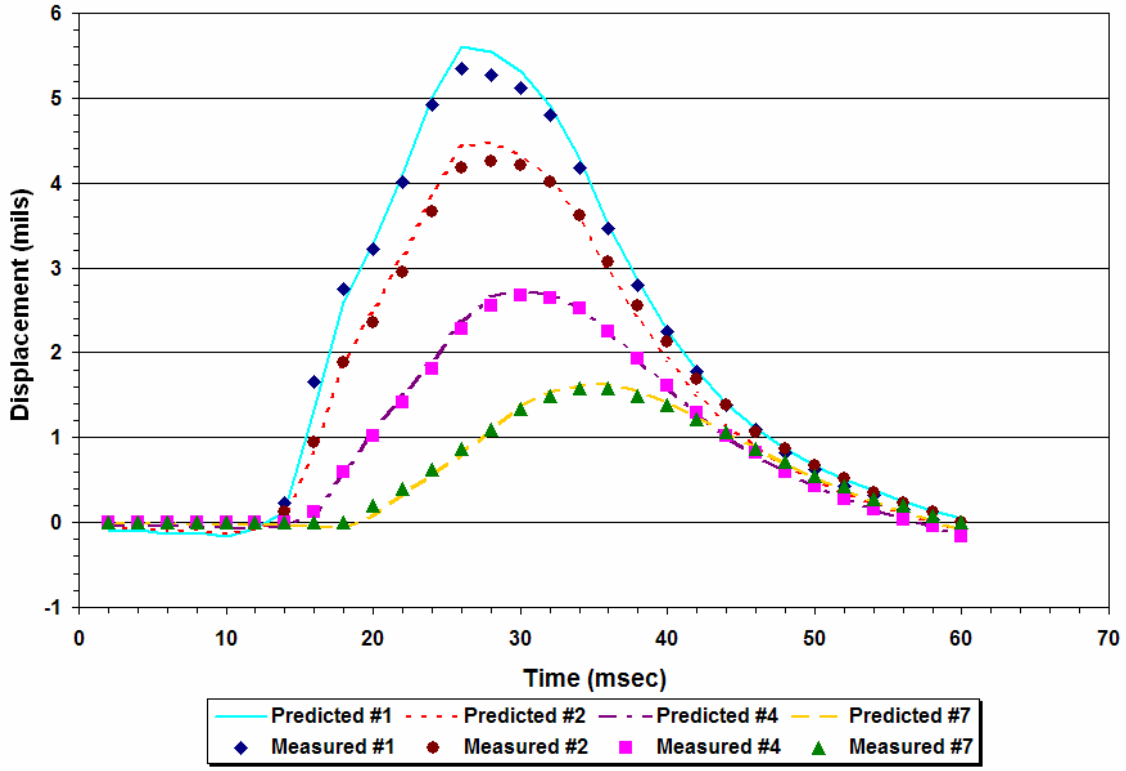

Figure D3. Comparison of Measured and Predicted FWD Displacement Histories on K6-29 (Data Collected in Feb 01).

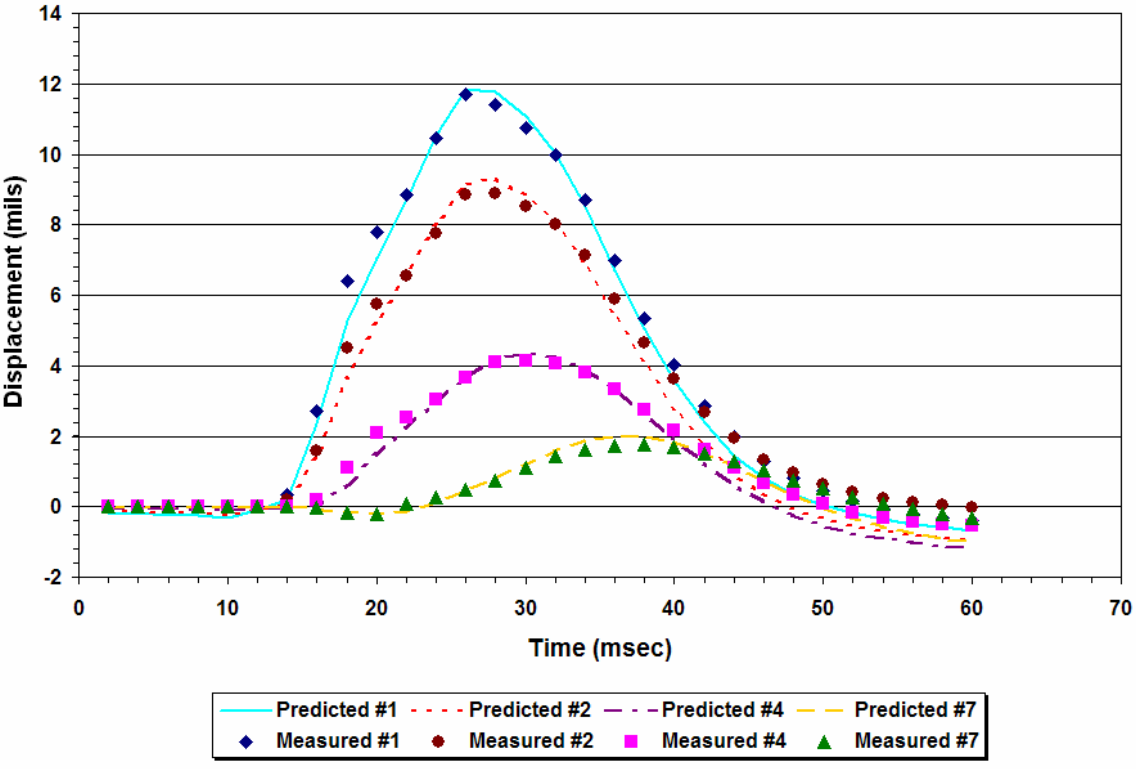

Figure D4. Comparison of Measured and Predicted FWD Displacement Histories on K6-35 (Data Collected in Feb 01).

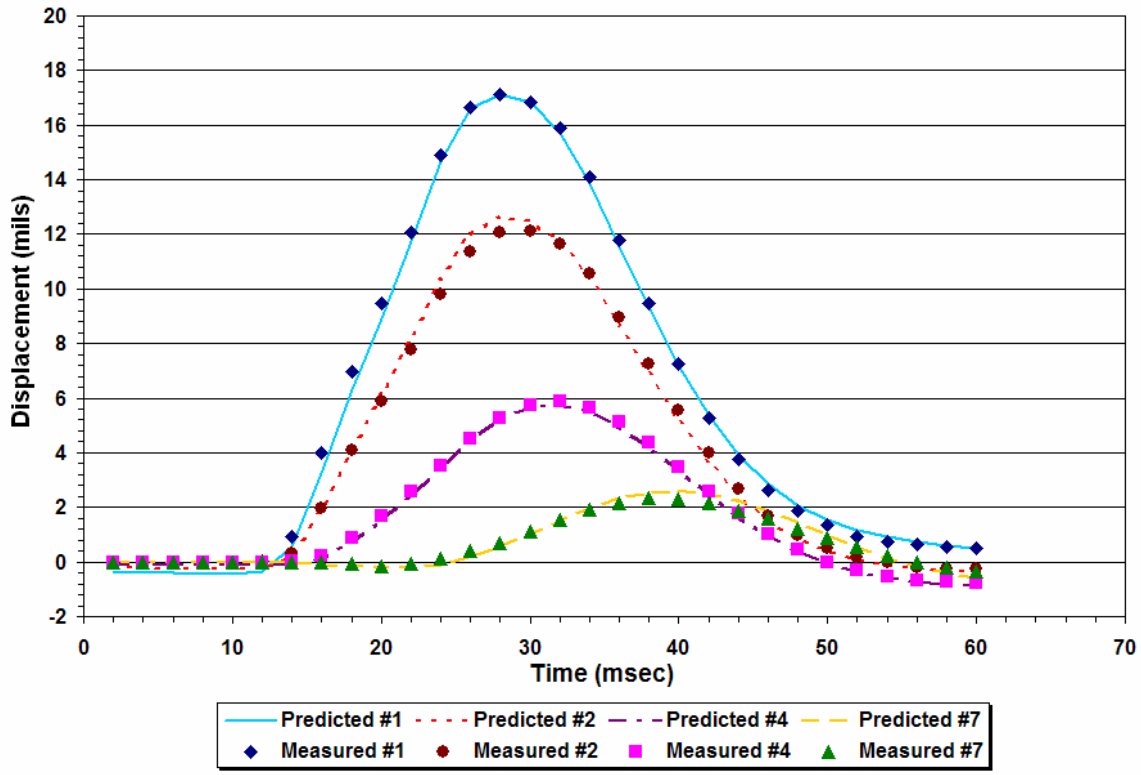

Figure D5. Comparison of Measured and Predicted FWD Displacement Histories on K6-48 (Data Collected in Feb 01).

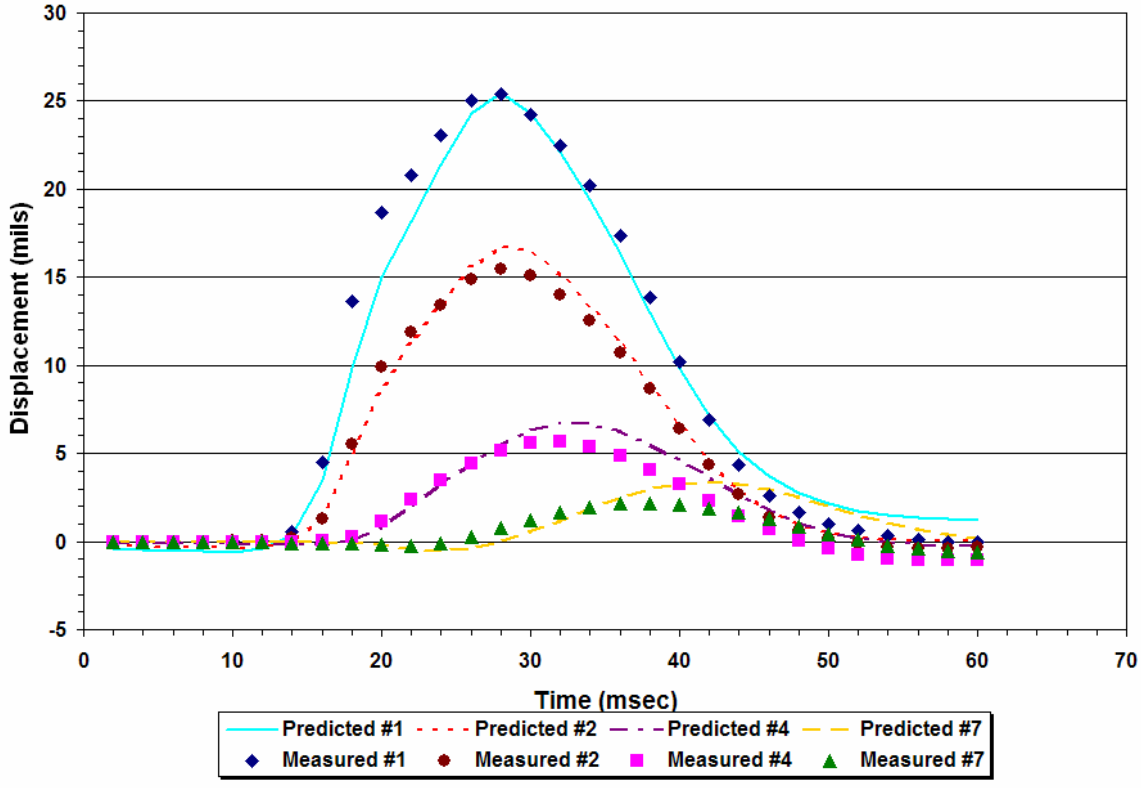

Figure D6. Comparison of Measured and Predicted FWD Displacement Histories on K6-1 (Data Collected in May 01).

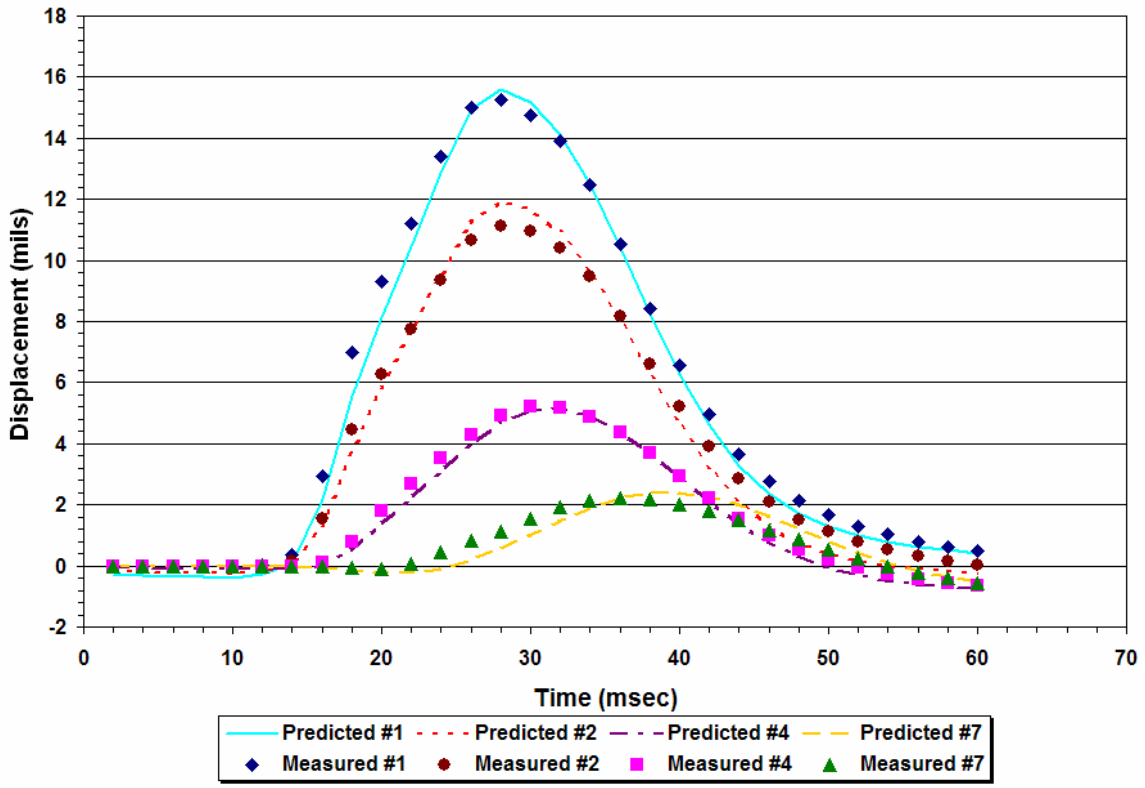

Figure D7. Comparison of Measured and Predicted FWD Displacement Histories on K6-4 (Data Collected in May 01).

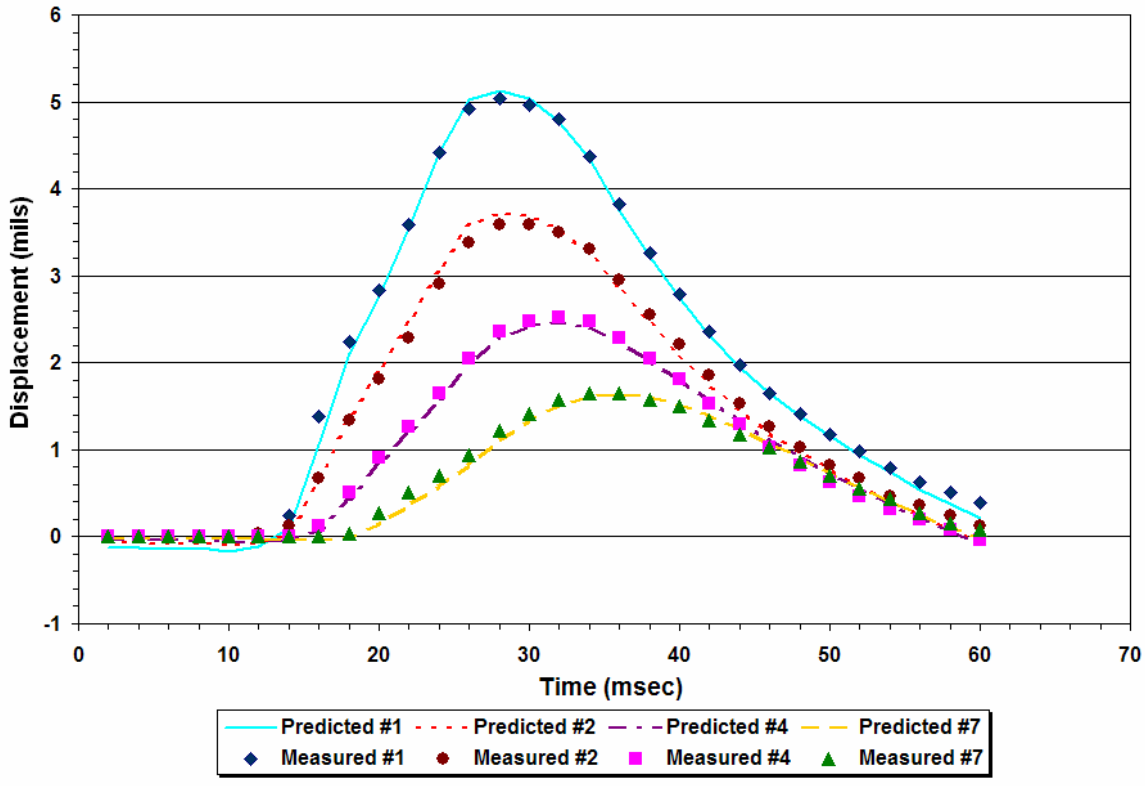

Figure D8. Comparison of Measured and Predicted FWD Displacement Histories on K6-11 (Data Collected in May 01).

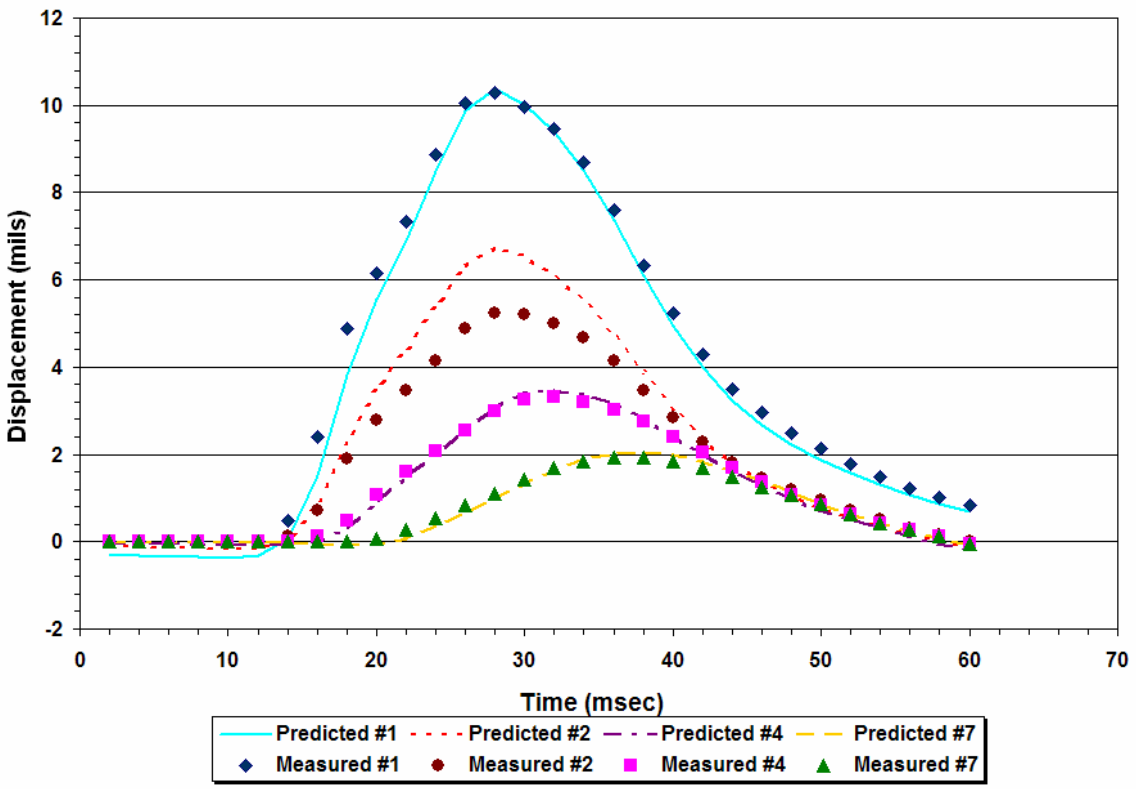

Figure D9. Comparison of Measured and Predicted FWD Displacement Histories on K6-23 (Data Collected in May 01).

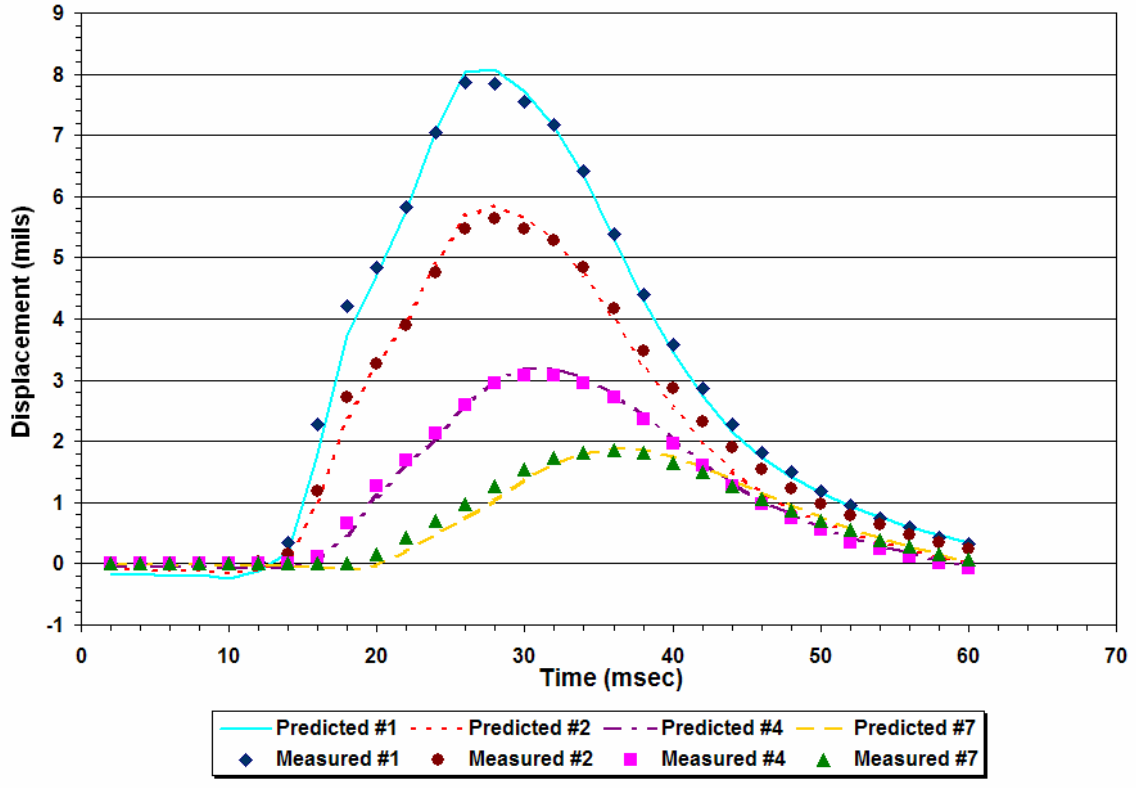

Figure D10. Comparison of Measured and Predicted FWD Displacement Histories on K6-29 (Data Collected in May 01).

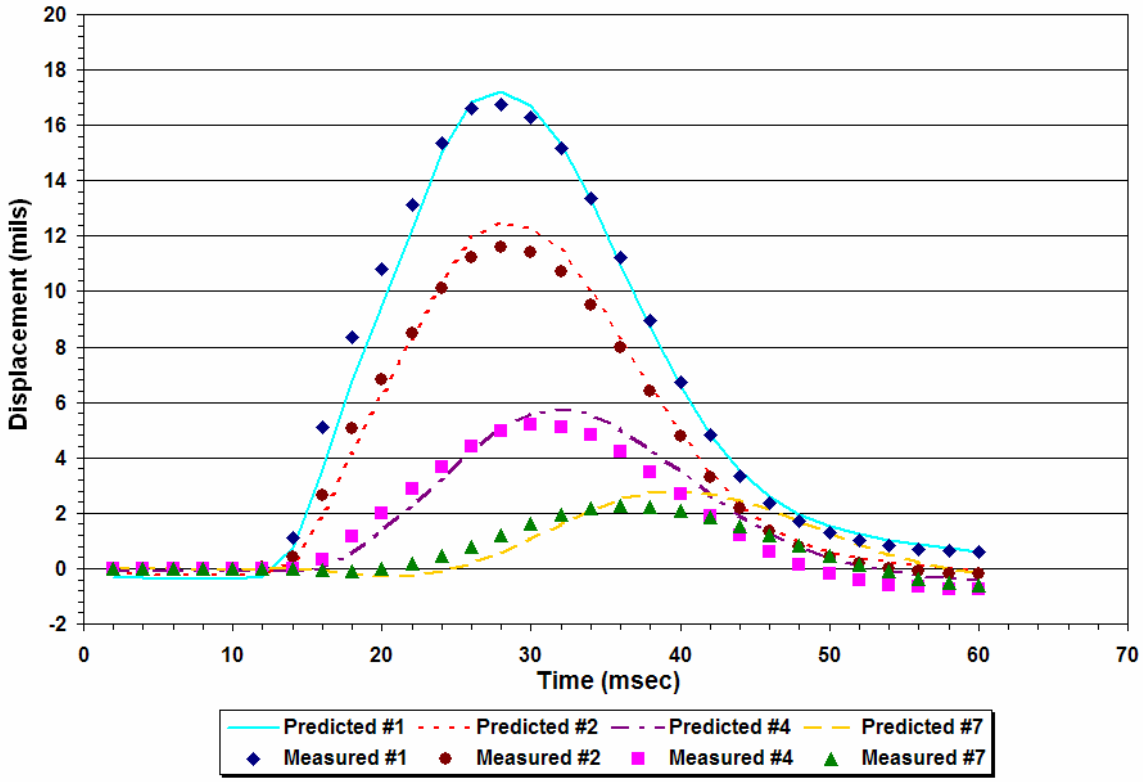

Figure D11. Comparison of Measured and Predicted FWD Displacement Histories on K6-1 (Data Collected in July 01).

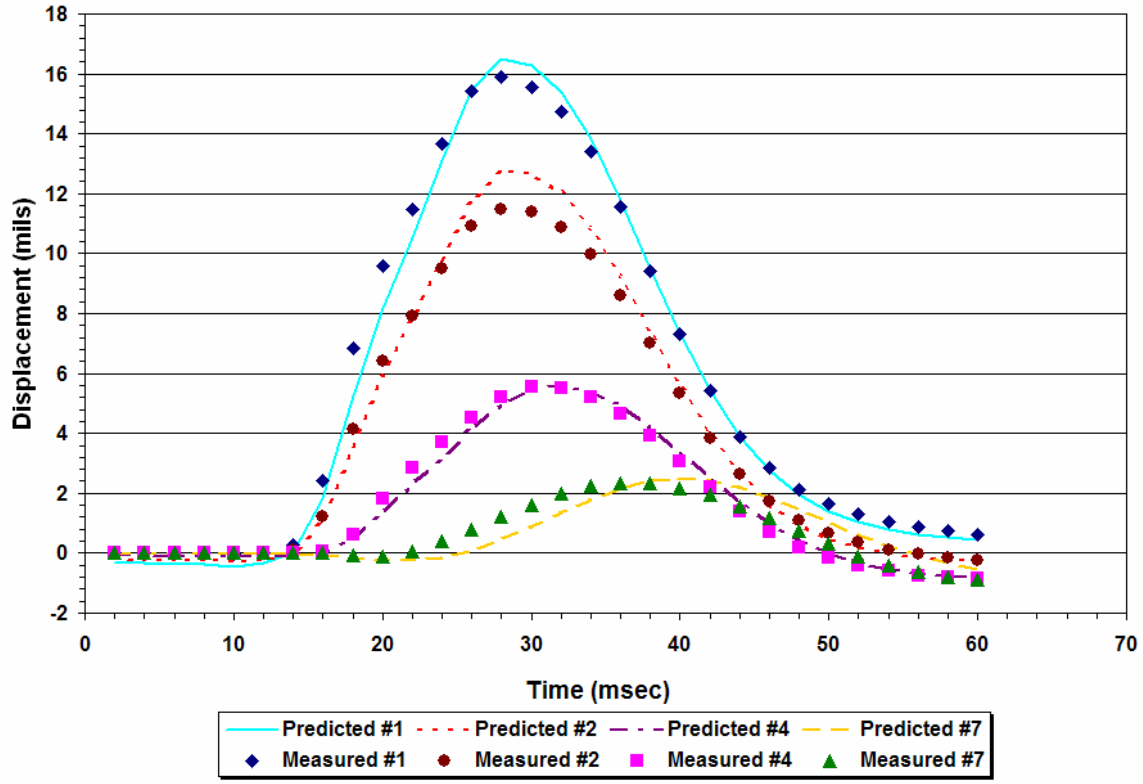

Figure D12. Comparison of Measured and Predicted FWD Displacement Histories on K6-4 (Data Collected in July 01).

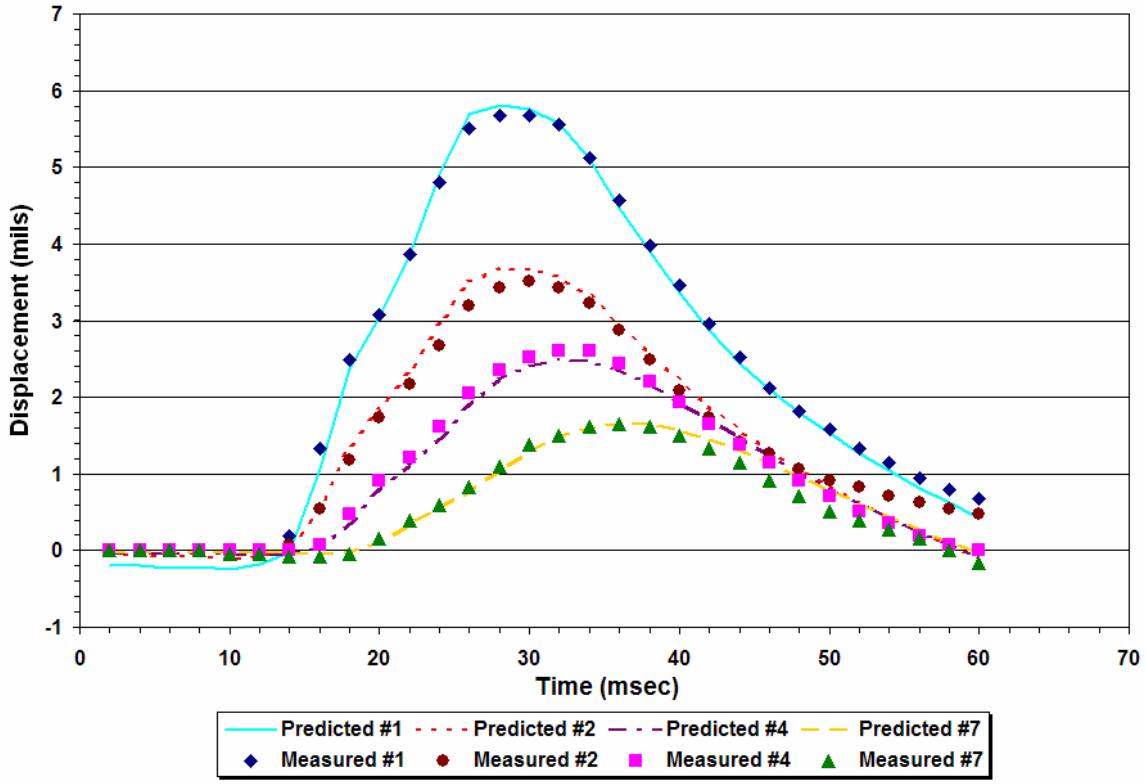

Figure D13. Comparison of Measured and Predicted FWD Displacement Histories on K6-11 (Data Collected in July 01).

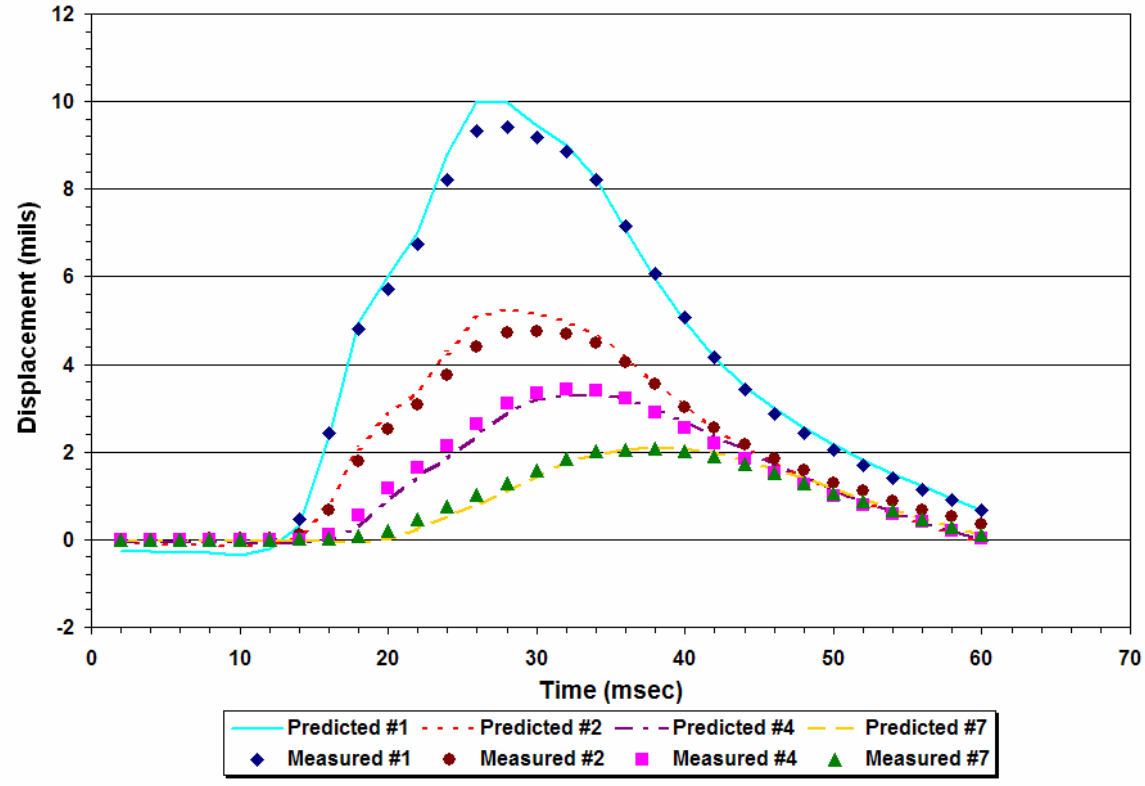

Figure D14. Comparison of Measured and Predicted FWD Displacement Histories on K6-23 (Data Collected in July 01).

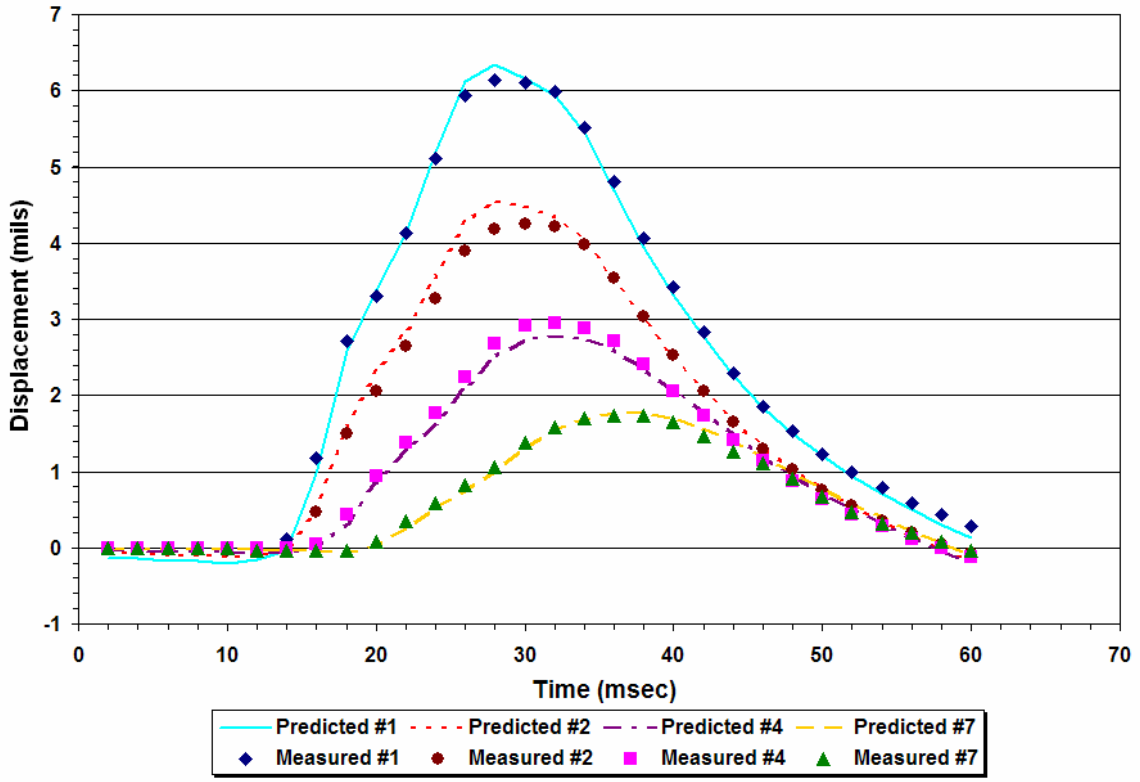

Figure D15. Comparison of Measured and Predicted FWD Displacement Histories on K6-29 (Data Collected in July 01).

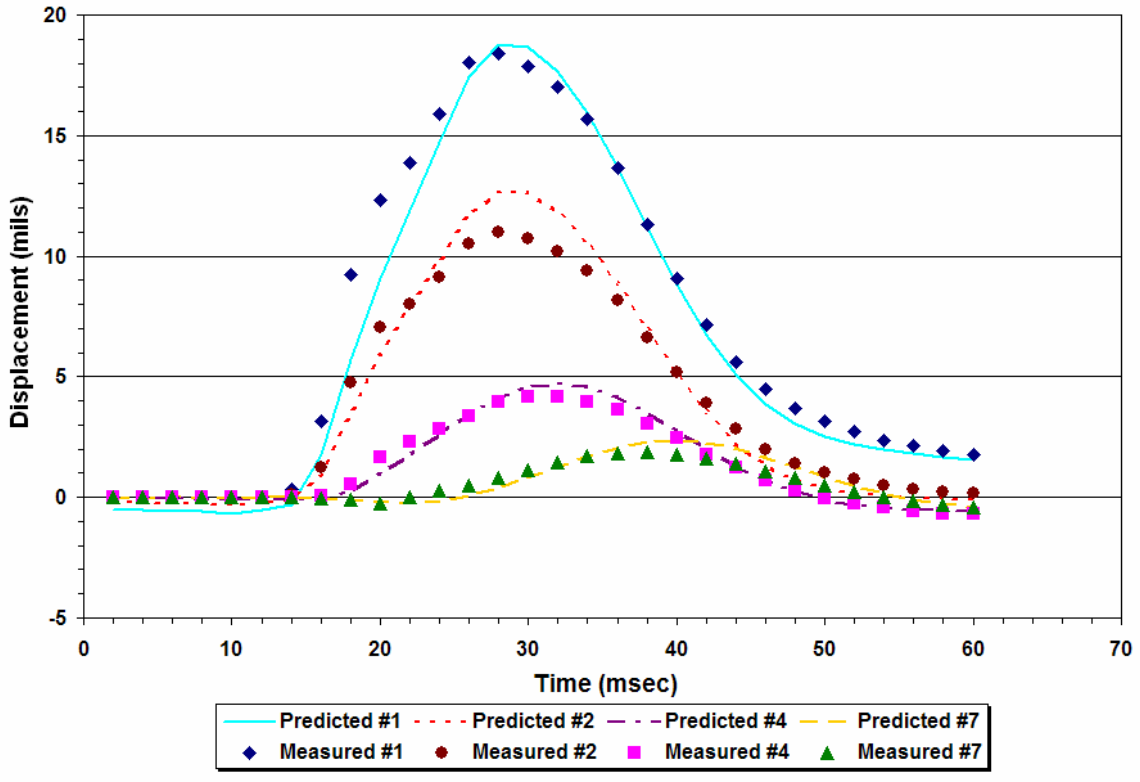

Figure D16. Comparison of Measured and Predicted FWD Displacement Histories on K6-35 (Data Collected in July 01).

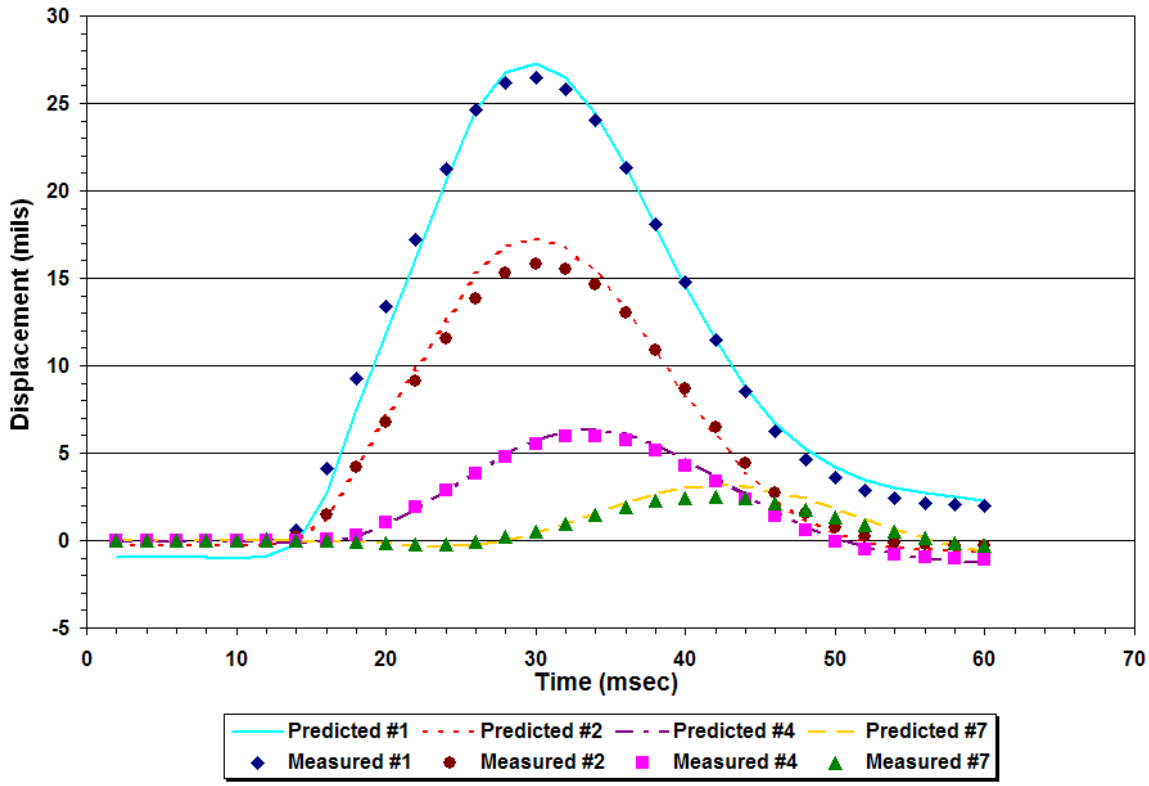

Figure D17. Comparison of Measured and Predicted FWD Displacement Histories on K6-48 (Data Collected in July 01).

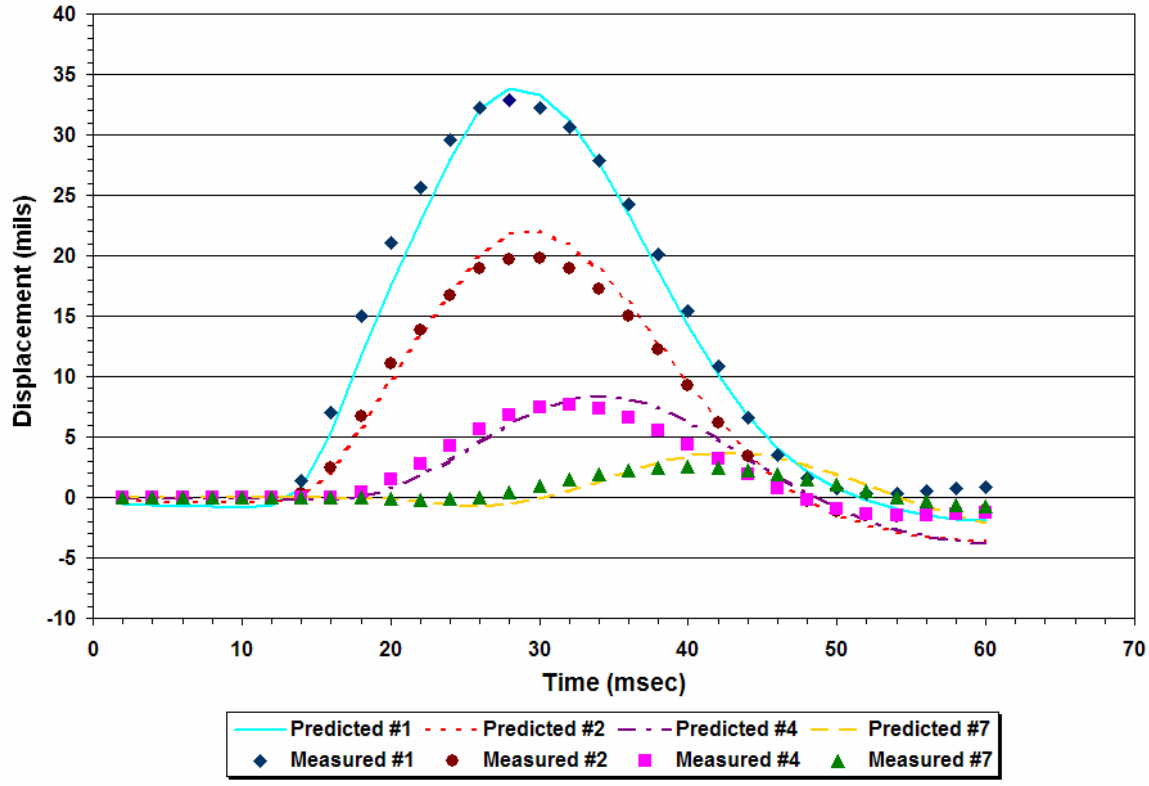

Figure D18. Comparison of Measured and Predicted FWD Displacement Histories on K6-1 (Data Collected in Aug 01).

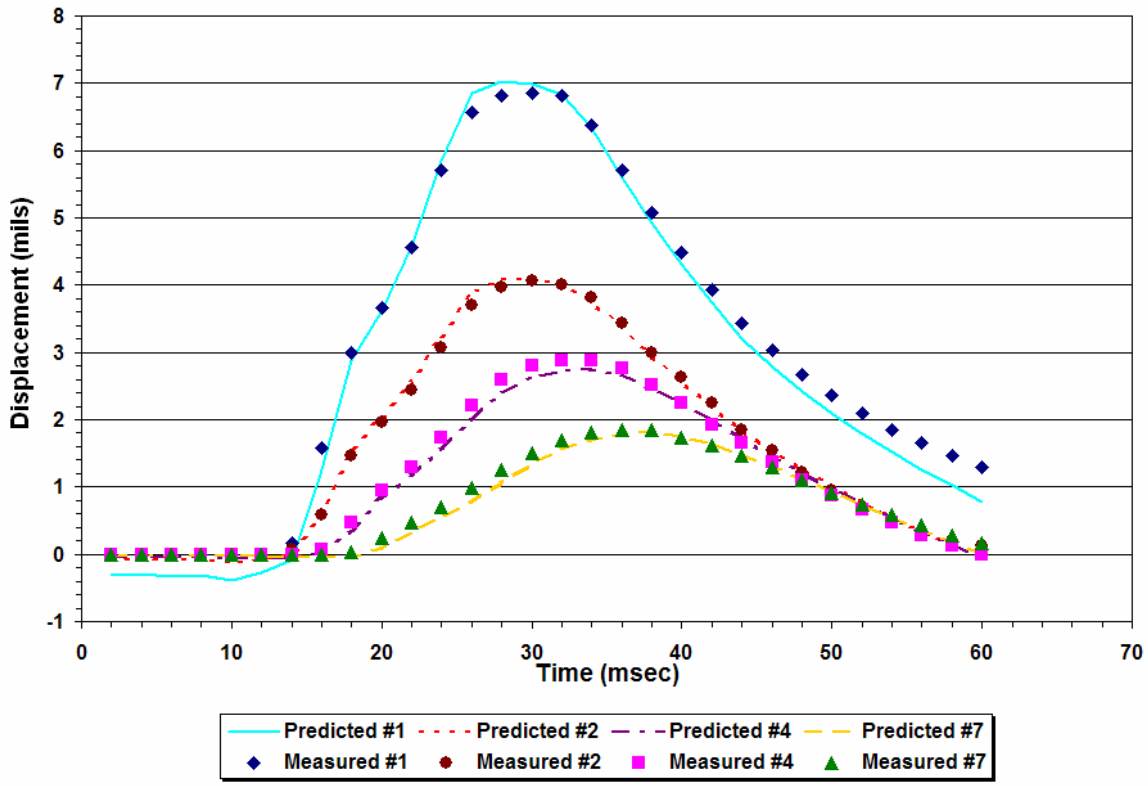

Figure D19. Comparison of Measured and Predicted FWD Displacement Histories on K6-11 (Data Collected in Aug 01).

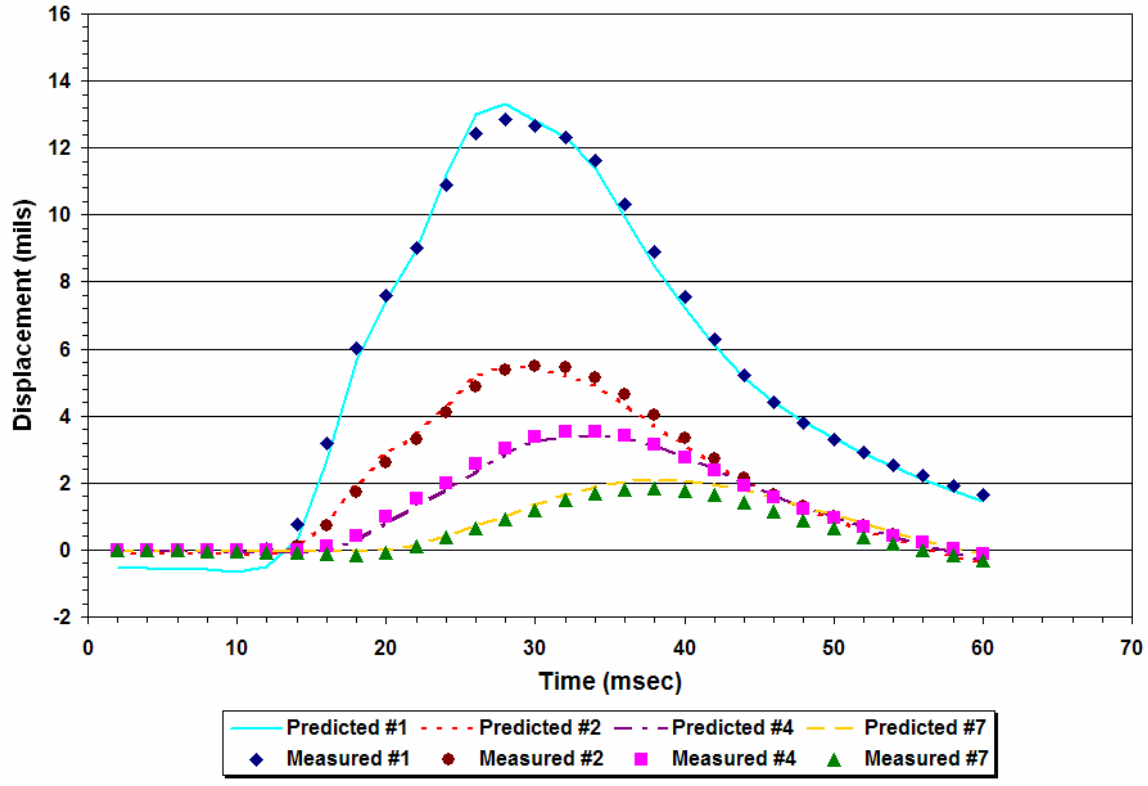

Figure D20. Comparison of Measured and Predicted FWD Displacement Histories on K6-23 (Data Collected in Aug 01).

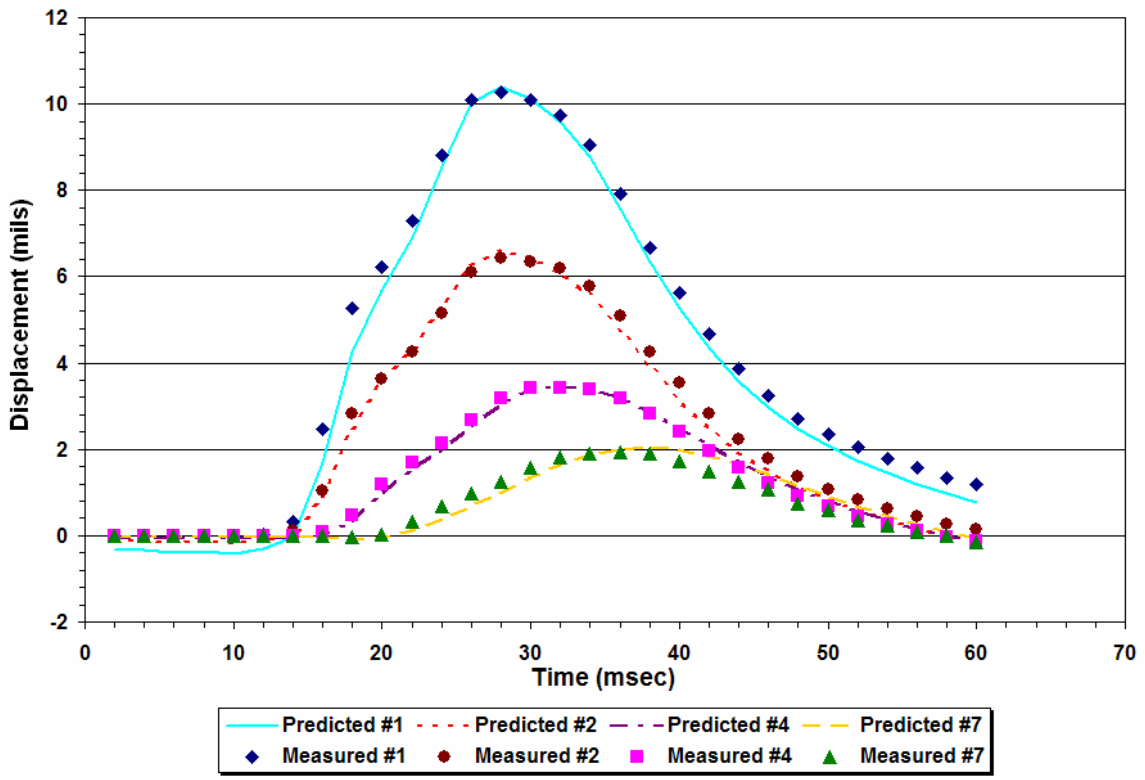

Figure D21. Comparison of Measured and Predicted FWD Displacement Histories on K6--29 (Data Collected in Aug 01).

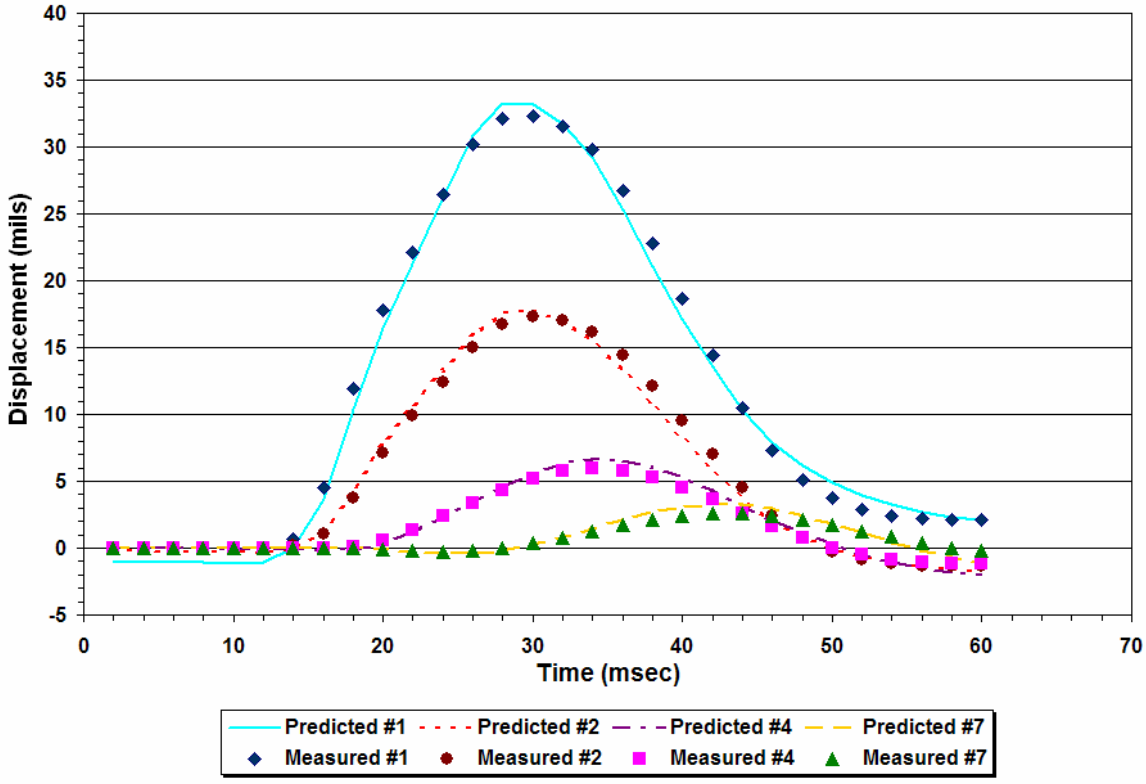

Figure D22. Comparison of Measured and Predicted FWD Displacement Histories on K6-48 (Data Collected in Aug 01).

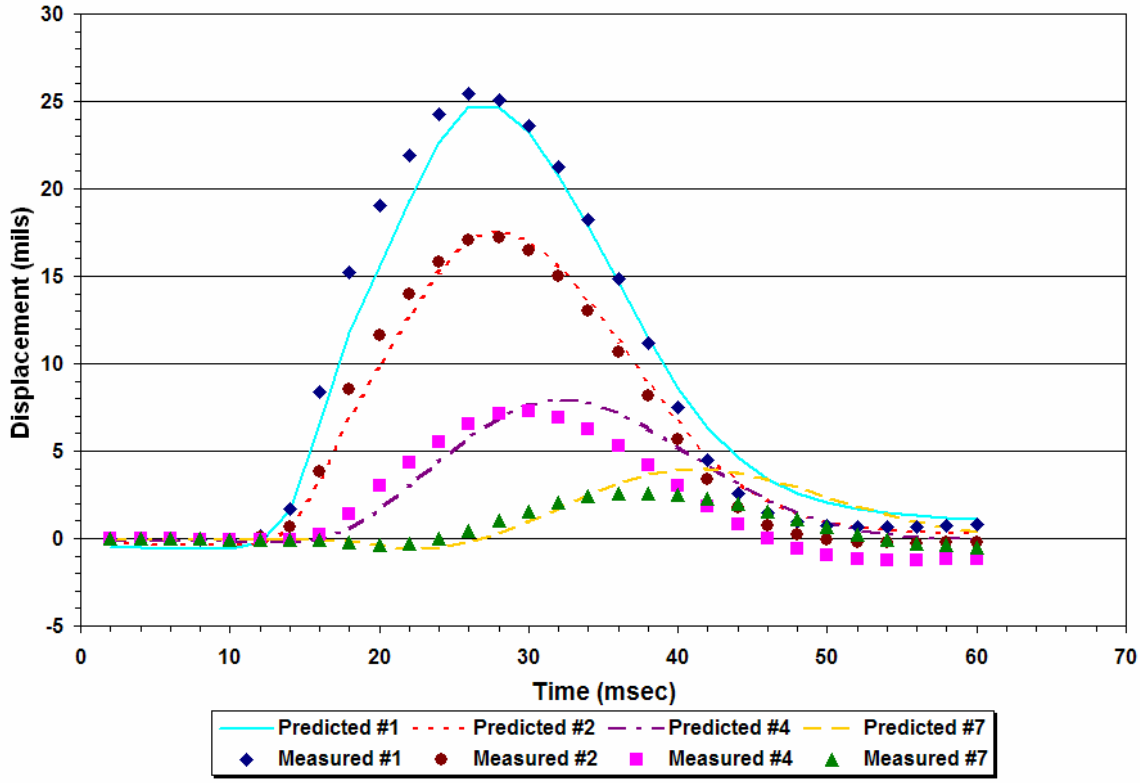

Figure D23. Comparison of Measured and Predicted FWD Displacement Histories on K6-1 (Data Collected in Mar 02).

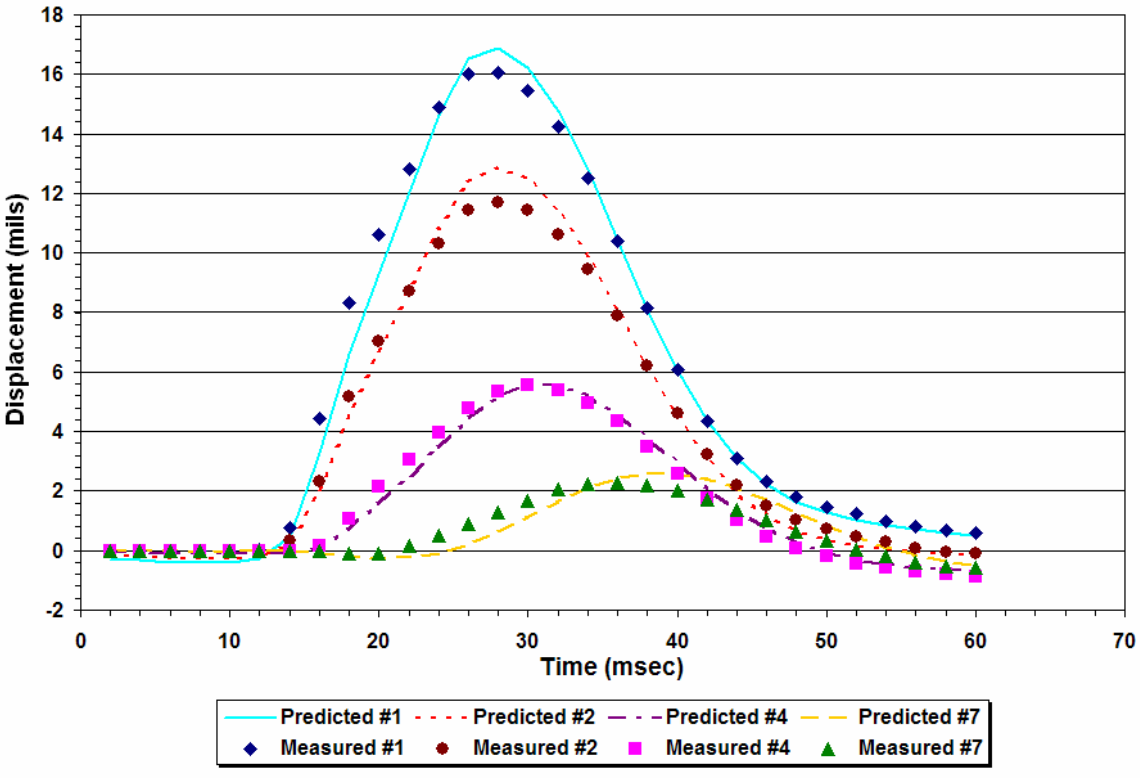

Figure D24. Comparison of Measured and Predicted FWD Displacement Histories on K6-4 (Data Collected in Mar 02).

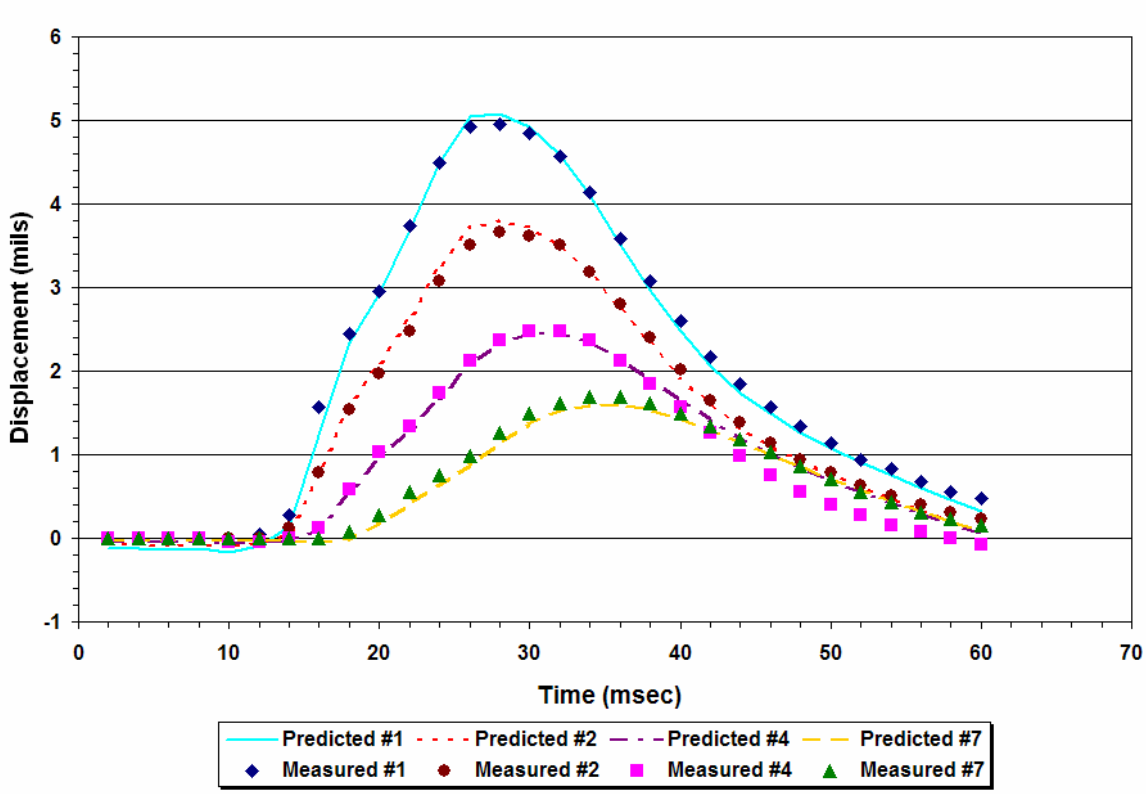

Figure D25. Comparison of Measured and Predicted FWD Displacement Histories on K6-11 (Data Collected in Mar 02).

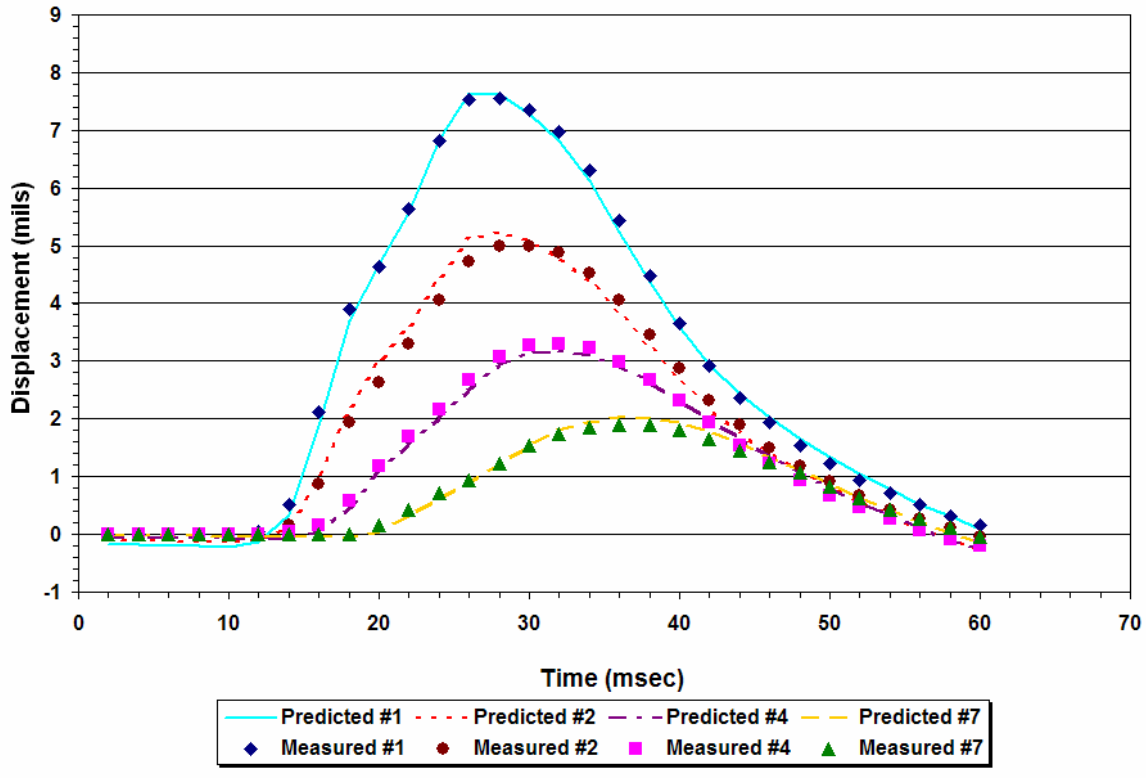

Figure D26. Comparison of Measured and Predicted FWD Displacement Histories on K6-23 (Data Collected in Mar 02).

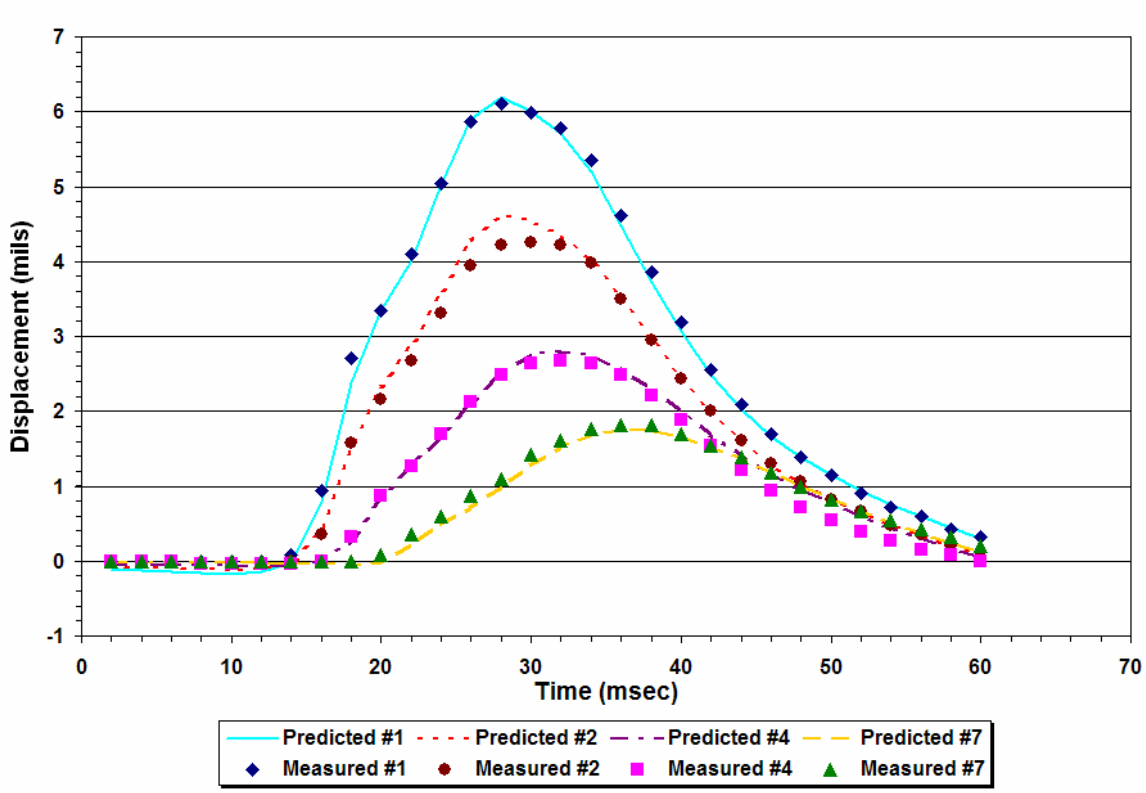

Figure D27. Comparison of Measured and Predicted FWD Displacement Histories on K6-29 (Data Collected in Mar 02).

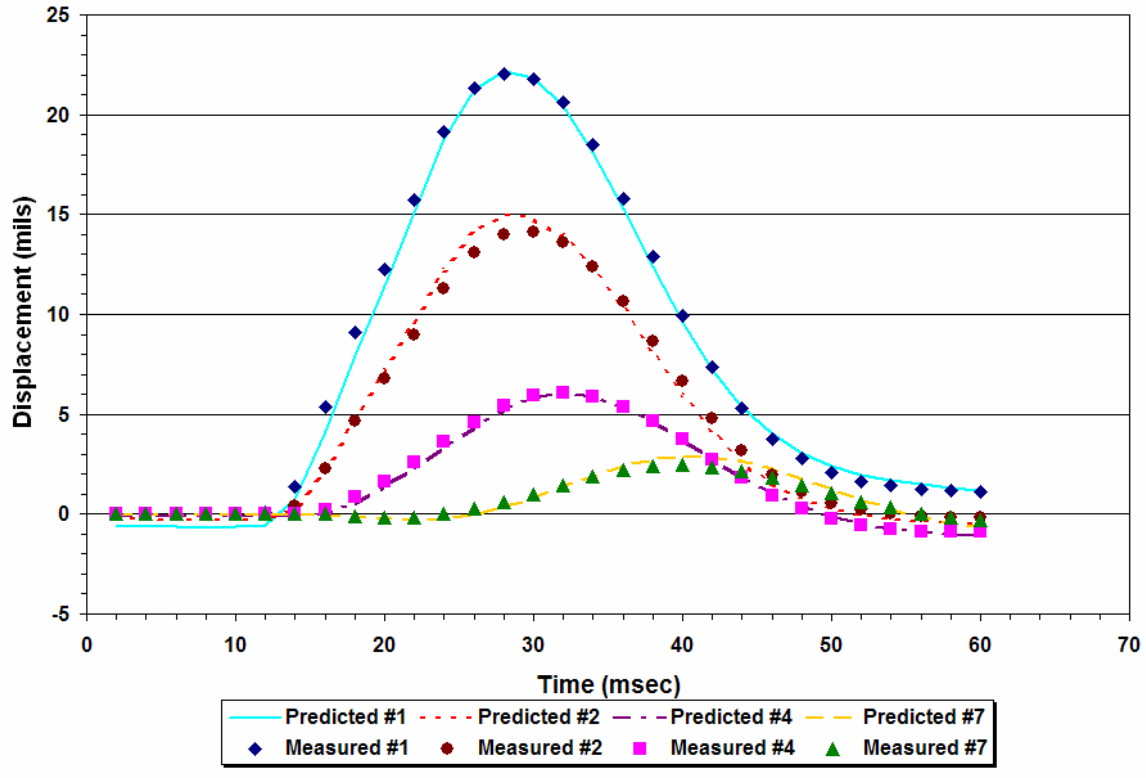

Figure D28. Comparison of Measured and Predicted FWD Displacement Histories on K6-48 (Data Collected in Mar 02).

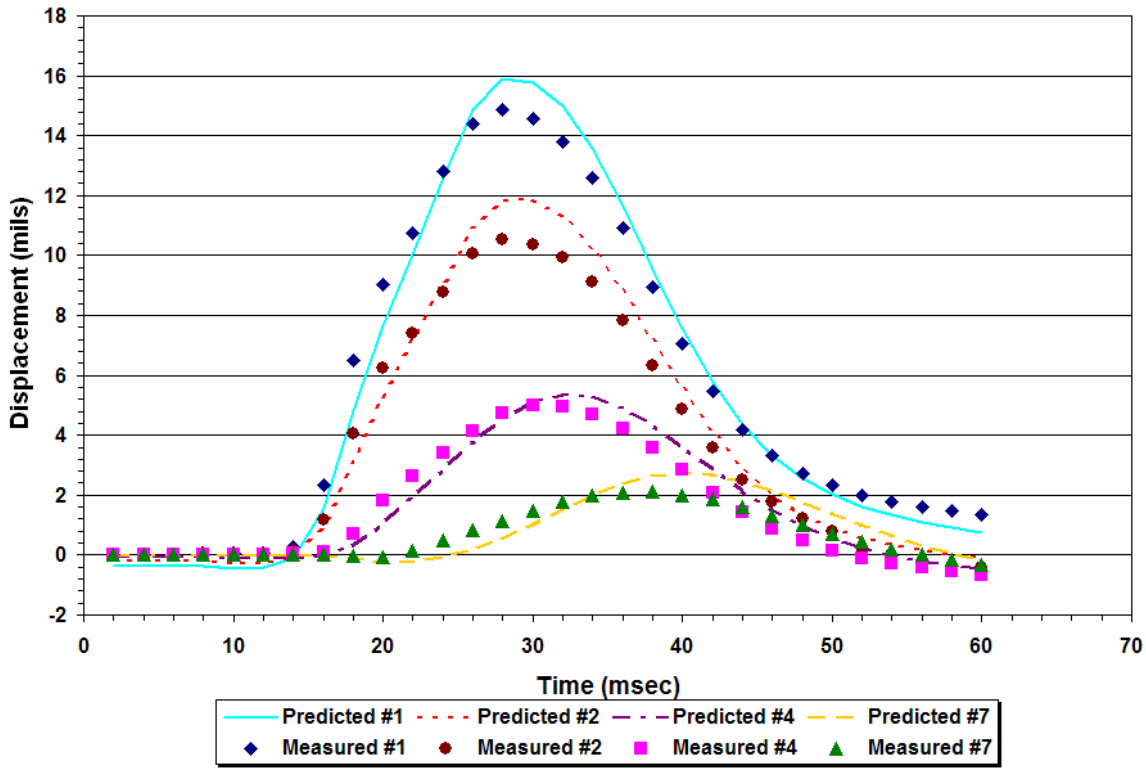

Figure D29. Comparison of Measured and Predicted FWD Displacement Histories on K6-4 (Data Collected in July 02).

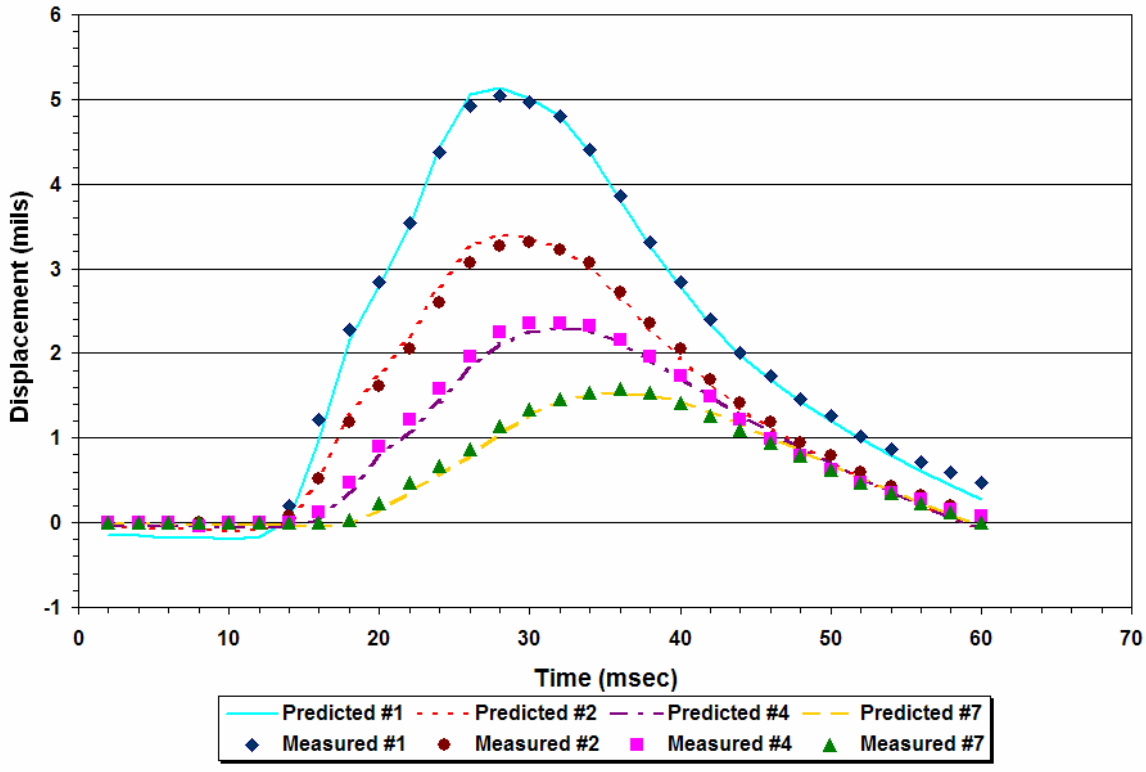

Figure D30. Comparison of Measured and Predicted FWD Displacement Histories on K6-11 (Data Collected in July 02).

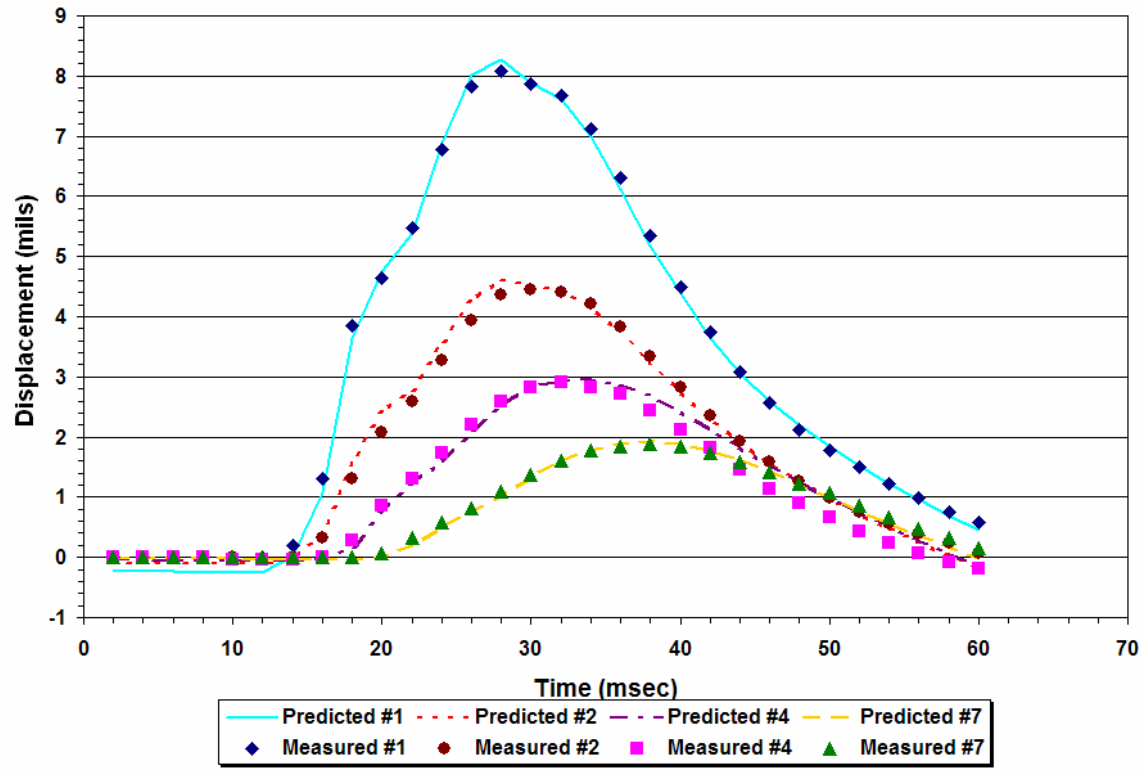

Figure D31. Comparison of Measured and Predicted FWD Displacement Histories on K6-23 (Data Collected in July 02).

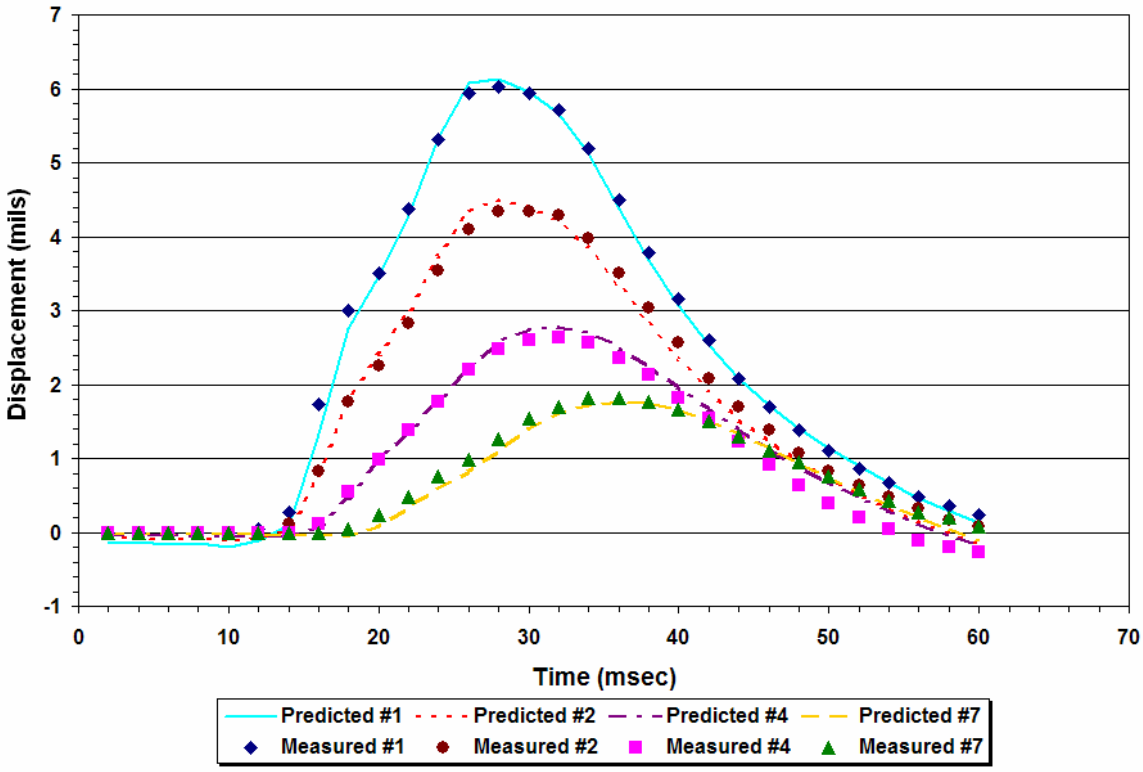

Figure D32. Comparison of Measured and Predicted FWD Displacement Histories on K6-29 (Data Collected in July 02).

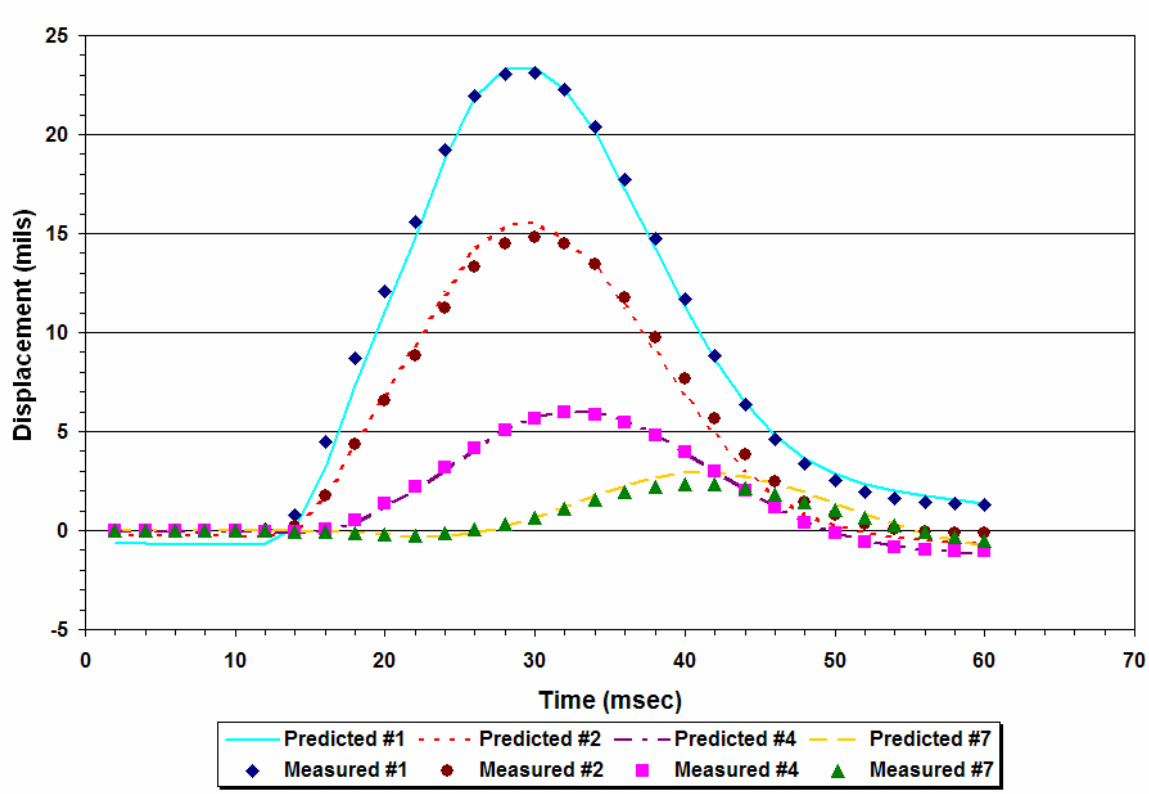

Figure D33. Comparison of Measured and Predicted FWD Displacement Histories on K6-48 (Data Collected in July 02).

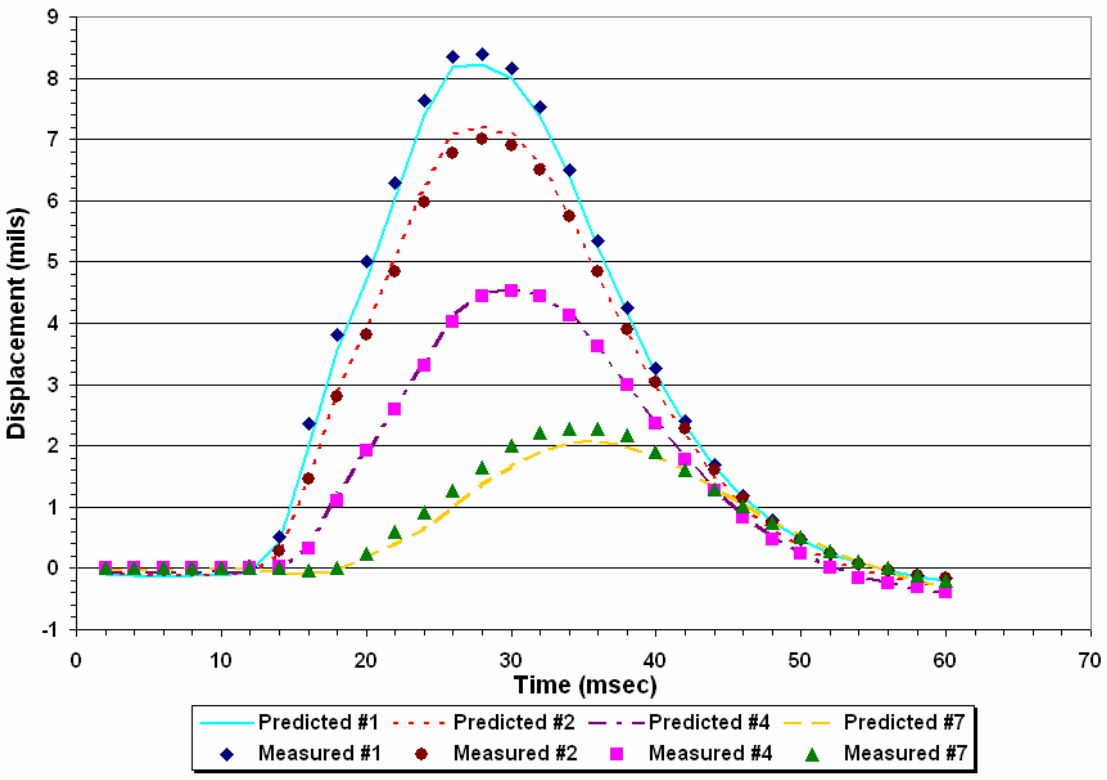

Figure D34. Comparison of Measured and Predicted FWD Displacement Histories on K7-9 (Data Collected in Feb 01).

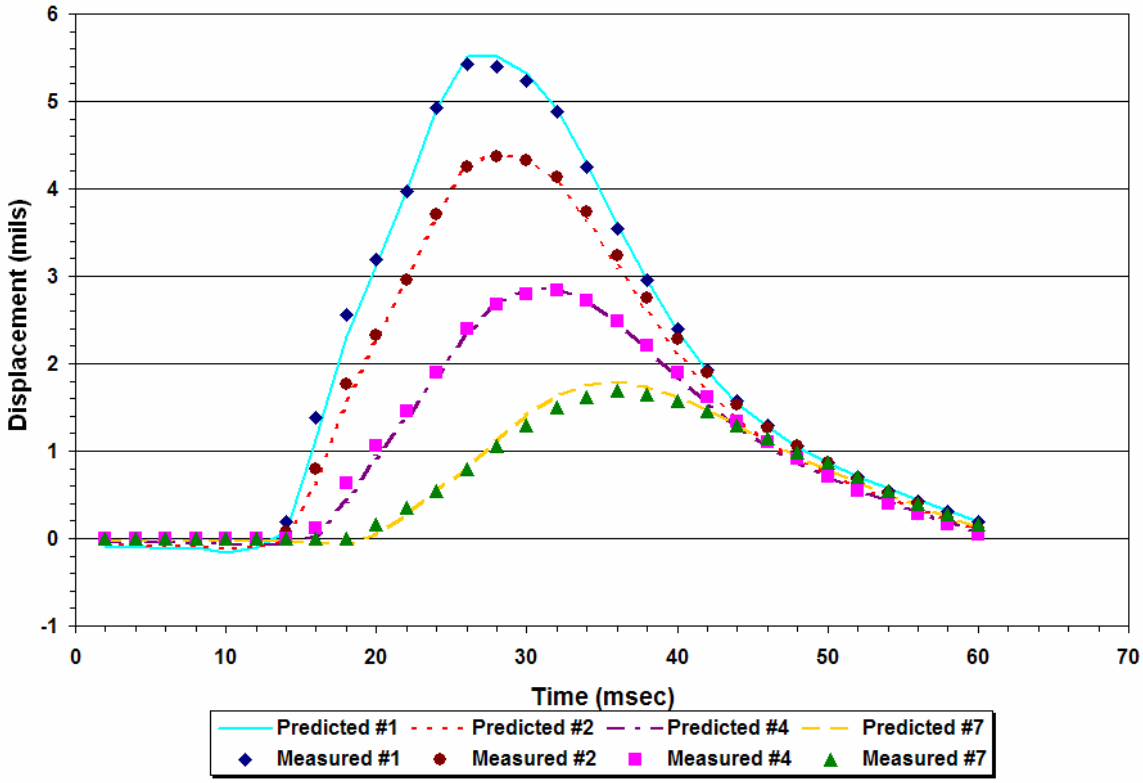

Figure D35. Comparison of Measured and Predicted FWD Displacement Histories on K7-20 (Data Collected in Feb 01).

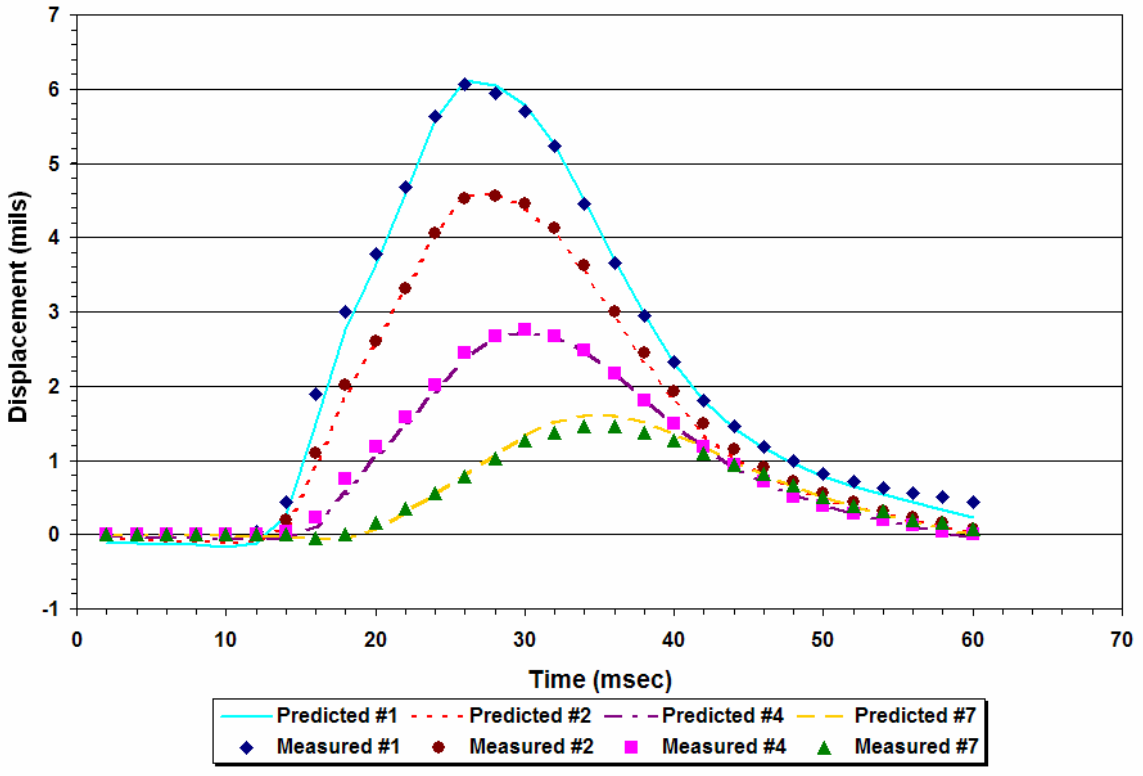

Figure D36. Comparison of Measured and Predicted FWD Displacement Histories on K7-37 (Data Collected in Feb 01).

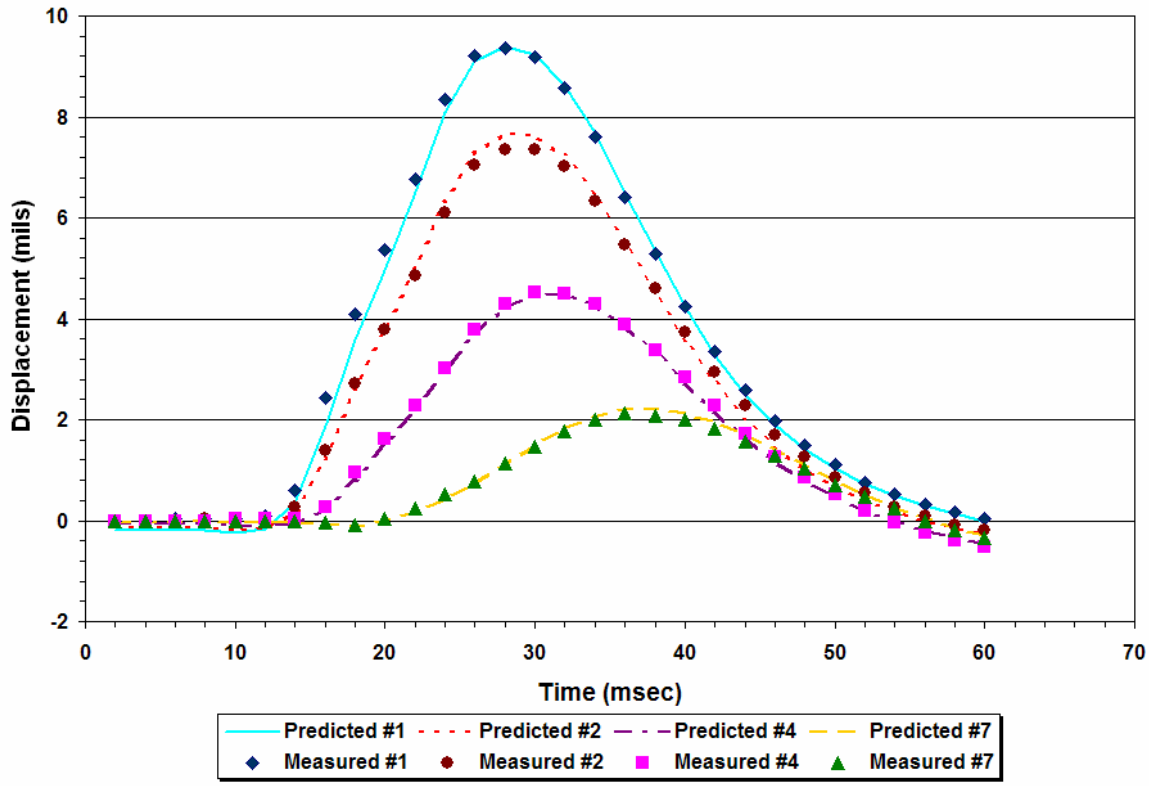

Figure D37. Comparison of Measured and Predicted FWD Displacement Histories on K7-40 (Data Collected in Feb 01).

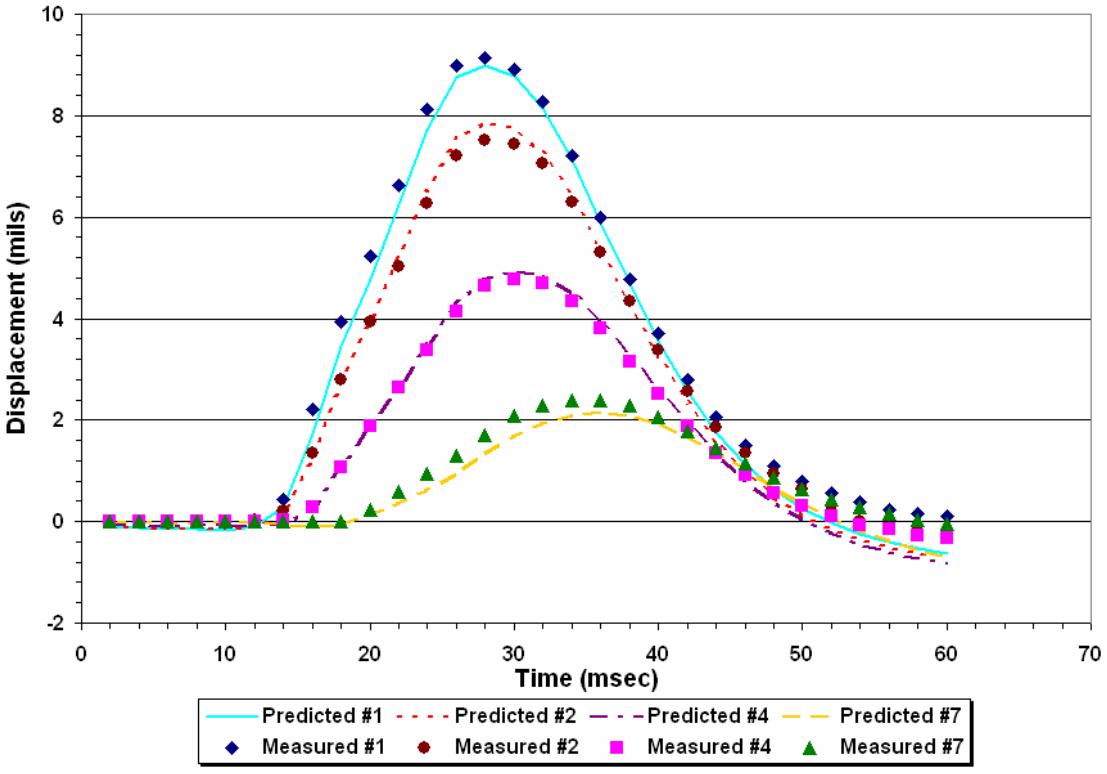

Figure D38. Comparison of Measured and Predicted FWD Displacement Histories on K7-9 (Data Collected in May 01).

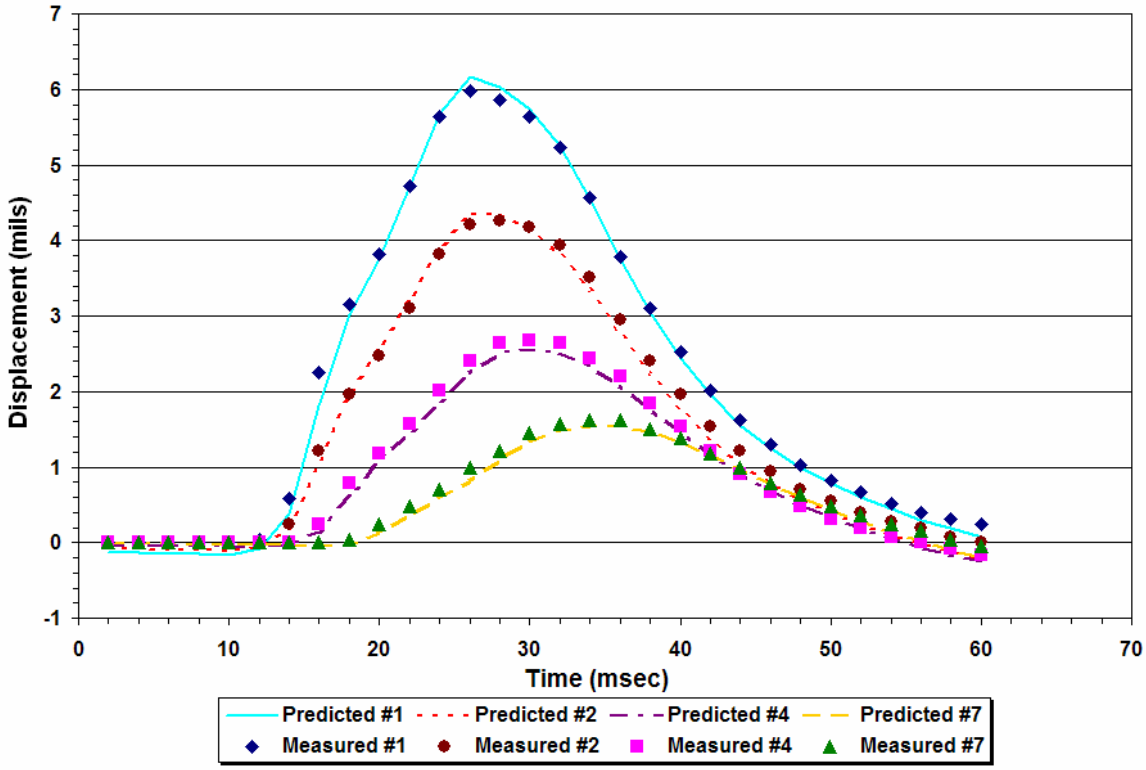

Figure D39. Comparison of Measured and Predicted FWD Displacement Histories on K7-11 (Data Collected in May 01).

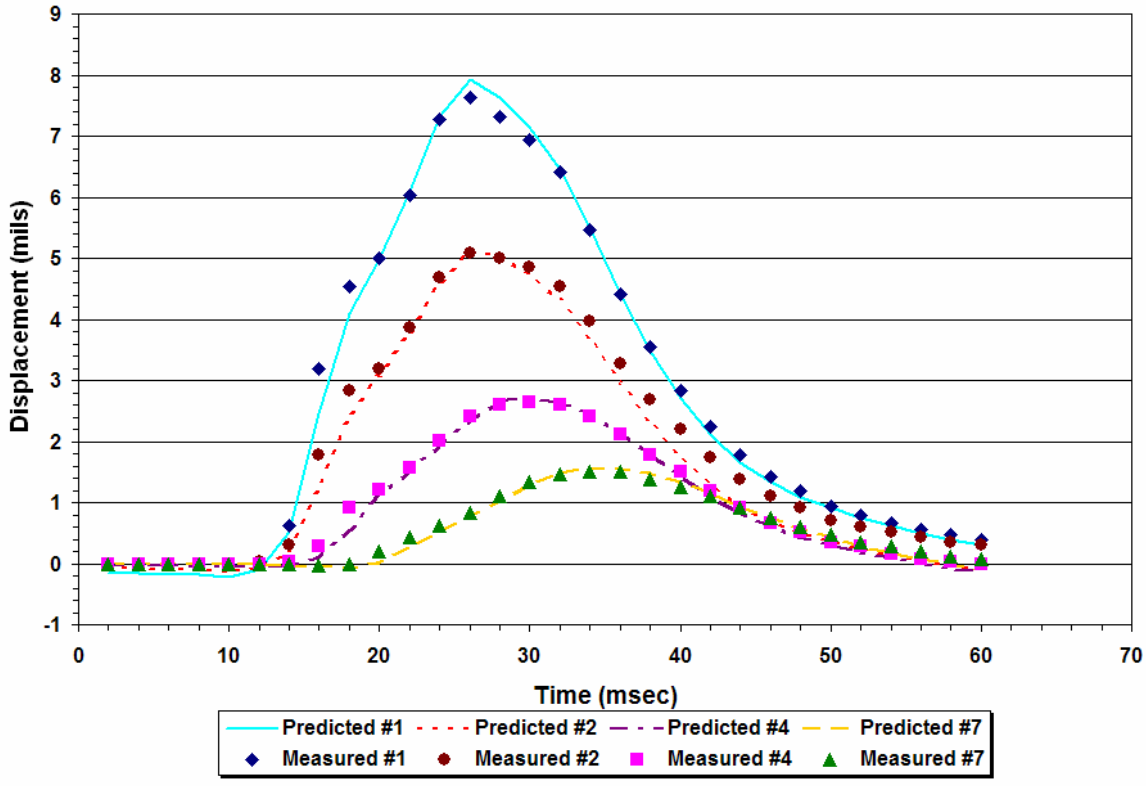

Figure D40. Comparison of Measured and Predicted FWD Displacement Histories on K7-15 (Data Collected in May 01).

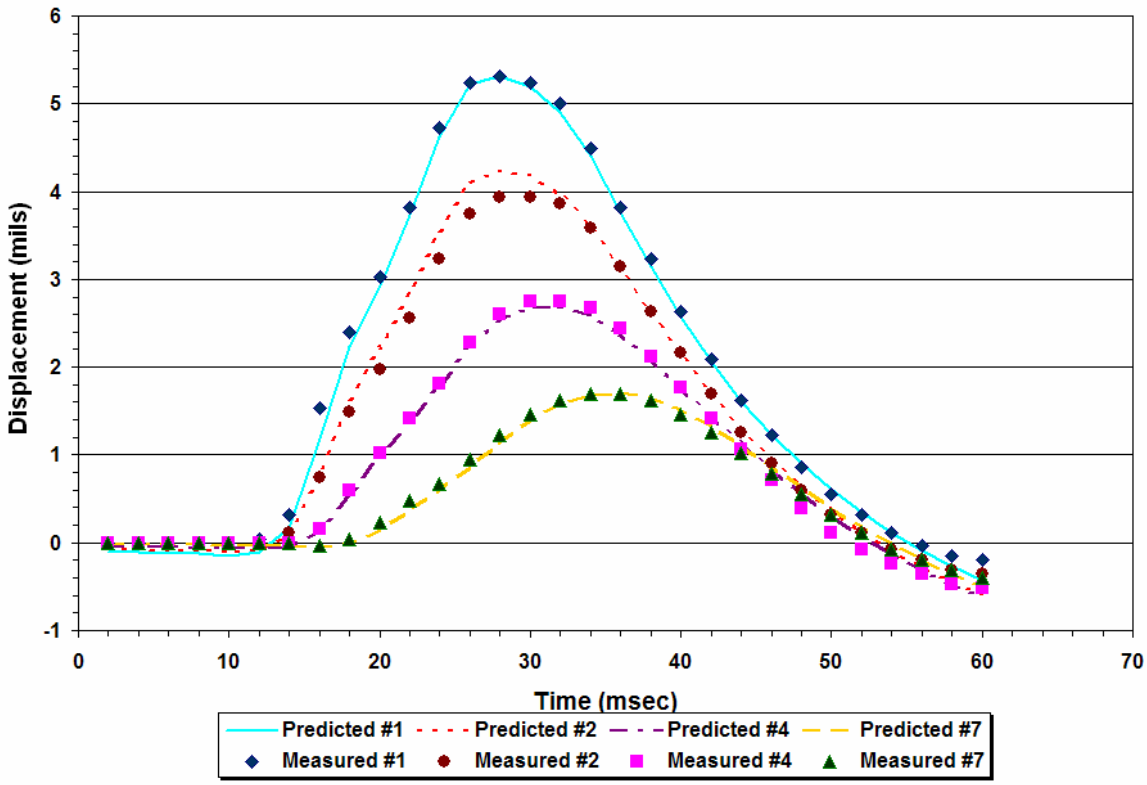

Figure D41. Comparison of Measured and Predicted FWD Displacement Histories on K7-31 (Data Collected in May 01).

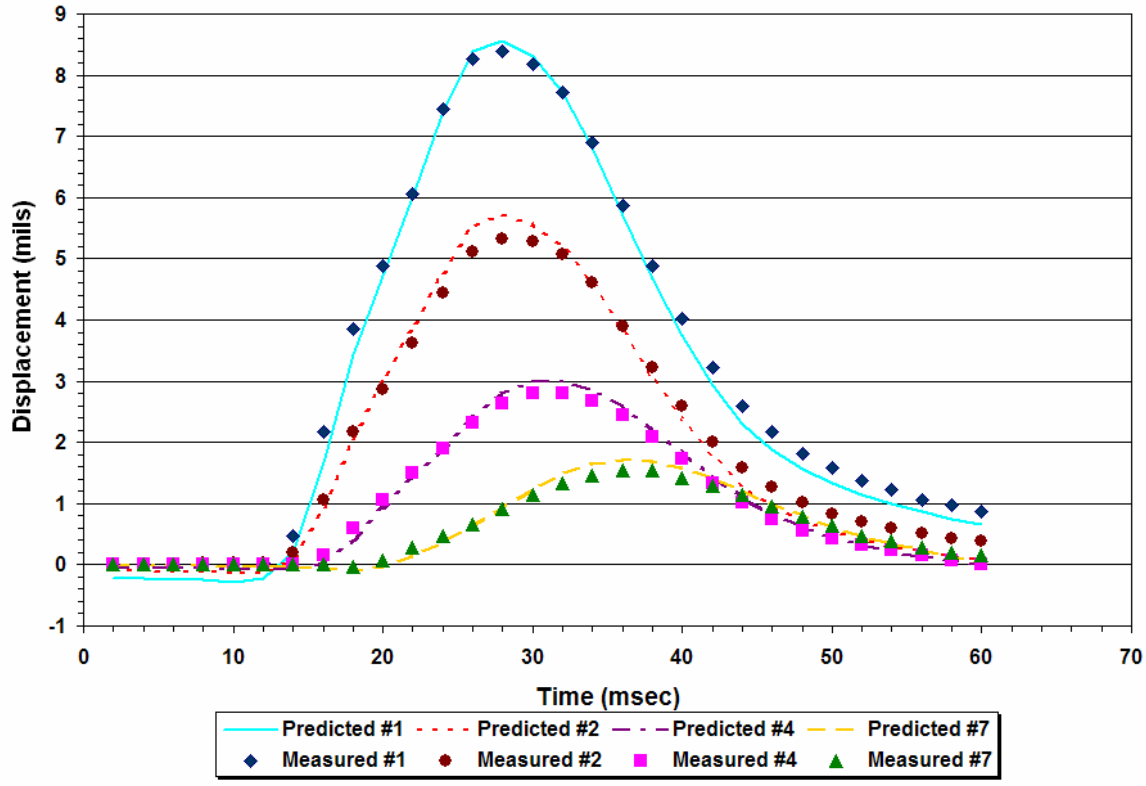

Figure D42. Comparison of Measured and Predicted FWD Displacement Histories on K7-37 (Data Collected in May 01).

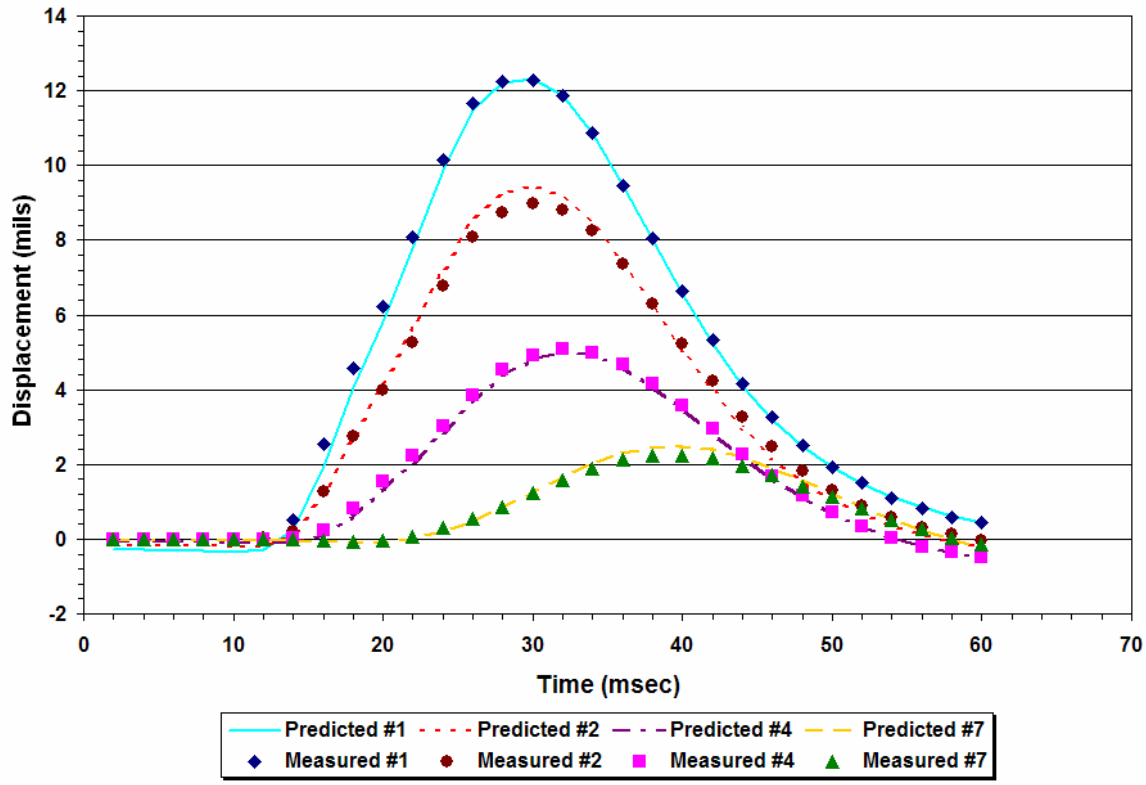

Figure D43. Comparison of Measured and Predicted FWD Displacement Histories on K7-40 (Data Collected in May 01).

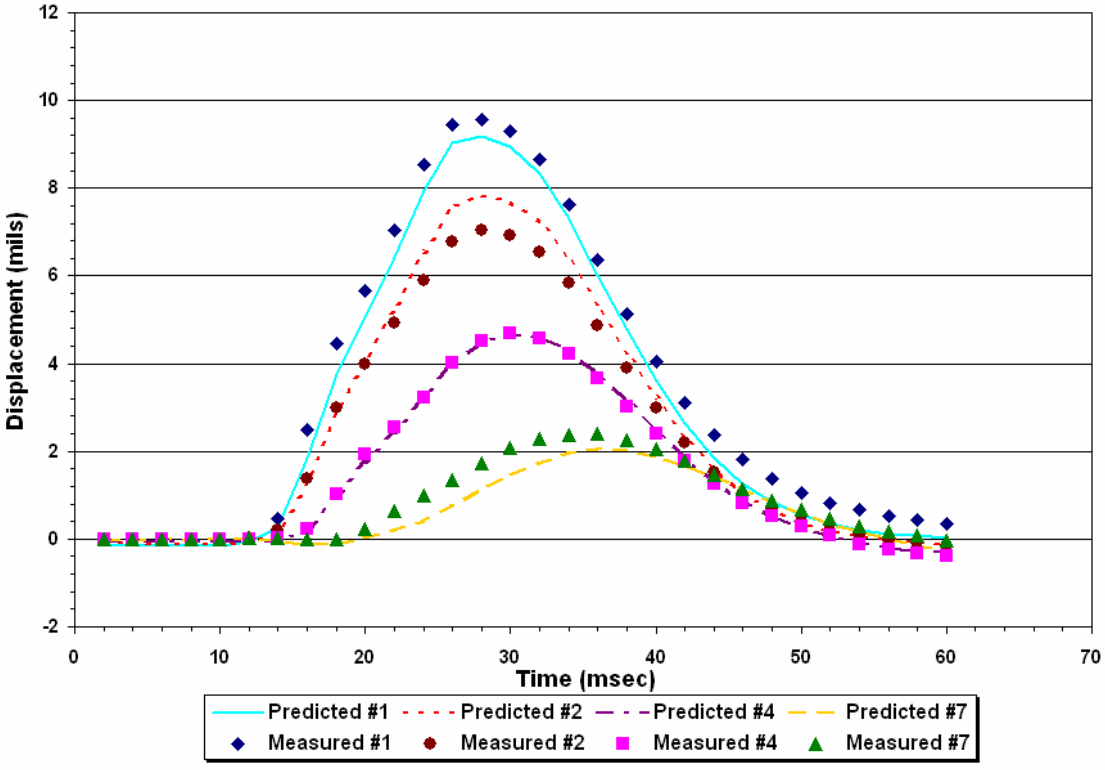

Figure D44. Comparison of Measured and Predicted FWD Displacement Histories on K7-9 (Data Collected in Aug 01).

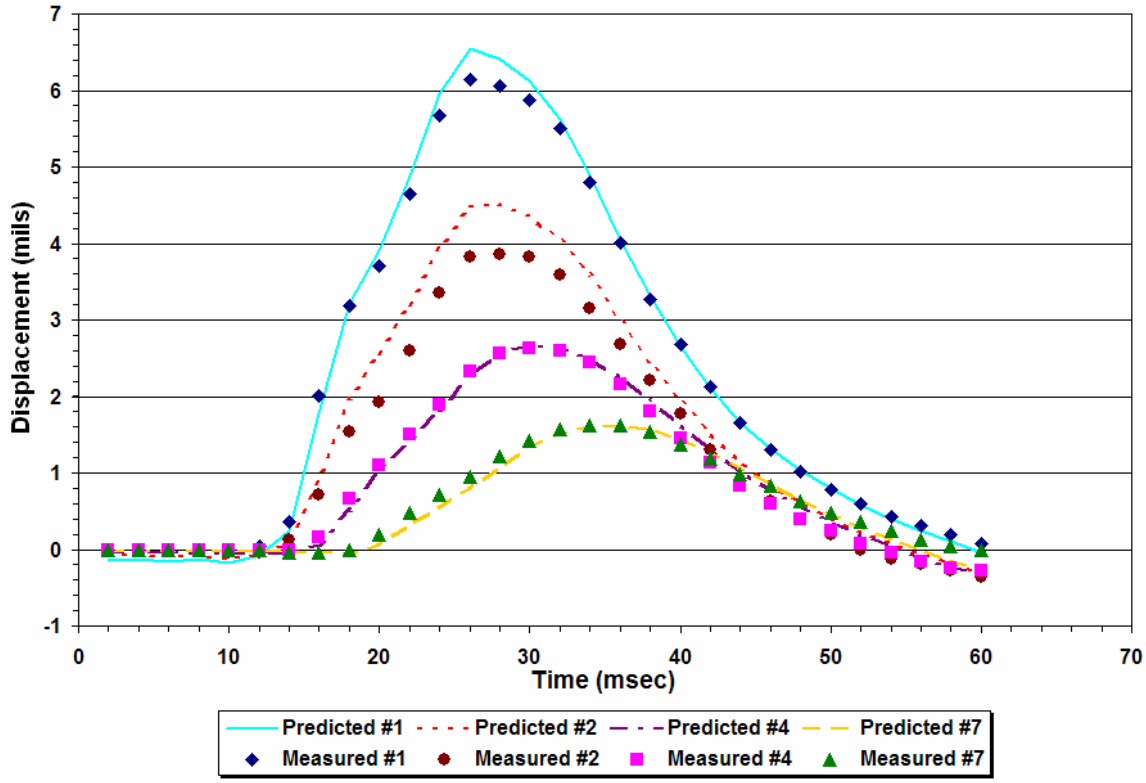

Figure D45. Comparison of Measured and Predicted FWD Displacement Histories on K7-11 (Data Collected in Aug 01).

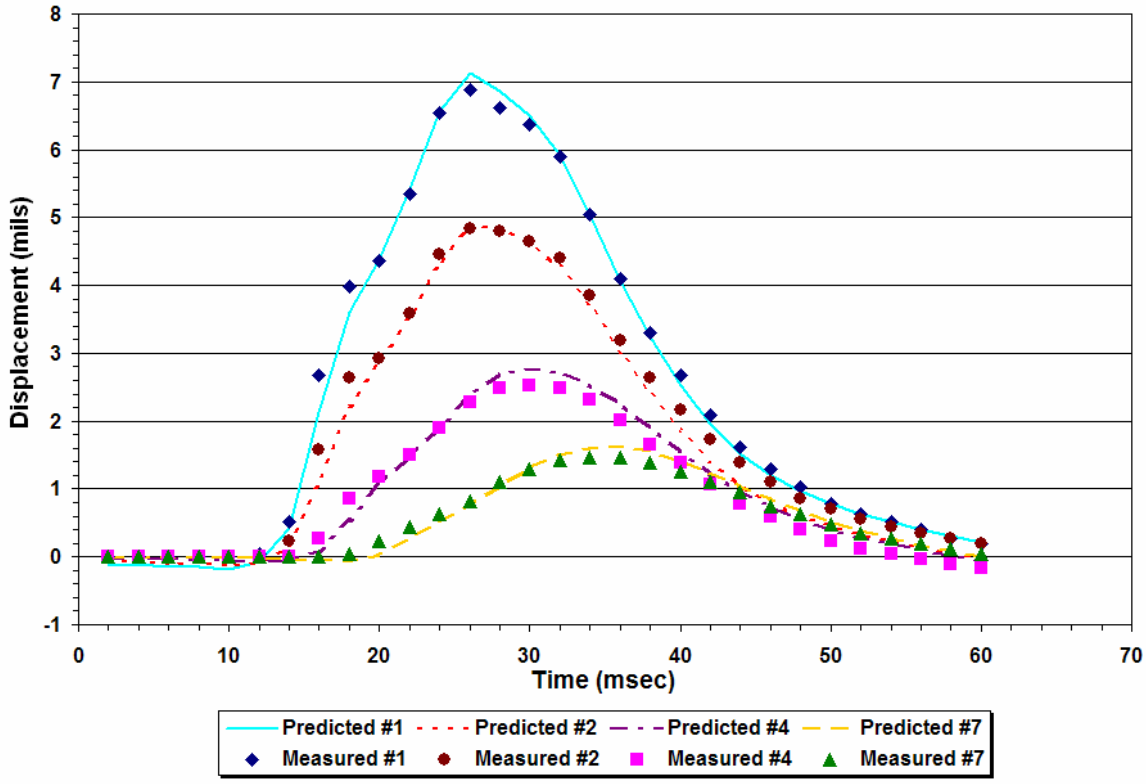

Figure D46. Comparison of Measured and Predicted FWD Displacement Histories on K7-15 (Data Collected in Aug 01).

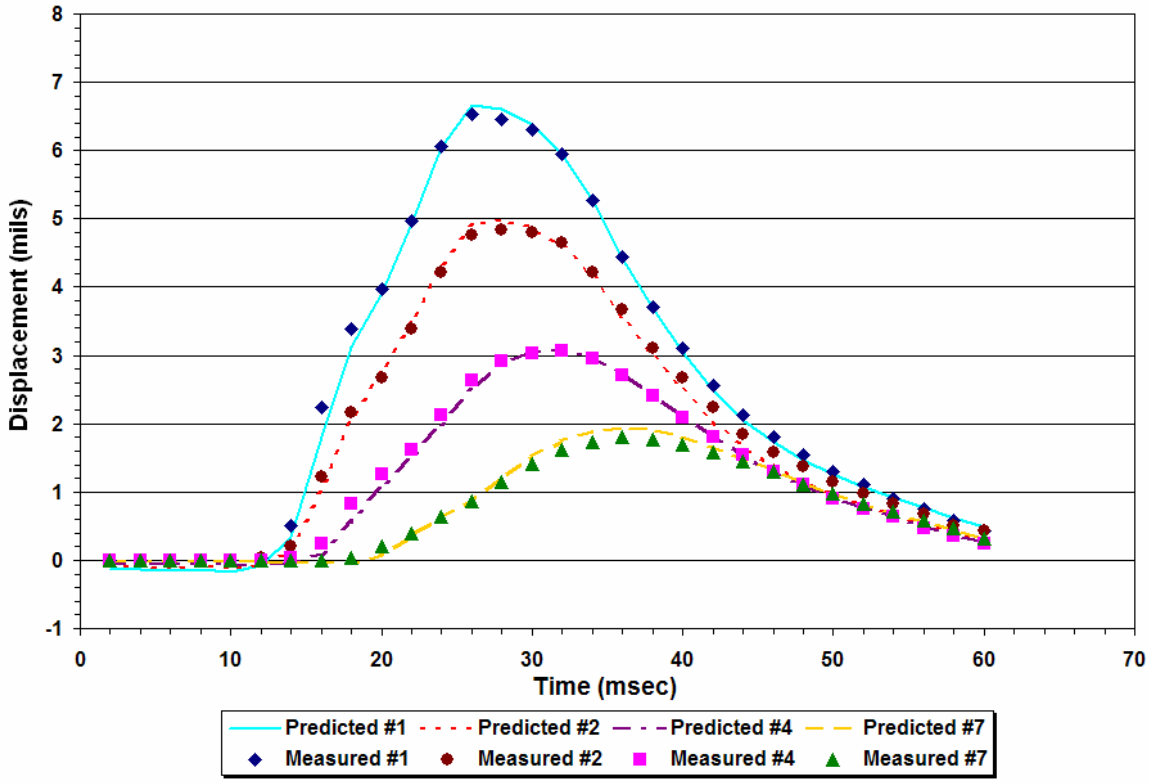

Figure D47. Comparison of Measured and Predicted FWD Displacement Histories on K7-20 (Data Collected in Aug 01).

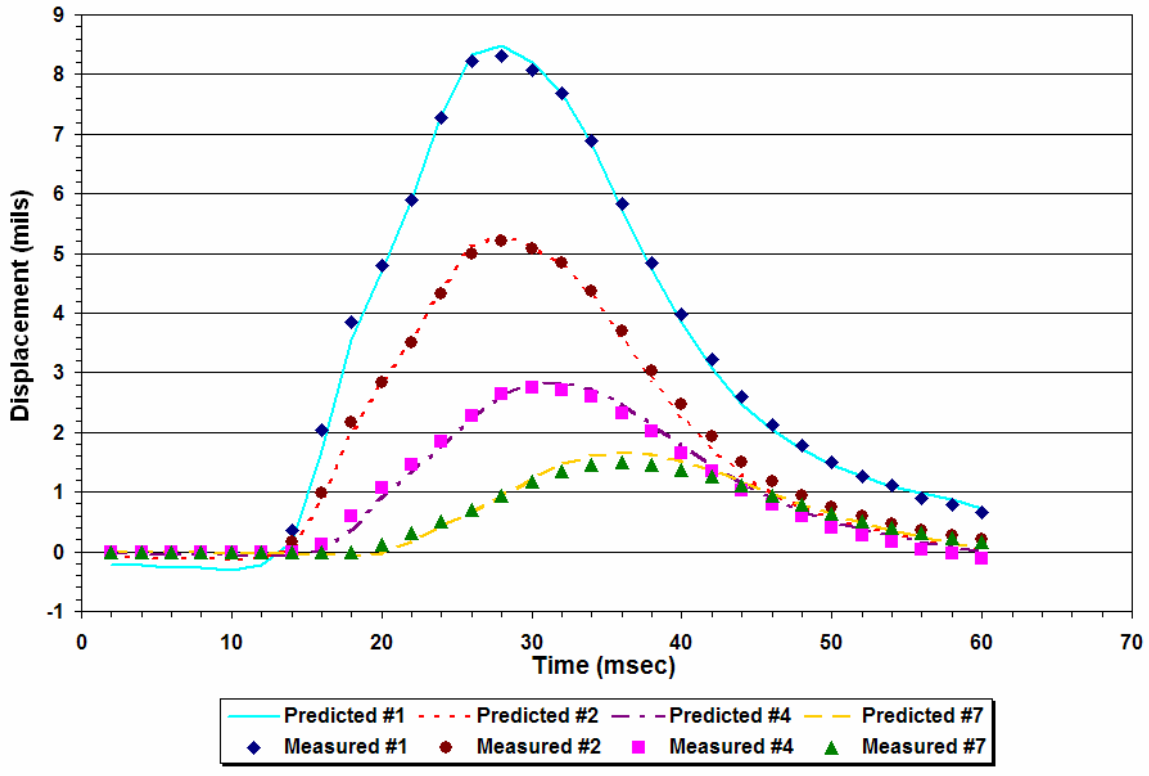

Figure D48. Comparison of Measured and Predicted FWD Displacement Histories on K7-37 (Data Collected in Aug 01).

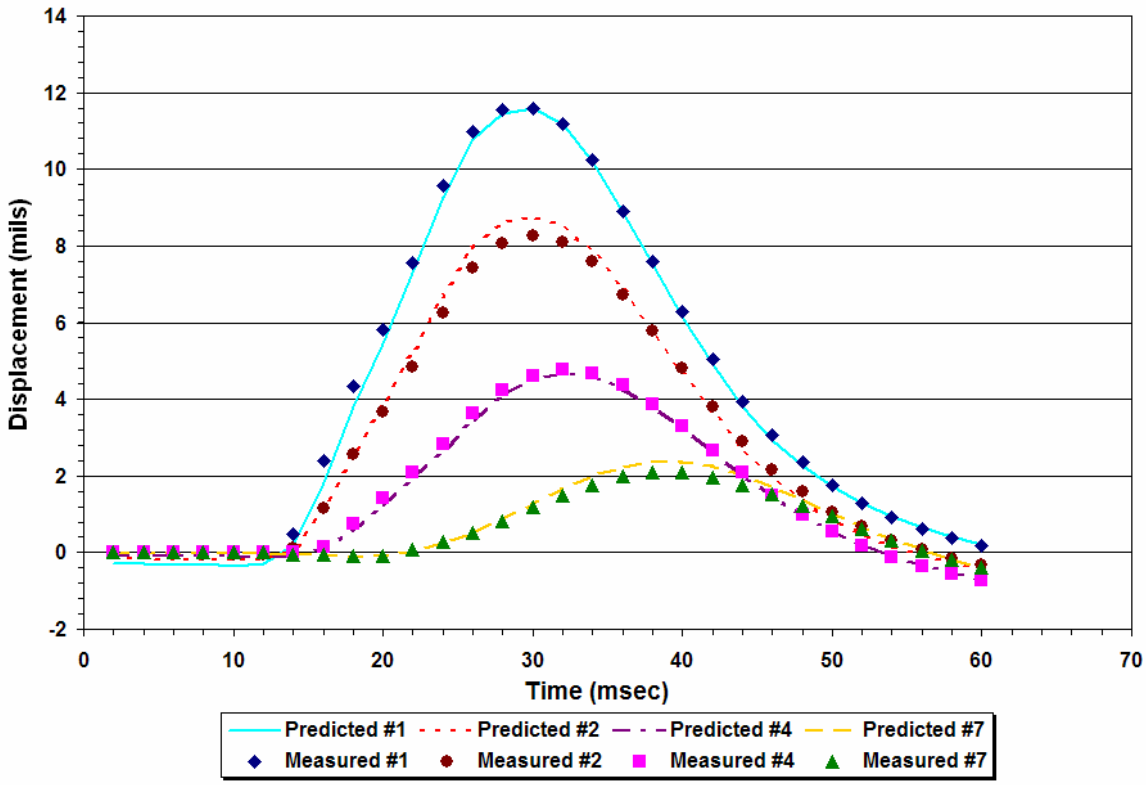

Figure D49. Comparison of Measured and Predicted FWD Displacement Histories on K7-40 (Data Collected in Aug 01).

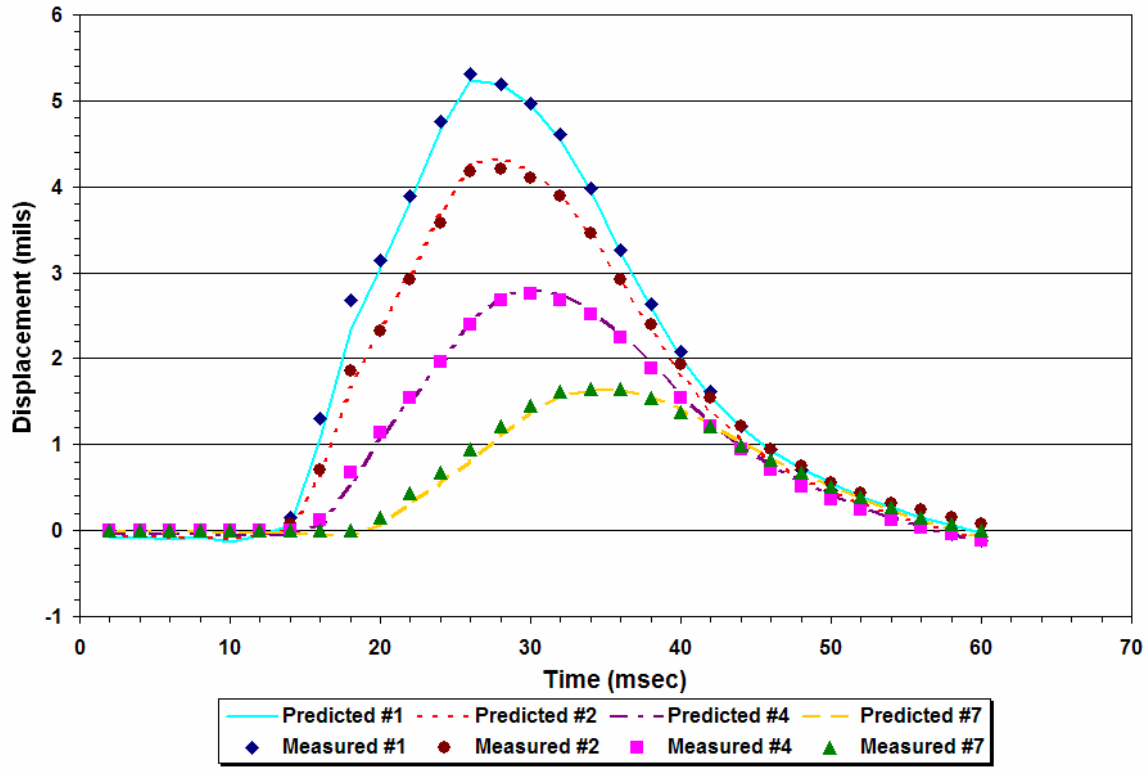

Figure D50. Comparison of Measured and Predicted FWD Displacement Histories on K7-11 (Data Collected in Mar 02).

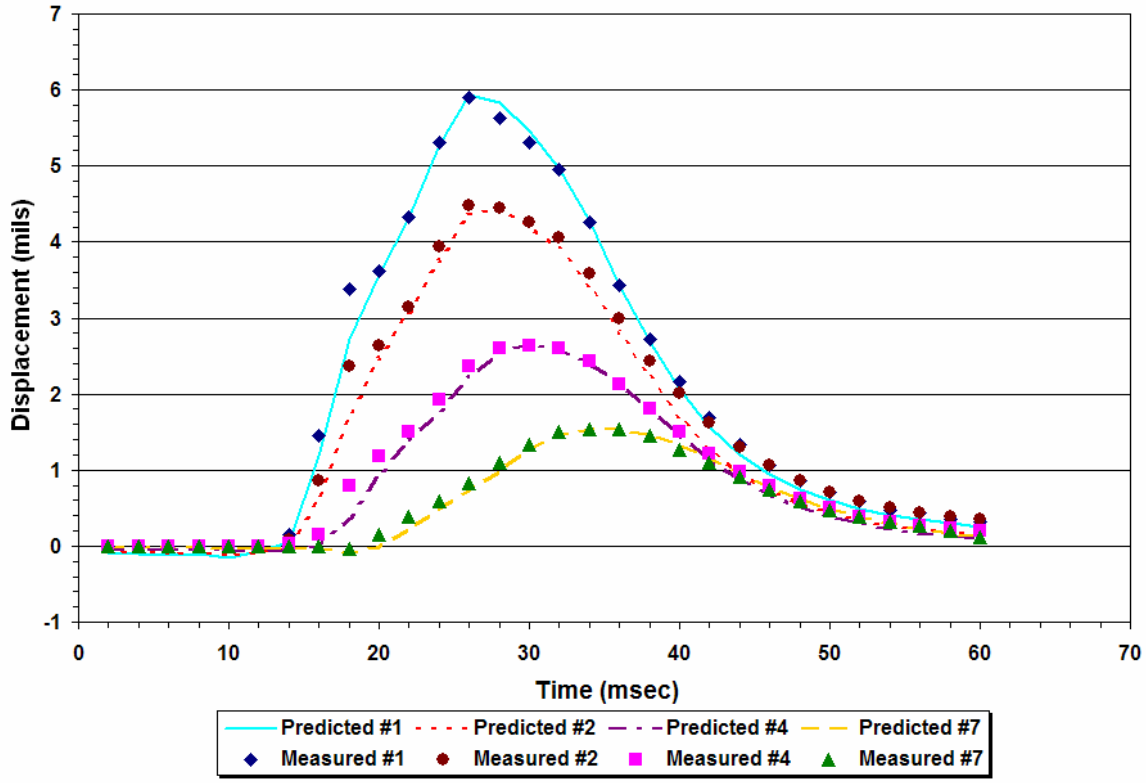

Figure D51. Comparison of Measured and Predicted FWD Displacement Histories on K7-15 (Data Collected in Mar 02).

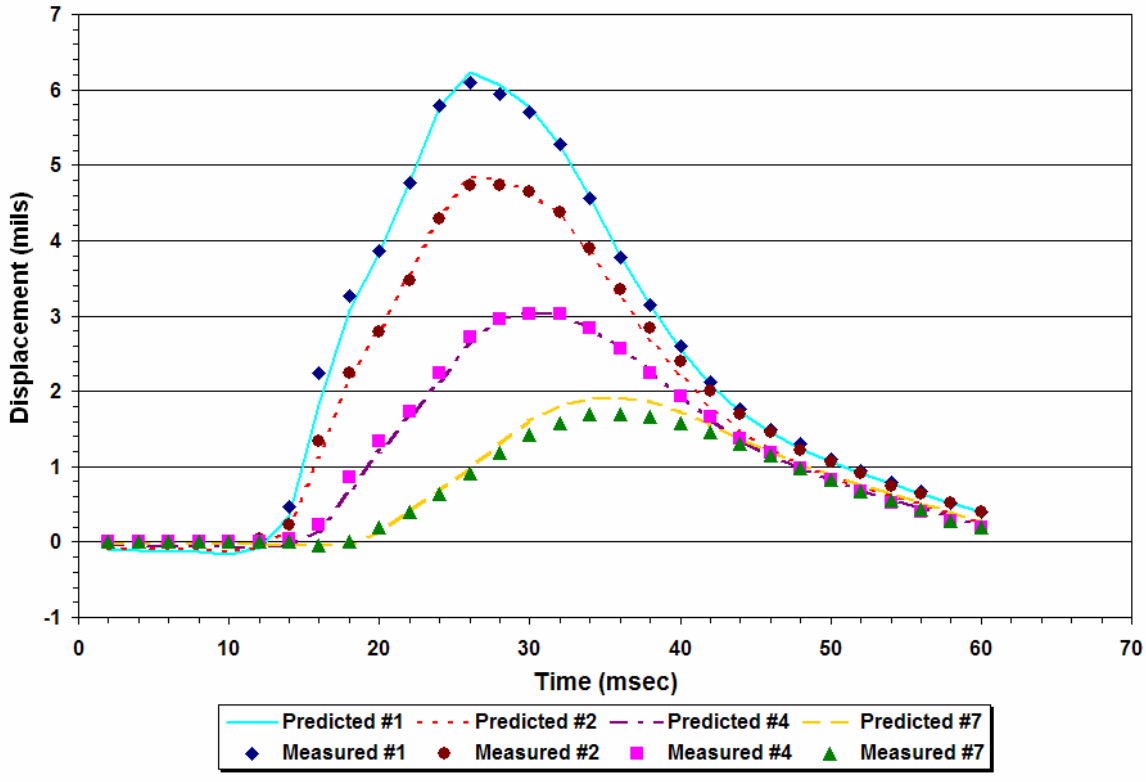

Figure D52. Comparison of Measured and Predicted FWD Displacement Histories on K7-20 (Data Collected in Mar 02).

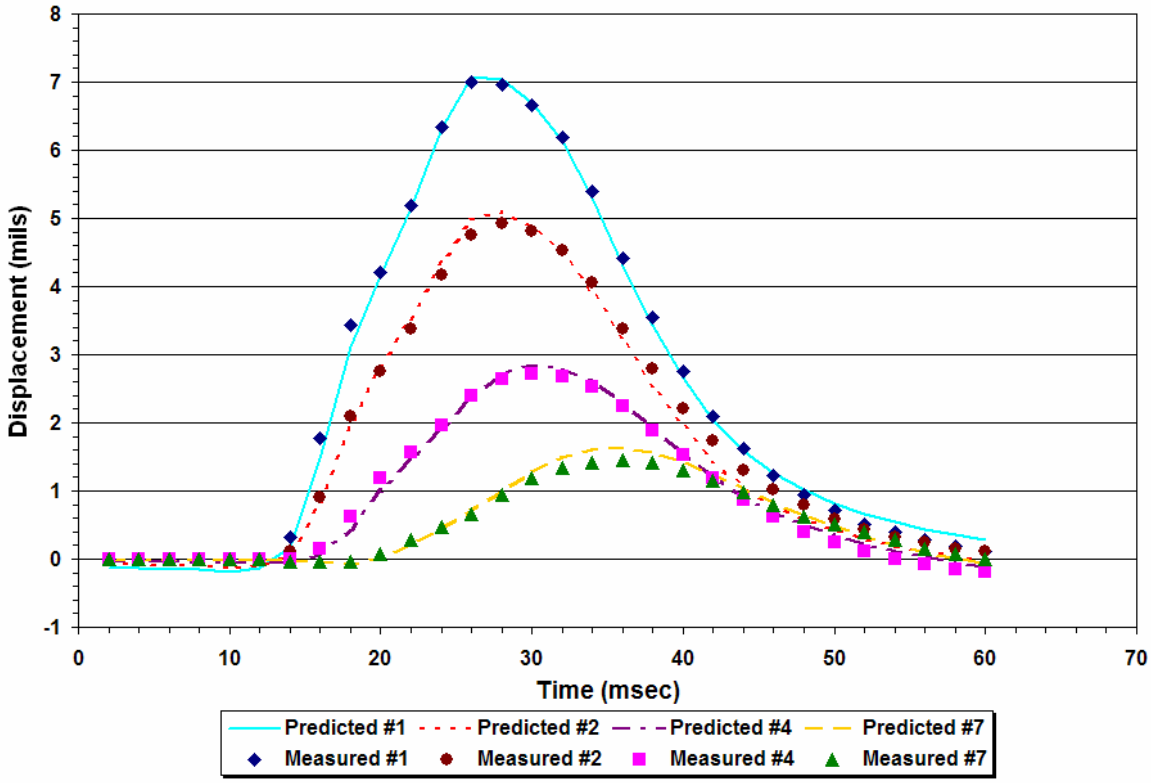

Figure D53. Comparison of Measured and Predicted FWD Displacement Histories on K7-37 (Data Collected in Mar 02).

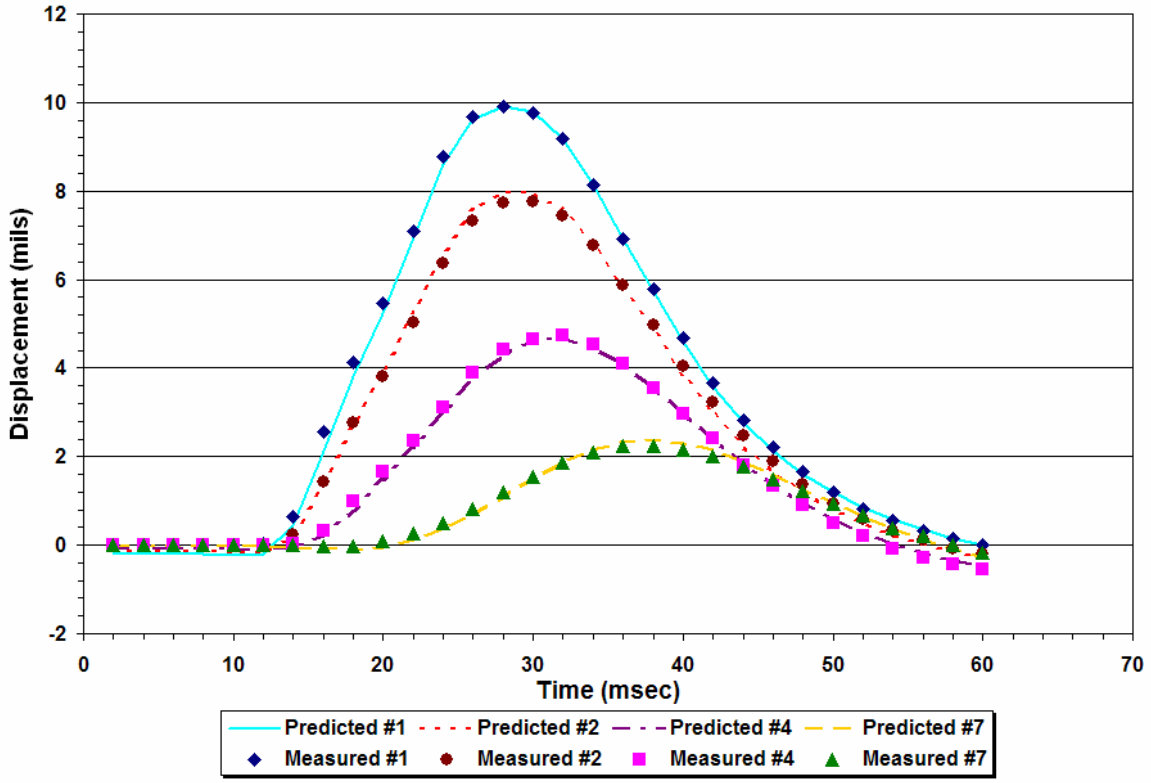

Figure D54. Comparison of Measured and Predicted FWD Displacement Histories on K7-40 (Data Collected in Mar 02).

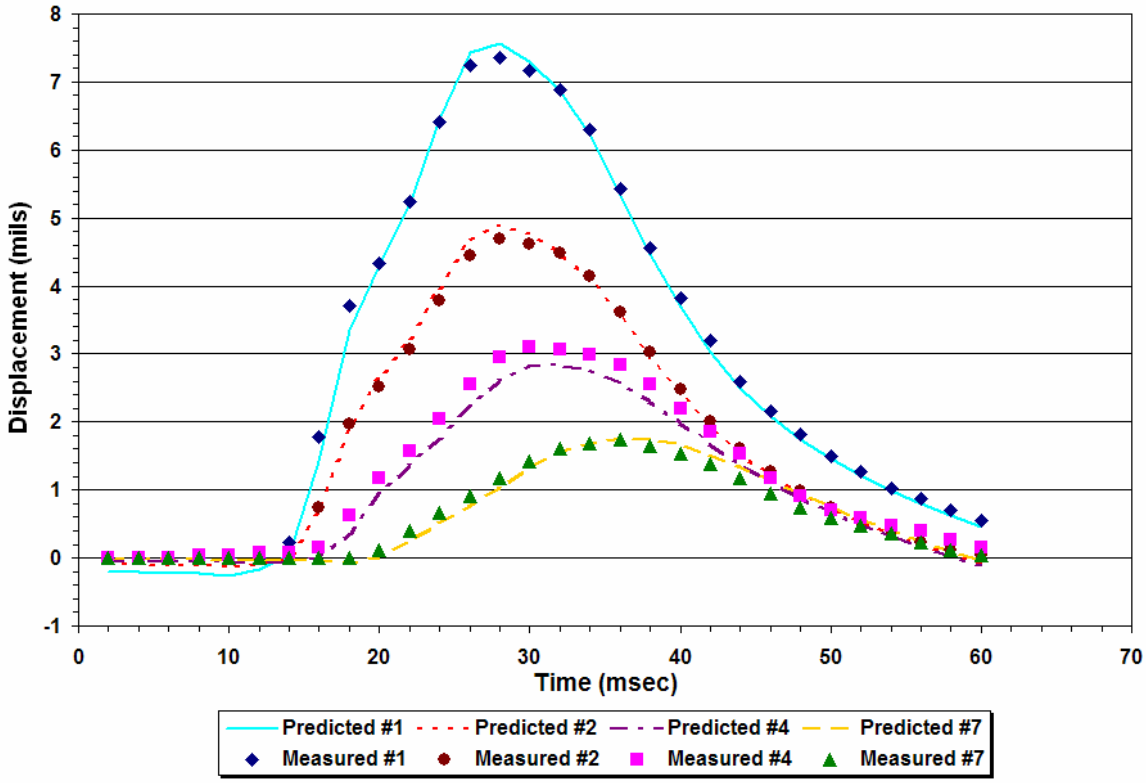

Figure D55. Comparison of Measured and Predicted FWD Displacement Histories on K7-11 (Data Collected in July 02).

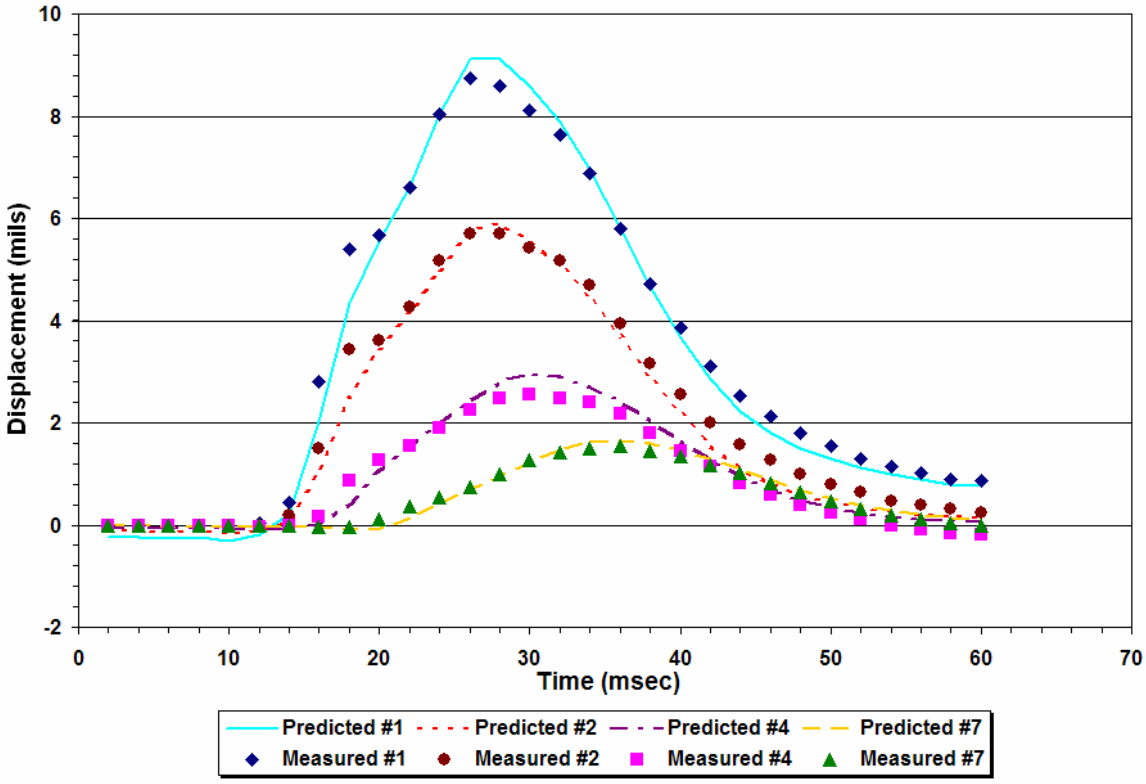

Figure D56. Comparison of Measured and Predicted FWD Displacement Histories on K7-15 (Data Collected in July 02).

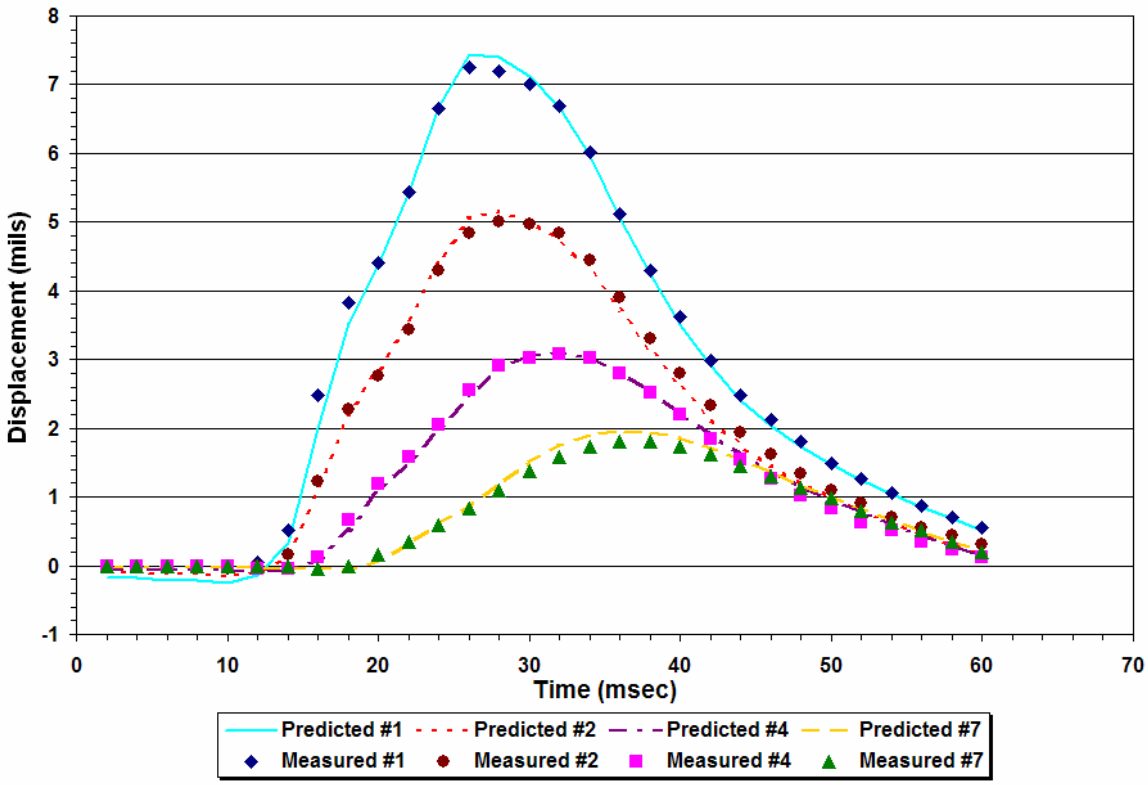

Figure D57. Comparison of Measured and Predicted FWD Displacement Histories on K7-20 (Data Collected in July 02).

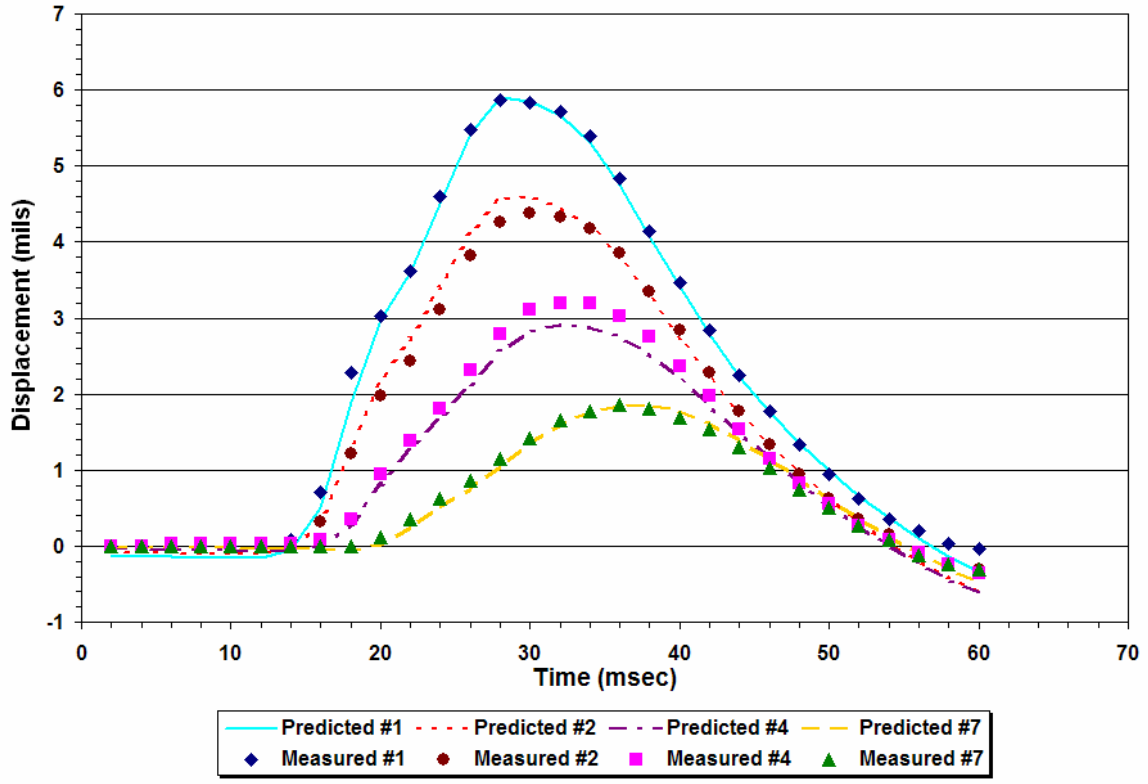

Figure D58. Comparison of Measured and Predicted FWD Displacement Histories on K7-31 (Data Collected in July 02).

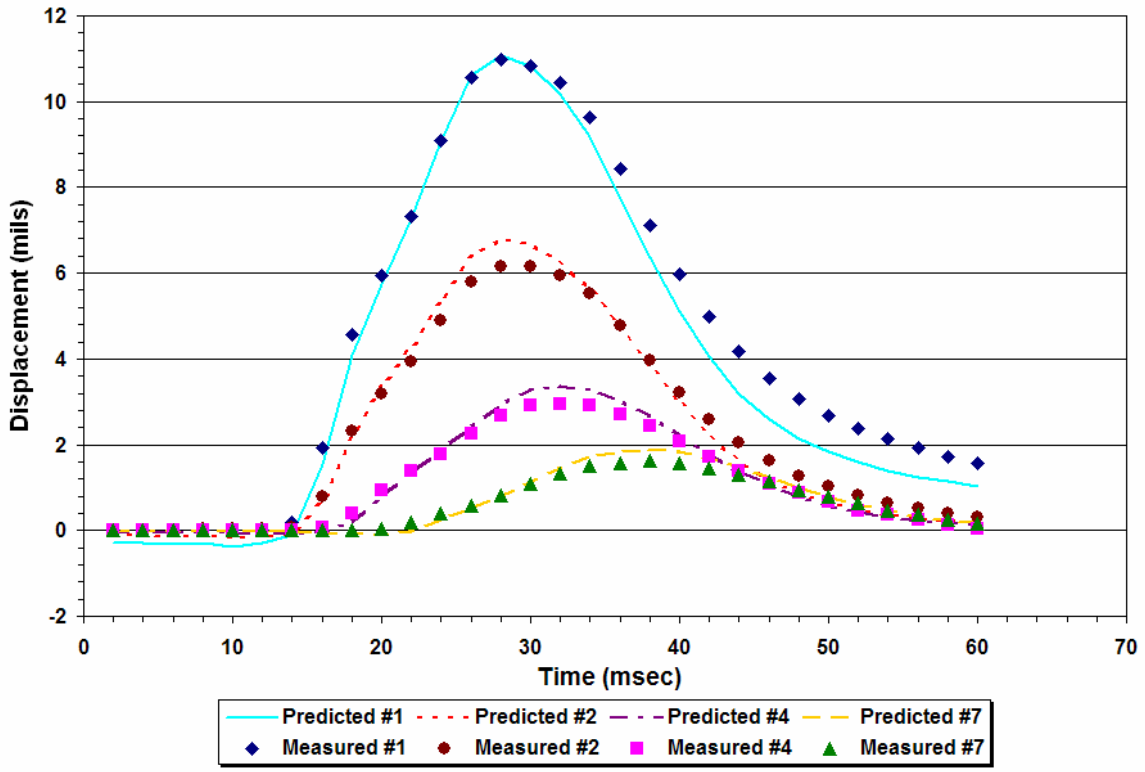

Figure D59. Comparison of Measured and Predicted FWD Displacement Histories on K7-37 (Data Collected in July 02).

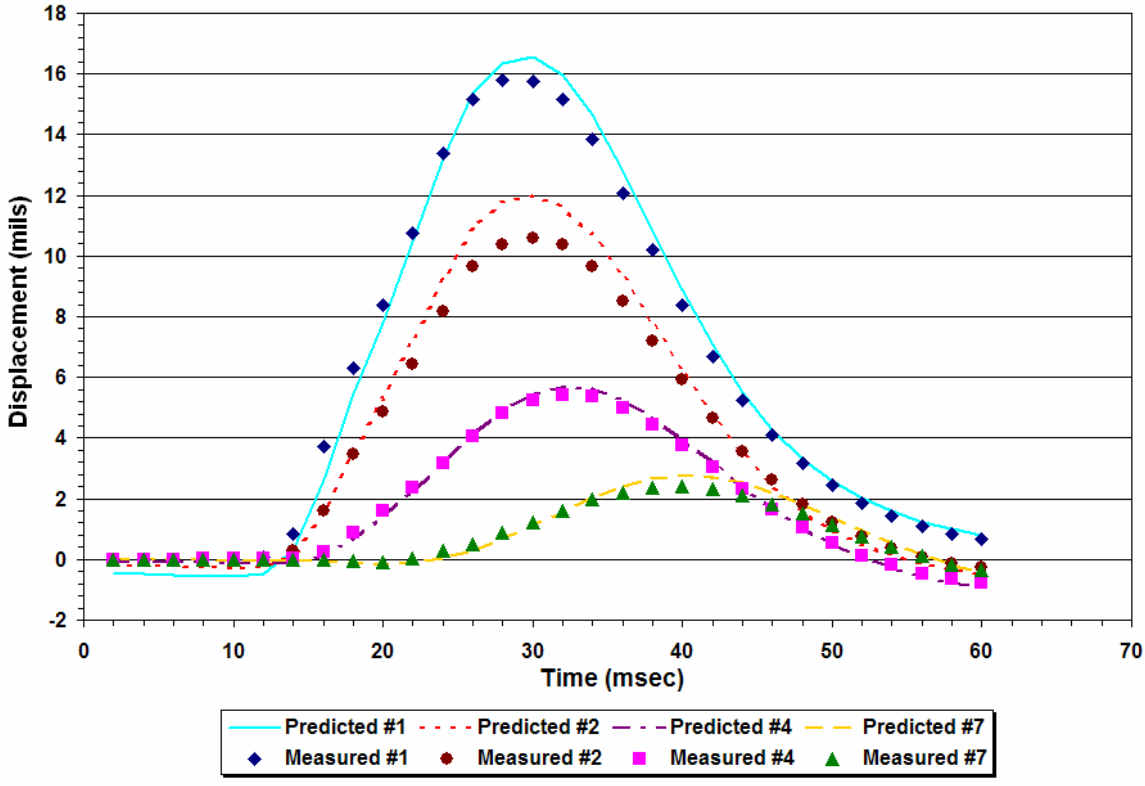

Figure D60. Comparison of Measured and Predicted FWD Displacement Histories on K7-40 (Data Collected in July 02).

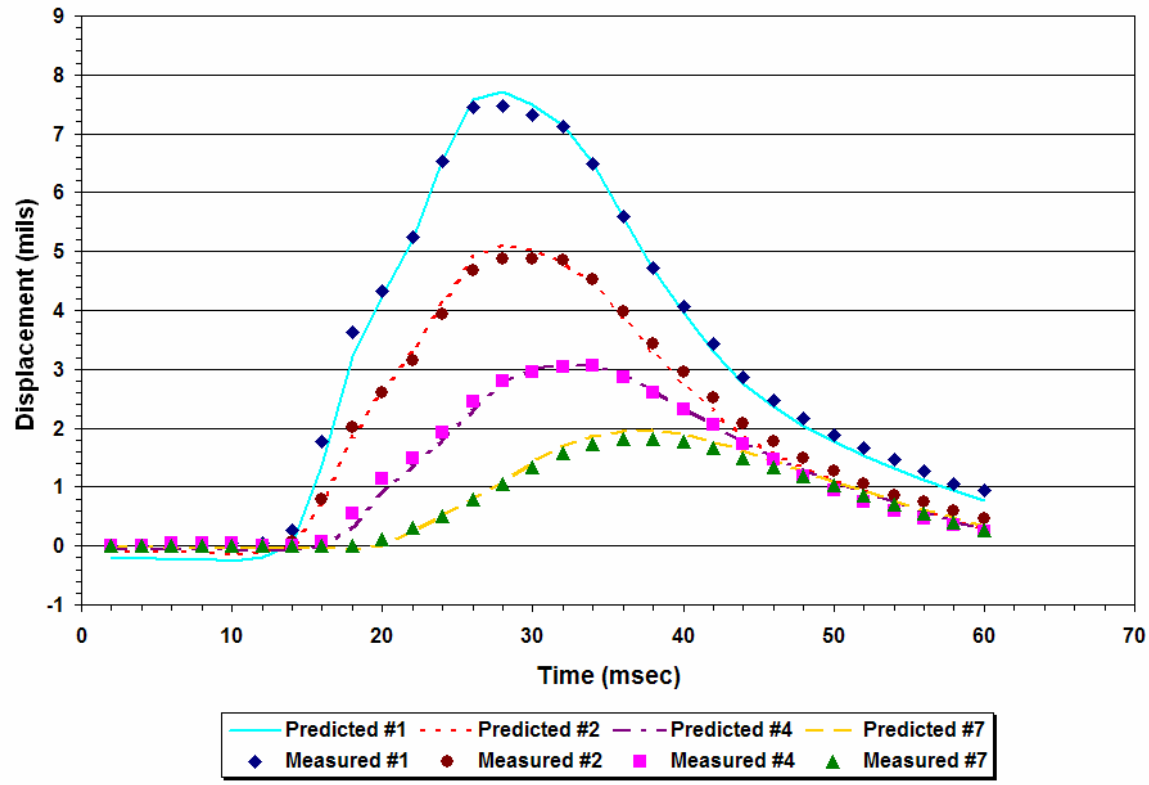

Figure D61. Comparison of Measured and Predicted FWD Displacement Histories on K7-20 (Data Collected in Oct 02).

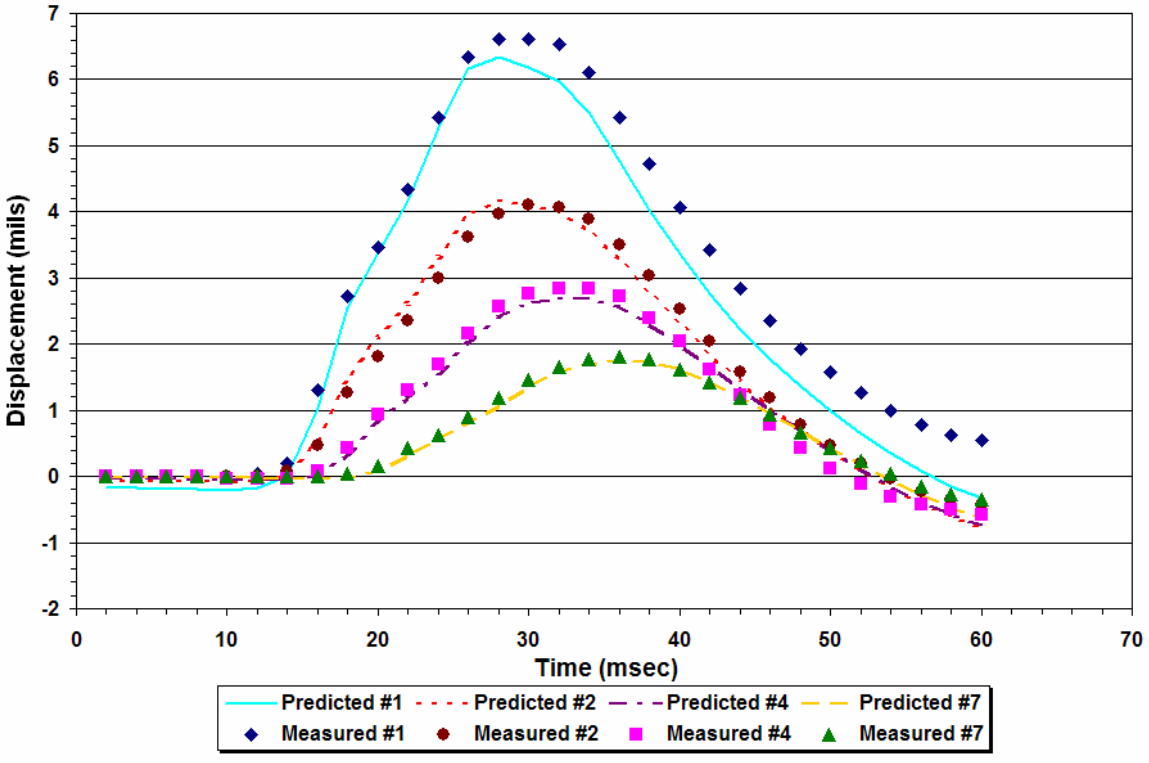

Figure D62. Comparison of Measured and Predicted FWD Displacement Histories on K7-31 (Data Collected in Oct 02).

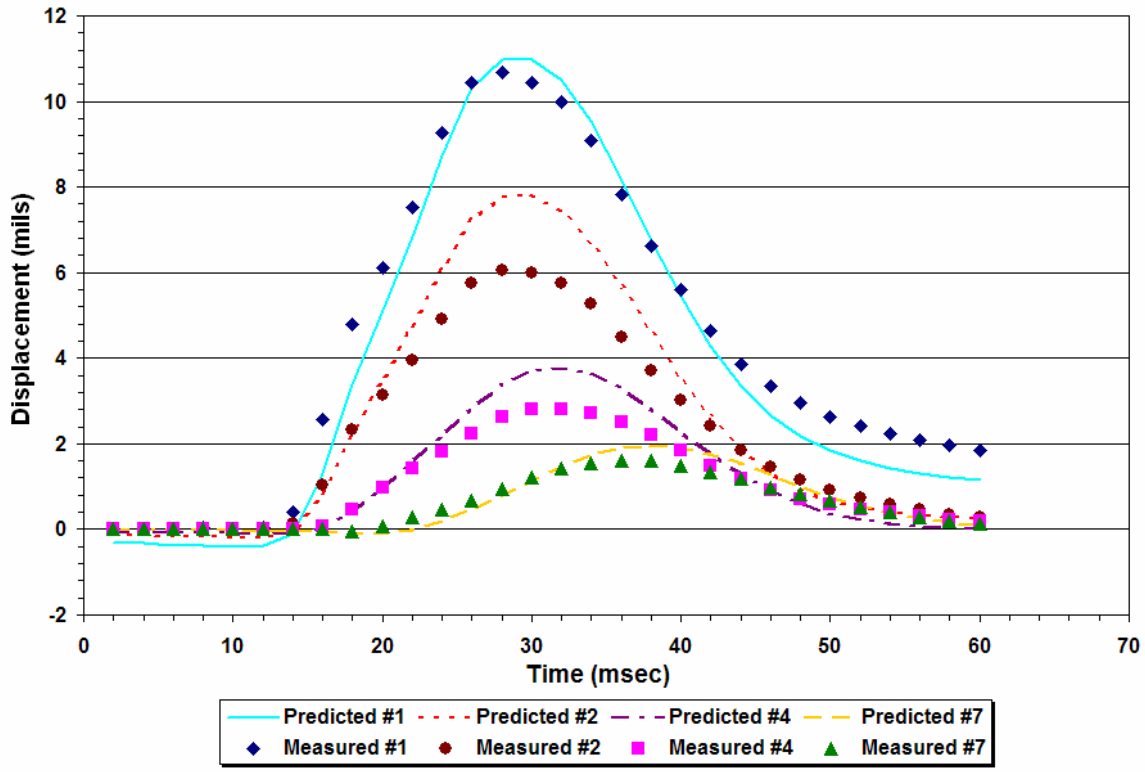

Figure D63. Comparison of Measured and Predicted FWD Displacement Histories on K7-37 (Data Collected in Oct 02).

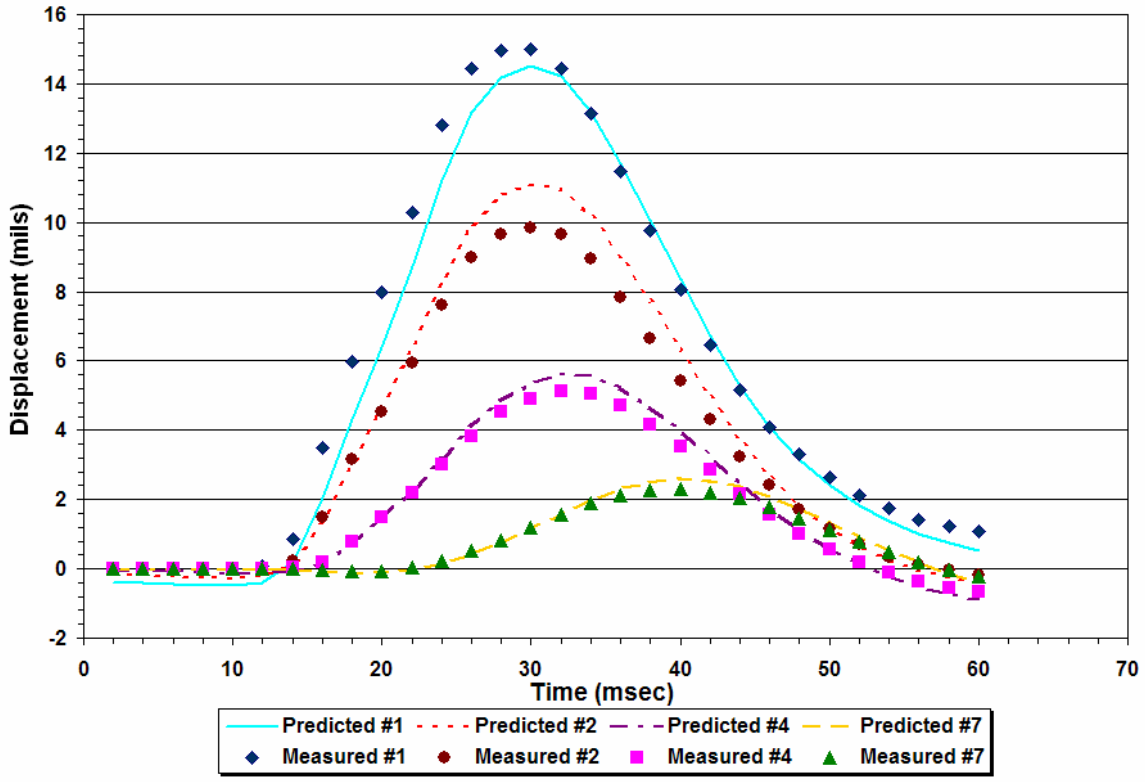

Figure D64. Comparison of Measured and Predicted FWD Displacement Histories on K7-40 (Data Collected in Oct 02).

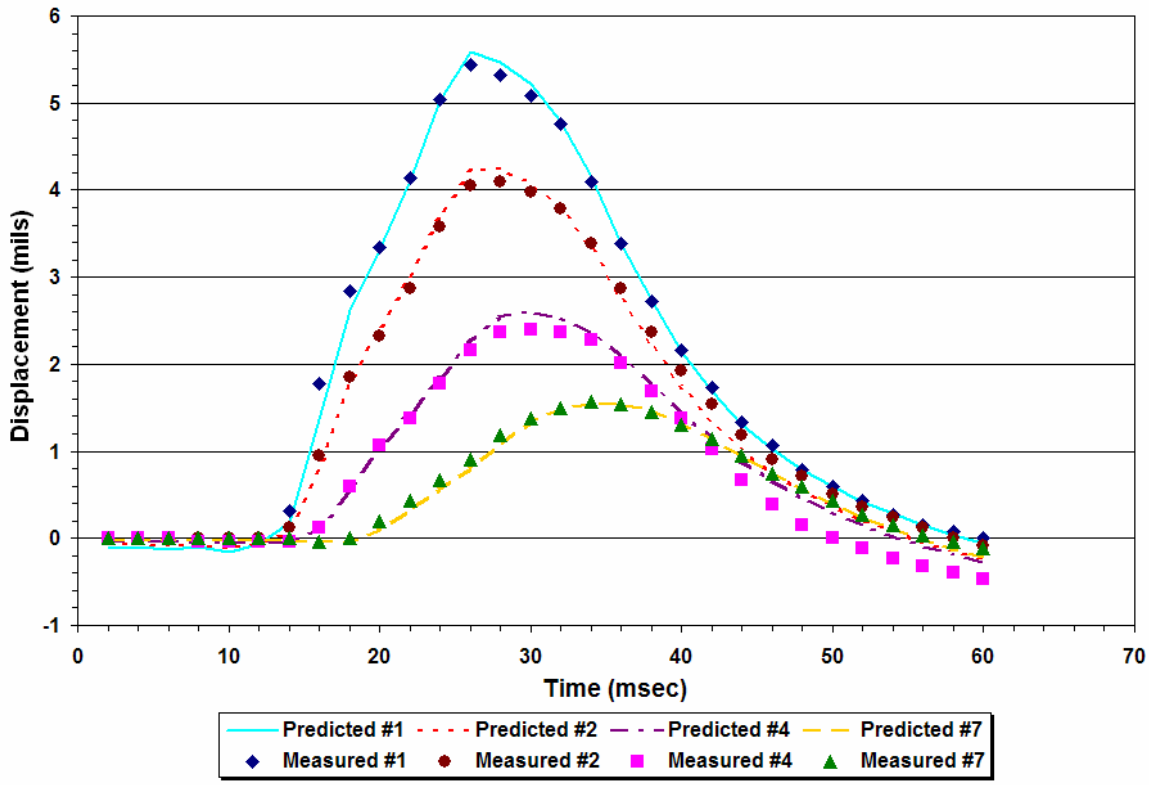

Figure D65. Comparison of Measured and Predicted FWD Displacement Histories on K7-11 (Data Collected in Apr 03).

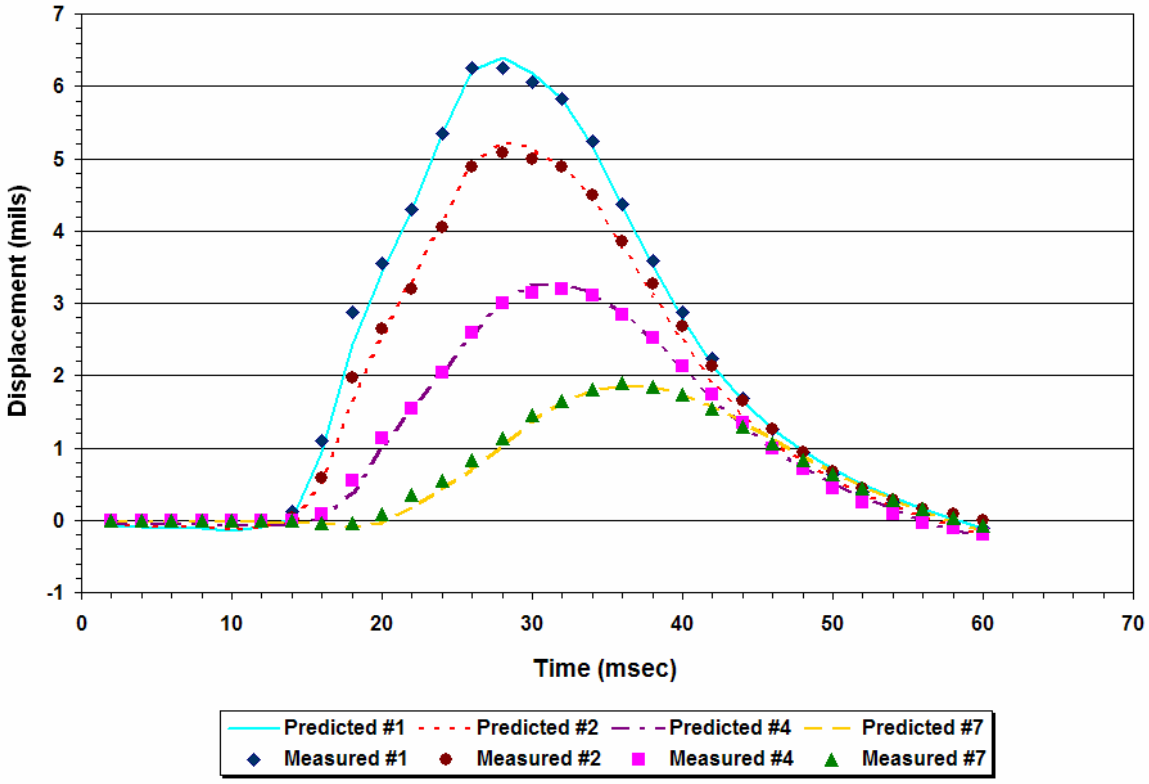

Figure D66. Comparison of Measured and Predicted FWD Displacement Histories on K7-15 (Data Collected in Apr 03).

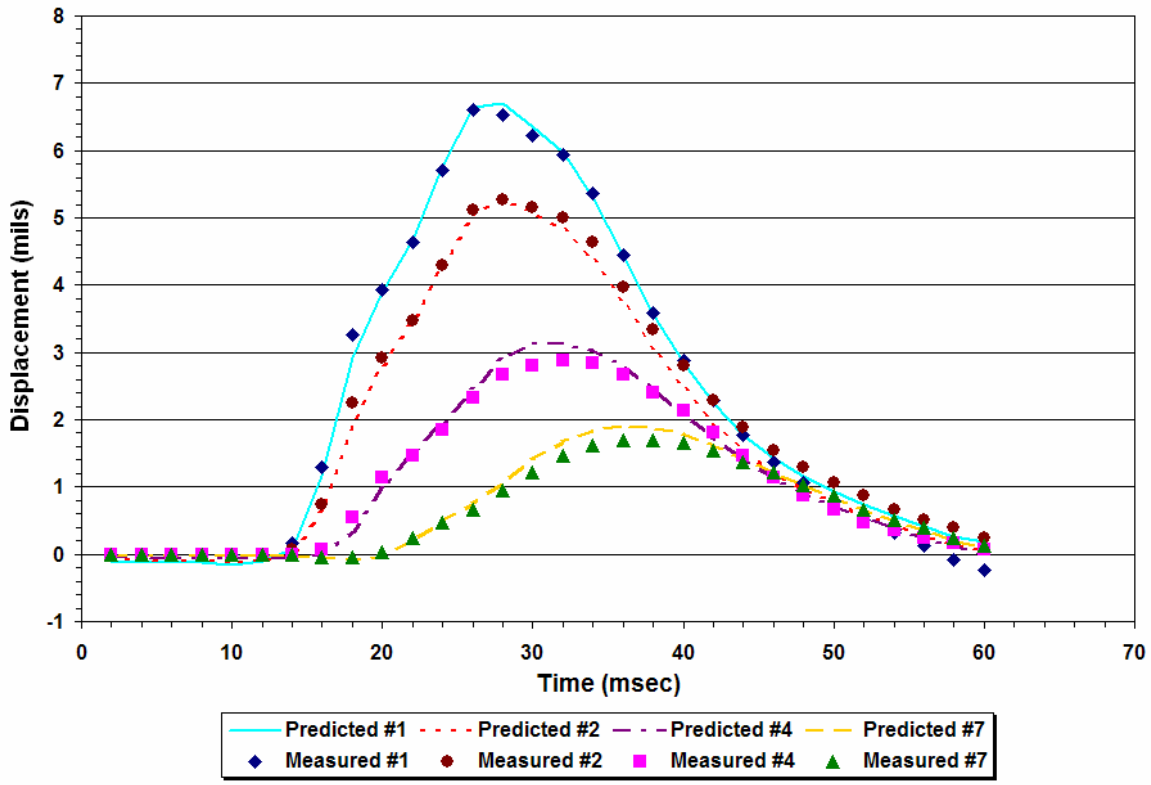

Figure D67. Comparison of Measured and Predicted FWD Displacement Histories on K7-20 (Data Collected in Apr 03).

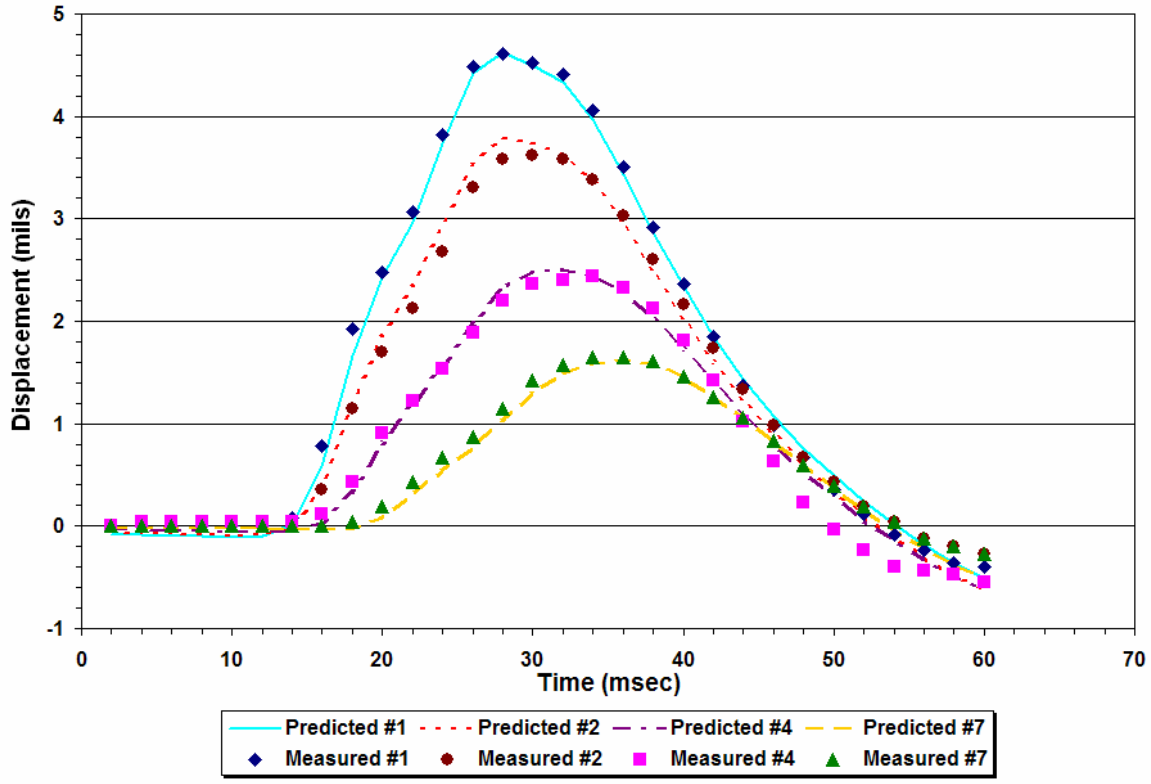

Figure D68. Comparison of Measured and Predicted FWD Displacement Histories on K7-31 (Data Collected in Apr 03).

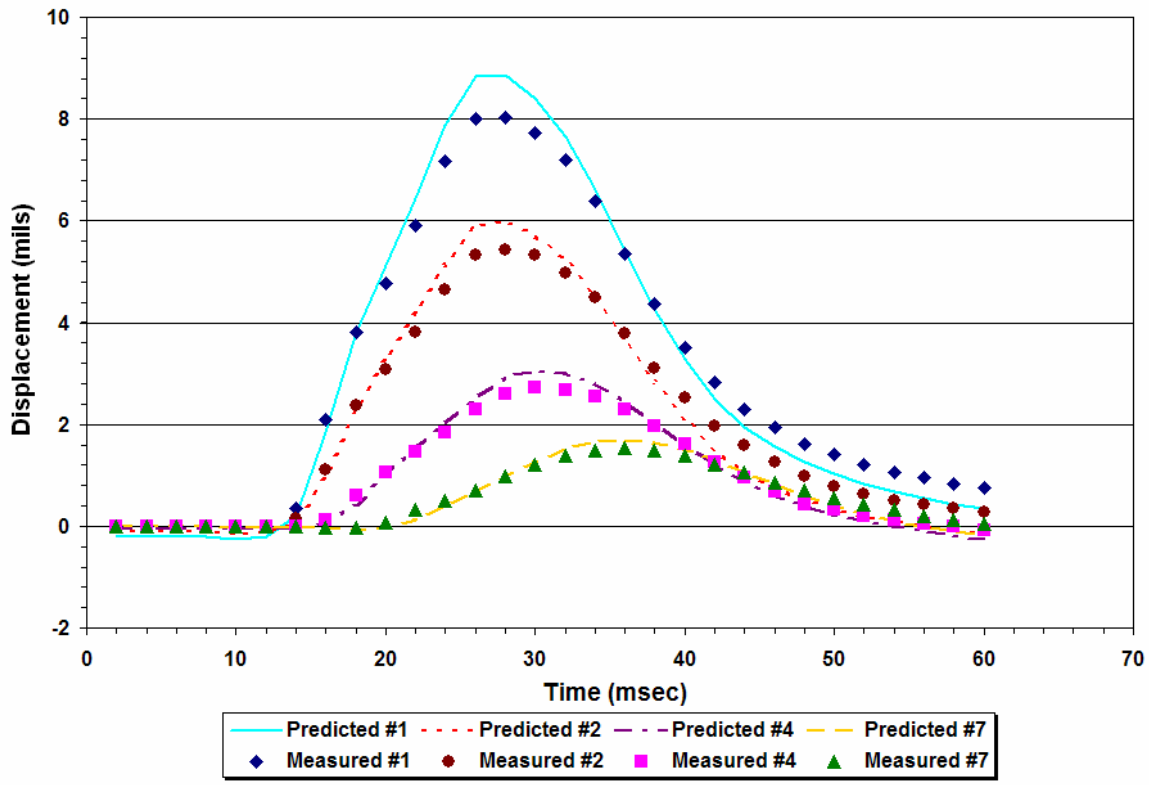

Figure D69. Comparison of Measured and Predicted FWD Displacement Histories on K7-37 (Data Collected in Apr 03).

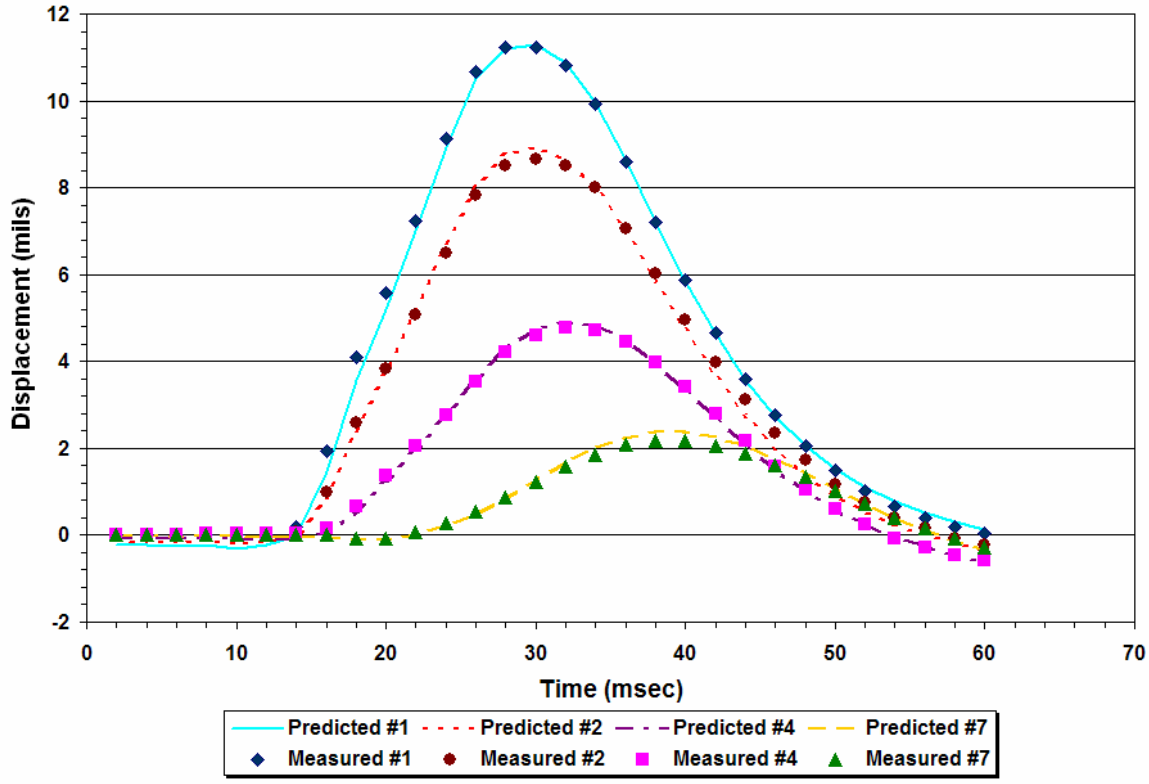

Figure D70. Comparison of Measured and Predicted FWD Displacement Histories on K7-40 (Data Collected in Apr 03).

APPENDIX E

COMPARISON OF MEASURED AND PREDICTED REAL AND IMAGINARY COMPONENTS OF THE COMPLEX COMPLIANCE OF CORES TESTED

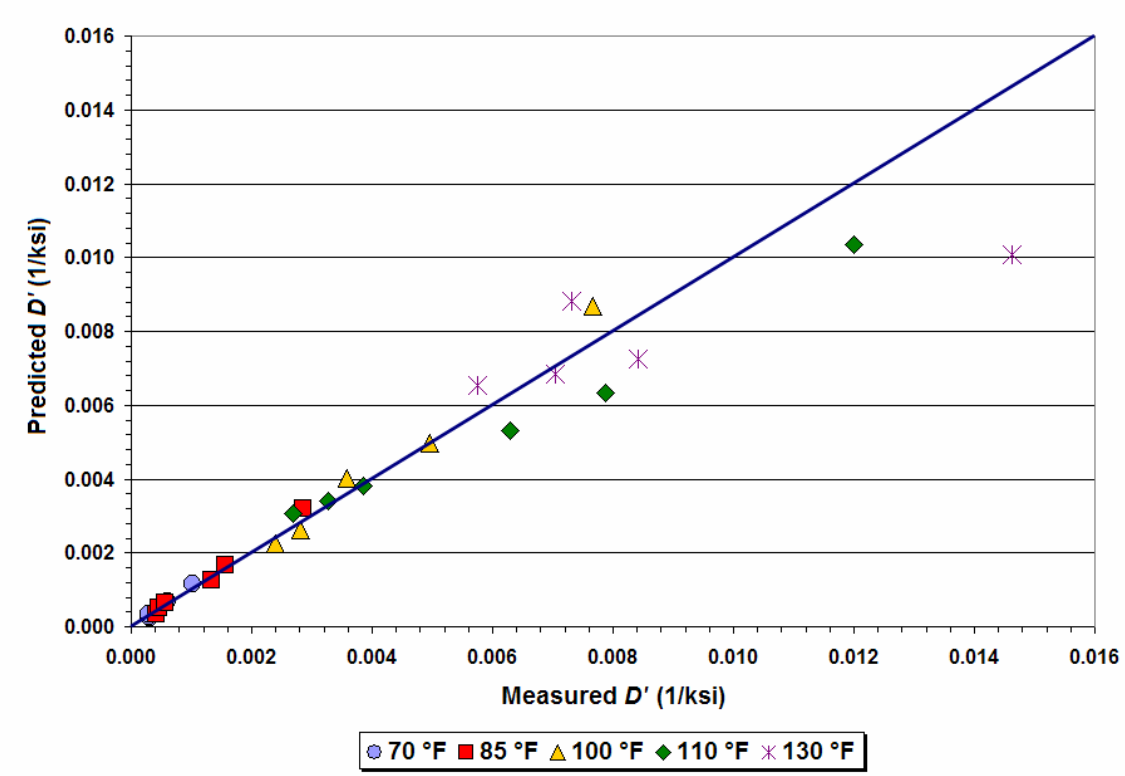

Figure E1. Comparison of Predicted and Measured Real Components of the Complex Compliance at Different Temperatures and Frequencies (K6-1 Core).

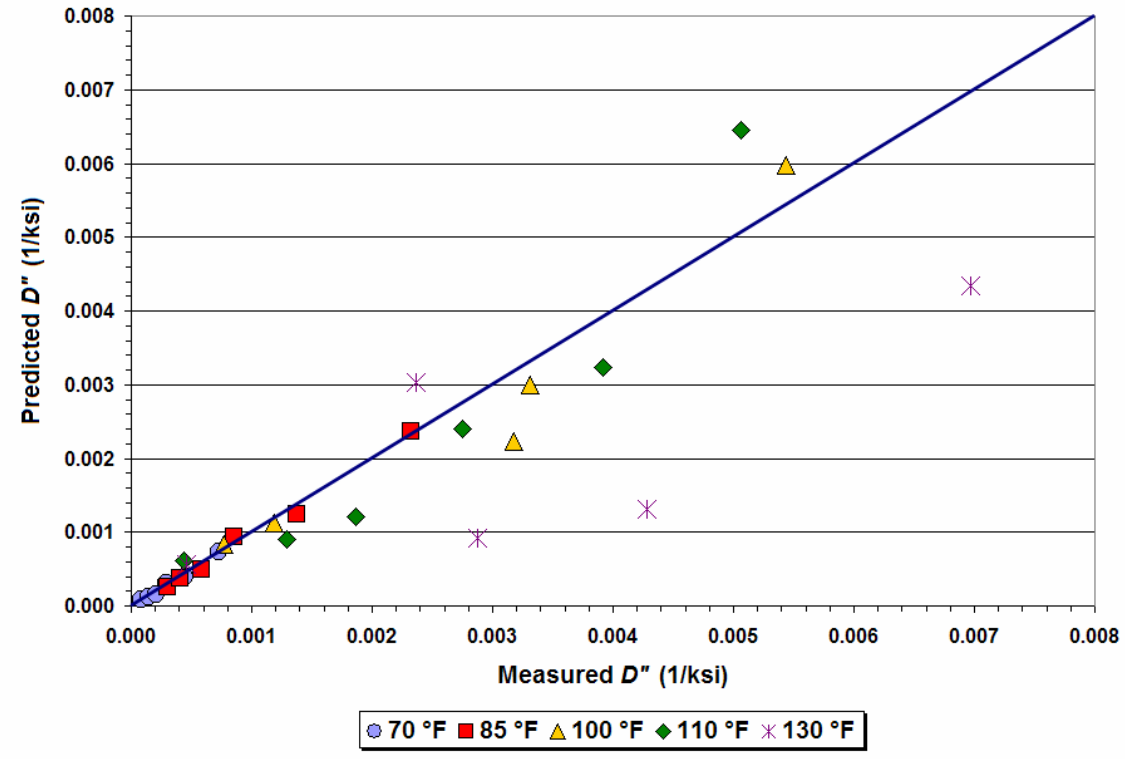

Figure E2. Comparison of Predicted and Measured Imaginary Components of the Complex Compliance at Different Temperatures and Frequencies (K6-1 Core).

Table E1. Predicted and Measured Real and Imaginary Components of the Complex Compliance at Different Temperatures and Frequencies (K6-1 Core).

Temperature (°F)	Frequency (Hz)	Real Component D' (ksi^{-1})		Imaginary Component D'' (ksi^{-1})	
		Measured	Predicted	Measured	Predicted
70	25	3.08E-04	2.26E-04	8.42E-05	8.63E-05
70	10	2.91E-04	2.79E-04	1.44E-04	1.24E-04
70	5	2.86E-04	3.33E-04	2.05E-04	1.61E-04
70	1	5.02E-04	5.34E-04	2.91E-04	3.03E-04
70	0.5	6.00E-04	6.67E-04	4.46E-04	3.96E-04
70	0.1	1.01E-03	1.16E-03	7.31E-04	7.38E-04
85	25	4.09E-04	3.42E-04	2.97E-04	2.53E-04
85	10	4.53E-04	4.96E-04	4.05E-04	3.67E-04
85	5	5.62E-04	6.57E-04	5.88E-04	4.86E-04
85	1	1.33E-03	1.26E-03	8.56E-04	9.32E-04
85	0.5	1.56E-03	1.67E-03	1.38E-03	1.24E-03
85	0.1	2.86E-03	3.21E-03	2.33E-03	2.37E-03
100	10	2.40E-03	2.26E-03	7.73E-04	8.28E-04
100	5	2.82E-03	2.62E-03	1.19E-03	1.12E-03
100	1	3.57E-03	4.00E-03	3.18E-03	2.23E-03
100	0.5	4.97E-03	4.97E-03	3.31E-03	2.99E-03
100	0.1	7.66E-03	8.69E-03	5.44E-03	5.98E-03
110	25	2.69E-03	3.05E-03	4.33E-04	6.07E-04
110	10	3.26E-03	3.42E-03	1.29E-03	8.97E-04
110	5	3.85E-03	3.80E-03	1.86E-03	1.21E-03
110	1	6.30E-03	5.31E-03	2.75E-03	2.41E-03
110	0.5	7.87E-03	6.35E-03	3.92E-03	3.24E-03
110	0.1	1.20E-02	1.04E-02	5.06E-03	6.44E-03
130	25	5.74E-03	6.53E-03	4.55E-04	5.69E-04
130	10	7.04E-03	6.85E-03	2.87E-03	9.18E-04
130	5	8.42E-03	7.25E-03	4.28E-03	1.31E-03
130	1	7.31E-03	8.83E-03	2.37E-03	3.03E-03
130	0.5	1.46E-02	1.01E-02	6.97E-03	4.34E-03

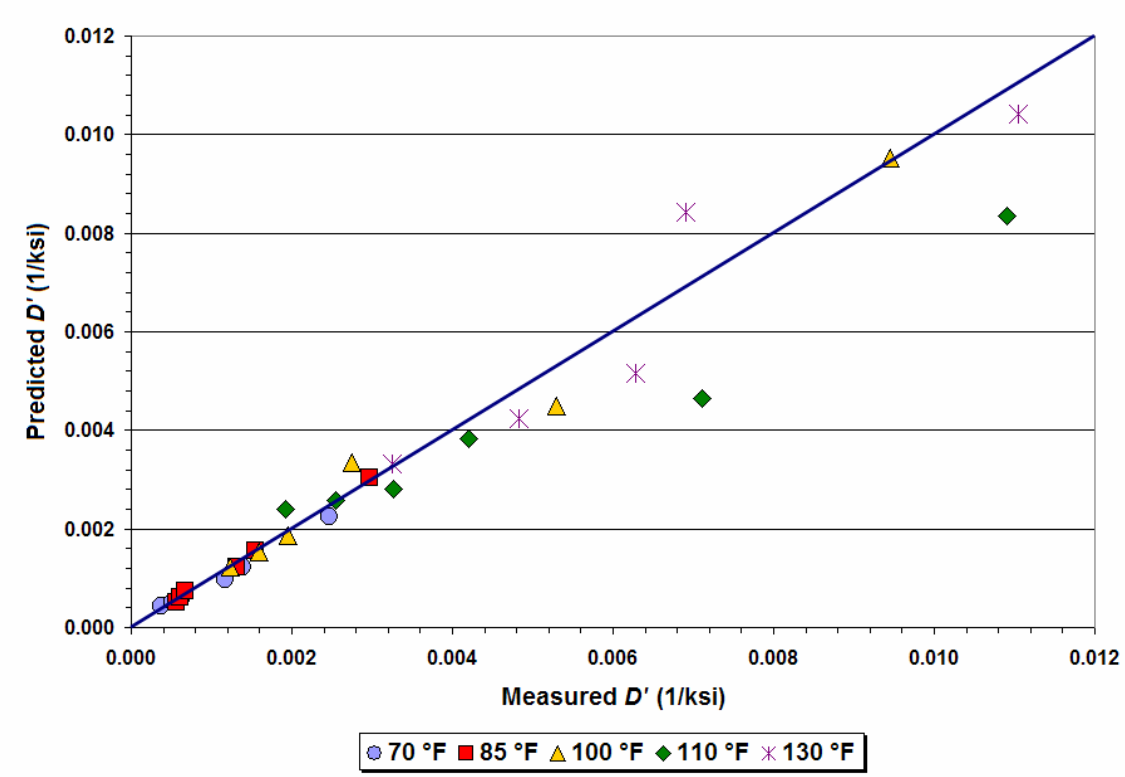

Figure E3. Comparison of Predicted and Measured Real Components of the Complex Compliance at Different Temperatures and Frequencies (K6-4 Core).

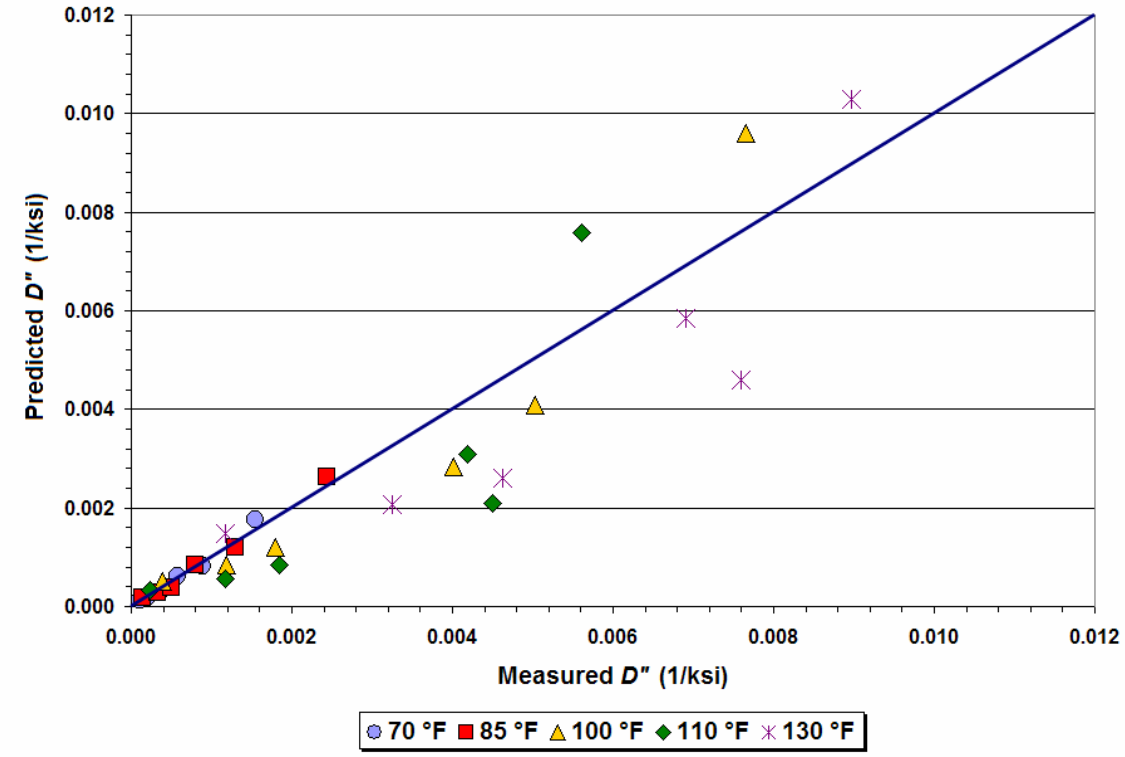

Figure E4. Comparison of Predicted and Measured Imaginary Components of the Complex Compliance at Different Temperatures and Frequencies (K6-4 Core).

Table E2. Predicted and Measured Real and Imaginary Components of the Complex Compliance at Different Temperatures and Frequencies (K6-4 Core).

Temperature (°F)	Frequency (Hz)	Real Component D' (ksi^{-1})		Imaginary Component D'' (ksi^{-1})	
		Measured	Predicted	Measured	Predicted
70	25	3.80E-04	4.35E-04	1.06E-04	1.35E-04
70	10	5.15E-04	5.15E-04	2.25E-04	2.07E-04
70	5	6.44E-04	6.03E-04	3.57E-04	2.85E-04
70	1	1.17E-03	9.59E-04	5.78E-04	6.02E-04
70	0.5	1.39E-03	1.21E-03	8.90E-04	8.28E-04
70	0.1	2.47E-03	2.25E-03	1.55E-03	1.75E-03
85	25	5.68E-04	5.18E-04	1.48E-04	1.75E-04
85	10	6.07E-04	6.20E-04	3.33E-04	2.75E-04
85	5	6.65E-04	7.38E-04	4.94E-04	3.86E-04
85	1	1.31E-03	1.21E-03	8.00E-04	8.49E-04
85	0.5	1.55E-03	1.57E-03	1.29E-03	1.19E-03
85	0.1	2.97E-03	3.04E-03	2.44E-03	2.62E-03
100	25	1.24E-03	1.24E-03	3.90E-04	5.13E-04
100	10	1.60E-03	1.52E-03	1.19E-03	8.35E-04
100	5	1.95E-03	1.86E-03	1.79E-03	1.21E-03
100	1	2.75E-03	3.34E-03	4.02E-03	2.83E-03
100	0.5	5.29E-03	4.49E-03	5.03E-03	4.09E-03
100	0.1	9.45E-03	9.52E-03	7.66E-03	9.59E-03
110	25	1.92E-03	2.39E-03	2.28E-04	3.42E-04
110	10	2.55E-03	2.58E-03	1.17E-03	5.72E-04
110	5	3.27E-03	2.81E-03	1.85E-03	8.42E-04
110	1	4.21E-03	3.83E-03	4.51E-03	2.09E-03
110	0.5	7.11E-03	4.64E-03	4.20E-03	3.08E-03
110	0.1	1.09E-02	8.35E-03	5.62E-03	7.59E-03
130	25	3.24E-03	3.32E-03	1.17E-03	1.49E-03
130	10	4.83E-03	4.24E-03	3.24E-03	2.06E-03
130	5	6.28E-03	5.16E-03	4.62E-03	2.62E-03
130	1	6.90E-03	8.42E-03	7.59E-03	4.59E-03
130	0.5	1.10E-02	1.04E-02	6.90E-03	5.84E-03
130	0.1	1.38E-02	1.77E-02	8.97E-03	1.03E-02

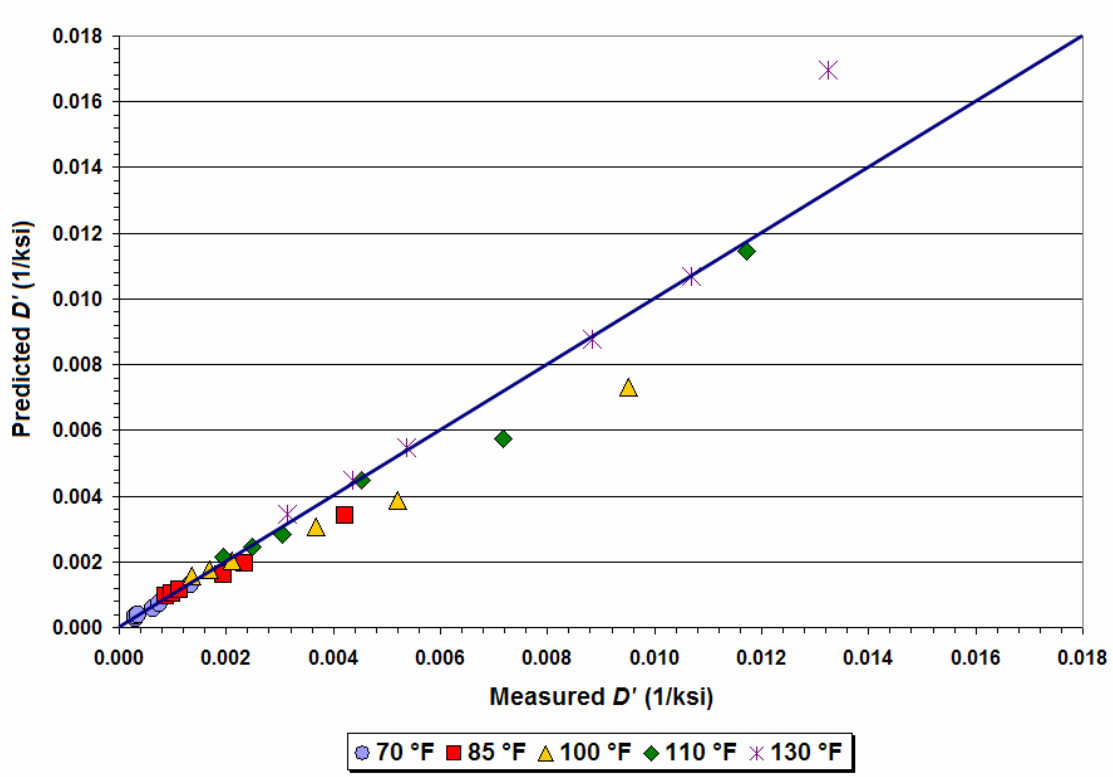

Figure E5. Comparison of Predicted and Measured Real Components of the Complex Compliance at Different Temperatures and Frequencies (K6-11 Core).

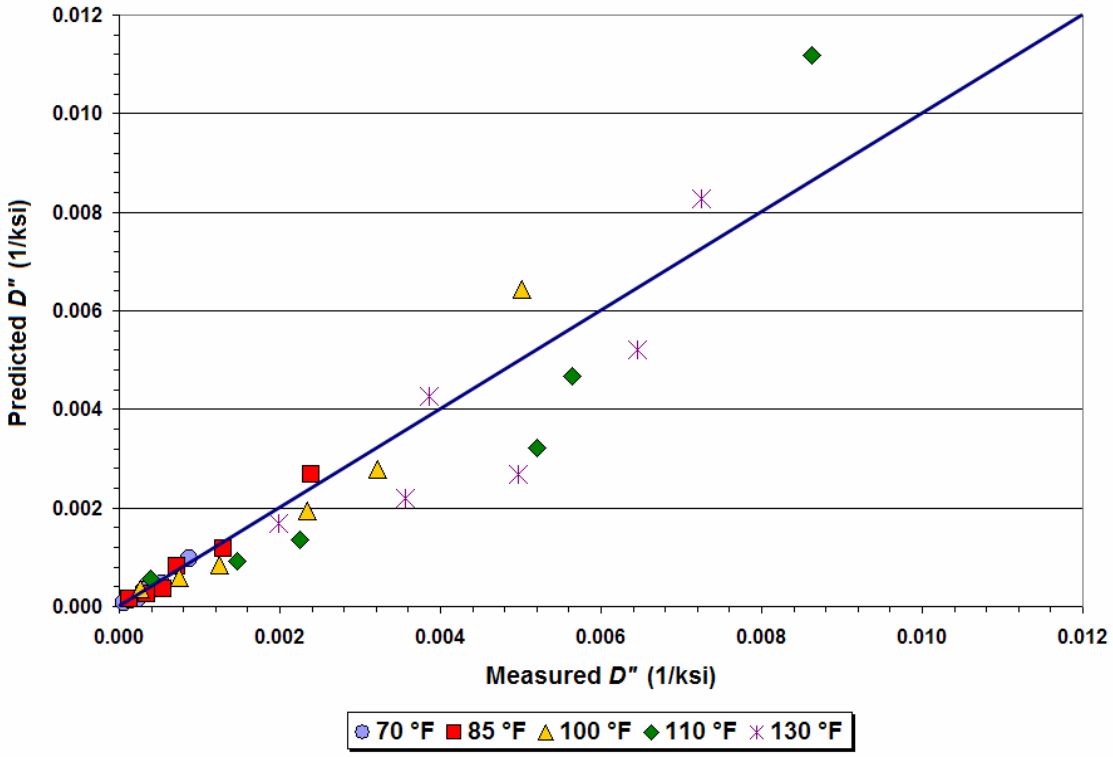

Figure E6. Comparison of Predicted and Measured Imaginary Components of the Complex Compliance at Different Temperatures and Frequencies (K6-11 Core).

Table E3. Predicted and Measured Real and Imaginary Components of the Complex Compliance at Different Temperatures and Frequencies (K6-11 Core).

Temperature (°F)	Frequency (Hz)	Real Component D' (ksi^{-1})		Imaginary Component D'' (ksi^{-1})	
		Measured	Predicted	Measured	Predicted
70	25	3.08E-04	2.81E-04	6.64E-05	8.00E-05
70	10	3.11E-04	3.28E-04	1.48E-04	1.21E-04
70	5	3.50E-04	3.81E-04	2.28E-04	1.66E-04
70	1	6.31E-04	5.87E-04	3.08E-04	3.42E-04
70	0.5	7.52E-04	7.31E-04	5.29E-04	4.66E-04
70	0.1	1.32E-03	1.31E-03	8.76E-04	9.59E-04
85	25	8.69E-04	9.59E-04	1.21E-04	1.60E-04
85	10	9.73E-04	1.05E-03	3.48E-04	2.55E-04
85	5	1.13E-03	1.15E-03	5.42E-04	3.64E-04
85	1	1.95E-03	1.60E-03	7.25E-04	8.28E-04
85	0.5	2.33E-03	1.95E-03	1.29E-03	1.18E-03
85	0.1	4.22E-03	3.39E-03	2.39E-03	2.68E-03
100	25	1.36E-03	1.56E-03	2.60E-04	3.70E-04
100	10	1.70E-03	1.77E-03	7.45E-04	5.94E-04
100	5	2.10E-03	2.01E-03	1.26E-03	8.49E-04
100	1	3.68E-03	3.06E-03	2.34E-03	1.95E-03
100	0.5	5.21E-03	3.86E-03	3.22E-03	2.79E-03
100	0.1	9.52E-03	7.31E-03	5.02E-03	6.42E-03
110	25	1.95E-03	2.15E-03	3.94E-04	5.62E-04
110	10	2.48E-03	2.47E-03	1.46E-03	9.25E-04
110	5	3.04E-03	2.84E-03	2.26E-03	1.35E-03
110	1	4.51E-03	4.48E-03	5.20E-03	3.21E-03
110	0.5	7.18E-03	5.76E-03	5.64E-03	4.67E-03
110	0.1	1.17E-02	1.15E-02	8.63E-03	1.12E-02
130	25	3.14E-03	3.45E-03	1.99E-03	1.68E-03
130	10	4.37E-03	4.49E-03	3.56E-03	2.19E-03
130	5	5.38E-03	5.49E-03	4.97E-03	2.68E-03
130	1	8.83E-03	8.76E-03	3.86E-03	4.26E-03
130	0.5	1.07E-02	1.07E-02	6.45E-03	5.20E-03
130	0.1	1.32E-02	1.70E-02	7.25E-03	8.28E-03

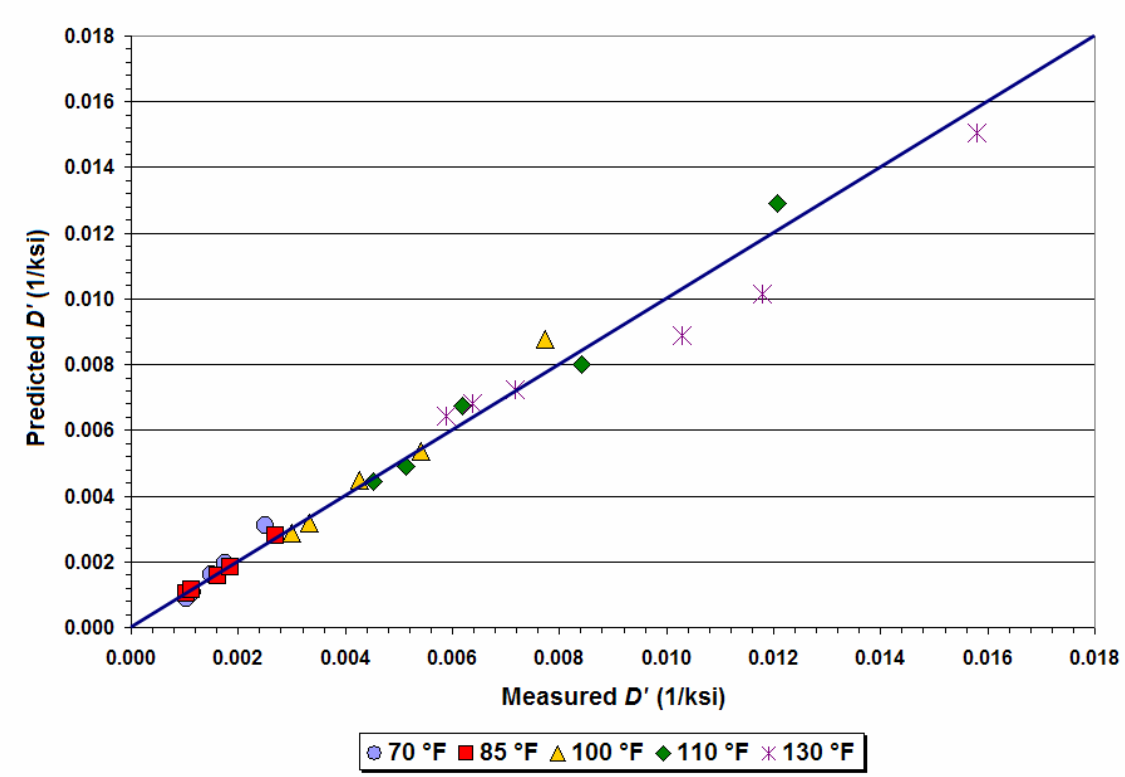

Figure E7. Comparison of Predicted and Measured Real Components of the Complex Compliance at Different Temperatures and Frequencies (K6-23 Core).

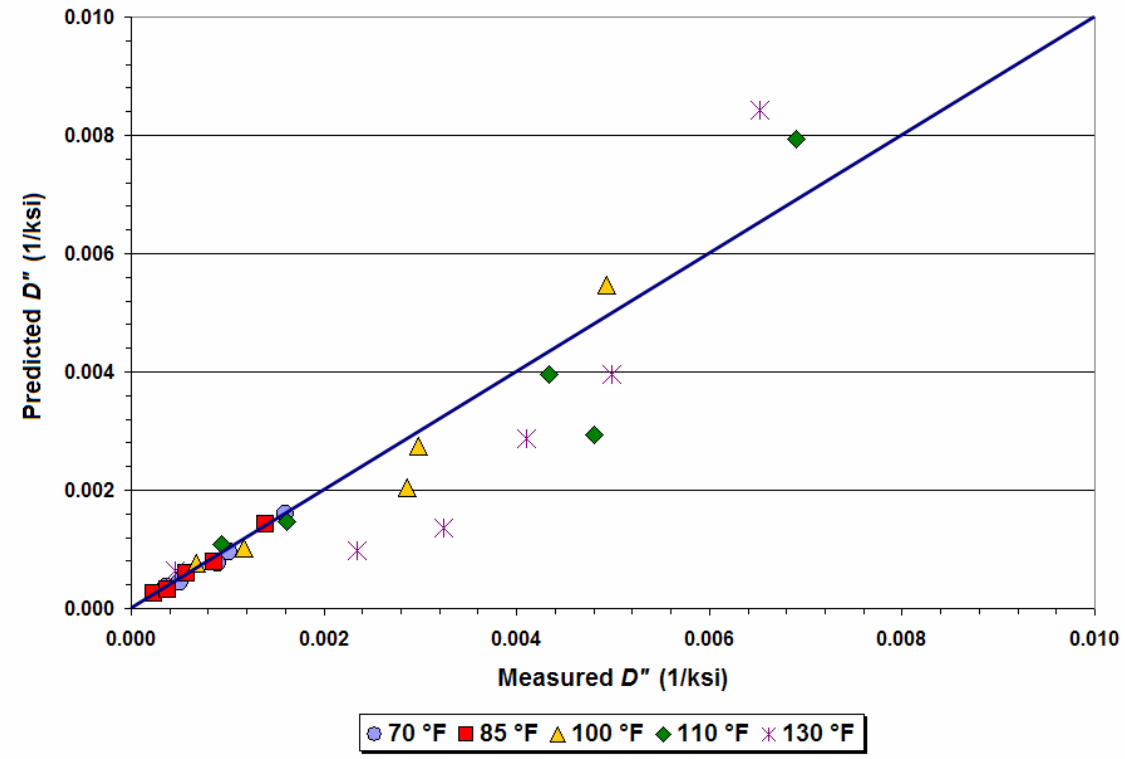

Figure E8. Comparison of Predicted and Measured Imaginary Components of the Complex Compliance at Different Temperatures and Frequencies (K6-23 Core).

Table E4. Predicted and Measured Real and Imaginary Components of the Complex Compliance at Different Temperatures and Frequencies (K6-23 Core).

Temperature (°F)	Frequency (Hz)	Real Component D' (ksi^{-1})		Imaginary Component D'' (ksi^{-1})	
		Measured	Predicted	Measured	Predicted
70	10	1.04E-03	8.90E-04	3.60E-04	3.60E-04
70	5	1.14E-03	1.06E-03	5.07E-04	4.51E-04
70	1	1.50E-03	1.61E-03	8.97E-04	7.59E-04
70	0.5	1.77E-03	1.95E-03	1.02E-03	9.52E-04
70	0.1	2.51E-03	3.12E-03	1.60E-03	1.60E-03
85	10	1.04E-03	1.04E-03	2.31E-04	2.52E-04
85	5	1.13E-03	1.15E-03	3.77E-04	3.27E-04
85	1	1.61E-03	1.55E-03	5.66E-04	6.00E-04
85	0.5	1.84E-03	1.82E-03	8.63E-04	7.80E-04
85	0.1	2.70E-03	2.79E-03	1.39E-03	1.44E-03
100	10	3.00E-03	2.86E-03	6.72E-04	7.66E-04
100	5	3.33E-03	3.19E-03	1.17E-03	1.03E-03
100	1	4.26E-03	4.47E-03	2.87E-03	2.04E-03
100	0.5	5.42E-03	5.35E-03	2.99E-03	2.75E-03
100	0.1	7.73E-03	8.76E-03	4.93E-03	5.46E-03
110	10	4.53E-03	4.43E-03	9.38E-04	1.09E-03
110	5	5.14E-03	4.91E-03	1.61E-03	1.47E-03
110	1	6.19E-03	6.73E-03	4.80E-03	2.94E-03
110	0.5	8.42E-03	8.00E-03	4.33E-03	3.96E-03
110	0.1	1.21E-02	1.29E-02	6.90E-03	7.94E-03
130	25	5.87E-03	6.43E-03	4.51E-04	6.34E-04
130	10	6.38E-03	6.81E-03	2.34E-03	9.73E-04
130	5	7.18E-03	7.25E-03	3.24E-03	1.35E-03
130	1	1.03E-02	8.90E-03	4.11E-03	2.87E-03
130	0.5	1.18E-02	1.01E-02	4.98E-03	3.97E-03
130	0.1	1.58E-02	1.50E-02	6.53E-03	8.42E-03

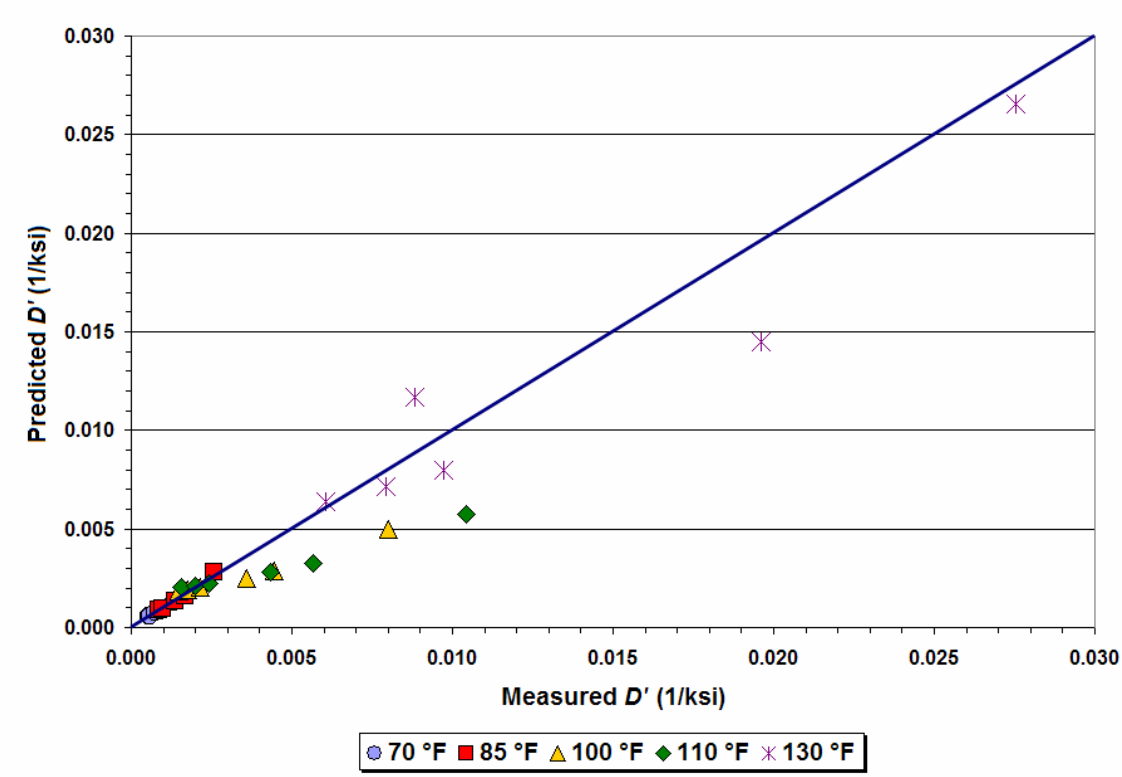

Figure E9. Comparison of Predicted and Measured Real Components of the Complex Compliance at Different Temperatures and Frequencies (K6-29 Core).

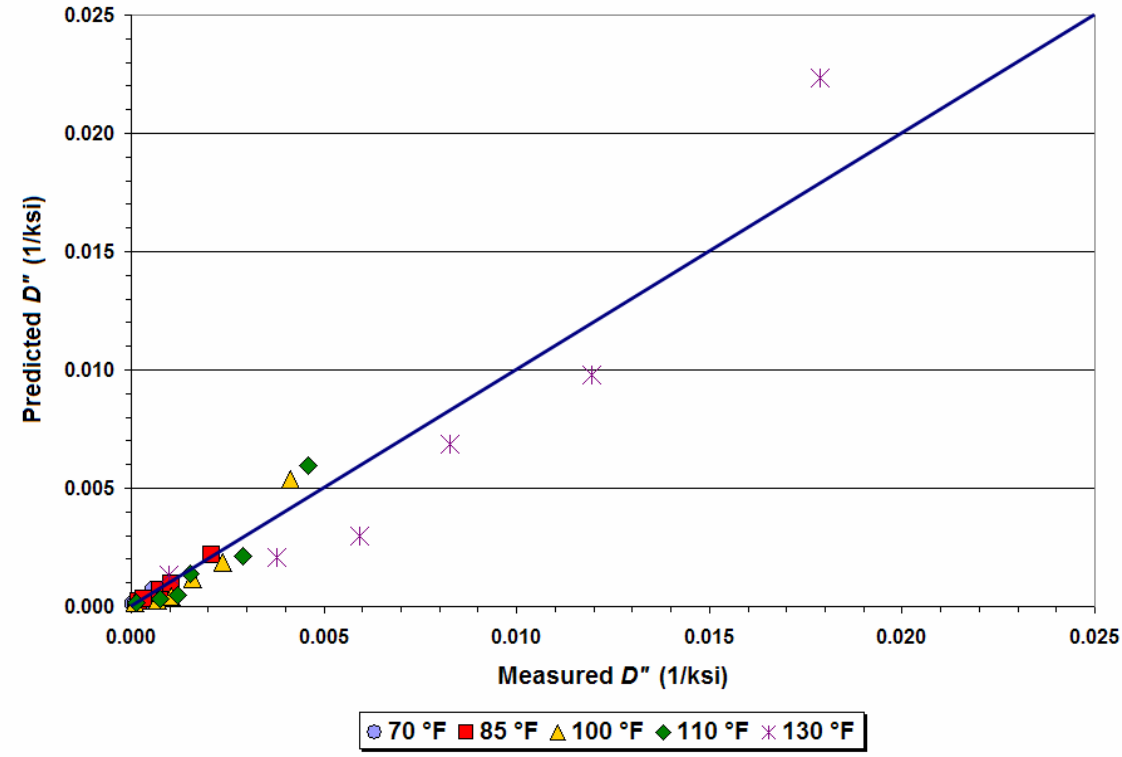

Figure E10. Comparison of Predicted and Measured Imaginary Components of the Complex Compliance at Different Temperatures and Frequencies (K6-29 Core).

Table E5. Predicted and Measured Real and Imaginary Components of the Complex Compliance at Different Temperatures and Frequencies (K6-29 Core).

Temperature (°F)	Frequency (Hz)	Real Component D' (ksi^{-1})		Imaginary Component D'' (ksi^{-1})	
		Measured	Predicted	Measured	Predicted
70	10	5.38E-04	5.67E-04	6.90E-05	8.35E-05
70	5	5.93E-04	6.02E-04	1.31E-04	1.14E-04
70	1	7.59E-04	7.45E-04	3.45E-04	2.37E-04
70	0.5	8.97E-04	8.49E-04	3.38E-04	3.24E-04
70	0.1	1.31E-03	1.25E-03	5.87E-04	6.71E-04
85	10	8.49E-04	8.69E-04	1.89E-04	2.08E-04
85	5	9.73E-04	9.59E-04	3.22E-04	2.97E-04
85	1	1.37E-03	1.32E-03	7.38E-04	6.78E-04
85	0.5	1.67E-03	1.60E-03	1.04E-03	9.66E-04
85	0.1	2.59E-03	2.79E-03	2.07E-03	2.20E-03
100	25	1.48E-03	1.86E-03	9.66E-05	1.43E-04
100	10	1.76E-03	1.93E-03	6.69E-04	2.61E-04
100	5	2.13E-03	2.02E-03	1.03E-03	4.11E-04
100	1	3.61E-03	2.48E-03	1.58E-03	1.19E-03
100	0.5	4.44E-03	2.89E-03	2.37E-03	1.87E-03
100	0.1	8.00E-03	4.99E-03	4.13E-03	5.40E-03
110	25	1.56E-03	2.04E-03	1.18E-04	1.75E-04
110	10	2.01E-03	2.13E-03	7.38E-04	3.14E-04
110	5	2.43E-03	2.24E-03	1.19E-03	4.89E-04
110	1	4.35E-03	2.80E-03	1.54E-03	1.37E-03
110	0.5	5.67E-03	3.28E-03	2.88E-03	2.13E-03
110	0.1	1.04E-02	5.72E-03	4.60E-03	5.96E-03
130	25	6.05E-03	6.40E-03	9.73E-04	1.31E-03
130	10	7.94E-03	7.18E-03	3.79E-03	2.10E-03
130	5	9.73E-03	8.00E-03	5.93E-03	2.99E-03
130	1	8.83E-03	1.17E-02	8.28E-03	6.84E-03
130	0.5	1.96E-02	1.45E-02	1.19E-02	9.80E-03
130	0.1	2.75E-02	2.66E-02	1.79E-02	2.24E-02

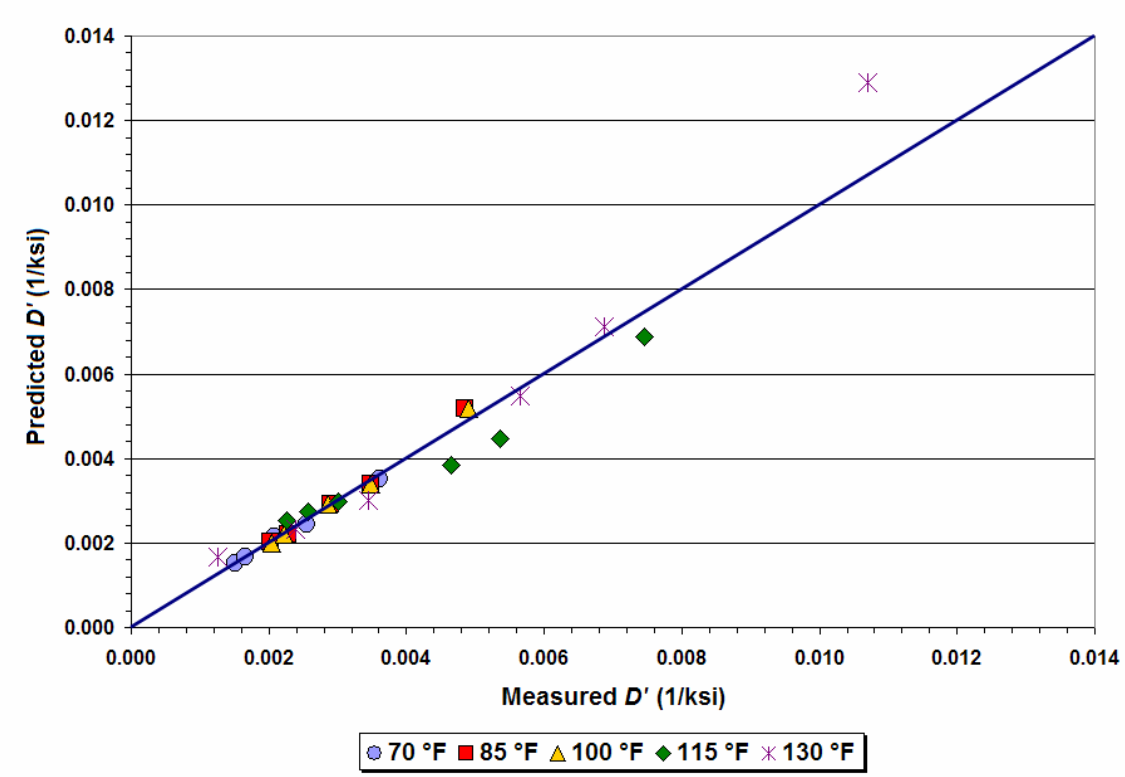

Figure E11. Comparison of Predicted and Measured Real Components of the Complex Compliance at Different Temperatures and Frequencies (K6-48 Core).

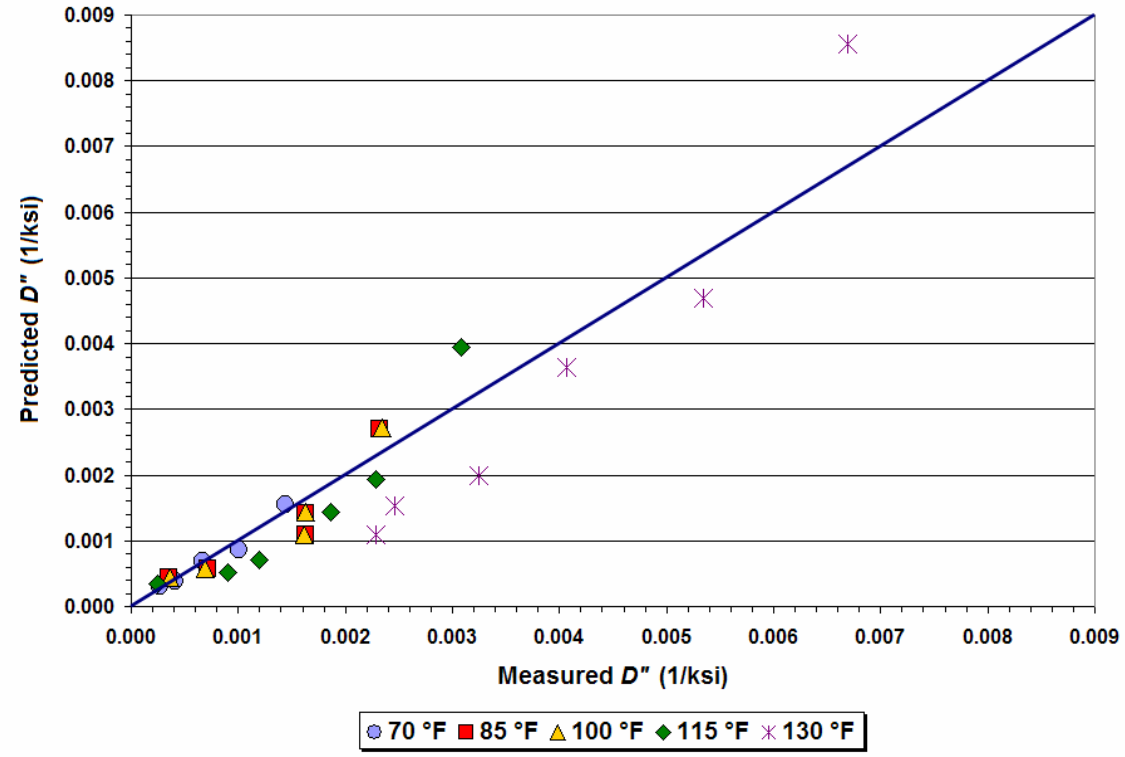

Figure E12. Comparison of Predicted and Measured Imaginary Components of the Complex Compliance at Different Temperatures and Frequencies (K6-48 Core).

Table E6. Predicted and Measured Real and Imaginary Components of the Complex Compliance at Different Temperatures and Frequencies (K6-48 Core).

Temperature (°F)	Frequency (Hz)	Real Component D' (ksi^{-1})		Imaginary Component D'' (ksi^{-1})	
		Measured	Predicted	Measured	Predicted
70	10	1.50E-03	1.53E-03	2.73E-04	2.97E-04
70	5	1.66E-03	1.66E-03	4.11E-04	3.82E-04
70	1	2.07E-03	2.13E-03	6.67E-04	6.80E-04
70	0.5	2.56E-03	2.44E-03	1.01E-03	8.69E-04
70	0.1	3.61E-03	3.52E-03	1.44E-03	1.55E-03
85	10	2.03E-03	2.02E-03	3.57E-04	4.35E-04
85	5	2.27E-03	2.21E-03	7.11E-04	5.73E-04
85	1	2.90E-03	2.93E-03	1.63E-03	1.08E-03
85	0.5	3.48E-03	3.41E-03	1.63E-03	1.42E-03
85	0.1	4.84E-03	5.18E-03	2.32E-03	2.69E-03
100	10	2.04E-03	2.01E-03	3.58E-04	4.34E-04
100	5	2.22E-03	2.20E-03	6.97E-04	5.72E-04
100	1	2.87E-03	2.91E-03	1.62E-03	1.09E-03
100	0.5	3.48E-03	3.39E-03	1.63E-03	1.44E-03
100	0.1	4.90E-03	5.18E-03	2.35E-03	2.72E-03
115	25	2.26E-03	2.55E-03	2.44E-04	3.45E-04
115	10	2.57E-03	2.75E-03	9.04E-04	5.17E-04
115	5	3.02E-03	2.97E-03	1.19E-03	7.04E-04
115	1	4.66E-03	3.85E-03	1.86E-03	1.43E-03
115	0.5	5.35E-03	4.46E-03	2.29E-03	1.94E-03
115	0.1	7.45E-03	6.88E-03	3.08E-03	3.95E-03
130	25	1.25E-03	1.66E-03	2.29E-03	1.10E-03
130	10	2.39E-03	2.33E-03	2.46E-03	1.54E-03
130	5	3.44E-03	3.02E-03	3.24E-03	1.99E-03
130	1	5.64E-03	5.49E-03	4.06E-03	3.63E-03
130	0.5	6.88E-03	7.11E-03	5.34E-03	4.70E-03
130	0.1	1.07E-02	1.29E-02	6.69E-03	8.56E-03

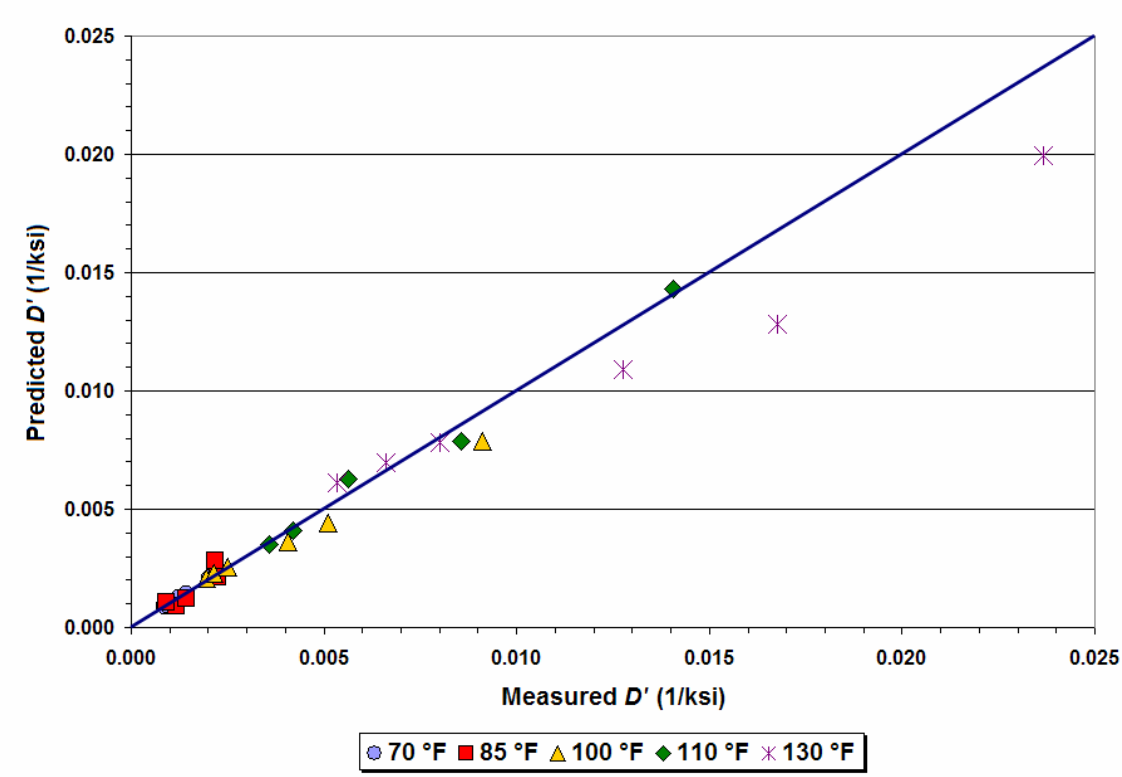

Figure E13. Comparison of Predicted and Measured Real Components of the Complex Compliance at Different Temperatures and Frequencies (K7-3 Core).

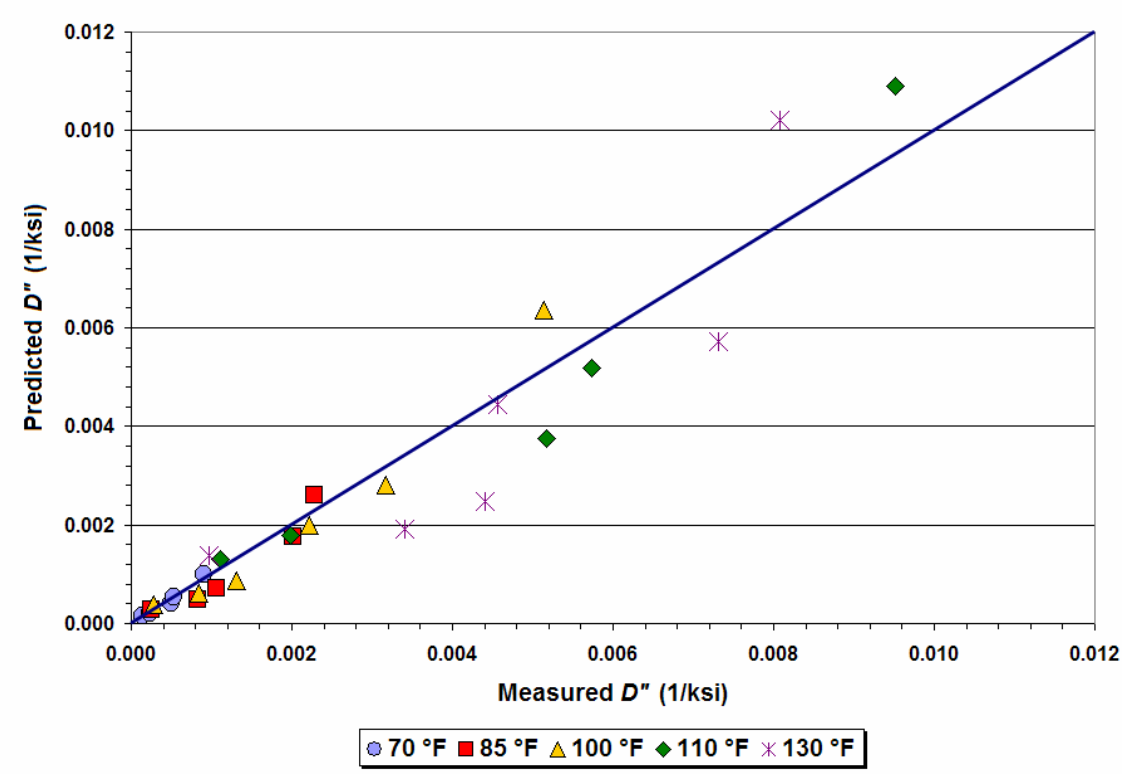

Figure E14. Comparison of Predicted and Measured Imaginary Components of the Complex Compliance at Different Temperatures and Frequencies (K7-3 Core).

Table E7. Predicted and Measured Real and Imaginary Components of the Complex Compliance at Different Temperatures and Frequencies (K7-3 Core).

Temperature (°F)	Frequency (Hz)	Real Component D' (ksi^{-1})		Imaginary Component D'' (ksi^{-1})	
		Measured	Predicted	Measured	Predicted
70	10	8.90E-04	8.97E-04	1.39E-04	1.59E-04
70	5	9.59E-04	9.66E-04	2.35E-04	2.10E-04
70	1	1.22E-03	1.23E-03	4.95E-04	3.98E-04
70	0.5	1.43E-03	1.40E-03	5.37E-04	5.24E-04
70	0.1	2.06E-03	2.05E-03	9.04E-04	9.94E-04
85	25	1.17E-03	8.97E-04	2.50E-04	2.90E-04
85	10	9.04E-04	1.06E-03	8.21E-04	4.86E-04
85	5	1.44E-03	1.25E-03	1.06E-03	7.18E-04
85	1	2.26E-03	2.11E-03	2.01E-03	1.77E-03
85	0.5	2.19E-03	2.81E-03	2.28E-03	2.62E-03
100	25	1.94E-03	2.06E-03	2.82E-04	3.86E-04
100	10	2.15E-03	2.28E-03	8.42E-04	6.15E-04
100	5	2.50E-03	2.54E-03	1.32E-03	8.76E-04
100	1	4.08E-03	3.62E-03	2.22E-03	1.98E-03
100	0.5	5.10E-03	4.43E-03	3.17E-03	2.81E-03
100	0.1	9.11E-03	7.87E-03	5.15E-03	6.35E-03
110	10	3.59E-03	3.53E-03	1.11E-03	1.29E-03
110	5	4.21E-03	4.07E-03	1.99E-03	1.78E-03
110	1	5.62E-03	6.29E-03	5.17E-03	3.75E-03
110	0.5	8.56E-03	7.87E-03	5.73E-03	5.18E-03
110	0.1	1.41E-02	1.43E-02	9.52E-03	1.09E-02
130	25	5.34E-03	6.11E-03	9.73E-04	1.38E-03
130	10	6.61E-03	6.97E-03	3.41E-03	1.93E-03
130	5	8.00E-03	7.80E-03	4.41E-03	2.48E-03
130	1	1.28E-02	1.09E-02	4.56E-03	4.44E-03
130	0.5	1.68E-02	1.28E-02	7.31E-03	5.71E-03
130	0.1	2.37E-02	1.99E-02	8.07E-03	1.02E-02

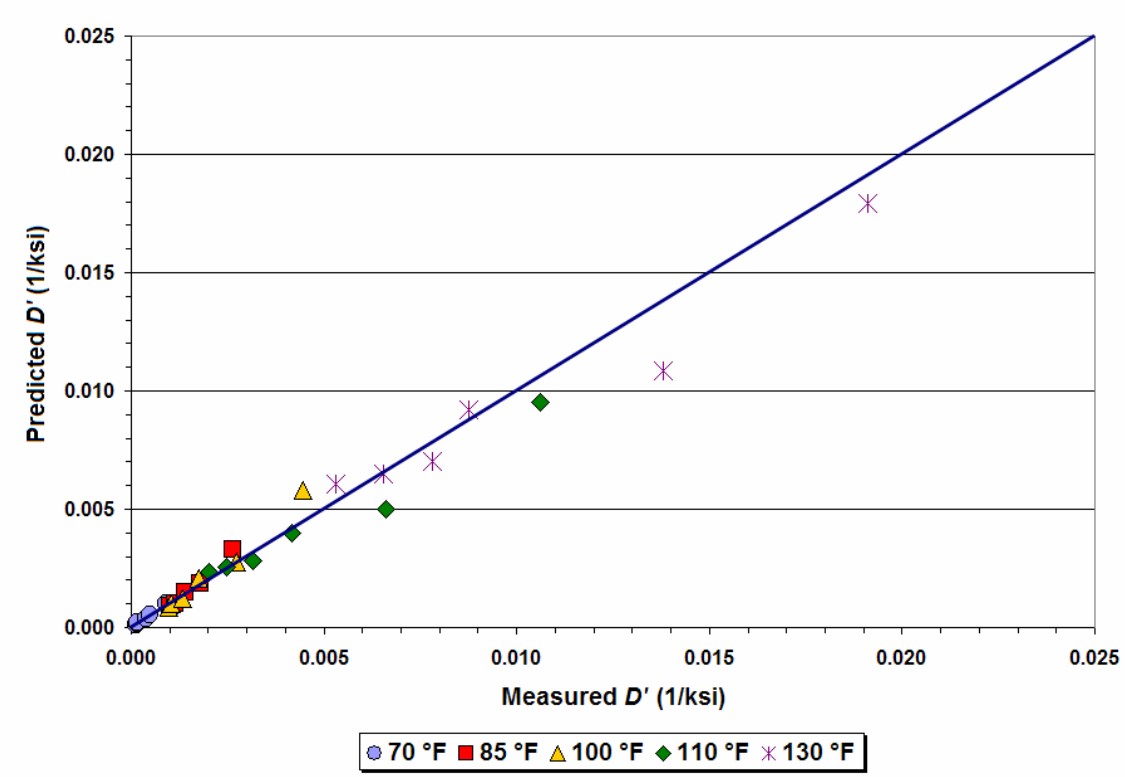

Figure E15. Comparison of Predicted and Measured Real Components of the Complex Compliance at Different Temperatures and Frequencies (K7-11 Core).

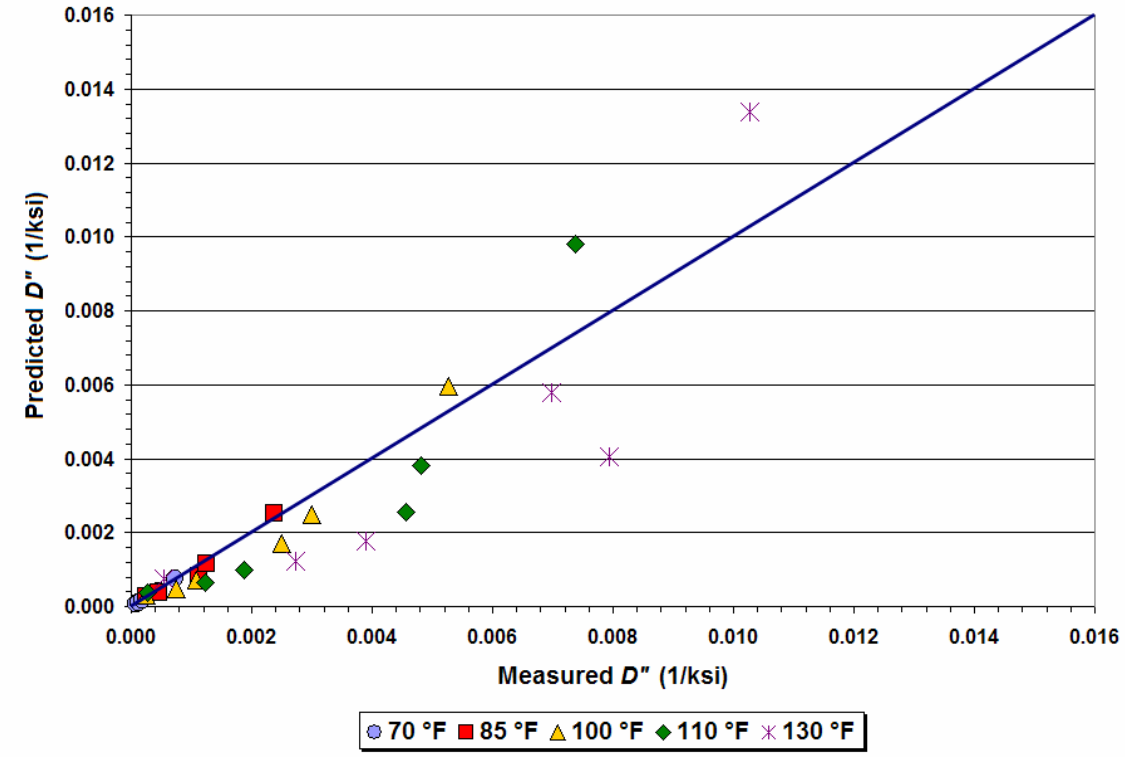

Figure E16. Comparison of Predicted and Measured Imaginary Components of the Complex Compliance at Different Temperatures and Frequencies (K7-11 Core).

Table E8. Predicted and Measured Real and Imaginary Components of the Complex Compliance at Different Temperatures and Frequencies (K7-11 Core).

Temperature (°F)	Frequency (Hz)	Real Component D' (ksi^{-1})		Imaginary Component D'' (ksi^{-1})	
		Measured	Predicted	Measured	Predicted
70	25	1.39E-04	1.07E-04	8.63E-05	8.00E-05
70	10	1.49E-04	1.55E-04	1.28E-04	1.16E-04
70	5	1.78E-04	2.06E-04	1.86E-04	1.54E-04
70	1	3.75E-04	3.98E-04	2.96E-04	2.97E-04
70	0.5	4.82E-04	5.28E-04	4.53E-04	3.93E-04
70	0.1	8.97E-04	1.01E-03	7.38E-04	7.59E-04
85	10	9.94E-04	9.11E-04	2.55E-04	2.74E-04
85	5	1.12E-03	1.03E-03	4.50E-04	3.82E-04
85	1	1.40E-03	1.50E-03	1.12E-03	8.28E-04
85	0.5	1.80E-03	1.85E-03	1.26E-03	1.16E-03
85	0.1	2.64E-03	3.28E-03	2.37E-03	2.51E-03
100	25	9.66E-04	8.63E-04	2.55E-04	2.99E-04
100	10	1.06E-03	1.04E-03	7.45E-04	4.91E-04
100	5	1.32E-03	1.23E-03	1.09E-03	7.18E-04
100	1	1.77E-03	2.10E-03	2.50E-03	1.71E-03
100	0.5	2.73E-03	2.78E-03	3.00E-03	2.48E-03
100	0.1	4.44E-03	5.82E-03	5.28E-03	5.95E-03
110	25	2.03E-03	2.35E-03	2.66E-04	3.88E-04
110	10	2.48E-03	2.56E-03	1.22E-03	6.64E-04
110	5	3.17E-03	2.82E-03	1.88E-03	9.94E-04
110	1	4.16E-03	4.00E-03	4.55E-03	2.55E-03
110	0.5	6.62E-03	4.97E-03	4.82E-03	3.82E-03
110	0.1	1.06E-02	9.52E-03	7.38E-03	9.80E-03
130	25	5.30E-03	6.07E-03	5.38E-04	7.66E-04
130	10	6.56E-03	6.51E-03	2.74E-03	1.23E-03
130	5	7.80E-03	7.04E-03	3.91E-03	1.76E-03
130	1	8.76E-03	9.18E-03	7.94E-03	4.05E-03
130	0.5	1.38E-02	1.08E-02	6.97E-03	5.80E-03
130	0.1	1.91E-02	1.79E-02	1.03E-02	1.34E-02

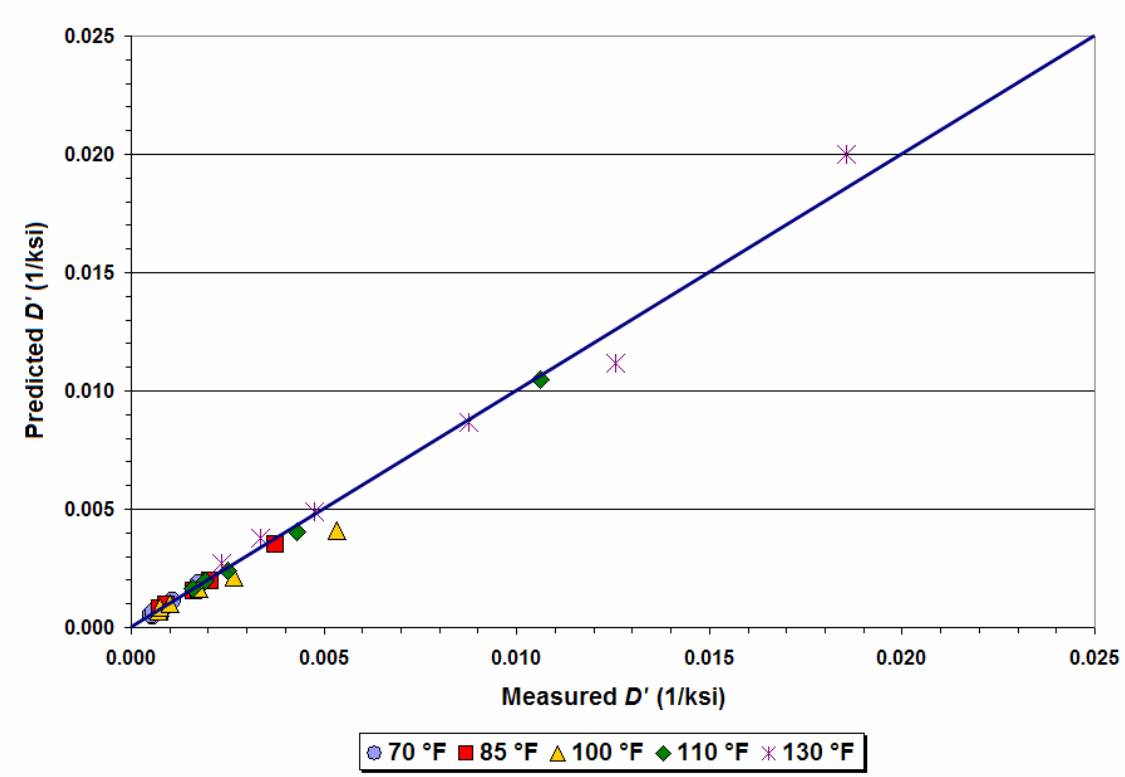

Figure E17. Comparison of Predicted and Measured Real Components of the Complex Compliance at Different Temperatures and Frequencies (K7-15 Core).

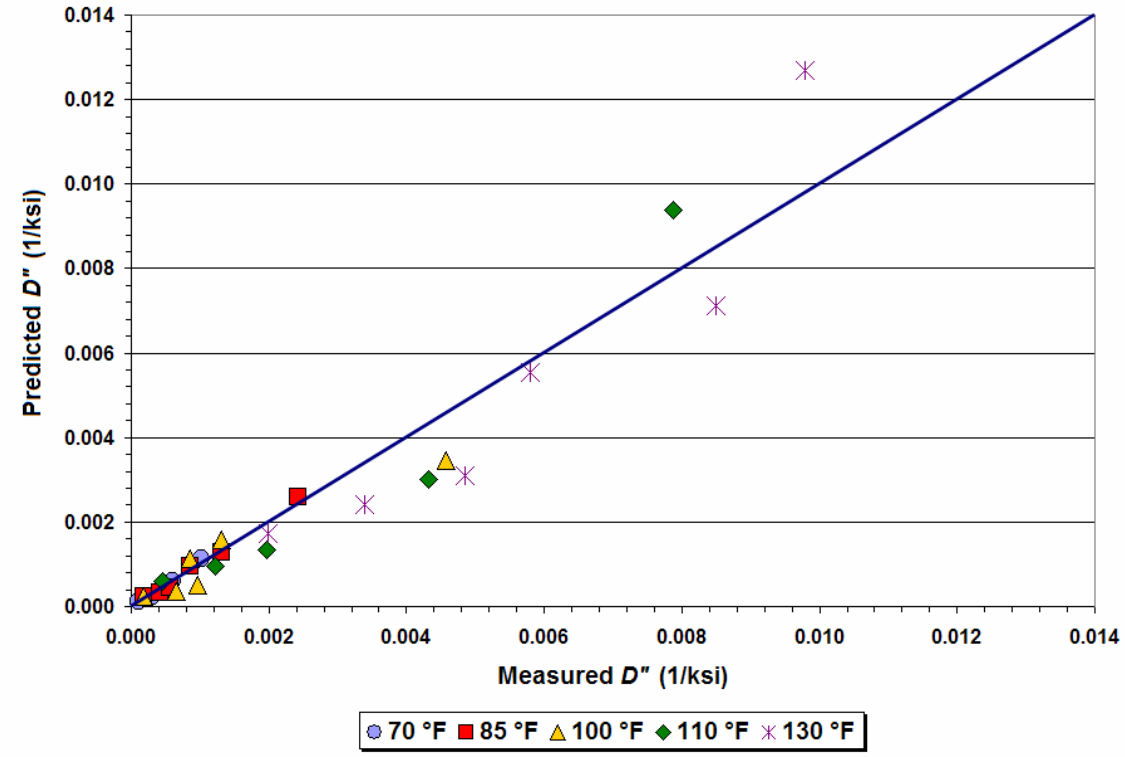

Figure E18. Comparison of Predicted and Measured Imaginary Components of the Complex Compliance at Different Temperatures and Frequencies (K7-15 Core).

Table E9. Predicted and Measured Real and Imaginary Components of the Complex Compliance at Different Temperatures and Frequencies (K7-15 Core).

Temperature °F	Frequency (Hz)	Real Component D' (ksi^{-1})		Imaginary Component D'' (ksi^{-1})	
		Measured	Predicted	Measured	Predicted
70	25	5.48E-04	4.68E-04	1.05E-04	1.24E-04
70	10	5.18E-04	5.43E-04	2.11E-04	1.78E-04
70	5	5.87E-04	6.22E-04	3.07E-04	2.35E-04
70	1	8.97E-04	9.11E-04	4.71E-04	4.46E-04
70	0.5	1.08E-03	1.11E-03	6.04E-04	5.88E-04
70	0.1	1.75E-03	1.84E-03	1.03E-03	1.12E-03
85	25	7.38E-04	6.82E-04	1.90E-04	2.27E-04
85	10	7.52E-04	8.14E-04	4.17E-04	3.40E-04
85	5	9.04E-04	9.66E-04	5.73E-04	4.62E-04
85	1	1.64E-03	1.54E-03	8.63E-04	9.38E-04
85	0.5	2.04E-03	1.95E-03	1.31E-03	1.28E-03
85	0.1	3.74E-03	3.53E-03	2.43E-03	2.59E-03
100	25	7.25E-04	7.18E-04	1.90E-04	2.35E-04
100	10	7.59E-04	8.56E-04	6.60E-04	3.68E-04
100	5	1.01E-03	1.01E-03	9.59E-04	5.15E-04
100	1	1.76E-03	1.65E-03	8.63E-04	1.12E-03
100	0.5	2.67E-03	2.12E-03	1.31E-03	1.58E-03
100	0.1	5.35E-03	4.08E-03	4.58E-03	3.45E-03
110	25	1.59E-03	1.64E-03	4.59E-04	6.07E-04
110	10	1.93E-03	1.99E-03	1.23E-03	9.52E-04
110	5	2.49E-03	2.38E-03	1.97E-03	1.35E-03
110	1	4.31E-03	4.05E-03	4.33E-03	2.99E-03
110	0.1	1.06E-02	1.05E-02	7.87E-03	9.38E-03
130	25	2.36E-03	2.73E-03	1.99E-03	1.74E-03
130	10	3.37E-03	3.80E-03	3.39E-03	2.42E-03
130	5	4.77E-03	4.88E-03	4.85E-03	3.10E-03
130	1	8.76E-03	8.69E-03	5.79E-03	5.53E-03
130	0.5	1.26E-02	1.12E-02	8.49E-03	7.11E-03
130	0.1	1.86E-02	2.00E-02	9.80E-03	1.27E-02

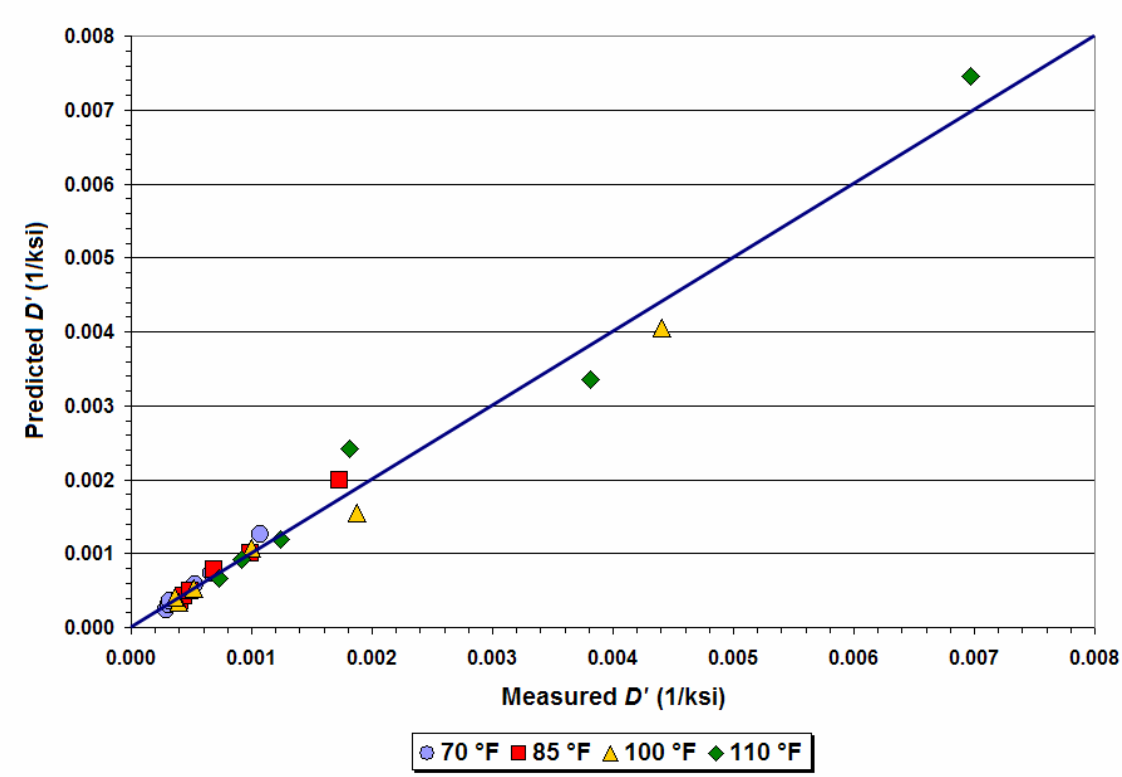

Figure E19. Comparison of Predicted and Measured Real Components of the Complex Compliance at Different Temperatures and Frequencies (K7-20 Core).

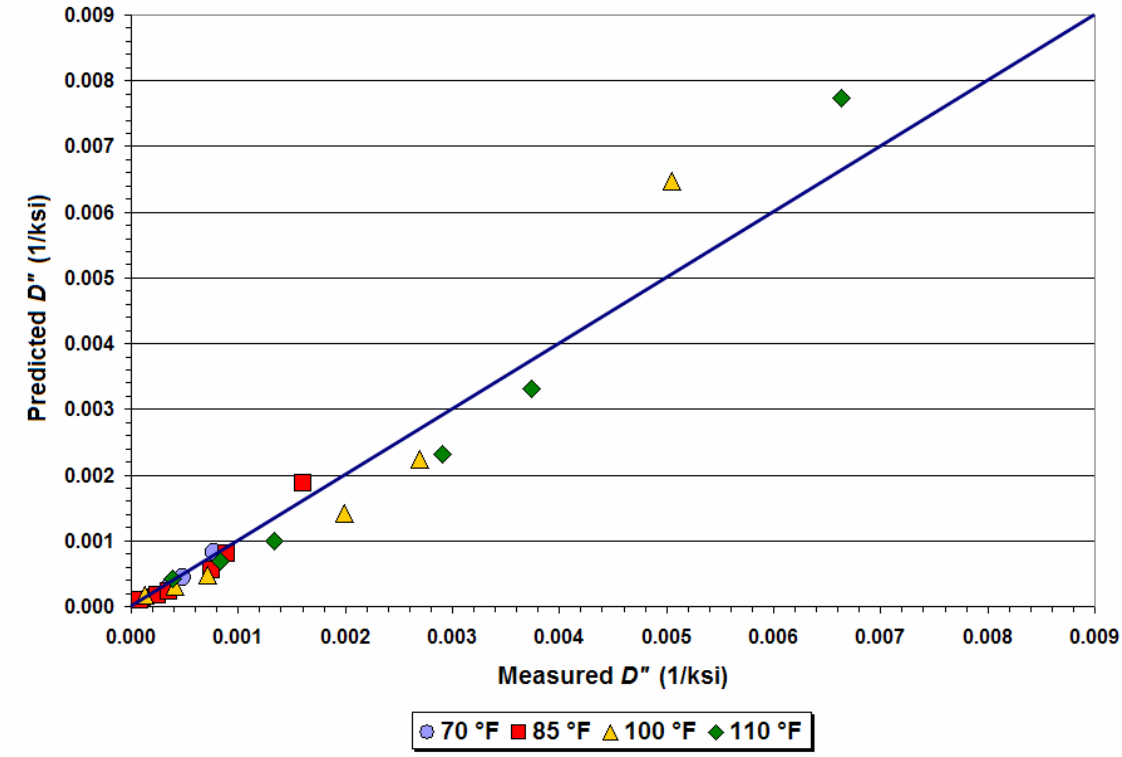

Figure E20. Comparison of Predicted and Measured Imaginary Components of the Complex Compliance at Different Temperatures and Frequencies (K7-20 Core).

Table E10. Predicted and Measured Real and Imaginary Components of the Complex Compliance at Different Temperatures and Frequencies (K7-20 Core).

Temperature (°F)	Frequency (Hz)	Real Component D' (ksi^{-1})		Imaginary Component D'' (ksi^{-1})	
		Measured	Predicted	Measured	Predicted
70	25	2.95E-04	2.41E-04	8.69E-05	9.38E-05
70	10	3.14E-04	2.98E-04	1.57E-04	1.35E-04
70	5	3.23E-04	3.57E-04	2.22E-04	1.77E-04
70	1	5.30E-04	5.77E-04	3.73E-04	3.33E-04
70	0.5	6.65E-04	7.25E-04	4.77E-04	4.36E-04
70	0.1	1.08E-03	1.26E-03	7.73E-04	8.21E-04
85	25	4.05E-04	3.66E-04	8.14E-05	1.01E-04
85	10	4.35E-04	4.23E-04	2.50E-04	1.65E-04
85	5	4.84E-04	4.90E-04	3.53E-04	2.37E-04
85	1	6.90E-04	7.80E-04	7.52E-04	5.55E-04
85	0.5	9.94E-04	1.01E-03	8.90E-04	8.00E-04
85	0.1	1.73E-03	1.99E-03	1.61E-03	1.88E-03
100	25	3.93E-04	3.33E-04	1.24E-04	1.68E-04
100	10	3.62E-04	4.16E-04	4.13E-04	3.08E-04
100	5	5.17E-04	5.22E-04	7.18E-04	4.88E-04
100	1	1.00E-03	1.07E-03	1.99E-03	1.41E-03
100	0.5	1.87E-03	1.55E-03	2.69E-03	2.24E-03
100	0.1	4.40E-03	4.05E-03	5.05E-03	6.48E-03
110	25	7.31E-04	6.68E-04	3.83E-04	4.28E-04
110	10	9.18E-04	9.11E-04	8.35E-04	6.90E-04
110	5	1.24E-03	1.19E-03	1.34E-03	9.94E-04
110	1	1.81E-03	2.42E-03	2.91E-03	2.31E-03
110	0.5	3.81E-03	3.35E-03	3.74E-03	3.32E-03
110	0.1	6.97E-03	7.45E-03	6.63E-03	7.73E-03

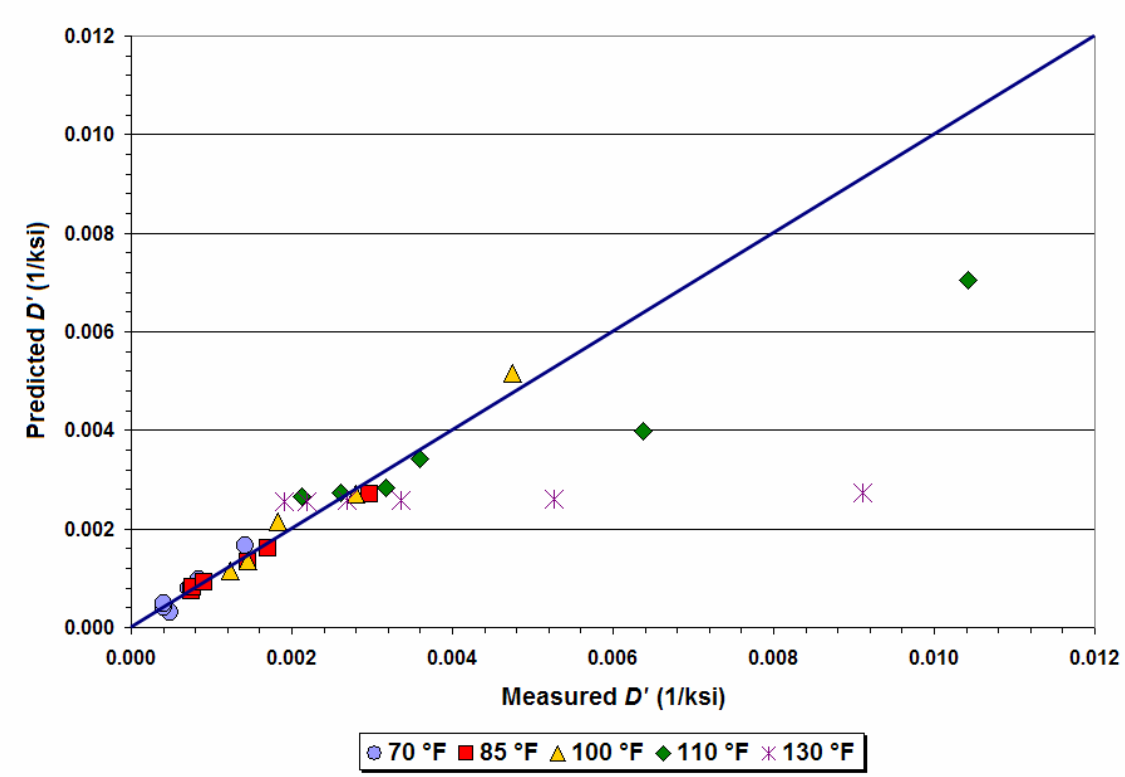

Figure E21. Comparison of Predicted and Measured Real Components of the Complex Compliance at Different Temperatures and Frequencies (K7-31 Core).

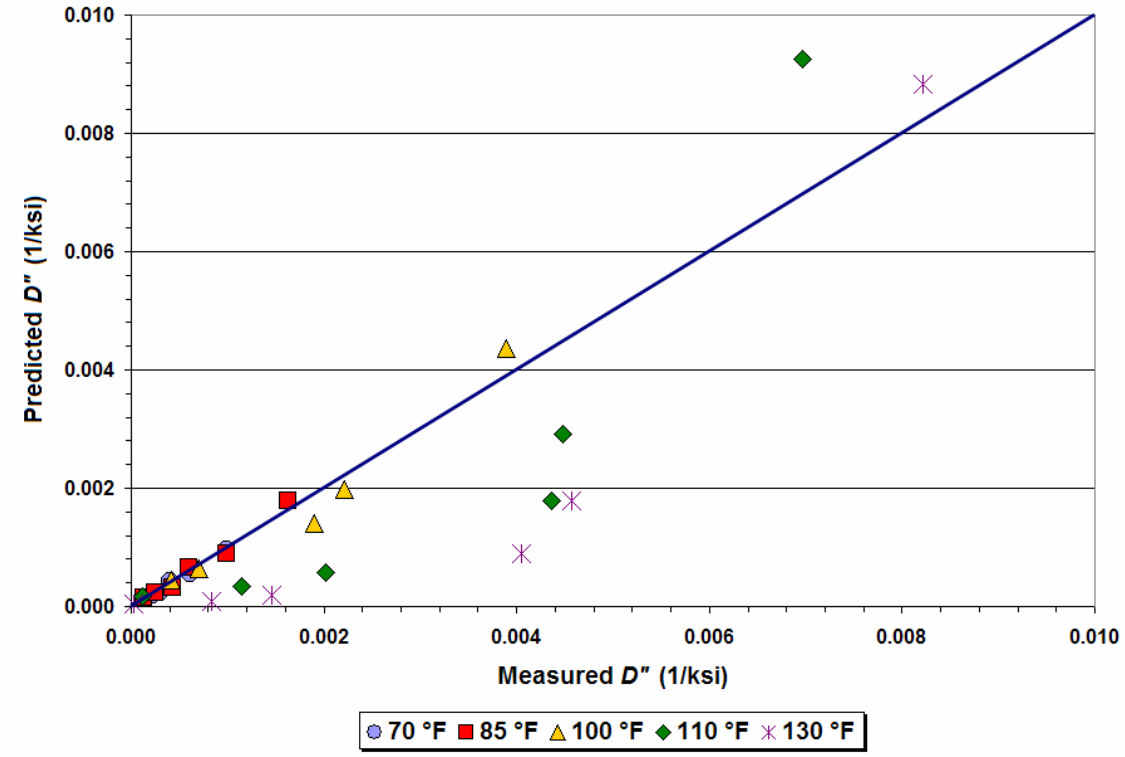

Figure E22. Comparison of Predicted and Measured Imaginary Components of the Complex Compliance at Different Temperatures and Frequencies (K7-31 Core).

Table E11. Predicted and Measured Real and Imaginary Components of the Complex Compliance at Different Temperatures and Frequencies (K7-31 Core).

Temperature °F	Frequency (Hz)	Real Component D' (ksi^{-1})		Imaginary Component D'' (ksi^{-1})	
		Measured	Predicted	Measured	Predicted
70	25	4.91E-04	3.12E-04	1.45E-04	1.39E-04
70	10	4.13E-04	3.97E-04	2.19E-04	1.90E-04
70	5	4.08E-04	4.83E-04	3.00E-04	2.43E-04
70	1	7.25E-04	7.80E-04	4.08E-04	4.27E-04
70	0.5	8.49E-04	9.73E-04	6.06E-04	5.44E-04
70	0.1	1.43E-03	1.65E-03	9.87E-04	9.59E-04
85	25	7.45E-04	7.31E-04	1.35E-04	1.58E-04
85	10	7.66E-04	8.28E-04	2.46E-04	2.37E-04
85	5	9.11E-04	9.32E-04	4.30E-04	3.21E-04
85	1	1.45E-03	1.33E-03	5.93E-04	6.51E-04
85	0.5	1.70E-03	1.61E-03	9.87E-04	8.83E-04
85	0.1	2.97E-03	2.71E-03	1.63E-03	1.79E-03
100	10	1.24E-03	1.16E-03	4.13E-04	4.51E-04
100	5	1.45E-03	1.35E-03	6.97E-04	6.34E-04
100	1	1.84E-03	2.13E-03	1.90E-03	1.40E-03
100	0.5	2.79E-03	2.72E-03	2.21E-03	1.97E-03
100	0.1	4.75E-03	5.16E-03	3.90E-03	4.37E-03
110	25	2.12E-03	2.66E-03	1.22E-04	1.79E-04
110	10	2.62E-03	2.73E-03	1.15E-03	3.44E-04
110	5	3.17E-03	2.84E-03	2.02E-03	5.64E-04
110	1	3.59E-03	3.43E-03	4.36E-03	1.78E-03
110	0.5	6.37E-03	3.97E-03	4.48E-03	2.92E-03
110	0.1	1.04E-02	7.04E-03	6.97E-03	9.25E-03
130	25	1.91E-03	2.56E-03	2.68E-05	3.76E-05
130	10	2.18E-03	2.56E-03	8.28E-04	9.32E-05
130	5	2.68E-03	2.57E-03	1.46E-03	1.84E-04
130	1	3.35E-03	2.58E-03	4.05E-03	9.04E-04
130	0.5	5.26E-03	2.59E-03	4.57E-03	1.79E-03
130	0.1	9.11E-03	2.73E-03	8.21E-03	8.83E-03

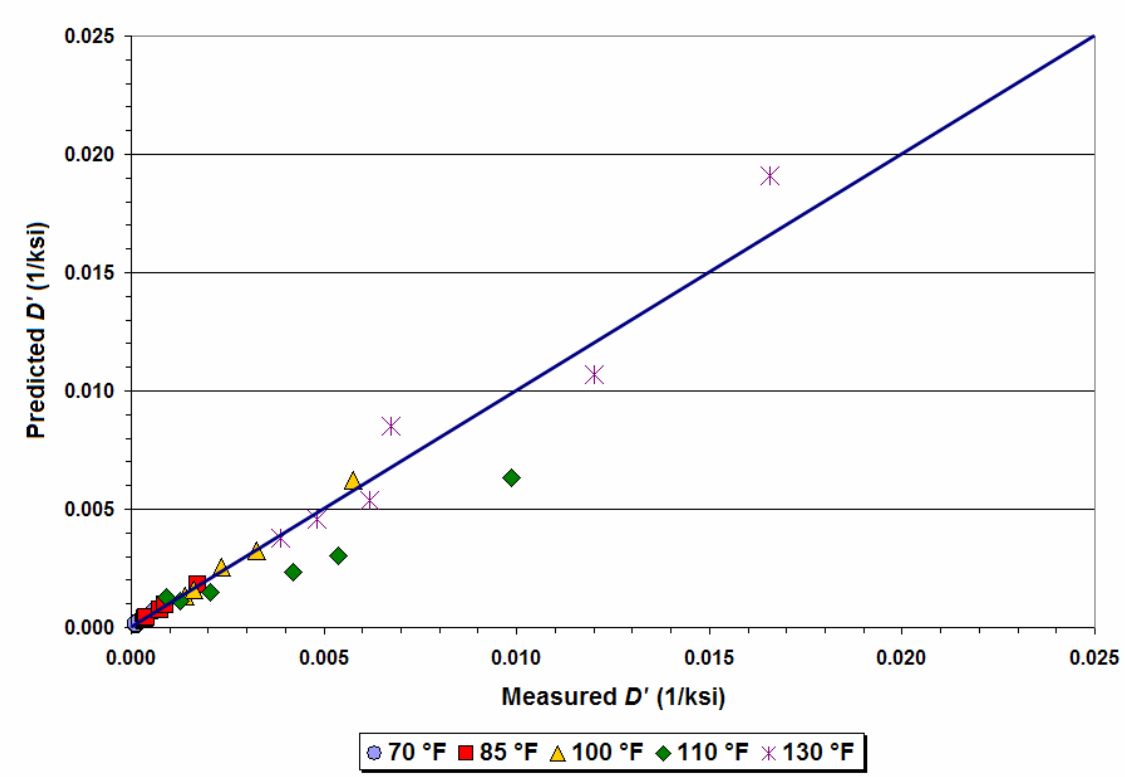

Figure E23. Comparison of Predicted and Measured Real Components of the Complex Compliance at Different Temperatures and Frequencies (K7-37 Core).

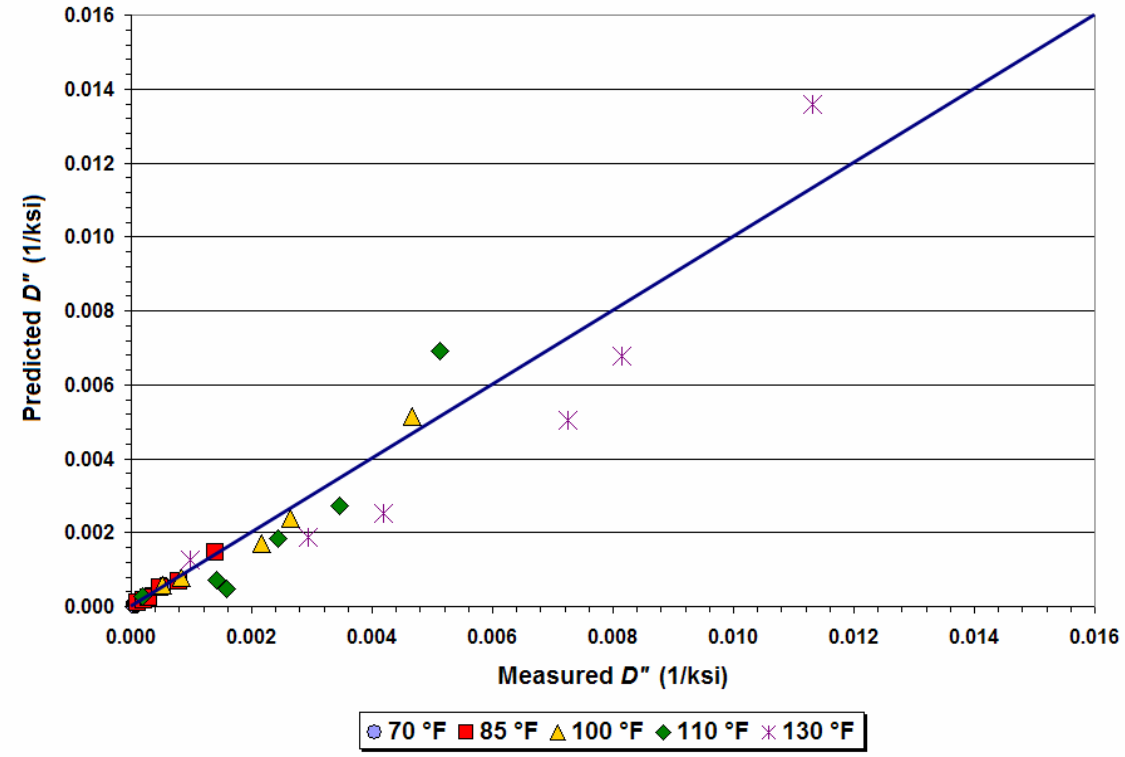

Figure E24. Comparison of Predicted and Measured Imaginary Components of the Complex Compliance at Different Temperatures and Frequencies (K7-37 Core).

Table E12. Predicted and Measured Real and Imaginary Components of the Complex Compliance at Different Temperatures and Frequencies (K7-37 Core).

Temperature °F	Frequency (Hz)	Real Component D' (ksi^{-1})		Imaginary Component D'' (ksi^{-1})	
		Measured	Predicted	Measured	Predicted
70	25	1.32E-04	9.94E-05	5.21E-05	4.84E-05
70	10	1.43E-04	1.28E-04	8.76E-05	7.25E-05
70	5	1.43E-04	1.60E-04	1.22E-04	9.80E-05
70	1	2.34E-04	2.82E-04	2.13E-04	1.99E-04
70	0.5	3.12E-04	3.68E-04	2.95E-04	2.70E-04
70	0.1	6.03E-04	7.04E-04	5.45E-04	5.46E-04
85	25	3.60E-04	3.07E-04	1.04E-04	1.13E-04
85	10	3.74E-04	3.75E-04	2.03E-04	1.73E-04
85	5	4.00E-04	4.49E-04	2.88E-04	2.39E-04
85	1	7.52E-04	7.45E-04	4.73E-04	5.03E-04
85	0.5	8.90E-04	9.59E-04	7.87E-04	6.90E-04
85	0.1	1.73E-03	1.82E-03	1.39E-03	1.46E-03
100	10	1.39E-03	1.33E-03	5.27E-04	5.68E-04
100	5	1.64E-03	1.57E-03	8.42E-04	7.94E-04
100	1	2.34E-03	2.55E-03	2.16E-03	1.71E-03
100	0.5	3.24E-03	3.27E-03	2.65E-03	2.38E-03
100	0.1	5.77E-03	6.23E-03	4.66E-03	5.15E-03
110	25	1.26E-03	1.13E-03	1.87E-04	2.84E-04
110	10	9.11E-04	1.28E-03	1.58E-03	4.83E-04
110	5	2.06E-03	1.47E-03	1.42E-03	7.25E-04
110	1	4.19E-03	2.33E-03	2.44E-03	1.83E-03
110	0.5	5.37E-03	3.04E-03	3.45E-03	2.73E-03
110	0.1	9.87E-03	6.31E-03	5.13E-03	6.90E-03
130	25	3.88E-03	3.80E-03	9.73E-04	1.26E-03
130	10	4.82E-03	4.55E-03	2.93E-03	1.86E-03
130	5	6.19E-03	5.36E-03	4.19E-03	2.51E-03
130	1	6.74E-03	8.49E-03	7.25E-03	5.04E-03
130	0.5	1.20E-02	1.07E-02	8.14E-03	6.79E-03
130	0.1	1.66E-02	1.91E-02	1.13E-02	1.36E-02

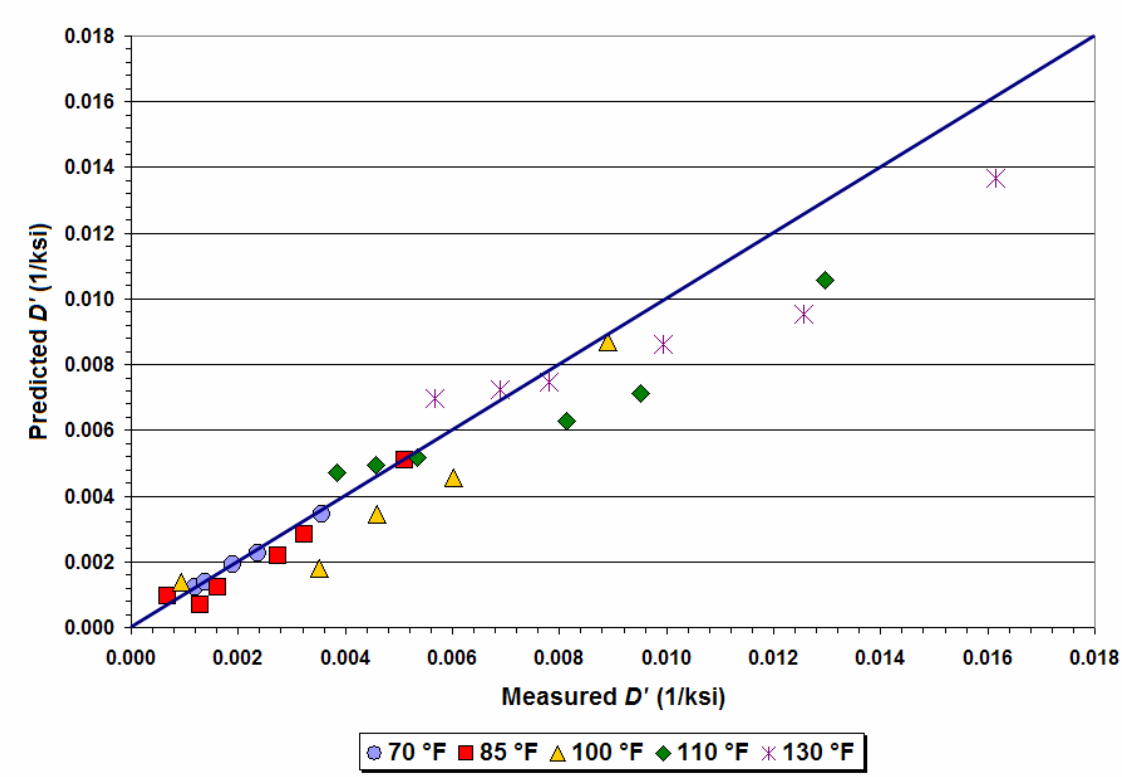

Figure E25. Comparison of Predicted and Measured Real Components of the Complex Compliance at Different Temperatures and Frequencies (K7-40 Core).

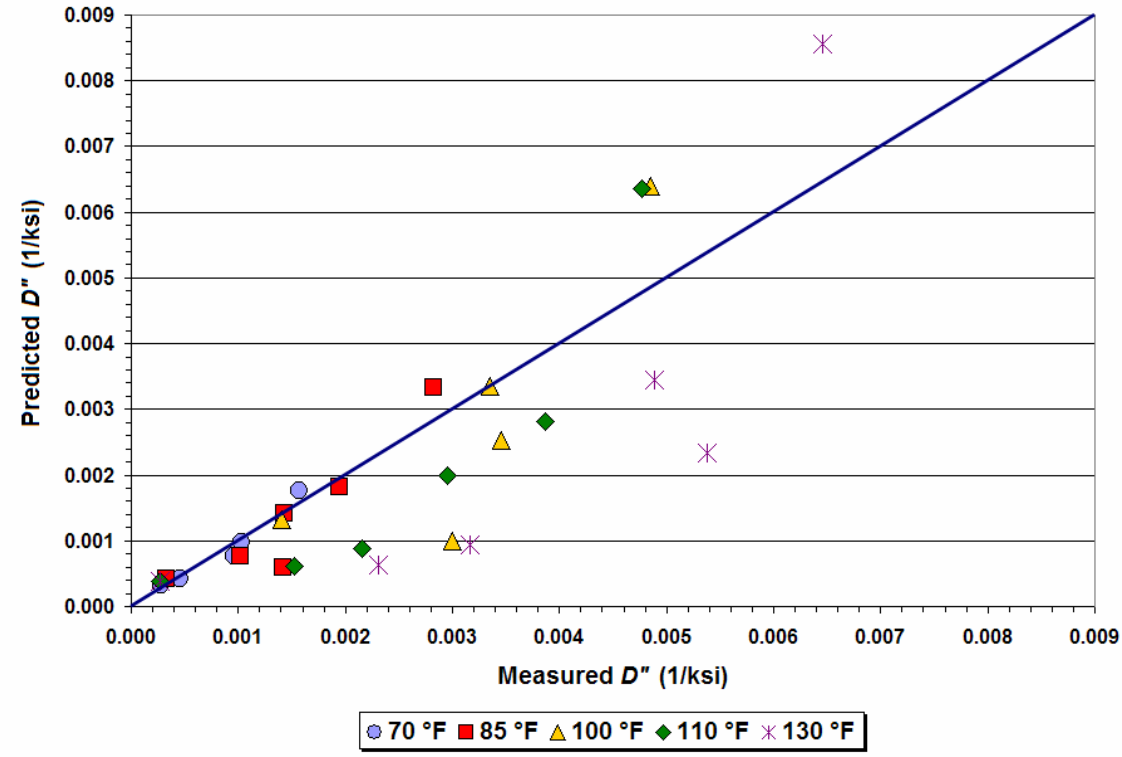

Figure E26. Comparison of Predicted and Measured Imaginary Components of the Complex Compliance at Different Temperatures and Frequencies (K7-40 Core).

Table E13. Predicted and Measured Real and Imaginary Components of the Complex Compliance at Different Temperatures and Frequencies (K7-40 Core).

Temperature °F	Frequency (Hz)	Real Component D' (ksi^{-1})		Imaginary Component D'' (ksi^{-1})	
		Measured	Predicted	Measured	Predicted
70	10	1.19E-03	1.23E-03	2.84E-04	3.29E-04
70	5	1.37E-03	1.38E-03	4.57E-04	4.24E-04
70	1	1.90E-03	1.90E-03	9.59E-04	7.59E-04
70	0.5	2.37E-03	2.24E-03	1.04E-03	9.80E-04
70	0.1	3.55E-03	3.46E-03	1.57E-03	1.77E-03
85	25	1.30E-03	7.04E-04	3.24E-04	4.24E-04
85	10	6.79E-04	9.66E-04	1.41E-03	5.98E-04
85	5	1.61E-03	1.23E-03	1.01E-03	7.73E-04
85	1	2.74E-03	2.19E-03	1.44E-03	1.41E-03
85	0.5	3.24E-03	2.82E-03	1.95E-03	1.83E-03
85	0.1	5.11E-03	5.08E-03	2.83E-03	3.33E-03
100	10	9.32E-04	1.37E-03	2.99E-03	1.00E-03
100	5	3.52E-03	1.81E-03	1.40E-03	1.32E-03
100	1	4.59E-03	3.46E-03	3.46E-03	2.53E-03
100	0.5	6.03E-03	4.57E-03	3.35E-03	3.35E-03
100	0.1	8.90E-03	8.69E-03	4.85E-03	6.39E-03
110	25	3.84E-03	4.71E-03	2.70E-04	3.91E-04
110	10	4.57E-03	4.93E-03	1.52E-03	6.20E-04
110	5	5.35E-03	5.19E-03	2.15E-03	8.83E-04
110	1	8.14E-03	6.27E-03	2.95E-03	1.99E-03
110	0.5	9.52E-03	7.11E-03	3.87E-03	2.82E-03
110	0.1	1.30E-02	1.06E-02	4.77E-03	6.35E-03
130	25	5.68E-03	6.97E-03	2.72E-04	3.82E-04
130	10	6.89E-03	7.25E-03	2.31E-03	6.39E-04
130	5	7.80E-03	7.45E-03	3.17E-03	9.45E-04
130	1	9.94E-03	8.63E-03	5.38E-03	2.34E-03
130	0.5	1.26E-02	9.52E-03	4.89E-03	3.45E-03
130	0.1	1.61E-02	1.37E-02	6.46E-03	8.56E-03

APPENDIX F

TEMPERATURE CORRECTED AC MODULI USING CHEN AND TxDOT EQUATIONS

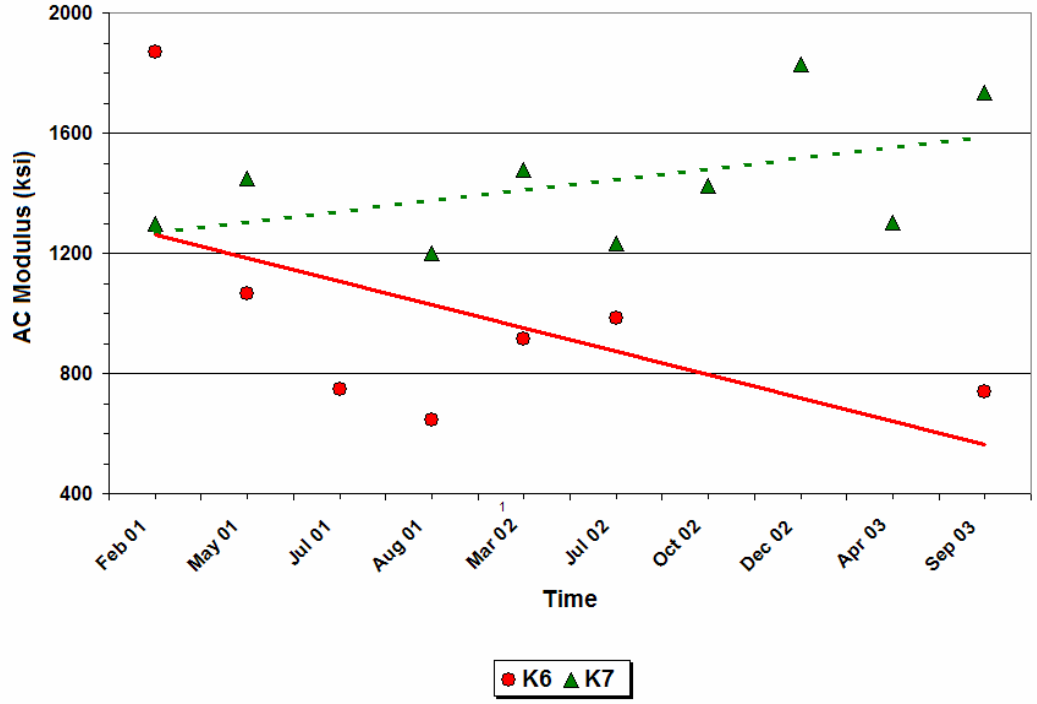

Figure F1. Corrected AC Moduli Using Eq. 7.2 (Group 1 FWD Stations).

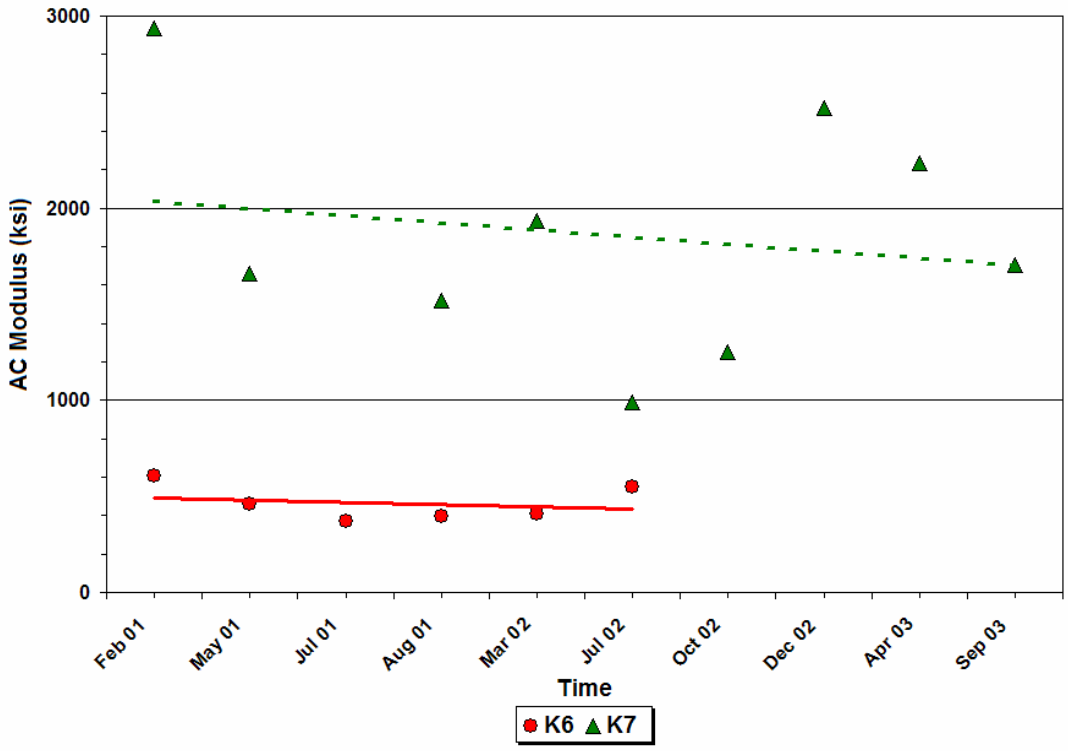

Figure F2. Corrected AC Moduli Using Eq. 7.2 (Group 2 FWD Stations).

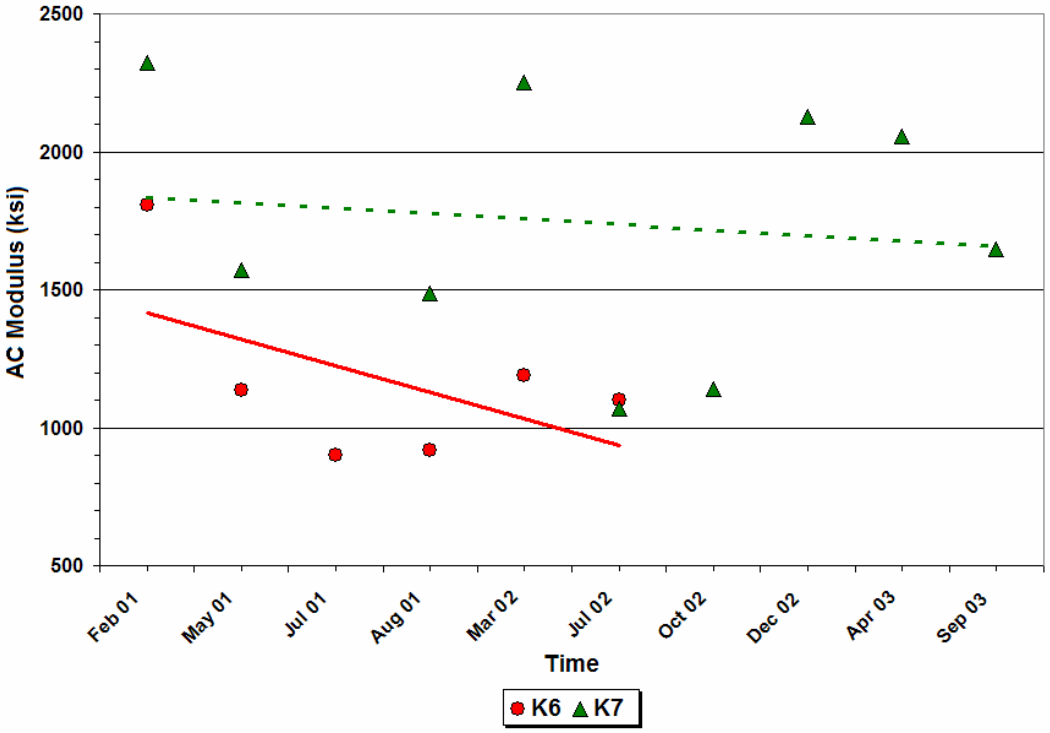

Figure F3. Corrected AC Moduli Using Eq. 7.2 (Group 3 FWD Stations).

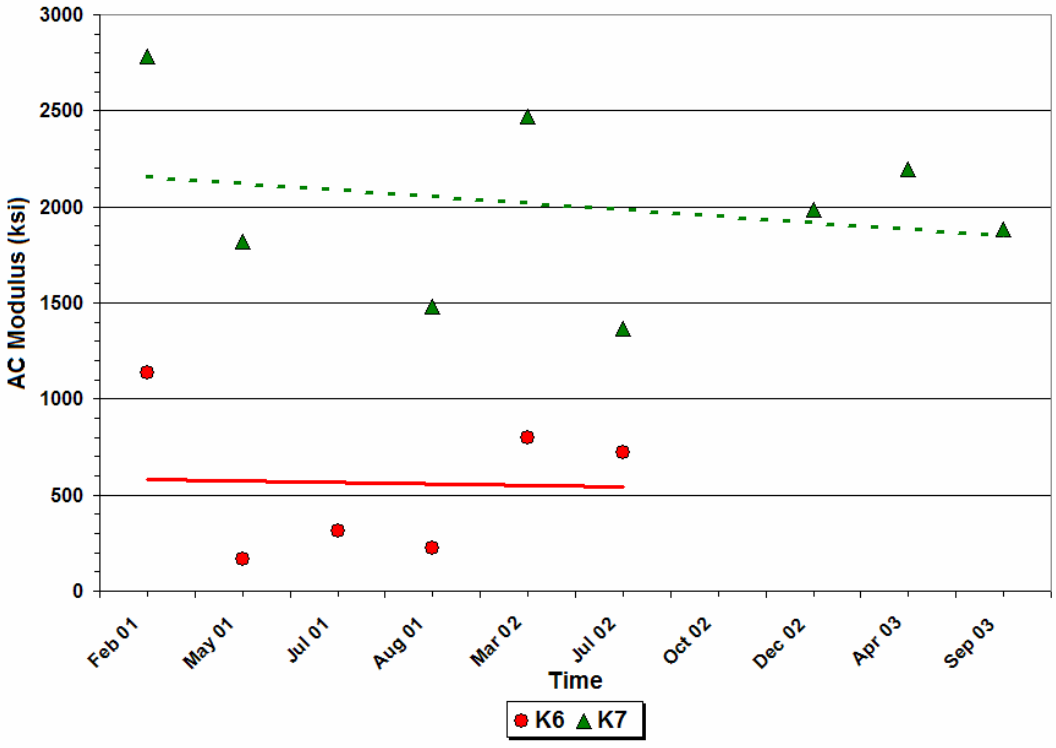

Figure F4. Corrected AC Moduli Using Eq. 7.2 (Group 4 FWD Stations).

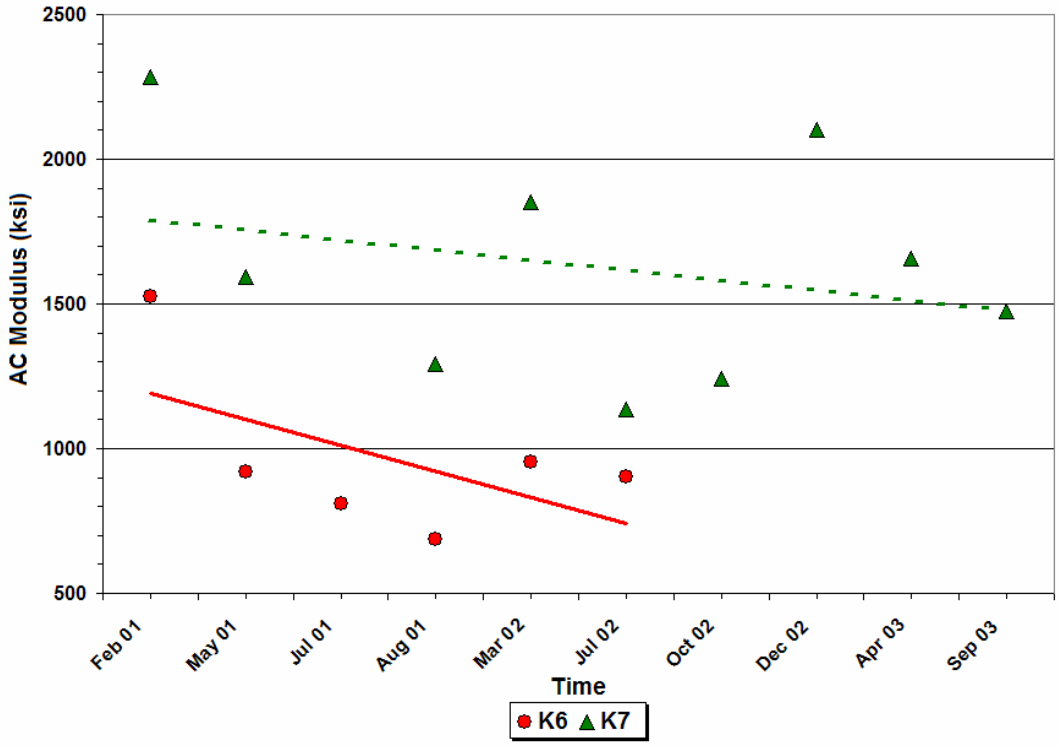

Figure F5. Corrected AC Moduli Using Eq. 7.2 (Group 5 FWD Stations).

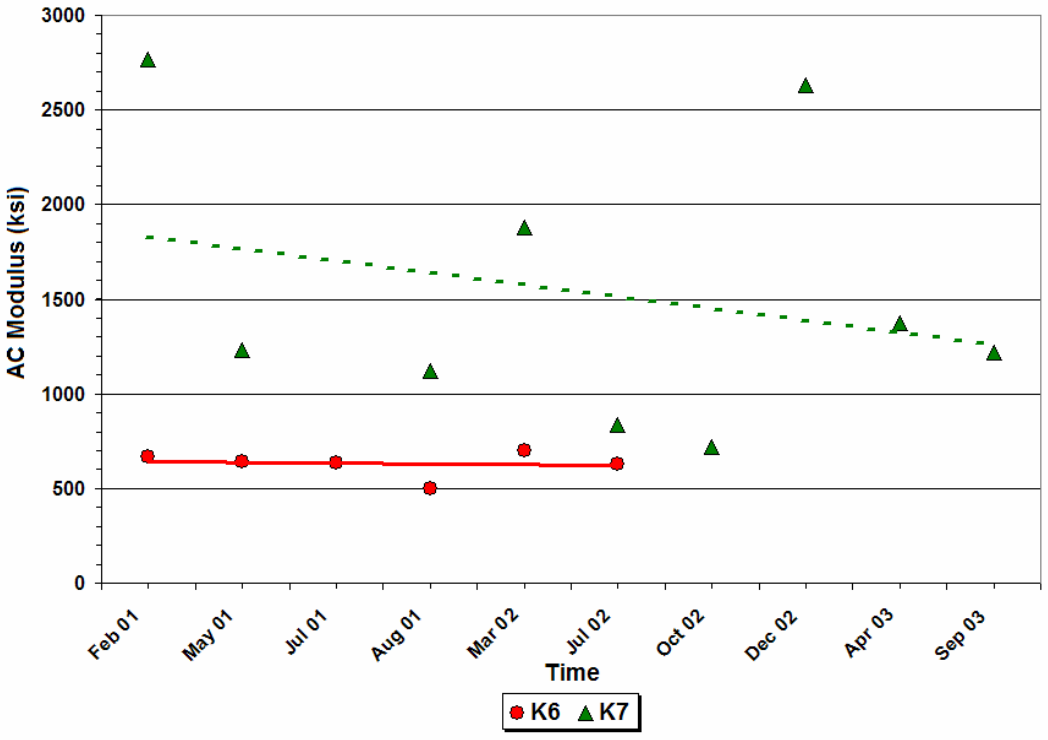

Figure F6. Corrected AC Moduli Using Eq. 7.2 (Group 6 FWD Stations).

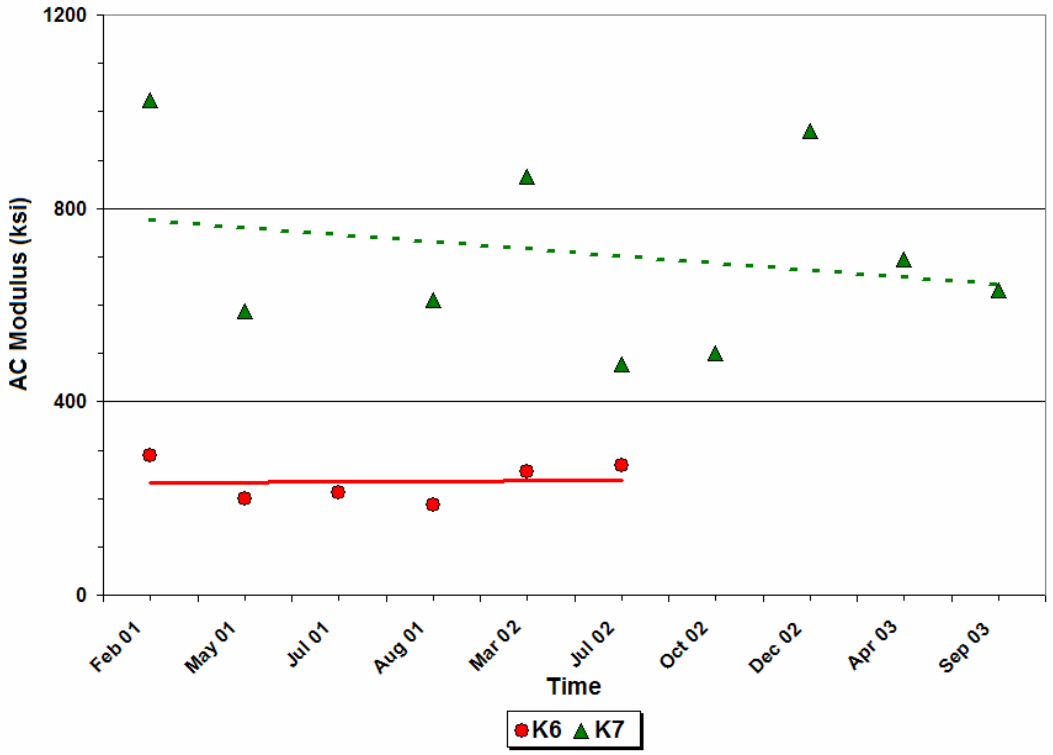

Figure F7. Corrected AC Moduli Using Eq. 7.2 (Group 7 FWD Stations).

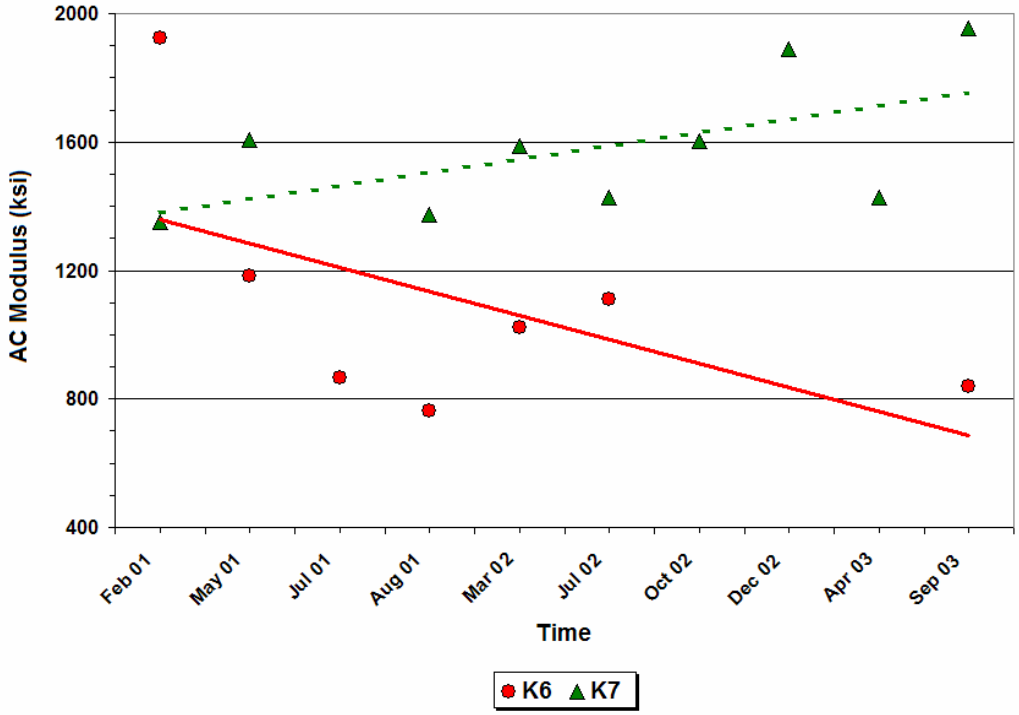

Figure F8. Corrected AC Moduli Using Eq. 7.3 (Group 1 FWD Stations).

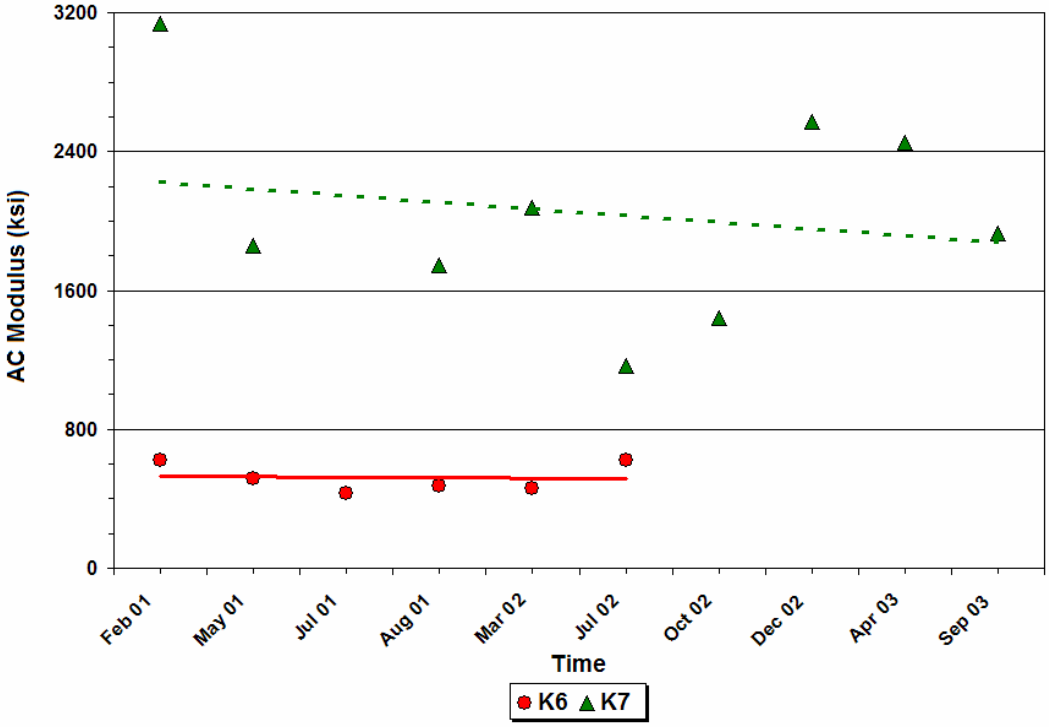

Figure F9. Corrected AC Moduli Using Eq. 7.3 (Group 2 FWD Stations).

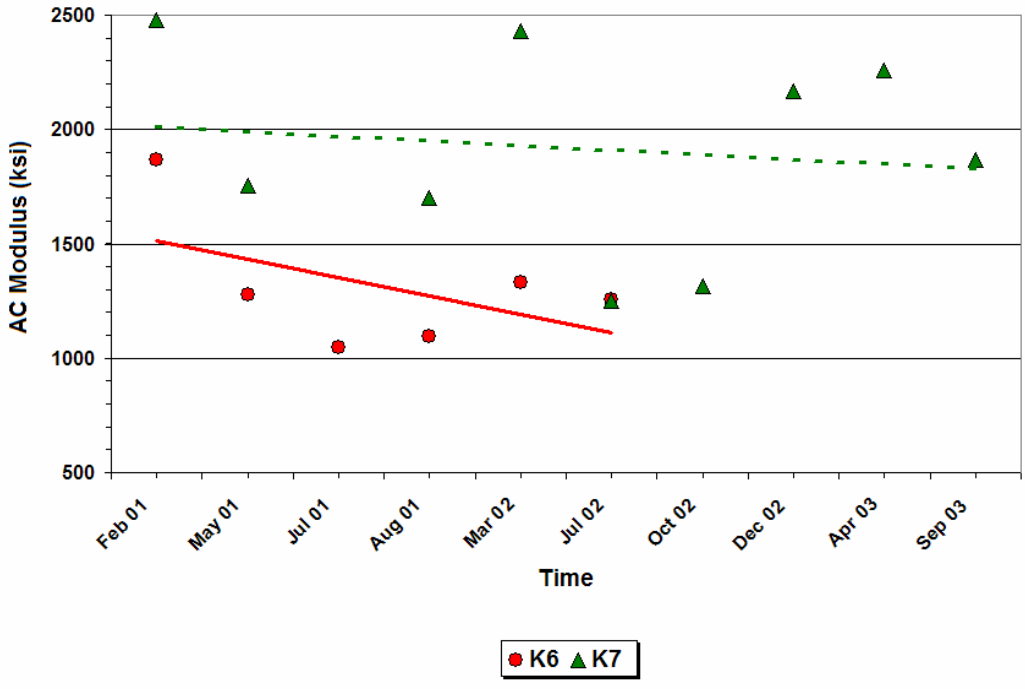

Figure F10. Corrected AC Moduli Using Eq. 7.3 (Group 3 FWD Stations).

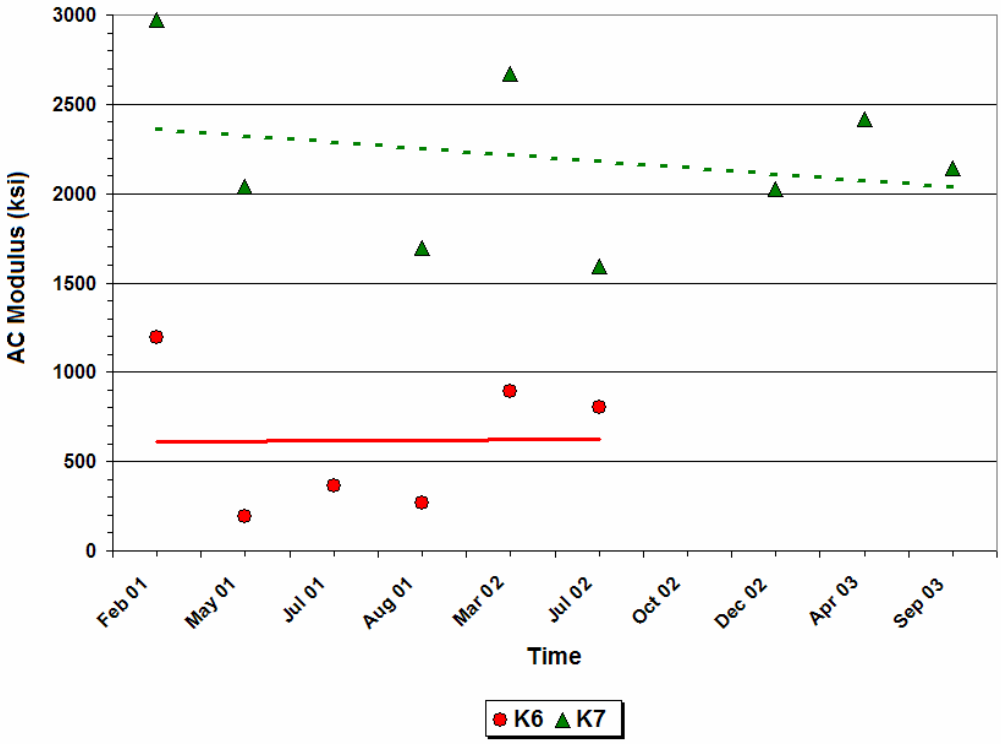

Figure F11. Corrected AC Moduli Using Eq. 7.3 (Group 4 FWD Stations).

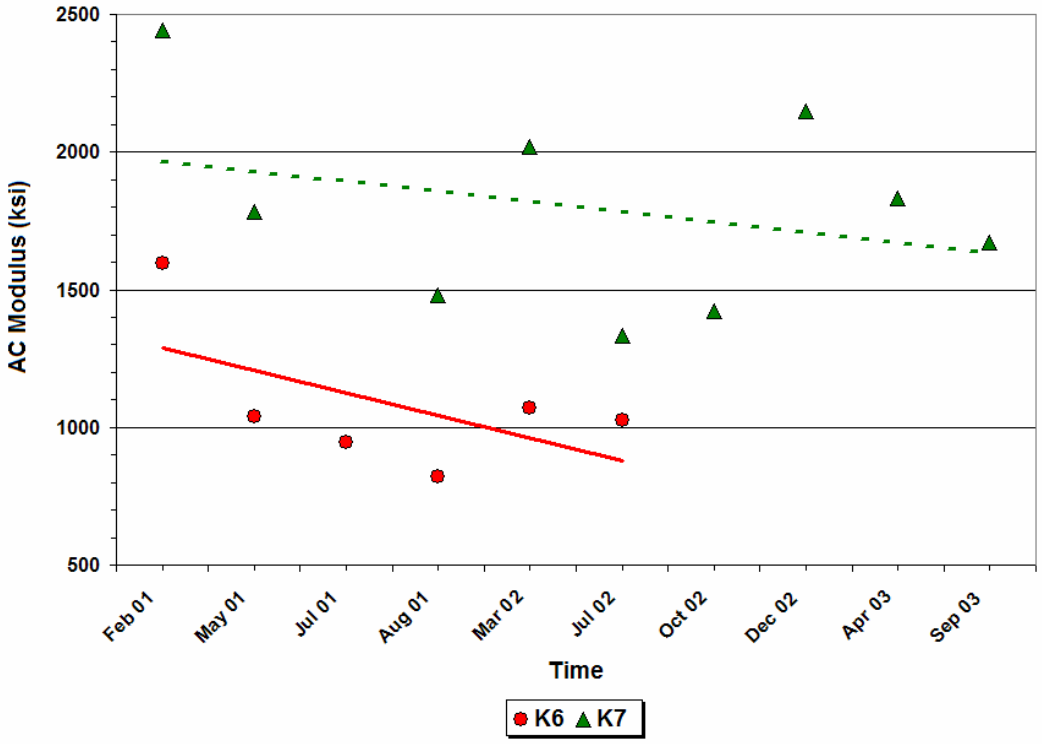

Figure F12. Corrected AC Moduli Using Eq. 7.3 (Group 5 FWD Stations).

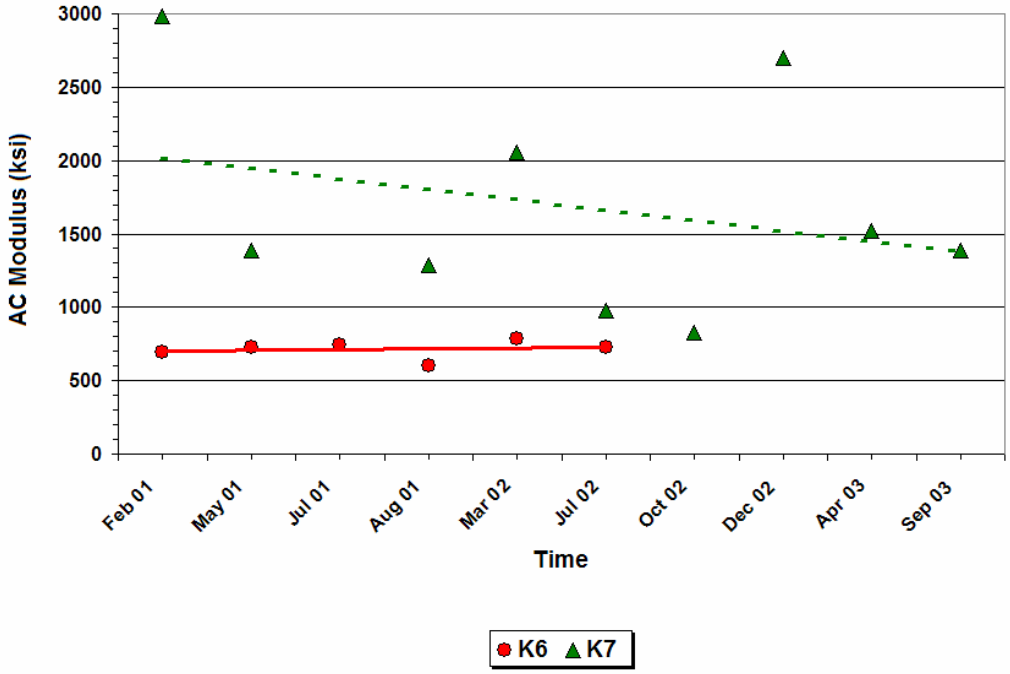

Figure F13. Corrected AC Moduli Using Eq. 7.3 (Group 6 FWD Stations).

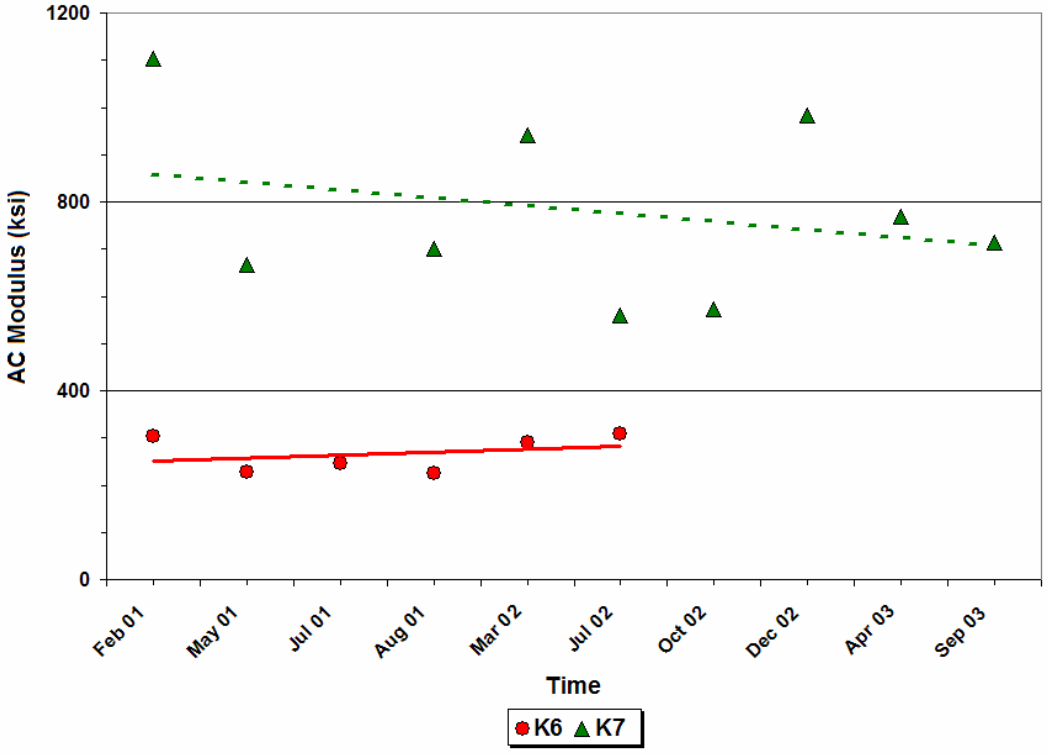

Figure F14. Corrected AC Moduli Using Eq. 7.3 (Group 7 FWD Stations).

APPENDIX G
CROSS-ANISOTROPIC FINITE ELEMENT MODEL FOR PREDICTING PAVEMENT RESPONSE

INTRODUCTION

Recent research suggests that directional or anisotropic modeling leads to reduced horizontal tensile stresses at the bottom of unbound granular layers and, in some instances, predicts compressive instead of tensile stresses. Since pavement damage is a function of the material response to traffic and environmental loads, it is important to verify whether realistic predictions are obtained from existing methods, and to ascertain the practical significance of differences between predictions based on the conventional assumption of linear elastic, isotropic behavior versus nonlinear elastic, anisotropic properties. Thus, in this project, researchers modified an existing finite element program to include the capability for modeling nonlinear, cross-anisotropic materials for the purpose of evaluating pavement response under given wheel loads. This finite element program for **N**onlinear **C**ross-anisotropic **P**avement **A**nalysis (NCPA) provides the flexibility of characterizing pavement materials as linear or nonlinear, and isotropic versus cross-anisotropic. It resulted from a modification of a finite element program previously developed by Jooste and Fernando (1994, 1995) to assess the potential for pavement damage due to superheavy load moves. Like the original program, NCPA uses 8-node quadratic serendipity elements with 9 Gauss integration points, allowing the calculation of displacements, strains and stresses at different coordinates. For the boundary conditions, the sides of the finite element mesh are assumed to be restrained in the horizontal direction. The bottom of the mesh is restrained in both the vertical and horizontal directions to represent a rigid bottom layer.

The surface wheel load is applied in an incremental fashion. At each load increment, the stress dependent moduli and Poisson's ratio are calculated iteratively for each element until convergence is achieved. Convergence depends on the percentage difference between new and previous values. In general, a 15 percent difference in the calculated moduli from the current and previous iterations is accepted. The same convergence criterion is implemented in NCPA. In addition to predicting pavement response, NCPA includes algorithms for predicting performance based on fatigue cracking, permanent deformation and ride quality criteria.

FINITE ELEMENT MODEL OF TWO-DIMENSIONAL AXISYMMETRIC SOLID

Virtual Work

The finite element method is based on the virtual work principle, which states that (Weave and Johnston, 1984):

> *If a general structure in equilibrium is subjected to a system of small virtual displacements within a comparable state of deformation, the virtual work of external actions is equal to the virtual strain energy of internal stresses*.

If a body is subjected to a set of body forces *b*, the virtual work principle can be written as follows (Owen and Hinton, 1980):

$$\int_{\Omega}[\delta\varepsilon]^{T}\sigma d\Omega-\int_{\Omega}[\delta u]^{T}bd\Omega-\int_{\Gamma t}[\delta u]^{T}td\Gamma=0 \qquad \text{(G1)}$$

where,

σ	=	the vector of stresses,
t	=	the vector of boundary tractions,
δu	=	the vector of virtual displacements,
$\delta\varepsilon$	=	the vector of associated virtual strains,
Ω	=	the domain of interest, and
Γ	=	the part of the boundary on which surface tractions are prescribed.

Governing Equation

In a finite element representation, the displacements and strains, and their virtual counterparts may be expressed by the relationships (Owen and Hinton, 1980):

$$u=\sum_{i=1}^{n}N_i d_i \qquad \delta u=\sum_{i=1}^{n}N_i\delta d_i \qquad \text{(G2)}$$

$$\varepsilon=\sum_{i=1}^{n}B_i d_i \qquad \delta\varepsilon=\sum_{i=1}^{n}B_i\delta d_i \qquad \text{(G3)}$$

where,

d_i = the vector of nodal variables,

δd_i = the vector of virtual nodal variables,

N_i = the matrix of global shape functions, and

B_i = the global strain-displacement matrix.

Substituting Eqs. (G2) and (G3) into Eq. (G1) yields:

$$\sum_{i=1}^{n}\left[\delta d_i\right]^T\left\{\int_\Omega\left[B_i\right]^T\sigma d\Omega-\int_\Omega\left[N_i\right]^T b d\Omega-\int_{\Gamma t}\left[N_i\right]^T t d\Gamma\right\}=0 \tag{G4}$$

Since there exists an arbitrary set of virtual displacements, Eq. (G4) can be re-written as:

$$\int_\Omega\left[B_i\right]^T\sigma d\Omega-\int_\Omega\left[N_i\right]^T b d\Omega-\int_{\Gamma t}\left[N_i\right]^T t d\Gamma=0 \tag{G5}$$

The stress-strain relationship at each element is given by:

$$\sigma=D\,\varepsilon=D\left(\sum_{j=1}^{n}B_j d_j\right) \tag{G6}$$

where D is the stress-strain matrix. From Eqs. (G5) and (G6), the following relationship between the element stiffness matrix K_{ij} and the vector of nodal variables is obtained:

$$\sum_{j=1}^{n}K_{ij}d_j=\int_\Omega\left[B_i\right]^T D\left(\sum_{j=1}^{n}B_j d_j\right)d\Omega \tag{G7}$$

Axisymmetric Solids

An axisymmetric solid is defined as a three-dimensional body that is developed by rotation of a planar section about an axis and is subjected to loads and boundary conditions that are symmetrical about this axis. Under this assumption, the behavior is independent of the circumferential coordinate θ. The displacements may be expressed as (Owen and Hinton, 1980):

$$u = \{u, v\} \tag{G8}$$

where u and v are the displacements in the radial (r) and vertical (z) directions, respectively. The nonzero strains are given as:

$$\varepsilon = \{\varepsilon_r, \varepsilon_\theta, \varepsilon_z, \gamma_{rz}\} \tag{G9}$$

where,

ε_r = $\frac{\partial u}{\partial r}$, normal strain in the r direction;

ε_θ = $\frac{u}{r}$, normal strain in the θ direction;

ε_z = $\frac{\partial v}{\partial z}$, normal strain in the z direction; and

γ_{rz} = $\frac{\partial u}{\partial z} + \frac{\partial v}{\partial r}$, shear strain on the r-z plane.

For linear isotropic materials, the strain-displacement matrix under the assumption of axisymmetry is given as:

$$B = \begin{bmatrix} \frac{\partial N_i}{\partial r} & 0 \\ \frac{N_i}{r} & 0 \\ 0 & \frac{\partial N_i}{\partial z} \\ \frac{\partial N_i}{\partial z} & \frac{\partial N_i}{\partial r} \end{bmatrix} \tag{G10}$$

Also, the stress-strain matrix for this case is:

$$D = \frac{E}{(1+\nu)(1-2\nu)} \begin{bmatrix} 1-\nu & \nu & 0 & 0 \\ \nu & 1-\nu & \nu & 0 \\ 0 & \nu & 1-\nu & 0 \\ 0 & 0 & 0 & \frac{1-2\nu}{2} \end{bmatrix} \tag{G11}$$

where, E is the modulus of elasticity and ν is the Poisson's ratio. Finally, an elemental volume is given by:

$$d\Omega = 2\pi r dr dz \tag{G12}$$

CROSS-ANISOTROPY UNDER AXISYMMETRIC ASSUMPTION

While the isotropic model uses the same resilient properties in all directions, a cross-anisotropic material has different resilient material properties in the horizontal and vertical directions. Zienkiewicz and Taylor (1989) suggested the general axisymmetric elasticity stress-strain relations for an anisotropic stratified layered system in terms of the in-plane and normal to the strata resilient moduli and Poisson's ratio. The constitutive axisymmetric anisotropic stress-strain relation matrix D takes the form:

$$D = \frac{M_R^V}{\alpha\beta}\begin{bmatrix} n(1-n\nu_{vh}^2) & n(\nu_{hh}+n\nu_{vh}^2) & n\nu_{vh}\alpha & 0 \\ n(\nu_{hh}+n\nu_{vh}^2) & n(1-n\nu_{vh}^2) & n\nu_{vh}\alpha & 0 \\ n\nu_{vh}\alpha & n\nu_{vh}\alpha & (1-\nu_{hh}^2) & 0 \\ 0 & 0 & 0 & m\alpha\beta \end{bmatrix} \tag{G13}$$

where,

α = $(1 + \nu_{hh})$,

β = $(1 - \nu_{hh} - 2n\nu_{vh}^2)$,

n = M_R^H / M_R^V,

m = G_{HV} / M_R^V,

G_{HV} = resilient shear modulus,

M_R^V = resilient modulus in the vertical direction,

M_R^H = resilient modulus in the horizontal direction,

ν_{vh} = Poisson's ratio determined from horizontal and vertical strains due to load in the vertical direction, and

ν_{hh} = Poisson's ratio determined from vertical and horizontal strains due to load in the horizontal direction.

Researchers incorporated the above stress-strain matrix into NCPA. The n and m values are used as input along with the parameter p defined as the ratio of ν_{hh} to ν_{vh}.

VERIFICATION OF CROSS-ANISOTROPIC FINITE ELEMENT MODEL

Gazetas (1982) studied the effect of soil cross-anisotropy on surface displacements and stress distributions in a homogeneous thick soil deposit (half-space) subjected to an axisymmetric parabolic vertical surface loading. The five independent material constants, M_R^H, M_R^V, ν_{vh}, ν_{hh} and G_{HV} cannot have arbitrary values; they are restricted by strain energy considerations expressed by the following constraints (Leknitskii, 1963):

$$M_R^H,\ M_R^V, G_{HV} \geq 0, \qquad -1 \leq \nu_{hh} \leq 1 - 2n\nu_{vh}^2 \tag{G14}$$

The theoretical solutions for the variation of vertical and radial stresses with depth z under the center of loading with radius R and magnitude p_0 are given by (Gazetas, 1982):

$$\sigma_z = \frac{p_0}{s_1 - s_2}\left[\frac{s_1}{(\lambda_2 + \sqrt{1+\lambda_2^2})^2} - \frac{s_2}{(\lambda_1 + \sqrt{1+\lambda_1^2})^2}\right] \tag{G15}$$

$$\sigma_r = \frac{p_0}{(s_1 - s_2)\sqrt{g}}\left\{\frac{s_1\left[1-(1-\nu_{hh})\frac{q_2}{2}\right]}{\left(\lambda_1 + \sqrt{1+\lambda_1^2}\right)^2} - \frac{s_2\left[1-(1-\nu_{hh})\frac{q_1}{2}\right]}{\left(\lambda_2 + \sqrt{1+\lambda_2^2}\right)^2}\right\} \tag{G16}$$

where,

$$s_1, s_2 = \left\{\frac{a + c \pm \left[(a+c)^2 - 4g\right]^{1/2}}{2g}\right\}^{\frac{1}{2}},$$

$$c = a - \frac{1}{m\left(n\nu_{vh}^2 - 1\right)},$$

$$a = \frac{\nu_{vh}\left(1+\nu_{hh}\right)}{n\nu_{vh}^2 - 1},$$

$$g = \frac{1-\nu_{hh}^2}{n\left(1 - n\nu_{vh}^2\right)}, \text{ and}$$

$$\lambda = \frac{z}{R};\ \ \lambda_i = \lambda s_i;\ \ q_i = 1 - a s_i^2;\ \ i = 1,2\,.$$

Figures G1 and G2 compare the predicted vertical and radial stresses from NCPA with the theoretical solutions given by Eqs. (G15) and (G16). Also shown are the predicted stresses from another layered elastic program called CIRCLY (1999). Table G1 shows the input parameters used in these comparisons. It is observed from Figure G1 that the vertical stresses predicted using NCPA fall midway between the theoretical values computed from Eq. (G15) and those obtained from CIRCLY. Of greater interest is the comparison of the radial stresses shown in Figure G2, which shows that NCPA predicts compressive radial stresses within the elastic half-space. However, the theoretical solution given by Eq. (G16) and CIRCLY predict small radial tensile stresses at depths greater than 9 inches that diminish to zero with increasing depths.

In addition to comparing finite element predictions with theoretical solutions for an elastic half-space, researchers analyzed a layered pavement system using NCPA and compared the predictions with those obtained from CIRCLY. Porter (2004) used this program to model the cross-anisotropic behavior of granular materials. As implemented within the Australian pavement design method, base and subgrade layers are characterized as cross-anisotropic according to the following assumptions:

- $n = 0.5$,
- $\nu_{vh} = \nu_{hh}$, and
- $G_{VH} = \dfrac{M_R^V}{1+\nu}$.

Researchers used the above properties in NCPA to model the pavement response to load for a three-layer pavement consisting of a 5-inch asphalt concrete layer, 16-inch granular base and subgrade. In this analysis, researchers characterized the asphalt and subgrade layers as linear elastic, isotropic materials, while the granular base was characterized as linear elastic, cross-anisotropic.

The predicted stresses with depth from NCPA and CIRCLY are shown in Figures G3 and G4. In the authors' opinion, the results from both programs are quite comparable. Note that the predicted radial stresses are close to zero at the bottom of the base layer. This reduction in the predicted radial tensile stress at the bottom of the base from a cross-anisotropic analysis has been reported in other studies by Tutumluer (1995) and Adu-Osei (2000).

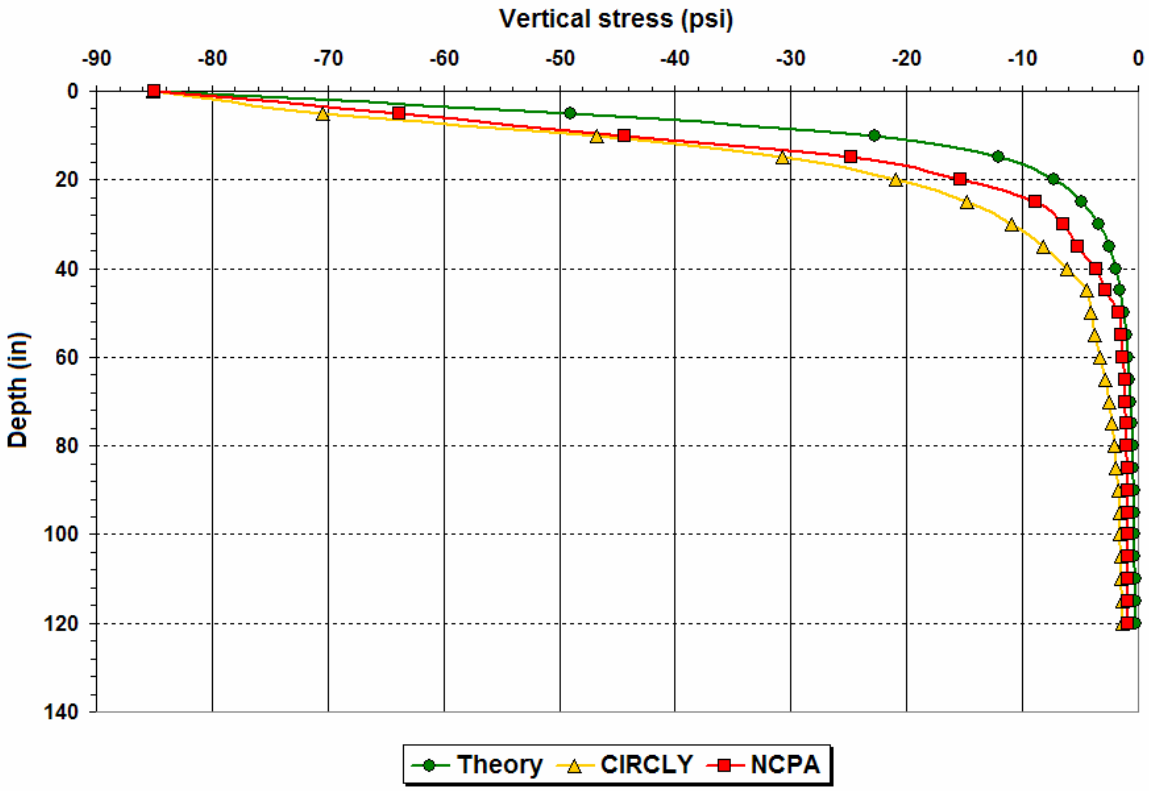

Figure G1. Comparison of Predicted Vertical Stresses from NCPA with Theoretical Solution for an Elastic Half-Space and with CIRCLY.

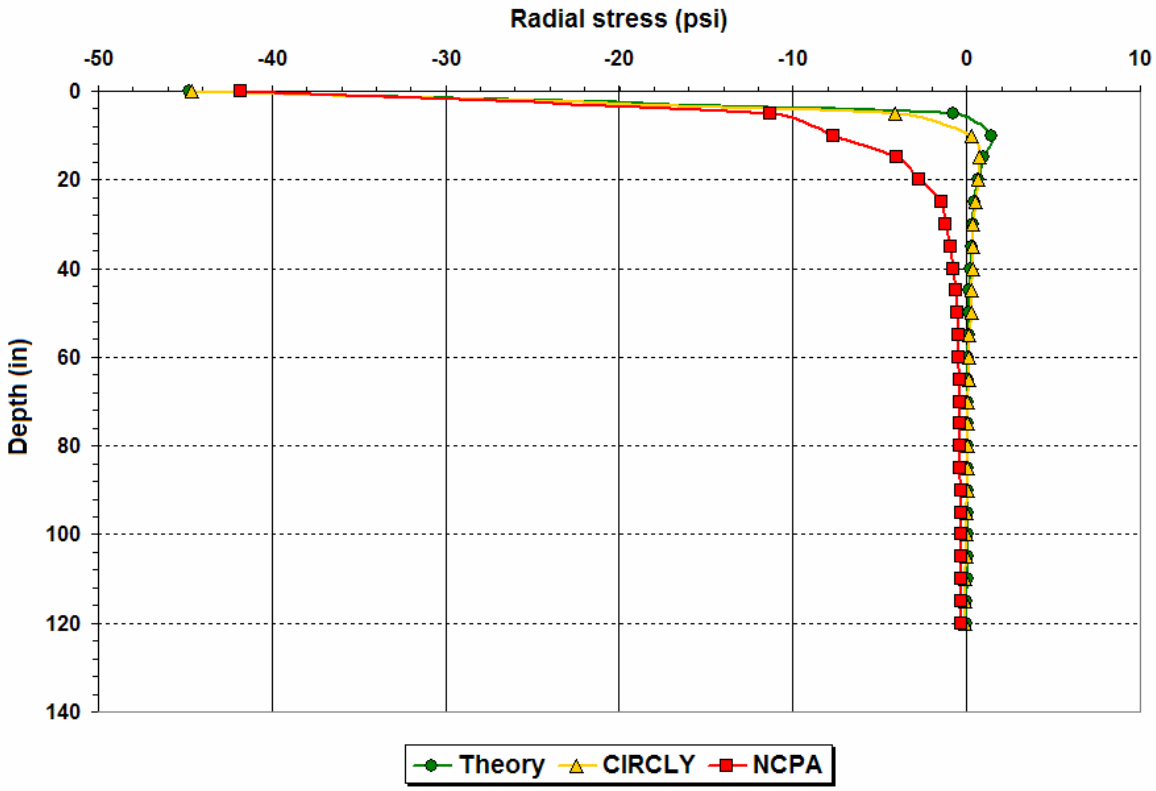

Figure G2. Comparison of Predicted Radial Stresses from NCPA with Theoretical Solution for an Elastic Half-Space and with CIRCLY.

Table G1. Input Parameters Used in Verification of NCPA with Theoretical Solutions.

Input Parameter	Value
ν_{vh}	0.2
ν_{hh}	0.3
n	0.5
m	0.3
p_0	85 psi

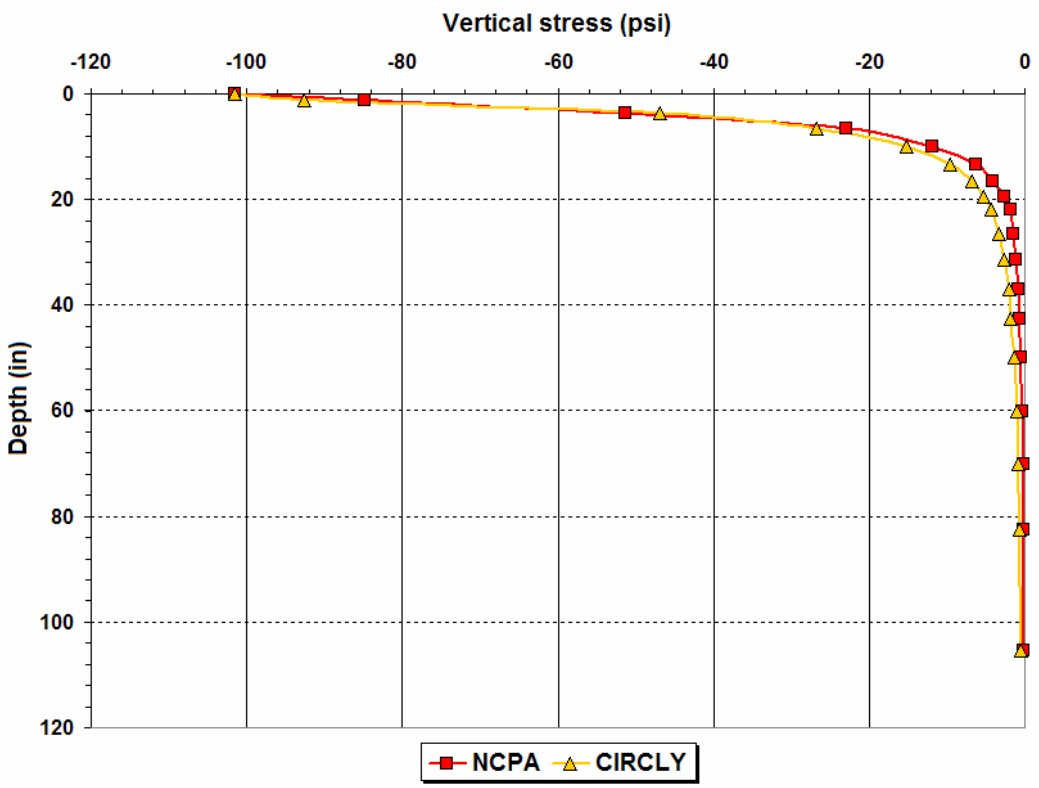

Figure G3. Comparison of Predicted Vertical Stresses from CIRCLY and NCPA.

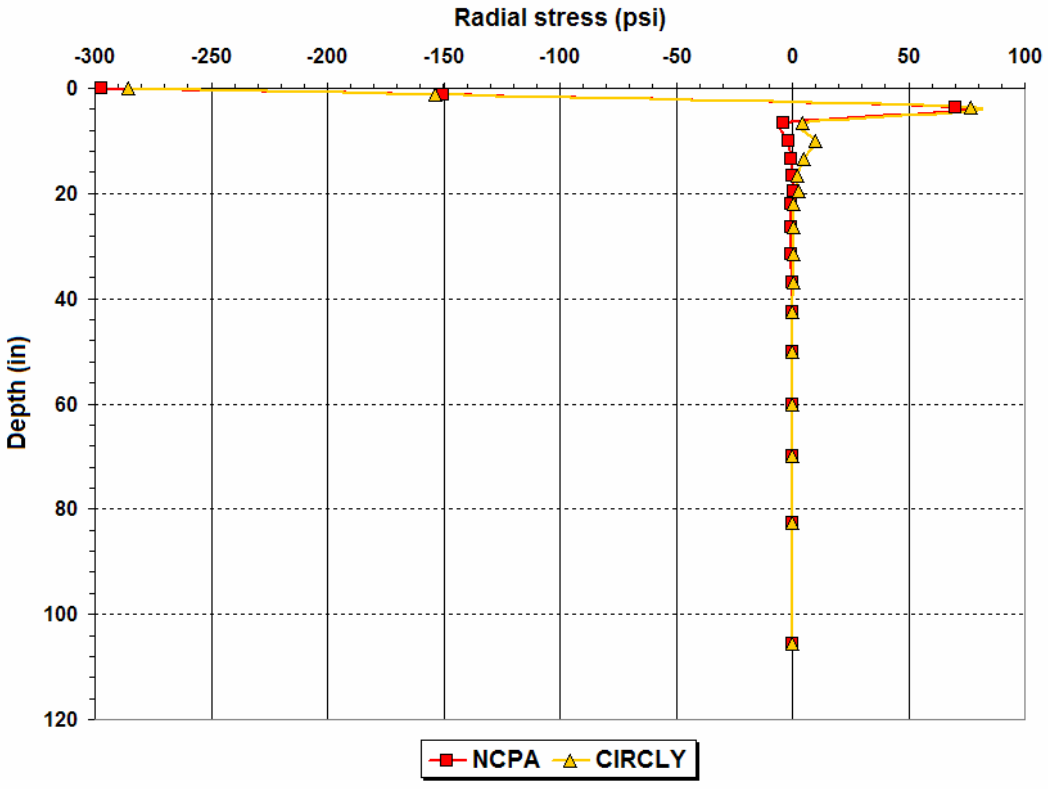

Figure G4. Comparison of Predicted Radial Stresses from CIRCLY and NCPA.

MODEL VERIFICATION WITH FIELD DEFLECTION MEASUREMENTS

As described in Appendix B, researchers installed two MDDs at the vicinity of the WIM site along SH48 in Brownsville. Deflection data obtained from the MDDs were also used to verify the finite element program described in this appendix. For this verification, researchers used deflection data measured under FWD loads and actual truck traffic at two different times to cover a range of pavement temperatures representative of summer and winter conditions in the Brownsville area. To account for the stress-dependency of pavement materials in the analysis (Lytton, 1989), pavement layer moduli were backcalculated from FWD data taken at load levels considered representative of measured truck tire loads on SH48. For backcalculation, researchers characterized the pavement cross-section at the WIM site as consisting of four layers, i.e., asphalt concrete, combined flexible base and salvage layers, lime-stabilized material, and the native subgrade. This four-layer cross-section is different from the three-layer system used in Chapter IV to backcalculate layer moduli at the FWD stations established along SH4/48. In general, the three-layer system resulted in the best agreement between measured and predicted surface deflection basins for all FWD stations established along the route. However, at the MDD stations, researchers found that the average absolute errors from a four-layer analysis were comparable with those obtained from a three-layer analysis. Thus, researchers used the backcalculated moduli from the four-layer analysis to verify the finite element program described in this appendix. Layer moduli were determined from FWD surface deflections using the MODULUS program (Michalak and Scullion, 1995).

Four constitutive models were considered in predicting the displacements at the LVDT locations of the MDDs. These models are:

- linear elastic, isotropic (LI),
- nonlinear elastic, isotropic (NI),
- linear elastic, cross-anisotropic (LA), and
- nonlinear elastic, cross-anisotropic (NA).

Isotropic materials are characterized in NCPA by setting $n = p = 1$. Nonlinear materials are characterized with modulus of elasticity and Poisson's ratio that are dependent on the bulk stress and the octahedral shear stress (Uzan, 1985 and Uzan, 1992). This model uses three material constants, K_1, K_2 and K_3, to characterize the stress-dependency of the resilient modulus and Poisson's ratio. Researchers conducted laboratory tests on specimens molded

from materials taken at the WIM site to characterize the cross-anisotropic and nonlinear material parameters needed in this analysis. For consistency with the results from the modulus backcalculation, the K_2 and K_3 values determined from laboratory tests were input to the finite element program. However, the K_1 value for each layer was determined to achieve compatibility with the backcalculated modulus of the material for the specified K_2 and K_3 parameters, and the FWD load level. This same procedure is implemented in TxDOT's program for superheavy load analysis (Fernando, 1997).

Researchers note that all layers except for the asphalt concrete material were characterized as stress-dependent in the nonlinear analysis. In addition, the NA analysis was conducted assuming that the *n* and *p* parameters for a given material were independent of the stress-state. Thus, the stress-dependency of M_R^H and ν_{hh} follows directly from the stress-dependency of M_R^V and ν_{vh} as determined from the K_1, K_2 and K_3 parameters specified for the material. The validity of this assumption needs to be verified in a future study.

Researchers verified the NCPA program by comparing measured MDD displacements with the corresponding predicted displacements. To determine the positions of the wheel loads that passed the MDDs, researchers viewed the video recordings that were made as the different trucks passed through the test site. The offset distance from a given tire and the MDD on the test lane was estimated from the position of the tire on the grid lines painted on the pavement.

In addition to the tire position, researchers needed to establish the truck tire loads corresponding to the measured MDD displacements. For overweight trucks, this information was taken from the permits issued at the Port of Brownsville, where trucks were weighed to verify that axle loads are within the allowable overweight limits. Researchers placed a tag on each overweight truck as it left the port that identified each truck as it passed the WIM site. For the non-permitted or legal trucks, researchers recorded the date and time each truck passed through the WIM site. In addition, the test lane was also recorded. With this information, researchers obtained the truck tire loads from the WIM data supplied by TxDOT.

Researchers first compared the predicted displacements from NCPA with the corresponding MDD displacements due to FWD loads. To quantify the accuracy of the predictions from the different constitutive models, the absolute differences between the predicted and measured peak displacements at the different LVDT positions were calculated

as percentages of the corresponding measured values. Figure G5 shows the overall average of the absolute differences for each model based on all test data included in this verification. Note that the largest errors are associated with the predictions for the fourth LVDT sensor. Researchers observed that the displacements from this sensor are quite small and exhibit little variation. Thus, the percentage errors would tend to be high, as shown in Figure G5. Because of the small variation in the sensor readings, researchers suspect that the fourth LVDT might have become faulty.

It is observed from Figure G5 that the lowest absolute errors were achieved with the NA model, followed by the nonlinear isotropic formulation. This result indicates the importance of modeling the stress-dependency of base and subgrade materials to predict pavement response for assessing the potential pavement damage due to routine overweight truck loads. It also suggests the need for considering the anisotropic behavior of pavement materials in predicting pavement response, and the need for additional research to characterize anisotropic properties, evaluate the factors that affect these properties and assess the impact to current design practice.

In addition to FWD tests, researchers used deflection data collected from actual truck traffic to verify NCPA and compare the accuracy of the different constitutive models. For this analysis, 40 trucks were selected from among those that were monitored at the K6 MDD station in August and December 2002. Researchers selected these months to cover high and low pavement temperatures in the Brownsville area.

Table G2 shows the input material parameters used in this analysis. To quantify the accuracy of the predictions, researchers determined the average difference, and the average of the absolute differences between the predicted and measured MDD peak displacements according to the following equations:

$$Ave.Difference = \frac{\sum_{i=1}^{4}(\delta_{FEMi} - \delta_{MDDi})}{4} \tag{G17}$$

$$Abs.Difference = \frac{\sum_{i=1}^{4}\left|\delta_{FEMi} - \delta_{MDDi}\right|}{4} \tag{G18}$$

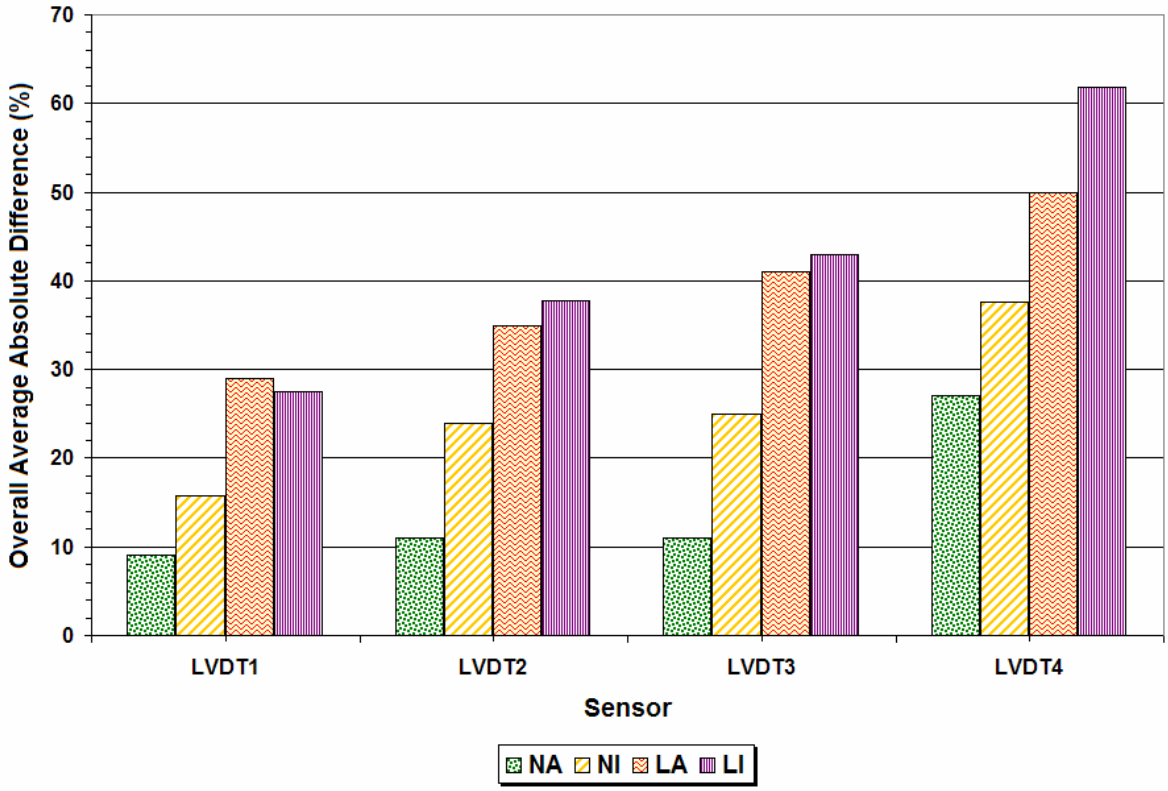

Figure G5. Percent Errors between Measured and Predicted MDD Displacements from Various Models Using FWD Test Data.

Table G2. Input Material Parameters for Model Comparisons Using Measured MDD Displacements from Truck Loads.

Property	August 2002				December 2002			
	AC	Flexible base	Stab. lime subbase	Subgrade	AC	Flexible base	Stab. lime subbase	Subgrade
E (ksi)	382	48	19	14	623	42	31	24
ν	0.4	0.3	0.3	0.4	0.4	0.3	0.3	0.4
K_1	24,120	2836	1347	830	39,290	2617	2164	1386
K_2	0.1	0.7	0.6	0.2	0.1	0.7	0.6	0.2
K_3	0.0	-0.2	-0.2	-0.4	0.0	-0.2	-0.2	-0.4
n	1.0	0.30	0.67	0.90	1.0	0.30	0.67	0.90
m	0.38	0.21	0.37	0.59	0.38	0.21	0.37	0.59
p	1.0	1.7	1.9	2.0	1.0	1.7	1.9	2.0

Table G3 summarizes the overall average error statistics determined from the data. It is observed that the NA model shows the least bias among the four models in terms of the overall average difference. In terms of the overall average absolute difference, the NA model also gave the closest predictions to the measured peak displacements relative to the other models considered in this evaluation. Similar to the previous finding, the NI model comes in second with respect to the accuracy of predicted displacements. These results again reflect the importance of modeling stress-dependency in the prediction of pavement response and the need for further study on the anisotropic behavior of pavement materials.

Table G3. Evaluation of Predictions from Various Models Using Measured MDD Displacements from Truck Loads.

Statistic (percent)	Constitutive Model							
	NA		NI		LA		LI	
	Aug. 2002	Dec. 2002	Aug. 2002	Dec. 2002	Aug. 2002	Dec. 2002	Aug. 2002	Dec. 2002
Overall average difference	-14	12	28	43	52	62	62	73
Overall average absolute difference	36	28	43	45	53	62	65	73

APPENDIX H

DISTRESS DATA FROM VISUAL SURVEYS

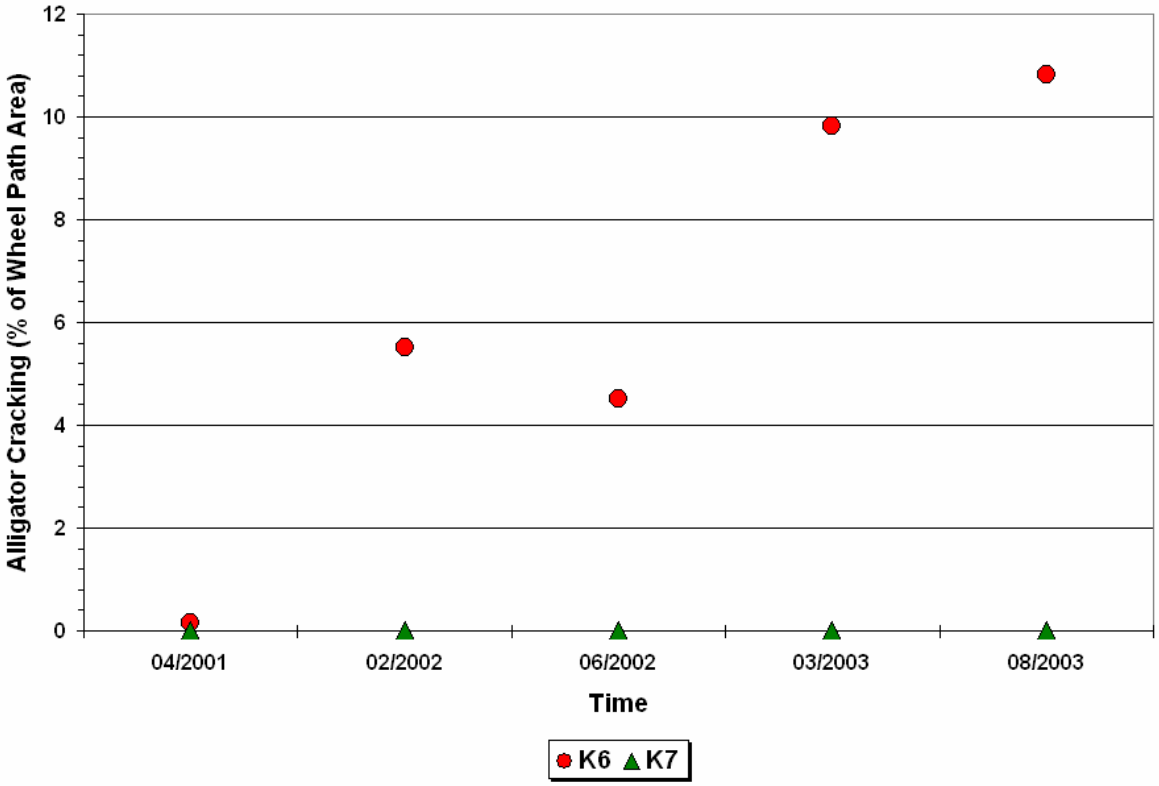

Figure H1. Alligator Cracking in Group 1 FWD Stations.

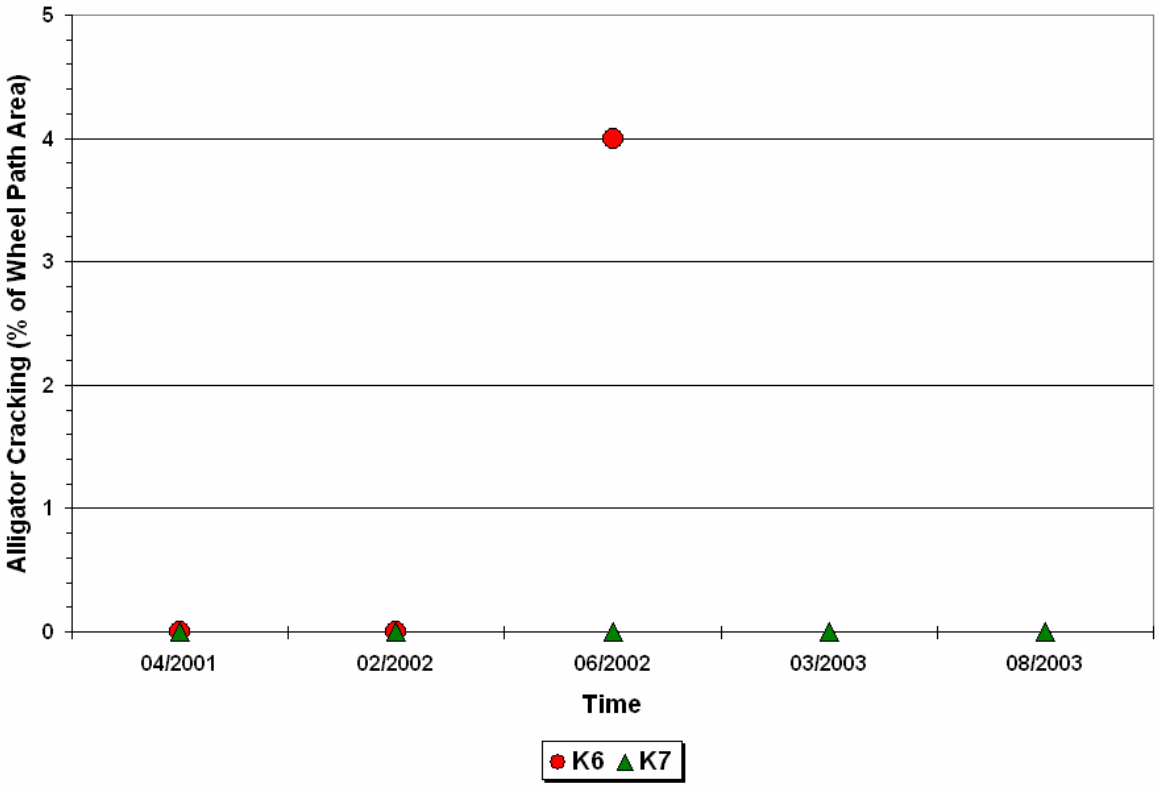

Figure H2. Alligator Cracking in Group 2 FWD Stations.

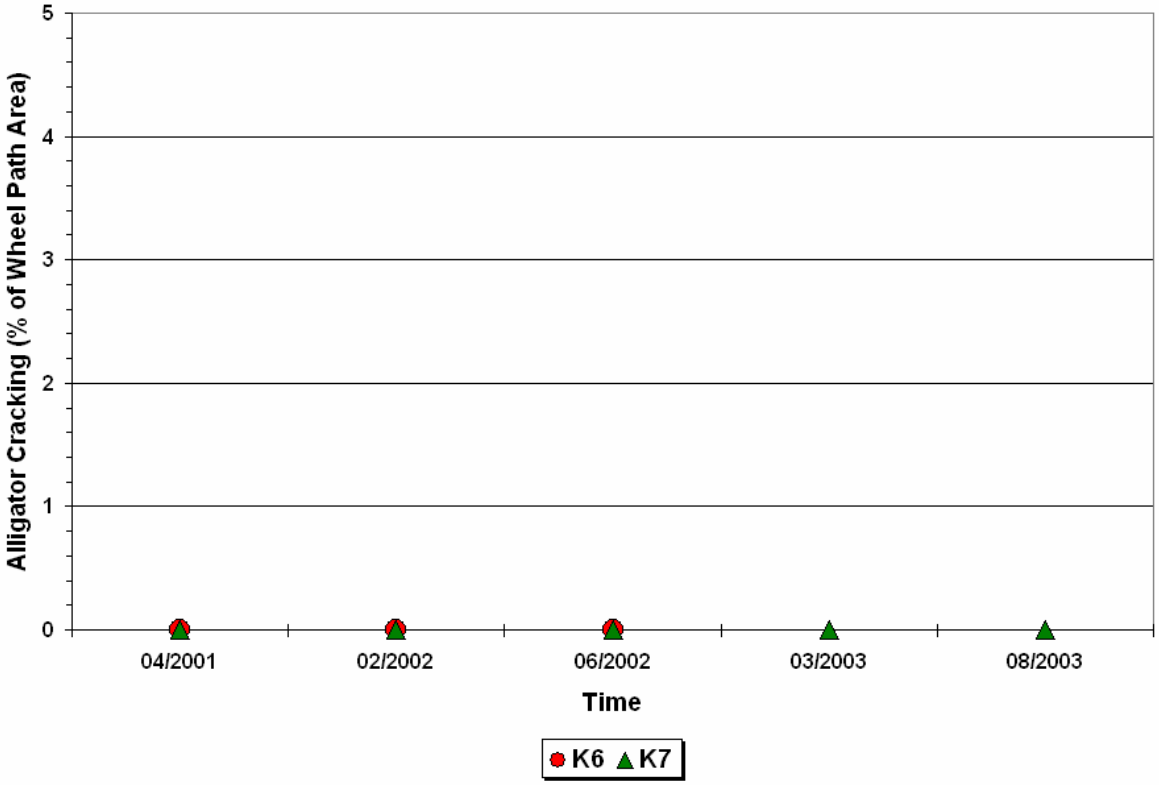

Figure H3. Alligator Cracking in Group 3 FWD Stations.

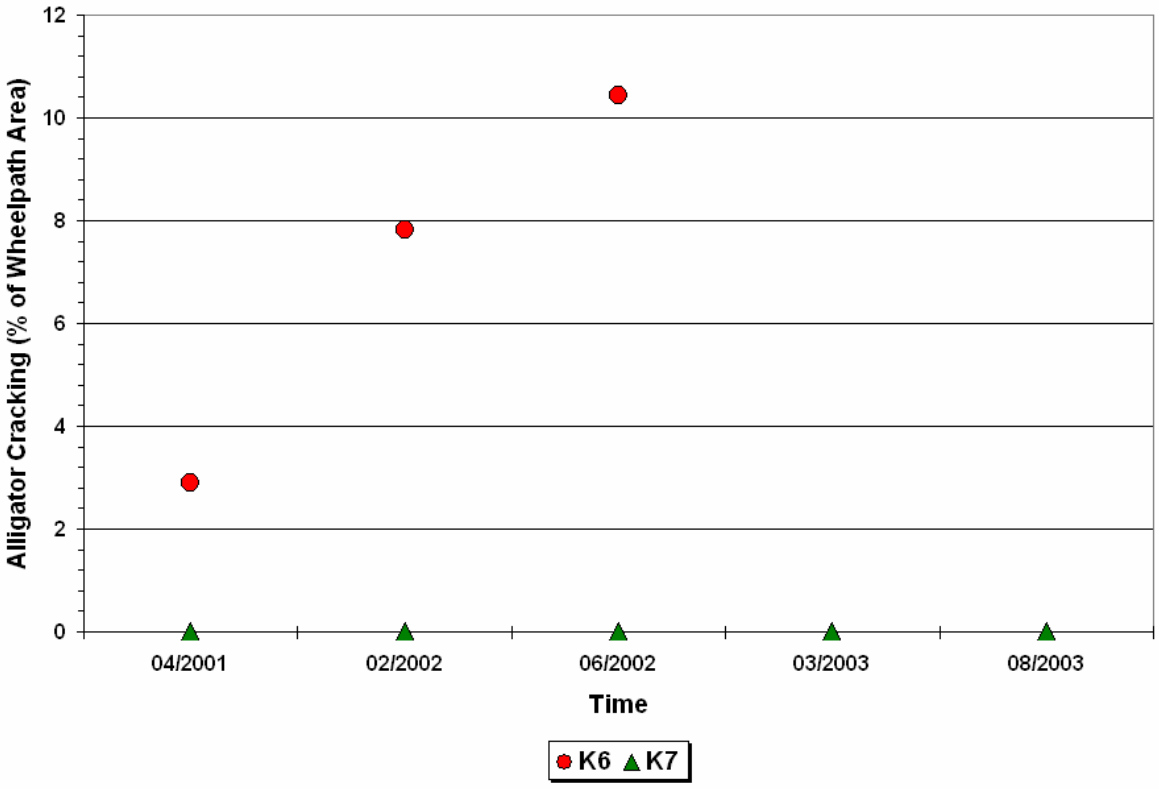

Figure H4. Alligator Cracking in Group 4 FWD Stations.

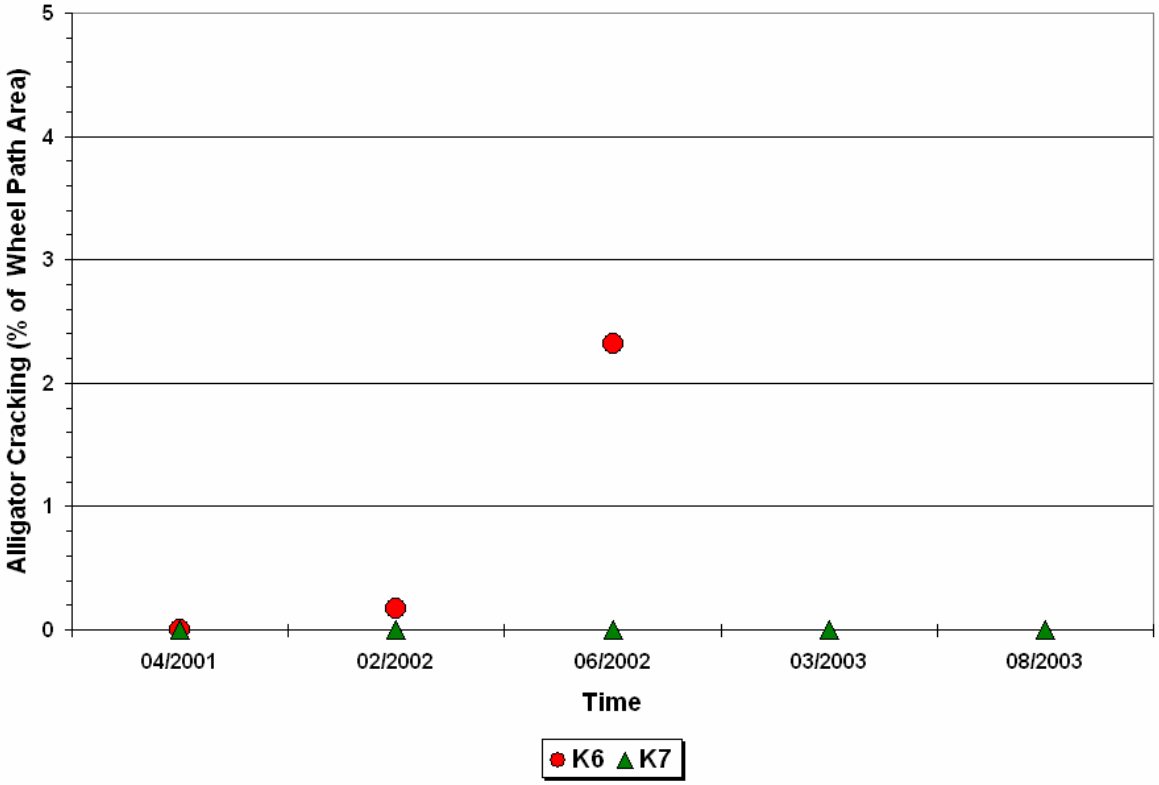

Figure H5. Alligator Cracking in Group 5 FWD Stations.

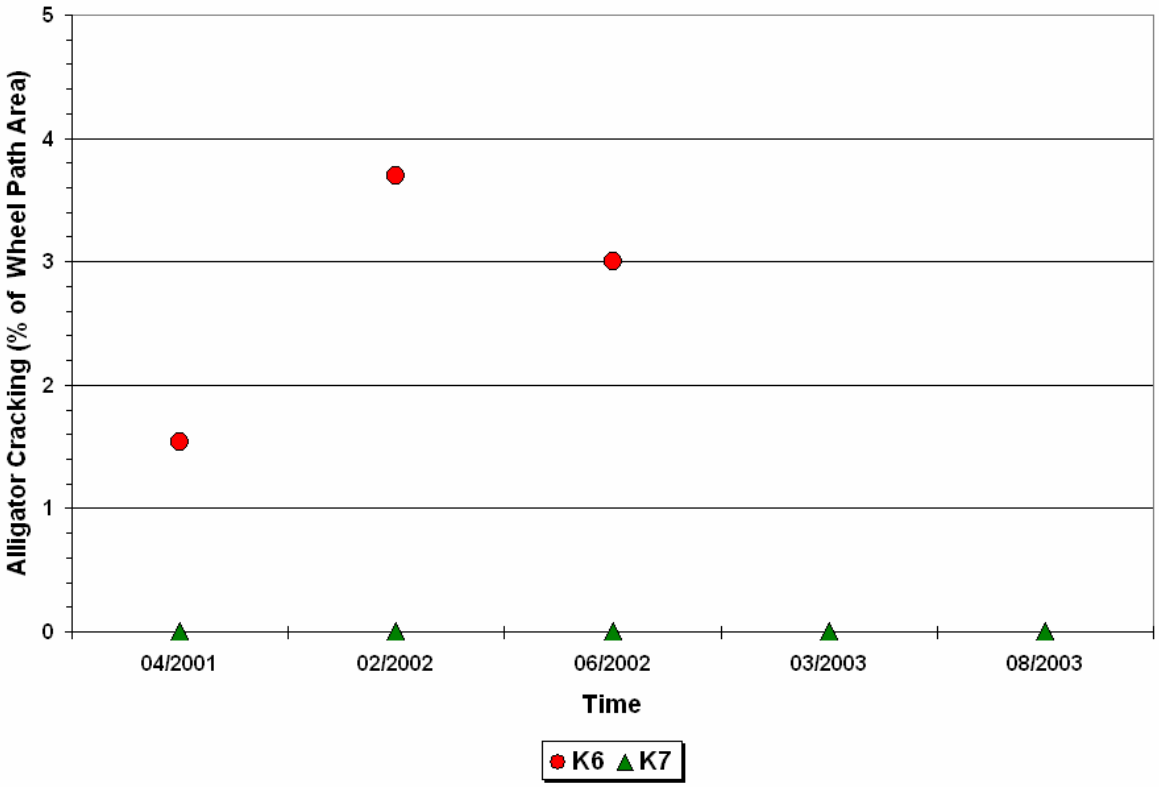

Figure H6. Alligator Cracking in Group 6 FWD Stations.

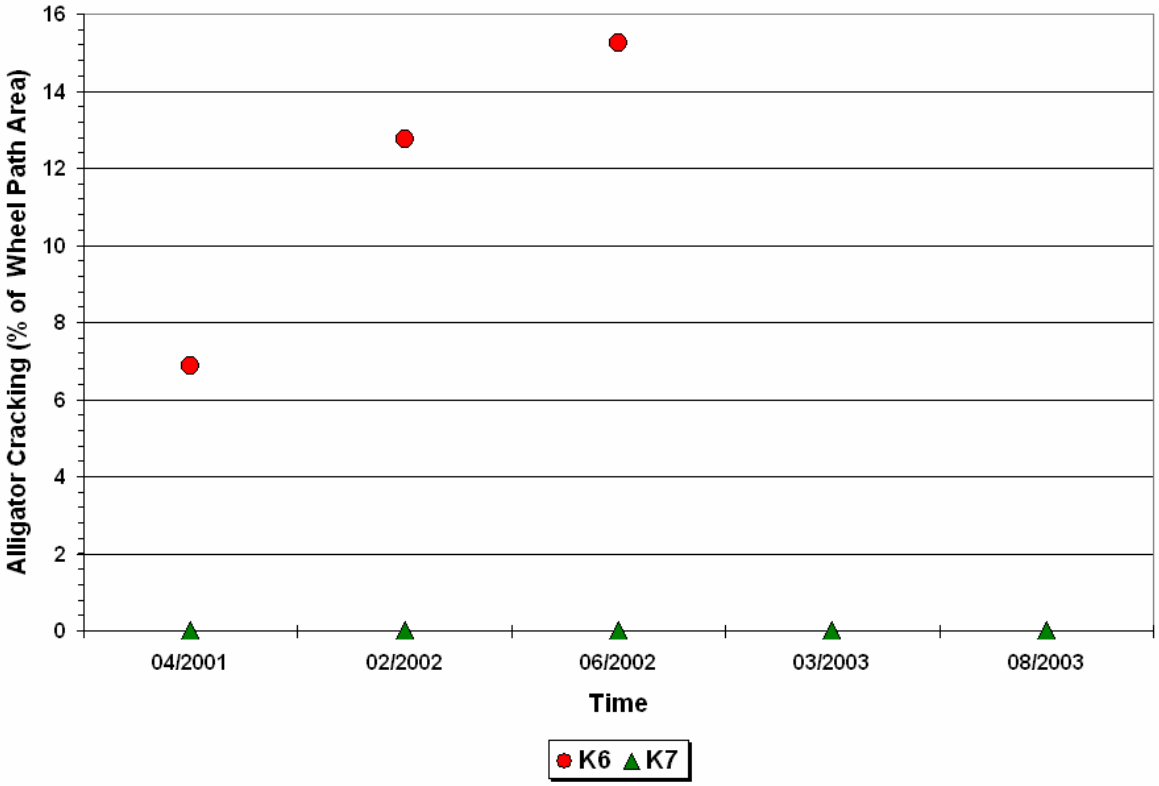

Figure H7. Alligator Cracking in Group 7 FWD Stations.

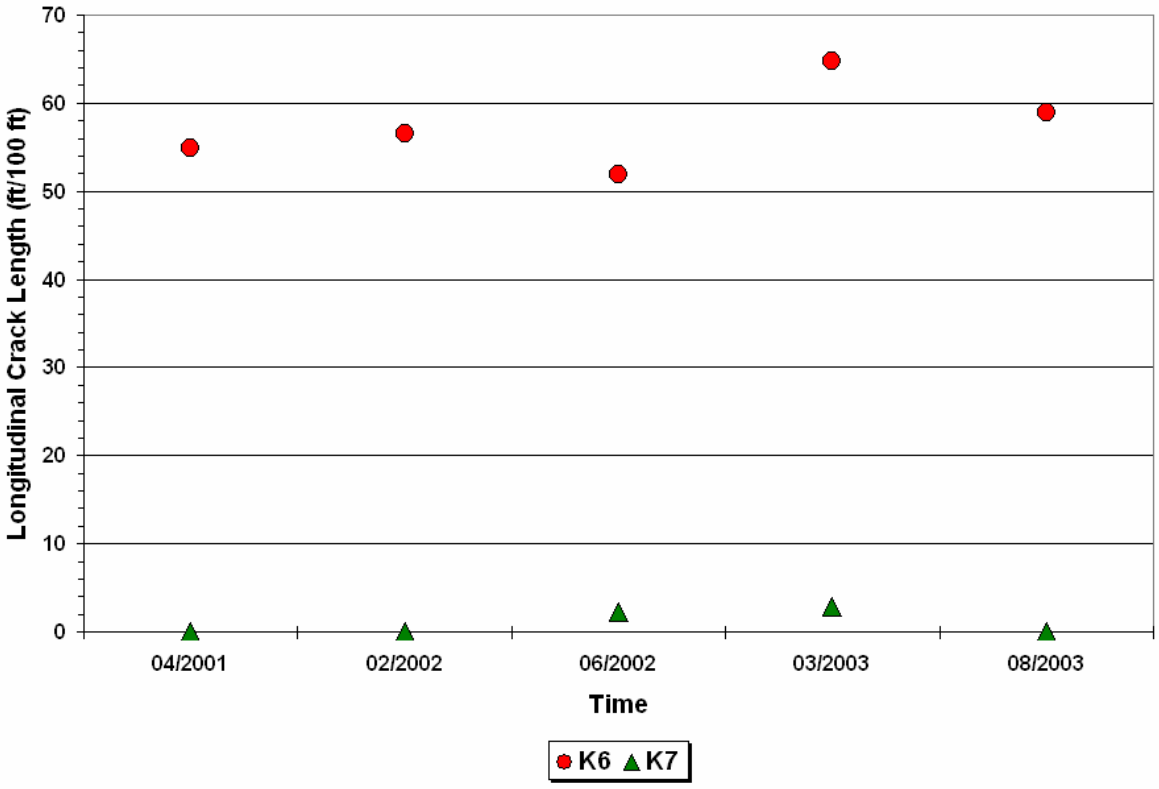

Figure H8. Longitudinal Cracking in Group 1 FWD Stations.

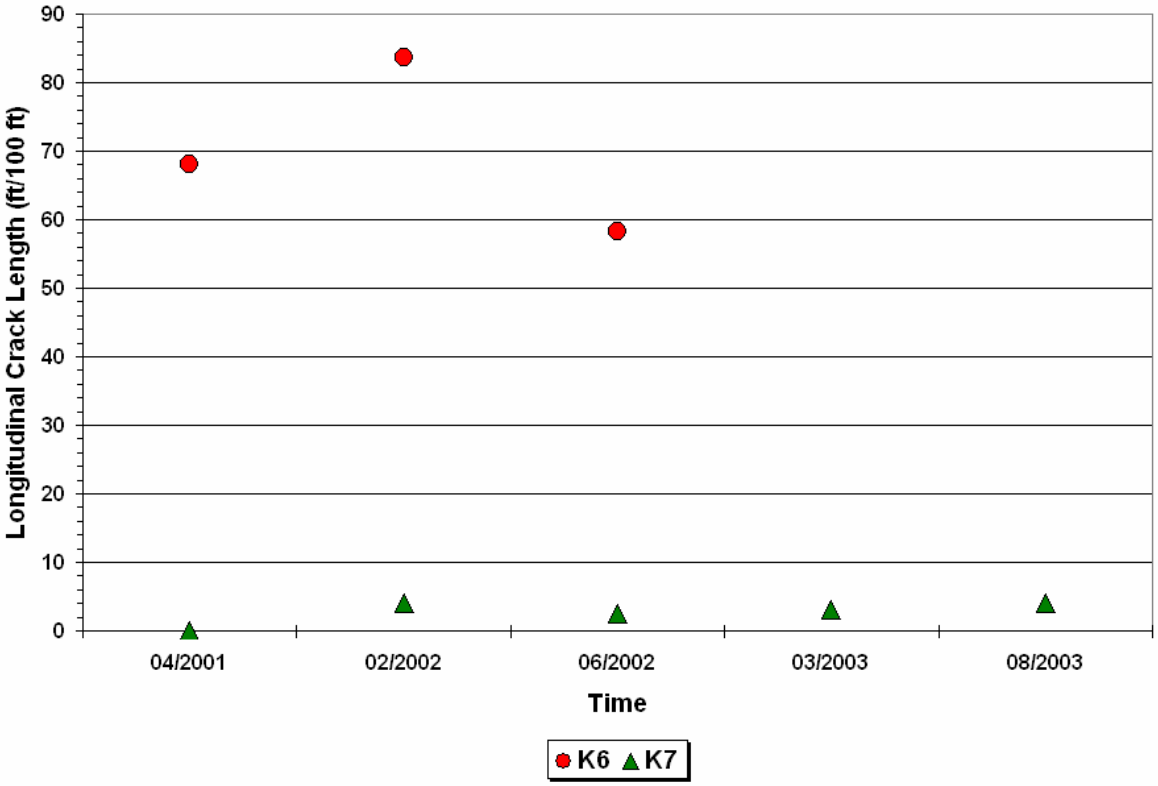

Figure H9. Longitudinal Cracking in Group 2 FWD Stations.

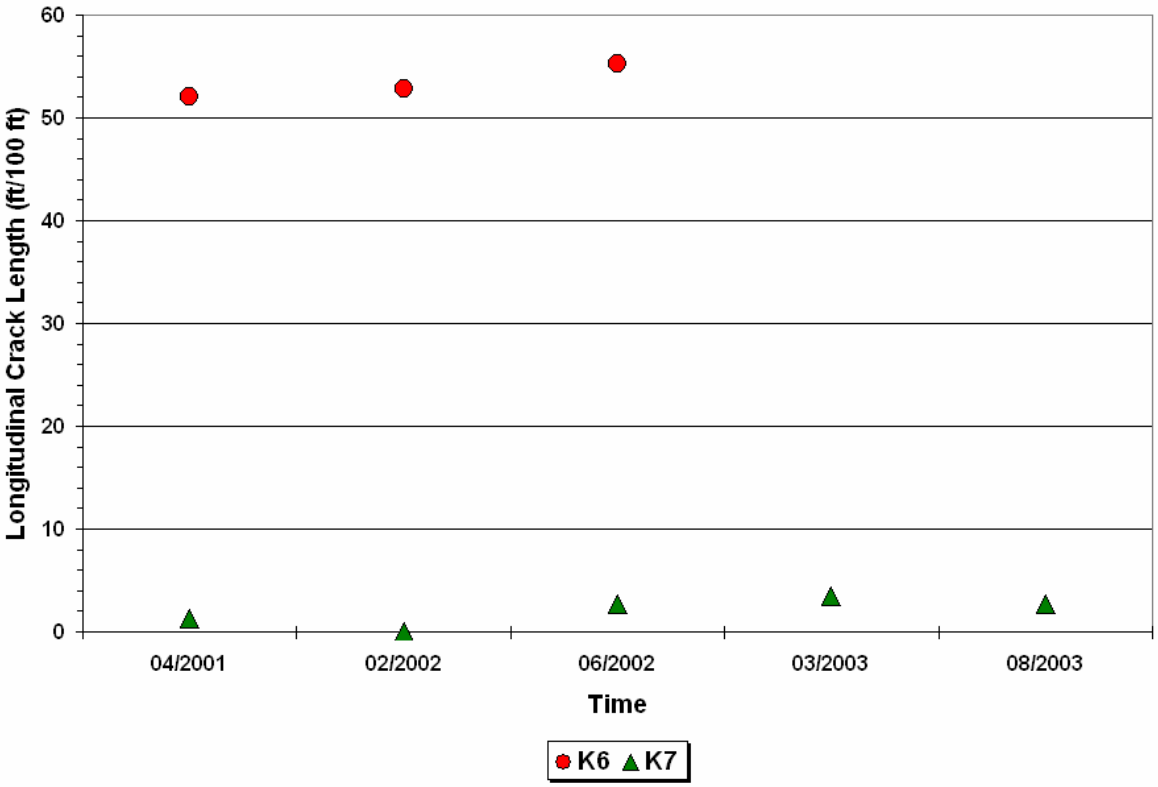

Figure H10. Longitudinal Cracking in Group 3 FWD Stations.

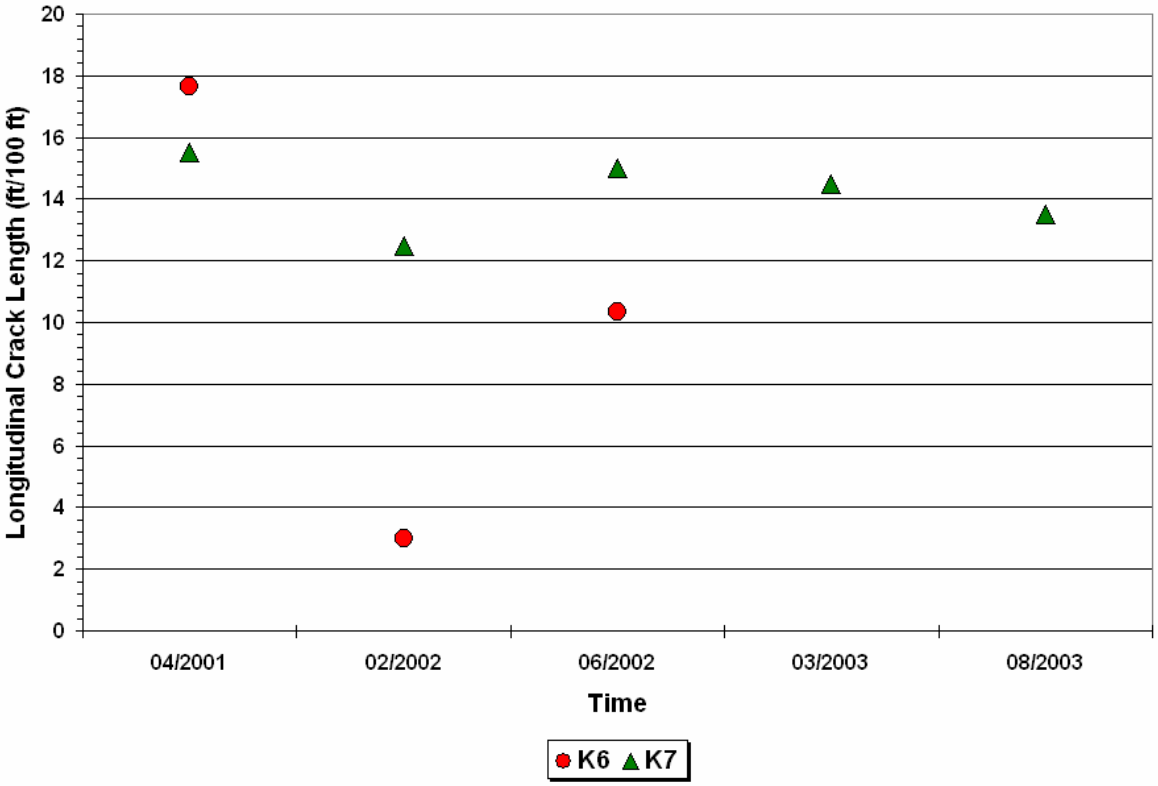

Figure H11. Longitudinal Cracking in Group 4 FWD Stations.

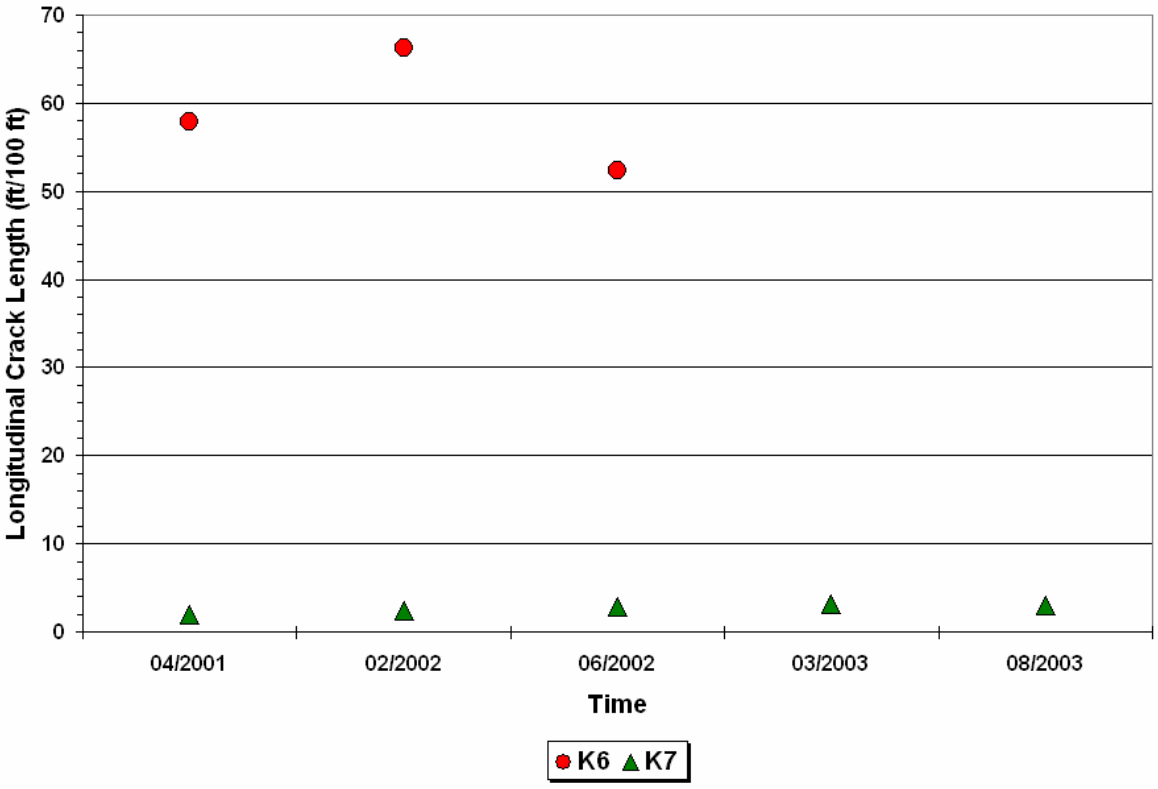

Figure H12. Longitudinal Cracking in Group 5 FWD Stations.

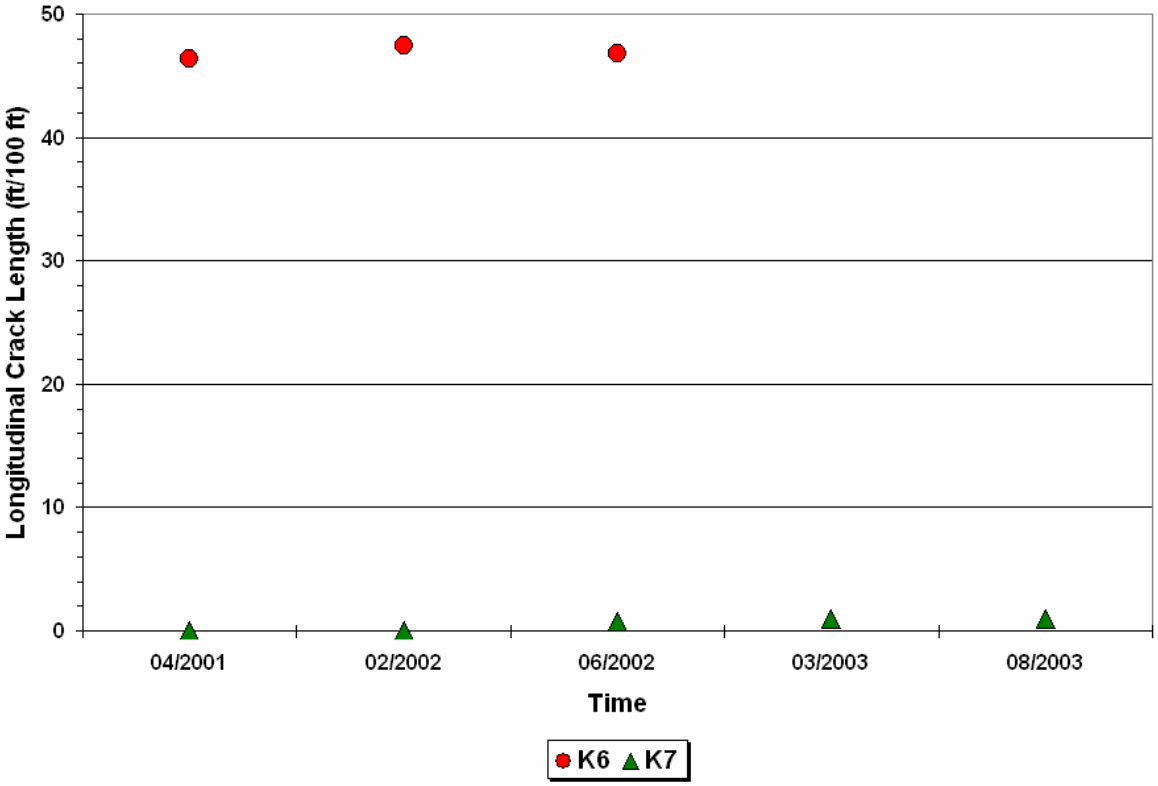

Figure H13. Longitudinal Cracking in Group 6 FWD Stations.

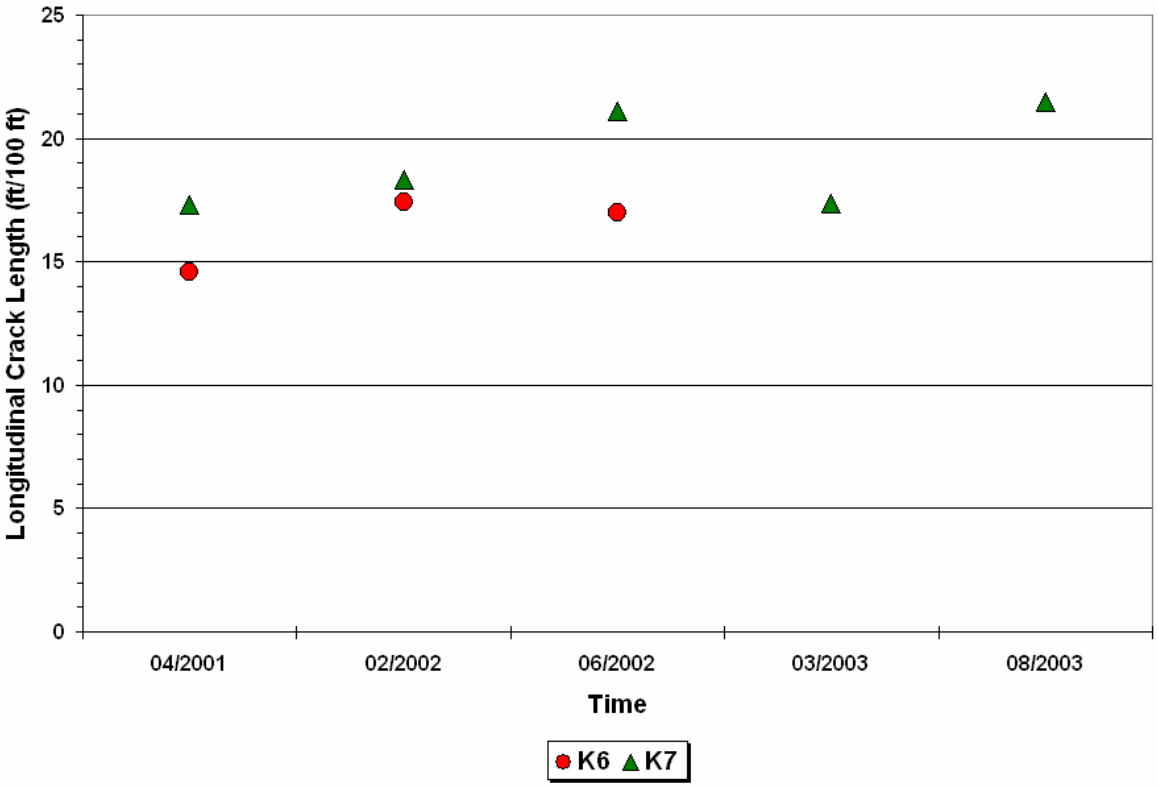

Figure H14. Longitudinal Cracking in Group 7 FWD Stations.

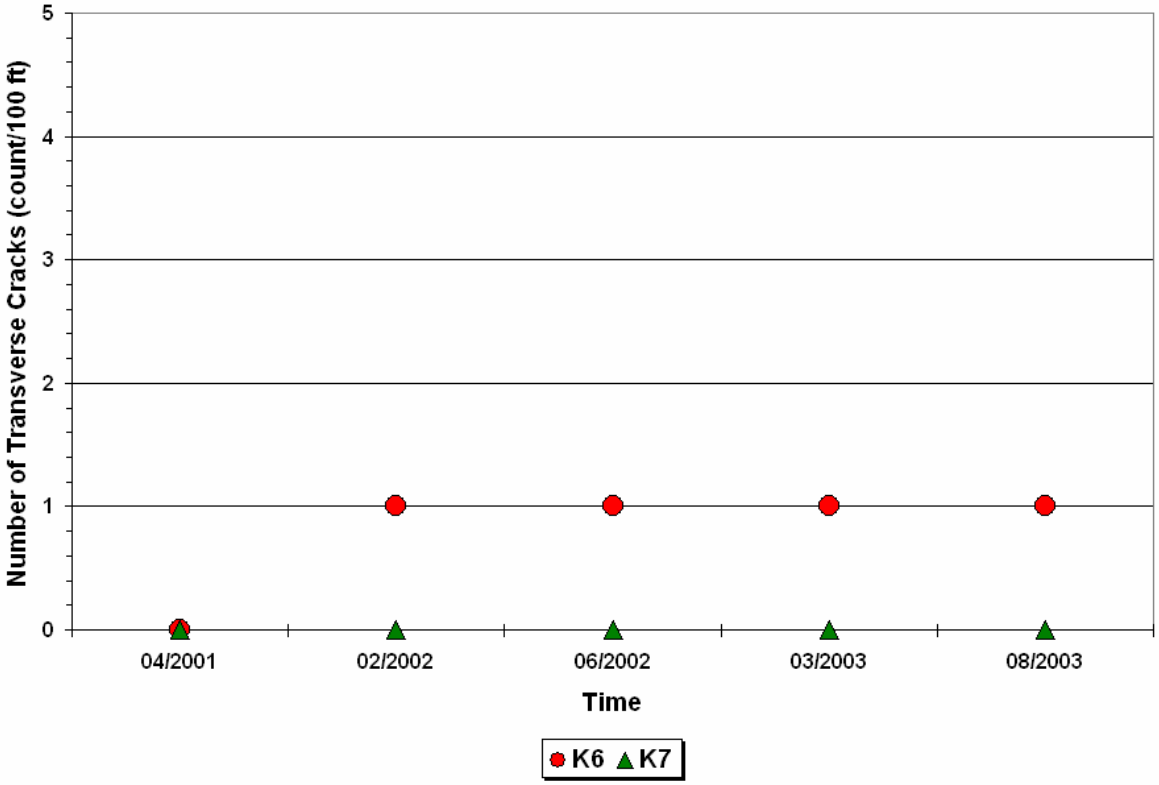

Figure H15. Transverse Cracking in Group 1 FWD Stations.

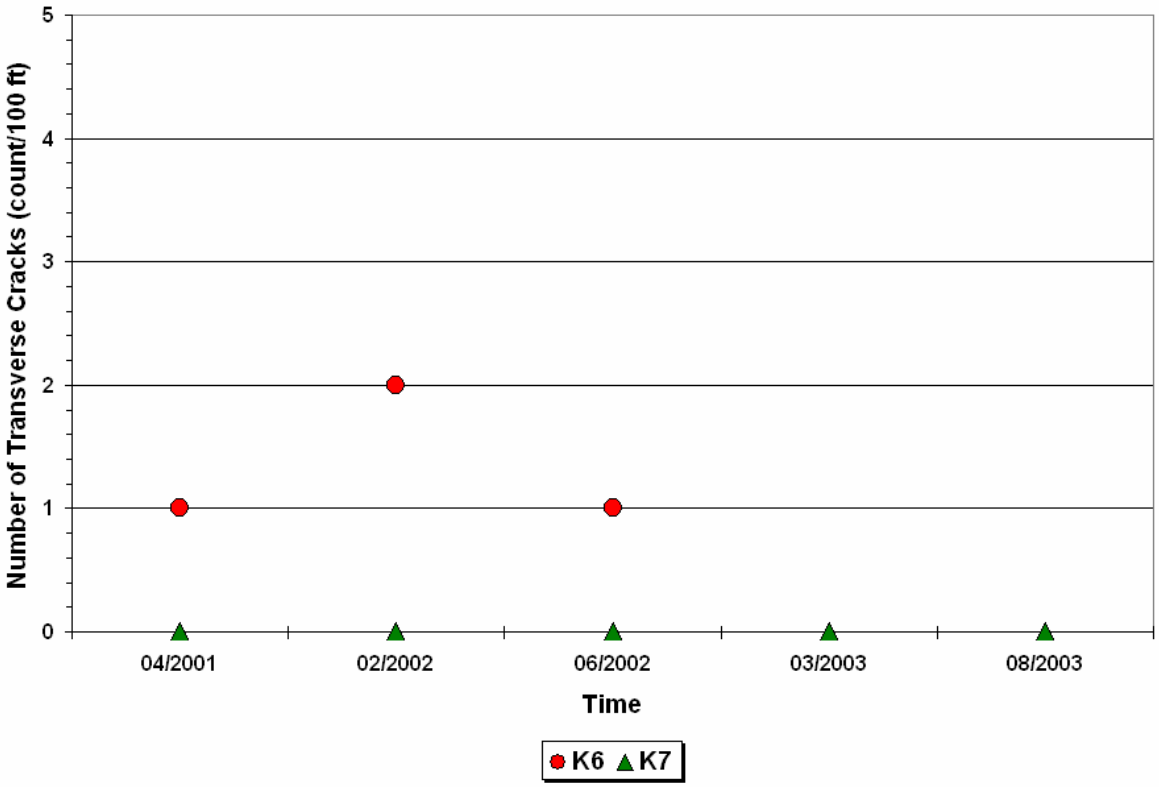

Figure H16. Transverse Cracking in Group 2 FWD Stations.

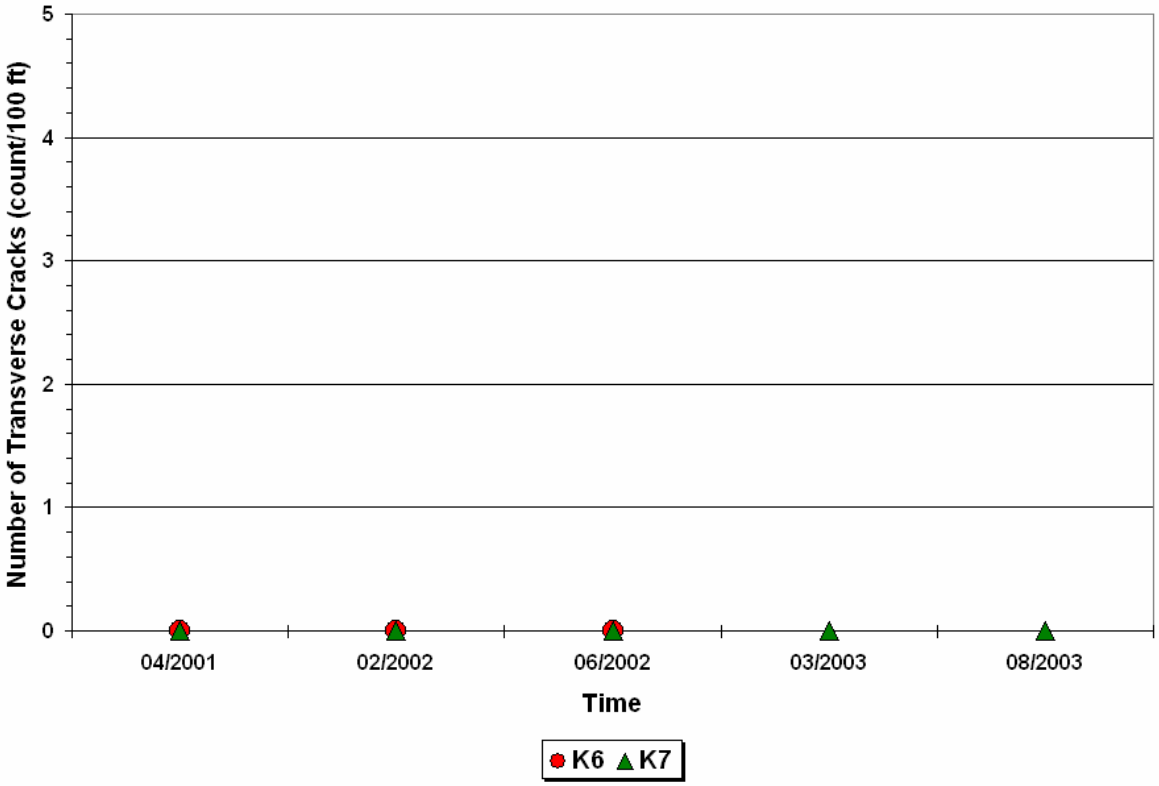

Figure H17. Transverse Cracking in Group 3 FWD Stations.

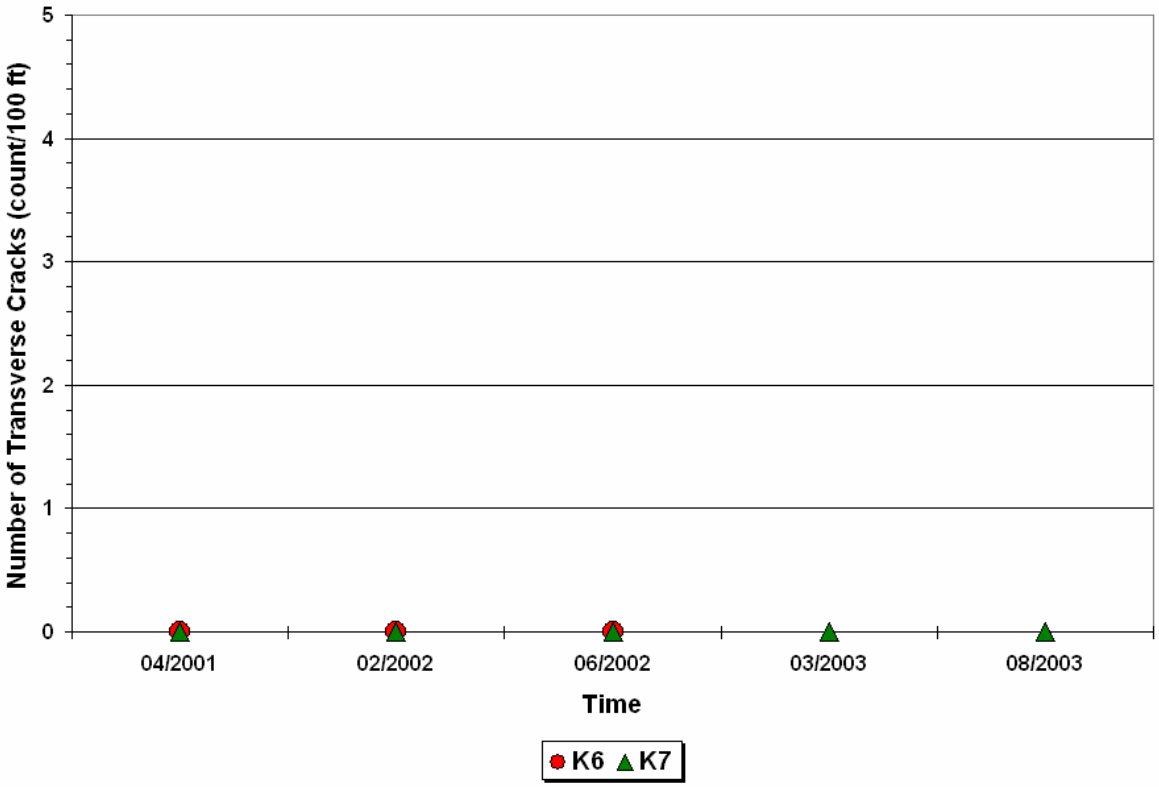

Figure H18. Transverse Cracking in Group 4 FWD Stations.

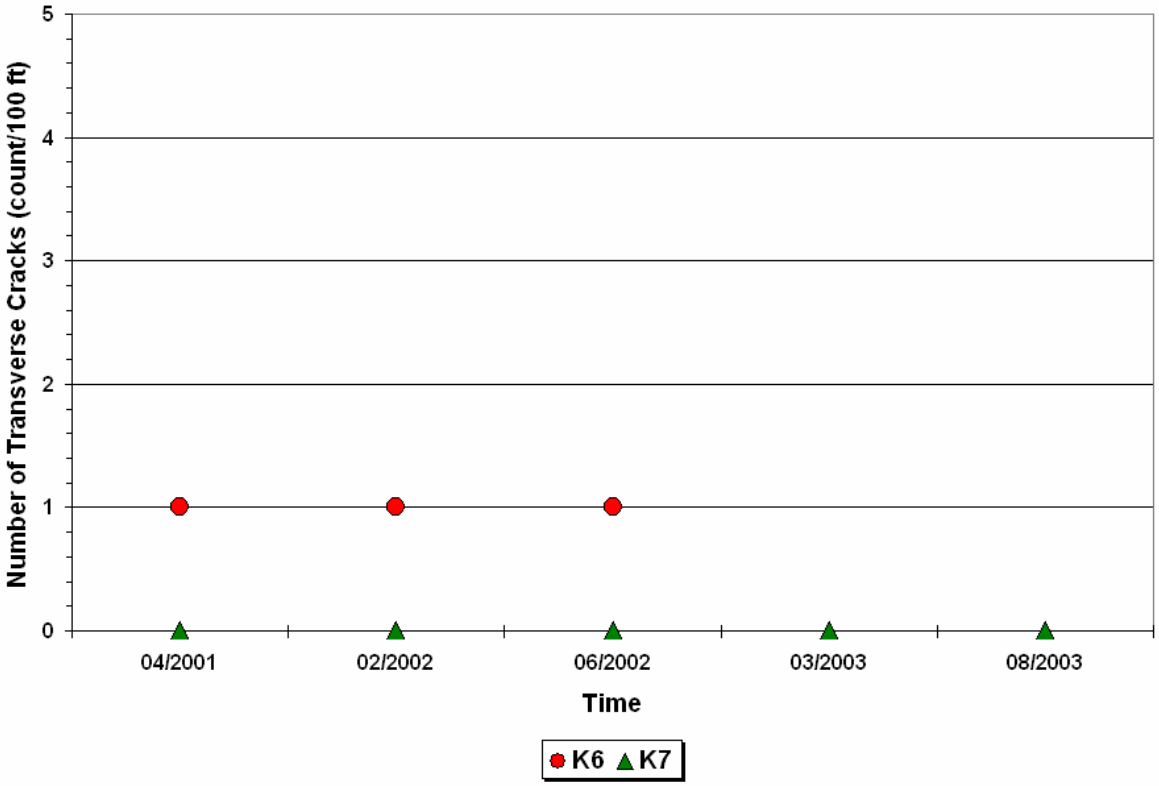

Figure H19. Transverse Cracking in Group 5 FWD Stations.

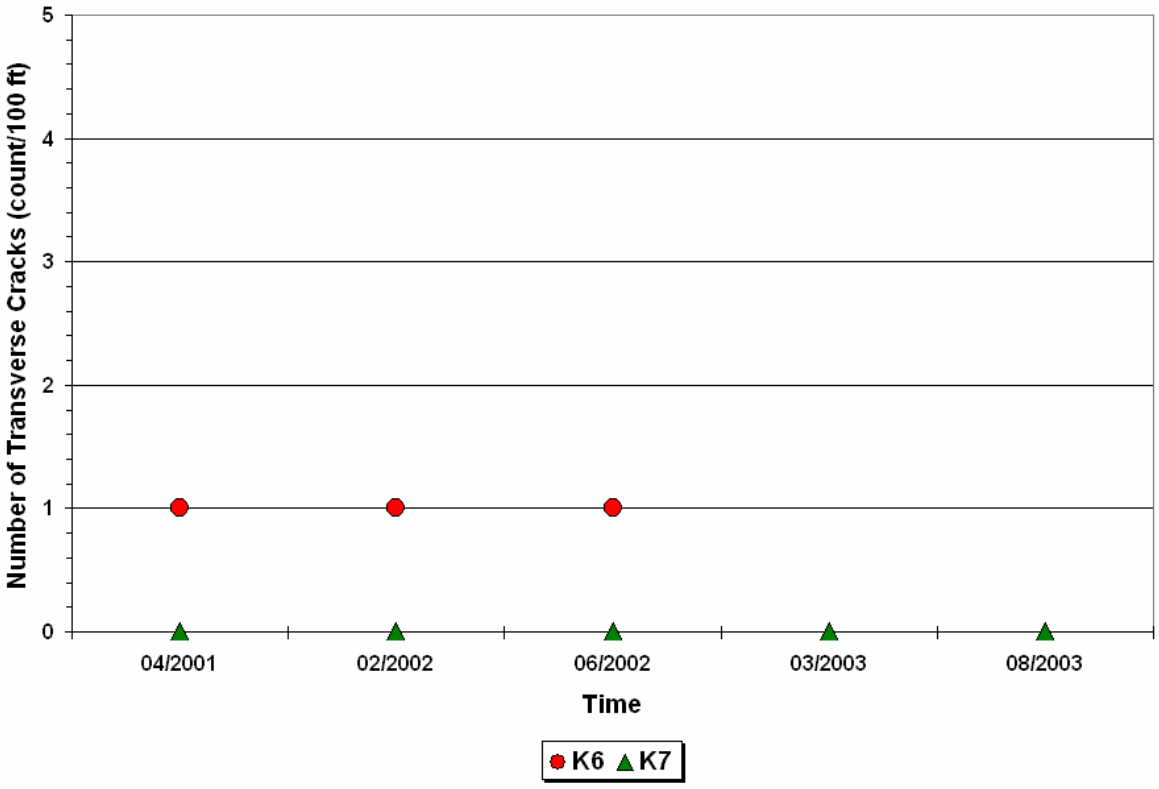

Figure H20. Transverse Cracking in Group 6 FWD Stations.

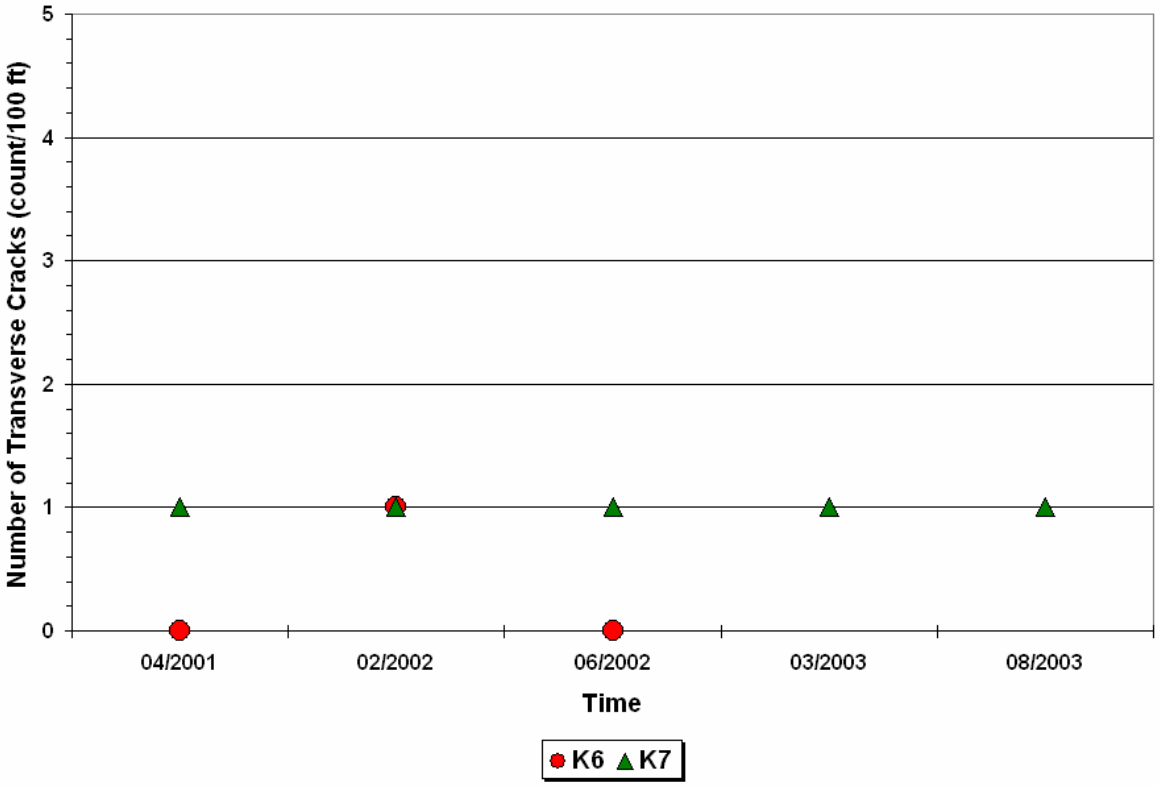

Figure H21. Transverse Cracking in Group 7 FWD Stations.

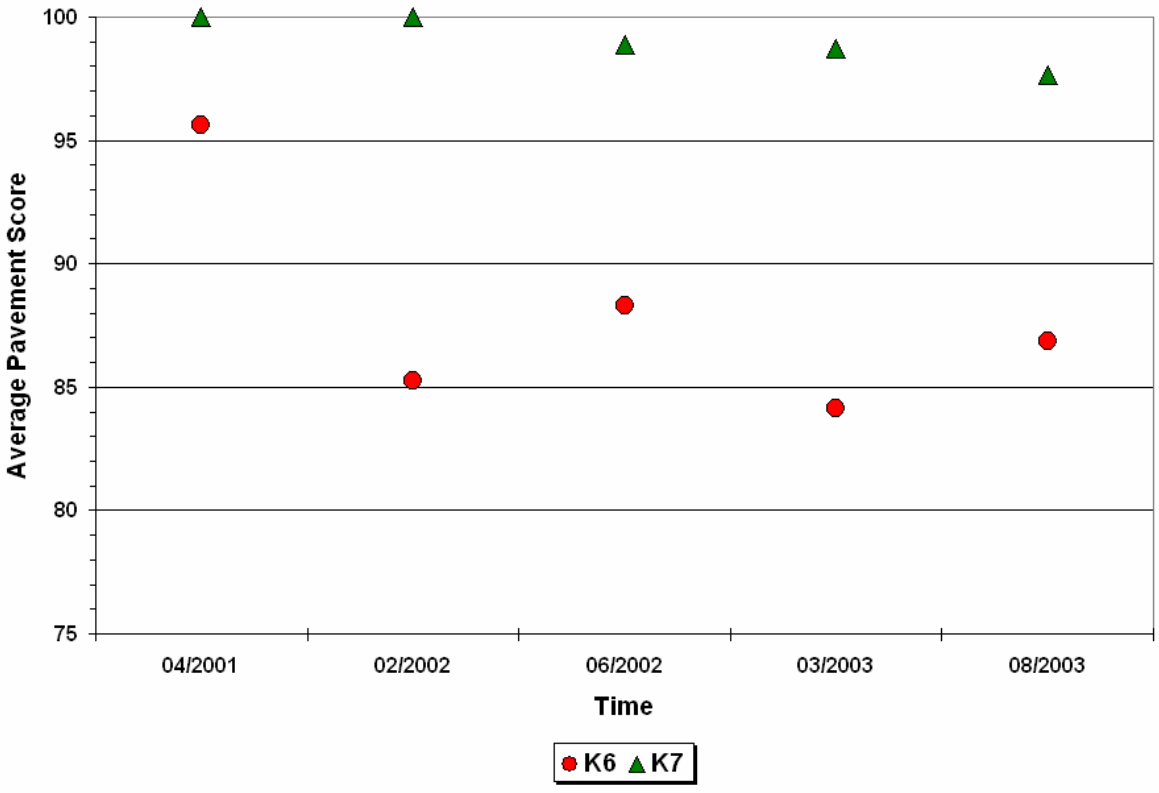

Figure H22. Average Pavement Scores in Group 1 FWD Stations.

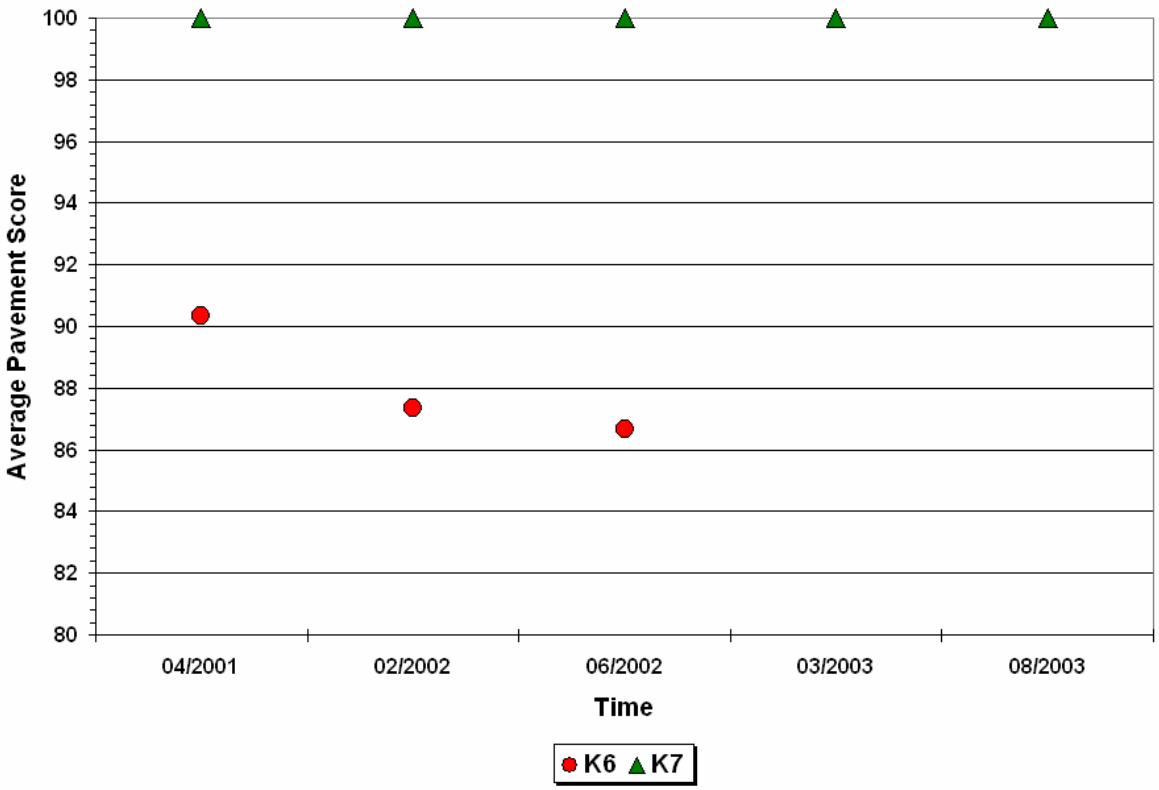

Figure H23. Average Pavement Scores in Group 2 FWD Stations.

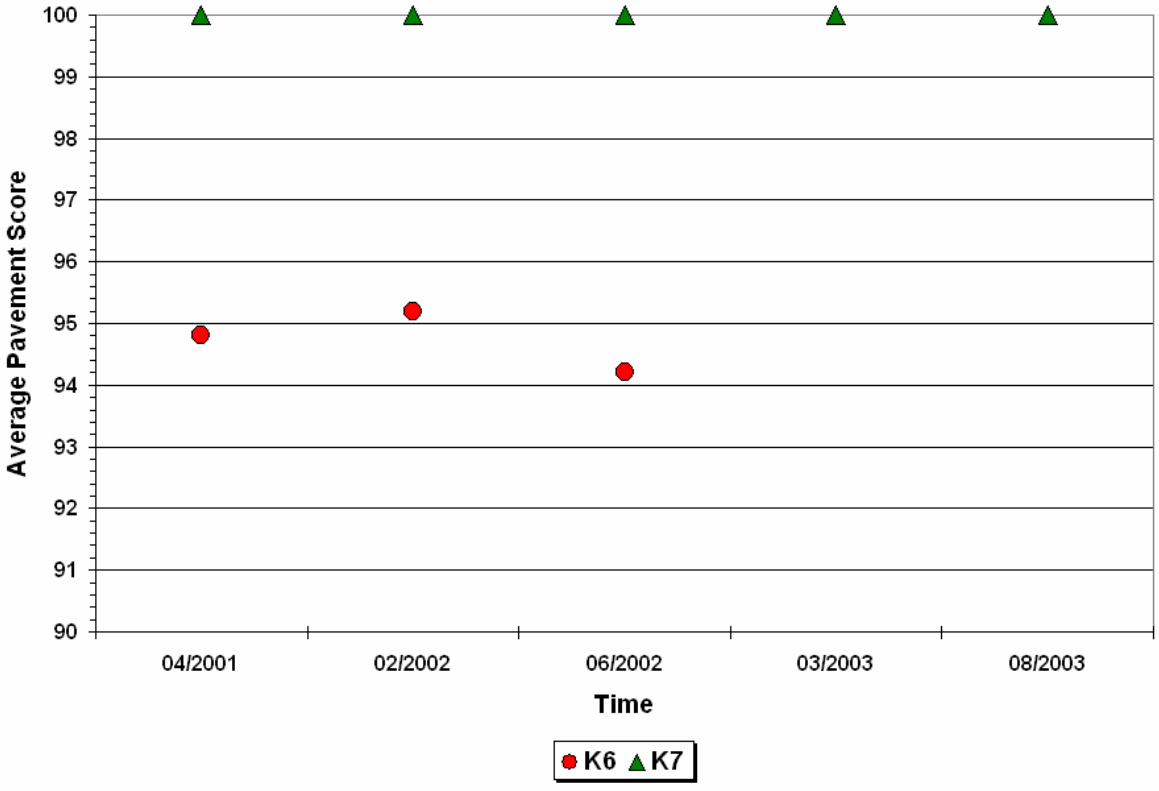

Figure H24. Average Pavement Scores in Group 3 FWD Stations.

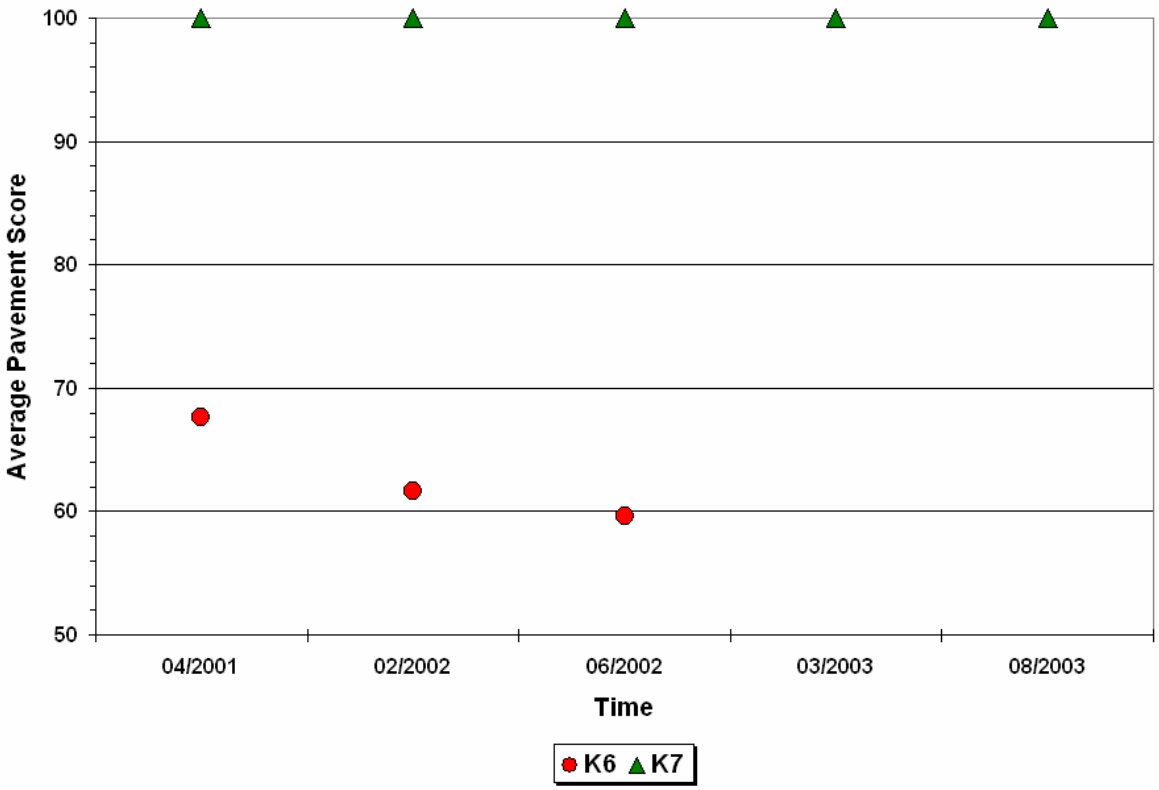

Figure H25. Average Pavement Scores in Group 4 FWD Stations.

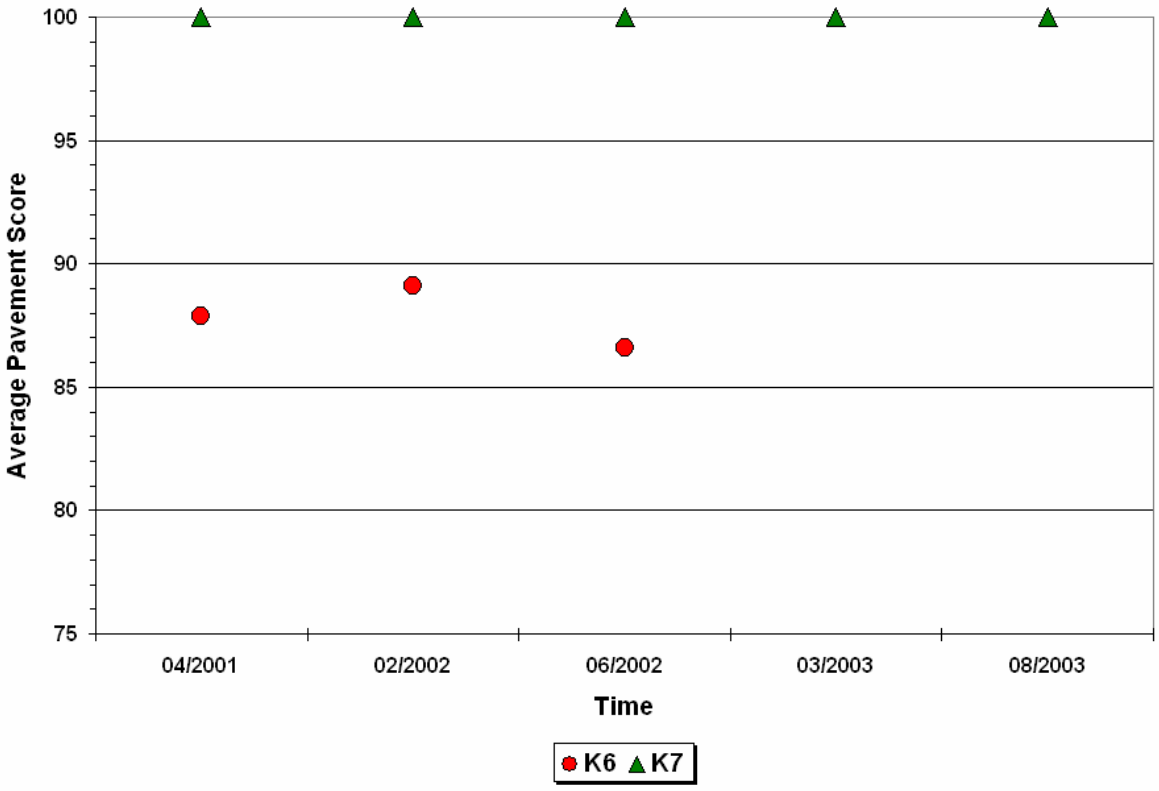

Figure H26. Average Pavement Scores in Group 5 FWD Stations.

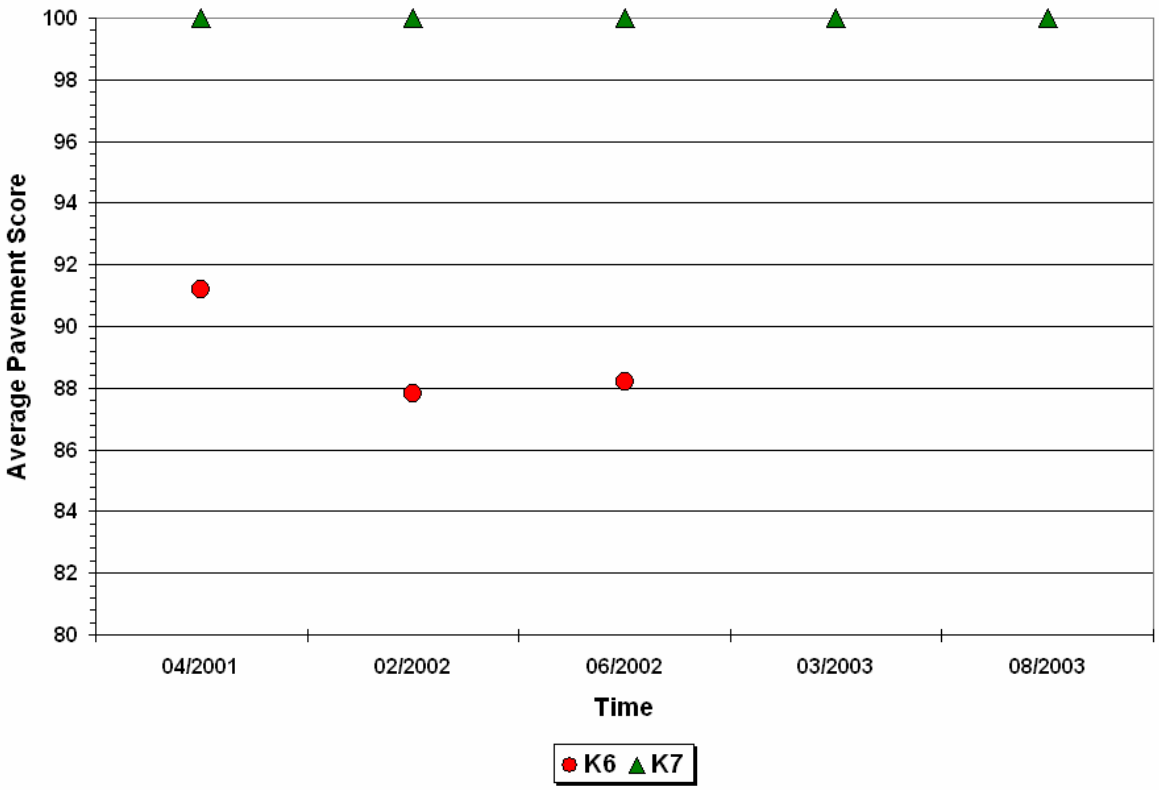

Figure H27. Average Pavement Scores in Group 6 FWD Stations.

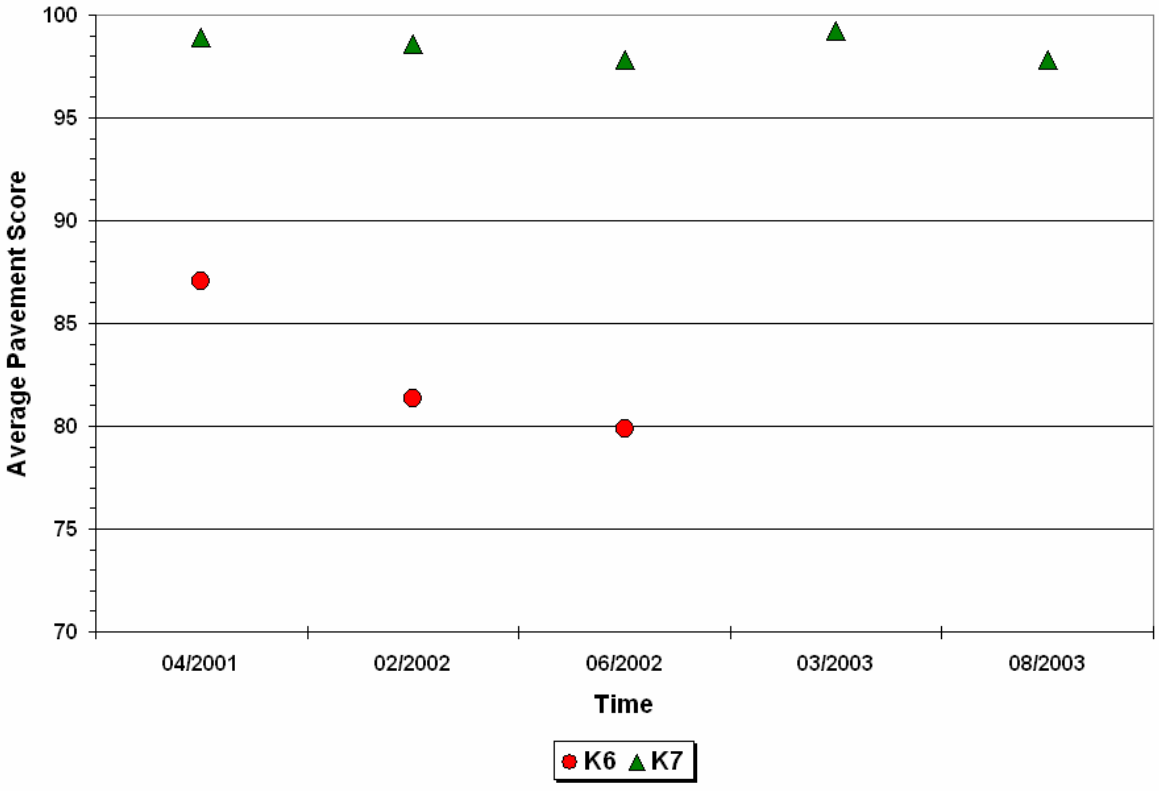

Figure H28. Average Pavement Scores in Group 7 FWD Stations.

APPENDIX I
INVESTIGATING THE APPLICATION OF FIBER-OPTIC SENSORS FOR WEIGH-IN-MOTION

INTRODUCTION

Researchers investigated the feasibility of using fiber Fabry-Perot optical sensors for weigh-in-motion measurement. Disadvantages of present-day piezoelectric-based WIM systems include: maintenance difficulties, susceptibility to corrosion, occurrence of erroneous readings and damage due to power surges, signal crosstalk from adjacent traffic lanes, and high cost. The fiber-optic Fabry-Perot sensor is considered to be more durable, immune from electromagnetic interference and crosstalk, electrically isolated from the monitoring equipment, free from corrosion effects, suitable for remote monitoring even when the signal conditioning unit (SCU) and sensors are far apart, and potentially cost-effective when many sensors are operated from a single SCU.

FIBER FABRY-PEROT SENSOR AND MONITORING SYSTEM

The sensing element is the fiber Fabry-Perot interferometer (FFPI), which functions as a strain gauge. Each FFPI sensor is composed of two dielectric internal mirrors separated by a length L (typically 12 mm) within a single mode fiber, as shown in Figure I1. The dielectric mirrors are formed by vacuum deposition of a 1000 nm-thick film of TiO_2 on the surface of the cleaved fiber end, followed by arc fusion splicing of the coated fiber to an uncoated fiber. The reflectivity of an internal mirror is controlled by varying the splicing parameters to achieve a desired value of about 5 percent. After the first mirror is formed, the fiber is cleaved to the desired cavity length and spliced with another coated fiber to produce the second mirror. The reflectivity of the second mirror is approximately the same as that of the first one.

A longitudinal strain applied to the fiber changes the optical path length nL of the interferometer, where n is the refractive index. The reflected optical power, which represents a coherent summation of the light wave amplitudes reflected by the two mirrors, is monitored using a laser light source. The output power is affected by changes in nL. Thus, the strain can be measured.

The sensor is bonded with polyimide in a 1/4-inch × 1/8-inch groove in a metal bar (Figure I2) with cross-sectional dimensions of 1-inch × 1-inch. The groove is then filled

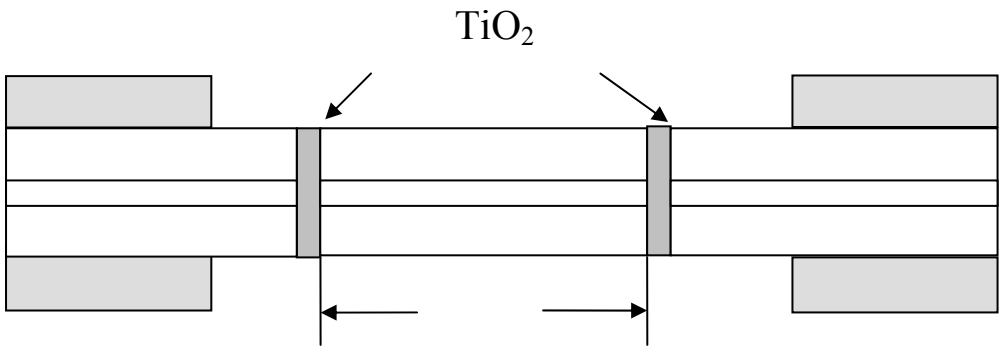

Figure I1. FFPI Sensor Diagram.

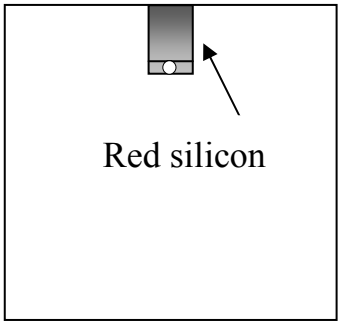

Figure I2. Configuration for Mounting of Fiber Sensor in a Metal Bar.

with high temperature red silicone. In this investigation, researchers embedded sensors in both steel and aluminum bars. The lengths of the bars were 1 ft for laboratory calibration and 4 ft for road testing.

The signal conditioning unit consists of four parts: the laser light source, signal processor, photo-detector, and the hand-held controller. For the experiments conducted, researchers used an SCU capable of monitoring as many as 16 FFPI sensors with a single 1310 nm distributed feedback laser and a digital signal processor. The laser is modulated at 2400 Hz with a periodic saw-tooth waveform so that the frequency of the emitted light varies linearly with time during the modulation cycle. Optical star couplers distribute the laser light to individual FFPI sensors and direct the reflected signal to an array of positive-intrinsic-negative (PIN) photo-detectors. The interference fringe data produced by reflected waves from the two mirrors in each sensor are processed with a microprocessor to determine the

phase shift in each fiber interferometer, and produce voltage outputs proportional to the phase shifts. The upper limit of 1200 Hz frequency response (half the sampling rate) is more than adequate for the WIM application.

The output data from the SCU is collected using a personal computer running a LabView data acquisition system and processed by a C++ program specifically designed for this research. The sampling rate can be varied, so that memory storage space can be saved by utilizing the minimum required sampling rate.

LABORATORY TEST RESULTS

Researchers conducted initial tests on the performance of the embedded FFPI sensors using an MTS machine at the TTI laboratory. For these experiments, the samples were 1-ft-long aluminum and steel bars, with an FFPI sensor embedded in the center of each bar. For each sample, the axis of the FFPI sensing fiber was parallel to the axis of the metal bar. During each test sequence, researchers set the MTS machine to strike the bar five times at a frequency of 5 Hz. The maximum applied force was varied from 200 to 4500 lb, with a minimum of 50 lb exerted on each strike to eliminate the bounce of the bar.

The response of the sensors embedded in steel and in aluminum with a maximum MTS striking force of 2000 lb is shown in Figures I3 and I4. The signal for the sensor embedded in the steel bar showed a single peak in response to an MTS strike, while the aluminum bar exhibited a pronounced ringing effect with two strain peaks for each strike.

Figure I5 shows the axial displacement of the steel bar and the fiber-optic sensor response as a function of the maximum MTS force. The axial displacement data were obtained with a linear variable differential transducer. Both the axial displacement and the fiber-optic sensor amplitude are nonlinear functions of the maximum force. However, as shown in Figure I6, the fiber-optic sensor response is a fairly linear function of the axial displacement, indicating the potential for using this sensor to measure strain for weigh-in-motion application.

RESULTS FROM HIGHWAY TESTING

Researchers conducted tests on bars instrumented with fiber-optic sensors along SH48 in Brownsville. As in the MTS tests, the sensors were embedded in steel and aluminum bars with cross-sectional dimensions of 1-inch × 1-inch. In the road tests, the bars

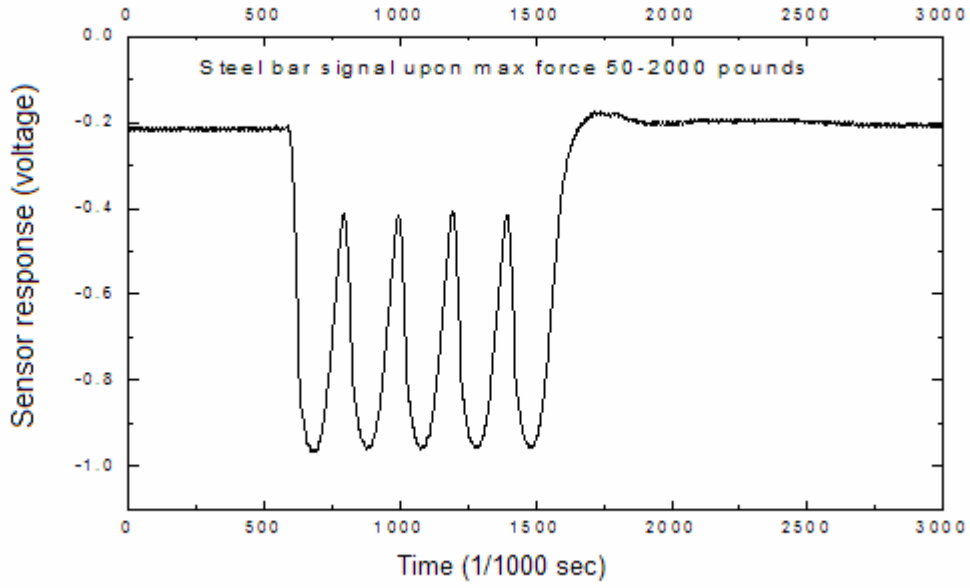

Figure I3. Response of Steel Bar Specimen During MTS Testing.

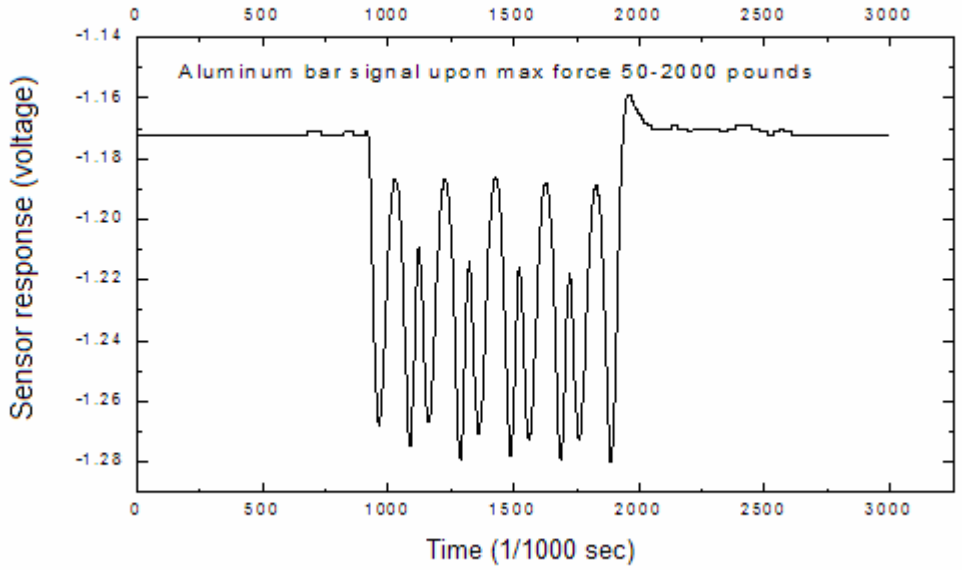

Figure I4. Response of Aluminum Bar Specimen During MTS Testing.

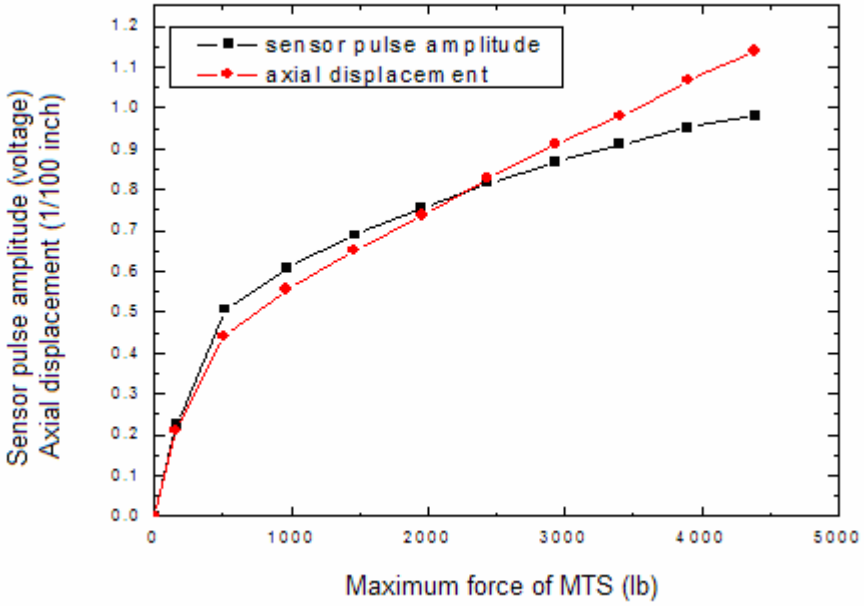

Figure I5. Dependence of Peak FFPI Sensor Response and Axial Displacement on Striking Force.

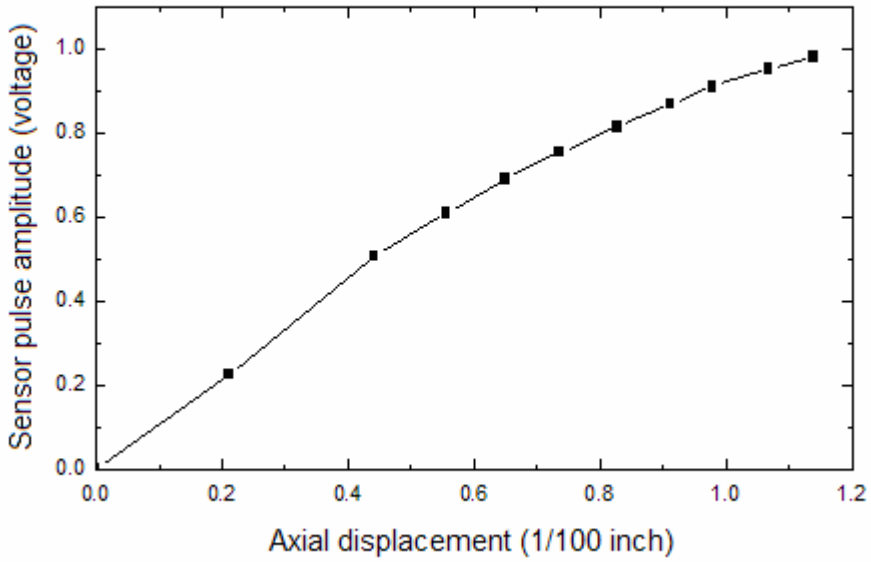

Figure I6. Dependence of Peak FFPI Sensor Response on Axial Displacement.

were 4 ft long, with 5 sensors embedded in each bar, as illustrated in Figure I7. Researchers spaced the sensors on the bar to ensure that the right side tires of a passing truck will come close to one or more of the sensors. Two saw cuts, each 1 inch wide and 2 inches deep, were made on the pavement across half of the travel lane. Researchers used hot bituminous sealant to secure the bars and fill in the sawed grooves. After the bar was bonded in place, researchers used solid hot-mix epoxy to fill in the grooves evenly to the level of the road surface, so that the sensors will measure the strain experienced by the surrounding pavement.

Representative data from the tests are shown in Figures I8 and I9. Because the signal amplitude is based on the position of the wheels relative to the sensor, the relative amplitudes are an indication of the position of the truck in the lane. In Figure I8, sensor 5 produces a larger signal than other sensors, indicating that the truck is in the right-hand portion of the lane. After the passage of the steering axle, the signal from each sensor resumes its starting value quickly, thus allowing for the collection of data from the drive and trailer axles of the passing truck. It is encouraging to see that each truck axle is clearly evident in the signals from the fiber-optic sensors, which exhibits a pattern similar to the MDD data.

Researchers monitored a total of 30 trucks using the sensors embedded in the aluminum bar and another 30 trucks with the sensors in the steel bar. An effort to correlate the fiber-optic sensor data with the measured static axle weights on trucks monitored by researchers was not successful. One factor that probably contributed to this poor correlation was the limited distance over which the FFPI sensors were placed across the test lane. Since there were only enough sensors to monitor one side of a passing truck, any uneven lateral distribution of loads carried by the truck would contribute to discrepancies between the measured static axle weights and the corresponding weights computed from fiber-optic measurements. Truck speed may be another factor that affects peak sensor response. In the researchers' opinion, calibration methods to relate the response of multiple sensors to actual truck weights would need to be investigated to establish the feasibility of using fiber-optic sensors for weigh-in-motion measurements.

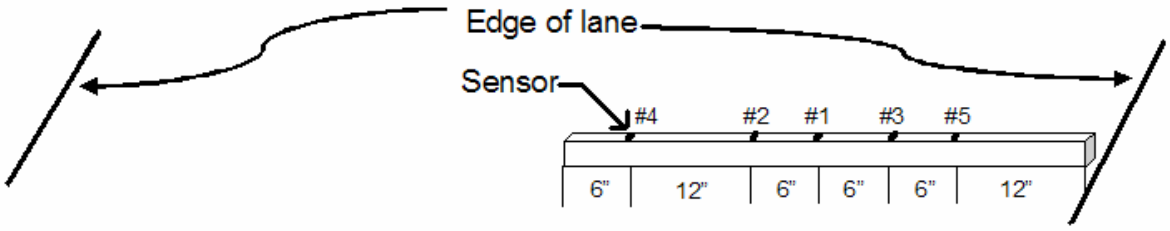

Figure I7. Locations of Fiber-Optic Sensors on Metal Bar.

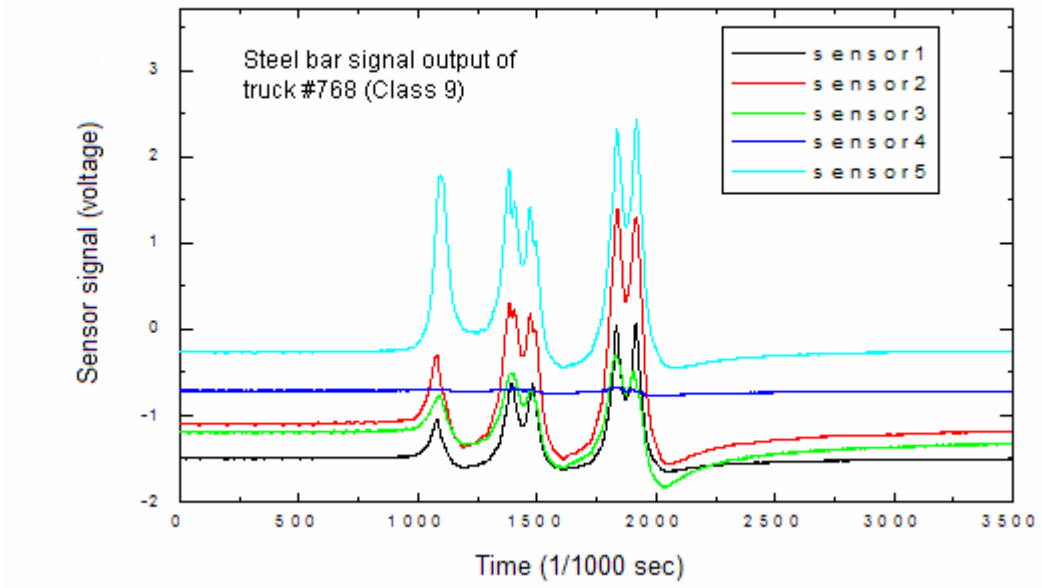

Figure I8. Data from FFPI Sensors Embedded in the Steel Bar with Passage of a Class 9 Truck.

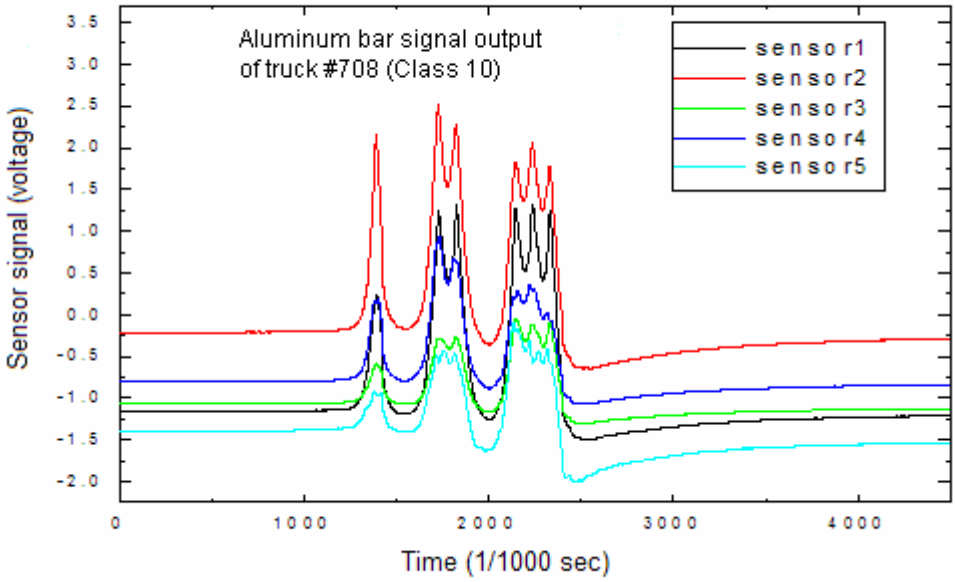

Figure I9. Data from FFPI Sensors Embedded in the Steel Bar with Passage of a Class 10 Truck.

CONCLUSIONS

An investigation of the application of FFPI sensors for weigh-in-motion measurement was conducted in this task. This investigation included laboratory tests conducted with an MTS machine to characterize the impulse response of fiber-optic sensors embedded in steel and aluminum bars. Test results showed significant ringing when the aluminum bar was struck with the MTS machine. However, this response was not observed with the steel bar specimen, indicating better performance during the tests compared to the aluminum bar. The peak strain response from the FFPI sensor in the steel bar showed a fairly linear dependence on axial displacement.

Researchers also conducted field tests along SH48 with FFPI sensors embedded in steel and aluminum bars. The FFPI sensors showed strong response and consistently reproduced the expected characteristics of truck wheel crossings. The axles of a passing truck were clearly observed in the signals. However, poor correlation was achieved between peak fiber-optic sensor response and truck weight data. Calibration methods to relate the response of multiple sensors to actual truck weights need to be investigated to determine whether the FFPI sensor can successfully be used to build WIM systems that are more affordable and accurate.